AUTOMATIC CONTROL OF

Aircraft *and* *Missiles* *Second Edition*

JOHN H. BLAKELOCK

Automatic Control of
Aircraft and Missiles

1 ∈1
1 - III
113
192?

Automatic Control
of Aircraft and Missiles

Second Edition

John H. Blakelock

Colonel, USAF (Ret)
Formerly Associate Professor of Electrical Engineering
Air Force Institute of Technology

Preface to Second Edition

In this second edition all the material from the first edition has been retained and the errors found in the first edition have been corrected. Considerable new material has been added, as discussed in the following paragraph.

In Chapter 4 the effectiveness of $\beta - \dot{\beta}$ feedback is discussed as a method of obtaining coordination during turns using the F-15 as the aircraft model. Chapter 7 has been expanded to cover the root locus analysis of a generic acceleration autopilot used in many air-to-air and surface-to-air guided missiles. The use of hinge moment commands to the canards for the control of missiles such as the AIM-9L Sidewinder is also covered. The guidance systems for these types of missiles as well as bank-to-turn missiles are covered in a new Chapter 8. The types of guidance include proportional navigation and line-of-sight and lead-angle command guidance. The discussion covers the complete root locus analysis of these guidance systems, and shows graphically why proportional navigation guidance is unstable for a navigation constant less than one, where a value of one yields pure pursuit. The coupling of the output of a director fire control system into the autopilot is presented in a new Chapter 9 along with the analysis of the resulting digital control system using the F-15 aircraft. The discrete analysis is performed in the z plane using traditional methods, as well as in the s plane using the Padé approximation to represent the e^{-Ts} of the zero-order hold. The results of a six-degree-of-freedom hybrid simulation showed that the system is capable of tracking a wide variety of target scenarios, including inverted flight to track an aircraft performing a split S, with the gun on track for a major portion of each run. The material in this chapter is based on research performed by the author under Air Force Contract F33615-78-C-3145EE40.

The analysis of multivariable control systems is covered in a new Chapter 10. Chapters 8 and 9 of the first edition become Chapters 11 and 12 of this edition with no changes. A new Chapter 13 covers methods for modeling the human pilot plus the integration of the human pilot into an aircraft flight control system. The longitudinal and lateral stability derivatives for an aircraft like the F-102 are calculated in Appendix D using the USAF Stability and Control Datcom. Longitudinal and lateral aerodynamic data for the F-15 aircraft have been added to Appendix F. Four new appendices have been added. Appendix G presents the derivation of the wind axis equations of motion, which are more useful than the body axis equations for full six-degree-of-freedom simulations. Appendix H gives a method for the digital simulation of first- and second-order system transfer functions. Appendix I contains the development of the equations for the solution of the air-to-air fire control problem including the calculation of projectile time of flight. Finally the A-1 and A-4 gunsights are described in Appendix J.

The new material for the second edition was typed by the author on an IBM PS/2 Model 50 computer using a scientific word processing system T^3 marketed by TCI Software Research Inc., Las Cruces, New Mexico.

I wish to express my appreciation to Professors John J. D'Azzo and Constantine H. Houpis of the Air Force Institute of Technology, Wright-Patterson Air Force Base, Ohio for their helpful suggestions for the second edition, especially for the material in Chapter 10. Finally I wish to express my deep appreciation to my wife for her encouragement, understanding, and assistance in the many hours of proofreading.

JOHN H. BLAKELOCK

Yellow Springs, Ohio
May 1990

Preface to First Edition

This book was conceived as early as 1958 when I gave a graduate course on the automatic control of aircraft and missiles at the Air Force Institute of Technology, Wright-Patterson Air Force Base, Dayton, Ohio, and I became aware that there was, and still is, with the exception of this book, no work extant which treats the whole subject. It is written for graduate and professional use, but at the same time its contents are presented in such a manner that it also can be used in the senior year of an undergraduate program.

The first four chapters make up the bulk of the book and contain most of the detailed analysis of various automatic control systems. In Chapter 1 the six-degree-of-freedom rigid body equations are derived in detail, followed by the linearization and separation of the equations of motion. The three-degree-of-freedom longitudinal equations are then derived along with the longitudinal stability derivatives, followed by the determination of the longitudinal transfer functions for a jet transport for an elevator input. The transient response of the aircraft as well as the effects of changes in altitude and airspeed on the longitudinal response are demonstrated through the use of analog computer traces. In Chapter 2 various control systems are analyzed by use of the root locus techniques along with the complete analysis and design of a glide slope coupler and automatic flare control, including automatic velocity control, as well as the results from the analog simulation. The same pattern is followed in Chapters 3 and 4 with the three lateral equations. The control systems analyzed in Chapter 4 include the damping of the Dutch roll, various techniques for achieving coordination during a turn (minimizing sideslip), the analysis of the complete lateral autopilot, and the design of a localizer coupler, which when used with the glide slope coupler and automatic flare control would provide an automatic landing system. Chapter 5

follows with an analysis of the effects of inertial cross-coupling including a control system for stabilizing the instability resulting therefrom. The subject of self-adaptive autopilots is discussed in Chapter 6 and includes a discussion of the forerunner of the self-adaptive control system used in the X-15. Chapter 7 follows with the analysis of missile control systems using the transfer function of the Vanguard missile, and Chapter 8 [now Chapter 11] with a study of the effects of flexibility and propellant sloshing, including the derivation of the appropriate transfer functions and a discussion of the methods of compensation. The book ends with a chapter [now Chapter 12] on the application of statistical design principles.

The final form of the equations of motion for the aircraft, and the aerodynamic terms, are the same as those discussed in a set of unpublished notes prepared by Professor J. Bicknell for a course in Airplane Stability and Control at the Massachusetts Institute of Technology. I have determined from experience that this is the most useful form for the equations for both numerical analysis and analog simulation. The aerodynamic stability derivatives used in the equations are the standard NACA nondimensional stability derivatives. The various control systems used in this book are not necessarily original with me, but are similar to actual control systems that have been proposed or used for high-performance aircraft. All the discussion, analysis, computer simulations, and interpretation of the behavior of the various control systems are original with me.

I wish to express my deep appreciation to Mrs. Jane Moone and Miss Charlasine Murph, who typed the original notes. Their efficiency and ability helped make this book possible. I also wish to thank the many students who used my material and made many helpful suggestions and corrections. Particular appreciation is expressed to Dr. C. M. Zieman, Head of the Electrical Engineering Department, and to Professors John J. D'Azzo and Constantine H. Houpis for their continued encouragement, and to Professor H. Phillip Whitaker, whose course in Automatic Control at MIT provided some of the basic concepts on which much of the analysis in this book is based. Finally, I wish to express my deep appreciation to my wife for her patience, understanding, and encouragement and for doing the necessary typing for the final manuscript.

JOHN H. BLAKELOCK

April, 1965

Contents

*Automatic Control of
Aircraft and Missiles*

Introduction

The seventeenth of December 1903 marked the date of the first successful flight of a powered aeroplane. The Wright brothers, in their efforts to succeed where others had failed, broke with tradition and designed their aeroplane to be unstable but controllable.[1] This break with tradition resulted in a more maneuverable and controllable vehicle that was less susceptible to atmospheric gusts. The approach taken by such pioneers as Lilienthal, Pilcher, Chanute, and Langley in the design of their flying machines was to make them inherently stable, leaving the pilot with no other duty than to steer the vehicle. The price paid for this stability was lack of maneuverability and susceptibility to atmospheric disturbances. The lack of stability introduced by the Wright brothers naturally made the pilot's job more difficult and tiring and more than likely hastened the development of the automatic pilot, often called simply an autopilot.

This inherent instability is still prevalent in aircraft of today in the form of the so-called "spiral divergence," which causes a slow divergence in heading and bank angle as a result of any small disturbance. The main purpose then of the early autopilots was to stabilize the aircraft and return it to the desired flight attitude after any disturbance. Such an autopilot was installed in a Glenn H. Curtis flying boat and first tested in late 1912. The autopilot, using gyros to sense the deviation of the aircraft from the desired attitude and servo motors to activate the elevators and ailerons, was developed and built by the Sperry Gyroscope Company of New York under the direction of Dr. E. A. Sperry. The apparatus, called the Sperry Aeroplane Stabilizer, installed in the Curtis flying boat, won prominence on the eighteenth of June 1914. While piloted by Lawrence Sperry, the son of Dr. Sperry, it won a safety prize of 50,000 francs offered by the Aero Club of France for the most

stable aeroplane.[1] It is worthy of note that this event took place only eleven years after the Wright brothers' historic flight. During this demonstration, while flying close to the ground under automatic control, with the pilot Lawrence Sperry standing in the cockpit with both hands over his head, the mechanic was standing and walking back and forth on the wing. In spite of the large yawing and rolling moment generated by the mechanic's presence on the wing, the aircraft maintained its original attitude.[2]

After 1915 public information on automatic pilots became nonexistent due to military security, and after the First World War there was little effort expended on advancing the state of the art. A break came in 1933 when Wiley Post insisted on the installation of the first prototype of the Sperry pneumatic-hydraulic Gyropilot in his aircraft, the "Winnie May," in which he flew around the world in less than eight days. This flight would have been impossible without the aid of this autopilot, which allowed Post to doze for short periods while the aircraft flew on under automatic control. The story goes that Post held a wrench tied to his finger by a piece of string; if he fell sound asleep the wrench would drop when his hand relaxed, and the subsequential jerk on his finger would awaken him so that he could check his progress and then doze again.[2] This flight aroused new interest in automatic flight, especially for the so-called navigational autopilots, and in 1947 an Air Force C-54 with a Sperry A-12 autopilot with an approach coupler and Bendix throttle control made a completely automatic trans-Atlantic flight including takeoff and landing. During the entire flight the control column was untouched by human hands, with everything controlled from a program stored on punched cards.[3] It is worthy of note that the development of the control system used for this feat was accomplished by the "tinker/inventors,"[3] and not by the application of classical feedback control system design techniques, which were just making their appearance.

These early autopilots, as already mentioned, were primarily designed to maintain the attitude and heading of the aircraft. With the advent of high-performance jet aircraft new problems have arisen. These problems are in addition to the heading instability already mentioned and are a matter of unsatisfactory dynamic characteristics. The situation may be best summarized as follows: In general, it may be said that if the period of oscillation inherent in an aircraft is 10 seconds or more, the pilot can adequately control or damp the oscillation, but if the period is 4 seconds or less, the pilot's reaction time is not short enough; thus, such oscillations should be well damped. The so-called "short period" pitch and "Dutch roll" oscillations inherent in all aircraft fall into the category of a 4-second oscillation. In the more conventional aircraft, the damping of these oscillations is effective enough that the handling characteristics of the aircraft are satisfactory. However, in almost all jet fighter and jet transport aircraft artificial damping must be provided by an automatic system. Probably the first successful application of a Dutch roll damper system was in a quasi fly-by-wire configuration installed in the YB-49 Northrop flying wing as early as 1948.[3] The resulting systems are referred to as pitch and yaw dampers and are analyzed in Chapters 2 and 4.

As the aircraft designers tried to obtain more performance from jet fighters, larger and larger engines were installed along with shorter and thinner wings; this trend resulted in significant changes in the moments of inertia of the aircraft which led to catastrophic results for some aircraft. The culprit was "inertial cross-coupling," which had safely been neglected in the past. This phenomenon, which is discussed in detail in Chapter 5, results when the aircraft rolls at high angular velocities. The normal correction is the installation of a larger and/or more effective vertical stabilizer. This requires a major modification of the airframe that is both costly and time consuming. As shown in Chapter 5 the effects of inertial cross-coupling can be eliminated with a properly designed control system.

Another stability problem that has manifested itself in some jet fighters is the problem of complete loss of longitudinal stability, or *pitch-up*, at high angles of attack. This phenomenon is more apt to occur when the horizontal stabilizer is placed on top of the vertical stabilizer to improve lateral stability. The actual cause of pitch-up and a control system that will stabilize the aircraft at these high angles of attack are discussed in Chapter 2. The same control system can be, and is, used to stabilize ballistic-type missiles, thus eliminating the necessity to add stabilizing surfaces at the aft end of the missile. This situation is discussed in Chapter 7 along with the analysis of autopilots for aerodynamic missiles.

There are many other problems that face the control engineer, such as the design of approach couplers to provide automatic approaches to landings in bad weather (Chapters 2 and 4), altitude and Mach hold control systems to improve fuel economy during cruise (Chapter 2), compensators to reduce the effects of body bending (Chapter 11), and control systems that automatically perform optimally under variations of air speed and altitude (Chapter 6). All these problems are discussed in the indicated chapters of this book.

The missile guidance systems are discussed in Chapter 8 and the analysis and design of the integrated flight/fire control system is presented in Chapter 9. The design of a multivariable control system that provides for independent control of the pitch and flight path angle while maintaining constant airspeed with an auto-throttle control system is covered in Chapter 10. Also in that chapter the design of the yaw orientational control system presented in Section 4-5 is validated by analyzing the system as a multiple-input multiple-output control system.

Regardless of its role, a particular control system will in general respond faster and more accurately but with less reliability than a human controller; the control system in general is unable to exercise judgment. The goal of the control system engineer is to optimize the performance of the system to meet the specified design requirements. But what generates the design requirements? The system design requirements result from the overall system design procedure discussed briefly in the next paragraph and in detail in Chapter 9 of Ref. 4.

The first step in the design procedure is the determination of the system purpose and overall system requirements, such as the mission phases and

operational requirements. The second step is the determination of the characteristics of the vehicle, control surface actuators, and feedback sensors. These steps are followed by the development of the candidate block diagrams that will satisfy the system requirements. As will be seen in Chapters 2, 4, 7, 8, and 9, there may be more than one possible block diagram configuration. The proposed systems are then analyzed to determine if any stability problems exist which would require system modifications to correct. The modifications could be in the form of different feedback quantities and/or the

TABLE 1   Cooper – Harper Pilot Rating Scale

Controllable	Acceptable	Satisfactory without improvements	Excellent, highly desirable — pilot compensation not a factor.	1
			Good, negligible deficiencies — pilot compensation not a factor.	2
			Fair, some mildly unpleasant deficiencies — minimal pilot compensation required.	3
		Deficiencies warrant improvement	Minor but annoying deficiencies — moderate pilot compensation required.	4
			Moderately objectional deficiencies — considerable pilot compensation required.	5
			Very objectional deficiencies — extensive pilot compensation required.	6
	Unacceptable	Deficiencies require improvements	Major deficiencies — adequate performance not attainable with maximum tolerable pilot compensation.	7
			Major deficiencies — considerable pilot compensation required for control.	8
			Major deficiencies — intense pilot compensation is required for control.	9
Uncontrollable		Improvement mandatory	Major deficiencies — control will be lost during some portion of required operation.	10

addition of some form of dynamic compensation. The designed system(s) can then be evaluated by developing a hybrid or digital simulation of the complete system(s) with actual hardware in the loop where possible. If more than one system configuration is being considered, the results of the simulation can be used to select the best system. As will be seen in Chapters 2, 4, 5, 7, 8, 9, and 10, all of the systems analyzed were simulated with the exception of the Vanguard system, and in some cases the simulations pointed out system deficiencies, which were corrected by system modifications. This book takes up the design process at step 2.

Another consideration that bears on how well the design requirements have been met is the pilot's rating of the final system. This can be accomplished by putting a pilot in the loop in the actual simulation and letting him fly a specific mission. How hard the pilot has to work to control the aircraft in the performance of the mission can be used to obtain the pilot's rating for that particular task. The pilot ratings are based on the Cooper–Harper pilot rating scale shown in Table 1; the ratings go from 1 to 10, where 1 is excellent and 10 is uncontrollable.[5,6] The compensation referred to in the table is the amount of compensation (lead or lag) that the pilot must introduce in order to control the vehicle. This plus the integration of the human pilot into an aircraft flight control system is analyzed in Chapter 13.

In the study of any airframe–autopilot combination, it is advantageous to represent the aircraft as a "block" in the block diagram of the control system so that the standard methods of analyzing servomechanisms may be employed. To make this representation, the transfer function of the aircraft relating a given input to a given output is required. By definition *the transfer function is the ratio of the Laplace transform of the output to the Laplace transform of the input with the initial conditions zero*. The longitudinal and lateral transfer functions are derived in Chapters 1 and 3, respectively.

To obtain the transfer functions of the aircraft it is necessary to define certain quantities, referred to as "stability derivatives," which relate the changes in the aerodynamic forces and moments acting on the aircraft caused by changes in its motion, orientation, or control surface motion. The stability derivatives used are the standard NACA nondimensional stability derivatives with the standard NACA sign conventions.

REFERENCES

1. C. S. Draper, "Flight Control," *Journal of the Royal Aeronautical Society*, July 1955, Vol. 59.

2. K. I. T. Richardson, *The Gyroscope Applied*, The Philosophical Library, New York, 1954, pp. 261–264.

3. D. McRuer and D. Graham, "Eighty Years of Flight Control: Triumphs and Pitfalls of the System Approach," *Journal of Guidance and Control*, July–August 1981, Vol. 4.

4. D. McRuer, I. Ashkenas, and D. Graham, *Aircraft Dynamics and Automatic Control*, Princeton University Press, Princeton, New Jersey, 1973.

5. J. D. Dillow and D. G. Picha, *Application of the Optimal Pilot Model to the Analysis of Aircraft Handling Qualities*, AFIT-TR-75-4, Wright-Patterson Air Force Base, Ohio: Air Force Institute of Technology, August 1975.

6. W. W. Richard, *Longitudinal Flying Qualities in the Landing Approach*, NASA TM X-73, 170, Proceedings of the 12th Annual Conference on Manual Control, May 1976.

1

Longitudinal Dynamics

1-1 INTRODUCTION

To obtain the transfer function of the aircraft it is first necessary to obtain the equations of motion for the aircraft. The equations of motion are derived by applying Newton's laws of motion, which relate the summation of the external forces and moments to the linear and angular accelerations of the system or body. To make this application, certain assumptions must be made and an axis system defined.

The center of the axis system is, by definition, located at the center of gravity of the aircraft. In general, the axis system is fixed to the aircraft and rotates with it. Such a set of axes is referred to as "body axes." It is not necessary to use such an axis system; an axis system could be fixed, for example, to the air mass, and the aircraft could rotate with respect to it. However, for the purposes of this text the axis system is taken as fixed to the aircraft.

The axis is taken with OX forward, OY out the right wing, and OZ downward as seen by the pilot, to form a right-handed axis system (see Figure 1-2, p. 15). Most aircraft are symmetrical with reference to a vertical plane aligned with the longitudinal axis of the aircraft. Thus, if the OX and OZ axes lie in this plane, the products of inertia J_{xy} and J_{yz} are zero. This result leads to the first assumption:

1. *The axes OX and OZ lie in the plane of symmetry of the aircraft, and J_{xy} and J_{yz} are equal to zero.* At this time, the exact direction of OX is not specified, but in general it is not along a principal axis; hence $J_{zx} \neq 0$.

7

1-2 THE MEANING OF VELOCITIES IN A MOVING AXIS SYSTEM

Very often a student has difficulty understanding what is meant by the velocity of a body with respect to an axis system that is moving with the body. How can there be any relative velocity in this situation? Statements about the velocity along the *OX* axis refer to the *component of velocity with respect to inertial space* taken along the instantaneous direction of the *OX* axis. At any instant, the aircraft has some resultant velocity vector with respect to inertial space. This vector is resolved into the instantaneous aircraft axes to obtain the velocity components *U*, *V*, and *W*. This resolution also applies to the angular velocity. Resolve the instantaneous angular velocity vector, with respect to inertial space, into the instantaneous direction of the *OX*, *OY*, and *OZ* axes to obtain *P*, *Q*, and *R*, respectively (see Figure 1-2, p. 15). It should be recalled that *P*, *Q*, and *R* are the components of the total angular velocity of the body (aircraft) with respect to inertial space. Thus, they are the angular velocities that would be measured by rate gyros fixed to these axes. It should also be recalled that inertial space is that space where Newton's laws apply. In general, a set of axes with their origin at the center of the earth but not rotating with the earth may be considered as an inertial coordinate system. Thus, the earth rotates once a day with respect to such an axis system.

1-3 DEVELOPMENT OF THE EQUATIONS OF MOTION (CONTROLS LOCKED)

The equations of motion for the aircraft can be derived from Newton's second law of motion, which states that the summation of all external forces acting on a body must be equal to the time rate of change of its momentum, and the summation of the external moments acting on a body must be equal to the time rate of change of its moment of momentum (angular momentum). The time rates of change are all taken with respect to inertial space. These laws can be expressed by two vector equations,

$$\sum \mathbf{F} = \frac{d}{dt}(m\mathbf{V}_T)\bigg]_I \qquad (1\text{-}1)$$

and

$$\sum \mathbf{M} = \frac{d\mathbf{H}}{dt}\bigg]_I \qquad (1\text{-}2)$$

where $]_I$ indicates the time rate of change of the vector with respect to inertial space. Rigorously Eq. 1-1 can be applied only to a constant-mass system. For systems with large mass variations, such as rockets, Lagrange's

equation (see Chapter 11) must be used; thus the constant-mass assumption discussed in the next paragraph. Now, the external forces and moments consist of equilibrium or steady-state forces and moments and changes in them which cause or result in a disturbance from this steady state or equilibrium condition. Thus,

$$\sum \mathbf{F} = \sum \mathbf{F}_0 + \sum \Delta \mathbf{F}$$

and

$$\sum \mathbf{M} = \sum \mathbf{M}_0 + \sum \Delta \mathbf{M} \tag{1-3}$$

where $\sum \mathbf{F}_0$ and $\sum \mathbf{M}_0$ are the summations of the equilibrium forces and moments. In the dynamic analyses to follow, the aircraft is always considered to be in equilibrium before a disturbance is introduced. Thus, $\sum \mathbf{F}_0$ and $\sum \mathbf{M}_0$ are identically zero. The equilibrium forces consist of lift, drag, thrust, and gravity, and the equilibrium moments consist of moments resulting from the lift and drag generated by the various portions of the aircraft and the thrust. Therefore, the aircraft is initially in unaccelerated flight, and the disturbances in general arise from either control surface deflections or atmospheric turbulence. Under these conditions, Eqs. 1-1 and 1-2 can be written in the form of

$$\sum \Delta \mathbf{F} = \frac{d}{dt} (m \mathbf{V}_T) \bigg]_I \tag{1-4}$$

and

$$\sum \Delta \mathbf{M} = \frac{d \mathbf{H}}{dt} \bigg]_I \tag{1-5}$$

Before proceeding with the derivation, it is necessary to make some additional assumptions:

2. *The mass of the aircraft remains constant during any particular dynamic analysis.* Actually, there is considerable difference in the mass of an aircraft with and without fuel, but the amount of fuel consumed during the period of the dynamic analysis may be safely neglected.

3. *The aircraft is a rigid body.* Thus, any two points on or within the airframe remain fixed with respect to each other. This assumption greatly simplifies the equations and is quite valid for fighter type aircraft. The effects of aeroelastic deflection of the airframe will be discussed in Chapter 11.

4. *The earth is an inertial reference, and unless otherwise stated the atmosphere is fixed with respect to the earth.* Although this assumption is

invalid for the analysis of inertial guidance systems, it is valid for analyzing automatic control systems for both aircraft and missiles, and it greatly simplifies the final equations. The validity of this assumption is based upon the fact that normally the gyros and accelerometers used for control systems are incapable of sensing the angular velocity of the earth or accelerations resulting from this angular velocity such as the Coriolis acceleration.

It is now time to consider the motion of an aircraft with respect to the earth. Equation 1-4 can be expanded to obtain

$$\sum \Delta \mathbf{F} = m \frac{d\mathbf{V}_T}{dt}\bigg]_I \qquad (1\text{-}6)$$

As the mass is considered constant, and using the fourth assumption, Eq. 1-6 reduces to

$$\sum \Delta \mathbf{F} = m \frac{d\mathbf{V}_T}{dt}\bigg]_E \qquad (1\text{-}7)$$

It is necessary to obtain an expression for the time rate of change of the velocity vector with respect to the earth. This process is complicated by the fact that the velocity vector may be rotating while it is changing in magnitude. This fact leads to the expression for the total derivative of a vector given below (see Appendix A)

$$\frac{d\mathbf{V}_T}{dt}\bigg]_E = \mathbf{1}_{V_T}\frac{dV_T}{dt} + \boldsymbol{\omega} \times \mathbf{V}_T \qquad (1\text{-}8)$$

where $\mathbf{1}_{V_T}(dV_T/dt)$ is the change in the linear velocity, $\boldsymbol{\omega}$ is the total angular velocity of the aircraft with respect to the earth, and $\times$ signifies the cross product. $\mathbf{V}_T$ and $\boldsymbol{\omega}$ can be written in terms of their components, so that

$$\mathbf{V}_T = \mathbf{i}U + \mathbf{j}V + \mathbf{k}W \qquad (1\text{-}9)$$

and

$$\boldsymbol{\omega} = \mathbf{i}P + \mathbf{j}Q + \mathbf{k}R \qquad (1\text{-}10)$$

where **i**, **j**, and **k** are unit vectors along the aircraft's X, Y, and Z axes, respectively. Then from Eq. 1-8

$$\mathbf{1}_{V_T}\frac{dV_T}{dt} = \mathbf{i}\dot{U} + \mathbf{j}\dot{V} + \mathbf{k}\dot{W} \qquad (1\text{-}11)$$

and

$$\boldsymbol{\omega} \times \mathbf{V}_T = \begin{vmatrix} \mathbf{i} & \mathbf{j} & \mathbf{k} \\ P & Q & R \\ U & V & W \end{vmatrix} \qquad (1\text{-}12)$$

Expanding,

$$\boldsymbol{\omega} \times \mathbf{V}_T = \mathbf{i}(WQ - VR) + \mathbf{j}(UR - WP) + \mathbf{k}(VP - UQ) \qquad (1\text{-}13)$$

$\Sigma \Delta \mathbf{F}$ can be written in terms of its components as follows:

$$\sum \Delta \mathbf{F} = \mathbf{i} \sum \Delta F_x + \mathbf{j} \sum \Delta F_y + \mathbf{k} \sum \Delta F_z \qquad (1\text{-}14)$$

Equating the components of Eqs. 1-14, 1-11, and 1-13, the equations of linear motion are obtained:

$$\sum \Delta F_x = m(\dot{U} + WQ - VR)$$

$$\sum \Delta F_y = m(\dot{V} + UR - WP)$$

$$\sum \Delta F_z = m(\dot{W} + VP - UQ) \qquad (1\text{-}15)$$

To obtain the equations of angular motion, it is necessary to return to Eq. 1-5, which is repeated here:

$$\sum \Delta \mathbf{M} = \frac{d\mathbf{H}}{dt} \bigg]_I \qquad (1\text{-}16)$$

Before proceeding, it is necessary to obtain an expression for **H**. By definition, **H** is the angular momentum, or moment of momentum, of a revolving body. The momentum of the element of mass *dm* due to the angular velocity $\boldsymbol{\omega}$ will be equal to the tangential velocity of the element of mass about the instantaneous center of rotation times *dm*. The tangential velocity can be expressed by the vector cross product as follows (see Figure 1-1):

$$\mathbf{V}_{\text{tan}} = \boldsymbol{\omega} \times \mathbf{R} \qquad (1\text{-}17)$$
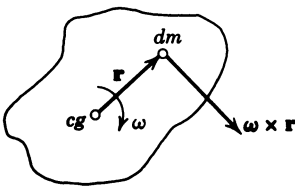
Figure 1-1 *General body with an angular velocity $\boldsymbol{\omega}$ about its center of gravity.*

Then the incremental momentum resulting from this tangential velocity of the element of mass can be expressed as

$$d\mathbf{M} = (\boldsymbol{\omega} \times \mathbf{r})\, dm \tag{1-18}$$

The moment of momentum is the momentum times the lever arm, or, as a vector equation,

$$d\mathbf{H} = \mathbf{r} \times (\boldsymbol{\omega} \times \mathbf{r})\, dm \tag{1-19}$$

But $\mathbf{H} = \int d\mathbf{H}$ over the entire mass of the aircraft. Thus

$$\mathbf{H} = \int \mathbf{r} \times (\boldsymbol{\omega} \times \mathbf{r})\, dm \tag{1-20}$$

In evaluating the triple cross product, if

$$\boldsymbol{\omega} = \mathbf{i}P + \mathbf{j}Q + \mathbf{k}R$$

and

$$\mathbf{r} = \mathbf{i}x + \mathbf{j}y + \mathbf{k}z$$

then

$$\boldsymbol{\omega} \times \mathbf{r} = \begin{vmatrix} \mathbf{i} & \mathbf{j} & \mathbf{k} \\ P & Q & R \\ x & y & z \end{vmatrix} \tag{1-21}$$

Expanding,

$$\boldsymbol{\omega} \times \mathbf{r} = \mathbf{i}(zQ - yR) + \mathbf{j}(xR - zP) + \mathbf{k}(yP - xQ) \tag{1-22}$$

Then

$$\mathbf{r} \times (\boldsymbol{\omega} \times \mathbf{r}) = \begin{vmatrix} \mathbf{i} & \mathbf{j} & \mathbf{k} \\ x & y & z \\ zQ - yR & xR - zP & yP - xQ \end{vmatrix} \tag{1-23}$$

Expanding,

$$\mathbf{r} \times (\boldsymbol{\omega} \times \mathbf{r}) = \mathbf{i}\big[(y^2 + z^2)P - xyQ - xzR\big] + \mathbf{j}\big[(z^2 + x^2)Q - yzR - xyP\big]$$
$$+ \mathbf{k}\big[(x^2 + y^2)R - xzP - yzQ\big] \tag{1-24}$$

Substituting Eq. 1-24 into Eq. 1-20, it becomes

$$\mathbf{H} = \int \mathbf{i}\big[(y^2 + z^2)P - xyQ - xzR\big]\,dm$$

$$+ \int \mathbf{j}\big[(z^2 + x^2)Q - yzR - xyP\big]\,dm$$

$$+ \int \mathbf{k}\big[(x^2 + y^2)R - xzP - yzQ\big]\,dm \qquad (1\text{-}25)$$

But $\int(y^2 + z^2)\,dm$ is defined to be the moment of inertia I_x, and $\int xy\,dm$ is defined to be the product of inertia J_{xy}. The remaining integrals of Eq. 1-25 are similarly defined. By remembering from the first assumption that $J_{xy} = J_{yz} = 0$, Eq. 1-25 can be rewritten in component form as

$$H_x = PI_x - RJ_{xz}$$
$$H_y = QI_y$$
$$H_z = RI_z - PJ_{xz} \qquad (1\text{-}26)$$

However, Eq. 1-16 indicates that the time rate of change of **H** is required. As **H** can change in magnitude and direction, Eq. 1-16 can be written as

$$\sum \Delta \mathbf{M} = \mathbf{1}_H \frac{dH}{dt} + \boldsymbol{\omega} \times \mathbf{H} \qquad (1\text{-}27)$$

The components of $\mathbf{1}_H\, dH/dt$ are

$$\frac{dH_x}{dt} = \dot{P}I_x - \dot{R}J_{xz}$$

$$\frac{dH_y}{dt} = \dot{Q}I_y$$

$$\frac{dH_z}{dt} = \dot{R}I_z - \dot{P}J_{xz} \qquad (1\text{-}28)$$

As the aircraft is assumed to be a rigid body of constant mass, the time rates of change of the moments and products of inertia are zero. Now,

$$\boldsymbol{\omega} \times \mathbf{H} = \begin{vmatrix} \mathbf{i} & \mathbf{j} & \mathbf{k} \\ P & Q & R \\ H_x & H_y & H_z \end{vmatrix} \qquad (1\text{-}29)$$

Expanding,

$$\boldsymbol{\omega} \times \mathbf{H} = \mathbf{i}(QH_z - RH_y) + \mathbf{j}(RH_x - PH_z) + \mathbf{k}(PH_y - QH_x) \quad (1\text{-}30)$$

Also $\sum \Delta \mathbf{M}$ can be written as

$$\sum \Delta \mathbf{M} = \mathbf{i} \sum \Delta \mathcal{L} + \mathbf{j} \sum \Delta \mathcal{M} + \mathbf{k} \sum \Delta \mathcal{N} \qquad (1\text{-}31)$$

By equating components of Eqs. 1-28, 1-30, and 1-31 and substituting for H_x, H_y, and H_z from Eq. 1-26, the angular equations of motion are obtained:

$$\sum \Delta \mathcal{L} = \dot{P}I_x - \dot{R}J_{xz} + QR(I_z - I_y) - PQJ_{xz}$$

$$\sum \Delta \mathcal{M} = \dot{Q}I_y + PR(I_x - I_z) + (P^2 - R^2)J_{xz}$$

$$\sum \Delta \mathcal{N} = \dot{R}I_z - \dot{P}J_{xz} + PQ(I_y - I_x) + QRJ_{xz} \qquad (1\text{-}32)$$

The equations of linear motion from Eq. 1-15 are

$$\sum \Delta F_x = m(\dot{U} + WQ - VR)$$

$$\sum \Delta F_y = m(\dot{V} + UR - WP)$$

$$\sum \Delta F_z = m(\dot{W} + VP - UQ) \qquad (1\text{-}33)$$

Equations 1-32 and 1-33 are the complete equations of motion for the aircraft. It will next be necessary to linearize the equations and expand the left-hand sides.

Summary of Nomenclature

Axis	Direction	Name	Linear Velocity	Small Angular Displacement	Angular Velocity
OX	Forward	Roll	U	ϕ	P
OY	Right wing	Pitch	V	θ	Q
OZ	Downward	Yaw	W	ψ	R

Axis	Moment of Inertia	Product of Inertia	Force	Moment
OX	I_x	$J_{xy} = 0$	F_x	$\mathcal{L}$
OY	I_y	$J_{yz} = 0$	F_y	$\mathcal{M}$
OZ	I_z	$J_{zx} \neq 0$	F_z	$\mathcal{N}$

These conclusions are based on the assumptions that:

1. *OX* and *OZ* are in the plane of symmetry.
2. The mass of the aircraft is constant.
3. The aircraft is a rigid body.
4. The earth is an inertial reference.

1-4   AIRCRAFT ATTITUDE WITH RESPECT TO THE EARTH

In order to describe the motion of the aircraft with respect to the earth or inertial space, it is necessary to be able to specify the orientation of one axis system with respect to another. This can be done through the use of a set of angles called "Euler angles." Consider an earth axis system with its origin at the center of gravity of the aircraft and nonrotating with respect to the earth. Let OX_E and OY_E be in the horizontal plane, and OZ_E vertical and down. OX_E may be taken as north or any other fixed direction. Referring to Figure 1-2, let the following angles indicate the rotation of the *XYZ* axis from the
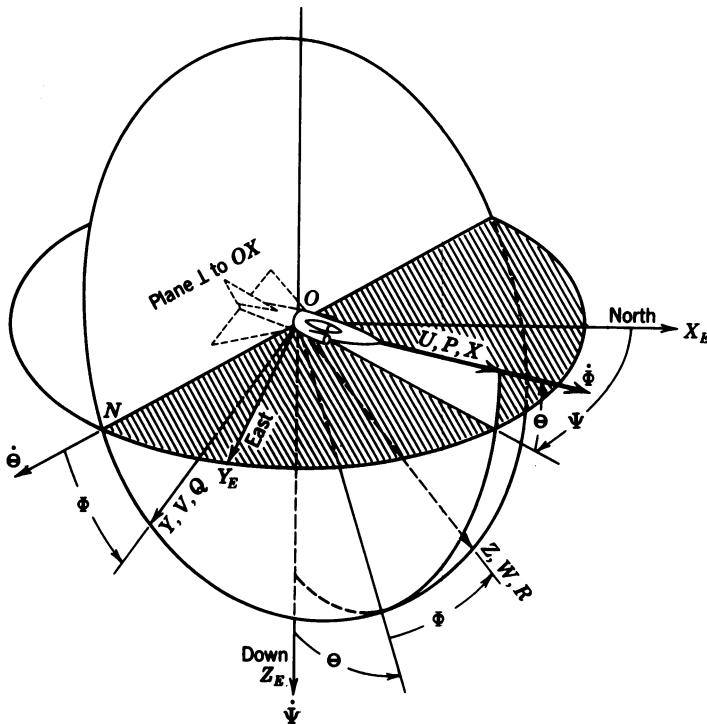
Figure 1-2   *Sketch of fixed and aircraft axes.*

earth axis:

> Ψ is the angle between OX_E and the projection of the OX axis on the horizontal plane.
> $\dot{\Psi}$ is a vector along OZ_E.
> Θ is the angle between the horizontal and the OX axis measured in the vertical plane.
> $\dot{\Theta}$ is a vector along ON, the line of nodes.
> Φ is the angle between ON and the OY axis measured in the OYZ plane. Note that this plane is not necessarily vertical.
> $\dot{\Phi}$ is a vector along OX.

Thus, the angles Ψ, Θ, and Φ specify the orientation of the aircraft axis system with respect to the earth. The positive direction of these angles is indicated in Figure 1-2.

To transform the components of the angular velocity of the aircraft from the earth axis to the aircraft axis system, take the components $\dot{\Psi}$, $\dot{\Theta}$, and $\dot{\Phi}$ and project them along the OX, OY, and OZ axes to obtain

$$P = \dot{\Phi} - \dot{\Psi} \sin \Theta$$
$$Q = \dot{\Theta} \cos \Phi + \dot{\Psi} \cos \Theta \sin \Phi$$
$$R = -\dot{\Theta} \sin \Phi + \dot{\Psi} \cos \Theta \cos \Phi \qquad (1\text{-}34)$$

These equations can be solved for $\dot{\Phi}$, $\dot{\Theta}$, and $\dot{\Psi}$ to yield

$$\dot{\Theta} = Q \cos \Phi - R \sin \Phi$$
$$\dot{\Phi} = P + Q \sin \Phi \tan \Theta + R \cos \Phi \tan \Theta = P + \dot{\Psi} \sin \Theta$$
$$\dot{\Psi} = Q \frac{\sin \Phi}{\cos \Theta} + R \frac{\cos \Phi}{\cos \Theta} \qquad (1\text{-}34a)$$

A similar transformation can be made for linear velocities. It should be noted that $\dot{\Phi}$, $\dot{\Theta}$, and $\dot{\Psi}$ are not orthogonal vectors. Equations 1-34a can be integrated with respect to time, and by knowing the initial conditions, Θ, Φ, and Ψ can be determined; however, as the rates of change of these angles are a function of the angles themselves, this is best done on a computer.

The components of the gravity force along the aircraft axes are along

$$OX: \quad -mg \sin \Theta$$
$$OY: \quad mg \cos \Theta \sin \Phi$$
$$OZ: \quad mg \cos \Theta \cos \Phi \qquad (1\text{-}35)$$

1-5   LINEARIZATION AND SEPARATION OF THE EQUATIONS OF MOTION

A study of Eqs. 1-32 and 1-33 shows that it takes six simultaneous nonlinear equations of motion to completely describe the behavior of a rigid aircraft. In this form, a solution can be obtained only by the use of analog or digital computers or by manual numerical integration. In most cases, however, by the use of proper assumptions the equations can be broken down into two sets of three equations each and these linearized to obtain equations amenable to analytic solutions of sufficient accuracy.

The six equations are first broken up into two sets of three simultaneous equations. To accomplish this the aircraft is considered to be in straight and level unaccelerated flight and then to be disturbed by deflection of the elevator. This deflection applies a pitching moment about the OY axis, causing a rotation about this axis which eventually causes a change in F_x and F_z, but does not cause a rolling or yawing moment or any change in F_y; thus $P = R = V = 0$ and the $\sum \Delta F_y$, $\sum \Delta \mathscr{L}$, and $\sum \Delta \mathscr{N}$ equations may be eliminated. This leaves

$$\left. \begin{aligned} \sum \Delta F_x &= m(\dot{U} + WQ) \\ \sum \Delta F_z &= m(\dot{W} - UQ) \\ \sum \Delta \mathscr{M} &= \dot{Q}I_y \end{aligned} \right\} \quad \text{longitudinal equations for } P = R = V = 0$$

$$(1\text{-}36)$$

An investigation of the remaining three equations, especially the $\mathscr{L}$ and $\mathscr{N}$ equations, shows that a rolling or yawing moment excites angular velocities about all three axes; thus except for certain cases the equations cannot be decoupled. The assumptions necessary for this decoupling will be discussed in Chapter 3 on the lateral dynamics of the aircraft, and the condition when this separation of the equations is not valid will be discussed in Chapter 5 on inertial cross-coupling. The rest of this chapter will be devoted to the expansion of the longitudinal equations of motion.

1-6   LONGITUDINAL EQUATIONS OF MOTION

Previously, the components of the total instantaneous values of the linear and angular velocities resolved into the aircraft axes were designated as U, V, W, P, Q, and R. As these values include an equilibrium value and the

Figure 1-3 *Equilibrium and disturbed aircraft stability axes:*

$$'\alpha \simeq W / U$$
$$\alpha = \alpha_0 + '\alpha$$
$$\Theta = \Theta_0 + \theta$$
$$\gamma = \Theta - '\alpha$$
$$or \quad \gamma = \theta - '\alpha \text{ for } \Theta_0 = 0$$

change from the steady state, they may be expressed as

$$U = U_0 + u \qquad P = P_0 + p$$
$$V = V_0 + v \qquad Q = Q_0 + q$$
$$W = W_0 + w \qquad R = R_0 + r$$

where U_0, V_0, etc., are the equilibrium values and u, v, etc., are the changes in these values resulting from some disturbance. In Section 1-1 a body axis system for the aircraft was discussed and the OX axis was taken forward, but the exact orientation was not specified. The OX axis could be aligned with the longitudinal axis of the aircraft; however, if it is originally aligned with the equilibrium direction of the velocity vector of the aircraft, $W_0 = 0$ (see Figure 1-3). In Figure 1-3 the axes X_E, Y_E, Z_E are earth reference axes; the X_0, Y_0, Z_0 are equilibrium aircraft axes; and X, Y, Z are the disturbed

aircraft axes. For any particular problem the aircraft axes, after being aligned with the X axis into the relative wind, remain fixed to the aircraft during the study of perturbations from that initial flight condition. Such a set of aircraft axes are referred to as "stability axes." The stability axes will be used in all the dynamic analysis to follow. As can be seen from Figure 1-3, Θ_0 and γ_0 are measured from the horizontal to the stability X_0 axis. The angle γ is often referred to as the "flight path angle" and is defined as the angle measured, in the vertical plane, between the horizontal and the velocity vector of the aircraft. By using stability axes, Θ_0 and γ_0 are equal. The definition of the angle of attack is standard, that is, the angle between the velocity vector (or the relative wind) and the wing chord. As the change in Θ, which is equal to θ, is caused by a rotation about the Y axis, then $q = \dot{\theta}$. Under these conditions $U = U_0 + u$, $W = w$, and, as U_0 is a constant, $\dot{U} = \dot{u}$ and $\dot{W} = \dot{w}$. As the aircraft is initially in unaccelerated flight, Q_0 must be zero; then $Q = q$. Making these substitutions the force equations of Eq. 1-36 become

$$\sum \Delta F_x = m(\dot{u} + wq)$$

$$\sum \Delta F_z = m(\dot{w} - U_0 q - uq) \qquad (1\text{-}37)$$

5. *By restricting the disturbances to small perturbations about the equilibrium condition, the product of the variations will be small in comparison with the variations and can be neglected, and the small-angle assumptions can be made relative to the angles between the equilibrium and disturbed axes. This fifth assumption somewhat limits the applicability of the equations but reduces them to linear equations.*

Thus Eq. 1-37 can be written as follows with the addition of the pitching moment equation from Eq. 1-36:

$$\sum \Delta F_x = m(\dot{u})$$

$$\sum \Delta F_z = m(\dot{w} - U_0 q) = m(\dot{w} - U_0 \dot{\theta})$$

$$\sum \Delta \mathcal{M} = I_y \dot{q} = I_y \ddot{\theta} \qquad (1\text{-}38)$$

It is now necessary to expand the applied forces and moments and to express them in terms of the changes in the forces and moments that cause or result from these perturbations. These latter forces are usually of an aerodynamic and gravitational origin. For instance, the components of gravity
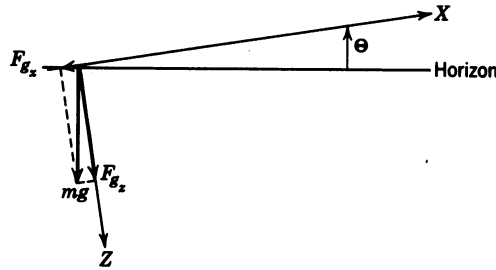
Figure 1-4   *Components of gravity resolved into aircraft axes.*

along the X and Z axes are a function of the angle Θ, as shown in Figure 1-4:

$$F_{g_x} = - mg \sin \Theta \quad \text{and} \quad F_{g_z} = mg \cos \Theta \qquad (1\text{-}39)$$

The changes in these forces with respect to Θ are

$$\frac{\partial F_{g_x}}{\partial \Theta} = - mg \cos \Theta \quad \text{and} \quad \frac{\partial F_{g_z}}{\partial \Theta} = - mg \sin \Theta \qquad (1\text{-}40)$$

The forces in the X direction are a function of U, W, $\dot{W}$, Θ, and $\dot{\Theta}$. Thus the total differential of F_x can be expressed as

$$\sum dF_x = \frac{\partial F_x}{\partial U} dU + \frac{\partial F_x}{\partial W} dW + \frac{\partial F_x}{\partial \dot{W}} d\dot{W} + \frac{\partial F_x}{\partial \Theta} d\Theta + \frac{\partial F_x}{\partial \dot{\Theta}} d\dot{\Theta} \qquad (1\text{-}41)$$

The reason for not including $\partial F_x / \partial \dot{U}$ will be explained in Section 1-6.
   If it is assumed that, as the disturbances are small, the partial derivatives are linear, the differentials can be replaced by the actual increments, and Eq. 1-41 becomes

$$\sum \Delta F_x = \frac{\partial F_x}{\partial u} \Delta U + \frac{\partial F_x}{\partial w} \Delta W + \frac{\partial F_x}{\partial \dot{w}} \Delta \dot{W} + \frac{\partial F_x}{\partial \theta} \Delta \Theta + \frac{\partial F_x}{\partial \dot{\theta}} \Delta \dot{\Theta} \qquad (1\text{-}42)$$

But u, w, etc., are the changes in the parameters, and as the perturbations are small, $u = \Delta U$, etc. Therefore Eq. 1-42 becomes

$$\sum \Delta F_x = \frac{\partial F_x}{\partial u} u + \frac{\partial F_x}{\partial \dot{w}} \dot{w} + \frac{\partial F_x}{\partial w} w + \frac{\partial F_x}{\partial \theta} \theta + \frac{\partial F_x}{\partial \dot{\theta}} \dot{\theta} \qquad (1\text{-}43)$$

Multiplying and dividing the first three terms of Eq. 1-43 by U_0, it becomes

$$\sum \Delta F_x = U_0 \frac{\partial F_x}{\partial u} \frac{u}{U_0} + U_0 \frac{\partial F_x}{\partial w} \frac{w}{U_0} + U_0 \frac{\partial F_x}{\partial \dot{w}} \frac{\dot{w}}{U_0} + \frac{\partial F_x}{\partial \theta} \theta + \frac{\partial F_x}{\partial \dot{\theta}} \dot{\theta} \quad (1\text{-}44)$$

As the perturbations have been assumed small, then $U \simeq U_0$, hereafter no distinction will be made, and the subscript zero will be dropped. However, the value of U that appears explicitly in the equations of motion is the equilibrium value of U. The dimensionless ratios u/U, w/U, and $\dot{w}/U$ are defined as

$$u/U = {}'u$$
$$w/U = {}'\alpha$$

(which is the variation in the angle of attack from equilibrium), and

$$\dot{w}/U = {}'\dot{\alpha}$$

Substituting these values into Eq. 1-44 yields

$$\sum \Delta F_x = U \frac{\partial F_x}{\partial u} {}'u + \frac{\partial F_x}{\partial \alpha} {}'\alpha + \frac{\partial F_x}{\partial \dot{\alpha}} {}'\dot{\alpha} + \frac{\partial F_x}{\partial \theta} \theta + \frac{\partial F_x}{\partial \dot{\theta}} \dot{\theta} \quad (1\text{-}45)$$

as

$$U \frac{\partial F_x}{\partial w} = \frac{\partial F_x}{\partial w/U} = \frac{\partial F_x}{\partial {}'\alpha} = \frac{\partial F_x}{\partial \alpha} \quad \text{as} \quad \frac{\partial {}'\alpha}{\partial \alpha} \equiv 1$$

From Eq. 1-38

$$\sum \Delta F_x = m\dot{u} = m\dot{u} \left(\frac{U}{U} \right) = mU \frac{\dot{u}}{U} = mU {}'\dot{u}$$

Substituting this expression for $\sum \Delta F_x$ in Eq. 1-45, taking the other terms over to the left-hand side of the equation, and dividing by Sq, the X equation becomes

$$\frac{mU}{Sq} {}'\dot{u} - \frac{U}{Sq} \frac{\partial F_x}{\partial u} {}'u - \frac{1}{Sq} \frac{\partial F_x}{\partial \alpha} {}'\alpha$$

$$- \frac{1}{Sq} \frac{\partial F_x}{\partial \dot{\alpha}} {}'\dot{\alpha} - \frac{1}{Sq} \frac{\partial F_x}{\partial \theta} \theta - \frac{1}{Sq} \frac{\partial F_x}{\partial \dot{\theta}} \dot{\theta} = \frac{F_{x_a}}{Sq} \quad (1\text{-}46)$$

where F_{x_a} is an applied aerodynamic force of unspecified origin to be explained in Section 1-7. S is the wing area as defined in Appendix D, $q = \frac{1}{2}\rho U^2$, the dynamic pressure in lb/sq ft, and ρ is the air density. Substitut-

ing for $\partial F_x / \partial\theta$ from Eq. 1-40 and multiplying and dividing the fourth and sixth terms by $c/2U$, where c is the mean aerodynamic chord (see Appendix D), Eq. 1-46 becomes

$$\frac{mU}{Sq}'\dot{u} - \frac{U}{Sq}\frac{\partial F_x}{\partial u}'u - \frac{1}{Sq}\frac{\partial F_x}{\partial\alpha}'\alpha - \frac{c}{2U}\left(\frac{1}{Sq}\right)\left(\frac{2U}{c}\right)\frac{\partial F_x}{\partial\dot{\alpha}}'\dot{\alpha}$$

$$+ \frac{mg}{Sq}(\cos\Theta)\theta - \frac{c}{2U}\left(\frac{1}{Sq}\right)\left(\frac{2U}{c}\right)\frac{\partial F_x}{\partial\dot{\theta}}\dot{\theta} = \frac{F_{x_a}}{Sq} = C_{F_{x_a}} \qquad (1\text{-}47)$$

To show how Eq. 1-47 was nondimensionalized, the $'\dot{\alpha}$ term will be analyzed. First take

$$\left(\frac{1}{Sq}\right)\left(\frac{2U}{c}\right)\frac{\partial F_x}{\partial\dot{\alpha}}$$

As F_x and Sq both have the dimensions of a force (lb), the units of these two terms cancel, leaving $2U/c$ and $1/\dot{\alpha}$. The dimensions of $2U/c$ and $1/\dot{\alpha}$ are $1/\sec$ and sec, respectively; therefore this portion of the $'\dot{\alpha}$ term is nondimensional and can be replaced by a nondimensional coefficient. The remaining portion of the $'\dot{\alpha}$ term, which is $(c/2U)'\dot{\alpha}$, is also nondimensional. The remaining terms are handled in a similar manner. These nondimensional coefficients are referred to as "stability derivatives," and although there are several forms of these coefficients, the ones used in this text and listed in Table 1-1 are essentially the NACA standard longitudinal stability derivatives. All the terms in Table 1-1 are explained later in Section 1-7, except for C_D and C_L, which are discussed in Appendix D.

Introducing these terms, Eq. 1-47 becomes

$$\frac{mU}{Sq}'\dot{u} - C_{x_u}'u - C_{x_\alpha}'\alpha - \frac{c}{2U}C_{x_{\dot{\alpha}}}'\dot{\alpha} + \frac{mg}{Sq}(\cos\Theta)\theta - \frac{c}{2U}C_{x_q}\dot{\theta} = C_{F_{x_a}} \quad (1\text{-}48)$$

Sometimes mg/Sq is replaced by $-C_w$. If this is done, Eq. 1-48 becomes

$$\frac{mU}{Sq}'\dot{u} - C_{x_u}'u - C_{x_\alpha}'\alpha - \frac{c}{2U}C_{x_{\dot{\alpha}}}'\dot{\alpha} - C_w(\cos\Theta)\theta - \frac{c}{2U}C_{x_q}\dot{\theta} = C_{F_{x_a}} \quad (1\text{-}49)$$

In like manner the F_z and $\mathcal{M}$ equation can be obtained. The F_z equation can be written

$$\sum \Delta F_z = \frac{\partial F_z}{\partial u}u + \frac{\partial F_z}{\partial w}w + \frac{\partial F_z}{\partial\dot{w}}\dot{w} + \frac{\partial F_z}{\partial\theta}\theta + \frac{\partial F_z}{\partial\dot{\theta}}\dot{\theta} \qquad (1\text{-}50)$$

Multiplying and dividing the first three terms by U and using the definitions of the dimensionless ratios previously stated, following Eq. 1-44, Eq. 1-50

TABLE 1-1   Definitions and Equations for Longitudinal Stability Derivatives

Symbol	Definition	Origin	Equation	Typical Values
C_{x_u}	$\dfrac{U}{Sq}\dfrac{\partial F_x}{\partial u}$	Variation of drag and thrust with u	$-2C_D - U\dfrac{\partial C_D}{\partial u}$	-0.05
C_{x_α}	$\dfrac{1}{Sq}\dfrac{\partial F_x}{\partial \alpha}$	Lift and drag variations along the X axis	$C_L - \dfrac{\partial C_D}{\partial \alpha}$	$+0.1$
C_w	—	Gravity	$-\dfrac{mg}{Sq}$	
$C_{x_{\dot\alpha}}$	$\dfrac{1}{Sq}\left(\dfrac{2U}{c}\right)\dfrac{\partial F_x}{\partial \dot\alpha}$	Downwash lag on drag	Neglect	
C_{x_q}	$\dfrac{1}{Sq}\left(\dfrac{2U}{c}\right)\dfrac{\partial F_x}{\partial \dot\theta}$	Effect of pitch rate on drag	Neglect	
C_{z_u}	$\dfrac{U}{Sq}\dfrac{\partial F_z}{\partial u}$	Variation of normal force with u	$-2C_L - U\dfrac{\partial C_L}{\partial u}$	-0.5
C_{z_α}	$\dfrac{1}{Sq}\dfrac{\partial F_z}{\partial \alpha}$	Slope of the normal force curve	$-C_D - \dfrac{\partial C_L}{\partial \alpha} \approx -\dfrac{\partial C_L}{\partial \alpha}$	-4
C_w	—	Gravity	$-\dfrac{mg}{Sq}$	
$C_{z_{\dot\alpha}}$	$\dfrac{1}{Sq}\left(\dfrac{2U}{c}\right)\dfrac{\partial F_z}{\partial \dot\alpha}$	Downwash lag on lift of tail	$2\left(\dfrac{\partial C_m}{\partial i_t}\right)\left(\dfrac{d\epsilon}{d\alpha}\right)$	-1
C_{z_q}	$\dfrac{1}{Sq}\left(\dfrac{2U}{c}\right)\dfrac{\partial F_z}{\partial \dot\theta}$	Effect of pitch rate on lift	$2K\left(\dfrac{\partial C_m}{\partial i_t}\right)$	-2
C_{m_u}	$\dfrac{U}{Sqc}\dfrac{\partial \mathcal{M}}{\partial u}$	Effects of thrust, slipstream, and flexibility	No simple relation; usually neglected for jets	
C_{m_α}	$\dfrac{1}{Sqc}\dfrac{\partial \mathcal{M}}{\partial \alpha}$	Static longitudinal stability	$(SM)\left(\dfrac{dC_L}{d\alpha}\right)_\delta^a$	-0.3
$C_{m_{\dot\alpha}}$	$\dfrac{1}{Sqc}\left(\dfrac{2U}{c}\right)\dfrac{\partial \mathcal{M}}{\partial \dot\alpha}$	Downwash lag on moment	$2\left(\dfrac{\partial C_m}{\partial i_t}\right)\dfrac{d\epsilon}{d\alpha}\dfrac{l_t}{c}$	-3
C_{m_q}	$\dfrac{1}{Sqc}\left(\dfrac{2U}{c}\right)\dfrac{\partial \mathcal{M}}{\partial \dot\theta}$	Damping in pitch	$2K\left(\dfrac{\partial C_m}{\partial i_t}\right)\dfrac{l_t}{c}$	-8

becomes

$$\sum \Delta F_z = U\frac{\partial F_z}{\partial u}{}'u + \frac{\partial F_z}{\partial \alpha}{}'\alpha + \frac{\partial F_z}{\partial \dot\alpha}{}'\dot\alpha + \frac{\partial F_z}{\partial \theta}\theta + \frac{\partial F_z}{\partial \dot\theta}\dot\theta \qquad (1\text{-}51)$$

From Eq. 1-38,

$$\sum \Delta F_z = m(\dot w - U\dot\theta)$$

Then

$$\sum \Delta F_z = m\left(\frac{\dot w}{U}U - U\dot\theta\right) = mU'\dot\alpha - mU\dot\theta \qquad (1\text{-}52)$$

Substituting this into Eq. 1-51, and dividing by Sq, it becomes

$$-\frac{U}{Sq}\frac{\partial F_z}{\partial u}{}'u + \left(\frac{mU}{Sq} - \frac{1}{Sq}\frac{\partial F_z}{\partial \dot\alpha}\right){}'\dot\alpha - \frac{1}{Sq}\frac{\partial F_z}{\partial \alpha}{}'\alpha$$

$$+\left(-\frac{mU}{Sq} - \frac{1}{Sq}\frac{\partial F_z}{\partial \dot\theta}\right)\dot\theta - \frac{1}{Sq}\frac{\partial F_z}{\partial \theta}\theta = \frac{F_{z_a}}{Sq} = C_{F_{z_a}} \qquad (1\text{-}53)$$

Going to the coefficient form of Table 1-1, Eq. 1-53 becomes

$$-C_{z_u}{}'u + \left(\frac{mU}{Sq} - \frac{c}{2U}C_{z_{\dot\alpha}}\right){}'\dot\alpha - C_{z_\alpha}{}'\alpha + \left(-\frac{mU}{Sq} - \frac{c}{2U}C_{z_q}\right)\dot\theta$$

$$-C_w(\sin\Theta)\theta = C_{F_{z_a}} \quad (1\text{-}54)$$

The moment equation can be written as

$$\sum \Delta\mathcal{M} = \frac{\partial\mathcal{M}}{\partial u}u + \frac{\partial\mathcal{M}}{\partial w}w + \frac{\partial\mathcal{M}}{\partial \dot w}\dot w + \frac{\partial\mathcal{M}}{\partial \dot\theta}\dot\theta \qquad (1\text{-}55)$$

[as $\partial\mathcal{M}/\partial\theta = 0$, for there is no change in $\mathcal{M}$ due to a change in θ if all the other parameters are held constant.]
   Multiplying and dividing the first three terms by U and using the definitions of the dimensionless ratios previously stated, Eq. 1-55 becomes

$$\sum \Delta\mathcal{M} = U\frac{\partial\mathcal{M}}{\partial u}{}'u + \frac{\partial\mathcal{M}}{\partial \alpha}{}'\alpha + \frac{\partial\mathcal{M}}{\partial \dot\alpha}{}'\dot\alpha + \frac{\partial\mathcal{M}}{\partial \dot\theta}\dot\theta \qquad (1\text{-}56)$$

But from Eq. 1-38, $\Sigma \Delta \mathcal{M} = I_y \ddot{\theta}$, and after dividing by Sqc, Eq. 1-56 becomes

$$-\frac{U}{Sqc}\frac{\partial \mathcal{M}}{\partial u}'u - \frac{1}{Sqc}\frac{\partial \mathcal{M}}{\partial \dot{\alpha}}'\dot{\alpha} - \frac{1}{Sqc}\frac{\partial \mathcal{M}}{\partial \alpha}'\alpha + \frac{I_y}{Sqc}\ddot{\theta} - \frac{1}{Sqc}\frac{\partial \mathcal{M}}{\partial \theta}\dot{\theta} = \frac{\mathcal{M}_a}{Sqc} = C_{m_a}$$

$$(1\text{-}57)$$

Going to the coefficient form of Table 1-1, Eq. 1-57 becomes

$$-C_{m_u}'u - \frac{c}{2U}C_{m_{\dot{\alpha}}}'\dot{\alpha} - C_{m_\alpha}'\alpha + \frac{I_y}{Sqc}\ddot{\theta} - \frac{c}{2U}C_{m_q}\dot{\theta} = C_{m_a} \qquad (1\text{-}58)$$

Equations 1-49, 1-54, and 1-58 are the longitudinal equations of motion for the aircraft and are rewritten here for reference:

$$\left(\frac{mU}{Sq}'\dot{u} - C_{x_u}'u\right) + \left(-\frac{c}{2U}C_{x_{\dot{\alpha}}}'\dot{\alpha} - C_{x_\alpha}'\alpha\right)$$

$$+\left[-\frac{c}{2U}C_{x_q}\dot{\theta} - C_w(\cos\Theta)\theta\right] = C_{F_{x_a}}$$

$$-\left(C_{z_u}'u\right) + \left[\left(\frac{mU}{Sq} - \frac{c}{2U}C_{z_{\dot{\alpha}}}\right)'\dot{\alpha} - C_{z_\alpha}'\alpha\right]$$

$$+\left[\left(-\frac{mU}{Sq} - \frac{c}{2U}C_{z_q}\right)\dot{\theta} - C_w(\sin\Theta)\theta\right] = C_{F_{z_a}}$$

$$\left(-C_{m_u}'u\right) + \left(-\frac{c}{2U}C_{m_{\dot{\alpha}}}'\dot{\alpha} - C_{m_\alpha}'\alpha\right) + \left(\frac{I_y}{Sqc}\ddot{\theta} - \frac{c}{2U}C_{m_q}\dot{\theta}\right) = C_{m_a}$$

$$(1\text{-}59)$$

These equations assume that:

1. The X and Z axes lie in the plane of symmetry and the origin of the axis system is at the center of gravity of the aircraft.
2. The mass of the aircraft is constant.
3. The aircraft is a rigid body.
4. The earth is an inertial reference.
5. The perturbations from equilibrium are small.
6. The flow is quasisteady (to be explained in Section 1-7).

These equations require that the X axis be aligned with the aircraft velocity vector while the aircraft is in equilibrium flight. The stability derivatives are defined in Table 1-1 and are derived in Section 1-7.

It should be remembered that in these equations $U = U_0$, $q = \frac{1}{2}\rho U_0^2$, $'u = u / U_0$, $'\alpha = w / U_0$, and $'\dot{\alpha} = \dot{w} / U_0$.

These equations are nondimensional; thus all angles and their derivatives must be in radian measure.

In deriving the longitudinal equations of motion certain nondimensional coefficients, referred to as stability derivatives, were introduced. In Section 1-7 the equations for the stability derivatives will be derived and their origin determined.

1-7 DERIVATION OF EQUATIONS FOR THE LONGITUDINAL STABILITY DERIVATIVES

The student probably wondered why in the expansion of the forces and moments the partial derivative with respect to $\dot{u}$ was missing, while the partial derivative with respect to $\dot{w}$ was included. This was based on the assumption of "quasisteady flow." Quasisteady flow assumes that the airflow around the aircraft changes instantaneously when the aircraft is disturbed from equilibrium. This, of course, is not true. If the aircraft is accelerated, it must in turn accelerate a certain mass of air; this effect is called the "apparent mass effect." However, the assumption of quasisteady flow makes the problem simpler, and for low Mach numbers it is completely adequate. For higher Mach numbers (0.8 or higher) this assumption can lead to theoretical results that do not satisfactorily predict the actual performance of the aircraft. For these cases the compressibility effects can be taken into account by use of stability derivatives for the Mach number in question. These, as well as the subsonic stability derivatives, are most accurately determined from wind tunnel tests. However, for the examples used in this book it will be assumed that

6. *Quasisteady flow does exist.* As a result of this assumption, all derivatives with respect to the rates of change of velocities are omitted except for those with respect to $\dot{w}$, which are retained to account for the effects of downwash on the horizontal stabilizer, to be explained in the next paragraph. When the forces and moments caused by control surface displacement are discussed, the rates of change of the control surface movement will also be neglected according to this same assumption.

The retention of the derivatives with respect to $\dot{w}$ is not in contradiction with the assumption of quasisteady flow; it takes into account the time required for the effect of the downwash produced *by* the wing to reach the horizontal tail. The downwash is caused by the wing tip vortices and is explained as follows: A wing producing lift experiences a low-pressure area on the upper surface of the wing and a high pressure area below the wing. At
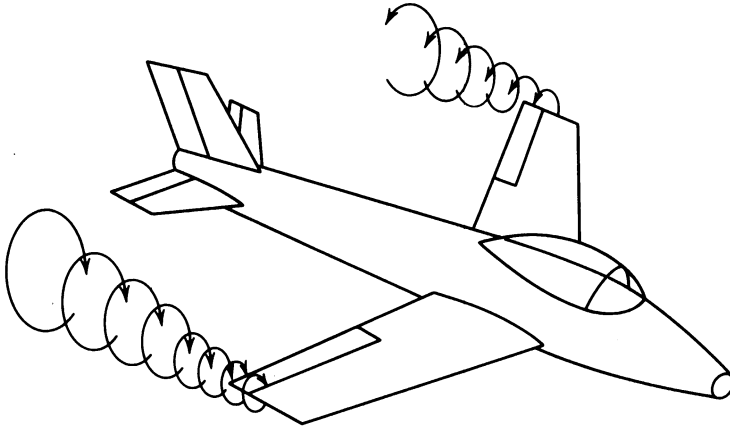
Figure 1-5   *An aircraft with wing tip vortices.*

the wing tip the air in the high-pressure area below the wing flows up into the area of low pressure on the upper surface of the wing. As the aircraft moves through the air the wing tips leave this circular pattern of air behind in the form of a spiral. These spirals are called "wing tip vortices" and are shown in Figure 1-5. The result of this wing vortex system is to induce a downward component of velocity to the air flow, which is referred to as downwash. Actually, as shown by Prandtl[1] in his lifting line theory, the vortex is not restricted to the wing tips but consists of a whole vortex sheet behind the wing. This vortex sheet accounts for the downwash at the wing and at the tail. The downwash velocities are not constant across the span of the wing unless the lift distribution is elliptical. Thus the downwash velocities at a given distance behind the wing vary with the distance from the fuselage. But, as the span of the horizontal tail is small compared to the wing span, the downwash velocity experienced by the tail is almost constant across its span. The effect of the downwash is to reduce the angle of attack of the tail (see Figure 1-6). The angle of attack of the tail can be expressed as

$$\alpha_t = i + \alpha - \epsilon \tag{1-60}$$

Figure 1-6   *Effect of downwash on the angle of attack of the horizontal stabilizer.*

where i is the angle of incidence of the stabilizer with respect to the α reference line, α is the wing angle of attack, Dw is the downwash velocity at the tail, and ϵ is the downwash angle $= Dw/U$ in radians.
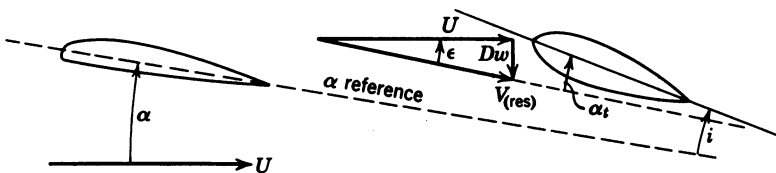
The downwash is the result of the lifting action of the wing and increases as the lift and angle of attack of the wing increase. If the vertical velocity of the aircraft is changed, the angle of attack changes; thus the downwash varies with w. Therefore, it is necessary to investigate the effect of a change of w, the vertical velocity, on the angle of attack of the tail. Referring to Figure 1-3, it can be seen that

$$\Delta\alpha \simeq \frac{w}{U} \quad \text{for} \quad W_0 = 0 \tag{1-61}$$

If it is assumed that w is still changing,

$$w_2 = w_1 + \frac{dw}{dt}\Delta t \tag{1-62}$$

where w_1 is the value of w at t_1, w_2 is the value of w at t_2, and $\Delta t = t_2 - t_1$.

As the aircraft is moving at a finite velocity through the air mass it takes a finite time for the effect of this change in w to reach the tail. This time can be expressed by the relation

$$\Delta t = \frac{l_t}{U} \tag{1-63}$$

where l_t is the distance between the quarter chord point of the wing MAC, or some other reference point, and the quarter chord point of the horizontal stabilizer MAC. Let

$$\Delta w = w_2 - w_1 \tag{1-64}$$

Then from Eq. 1-62

$$w_2 - w_1 = \Delta w = \frac{dw}{dt}\Delta t \tag{1-65}$$

Substituting for Δt, Eq. 1-65 becomes

$$\Delta w = \frac{dw}{dt}\frac{l_t}{U} \tag{1-66}$$

As explained following Eq. 1-60, the amount of downwash at the tail is dependent on the angle of attack of the wing and thus dependent on the vertical velocity of the wing; therefore, it can be said that the downwash at the tail is proportional to the vertical velocity of the wing, or in equation

form

$$(Dw)_t = kw \qquad (1\text{-}67)$$

Then

$$\Delta(Dw)_t = k\,\Delta w \qquad (1\text{-}68)$$

Substituting for Δw from Eq. 1-66, Eq. 1-68 becomes

$$\Delta(Dw)_t = k\frac{l_t}{U}\frac{dw}{dt} = k\frac{l_t}{U}\dot{w} \qquad (1\text{-}69)$$

But $\dot{w}/U = {}'\dot{\alpha}$; thus Eq. 1-69 becomes

$$\Delta(Dw)_t = kl_t\,'\dot{\alpha} \qquad (1\text{-}70)$$

which is the change in the downwash at the tail due to a rate of change of the angle of attack of the wing. This results in a change of angle of attack of the tail causing a small change in the lift and thus in the Z force and in the pitching moment. Thus partial derivatives with respect to $\dot{w}({}'\dot{\alpha})$ must be included even for quasisteady flow.

It is now time to look at the rest of the stability derivatives. Table 1-1 indicates that $C_{x_{\dot{\alpha}}}$ and C_{x_q} are generally neglected. In the discussion of quasisteady flow the existence of a force due to ${}'\dot{\alpha}$ was explained. In this discussion it is pointed out that this rate of change of angle of attack of the wing results in a change of angle of attack of the horizontal stabilizer, thus changing its lift and drag. The change in drag is the main contribution to a change in the force in the X direction. As the drag of the horizontal stabilizer is usually very small in comparison with the drag of the rest of the aircraft (generally less than 10 percent of the zero-lift drag), any change in this drag can be neglected. In like manner, a pitching velocity $\dot{\theta}$ causes a change in the angle of attack of the horizontal stabilizer, but as in the case of ${}'\dot{\alpha}$ the change in the drag resulting from $\dot{\theta}$ can be neglected. Thus $C_{x_{\dot{\alpha}}}$ and C_{x_q} are usually negligible and are neglected in the following pages. The derivation of the equations for the rest of the stability derivatives follows.

C_{x_u} is the change in the force in the X direction due to a change in the forward velocity. The force in the X direction, when the aircraft is in equilibrium flight with $W_0 = 0$, depends on the thrust and the drag. The thrust vector may not be aligned with the velocity vector of the aircraft, but the angle between these two vectors normally is small. Thus by using small-angle assumptions the cosine of the angle can be replaced by 1. Then

$$F_x = T - D = T - C_D\rho\frac{U^2 S}{2} \qquad (1\text{-}71)$$

Differentiating with respect to u, keeping the other parameters constant, Eq. 1-71 becomes

$$\frac{\partial F_x}{\partial u} = \frac{\partial T}{\partial u} - C_D \rho US - \frac{\partial C_D}{\partial u} \rho \frac{U^2 S}{2} \qquad (1\text{-}72)$$

It should be noted that all these partial derivatives and C_D must be evaluated at the equilibrium flight condition. Now

$$C_{x_u} = \frac{U}{Sq} \frac{\partial F_x}{\partial u} \qquad \text{where} \quad q = \frac{\rho}{2} U^2$$

Multiplying Eq. 1-72 by U/Sq, it becomes

$$C_{x_u} = \frac{U}{Sq} \frac{\partial T}{\partial u} - 2C_D - U \frac{\partial C_D}{\partial u} \qquad (1\text{-}73)$$

For a jet aircraft the thrust is essentially constant; thus $\partial T/\partial u = 0$. However, for a propeller driven aircraft the thrust decreases as the velocity increases; thus $\partial T/\partial u$ is negative. The variation of drag with velocity is primarily due to Mach number effects, especially in the transonic region where C_D varies with Mach number at a constant angle of attack. Below Mach 0.6, $\partial C_D/\partial u \approx 0$ (see Appendix D).

C_{z_u} is the change in the force in the Z direction due to a change in the forward velocity. The component of thrust in the Z direction is much less than the lift, thus it may be neglected. Then

$$F_z = -L = -C_L \rho \frac{U^2 S}{2} \qquad (1\text{-}74)$$

Differentiating Eq. 1-74

$$\frac{\partial F_z}{\partial u} = -C_L \rho US - \frac{\partial C_L}{\partial u} \rho \frac{U^2 S}{2} \qquad (1\text{-}75)$$

Multiplying by U/Sq to obtain the nondimensional coefficient, Eq. 1-75 becomes

$$C_{z_u} = \frac{U}{Sq} \frac{\partial F_z}{\partial u} = -2C_L - U \frac{\partial C_L}{\partial u} \qquad (1\text{-}76)$$

The variation of lift coefficient with velocity is primarily due to Mach effects. The lift coefficient normally decreases very rapidly in the transonic region, then rises again. Below about Mach 0.6, $\partial C_L/\partial u \approx 0$ (see Appendix D).

C_{m_u} is the change in the pitching moment due to a change in forward velocity. This term is primarily a result of slipstream effects. However,
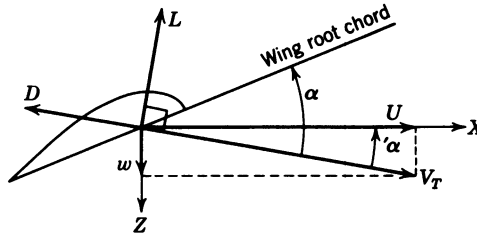
Figure 1-7   *Orientation of the lift and drag vectors after a disturbance producing a vertical velocity.*

aircraft flexibility and compressibility also affect this term. In the transonic region the static stability of the aircraft can vary considerably. Below the transonic region C_{m_u} can be safely neglected for jets. The changes in C_{m_u} are due to the shift, usually rearward, of the center of pressure as the aircraft enters the transonic region, making C_{m_u} negative.

C_{x_α} is the change in the force in the X direction due to a change in α caused by a change in w.

Because the aircraft axes are fixed to the aircraft, a disturbance resulting in a vertical velocity produces lift and drag vectors that are no longer perpendicular to and parallel to the X axis (see Figure 1-7). Thus to find the contributions of the lift and drag to the forces in the X direction it is necessary to resolve them into the X axis through the angle $'\alpha$. Then

$$F_x = L \sin'\alpha - D \cos'\alpha \tag{1-77}$$

Differentiating,

$$\frac{\partial F_x}{\partial'\alpha} = \frac{\partial L}{\partial'\alpha} \sin'\alpha + L \cos'\alpha - \frac{\partial D}{\partial'\alpha} \cos'\alpha + D \sin'\alpha \tag{1-78}$$

As before, the partial derivatives must be evaluated at the equilibrium condition, or when $'\alpha = 0$. Thus Eq. 1-78 becomes

$$\left(\frac{\partial F_x}{\partial'\alpha} \right)_{'\alpha = 0} = L - \frac{\partial D}{\partial'\alpha} = L - \frac{\partial D}{\partial\alpha} \qquad \text{as} \qquad \frac{\partial'\alpha}{\partial\alpha} = 1 \tag{1-79}$$

Multiplying by $1/Sq$ to obtain the nondimensional coefficient, Eq. 1-79 becomes

$$C_{x_\alpha} = \frac{1}{Sq} \left(\frac{\partial F_x}{\partial\alpha} \right) = C_L - \frac{\partial C_D}{\partial\alpha} \tag{1-80}$$

C_{z_α} is the variation of the Z force with angle of attack. This term is very similar to the case of C_{x_α}, and referring to Figure 1-7, the new force in the Z

direction can be expressed as

$$F_z = -L\cos'\alpha - D\sin'\alpha \tag{1-81}$$

Differentiating,

$$\frac{\partial F_z}{\partial'\alpha} = -\frac{\partial L}{\partial'\alpha}\cos'\alpha + L\sin'\alpha - \frac{\partial D}{\partial'\alpha}\sin'\alpha - D\cos'\alpha \tag{1-82}$$

Evaluating at $'\alpha = 0$, as before, Eq. 1-82 becomes

$$\left(\frac{\partial F_z}{\partial'\alpha}\right)_{'\alpha=0} = -\frac{\partial L}{\partial'\alpha} - D = -\frac{\partial L}{\partial\alpha} - D \tag{1-83}$$

Going to coefficient form, Eq. 1-83 becomes

$$C_{z_\alpha} = \frac{1}{Sq}\left(\frac{\partial F_z}{\partial\alpha}\right) = -C_D - \frac{\partial C_L}{\partial\alpha} \simeq -\frac{\partial C_L}{\partial\alpha} \tag{1-84}$$

NOTE. Both $\partial C_D/\partial\alpha$ and $\partial C_L/\partial\alpha$ are the slopes of the drag and lift coefficient curves per radian of angle of attack (see Appendix D).

C_{m_α} is the change in the pitching moment due to a change in angle of attack. This term determines the static longitudinal stability of the aircraft and must be negative for a "statically stable aircraft." A statically stable aircraft is one that tends to return to its equilibrium condition after a disturbance has occurred. A negative C_{m_α} means that as the angle of attack increases positively, the pitching moment becomes more negative, tending to decrease the angle of attack. The opposite is true for a positive C_{m_α}. The positive-C_{m_α} condition and an automatic system for controlling such an aircraft are discussed in Chapter 2.

Now

$$C_{m_\alpha} = \frac{\partial C_m}{\partial\alpha} = \left(\frac{dC_m}{dC_L}\right)_\delta^a \left(\frac{dC_L}{d\alpha}\right)_\delta^a \tag{1-85}$$

where $(dC_m/dC_L)_\delta^a$ means the change in C_m with respect to C_L for the aircraft (a) with the elevator fixed ($\delta = 0$). But $(dC_m/dC_L)_\delta^a$ is the same as the static margin SM, that is, $(dC_m/dC_L)_\delta^a = \text{SM}.$[3]

The static margin is equal to x/c, where x is the distance between the fixed control neutral point and the center of gravity of the aircraft and c is the mean aerodynamic chord (MAC). If the center of gravity is ahead of the fixed control neutral point, x is negative and the aircraft is stable. The fixed control neutral point is the location of the center of gravity for which the static margin is zero, or the point for which $dC_m/d\alpha$ is equal to zero.[1,3]

Therefore

$$C_{m_\alpha} = (SM)_\delta \left(\frac{dC_L}{d\alpha} \right)_\delta^a \tag{1-86}$$

$C_{m_{\dot{\alpha}}}$ is the effect of the rate of change of angle of attack caused by $\dot{w}$ on the pitching moment coefficient. As explained in the paragraph preceding Eq. 1-60, this derivative arises from the time lag required for the wing downwash to reach the tail. The change in the angle of attack of the tail due to a rate of change of the downwash is given by the equation

$$\Delta \alpha_t = \frac{d\epsilon}{dt} \Delta t \tag{1-87}$$

where $\Delta t = l_t / U$ from Eq. 1-63.
Multiplying Eq. 1-87 by $d\alpha / d\alpha$ and substituting for Δt yields

$$\Delta \alpha_t = \frac{d\epsilon}{d\alpha} \frac{d\alpha}{dt} \frac{l_t}{U} = \frac{d\epsilon}{d\alpha} \frac{l_t}{U} \dot{\alpha} \tag{1-88}$$

Taking the derivative with respect to $\dot{\alpha}$, Eq. 1-88 becomes

$$\frac{d(\Delta \alpha_t)}{d\dot{\alpha}} = \frac{d\epsilon}{d\alpha} \frac{l_t}{U} \tag{1-89}$$

Now

$$\frac{\partial C_m}{\partial \dot{\alpha}} = \left(\frac{dC_m}{di} \right)_{\delta,\alpha}^t \frac{d(\Delta \alpha_t)}{d\dot{\alpha}} \tag{1-90}$$

where $(dC_m / di)_{\delta,\alpha}^t$ is the rate of change of the pitching moment coefficient of the tail with respect to the angle of incidence with α and δ, the elevator deflection, constant. But

$$C_{m_{\dot{\alpha}}} = \frac{2U}{c} \frac{\partial C_m}{\partial \dot{\alpha}} = \left(\frac{1}{Sqc} \right) \left(\frac{2U}{c} \right) \left(\frac{\partial \mathcal{M}}{\partial \dot{\alpha}} \right) \tag{1-91}$$

as $\mathcal{M} = SqcC_m$. Multiplying Eq. 1-90 by $2U/c$, substituting for $d(\Delta \alpha_t)/d\dot{\alpha}$, and substituting this into Eq. 1-91, it becomes

$$C_{m_{\dot{\alpha}}} = 2 \left(\frac{dC_m}{di} \right)_{\delta,\alpha}^t \frac{d\epsilon}{d\alpha} \frac{l_t}{c} \tag{1-92}$$
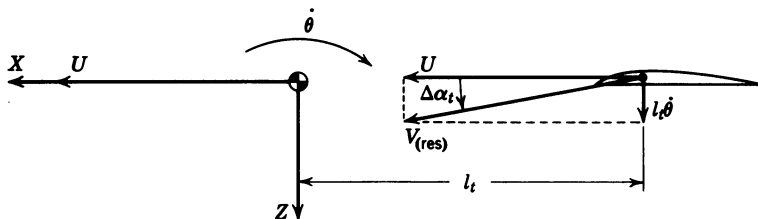
Figure 1-8 *Effect of $\dot\theta$ on the angle of attack of the tail.*

where the theoretical value of $d\epsilon/d\alpha$ is[1]

$$\frac{d\epsilon}{d\alpha} = \frac{2}{\pi R}\left(\frac{dC_L}{d\alpha}\right)^w$$

$C_{z_{\dot\alpha}}$ is the effect of the rate of change of angle of attack caused by $\dot w$ on the Z force. This derivative arises from the same cause as $C_{m_{\dot\alpha}}$ and can be derived from $C_{m_{\dot\alpha}}$ by dividing by a suitable length to obtain a force coefficient from a moment coefficient. The length used is l_t (see Figure 1-8).

To keep the coefficient nondimensional it is multiplied by c, the mean aerodynamic chord. Thus

$$C_{z_{\dot\alpha}} = \frac{c}{l_t}C_{m_{\dot\alpha}} = 2\left(\frac{dC_m}{di}\right)^t_{\delta,\alpha}\left(\frac{d\epsilon}{d\alpha}\right) \tag{1-93}$$

C_{m_q}, the effect on the pitching moment due to a pitch rate, arises from the curvature of the flight path, which causes a change in the angle of attack of the tail. From Figure 1-8 it can be seen that if the aircraft has a pitching velocity, the tail has a vertical velocity component equal to $l_t\dot\theta$. This velocity added vectorially to U yields $V_{(res)}$. Thus the change in the angle of attack resulting from this pitching velocity can be expressed as

$$\Delta\alpha_t = \frac{l_t\dot\theta}{U} \tag{1-94}$$

Differentiating,

$$\frac{d(\Delta\alpha_t)}{d\dot\theta} = \frac{l_t}{U} \tag{1-95}$$

Now

$$\frac{\partial C_m}{\partial\dot\theta} = \left(\frac{dC_m}{di}\right)^t_{\delta,\alpha}\frac{d(\Delta\alpha_t)}{d\dot\theta} = \left(\frac{dC_m}{di}\right)^t_{\delta,\alpha}\frac{l_t}{U} \tag{1-96}$$

But

$$C_{m_q} = \frac{2U}{c} \frac{\partial C_m}{\partial \dot{\theta}} = \left(\frac{1}{Sqc}\right)\left(\frac{2U}{c}\right)\frac{\partial \mathcal{M}}{\partial \dot{\theta}} \qquad (1\text{-}97)$$

Multiplying Eq. 1-96 by $2U/c$ yields

$$C_{m_q} = 2K\left(\frac{dC_m}{di}\right)_{\delta,\alpha}^{t}\left(\frac{l_t}{c}\right) \qquad (1\text{-}98)$$

where the factor K makes a rough allowance for the contribution of the rest of the aircraft to C_{m_q} and is usually about 1.1. For a swept wing aircraft the factor may be higher.

C_{z_q} is the change in the Z force due to a pitching velocity. As in the case of $C_{z_{\dot{\alpha}}}$, this stability derivative can be obtained from C_{m_q} by multiplying by c/l_t. Thus

$$C_{z_q} = \frac{c}{l_t}C_{m_q} = 2K\left(\frac{dC_m}{di}\right)_{\delta,\alpha}^{t} \qquad (1\text{-}99)$$

C_{z_q} and $C_{z_{\dot{\alpha}}}$ are often neglected in the final equations of motion. This results, not from the fact that these terms are negligible in comparison with the other stability derivatives (as in the case of $C_{x_{\dot{\alpha}}}$ and C_{x_q}), but from the fact that they are negligible when combined with the other terms which form the coefficients of $'\dot{\alpha}$ and q, respectively. Thus

$$\frac{c}{2U}C_{z_{\dot{\alpha}}} \ll \frac{mU}{Sq} \quad \text{and} \quad \frac{c}{2U}C_{z_q} \ll \frac{mU}{Sq}.$$

However, the relative magnitudes of these terms should be checked for any particular set of stability derivatives and flight conditions.

C_{m_a} is the effect on the pitching moment resulting from the movement of some external control surface, in this case and those to follow, the elevator. For an aircraft with conventional elevators

$$C_{m_a} = C_{m_{\delta_e}}\delta_e \qquad (1\text{-}100)$$

where $C_{m_{\delta_e}}$ is the elevator effectiveness. For an aircraft with a so-called "flying tail,"

$$C_{m_a} = C_{m_{i_t}}\delta_{i_t} = \left(\frac{\partial C_m}{\partial i}\right)_{\alpha}^{t}\delta_{i_t} \qquad (1\text{-}101)$$

$C_{F_{z_a}}$ is the effect on the forces in the Z direction due to the deflection of the elevator:

$$C_{F_{z_a}} = C_{z_{\delta_e}}\delta_e = \frac{c}{l_t}C_{m_{\delta_e}}\delta_e \qquad (1\text{-}102)$$

$C_{F_{x_a}}$ is the effect on the forces in the X direction due to the deflection of the elevator. This is a change in the drag due to the elevator deflection and is usually neglected.

For the longitudinal equations only the effect of the elevator has been considered. The gear, flaps, and dive brakes also cause changes in the forces and moments and would appear on the right hand side of the equations along with C_{m_a}, $C_{F_{z_a}}$, and $C_{F_{x_a}}$. However, for most cases, if it is necessary to study the dynamics of the aircraft with the gear and/or flaps down, it can be assumed that the aircraft is in equilibrium in the desired configuration. The stability derivatives for that configuration then are used when proceeding with the desired dynamic analysis. If it is necessary to study the effect of the operation of the gear, flaps, or other force or moment producing devices, this can best be done by simulation on an analog computer.

In Section 1-8 a particular aircraft is studied, and the equations of motions solved.

1-8 SOLUTION OF THE LONGITUDINAL EQUATIONS (STICK FIXED)

In solving the equations of motion it is first necessary to obtain the transient solution, which is obtained from the homogeneous equations, that is, with no external inputs: $C_{m_a} = C_{F_{z_a}} = C_{F_{x_a}} = 0$. Taking the Laplace transform[4] of Eq. 1-59 with the initial conditions zero and neglecting $C_{x_{\dot{a}}}$, C_{x_q}, and C_{m_u} yields

$$\left(\frac{mU}{Sq}s - C_{x_u}\right)'u(s) - C_{x_a}'\alpha(s) - C_w(\cos\Theta)\theta(s) = 0$$

$$-C_{z_u}'u(s) + \left[\left(+\frac{mU}{Sq} - \frac{c}{2U}C_{z_{\dot{a}}}\right)s - C_{z_a}\right]'\alpha(s) \cdot$$

$$+\left[\left(-\frac{mU}{Sq} - \frac{c}{2U}C_{z_q}\right)s - C_w(\sin\Theta)\right]\theta(s) = 0$$

$$\left(-\frac{c}{2U}C_{m_{\dot{a}}}s - C_{m_a}\right)'\alpha(s) + \left(\frac{I_y}{Sqc}s^2 - \frac{c}{2U}C_{m_q}s\right)\theta(s) = 0 \qquad (1\text{-}103)$$

For this example the values of the stability derivatives for a four-engine jet transport are used. The aircraft is flying in straight and level flight at 40,000 ft

with a velocity of 600 ft/sec (355 knots), and the compressibility effects will be neglected. For this aircraft the values are as follows:

$$\Theta = 0$$

$$\text{Mach} = 0.62$$

$$m = 5800 \text{ slugs}$$

$$U = 600 \text{ ft/sec}$$

$$S = 2400 \text{ sq ft}$$

$$I_y = 2.62 \times 10^6 \text{ slug ft}^2$$

$$C_{x_u} = -2C_D = -0.088$$

$$C_{x_\alpha} = -\frac{\partial C_D}{\partial \alpha} + C_L = 0.392$$

$$C_w = -\frac{mg}{Sq} = -C_L = -0.74$$

$$\frac{l_t}{c} = 2.89$$

$$c = 20.2 \text{ ft}$$

$$C_{z_u} = -2C_L = -1.48$$

$$C_{z_{\dot\alpha}} = \left(\frac{dC_m}{di_t}\right)^t_{\delta,\alpha} \left(\frac{d\epsilon}{d\alpha}\right)(2) = (-1.54)(0.367)(2) = -1.13$$

$$C_{z_\alpha} = -\frac{\partial C_L}{\partial \alpha} - C_D = -4.42 - 0.04 = -4.46$$

$$C_{z_q} = 2K\left(\frac{dC_m}{di}\right)^t_{\delta,\alpha} = 2.56(-1.54) = -3.94$$

$$C_{m_{\dot\alpha}} = 2\left(\frac{dC_m}{di}\right)^t_{\delta,\alpha}\left(\frac{d\epsilon}{d\alpha}\right)\frac{l_t}{c} = (-1.54)(0.367)(2)(2.89)$$

$$C_{m_{\dot\alpha}} = -3.27$$

$$C_{m_\alpha} = (\text{SM})_\delta\left(\frac{dC_L}{d\alpha}\right)^a_\delta = (-0.14)(4.42) = -0.619$$

$$C_{m_q} = 2K\left(\frac{dC_m}{di}\right)^t_{\delta,\alpha}\left(\frac{l_t}{c}\right)$$

$$C_{m_q} = (2.56)(-1.54)(2.89) = -11.4$$

Instead of 1.1, 1.28 is used for K, to take account of the increased contribution of the swept wing to C_{m_q} and C_{z_q}. Then

$$q = \frac{\rho}{2}U^2 = \frac{(0.000585)(600)^2}{2} = 105.1 \text{ lb/sq ft}$$

$$\frac{mU}{Sq} = \frac{(5800)(600)}{(2400)(105.1)} = 13.78 \text{ sec}$$

$$\frac{c}{2U}C_{z_{\dot{\alpha}}} = \frac{(20.2)(-1.13)}{(2)(600)} = -0.019 \text{ sec}$$

$$\frac{c}{2U}C_{z_q} = (0.0168)(-3.94) = -0.066 \text{ sec}$$

$$\frac{c}{2U}C_{m_{\dot{\alpha}}} = (0.0168)(-3.27) = -0.0552 \text{ sec}$$

$$\frac{c}{2U}C_{m_q} = (0.0168)(-11.4) = -0.192 \text{ sec}$$

$$\frac{I_y}{Sqc} = \frac{(2.62\times10^6)}{(2400)(105.1)(20.2)} = 0.514 \text{ sec}^2$$

From the preceding equations it can be seen that $(c/2U)C_{z_{\dot{\alpha}}}$ and $(c/2U)C_{z_q}$ are much smaller than mU/Sq and can be neglected in this case. Substituting these values into Eq. 1-103, it becomes

$$(13.78s +0.088)\,'u(s) -0.392\,'\alpha(s) +0.74\theta(s) = 0$$

$$1.48\,'u(s) +(13.78s +4.46)\,'\alpha(s) -13.78s\theta(s) = 0$$

$$0+(0.0552s +0.619)\,'\alpha(s) +(0.514s^2 +0.192s)\theta(s) = 0 \quad (1\text{-}104)$$

The only nonzero solution of these simultaneous equations requires that the determinant of the coefficients be zero. Thus

$$\begin{vmatrix} 13.78s +0.088 & -0.392 & 0.74 \\ 1.48 & 13.78s +4.46 & -13.78s \\ 0 & 0.0552s +0.619 & 0.514s^2 +0.192s \end{vmatrix} = 0 \quad (1\text{-}105)$$

Expanding this determinant, the following quartic equation is obtained (see Appendix E for method):

$$97.5s^4 +79s^3 +128.9s^2 +0.998s +0.677 = 0 \quad (1\text{-}106)$$

Dividing through by 97.5, the equation reduces to

$$s^4 + 0.811s^3 + 1.32s^2 + 0.0102s + 0.00695 = 0 \qquad (1\text{-}107)$$

At this time it is not necessary to determine the magnitudes of the variations of $'u$, $'\alpha$, and θ. [As the transient response of all three variables will be of the same form, their time variation is of greatest interest now.] In Section 1-9 the magnitude of these variations will be discussed. The response will be of the form $Ae^{s_1t} + Be^{s_2t} + Ce^{s_3t} + De^{s_4t}$, where s_1, s_2, etc. are the roots of the characteristic equation. Thus it is necessary to factor Eq. 1-107 to obtain the roots. Since the roots of this quartic lead to two sets of complex roots indicating two damped sinusoidal oscillations, and as a result of the relative magnitudes of the coefficients, Lin's[5] method provides the quickest procedure for obtaining the two quadratic factors, if a computer or calculator program is not available. To do this it is necessary to obtain the first trial divisor. This is done by dividing the coefficients of the last three terms by the coefficient of the s^2 term. Then using synthetic division,

```
1+0.0077+0.0053)  1  0.811    1.32     0.0102  0.00695
                  1  0.0077   0.0053
                  ─────────────────────
                     0.8033   1.3147   0.0102
                     0.8033   0.0062   0.0041
                     ─────────────────────────
                              1.3085   0.0061  0.00695
                              1.3085   0.0101  0.00694
                              ──────────────────────────
```

For the next trial divisor take $1.3085 + 0.0061 + 0.00695$ divided by 1.3085, or $1 + 0.00466 + 0.0053$. Then, again using synthetic division,

```
1+0.00466+0.0053)  1  0.811     1.32     0.0102  0.00695
                   1  0.00466   0.0053
                   ─────────────────────
                      0.80634   1.3147   0.0102
                      0.80634   0.0037   0.0043
                      ─────────────────────────
                                1.311    0.0059  0.00695
                                1.311    0.0061  0.00695
                                ───────────────────
                                         ~0
```

Therefore the two quadratic factors are

$$(s^2 + 0.00466s + 0.0053)(s^2 + 0.806s + 1.311) = 0 \qquad (1\text{-}108)$$

A common way to write such quadratics is to indicate the natural frequency ω_n and the damping ratio ζ as $(s^2 + 2\zeta\omega_n s + \omega_n^2)$. Doing this, Eq.

1-108 becomes

$$\left(s^2 + 2\zeta_p \omega_{np} s + \omega_{np}^2\right)\left(s^2 + 2\zeta_s \omega_{ns} s + \omega_{ns}^2\right) \tag{1-109}$$

Then

$$\left.\begin{array}{l} \zeta_s = 0.352 \\ \omega_{ns} = 1.145 \text{ rad/sec} \end{array}\right\} \quad \text{Short-period oscillation}$$

$$\left.\begin{array}{l} \zeta_p = 0.032 \\ \omega_{np} = 0.073 \text{ rad/sec} \end{array}\right\} \quad \text{Phugoid oscillation}$$

The characteristic modes for nearly all aircraft in most flight conditions are two oscillations: one of short period with relatively heavy damping, the other of long period with very light damping. The periods and the damping of these oscillations vary from aircraft to aircraft and with the flight conditions. The short-period oscillation is called the "short-period mode" and primarily consists of variations in $'\alpha$ and θ with very little change in the forward velocity. The long-period oscillation is called the "phugoid mode" and primarily consists of variations of θ and $'u$ with $'\alpha$ about constant. The phugoid mode can be thought of as an exchange of potential and kinetic energy. The aircraft tends to fly a sinusoidal flight path in the vertical plane. As the aircraft proceeds from the highest point of the flight path to the lowest point, it picks up speed, thus increasing the lift of the wing and curving the flight path until the aircraft starts climbing again and the velocity decreases; the lift decreases and the flight path curves downward. This condition continues until the motion is damped out, which generally requires a considerable number of cycles. However, the period is very long, and the pilot can damp the phugoid successfully even if it is slightly divergent or unstable.

A good measure of the damping of an oscillation is the time required for the oscillation to damp to one-half amplitude. This measure of the damping can be expressed as

$$T_{1/2} = \frac{0.693}{\zeta \omega_n} \tag{1-110}$$

as $e^{-0.693} = \frac{1}{2}$. For the short-period mode

$$T_{1/2} = \frac{0.693}{0.406} = 1.72 \text{ sec} \tag{1-111}$$

For the phugoid mode

$$T_{1/2} = \frac{0.693}{0.00233} = 298 \text{ sec} = 4.96 \text{ min} \tag{1-112}$$

The damping ratio for the short-period mode is fairly representative. Some conventional aircraft will have larger values; however, some of our jet fighters have much lower values, making it necessary to add damping by means of a servo system, which is discussed in Chapter 2.

1-9 LONGITUDINAL TRANSFER FUNCTION FOR ELEVATOR DISPLACEMENT

To obtain the transfer function it is necessary to obtain values for $C_{m_{\delta_e}}$ and $C_{z_{\delta_e}}$; these values are $C_{m_{\delta_e}} = -0.710$, $C_{z_{\delta_e}} = (c/l_t)C_{m_{\delta_e}} = (0.346)(-0.710) = -0.246$. $C_{x_{\delta_e}}$ will be neglected. The signs of these stability derivatives are determined by the elevator sign convention discussed in the next paragraph.

It is now necessary to define the positive deflection of the elevator. Down elevator (stick forward) is defined as "positive elevator" by NACA convention. Thus a positive elevator deflection produces a negative θ, which means that the transfer function for elevator deflection input to θ output is negative. For this reason some references reverse the elevator sign convention; however, that is not done in this book.

Taking the Laplace transform of Eq. 1-59 with the initial conditions zero, and after the substitution of the appropriate values, yields

$$(13.78s + 0.088)\,'u(s) - 0.392\,'\alpha(s) + 0.74\theta(s) = 0$$

$$1.48\,'u(s) + (13.78s + 4.46)\,'\alpha(s) - 13.78s\theta(s) = -0.246\delta_e(s)$$

$$(0.0552s + 0.619)\,'\alpha(s) + (0.514s^2 + 0.192s)\theta(s) = -0.710\delta_e(s) \tag{1-113}$$

where δ_e is the elevator deflection in radians. The transfer function for δ_e input to $'u$ output using determinants is (see Appendix E for method).

$$\frac{'u(s)}{\delta_e(s)} = \frac{\begin{vmatrix} 0 & -0.392 & 0.74 \\ -0.246 & 13.78s + 4.46 & -13.78s \\ -0.710 & 0.0552s + 0.619 & 0.514s^2 + 0.192s \end{vmatrix}}{\nabla} \tag{1-114}$$

where ∇ is the determinant of the homogeneous equation,

$$\nabla = 97.5(s^2 + 0.00466s + 0.0053)(s^2 + 0.806s + 1.311) \tag{1-115}$$

Expanding the numerator determinant, Eq. 1-114 becomes

$$\frac{'u(s)}{\delta_e(s)} = \frac{-0.0494(s^2 - 68.2s - 45)}{\nabla} \tag{1-116}$$

or

$$\frac{'u(s)}{\delta_e(s)} = \frac{-0.000506(s - 68.8)(s + 0.6)}{(s^2 + 0.00466s + 0.0053)(s^2 + 0.806s + 1.311)} \tag{1-117}$$

[An examination of Eq. 1-117 indicates that there is a zero in the right half plane, thus indicating a so-called nonminimum phase angle transfer function. This means that for a positive step input of δ_e the steady-state sign of $'u$ will be positive.] Putting this expression in the alternative form of the transfer function, Eq. 1-117 becomes (see Appendix C)

$$\frac{'u(s)}{\delta_e(s)} = \frac{-3\left(\dfrac{s}{68.8} - 1\right)\left(\dfrac{s}{0.6} + 1\right)}{\left[\left(\dfrac{s}{0.073}\right)^2 + \dfrac{2(0.032)}{0.073}s + 1\right]\left[\left(\dfrac{s}{1.145}\right)^2 + \dfrac{2(0.352)}{1.145}s + 1\right]} \tag{1-118}$$

To obtain the steady-state value of u per unit elevator step input, apply the final value theorem to Eq. 1-118 (see Appendix C).]

$$\frac{u}{\delta_e} = \frac{'uU}{\delta_e}\frac{\text{ft/sec}}{\text{rad}} = \frac{'uU}{57.3\delta_e}\frac{\text{ft/sec}}{\text{deg}} \tag{1-119}$$

but $U = 600$ ft/sec. Therefore

$$\frac{u}{\delta_e} = \frac{3(600)}{57.3} = 31.4\frac{\text{ft/sec}}{\text{deg}} \tag{1-120}$$

The transfer function for δ_e input to $'\alpha$ output in determinant form is

$$\frac{'\alpha(s)}{\delta_e(s)} = \frac{\begin{vmatrix} 13.78s + 0.088 & 0 & 0.74 \\ 1.48 & -0.246 & -13.78s \\ 0 & -0.710 & 0.514s^2 + 0.192s \end{vmatrix}}{\nabla} \tag{1-121}$$
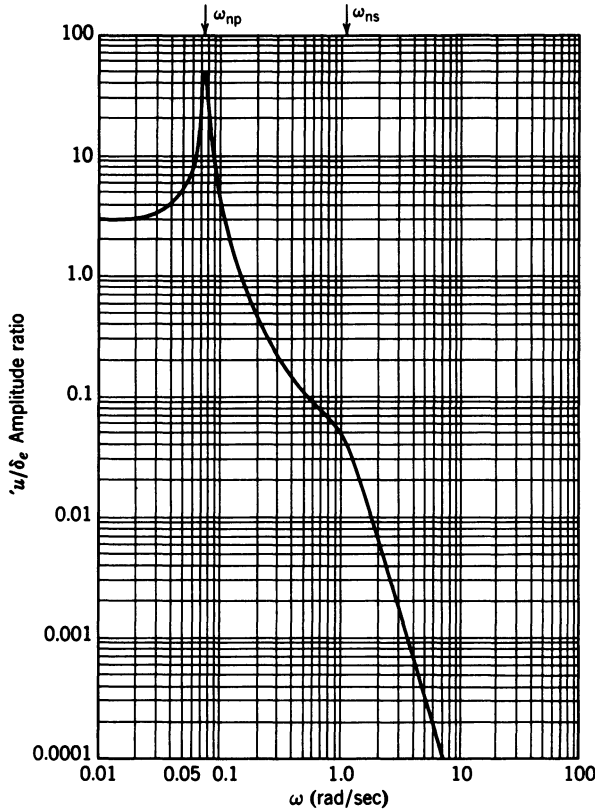
Expanding, Eq. 1-121 becomes

$$\frac{'\alpha(s)}{\delta_e(s)} = \frac{-0.01785(s^3 + 77.8s^2 + 0.496s + 0.446)}{(s^2 + 0.00466s + 0.0053)(s^2 + 0.806s + 1.311)} \tag{1-122}$$

Factoring the numerator,

$$\frac{'\alpha(s)}{\delta_e(s)} = \frac{-0.01785(s+77.79)(s^2+0.0063s+0.0057)}{(s^2+0.00466s+0.0053)(s^2+0.806s+1.311)} \quad (1\text{-}123)$$

Going to the alternative form, Eq. 1-123 becomes

$$\frac{'\alpha(s)}{\delta_e(s)} = \frac{-1.14\left(\dfrac{s}{77.79}+1\right)\left[\left(\dfrac{s}{0.0755}\right)^2+\dfrac{2(0.041)}{0.0755}s+1\right]}{\left[\left(\dfrac{s}{0.073}\right)^2+\dfrac{2(0.032)}{0.073}s+1\right]\left[\left(\dfrac{s}{1.145}\right)^2+\dfrac{2(0.352)}{1.145}s+1\right]} \quad (1\text{-}124)$$

Figure 1-9 Magnitude plot for $'u/\delta_e$ transfer function versus ω for $s = j\omega$.

For δ_e input to θ output,

$$\frac{\theta(s)}{\delta_e(s)} = \frac{\begin{vmatrix} 13.78s + 0.088 & -0.392 & 0 \\ 1.48 & 13.78s + 4.46 & -0.246 \\ 0 & 0.0552s + 0.619 & -0.710 \end{vmatrix}}{\nabla} \quad (1\text{-}125)$$

Expanding and factoring,

$$\frac{\theta(s)}{\delta_e(s)} = \frac{-1.31(s+0.016)(s+0.3)}{(s^2 + 0.00466s + 0.0053)(s^2 + 0.806s + 1.311)} \quad (1\text{-}126)$$
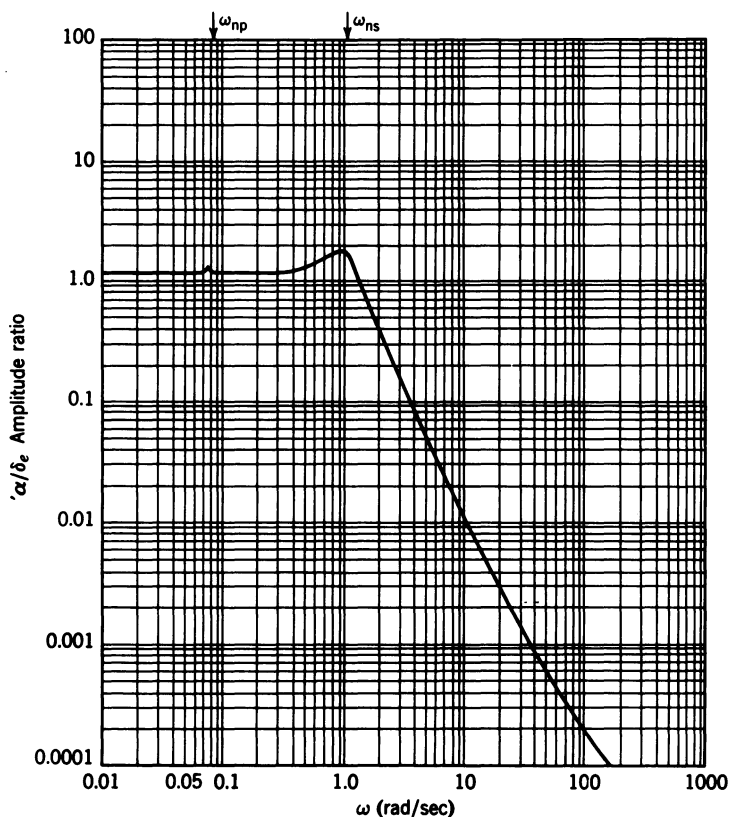
Figure 1-10   *Magnitude plot for 'α / δ_e transfer function versus ω for s = jω.*
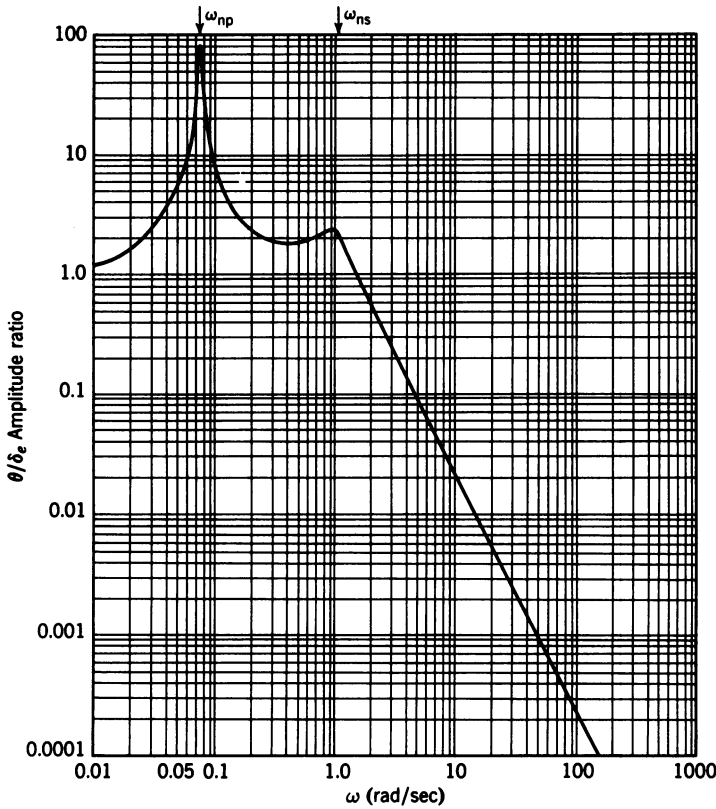
Figure 1-11 Magnitude plot for θ / δ_e transfer function versus ω for $s = j\omega$.

or in the alternative form

$$\frac{\theta(s)}{\delta_e(s)} = \frac{-0.95\left(\frac{s}{0.016}+1\right)\left(\frac{s}{0.3}+1\right)}{\left[\left(\frac{s}{0.073}\right)^2 + \frac{2(0.032)}{0.073}s+1\right]\left[\left(\frac{s}{1.145}\right)^2 + \frac{2(0.352)}{1.145}s+1\right]} \quad (1\text{-}127)$$

The steady-state values for $'\alpha(s)/\delta_e(s)$ and $\theta(s)/\delta_e(s)$ for a unit step input can be obtained directly from Eqs. 1-124 and 1-127, respectively; as both of these equations represent the ratios of two angles, the units may be either radians or degrees.

Figures 1-9, 1-10, and 1-11 are amplitude ratio plots of Eqs. 1-118, 1-124, and 1-127 against ω for $s = j\omega$. Figure 1-9 shows that the amplitude of the $'u/\delta_e$ response is very small at the natural frequency of the short-period

oscillation. This statement substantiates the one made in Section 1-8 that there is very little change in the forward velocity during the short-period oscillation.

An examination of Eq. 1-124 and Figure 1-10 indicates that the numerator quadratic effectively cancels the phugoid quadratic, thus substantiating the earlier statement that the phugoid oscillation takes place at almost constant angle of attack.

Figure 1-11 shows that a considerable variation in θ occurs at both the phugoid and short-period frequencies. These observations lead to the following approximations of the phugoid and short-period oscillations:

Short-Period Approximation. As mentioned earlier, the short-period oscillation occurs at almost constant forward speed; therefore, let $'u = 0$ in the equations of motion. The X equation can be neglected, as it does not contribute much to the short-period oscillation: forces in the X direction contribute mostly to changes in forward speed. With these assumptions and by neglecting $C_{z_{\dot{\alpha}}}$ and C_{z_q} and inserting $C_{z_{\delta_e}}$ and $C_{m_{\delta_e}}$, Eq. 1-103 becomes

$$\left(\frac{mU}{Sq}s - C_{z_\alpha}\right)'\alpha(s) + \left[-\frac{mU}{Sq}s - C_w(\sin\Theta)\right]\theta(s) = C_{z_{\delta_e}}\delta_e(s)$$

$$\left(-\frac{c}{2U}C_{m_{\dot{\alpha}}}s - C_{m_\alpha}\right)'\alpha(s) + \left(\frac{I_y}{Sqc}s^2 - \frac{c}{2U}C_{m_q}s\right)\theta(s) = C_{m_{\delta_e}}\delta_e(s) \quad (1\text{-}128)$$

Before evaluating the transfer functions to compare them with those obtained from the complete equations, the determinant of the homogeneous equation is first expanded in general terms. Thus with $\Theta = 0$ Eq. 1-128 becomes

$$\begin{vmatrix} \left(\dfrac{mU}{Sq}s - C_{z_\alpha}\right) & \dfrac{-mU}{Sq}s \\[2em] \left(\dfrac{-c}{2U}C_{m_{\dot{\alpha}}}s - C_{m_\alpha}\right) & \left(\dfrac{I_y}{Sqc}s^2 - \dfrac{c}{2U}C_{m_q}s\right) \end{vmatrix} = 0 \qquad (1\text{-}129)$$

The expansion of this expression can be written in the form of

$$s(As^2 + Bs + C) = 0$$

where

$$A = \left(\frac{I_y}{Sqc}\right)\left(\frac{mU}{Sq}\right)$$

$$B = \left(\frac{-c}{2U}C_{m_q}\right)\left(\frac{mU}{Sq}\right) - \frac{I_y}{Sqc}C_{z_\alpha} - \left(\frac{c}{2U}C_{m_{\dot{\alpha}}}\right)\left(\frac{mU}{Sq}\right)$$

$$C = \frac{c}{2U}C_{m_q}C_{z_\alpha} - \frac{mU}{Sq}C_{m_\alpha} \qquad\qquad (1\text{-}130)$$

If Eq. 1-130 is divided by A and written in the standard form of the quadratic with ζ and ω_n, then

$$2\zeta\omega_n = \frac{B}{A} \qquad\qquad (1\text{-}131)$$

and

$$\omega_n^2 = \frac{C}{A} \qquad\qquad (1\text{-}132)$$

Substituting for C/A and taking the square root, Eq. 1-132 becomes

$$\omega_n = \left|\frac{\dfrac{c}{2U}C_{m_q}C_{z_\alpha} - \dfrac{mU}{Sq}C_{m_\alpha}}{\left(\dfrac{I_y}{Sqc}\right)\left(\dfrac{mU}{Sq}\right)}\right|^{1/2} \qquad\qquad (1\text{-}133)$$

Substituting $(\rho/2)U^2$ for q and simplifying, Eq. 1-133 becomes

$$\omega_n = \frac{U\rho Sc}{2}\left|\frac{\dfrac{C_{m_q}C_{z_\alpha}}{2} - \dfrac{2m}{\rho Sc}C_{m_\alpha}}{I_y m}\right|^{1/2} \sim U\sqrt{\rho} \qquad\qquad (1\text{-}134)$$

Substituting for B/A and solving for ζ, Eq. 1-131 becomes

$$\zeta = \frac{-\dfrac{c}{2U}\dfrac{mU}{Sq}(C_{m_{\dot{\alpha}}}+C_{m_q})-\dfrac{I_y}{Sqc}C_{z_\alpha}}{\left(\dfrac{I_y}{Sqc}\right)\left(\dfrac{mU}{Sq}\right)(U\rho Sc)\left(\dfrac{\dfrac{C_{m_q}C_{z_\alpha}}{2}-\dfrac{2m}{\rho Sc}C_{m_\alpha}}{I_y m}\right)^{1/2}} \qquad (1\text{-}135)$$

Substituting for q and simplifying, Eq. 1-135 becomes

$$\zeta = -\frac{1}{4}\left(C_{m_q}+C_{m_{\dot{\alpha}}}+\frac{2I_y}{mc^2}C_{z_\alpha}\right)\left(\frac{mc^2}{I_y\left(\dfrac{C_{m_q}C_{z_\alpha}}{2}-\dfrac{2mC_{m_\alpha}}{\rho Sc}\right)}\right)^{1/2} \qquad (1\text{-}136)$$

From an investigation of Eqs. 1-134 and 1-136 we can see that, for a given altitude, the natural frequency of the short-period oscillation is proportional to U while the damping ratio is constant. However, both the natural frequency and the damping ratio vary with altitude. They are roughly proportional to $\sqrt{\rho}$ and decrease as the altitude increases (see Ref. 3 for a table of ρ versus altitude).

Let us calculate the transfer functions for the approximation to the short-period oscillation. The values of ζ and ω_n can be calculated from Eqs. 1-134 and 1-136, but the numerator must still be evaluated, so that it is just as easy to return to the basic equation. Substituting the proper values into Eq. 1-128, the determinant form for the $'\alpha(s)/\delta_e(s)$ transfer function is

$$\frac{'\alpha(s)}{\delta_e(s)} = \frac{\begin{vmatrix} -0.246 & -13.78s \\ -0.710 & 0.514s^2+0.192s \end{vmatrix}}{\begin{vmatrix} 13.78s+4.46 & -13.78s \\ 0.0552s+0.619 & 0.514s^2+0.192s \end{vmatrix}} \qquad (1\text{-}137)$$

Expanding,

$$\frac{'\alpha(s)}{\delta_e(s)} = \frac{-0.01782(s+77.8)}{s^2+0.805s+1.325} \qquad (1\text{-}138)$$

Going to the alternative form,

$$\frac{'\alpha(s)}{\delta_e(s)} = \frac{-1.05\left(\dfrac{s}{77.8}+1\right)}{\left(\dfrac{s}{1.15}\right)^2 + \dfrac{2(0.35)}{1.15}s + 1} \tag{1-139}$$

A comparison of Eqs. 1-139 and 1-124 shows excellent agreement, again substantiating the original assumption. The $\theta(s)/\delta_e(s)$ transfer function will now be evaluated. From Eq. 1-128

$$\frac{\theta(s)}{\delta_e(s)} = \frac{\begin{vmatrix} 13.78s+4.46 & -0.246 \\ 0.0552s+0.619 & -0.710 \end{vmatrix}}{\begin{vmatrix} 13.78s+4.46 & -13.78s \\ 0.0552s+0.619 & 0.514s^2+0.192s \end{vmatrix}} \tag{1-140}$$

Expanding,

$$\frac{\theta(s)}{\delta_e(s)} = \frac{-1.39(s+0.306)}{s(s^2+0.805s+1.325)} \tag{1-141}$$

Going to the alternative form,

$$\frac{\theta(s)}{\delta_e(s)} = \frac{-0.321\left(\dfrac{s}{0.306}+1\right)}{s\left[\left(\dfrac{s}{1.15}\right)^2 + \dfrac{2(0.35)}{1.15}s + 1\right]} \tag{1-142}$$

The magnitude plot of Eq. 1-142 is shown in Figure 1-12. A comparison of Figures 1-11 and 1-12 shows very good agreement in the vicinity of the natural frequency of the short-period mode. It should be noted that Eq. 1-142 has a pole at $s = 0$, that is, a root of the denominator of this equation is $s = 0$. This s in the denominator mathematically represents a pure integration. As a result, if δ_e is a step (that is, a constant), the output θ will be the integral of this constant and will approach infinity as time approaches infinity. However, $\dot{\theta}$ will reach a constant value for a step input of δ_e. Such a constant value results from the fact that multiplying by s is equivalent to differentiating; thus $\dot{\theta}(s)/\delta_e(s) = s\theta(s)/\delta_e(s)$. The s in the denominator of Eq. 1-142 results from the fact that Θ was taken as zero in Eq. 1-128, which effectively eliminates the effects of gravity from the short-period approximation. However, this does not invalidate the use of the short-period approximation for studying the short-period mode of oscillation. For these studies the frequency of oscillation and the damping after the aircraft has been disturbed from equilibrium are of primary interest. This information can be
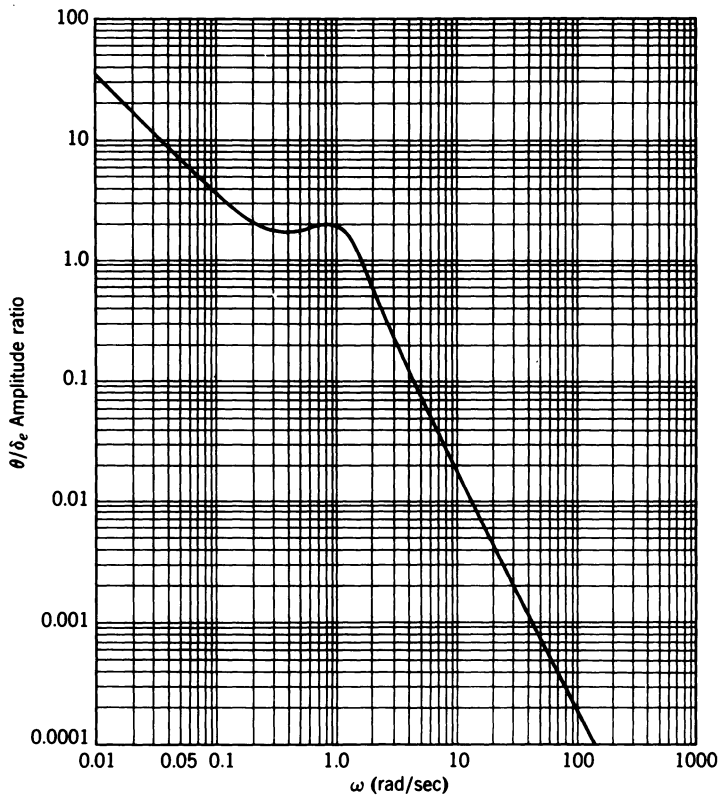
Figure 1-12 *Magnitude plot for* θ / δ_e *transfer function versus* ω *for* $s = j\omega$, *short-period approximation.*

obtained from the short-period approximation; thus it will be used in the study of the longitudinal autopilots.

Phugoid Approximation. As stated in Section 1-8, the phugoid oscillation takes place at almost constant angle of attack; thus $'\alpha$ can be set equal to zero in Eq. 1-103. The next problem is to determine which two of the three equations to retain. As the phugoid oscillation is of long period, θ is varying quite slowly; therefore, the inertia forces can be neglected, leaving for the $\mathcal{M}$ equation

$$\frac{-c}{2U} C_{m_q} s\theta(s) = C_{m_{\delta_e}} \delta_e(s) \tag{1-143}$$

If this equation is combined with either the X or the Z equation with $'\alpha = 0$, the resulting homogeneous equation is not oscillatory. This could hardly represent the phugoid mode. Thus it is necessary to use the X and Z equations.

Then, for $\Theta = 0$ and neglecting C_{z_q}, Eq. 1-103 becomes

$$\left(\frac{mU}{Sq}s - C_{x_u}\right)'u(s) - C_w\theta(s) = 0$$

$$- C_{z_u}'u(s) - \left(\frac{mU}{Sq}s\right)\theta(s) = 0 \tag{1-144}$$

In determinant form,

$$\begin{vmatrix} \left(\dfrac{mU}{Sq}s - C_{x_u}\right) & -C_w \\ -C_{z_u} & -\dfrac{mU}{Sq}s \end{vmatrix} = 0$$

Expanding,

$$-\left(\frac{mU}{Sq}\right)^2 s^2 + \frac{mU}{Sq}C_{x_u}s - C_w C_{z_u} = 0 \tag{1-145}$$

But $C_w = -C_L$. Substituting for C_w and dividing by $-(mU/Sq)^2$, Eq. 1-145 becomes

$$s^2 - \frac{C_{x_u}}{mU/Sq}s - \frac{C_{z_u}C_L}{(mU/Sq)^2} = 0 \tag{1-146}$$

Then

$$\omega_{np} = \frac{\sqrt{-C_{z_u}C_L}}{mU/Sq} \qquad \text{but} \qquad \frac{mU}{Sq} = \frac{2mU}{S\rho U^2} = \frac{2m}{\rho SU}$$

Substituting for mU/Sq,

$$\omega_{np} = \frac{\rho SU\sqrt{-C_{z_u}C_L}}{2m} \tag{1-147}$$

But from Table 1-1, $C_{z_u} \approx -2C_L = -2(2mg/\rho SU^2)$. Substituting, Eq. 1-147 becomes

$$\omega_{np} = \frac{g}{U}\sqrt{2} \qquad \text{or} \qquad T_p = 0.138U \tag{1-148}$$

The damping ratio can also be obtained from Eq. 1-146:

$$\zeta_p = \frac{-C_{x_u}}{2\dfrac{mU}{Sq}\sqrt{\dfrac{-C_{z_u}C_L}{mU/Sq}}} = \frac{-C_{x_u}}{2\sqrt{-C_{z_u}C_L}} \qquad (1\text{-}149)$$

From Table 1-1, $C_{x_u} \simeq -2C_D$ and $C_{z_u} \simeq -2C_L$. Substituting this, Eq. 1-149 becomes

$$\zeta_p = \frac{2C_D}{2\sqrt{2C_L^2}} = \frac{C_D}{C_L\sqrt{2}} = \frac{D}{W\sqrt{2}} \qquad (1\text{-}150)$$

This operation assumes that the $\partial C_D/\partial u = \partial C_L/\partial u \simeq 0$, which is valid for low Mach numbers as explained in Section 1-7. If this is not true, the damping of the phugoid mode is also dependent upon the forward velocity.

   With this assumption it can be seen from Eq. 1-150 that the damping of the phugoid mode is dependent upon the drag. Thus for present-day jet aircraft, where the emphasis is on low drag, the damping is very low. An examination of Eq. 1-148 indicates that the natural frequency of the phugoid mode is inversely proportional to the forward speed and is independent of ρ. The validity of these conclusions is checked in Section 1-10, where the effects of changes in airspeed and altitude on the short-period and phugoid modes are studied in detail.

   The two transfer functions for the phugoid mode can be evaluated from Eq. 1-113 with $'\alpha(s) = 0$ and by taking the X and Z equations. The $'u(s)/\delta_e(s)$ transfer function is

$$\frac{'u(s)}{\delta_e(s)} = \frac{-0.0009}{s^2 + 0.00645s + 0.00582} \qquad (1\text{-}151)$$

or

$$\frac{'u(s)}{\delta_e(s)} = \frac{-0.165}{\left(\dfrac{s}{0.0765}\right)^2 + \dfrac{2(0.042)}{0.0765}s + 1} \qquad (1\text{-}152)$$

   A comparison of Eqs. 1-152 and 1-118 shows good agreement for the natural frequencies and damping ratios, but here the agreement ends. The error coefficient K' is 0.165 instead of 3, and, as discussed in Section 1-10, there is a 180° phase shift between the two equations. For the complete equation a positive elevator deflection gives a positive value of $'u$, while from the approximation the initial value of $'u$ will be negative. This means that for a down elevator, which should cause the aircraft to accelerate, the aircraft slows. This condition results from the elimination of the $\mathscr{M}$ equation, that is,

$C_{z_{\delta_e}}$ is the only input. For a positive elevator deflection this gives a force in the $-Z$ direction causing the 180° phase shift from the true picture. The $\theta(s)/\delta_e(s)$ transfer function is

$$\frac{\theta(s)}{\delta_e(s)} = \frac{0.018(s + 0.00637)}{s^2 + 0.00645s + 0.00582} \qquad (1\text{-}153)$$

or

$$\frac{\theta(s)}{\delta_e(s)} = \frac{0.0196\left(\dfrac{s}{0.00637} + 1\right)}{\left(\dfrac{s}{0.0765}\right)^2 + \dfrac{2(0.042)}{0.0765}s + 1} \qquad (1\text{-}154)$$

When comparing Eqs. 1-127 and 1-154 it can be seen that the only real comparison is in the natural frequency and the damping ratio. Again K' is way off, and there is the 180° phase difference. From this it can be concluded that the only real usefulness of the phugoid approximation is to obtain good approximate values of the natural frequency and damping ratio. Thus, as discussed in Section 1-10, the phugoid approximation is not satisfactory for simulation purposes.

1-10 TRANSIENT RESPONSE OF THE AIRCRAFT

In the preceding section the transfer functions for the longitudinal equations were obtained and analyzed. In this section the effects of changes in airspeed and altitude on the transient response of the aircraft, as obtained by use of an analog computer, are studied. The usefulness of the short-period approximation and the shortcomings of the phugoid approximation are illustrated. In the computer simulation, the slope of the lift curve was assumed constant, as were C_{m_α}, $C_{m_{\dot\alpha}}$, and C_{m_q}. In general, this is a valid assumption at the lower Mach numbers. In addition the mass and moment of inertia were held constant. The other stability derivatives were allowed to vary and were calculated using the equations given in Table 1-1. To displace the aircraft from equilibrium a 6° up-elevator deflection of approximately 1-sec duration was applied. Three different altitudes and airspeeds were studied. The results are presented in Figures 1-13, 1-14, 1-15 and are summarized in Table 1-2.

In the discussion of the short-period approximation certain predictions were made concerning the effects on the short-period dynamics of changes in airspeed and altitude. Table 1-2(a) shows that these predictions are very well substantiated by the results of the three-degree-of-freedom simulation. The discussion of the phugoid mode shows that the period of the phugoid mode
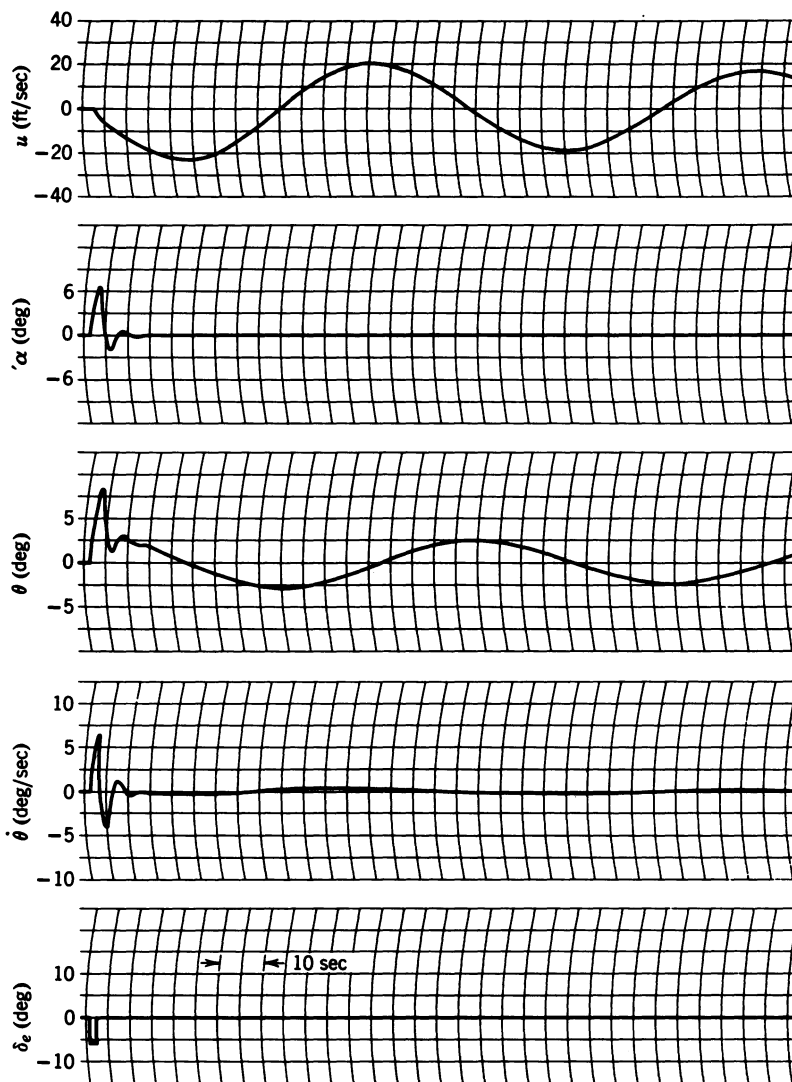
Figure 1-13 *Transient response of the aircraft for a pulse elevator deflection (complete longitudinal equations for 600 ft / sec at 40,000 ft).*

(T_p) was proportional to the airspeed and independent of air density or altitude. The three-degree-of-freedom simulation, as summarized in Table 1-2(*b*), verifies this proportionality; however, the proportionality constant is not independent of altitude nor equal to the theoretical value. Perkins and Hage in their book[1] state that this constant is nearly 0.178. The dependence on altitude and variation from the theoretical value probably results from the
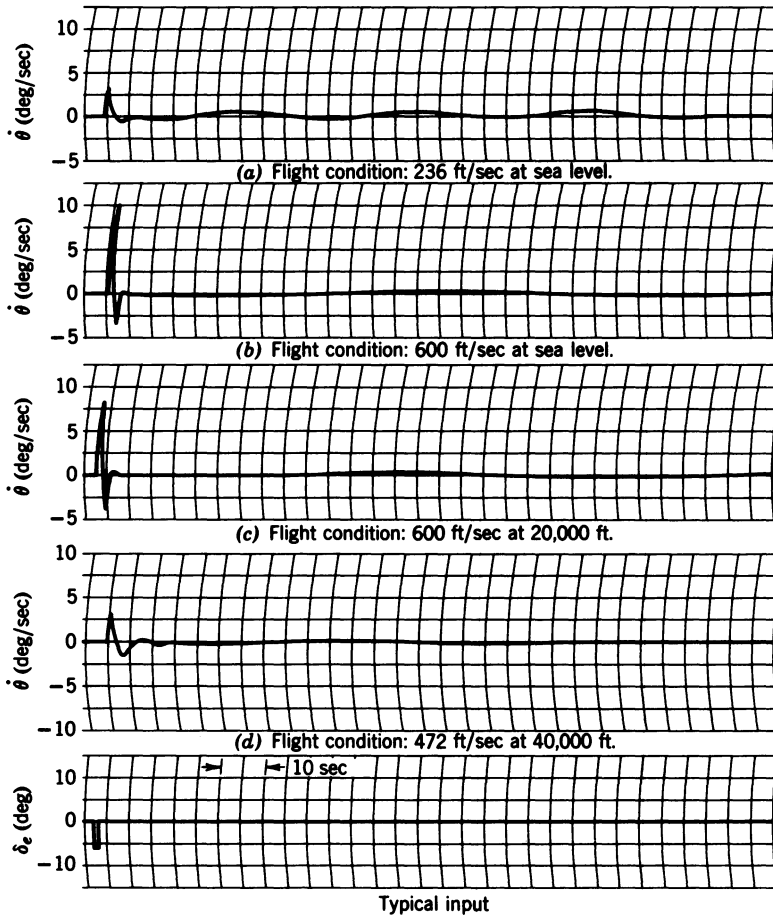
Figure 1-14 *Computer results showing the effects of changes in airspeed and altitude on the short-period mode (complete longitudinal equations).*

second-order effects of the terms neglected in obtaining the phugoid approximation.

From the phugoid approximation the damping ratio is given by the formula

$$\zeta_p = \frac{C_D}{C_L\sqrt{2}} \qquad (1\text{-}155)$$

Multiplying the numerator and denominator of Eq. 1-155 by qS yields

$$\zeta_p = \frac{qSC_D}{qSC_L\sqrt{2}} = \frac{D}{L\sqrt{2}} = \frac{D}{mg\sqrt{2}} \qquad (1\text{-}156)$$
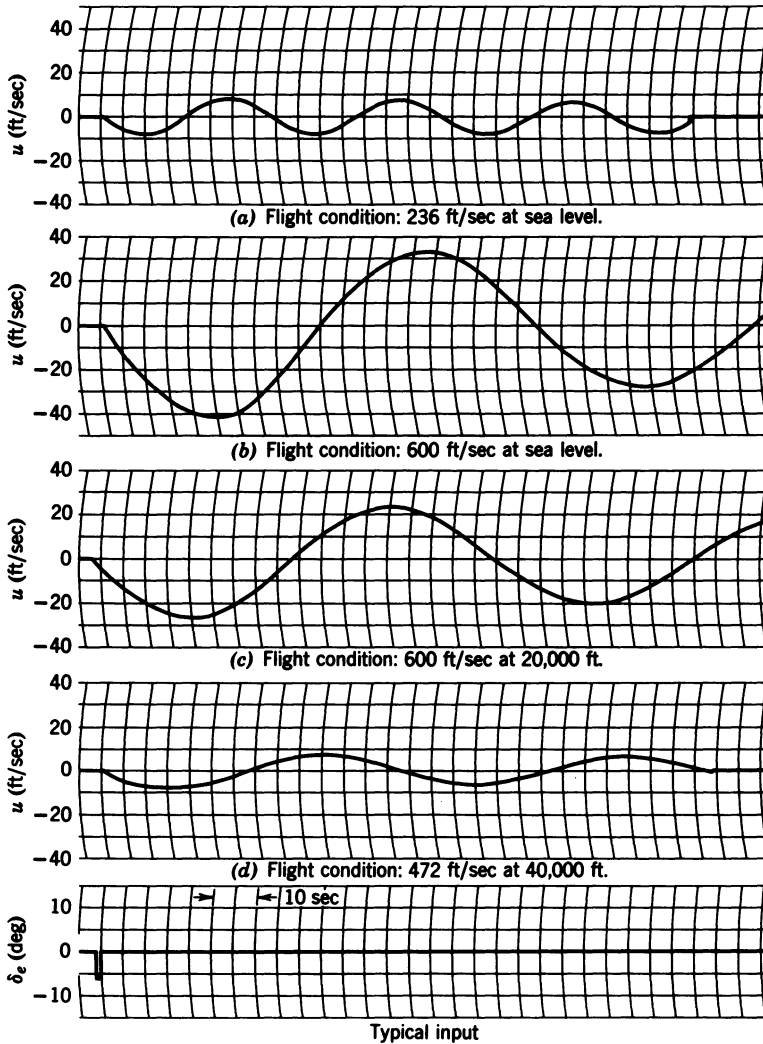
Figure 1-15 *Computer results showing the effects of changes in airspeed and altitude on the phugoid mode (complete longitudinal equations).*

Thus the damping of the phugoid mode is proportional to the ratio of the drag to the lift. If the aircraft is in straight and level flight, the lift is equal to the weight and thus constant. Under these conditions the damping of the phugoid is proportional to the total drag. As the airspeed is increased at a given altitude, the total drag increases and thus the phugoid damping should increase. Similarly, if the airspeed remains constant but the altitude is increased, the damping should decrease due to the decrease in drag resulting

TABLE 1-2   Comparison of the Predicted and Actual Effects of the Variation of Airspeed and Altitude on the Longitudinal Dynamic Response

(a) Short-Period Mode

Flight Condition		Change in ζ $\zeta = K_1\sqrt{\rho}$		Change in ω_n $\omega_n = K_2 U\sqrt{\rho}$	
Altitude (ft)	U_0 (ft / sec)	Predicted	Actual	Predicted	Actual
Sea level	236 600	None	Negligible	2.54	~ 2
40,000	472 600	None	None	1.27	1.3
Sea level to 40,000	600	0.496	~ 0.5	0.496	~ 0.5

(b) Phugoid Mode

Flight Condition		Change in ζ $\zeta = D / mg\sqrt{2}$		Value of K $T_p = KU$	
Altitude (ft)	U_0 (ft / sec)	Predicted	Actual	Predicted	Actual
Sea level	236 600	Increases	Increases	0.138	0.161 0.162
40,000	472 600	Increases	Increases	0.138	0.148 0.145
Sea level to 40,000	600	Less at 40,000 ft	Less at 40,000 ft	0.138	0.162 0.145

from the lower air density at the higher altitude. These two observations are verified by the computer runs and are summarized in Table 1-2(*b*).

In deriving the short-period approximate equations it is assumed that the forward velocity remains constant during this oscillation. The computer simulation does not completely verify this, especially at the lower dynamic pressures where the amplitude of the phugoid is small and the period relatively short. However, this result does not invalidate the use of the short-period approximation. The assumption that the angle of attack is constant and that the inertia forces are negligible (that is, that $\ddot{\theta}$ is very small) during the phugoid oscillation is confirmed by Figures 1-13 and 1-14 ($\ddot{\theta}$ would be much smaller than $\dot{\theta}$).

Examination of Figure 1-16 shows that the short-period approximation is a perfect duplication of the short-period oscillation in Figure 1-13. The fact that θ does not return to zero was explained in Section 1-9, following Eq. 1-142, and results from dropping the X equation. The fact that the short-period approximation does give such a true picture of the short-period
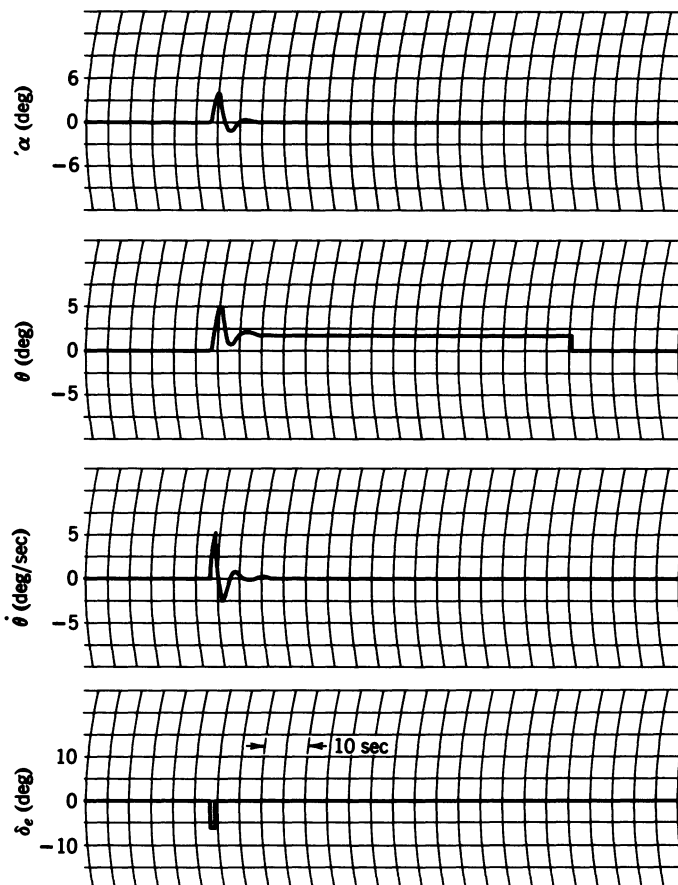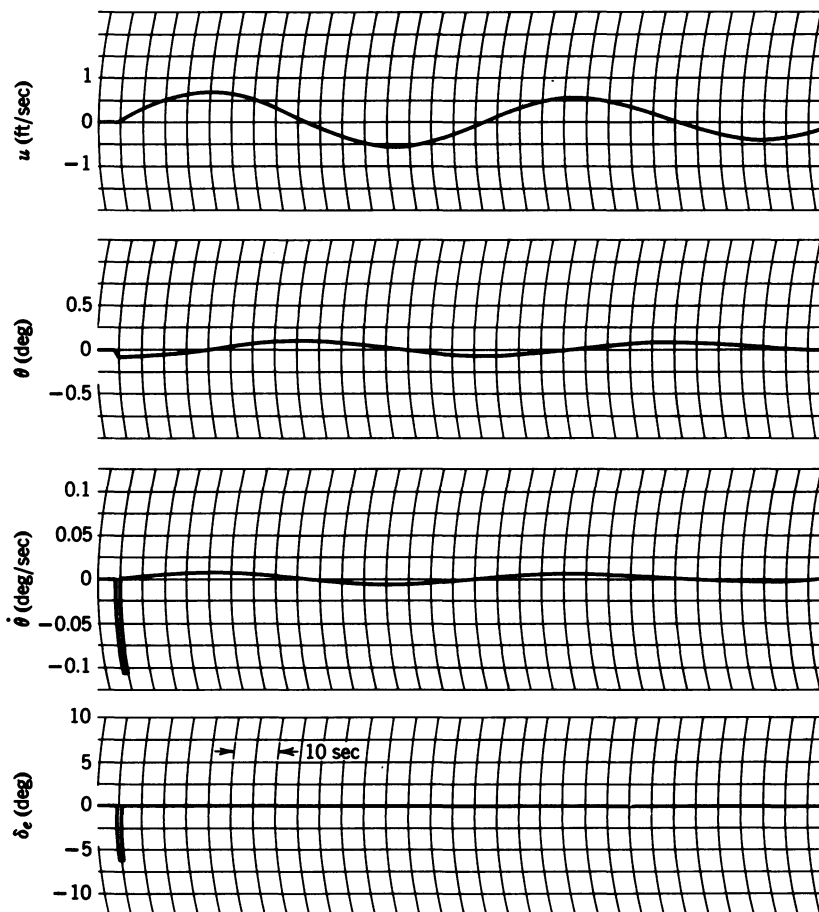
Figure 1-16   *Transient response of the aircraft for a pulse elevator deflection. Short-period approximation for 600 ft / sec at 40,000 ft.*

oscillation makes it very useful for simulation purposes. On the other hand, as can be seen from Figure 1-17, the phugoid approximation, except for fairly accurately yielding the natural frequency and damping ratio, does not accurately reproduce the phugoid oscillation. The magnitudes of the oscillations are very much smaller than those obtained from the complete longitudinal equations, and the 180° phase shift is evident.

1-11   EFFECT OF VARIATION OF STABILITY DERIVATIVES ON AIRCRAFT PERFORMANCE

This section presents the effects of variation of the stability derivatives on the damping ratios and natural frequencies of the longitudinal modes of oscilla-

Figure 1-17 Transient response of the aircraft for a pulse elevator deflection. Phugoid approximation for 600 ft / sec at 40,000 ft.

tion of the aircraft. The data for Table 1-3 was obtained for an airspeed of 600 ft/sec at 40,000 ft, through the use of the analog computer, by varying each stability derivative individually and then determining the damping ratios and the natural frequencies from the time recordings. This is an artificial situation; in general, any one of the stability derivatives cannot be changed without changing at least some of the other stability derivatives. However, in performing a dynamic simulation of an aircraft in connection with the design of an autopilot, the engineer must know, or be able to estimate, the values of the stability derivatives that he needs. By knowing which ones are most likely to affect the damping ratios and natural frequencies, and by how much, the engineer knows which stability derivatives should be known most accurately for his particular design problem. The data in Table 1-3 could also aid the

TABLE 1-3 Effects of Variation of the Stability Derivatives on the Damping Ratios and Natural Frequencies of the Longitudinal Modes of Oscillation

Stability Derivative	Basic Value	Change	Short Period ζ	Short Period ω_n	Phugoid ζ	Phugoid ω_n
C_{x_u}	−0.088	×10	0.35	1.15	0.4	0.08
		×2			0.07	0.077
		×$\frac{1}{2}$			0.007	0.073
		×$\frac{1}{10}$			−0.007*	0.073
C_{x_α}	0.392	×10			0.075	0.073
		×$\frac{1}{10}$			0.025	0.073
C_{z_u}	−1.48	×10			−0.018	0.228
		×2			0.007	0.103
		×$\frac{1}{2}$			0.058	0.051
		×$\frac{1}{10}$			0.1	0.0226
C_{z_α}	−4.46	×4	~ 0.8	1.53	0.025	0.064
		×2	0.47	1.21	0.035	0.069
		×$\frac{1}{2}$	0.27	1.1	0.05	0.075
		×$\frac{1}{4}$	0.25	1.05	0.13	0.0757
$C_{m_{\dot\alpha}}$	−3.27	×10	~ 1	1.38	0.035	0.073
		×2	0.4	1.18		
		×$\frac{1}{2}$	0.32	1.13		
		×$\frac{1}{10}$	0.31	1.11		
C_{m_α}	−0.619	×2	0.23	1.62		
		×$\frac{1}{2}$	0.45	0.92		0.07
C_{m_q}	−11.4	×4	~ 1	1.85		0.064
		×2	0.52	1.2		0.069
		×$\frac{1}{2}$	0.27	1.12		0.075
		×$\frac{1}{10}$	0.2	1.1		0.076

*Negative damping or instability.

engineer in locating errors in his simulation if the damping ratio and/or natural frequency as determined by the simulation differs from the calculated value. For example, if in simulating the short-period mode it is found that the damping is too heavy but that the natural frequency has only increased slightly, the first guess might be that an error in C_{m_q} is the cause. A check of the value of the potentiometer setting that determines this stability derivative, the potentiometer setting itself, or the patch board wiring just ahead or behind this potentiometer might disclose the error and thus save a considerable amount of time that might otherwise be spent trouble-shooting the whole circuit. It is for these reasons that this section is included in this book.

In Table 1-3 the maximum amount that the stability derivatives are increased or decreased is one order of magnitude; however, if a smaller change gives extremely large variations of the damping ratio or natural frequency, the stability derivatives are not changed by that much. It should be remembered that the data in Table 1-3 is calculated from computer traces similar to those in Figure 1-14; thus extremely small changes in the damping

TABLE 1-4   List of Stability Derivatives That Have the Largest Effects on the Damping Ratios and Natural Frequencies of the Longitudinal Modes of Oscillation

Stability Derivative	Quantity Most Affected	How Affected
C_{m_q}	Damping of the short period, ζ_s	Increase C_{m_q} to increase the damping
C_{m_α}	Natural frequency of the short period, ω_{ns}	Increase C_{m_α} to increase the frequency
C_{x_u}	Damping of the phugoid, ζ_p	Increase C_{x_u} to increase the damping
C_{z_u}	Natural frequency of the phugoid, ω_{np}	Increase C_{z_u} to increase the frequency

ratios or natural frequencies cannot be detected. But as this data is primarily to aid in analog simulation of the aircraft, the accuracy obtained should be satisfactory. In addition, the main purpose here is to show the trend, for the amount of change will vary with aircraft. For reference, the basic values of the damping ratios and natural frequencies, as measured from the computer traces, are

Short period: $\zeta_s = 0.35$

$\omega_{ns} = 1.15$ rad/sec

Phugoid: $\zeta_p = 0.035$

$\omega_{np} = 0.073$ rad/sec

From Table 1-3 it can be concluded that the stability derivatives shown in Table 1-4 have the most effect on the damping ratios and/or natural frequencies.

REFERENCES

1. C. D. Perkins and R. E. Hage, *Airplane Performance, Stability, and Control*, John Wiley and Sons, New York, 1949.

2. B. Etkin, *Dynamics of Flight: Stability and Control*, 2nd ed., John Wiley and Sons, New York, 1982.

3. D. O. Dommash, S. S. Sherby, and T. F. Connolly, *Airplane Aerodynamics*, Pitman Publishing Corp., New York, 1951.

4. M. F. Gardner and J. L. Barnes, *Transients in Linear Systems*, Vol. 1, John Wiley and Sons, New York, 1942.

5. Shih-Nge Lin, "A Method of Successive Approximations of Evaluating the Real and Complex Roots of Cubic and Higher Order Equations," *Journal of Mathematics and Physics*, August 1941, Vol. XX, No. 3.

2

Longitudinal Autopilots

2-1 DISPLACEMENT AUTOPILOT

The simplest form of autopilot, which is the type that first appeared in aircraft and is still being used in some of the older transport aircraft, is the displacement-type autopilot. This autopilot was designed to hold the aircraft in straight and level flight with little or no maneuvering capability. A block diagram for such an autopilot is shown in Figure 2-1.

For this type of autopilot the aircraft is initially trimmed to straight and level flight, the reference aligned, and then the autopilot engaged. If the pitch attitude varies from the reference, a voltage e_g is produced by the signal generator on the vertical gyro. This voltage is then amplified and fed to the elevator servo. The elevator servo can be electromechanical or hydraulic with an electrically operated valve. The servo then positions the elevator, causing the aircraft to pitch about the Y axis and so returning it to the desired pitch attitude. The elevator servo is, in general, at least a second-order system; but if properly designed, its natural frequency is higher than that of the aircraft. If the damping ratio is high enough, the elevator servo can be represented by a sensitivity (gain) multiplied by a first-order time lag. Representative characteristic times vary from 0.1 to 0.03 sec. The transfer function used to represent the aircraft can be the complete three-degree-of-freedom longitudinal transfer function or the transfer function of the short-period approximation. The choice depends on what characteristic of the aircraft behavior is being studied.

There is one disadvantage of this system, from a servo point of view; that is, it is a Type 0 system (see Appendix C). This means that there are no
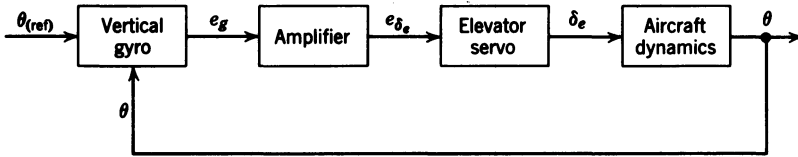
Figure 2-1   *Displacement autopilot.*

integrations in the forward loop. Thus if some fixed external moment were applied, resulting from a change in trim, for example, there would have to be an error in θ to generate a voltage to drive the elevator servo, thus producing an elevator deflection to balance the interfering moment. This, then, would require the pilot to make occasional adjustments of the reference to maintain the desired flight path.

Another disadvantage of this system can be illustrated by studying the root locus of Figure 2-1, for two different aircraft. The short-period approximation for both aircraft is used here. The first aircraft is a conventional transport flying at 150 mph at sea level, and the second aircraft is the jet transport studied in Chapter 1, flying at 600 ft/sec at 40,000 ft. Figure 2-2 is the block diagram for the first aircraft obtained by inserting the transfer functions for the components represented by the blocks in Figure 2-1. The amplifier and the elevator servo are combined into one block, and the vertical gyro replaced by a summer. As the aircraft transfer function is negative, the sign of the elevator servo transfer function is made negative so that the forward transfer function is positive. This is done so that a positive $\theta_{(ref)}$ causes a positive change in θ, which will be helpful when analyzing the glide slope control system. If the sign of the transfer function of the elevator servo had been left positive, the sign at the summer for the feedback signal would have been positive, so that the sign of the open loop transfer function would have been negative (see Appendix C). In either case the analysis would have been the same. Figure 2-3 is the root locus for the conventional transport; Figure 2-4 is the block diagram for the jet aircraft; and Figure 2-5 the corresponding root locus. As can be seen in Figure 2-3, the short-period oscillation for the first aircraft is well damped, the damping ratio being 0.78. As $S_{(es)}$—the gain of the elevator servo—is increased from zero, the damping decreases, and when $S_{(es)}$ is increased to 8.8 deg/volt, the damping ratio
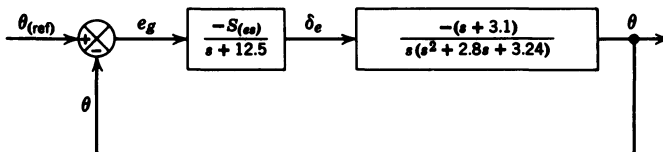
Figure 2-2   *Block diagram for the conventional transport and autopilot.*
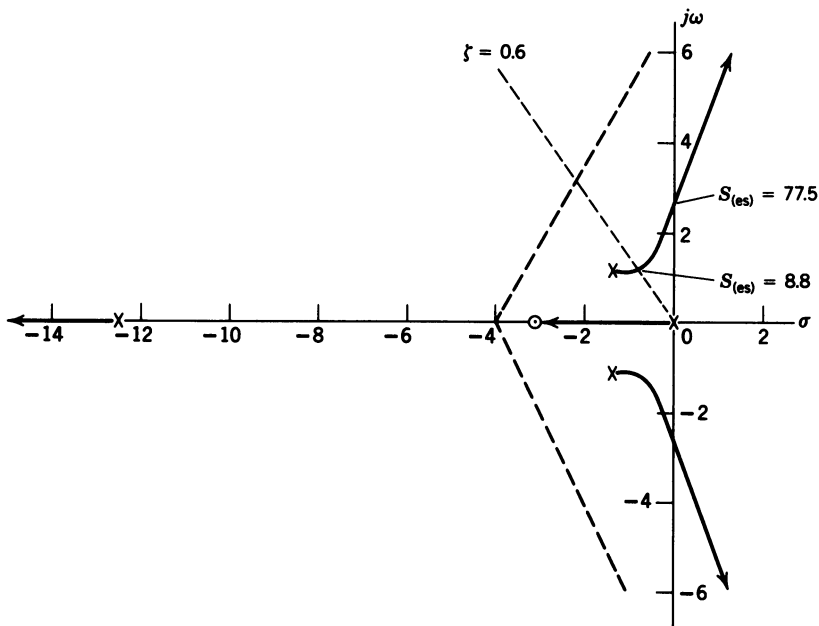
Figure 2-3 *Root locus for conventional transport and autopilot.*

decreases to 0.6, which is still sufficient. In contrast, Figure 2-5 shows that for the jet transport the damping ratio, which is already too low for satisfactory dynamic response, decreases rapidly as the $S_{(es)}$ is increased. Another consideration is the value of $S_{(es)}$ for instability. For the first aircraft this value of $S_{(es)}$ is 77.5 deg/volt, while for the second aircraft it is only 38.4 deg/volt. From this example it can be seen that the displacement autopilot, while satisfactory for conventional transports, is not satisfactory for jet transports similar to the one studied in Chapter 1.

The s appearing in the denominator of the aircraft transfer function results from dropping the gravity term ($C_w \sin \Theta$) in Eq. 1-128, that is, $\Theta = 0$. If Θ is not zero, which would be the case after a disturbance or if Θ_0 were not zero, the s in the denominator becomes a real pole near the origin. For this reason, although the systems shown in Figures 2-2 and 2-4 are technically Type 1 systems (see Appendix C), they will be considered here as Type 0
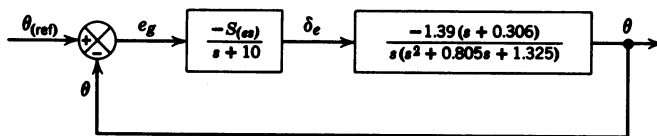
Figure 2-4 *Block diagram for the jet transport and autopilot.*
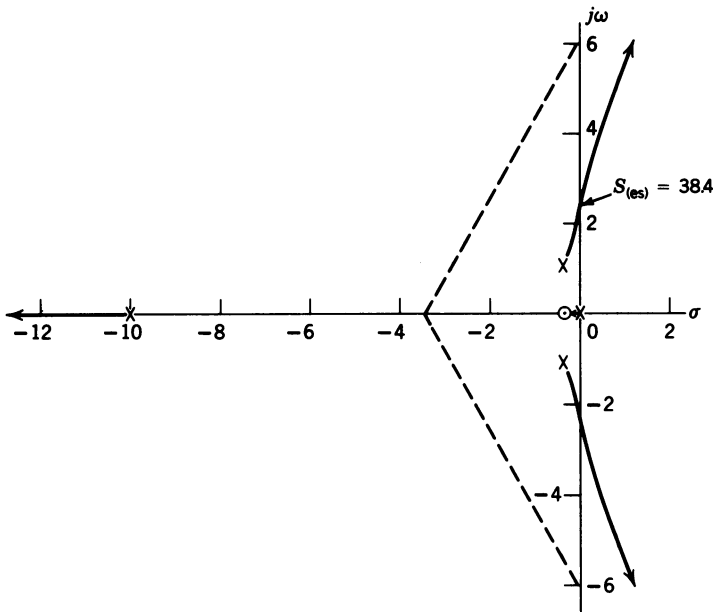
Figure 2-5 *Root locus for jet transport and autopilot.*

systems. This in no way affects the validity of the analysis to follow, for even if Θ_0 is not zero, the real pole introduced is so close to the origin as to be indistinguishable from a pole at the origin when plotting the root locus.

If, in the case of the jet aircraft, it is desired to increase the damping of the short-period oscillation, this can be accomplished by adding an inner feedback loop utilizing a rate gyro. Figure 2-6 is a block diagram of such a system. A root locus analysis is presented here to show the effect of the rate gyro feedback. First, Figure 2-6 is redrawn indicating the transfer functions for the various blocks, which yields Figure 2-7. Figure 2-8 shows the root locus for the inner loop as the rate gyro sensitivity is increased from zero. As seen in Figure 2-8, there is a range of rate gyro sensitivities that yields all real
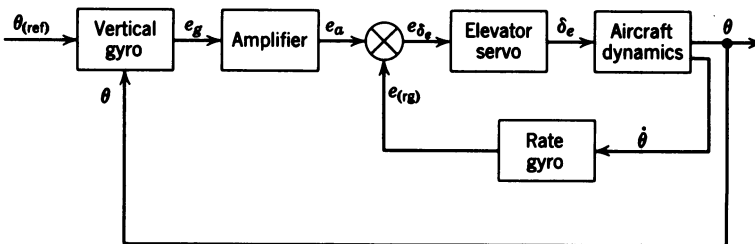
Figure 2-6 *Displacement autopilot with pitch rate feedback for damping.*
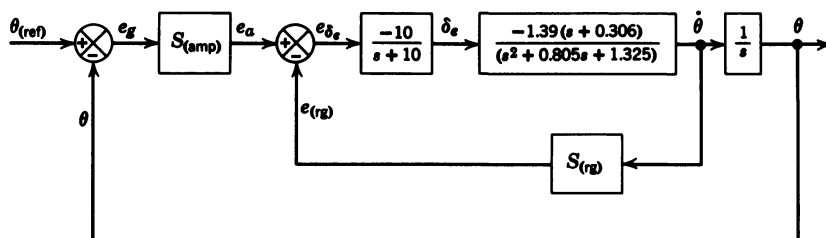
Figure 2-7   *Block diagram for the jet transport and displacement autopilot with pitch rate feedback added for damping.*

roots. The question that now arises is what value of rate gyro sensitivity should be used to obtain the best overall system response after closing the outer loop. There is no simple rule to aid the engineer in selecting the final sensitivity. The final choice usually results in a compromise between the desirability of rapid response and the desire to reduce excessive overshoot. For illustration, two rate gyro sensitivities are chosen, as indicated in Figure 2-8. Using these closed loop poles a root locus can now be drawn for each rate gyro sensitivity for the outer loop (see Figures 2-9 and 2-10). For each root locus the value of the amplifier sensitivity required to reduce the
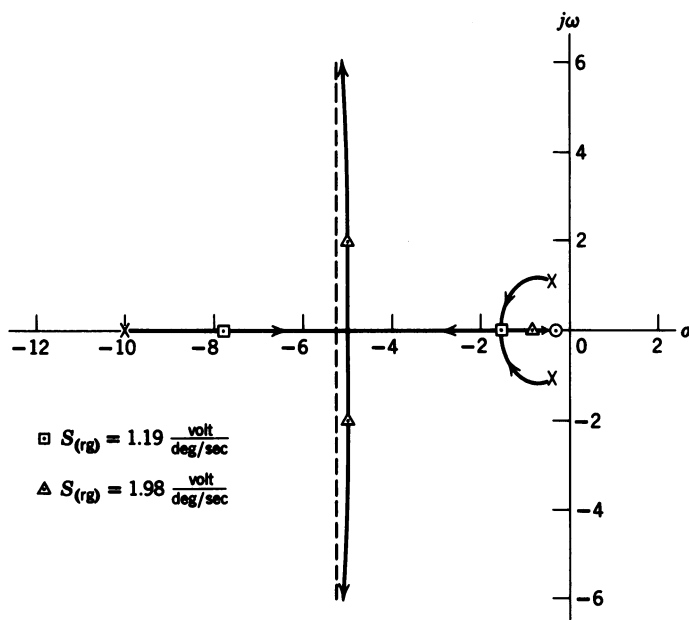
Figure 2-8   *Root locus for the inner loop of the jet transport and autopilot with pitch rate feedback.*
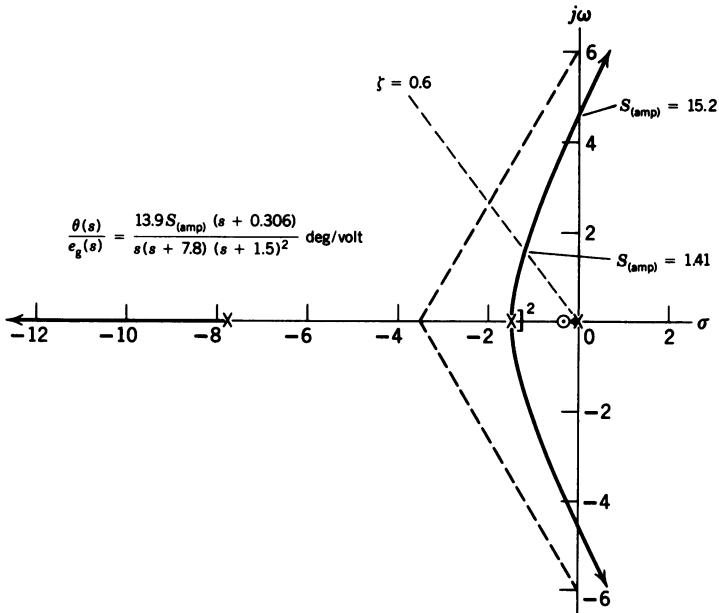
Figure 2-9   Root locus for the outer loop of the jet transport and autopilot for $S_{(rg)} = 1.19$ volt / (deg / sec).

$$\frac{\theta(s)}{e_g(s)} = \frac{13.9 S_{(amp)} (s + 0.306)}{s(s + 7.8)(s + 1.5)^2} \text{ deg/volt}$$
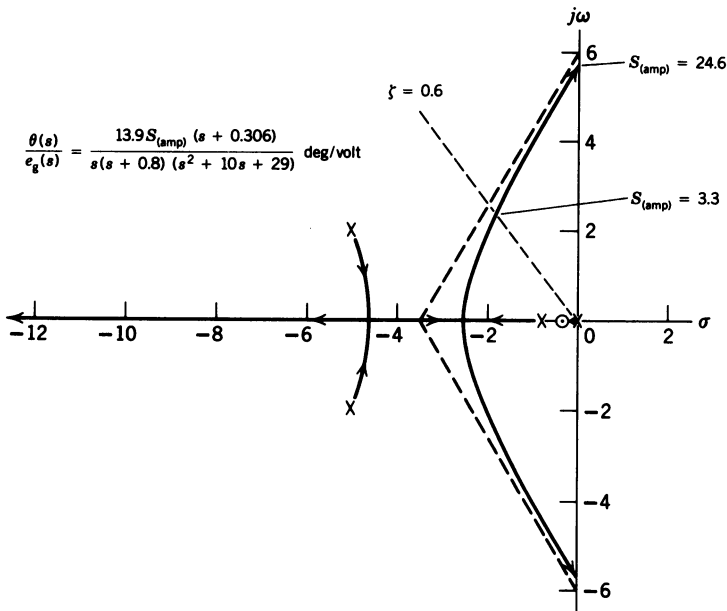
Figure 2-10   Root locus for the outer loop of the jet transport and autopilot for $S_{(rg)} = 1.98$ volt / (deg / sec).

$$\frac{\theta(s)}{e_g(s)} = \frac{13.9 S_{(amp)} (s + 0.306)}{s(s + 0.8)(s^2 + 10s + 29)} \text{ deg/volt}$$

TABLE 2-1 Amplifier Sensitivities Required for the Conditions Indicated for Displacement Autopilot for Two Values of Rate Gyro Sensitivity

$S_{(rg)} \left(\dfrac{\text{volt}}{\text{deg} / \text{sec}} \right)$	$S_{(amp)}$ (volt / volt)	
	For $\zeta = 0.6$	For $\zeta = 0$
1.19	1.41	15.2
1.98	3.3	24.6

damping ratio to 0.6 and to zero is tabulated in Table 2-1. The result of this root locus study illustrates an important point; that is, the higher the gain of the inner loop, the higher the allowable gain for neutral stability for the outer loop. However, too high an inner loop gain results in higher natural frequencies and lower damping as the inner loop poles move out along the 90° asymptotes.

Although the displacement autopilot with rate feedback adequately controls a jet transport, it is desirable to obtain a Type 1 system to eliminate the steady-state error for a step input. This fact plus the desirability for more maneuverability, especially in fighter aircraft, has led to the pitch orientational control system with control stick steering.

2-2 PITCH ORIENTATIONAL CONTROL SYSTEM

The pitch orientational control system has as its input a desired pitch rate; such an input, plus the desire to obtain a Type 1 system, which calls for an integration in the forward loop, makes it advisable to use an integrating gyro as the command receiver. Figure 2-11 is a block diagram of a pitch orientational control system. The necessity for the rate gyro depends upon the characteristics of the system. If this system is to be used to control the attitude of the aircraft, an altitude or Mach hold control system can be used
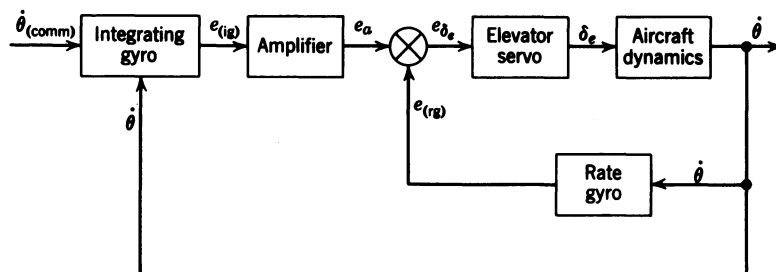
Figure 2-11 *Pitch orientational control system.*

for the third and outer loop (see Section 2-4) and thus provide the $\dot{\theta}_{(comm)}$ signal. The command signal can also come from the pilot.

The pilot's input might come from a so-called "maneuver stick," a small control stick which, when moved, positions a potentiometer and thus produces a voltage. Such a system is referred to as a fly-by-wire control system. The introduction of component redundancy and digital flight control systems, capable of detecting sensor or other component failure, has made fly-by-wire control systems practical. In these systems the software detects the failure of any component, isolates the failed component, and transfers operation or control to a redundant operational component.

However, the maneuver stick does not provide any feel to the pilot; that is, the pilot does not have to exert any force to move the handle. The alternative method is to use a force stick. For this a portion of the stick is necked down so that the stick will flex slightly when a force is applied. The stick is so installed that with the system on, the force exerted by the pilot on the stick is resisted by the servo actuator, which is locked by the fluid trapped when the actuating valve is in the off position (see Figure 2-12). The result of the applied force is to cause a deflection of the control stick at the necked-down area. Strain gauges on this portion of the stick sense this deflection, producing a voltage which is the command signal. For the case in question, this voltage is amplified and fed as torquing current to the torque generator of the integrating gyro. As a result of this torquing current a signal is produced
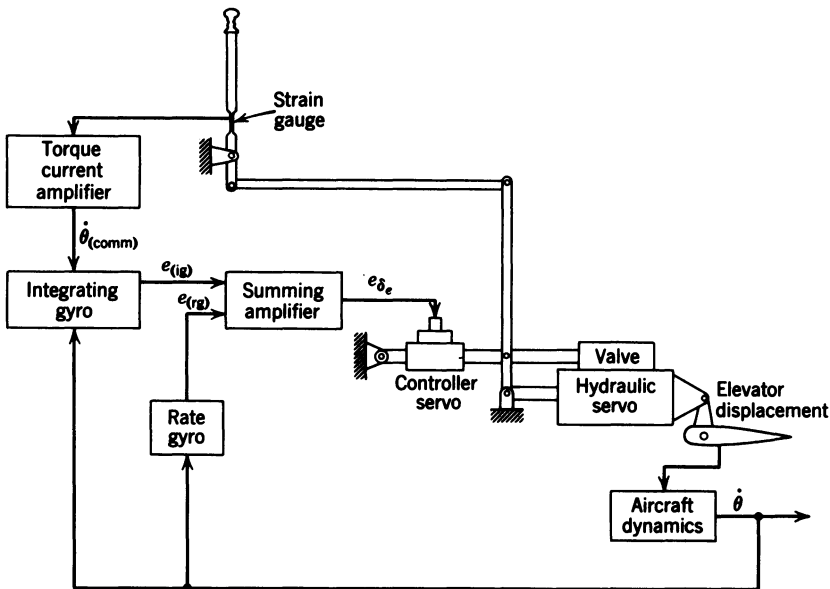
Figure 2-12 *Functional diagram of a pitch orientational control system with control stick steering.*[1]

from the integrating gyro signal generator. This signal is amplified and used to position the selector valve of the elevator servo positioning the elevator. As the elevator is positioned, the stick follows this movement, and the aircraft acquires the desired pitch rate. To maintain a steady pitch rate the pilot must continue to apply pressure to the stick. The system can be adjusted to provide any stick force gradient per g of acceleration desired, thus providing the desired feel to the pilot. In the future discussion of the pitch orientational control system it will be assumed that the command to the integrating gyro comes from the force stick; this is often referred to as "control stick steering." This autopilot configuration can be used to provide an all attitude autopilot; however, one very important application is the control of an aircraft that is longitudinally unstable, that is, C_{m_α} is positive.

Although most aircraft are designed to be statically stable (C_{m_α} negative), certain flight conditions can result in large changes in the longitudinal stability. Such changes occur in some high-performance aircraft as they enter the transonic region. However, an even more severe shift in the longitudinal stability results in some high-performance aircraft at high angles of attack, a phenomenon referred to as "pitch-up." An aircraft that is subject to pitch-up might have a curve of C_m versus α similar to the one shown in Figure 2-13. As long as the slope of the curve in Figure 2-13 is negative the aircraft is stable, but as the angle of attack is increased, the slope changes sign and the aircraft becomes unstable. If corrective action is not taken, the angle of attack increases until the aircraft stalls. This usually happens so rapidly that the pilot is unable to control or stop the pitch-up. Before proceeding with the study of the pitch orientational control system, the aerodynamic causes of pitch-up will be discussed.

Pitch-up is most likely to occur in aircraft that have the horizontal stabilizer mounted well above the wing of the aircraft; a common place is the top of the vertical stabilizer. This is sometimes done to obtain the end-plate effect on the vertical stabilizer and thus increase the effectiveness of the vertical stabilizer. Another factor that contributes to this unstable flight condition is a wing with a low aspect ratio. Such a wing has a large downwash velocity that increases rapidly as the angle of attack of the wing is increased.
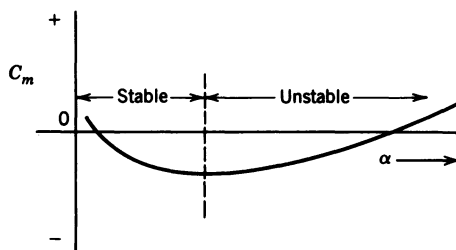
Figure 2-13 C_m *versus* α *for an aircraft subject to pitch-up.*
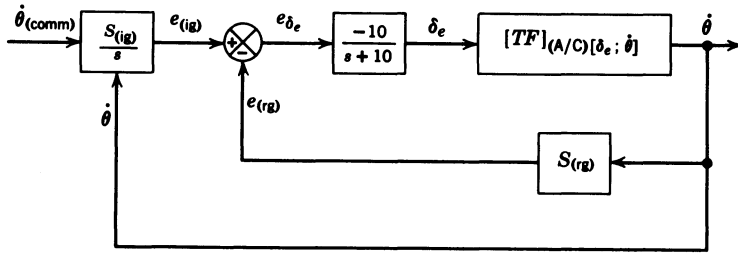
Figure 2-14 Block diagram of pitch orientational control system for the control of pitch-up.
For low angles of attack (stable condition),

$$[\text{TF}]_{(A/C)[\delta_e;\,\dot\theta]} = \frac{-15(s+0.4)}{s^2+0.9s+8} \quad \frac{\text{deg}/\sec}{\text{deg}}$$

For high angles of attack (unstable condition),

$$[\text{TF}]_{(A/C)[\delta_e;\,\dot\theta]} = \frac{-9(s+0.3)}{(s+3.8)(s-2.9)} \quad \frac{\text{deg}/\sec}{\text{deg}}$$

As the high horizontal tail moves down into this wing wake, pitch-up occurs if the downwash velocity becomes high enough. Pitch-up may occur in straight-wing as well as swept-wing aircraft. For the swept-wing aircraft the forward shift of the center of pressure of the wing at high angles of attack is also a contributing factor. A practical solution of the pitch-up problem is to limit the aircraft to angles of attack below the critical angle of attack; however, this also limits the performance of the aircraft. An aircraft that is subject to pitch-up generally will fly at these higher angles of attack; thus an automatic control system that makes the aircraft flyable at angles of attack greater than the critical angle of attack increases the performance capabilities of the aircraft. The pitch orientational control system, if properly designed, provides this control.

The rest of this section will be devoted to a root locus study of this control system to show how the sensitivities of the rate gyro and the integrating gyro should be determined to obtain the desired control. Included also will be the results of some computer runs showing the effectiveness of this control. The transfer function used to represent the aircraft is representative of modern high-performance fighter aircraft, although not the transfer function of any actual aircraft. Figure 2-14 is the block diagram of the system. The amplifier that was shown in Figure 2-11 is combined with the elevator servo. A root locus study for both the stable and unstable condition demonstrates the factors that influence the selection of the rate gyro and integrating gyro sensitivities.

Figure 2-15 is the root locus for the inner loop for low angles of attack as the rate gyro sensitivity is varied. The location of the closed loop poles for
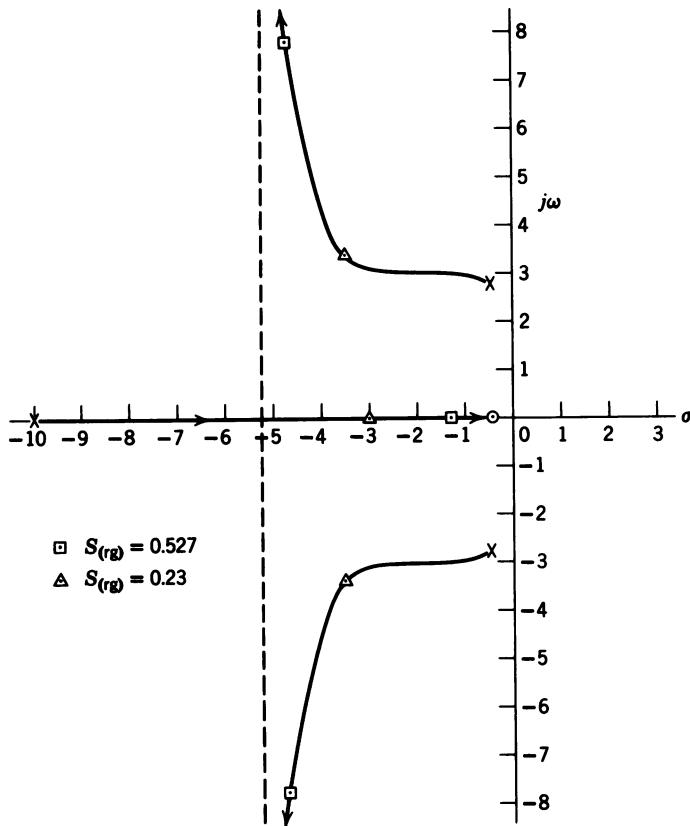
Figure 2-15 *Root locus for the inner loop of the control system shown in Figure 2-14, for low angles of attack.*

two values of rate gyro sensitivity are illustrated. One value results in the maximum damping; the reason for the higher rate gyro sensitivity will be shown later. Figure 2-16 is the root locus for the inner loop for high angles of attack. From this root locus it can be seen that as the rate gyro sensitivity is increased, the pole in the right half plane moves toward the zero in the left half plane. The locations of the closed loop poles for the same rate gyro sensitivities as were used in Figure 2-15 are shown. These closed loop poles are the open loop poles for the outer loop. The root locus for the outer loop for the unstable condition is seen in Figure 2-17. Note the additional pole at the origin, which results from the integrating gyro. Now the reason for selecting the higher rate gyro sensitivity is evident. If the rate gyro sensitivity is not high enough, that is, the pole in the right half plane is too far to the right, the system is only stable for a limited range of integrating gyro sensitivities. As is shown in Table 2-2, the higher the rate gyro sensitivity, the wider the allowable range of integrating gyro sensitivities. In fact, if the pole
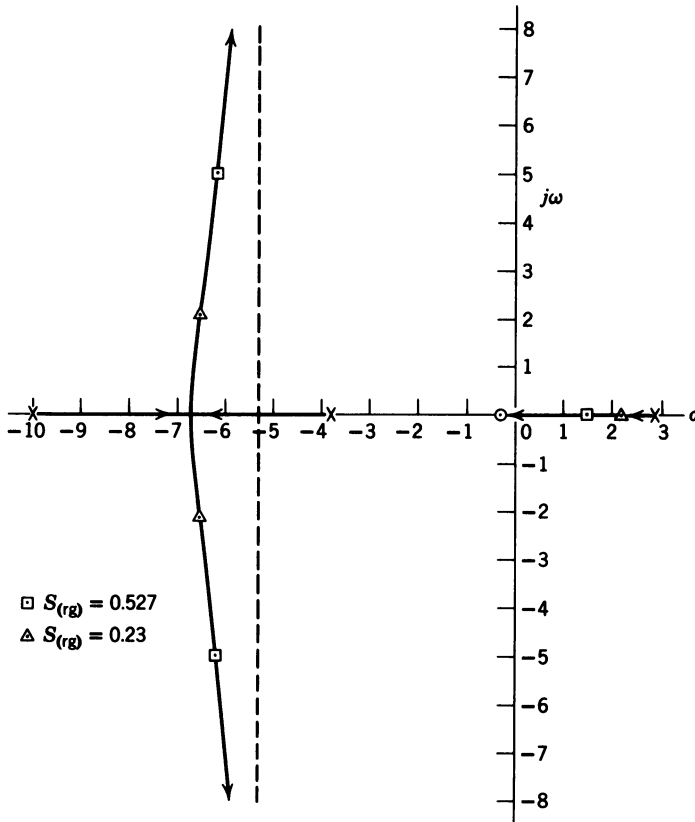
Figure 2-16 *Root locus for the inner loop of the control system shown in Figure 2-14, for high angles of attack.*

in the right half plane is too far to the right, then regardless of the integrating gyro sensitivity, the system is unstable. The locations of the final closed loop poles for the whole system which result in the fastest response time are indicated by Figure 2-17. Figure 2-18 is the root locus for the outer loop at low angles of attack. The locations of the closed loop poles for the same integrating gyro sensitivity used at large angles of attack are indicated in Figure 2-18. The integrating gyro sensitivities to produce instability are listed in Table 2-3. From this table it can be seen that stability at high angles of attack can be obtained without producing instability at low angles of attack.

To check the ability of this system to control an aircraft that is subject to pitch-up at high angles of attack, the aircraft and control systems were simulated on an analog computer. To add realism, a mock-up of an elevator servo with force stick input was "tied" into the computer. The angle of attack was displayed on an oscilloscope. Several runs were made, during which the angle of attack was varied from the trim angle of attack for straight and level
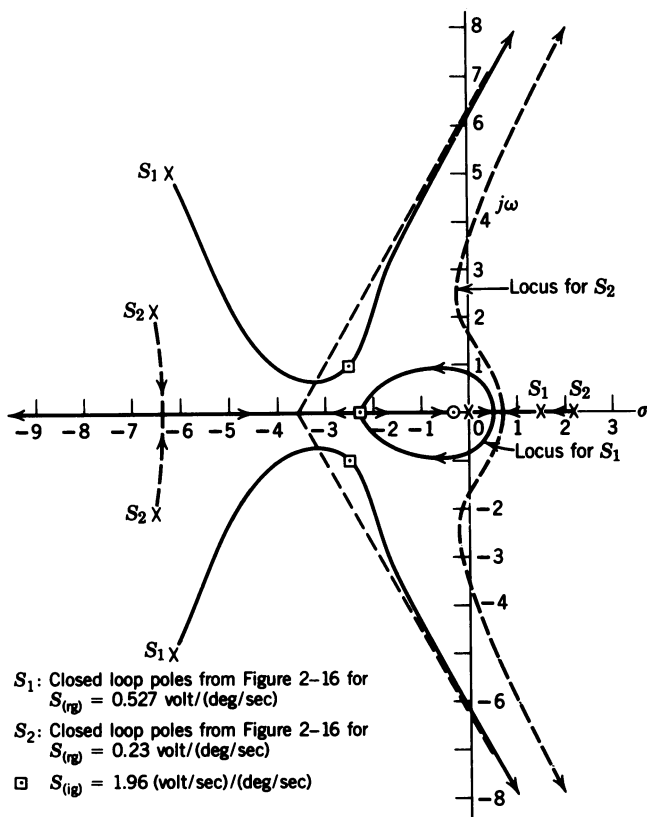
Figure 2-17   *Root locus for the complete pitch orientational control system for high angles of attack.*

TABLE 2-2   Maximum and Minimum Integrating Gyro Sensitivities for System Stability for Two Rate Gyro Sensitivities (High Angle of Attack)

Rate Gyro Sensitivities [volt / (deg / sec)]	Integrating Gyro Sensitivities [volt / (deg / sec)]	
	Minimum	Maximum
0.23	1.56	2.63
0.527	1.12	5.78
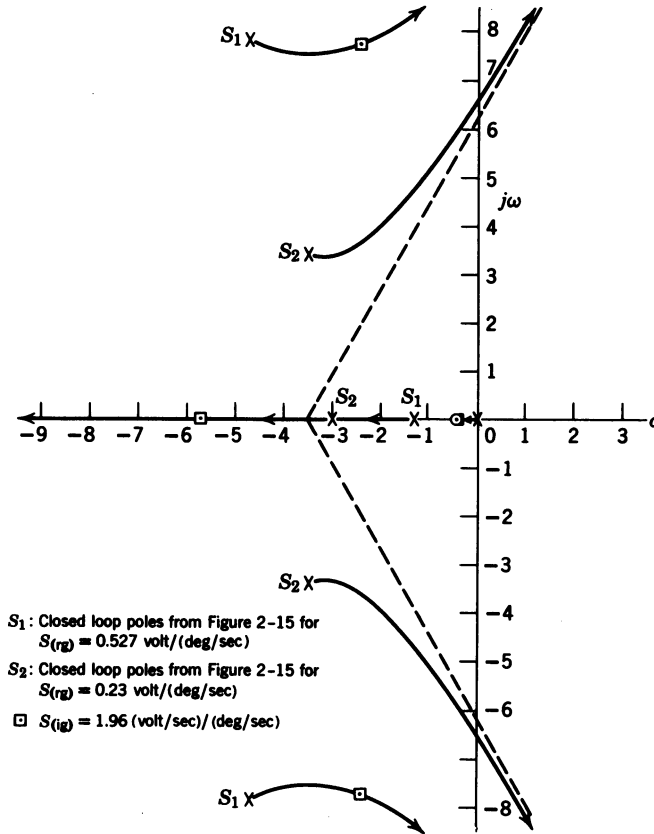
Figure 2-18 *Root locus for the complete pitch orientational control system for low angles of attack.*

flight up to about 23° angle of attack. Figure 2-19 is a recording of one of these runs. Neutral stability occurred at about 13° angle of attack, at which point the elevator angle started decreasing, and as the angle of attack increased still further, the elevator angle went through zero and became positive. As the force stick was used, the stick moved forward as the elevator angle went positive; however, it was still necessary to apply "back pressure"

TABLE 2-3 Integrating Gyro Sensitivities for Instability for Two Rate Gyro Sensitivities (Low Angle of Attack)

Rate Gyro Sensitivity [volt / (deg / sec)]	Integrating Gyro Sensitivity [volt / (deg / sec)]
0.23	2.36
0.527	5.64
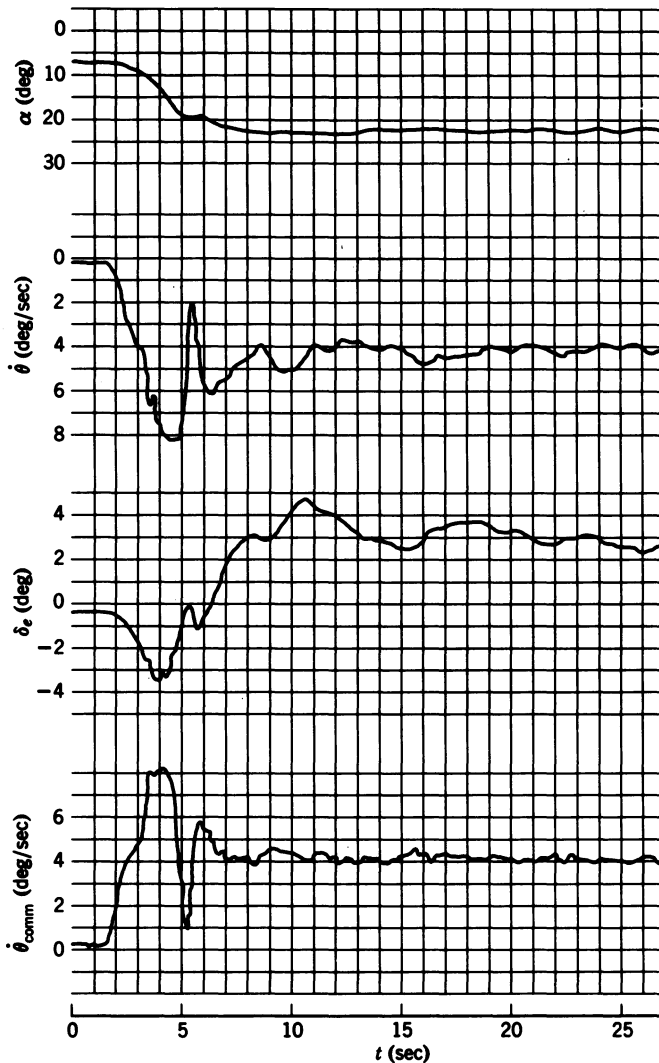
Figure 2-19 *Response of the pitch orientational control system for force stick input for Mach 0.8 at 40,000 ft.*

to the stick. By simply releasing the back pressure the commanded pitch rate became zero and the angle of attack returned to the trim angle of attack. Besides being able to control an aircraft that is subject to pitch-up, this control system would also take care of trim changes encountered when an aircraft passes through the transonic region. The characteristics of the integrating gyro as discussed in Section 2-7 make this control possible.

Until now, we have studied longitudinal autopilots in which either the pitch angle or the pitch rate was used to obtain control or to add damping. It

is sometimes desirable or necessary to control the acceleration along the aircraft's Z axis. This type of autopilot is referred to as an acceleration autopilot and is discussed in Section 2-3.

2-3 ACCELERATION CONTROL SYSTEM

Figure 2-20 is a block diagram for an acceleration control system. A pure integration is introduced in the forward loop to provide a Type 1 system. To understand the requirement for the rate gyro feedback loop and the reason for the signs used at the summers, we must examine the transfer function for the aircraft for an elevator input to an acceleration output. The required transfer function can be derived from the Z force equation of Eq. 1-38, which is repeated here:

$$a_z = \dot{w} - U_0 \dot{\theta} \qquad (2\text{-}1)$$

Factoring U_0 out of the right hand side of Eq. 2-1 yields

$$a_z = U_0 \left(\frac{\dot{w}}{U_0} - \dot{\theta} \right) = U_0('\dot{\alpha} - \dot{\theta}) \qquad (2\text{-}2)$$

as $\dot{w}/U_0 = '\dot{\alpha}$. The transfer function can be obtained by dividing Eq. 2-2 by δ_e, which yields

$$\frac{a_z}{\delta_e} = U_0 \left(\frac{'\dot{\alpha}}{\delta_e} - \frac{\dot{\theta}}{\delta_e} \right) \qquad (2\text{-}3)$$

Thus the acceleration transfer function is simply the forward velocity, times the $'\dot{\alpha}$ transfer function, minus the $\dot{\theta}$ transfer function. The question that now arises is whether to use the three-degree-of-freedom equations or the short-period approximation. In Section 1-10 it was shown that during the
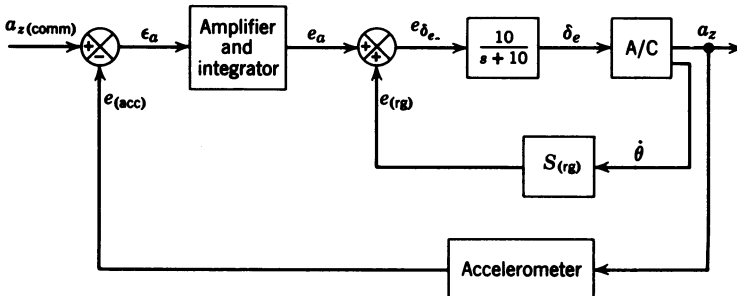
Figure 2-20 Block diagram of an acceleration control system. $S_{(acc)} = 1 \text{ volt } / g$.

phugoid oscillation $'\dot{\alpha}$ and $\dot{\theta}$ were almost zero. From this it can be concluded that the short-period approximation can be used for the acceleration transfer function.

As an acceleration control system is used generally in fighter-type aircraft, the transfer functions used are typical of a high-performance fighter. For the aircraft used in Section 2-2, the $'\dot{\alpha}$ and $\dot{\theta}$ transfer functions are:

$$\frac{'\dot{\alpha}(s)}{\delta_e(s)} = \frac{-(0.1s^2 + 15s)}{s^2 + 0.9s + 8} \tag{2-4}$$

$$\frac{\dot{\theta}(s)}{\delta_e(s)} = \frac{-(15s + 6)}{s^2 + 0.9s + 8} \tag{2-5}$$

Subtracting Eq. 2-5 from Eq. 2-4, multiplying by U_0, and substituting into Eq. 2-3 yields

$$\frac{a_z(s)}{\delta_e(s)} = \frac{-77.7(s^2 - 60)}{s^2 + 0.9s + 8} \tag{2-6}$$

Factoring,

$$\frac{a_z(s)}{\delta_e(s)} = \frac{-77.7(s + 7.75)(s - 7.75)}{s^2 + 0.9s + 8} \frac{\text{ft/sec}^2}{\text{rad}} \tag{2-7}$$

But the units for the transfer function of the elevator servo are deg/volt, and for the accelerometer they are volt/g. The units of Eq. 2-7 can be changed to g/deg by dividing by 32.2 (ft/sec^2)/g and 57.3 deg/rad. Thus Eq. 2-7 becomes

$$\frac{a_z(s)}{\delta_e(s)} = \frac{-0.042(s + 7.75)(s - 7.75)}{s^2 + 0.9s + 8} \frac{g}{\text{deg}} \tag{2-8}$$

An examination of Eq. 2-8 indicates that there is a zero in the right half plane, thus indicating a so-called nonminimum phase angle transfer function. This means that for a positive step input of δ_e the steady-state sign of a_z will be positive, which is consistent with the sign convention already established. Thus the sign at the summer for the acceleration feedback must be negative for negative feedback. The sign for the elevator servo remains positive, so that a positive $a_{z(\text{comm})}$ yields a positive a_z output.

Having settled on the sign of the feedback element, the sign of the open loop transfer function can be determined (see Appendix C) from the sign of each transfer function and the sign at the summer for the feedback element. Thus the sign of the open loop transfer function is positive (the zero in the right half plane has no effect on the sign of the open loop transfer function).
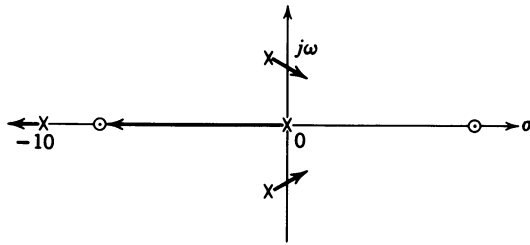
Figure 2-21 Angle of departure of the complex poles for the acceleration control system without rate feedback (zero-angle root locus).

The denominator of the closed loop transfer function is $1 - [\text{TF}]_{\text{OL}}$, which, as the sign of $[\text{TF}]_{\text{OL}}$ is plus, means that $G(s)H(s) = +1$, and the zero angle root locus must be plotted. If the rate gyro loop were not included, the complex poles of the aircraft would move toward the imaginary axis as shown in Figure 2-21. The complex poles of the aircraft must therefore be moved further to the left before closing the accelerometer feedback loop. This can be accomplished by using pitch-rate feedback.

The block diagram for the rate feedback loop is shown in Figure 2-22. The system depicted there is the same as the inner loop of the pitch orientational control system for low angles of attack, the root locus of which was seen in Figure 2-15. The closed loop transfer function for the inner loop of the acceleration control system for $S_{(\text{rg})} = 0.23$ is

$$\frac{\dot{\theta}(s)}{e_a(s)} = \frac{-150(s + 0.4)}{(s + 3)(s^2 + 7s + 24)} \quad \frac{\text{deg/sec}}{\text{volt}} \tag{2-9}$$

The block diagram for the outer loop is shown in Figure 2-23 for $S_{(\text{rg})} = 0.23$. The $a_z / \dot{\theta}$ block is required to change the output of the inner loop $\dot{\theta}$ to the required output for the outer loop a_z. The transfer function for this block can be obtained by taking the ratio of the $a_z(s)/\delta_e(s)$ and $\dot{\theta}(s)/\delta_e(s)$
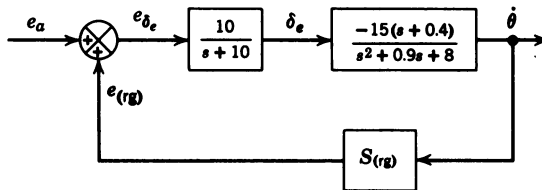
Figure 2-22 Block diagram for the inner loop of the acceleration control system.
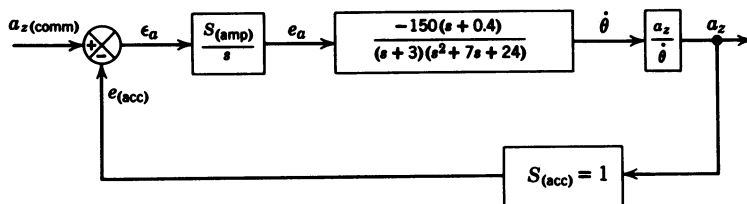
Figure 2-23   Block diagram for the outer loop for the acceleration control system.

transfer functions; thus

$$\frac{a_z(s)}{\dot{\theta}(s)} = \frac{-0.042(s+7.75)(s-7.75)}{-15(s+0.4)} \quad \frac{g}{\deg/\sec} \tag{2-10}$$

Then the $a_z(s)/e_a(s)$ transfer function is the product of Eqs. 2-9 and 2-10, or

$$\frac{a_z(s)}{e_a(s)} = \frac{-0.42(s+7.75)(s-7.75)}{(s+3)(s^2+7s+24)} \quad \frac{g}{\text{volt}} \tag{2-11}$$

This operation changes only the numerator of the forward transfer function by replacing the zero of the $\dot{\theta}(s)/\delta_e(s)$ transfer function with the zeros of the $a_z(s)/\delta_e(s)$ transfer function. The denominator remains the same.

Using Eq. 2-11 with the transfer function of the amplifier and integrator, the root locus for the outer loop can now be drawn and is shown in Figure 2-24. The closed loop poles for $S_{(amp)} = 2.22$ are illustrated in Figure 2-24, and the closed loop transfer function is

$$\frac{a_z(s)}{a_{z(comm)}(s)} = \frac{-0.93(s+7.75)(s-7.75)}{(s^2+2.2s+2.4)(s^2+7.8s+24)} \tag{2-12}$$

Although the accelerometer control system provides good operation, there are some practical problems. One of these is that the accelerometer cannot distinguish between the acceleration due to gravity and accelerations caused by aircraft motion. The acceleration of gravity can be balanced out so that in straight and level flight at normal cruise air speed and altitude the output of the accelerometer would be zero. However, at different angles of attack the accelerometer output would not be zero. For example, if the angle of attack changed by 10° from the value at which the accelerometer was nulled, the output would correspond to ± 0.5 ft/sec^2. The accelerometer can be adjusted so that it is insensitive to accelerations that are less than 1 ft/sec^2, thus eliminating this problem. Another problem which would probably be harder to overcome is the unwanted accelerations arising from turbulence. This shows up as noise and has to be filtered out. As a result of these
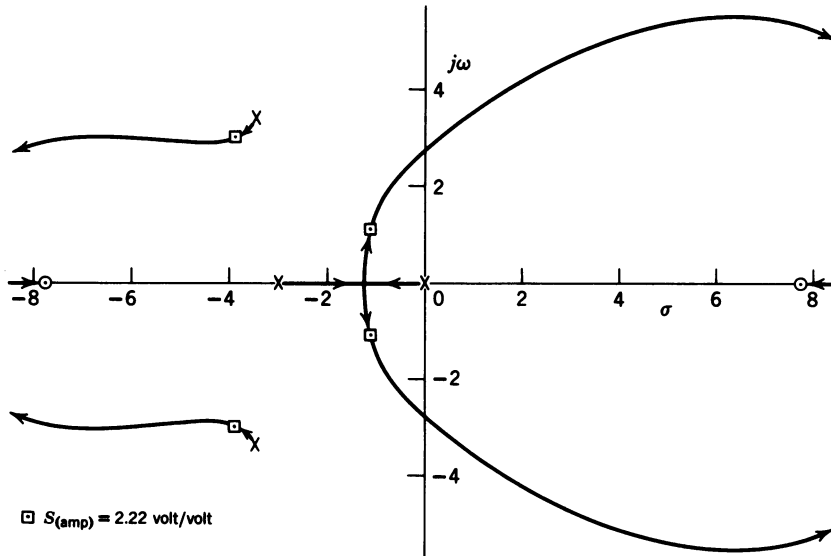
Figure 2-24 *Root locus of the outer loop of the acceleration control system (zero-angle root locus).*

problems, and because there are not many requirements that call for an aircraft maneuvering at constant acceleration, the acceleration autopilot is not often employed. However, there are some requirements that make the acceleration autopilot ideal. An example is the necessity to perform a maximum performance pull-up in connection with a particular tactical maneuver. The system can be adjusted so that the maximum allowable accelerations for the aircraft are experienced during pull-up. Another example will be discussed in Chapter 7, where an acceleration control system is used for the control of a surface-to-air guided missile.

    Now that we have looked at some of the basic longitudinal control systems, their integration into various automatic flight control systems is discussed in Sections 2-4 and 2-5.

2-4   GLIDE SLOPE COUPLER AND AUTOMATIC FLARE CONTROL

The ultimate goal for both military and commercial aviation is all-weather operation. To achieve this goal, it must be possible to land the aircraft without visual reference to the runway. This can be accomplished by an automatic landing system which will guide the aircraft down a predetermined glide slope and then at a preselected altitude reduce the rate of descent and cause the aircraft to "flare" out and touch down with an acceptably low rate of descent. This section covers the longitudinal control portion of such a

system; lateral control is covered in Chapter 4. The design of a glide slope coupler, an automatic flare control system, and an altitude hold control system (to be studied in Section 2-5) have one thing in common, that is, the control of the flight path angle γ. The automatic control of the flight path angle without simultaneous control of the airspeed, either manual or automatic, is impossible. This point is illustrated by studying the response of the attitude control system, without velocity control, that will later be coupled to the glide slope. For this analysis the jet transport in the landing configuration is used. The appropriate longitudinal equations for sea level at 280 ft/sec are

$$(7.4s + 0.15)'u(s) - 0.25'\alpha(s) + 0.85\theta(s) = C_{x_T}\delta_{(rpm)}(s)$$

$$1.7'u(s) + (7.4s + 4.5)'\alpha(s) - 7.4s\theta(s) = -0.246\delta_e(s)$$

$$(0.118s + 0.619)'\alpha(s) + (0.59s^2 + 0.41s)\theta(s) = -0.71\delta_e(s) \quad (2-13)$$

where

$$C_{x_T} = \frac{1}{Sq} \frac{\partial T}{\partial \delta_{(rpm)}} \text{ rpm}^{-1}.$$

For the basic autopilot, $\delta_{(rpm)}$ is considered zero.

Figure 2-25 is a block diagram of the basic autopilot used in this analysis. The root locus for the inner loop is shown in Figure 2-26. The rate gyro sensitivity was selected so the complex poles would lie on the branches approaching the 90° asymptotes with a damping ratio greater than 0.7, in this case 0.866. The higher damping ratio was chosen because the outer loop tends to decrease the damping of the complex roots. For the closed loop poles indicated in Figure 2-26, $S_{(rg)} = 2.5$ volt/(rad/sec). Using the closed loop poles from the root locus shown in Figure 2-26, the block diagram for the outer loop can be drawn and is seen in Figure 2-27. The root locus for the outer loop is shown in Figure 2-28, with the location of the closed loop poles for $S_{(amp)} = 3.88$ volt/volt, which yields a damping ratio of 0.8. The reason for this selection will be more obvious when the root locus for the final outer loop through the glide slope coupler is examined later in this section.
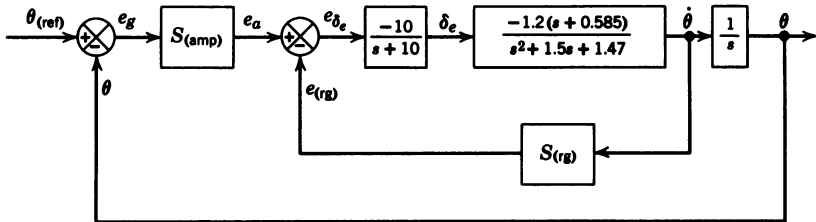
Figure 2-25 *Basic autopilot for the jet transport, landing configuration.*
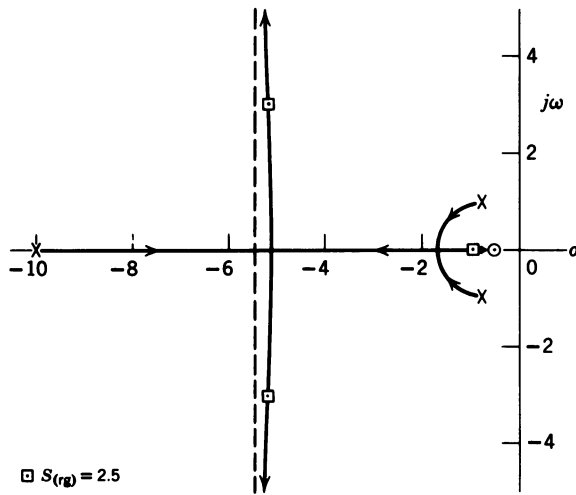
Figure 2-26 *Root locus for the inner loop of the basic autopilot for the jet transport.*

After selection of the gains for the two loops of the basic autopilot, the aircraft and the basic autopilot were simulated on the analog computer. For the aircraft simulation the complete three-degree-of-freedom longitudinal equations were used. The response of the aircraft alone, for a step elevator input with no velocity control, is depicted in Figure 2-29. The effect of adding rate gyro feedback is shown in Figure 2-30. It is evident that the rate gyro has little effect on the damping of the phugoid mode. The response of the aircraft, including the basic autopilot for a step $\theta_{(comm)}$ can be seen in Figure 2-31. The necessity for velocity control is now evident, since the steady-state value of γ is $-0.2°$. This value results from a positive θ command, which it is hoped will cause the aircraft to climb (positive γ). However, as the nose of the aircraft rises and the aircraft starts to climb, the airspeed decreases, requiring an increase in the angle of attack to maintain the required lift. In the steady state this increase in the angle of attack is greater than the change in θ, and as $\gamma = \theta - '\alpha$, the result is that the aircraft starts a very shallow glide. In order for γ to have the same steady-state sign as $\theta_{(comm)}$, some form of velocity control must be employed.
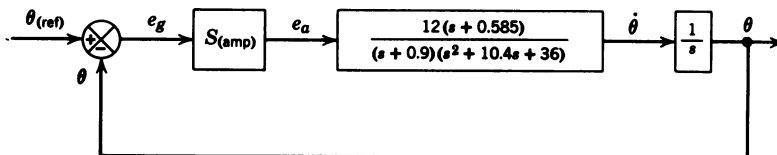
Figure 2-27 *Block diagram for the root locus of the outer loop of the basic autopilot.*
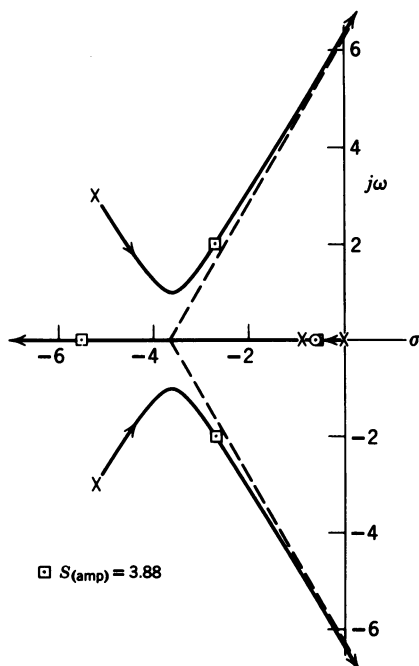
Figure 2-28   *Root locus for the outer loop of the basic autopilot for the jet transport.*

An automatic velocity control system, sometimes referred to as "phugoid damping," is shown in Figure 2-32. The time constant for the jet engine is taken as 10 sec and may be excessive; however, if the system can be made to operate with this lag, its performance would be even better if the actual engine time constant were less. This time lag represents the time required for the thrust of the jet engine to build up after a movement T_p of the throttle. Since u is the change in airspeed, the input to the aircraft block is the change in the engine speed from that required for straight and level unaccelerated flight. The first block in the forward loop of Figure 2-32 is a proportional plus integral network which makes the system Type 1 and also provides compensation by adding a zero at $s = -0.1$. Velocity and the rate of change of velocity are used in the feedback path. Both the velocity error (actually airspeed error) and the velocity rate signal can be supplied by a single instrument.[2] The aircraft transfer function can be obtained from Eq. 2-13 and is

$$\frac{u(s)}{\delta_{(rpm)}(s)} = \frac{37.9 C_{x_{T}} s(s^2 + 1.5s + 1.47)}{(s^2 + 1.51s + 1.48)(s^2 + 0.009s + 0.0186)} \quad \frac{\text{ft/sec}}{\text{rpm}} \quad (2\text{-}14)$$

The existence of the quadratic, in the numerator of Eq. 2-14, that almost exactly cancels the short-period quadratic in the denominator is not a
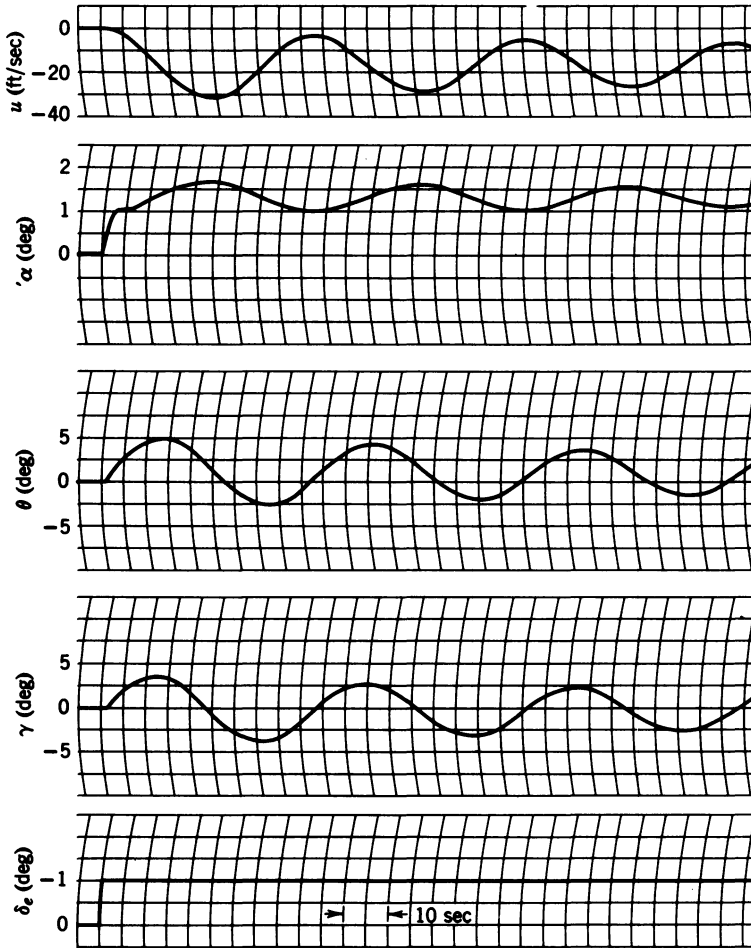
Figure 2-29 *Transient response of the jet transport in the landing configuration at sea level at 280 ft / sec for an elevator step input.*

coincidence. The reason for this can be seen by examining the determinant of the numerator used to determine Eq. 2-14. This determinant is

$$\begin{vmatrix} C_{x_T} & -0.25 & 0.85 \\ 0 & 7.4s+4.5 & -7.4s \\ 0 & 0.118s+0.619 & 0.59s^2+0.41s \end{vmatrix}$$

The result of expanding the foregoing determinant yields C_{x_T} times its minor, but the minor of C_{x_T} is identical to the determinant of the denominator for any of the transfer functions obtained by using the short-period approxima-
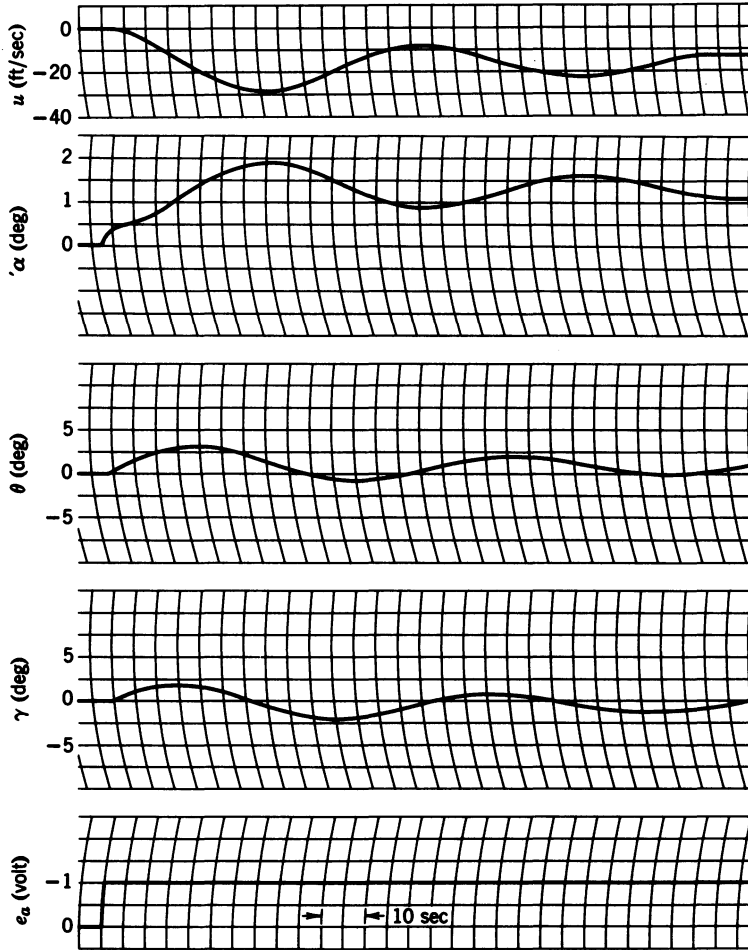
Figure 2-30 *Transient response of the jet transport with pitch-rate feedback for $S_{(rg)} = 2.5$ volt / (deg / sec), for step input of e_a.*

tion. As the short-period poles are effectively canceled by the complex zeros for the $u(s)/\delta_{(rpm)}(s)$ transfer function, the velocity control loop has no effect on the short-period mode. This characteristic of the velocity control loop is used to simplify the remaining analysis.

In Figure 2-32 the open loop transfer function using Eq. 2-14 is

$$[TF]_{OL} = \frac{-3790 C_{x_T} S_e (s + 0.1)}{(s + 10)(s^2 + 0.009s + 0.0186)} \tag{2-15}$$

Figure 2-33 is a sketch of the root locus for the velocity control loop. The
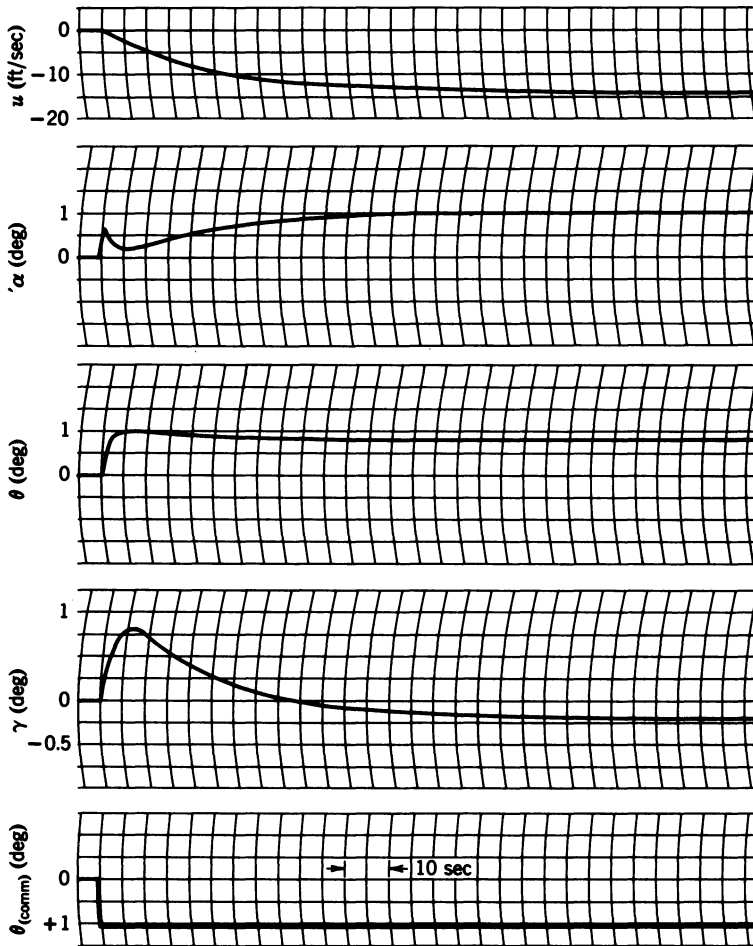
Figure 2-31   Transient response of the jet transport and basic autopilot for $S_{(amp)} = 3.88$ volt / volt, for a θ step command.
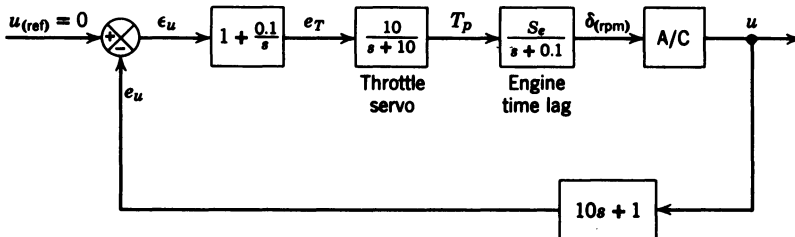
Figure 2-32   Velocity control system using throttle.

$$[TF]_{CL} = \frac{75.8}{(s + 0.1004)(s^2 + 9.908s + 757.1)}$$
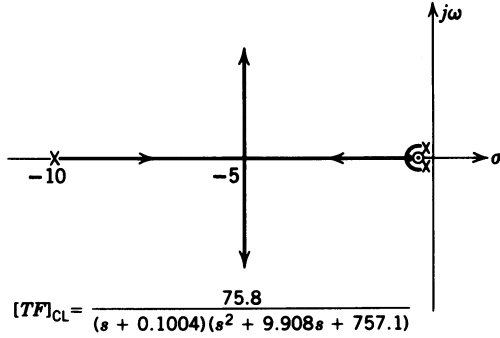
Figure 2-33   Sketch of root locus for the velocity control loop (not to scale).

effectiveness of the velocity control loop for damping the phugoid mode is very apparent. The value of the product of $C_{x_T}S_e$ selected is 0.2. This value is determined experimentally from the results of the computer simulation. For this value, the complex poles on the vertical branches of Figure 2-33 have a damping ratio of 0.182 and a natural frequency of 27.5 rad/sec. The real pole near the real zero is thus the dominant root. The effect of the velocity control loop for the basic aircraft with no other feedback is illustrated in Figure 2-34(a), and its effect on the aircraft with the basic autopilot is shown in Figure 2-34(b). As can be seen from Figure 2-34(b), the steady-state sign of γ is not only positive for a positive $\theta_{(\text{comm})}$ but also is equal to the commanded pitch angle. It should also be noted that the velocity control loop has not affected the initial portion of the transient response of $'\alpha$, θ, and the initial signs of the γ trace [Figure 2-34(b)]. From this and the fact that the short-period quadratic is canceled by the numerator quadratic in Eq. 2-14, it can be concluded that the velocity control loop does not affect the short-period dynamics of the aircraft. Therefore if velocity control is assumed, either manual or automatic, the short-period transfer functions can be used for any analysis of any control system employed for the control of the flight path angle.

The effect of velocity control has been illustrated, and the design and analysis of a glide slope coupler may now be continued.

The geometry associated with the glide slope problem is shown in Figure 2-35. If the aircraft is below the centerline of the glide slope (Figure 2-35), then d is considered negative, as is γ, when the velocity vector is below the horizon, that is, the aircraft descending. The component of U perpendicular to the glide slope center line is $\dot{d}$ and is given by

$$\dot{d} = U \sin\left(\gamma + 2\tfrac{1}{2}\right)^{\circ} \simeq \frac{U}{57.3}\left(\gamma + 2\tfrac{1}{2}\right)^{\circ} \tag{2-16}$$

for small angles. For the condition shown as $\gamma < 2\tfrac{1}{2}^{\circ}$ in Figure 2-35, then

(a) Basic aircraft.   (b) Basic aircraft and autopilot.
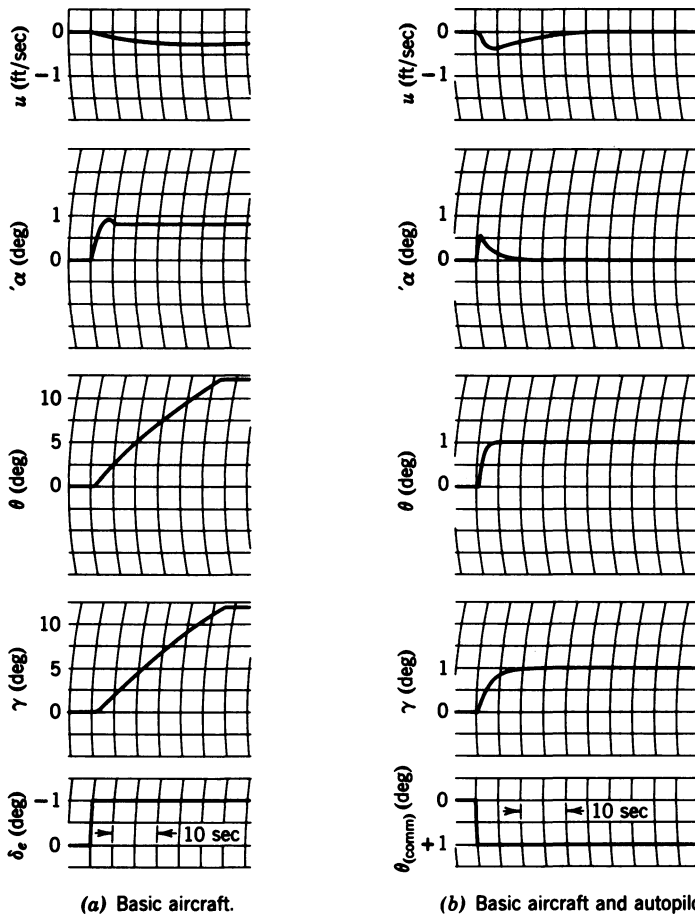
Figure 2-34 Transient response of jet transport, with and without the basic autopilot, showing the effects of velocity control.
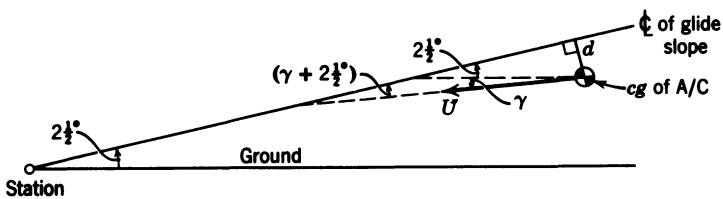
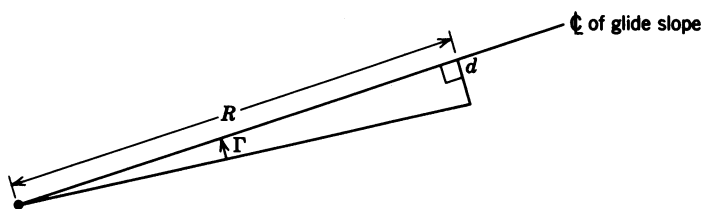**Figure 2-35** Geometry of the glide slope problem. Note: d and γ are negative.

Figure 2-36 *Effect of beam narrowing.*

$\gamma + 2\frac{1}{2}°$ is positive; therefore $\dot{d}$ is positive, and as d initially was negative, the aircraft is approaching the glide path from below. Integrating Eq. 2-16 yields

$$d \approx \frac{U}{57.3s}(\gamma + 2\frac{1}{2})° \qquad (2\text{-}17)$$

One other factor must be included, and that is that the glide slope receiver does not measure the perpendicular distance to the glide slope centerline but the angular error resulting therefrom. Thus for a given value of d the angular error increases as the aircraft nears the station, which has the effect of increasing the system gain as the range to the station decreases as shown in Figure 2-36. From Figure 2-36, $\tan \Gamma = d/R$, or for small angles and Γ in degrees

$$\Gamma \approx 57.3d/R \text{ deg} \qquad (2\text{-}18)$$

Through the use of Eqs. 2-17 and 2-18 the flight path angle γ can be related to the angular error of the aircraft from the glide slope centerline, and the block diagram for the glide slope control system can be drawn, including the geometry (see Figure 2-37). Figure 2-37 shows that the coupler contains a proportional plus integral circuit, plus a lead compensator. The zero of the lead network is selected so that it cancels the closed loop pole at $s = -0.5$ from the basic autopilot (see Figure 2-28). The factor of 10 is included to provide a steady-state gain of 1 for the lead circuit. The $\gamma(s)/\theta(s)$ transfer function is required to convert the θ output from the aircraft and autopilot
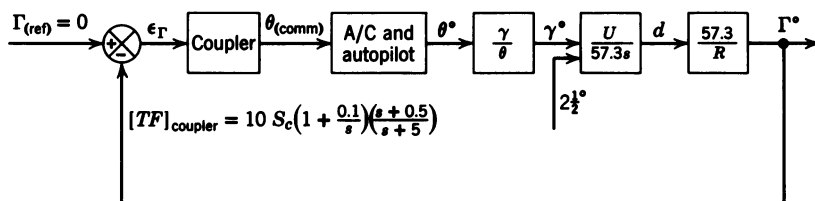
Figure 2-37 *Block diagram of automatic glide slope control system.*

transfer function to γ, and can be derived from the relation $\gamma = \theta - {}'\alpha$ (see Figure 1-3). Then

$$\frac{\gamma(s)}{\theta(s)} = 1 - \frac{{}'\alpha(s)}{\theta(s)}$$

but

$$\frac{{}'\alpha(s)}{\theta(s)} = \left[\frac{{}'\alpha(s)}{\delta_e(s)}\right]\left[\frac{\delta_e(s)}{\theta(s)}\right] = \frac{0.0276s(s+36.7)}{s+0.585}$$

as

$$\frac{\theta(s)}{\delta_e(s)} = \frac{-1.2(s+0.585)}{s(s^2+1.5s+1.47)}$$

and

$$\frac{{}'\alpha(s)}{\delta_e(s)} = \frac{-0.0332(s+36.7)}{s^2+1.5s+1.47}$$

Substituting and simplifying,

$$\frac{\gamma(s)}{\theta(s)} = -\frac{0.0276(s+4.85)(s-4.35)}{s+0.585} \qquad (2\text{-}19)$$

Equation 2-19 is the required transfer function; however, most control system designers use a simplified form of Eq. 2-19, which is

$$\frac{\gamma(s)}{\theta(s)} = \frac{0.585}{s+0.585} \qquad (2\text{-}20)$$

Equation 2-20 can be obtained by neglecting the s terms in the numerator of Eq. 2-19. Although a root locus analysis using Eq. 2-20 gives good results, Eq. 2-19 is used in the analysis to follow. For the closed loop poles shown in Figure 2-28,

$$\frac{\theta(s)}{\theta_{(comm)}(s)} = \frac{46.5(s+0.585)}{(s+0.5)(s+5.5)(s^2+5.4s+11.4)} \qquad (2\text{-}21)$$

Using the transfer functions shown in Figure 2-37 and Eqs. 2-19 and 2-21, the forward transfer function for the glide slope control system can be obtained and is given in Figure 2-38 for $U = 280$ ft/sec. The zero-angle root locus for the glide slope control system is shown in Figure 2-39. For this root locus the coupler sensitivity is constant at a value of $10°$ of $\theta_{(comm)}$ per degree of ϵ_Γ,
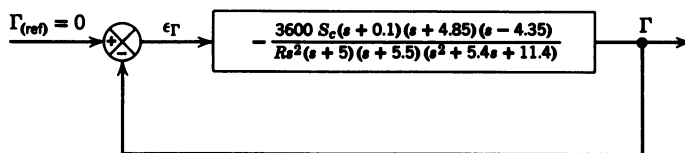
Figure 2-38 Simplified block diagram of automatic glide slope control system.

and the range to the station, R, provides the variable gain. Thus it can be seen that the dynamics of the system change as the aircraft approaches the station. The problem involved in the design of a satisfactory glide slope coupler results from the two poles at the origin, one from the coupler, the other from the geometry. Without the zero at $s = -0.1$, from the proportional plus integral network, the poles at the origin would move immediately into the right half plane. Even with the zero at $s = -0.1$, if the pole at $s = -0.5$ were not canceled by the zero of the compensator, the system would, at best, be only marginally stable for a limited range of R. Since the range to the station provides the variable gain for the glide slope control system, the root locus can be used to determine the minimum range for stable operation. For this case, the magnitude condition for the point where the root locus crosses the imaginary axis yields a K of 27, which must be equal to $3600 S_c / R$. Therefore $R = 134 S_c$, which for $S_c = 10$ gives a minimum range of 1340 ft. From the computer simulation the minimum range was determined as 1300 ft, thus further verifying the validity of using the short-period approximation for the root locus analysis, if velocity control is assumed.
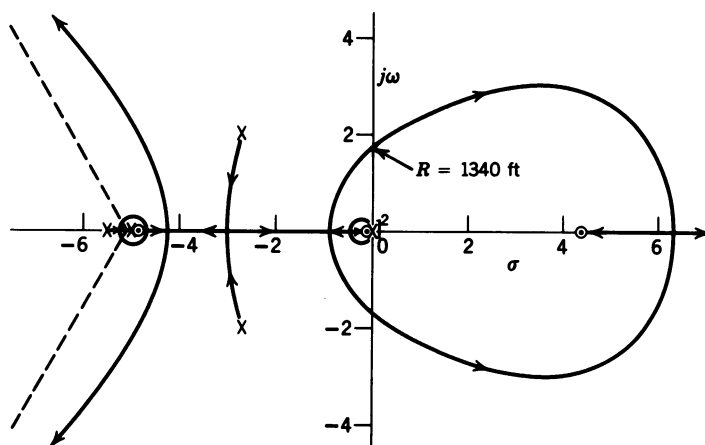
Figure 2-39 Root locus for the automatic glide slope control system for $S_c = 10$ (zero-angle root locus).
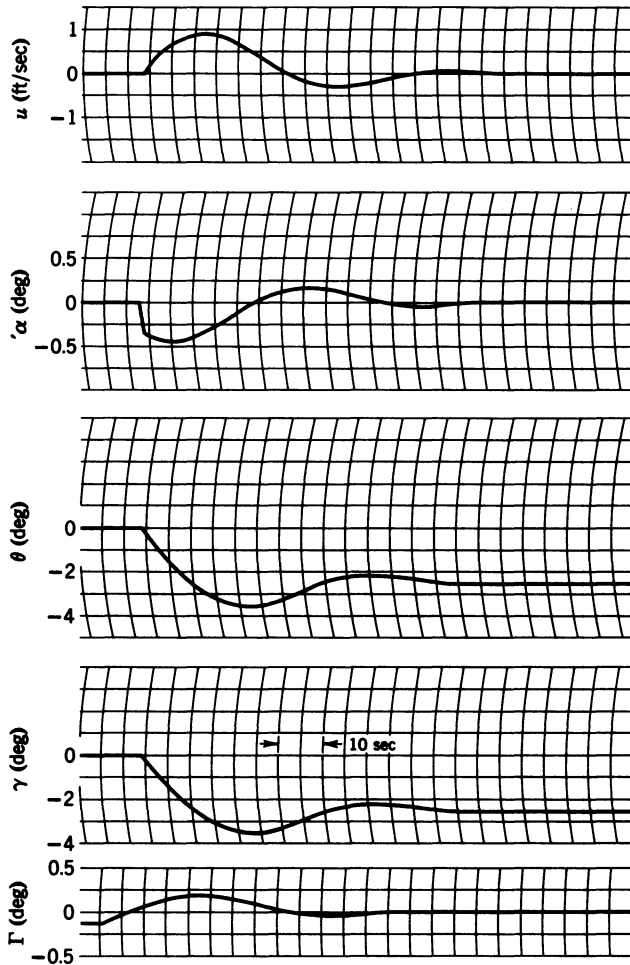
Figure 2-40   *Time response of the automatic glide slope control system for S_c = 10 deg / deg.*

The results of the computer simulation of the complete longitudinal equations of motion plus the basic autopilot and the velocity control system (see Figure 2-32) are shown in Figures 2-40 and 2-41. The aircraft was placed initially at 1400 ft above the station (100 ft below the glide slope) in straight and level flight. The glide slope control system was engaged as the aircraft passed through the glide slope centerline. As can be observed in Figure 2-41, the aircraft has settled onto the glide slope while still about three miles from the station. From Figure 2-40 it can be seen that the maximum overshoot is only 0.15°, which is much less than the maximum deflection of ±0.5° for the pilot's glide slope indicator.
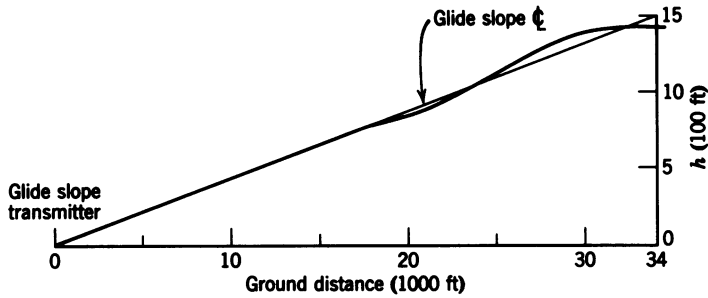
Figure 2-41 *Response of the automatic glide slope control system for $S_c = 10$ deg / deg.*

As mentioned earlier, the forward loop gain is dependent upon the range to the station, which leads to instability as the range decreases. To combat this the coupler sensitivity can be decreased as the range is decreased; however, to do this accurately requires the instantaneous range to the station, which is normally not available. This difficulty can be overcome by using a self-adaptive control system to be discussed in Chapter 6.

The final phase of the landing is the transition from the glide slope to the actual touchdown, generally referred to as "the flare." The rest of this section deals with the analysis and design of an automatic flare control.

Flight test data has shown that when a pilot performs the flare from the approach glide to the final touchdown he generally decreases his rate of descent in an exponential manner, thus tending to make the aircraft fly an exponential path during the flare. For the automatic flare control, then, the aircraft is commanded to fly an exponential path from the initiation of the flare until touchdown. Thus

$$h = h_0 e^{-t/\tau} \tag{2-22}$$

where h is the height above the runway, and h_0 is the height at the start of the flare. Differentiating Eq. 2-22 yields

$$\dot{h} = -\frac{h_0}{\tau} e^{-t/\tau} = -\frac{h}{\tau} \tag{2-23}$$

The geometry of the flare path is illustrated in Figure 2-42. Equation 2-23 can be used to determine h_0 if τ is known, that is, for $t = 0$, $h_0 = -\tau \dot{h}_0$. Since $\dot{h}_0$ is the rate of descent at the initiation of the flare, then for a $2\frac{1}{2}°$ glide slope and a velocity of 280 ft/sec, $\dot{h}_0 = -12.2$ ft/sec. The desired value of τ can be obtained by specifying the distance to the touchdown point from the glide slope transmitter. If this distance is to be 1000 ft and if it is assumed that the aircraft touches down in four time constants, then the ground
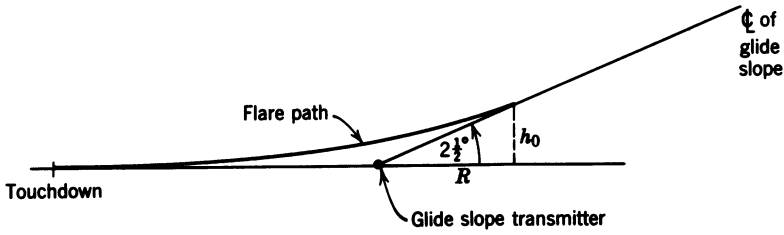
Figure 2-42 Geometry of flare path.

distance traveled during the flare, if the aircraft's velocity is constant, is

$$R + 1000 = (280)(4\tau) \tag{2-24}$$

But $h_0 = 12.2\tau$, and from Figure 2-42, $\tan 2\frac{1}{2}° = h_0/R = 12.2\tau/R$; therefore $R = 280\tau$.

Substituting for R in Eq. 2-24 and solving for τ yields $\tau = 1.18$ and $\dot{h} = -h/1.18 \simeq -0.8h$. Then $h_0 = 12.2/0.8 = 15.2$ ft. The control equation for the automatic flare control system is then

$$\dot{h}_r = -0.8h \tag{2-25}$$

The block diagram for the automatic flare control system can be seen in Figure 2-43. The outer loop simply supplies the rate-of-descent command, $\dot{h}_r$. The transfer function for the aircraft and autopilot is the same as the one used for the glide slope analysis and as given in Eq. 2-21. The $\dot{h}(s)/\theta(s)$ transfer function can be obtained from the $\gamma(s)/\theta(s)$ transfer function and is

$$\frac{\dot{h}(s)}{\theta(s)} = \frac{U}{57.3}\left[\frac{\gamma(s)}{\theta(s)}\right] = \frac{-7.73(s+4.85)(s-4.35)}{57.3(s+0.585)} \tag{2-26}$$
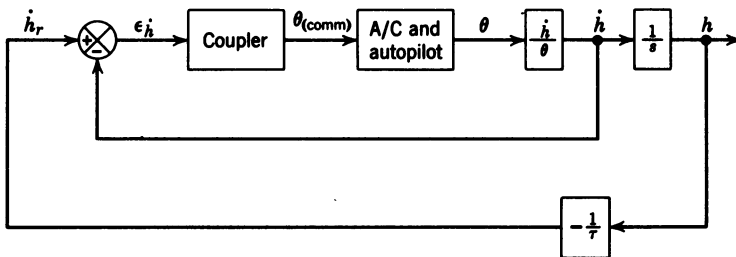
Figure 2-43 Block diagram of automatic flare control system.
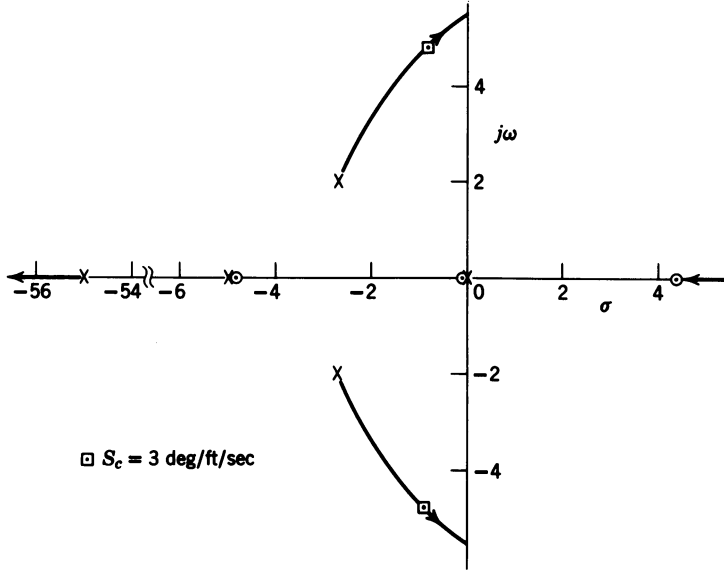
Figure 2-44   *Root locus for the automatic flare control system.*

The coupler transfer function is

$$[TF]_{coupler} = 10S_c \left(1 + \frac{0.1}{s}\right)\left(\frac{s+0.5}{s+5}\right)\left(\frac{s+5.5}{s+55}\right) \qquad (2\text{-}27)$$

which is the same as that for the glide slope control system, plus an additional lead network. The second lead network is added to obtain a higher value of coupler sensitivity, thus preventing the aircraft from flying into the runway too soon. The open loop transfer function from Eqs. 2-21, 2-26, and 2-27 is

$$[TF]_{OL} = \frac{63S_c(s+0.1)(s+4.85)(s-4.35)}{s(s+5)(s+55)(s^2+5.4s+11.4)} \qquad (2\text{-}28)$$

The root locus for the automatic flare control system is shown in Figure 2-44, with the location of the complex poles indicated for a coupler sensitivity of $3°$ of $\theta_{(comm)}$ per ft/sec error in rate of descent. The results of the computer simulation are shown in Figures 2-45 and 2-46. It is found that the command equation must be changed to $\dot{h}_r = -0.6h$ for satisfactory operation. An examination of Figure 2-45 yields a natural frequency of 4.6 rad/sec as compared with 4.8 rad/sec from the root locus analysis. The damping ratio is difficult to measure because the oscillation is superimposed on a first-order response, but it is probably between 0.15 and 0.2. The damping ratio from
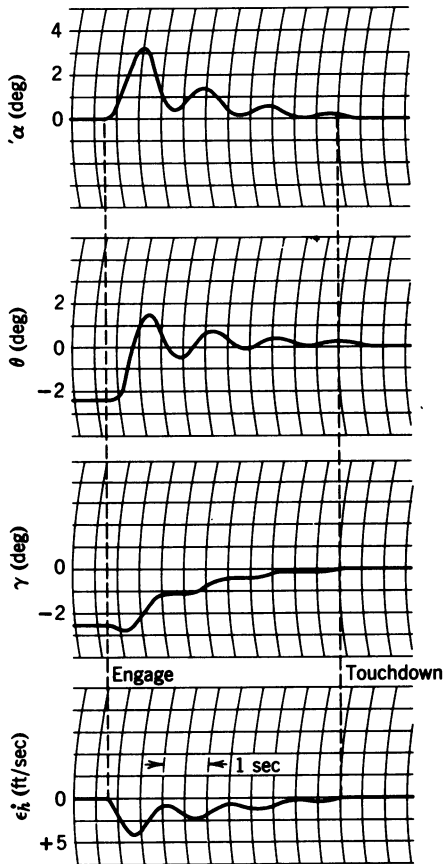
Figure 2-45 Time response of the automatic flare control system for $S_c = 3$ deg / (ft / sec) and $\dot{h}_r = -0.6h$.
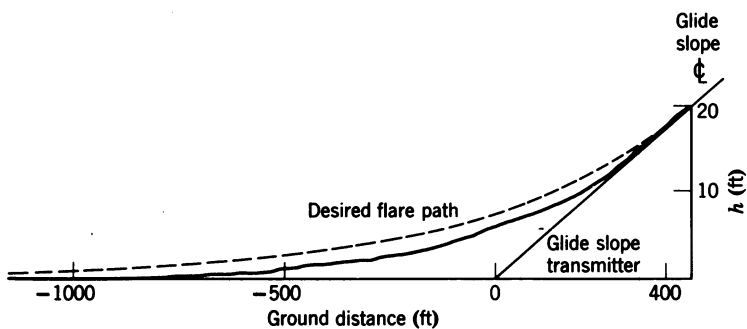
Figure 2-46 Response of the automatic flare control system for $S_c = 3$ deg / (ft / sec) and $\dot{h}_r = -0.6h$.

the root locus is 0.19. The agreement is considered excellent. In Figure 2-46 the actual path is compared with the desired flare path and is considered better than acceptable. The rate of descent at touchdown is approximately 30 ft/min, which does not include the ground effect that would be present for an actual landing and thus reduce the rate of descent further. This would be considered an excellent landing by any pilot.

2-5 FLIGHT PATH STABILIZATION

The two modes of operation of a complete longitudinal flight control system investigated here are referred to as "Mach hold" and "altitude hold." These modes are generally used during cruise operation, and one or the other selected depending on the mission requirement. In the Mach hold mode the aircraft is made to fly at a constant Mach number by automatically controlling the flight path angle through the elevators. For this mode of operation the aircraft is first trimmed to fly straight and level and the power adjusted to yield the desired Mach number. The Mach hold mode of the flight control system is then engaged. As the aircraft (usually a jet type) cruises, fuel is used, the weight of the aircraft decreases, and the speed tends to increase. The increase in speed is sensed by the control system and corrected for by an up-elevator signal causing the aircraft to climb. The net result of operation in the Mach hold mode is that the aircraft is made to climb slowly as fuel is consumed in order to maintain a constant Mach number. Since the fuel consumption of a jet aircraft decreases as the altitude increases, this mode of operation is desirable for long-range operation; however, there are many times when it is necessary to fly at a constant altitude. Under these conditions the altitude hold mode is selected: the aircraft's flight path angle (and thus its altitude) is controlled by the elevators, and the airspeed or Mach number is controlled, either manually or automatically, by use of the throttle. For the analysis of these two modes, the transfer functions for the jet transport cruising at 600 ft/sec at 40,000 ft are used.

For the analysis of the Mach hold mode it is assumed that the altitude variations are small so that the variations in Mach number can be represented by variations in velocity. Figure 2-47 is a block diagram of the Mach hold mode of the flight control system. As the change in the velocity is needed for the outer loop, the complete three-degree-of-freedom longitudinal equations must be used for the root locus analysis of both the inner and outer loops. For this aircraft, the required $\dot{\theta}(s)/\delta_e(s)$ transfer function can be obtained from Eq. 1-126, which is repeated here:

$$\frac{\dot{\theta}(s)}{\delta_e(s)} = \frac{-1.31s(s+0.016)(s+0.3)}{(s^2+0.00466s+0.0053)(s^2+0.806s+1.311)} \frac{\text{deg/sec}}{\text{deg}} \quad (2\text{-}29)$$

Because the short-period portion of Eq. 2-29 is almost identical to the short-period approximate transfer function for $\dot{\theta}(s)/\delta_e(s)$, Figure 2-8 is still
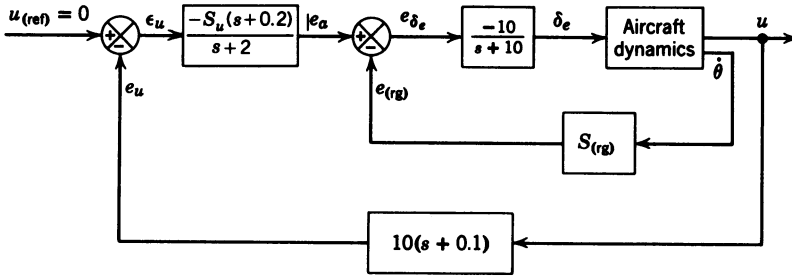
Figure 2-47   Mach hold mode of the flight control system.

valid for the short-period portion of the inner loop of the Mach hold mode. If the remaining poles and zeros from Eq. 2-29 were plotted on Figure 2-8, they would all appear as if located at the origin and therefore would not change the root locus in Figure 2-8. Since the aircraft gain for the three-degree-of-freedom transfer function is 1.31 instead of the 1.39 from the short-period transfer function (see Figure 2-7), the rate gyro sensitivity corresponding to $S_{(rg)} = 1.98$ for Figure 2-8 is 2.1 volt/(deg/sec).

It is still necessary to determine the location of the phugoid poles for this value of rate gyro sensitivity. To do this the portion of the root locus near the origin must be expanded as shown in Figure 2-48. To obtain the portion of the root locus in the vicinity of the origin, it is assumed that the angle and magnitude contributions from the poles and zeros not shown in Figure 2-48 are constant. The closed loop location of the phugoid poles is shown in Figure 2-48. Combining the results of Figures 2-8 and 2-48, the closed loop transfer function for the inner loop for $S_{(rg)} = 2.1$ volt/(deg/sec) can be obtained and is given by

$$\frac{\dot{\theta}(s)}{e_a(s)}\bigg]_{CL} = \frac{13.1s(s+0.3)(s+0.016)}{(s+0.8)(s^2+10s+29)(s^2+0.01s+0.003)} \frac{deg/sec}{volt} \quad (2\text{-}30)$$

□ Closed loop phugoid poles for
  $S_{(rg)} = 2.1$ volt/deg/sec
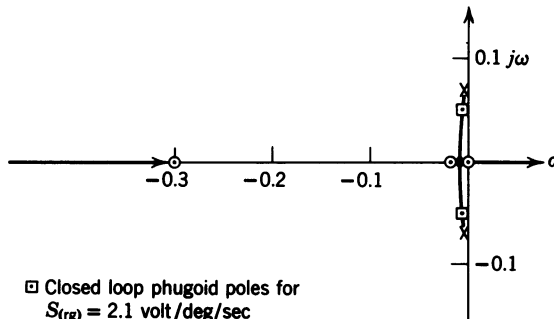
Figure 2-48   Sketch of expanded portion of the root locus for the inner loop of Figure 2-47.

$$u_{(ref)} = 0 \quad \epsilon_u \quad \frac{-0.0525 S_u (s - 68.8)(s + 0.6)(s + 0.2)}{(s + 0.8)(s^2 + 0.01s + 0.003)(s^2 + 10s + 29)(s + 2)} \quad u$$

$$e_u$$

$$10(s + 0.1)$$
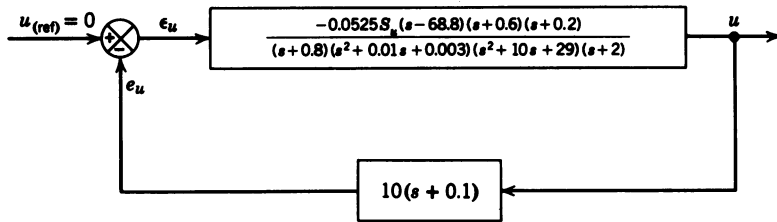
Figure 2-49 *Block diagram for the root locus analysis of the outer loop.*

As in the case of the glide slope, the $\dot{\theta}$ output of the inner loop must be changed to u, the required output for the outer loop. This requires the $u(s)/\dot{\theta}(s)$ transfer function which is U times the ratio of the $'u(s)/\delta_e(s)$ transfer function to the $\dot{\theta}(s)/\delta_e(s)$ transfer function. The transfer function is

$$\frac{u(s)}{\dot{\theta}(s)} = \frac{0.23(s - 68.8)(s + 0.6)}{57.3s(s + 0.016)(s + 0.3)} \frac{\text{ft/sec}}{\text{deg/sec}} \tag{2-31}$$

The 57.3 in the denominator of Eq. 2-31 is required to convert $'u(s)/\delta_e(s)$ from radians to degrees. Using Eqs. 2-30 and 2-31, the simplified block diagram for the outer loop root locus can be drawn and is shown in Figure 2-49. Due to the zero in the right half plane of the forward transfer function in Figure 2-49, the steady-state sign of u for a positive input is positive. Therefore the minus sign is required at the summer for the feedback signal, and the zero-angle root locus must be plotted. The root locus is seen in Figure 2-50 with the location of the complex roots for $S_u = 1.19$ volt/volt. As these poles move into the right half plane at some value of S_u, their closed

□ $S_u = 1.19$ volt/volt
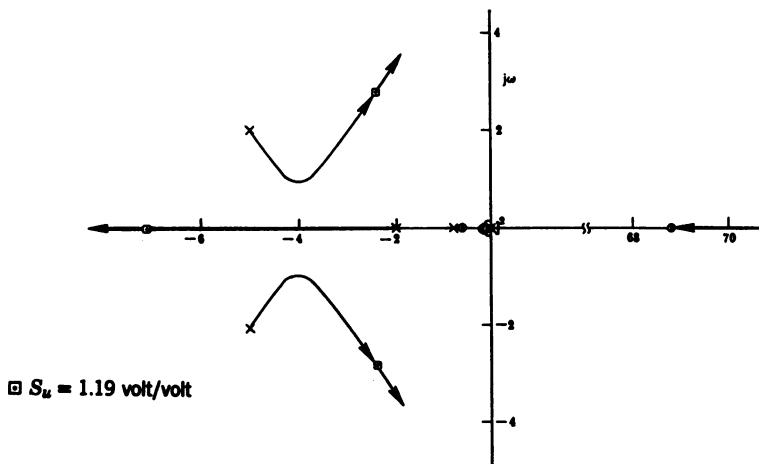
Figure 2-50 *Root locus for the outer loop of the Mach hold mode (zero-angle root locus).*
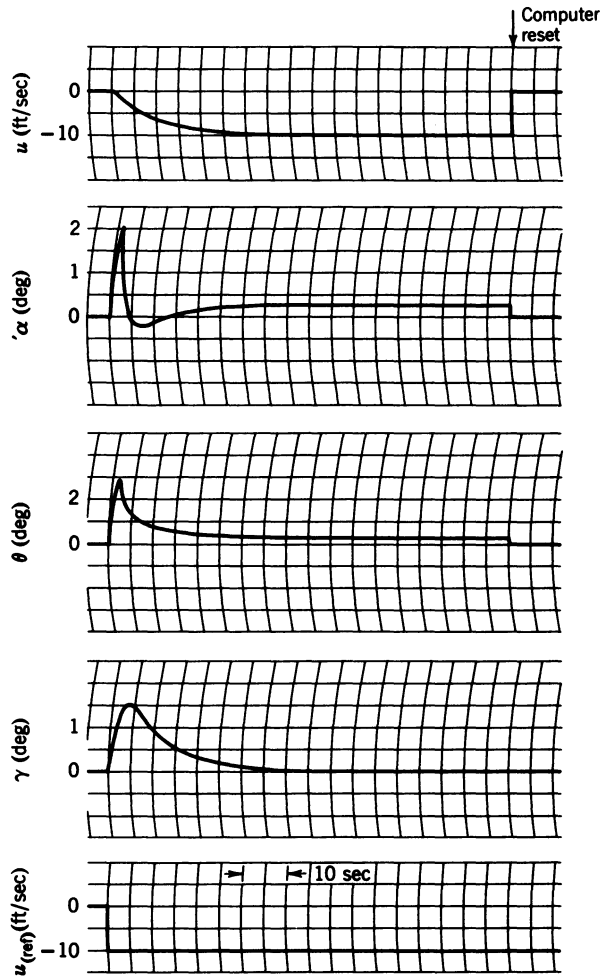
Figure 2-51 *Response of the Mach hold control system to a step input of $u_{(ref)}$ for $S_u = 1$.*

loop location determines the degree of stability of the system. The poles near the origin representing the phugoid mode move around, break into the real axis, and are the dominant roots. The response of the system to a step command of $u_{(ref)}$ is depicted in Figure 2-51. The dominance of the real pole near the origin is evident, especially in the velocity response. The fact that the velocity response exhibits a pure first-order response characteristic and that the steady state condition is reached in 40 sec suggests an almost ideal response.

The block diagram for the altitude hold mode is drawn in Figure 2-52. As in the case of the acceleration control system, the short-period approximation
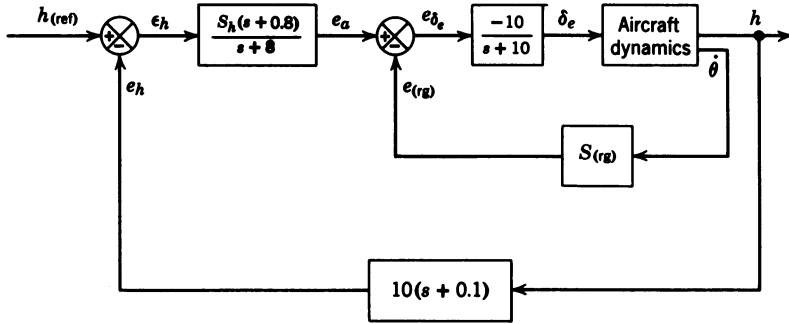
Figure 2-52 Altitude hold mode of flight control system.

can be used for the analysis of the altitude hold mode. Since the jet transport is being used for this analysis, the root locus for the inner loop is the same as the one shown in Figure 2-8, and for $S_{(rg)} = 1.98$ the closed loop transfer function for the inner loop is

$$\frac{\dot{\theta}(s)}{e_a(s)} = \frac{13.9(s+0.306)}{(s+0.8)(s^2+10s+29)} \quad \frac{\text{deg/sec}}{\text{volt}} \qquad (2\text{-}32)$$

The block diagram for the outer loop analysis can now be drawn and is shown in Figure 2-53. The minus sign that appears in the $h(s)/\dot{\theta}(s)$ transfer function arises from the sign convention used. As γ is taken as positive for an aircraft in a climb, the rate of climb $(\dot{h})$ resulting from a positive γ is taken as positive, and therefore h is considered positive for an aircraft whose altitude has increased. This is also consistent with the measurement of altitude. Since a_z is taken as positive downward, $h = (-1/s^2)a_z$. The sign at the summer for the feedback signal must be negative for the same reasons as those discussed for the acceleration control system. The zero-angle root locus for the altitude hold mode can be seen in Figure 2-54, with the location of the closed loop poles for $S_h = 0.493$.
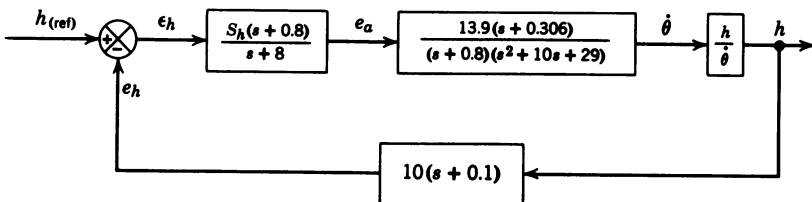
Figure 2-53 Block diagram for the outer loop of the altitude hold mode, where

$$\frac{h(s)}{\dot{\theta}(s)} = -\frac{1}{s^3}\frac{a_z(s)}{\theta(s)} = \frac{-0.135(s-4.89)(s+4.89)}{s^2(s+0.306)} \quad \frac{\text{ft}}{\text{deg/sec}}$$

$\boxdot$ S_h = 0.493 volt/volt
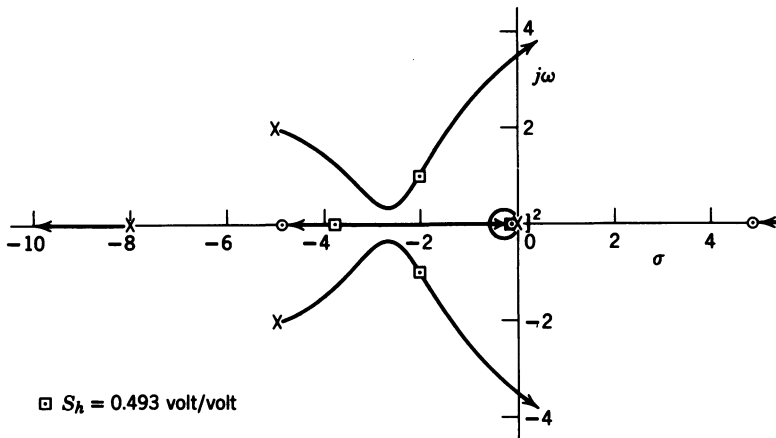
Figure 2-54 *Root locus for the outer loop of the altitude hold mode (zero-angle root locus).*
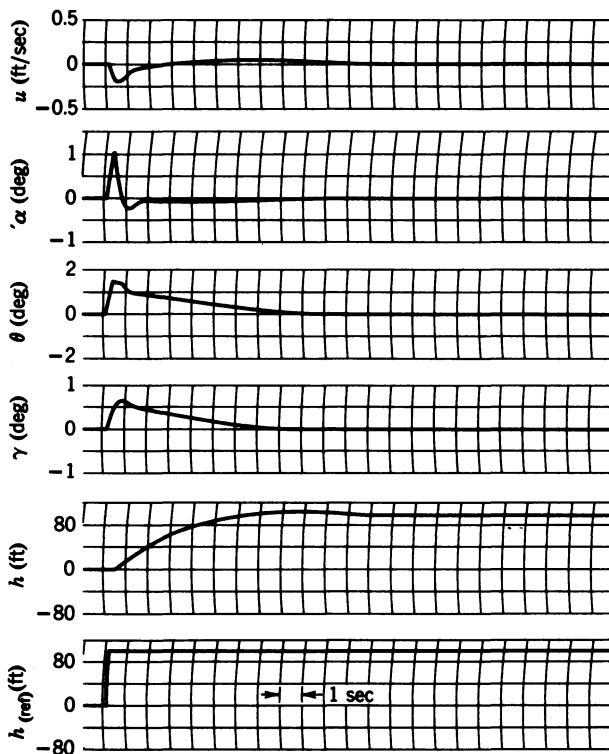
Figure 2-55 *Response of the altitude hold mode control system to a step input of $h_{(ref)}$ for $S_h = 0.5$.*

In Section 2-4 it was observed that it is impossible to control the flight path angle without simultaneous control of the velocity. Therefore, although the short-period equations are used for the analysis, the complete three-degree-of-freedom equations are employed for the simulation combined with the velocity control system that was used for the glide slope control system. The response of the altitude hold mode is shown in Figure 2-55, for a step input of 100 ft for $h_{(ref)}$. This value is equivalent to engaging the altitude hold mode with an error of 100 ft between the actual and reference altitudes. As can be seen from the computer traces, the change in altitude is smooth, with no violent changes in angle of attack or pitch attitude.

This discussion completes the analysis of the two modes of flight path stabilization.

2-6   VERTICAL GYRO AS THE BASIC ATTITUDE REFERENCE

For some of the autopilot configurations discussed in this chapter it is necessary to determine the actual pitch attitude of the aircraft. This can be accomplished by use of a vertical gyro. The vertical gyro also provides an indication of bank angle for use in conjunction with the lateral autopilots to be discussed in Chapter 4. A vertical gyro is basically a two-degree-of-freedom gyro constructed so that the angular momentum vector (direction of the spin axis) is along the local vertical. The two gimbal axes are then aligned so that the roll axis is horizontal and lies in the XZ plane of the aircraft and the pitch axis is parallel to the aircraft's Y axis, as illustrated schematically in Figure 2-56. Due to its gyroscopic action, the spin axis of the gyro tends to remain nonrotating with respect to inertial space or to the so-called "fixed"
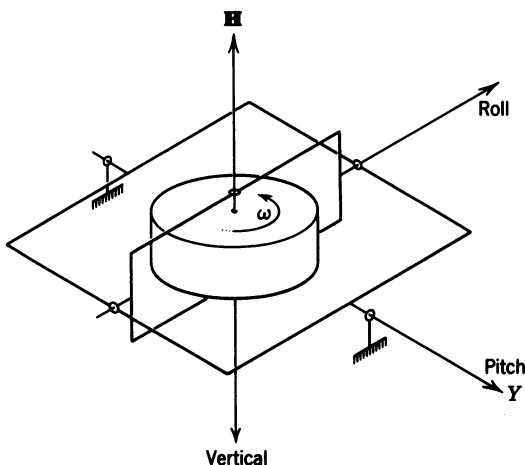
Figure 2-56   *Orientation of a vertical gyro.*

stars. Therefore, to maintain the spin axis vertical, a suitable torque must be applied to precess the gyro. This torque must be applied about the pitch axis to precess the gyro about the roll axis, and about the roll axis for precession about the pitch axis in obedience to the law of the gyro as discussed in Appendix B. To precess the spin axis of the gyro into alignment with the vertical (the direction as indicated by a plumb bob whose pivot is stationary with respect to the earth), commonly referred to as "erection," there must be some method for detecting the misalignment and then generating the required torque. Such a method requires some form of pendulous or acceleration sensitive device. As these devices are incapable of distinguishing between accelerations caused by vehicle motion (kinematic accelerations) and the acceleration of gravity, the vertical gyro attempts to align its spin axis in the direction of the total acceleration (vector sum of the kinematic and gravitational accelerations), usually referred to as the "apparent vertical." If the kinematic accelerations are random, such as atmospheric turbulence, with a zero average, then, due to the slow erection rates (around 2 to 6 deg/min) of the gyro, the average direction of the spin axis will align with the direction of the vertical. However, during periods of sustained horizontal acceleration (takeoff, landing, acceleration from subsonic to supersonic, etc.) or lateral acceleration (sustained turn), the gyro tends to erect to a false vertical. As the autopilot is not generally engaged during takeoff and landing, there is no problem encountered here; however, the autopilot may be engaged during accelerations from subsonic to supersonic flight and back again, and the resulting misalignment would cause an error in the pitch attitude.

The behavior of a vertical gyro during a sustained turn is much more complicated than in the case of sustained longitudinal acceleration. For a coordinated turn the lift vector is normal to the plane of the wings (see Figure 4-13). The gyro then considers this the direction of the vertical and attempts to align its spin axis with the lift vector. However, because the aircraft is in a turn, the lift vector is rotating; thus if the spin axis of the gyro is to align itself with the lift vector, the momentum vector ($\mathbf{H}$) of the gyro must have an angular velocity, which in turn requires a torque to be applied. This torque can be developed only by a pitch misalignment. For this reason it is desirable to be able to cut out the erecting torque during turns when the aircraft is under control of the autopilot. One method of accomplishing this is to use mercury switches in the form of levels. If the gyro is erect, the ball of mercury will lie at the center of the tube and no erection signal will be generated; however, if the gyro is misaligned, the ball will move to one end of the tube and close the circuit to an electromagnetic torque generator on the proper axis for erection (this must be done about both axes). With this type of erection scheme the erection signals can be cut out any time a heading command is fed to the autopilot. Using this type of erection mechanism the gyro can be made to indicate the vertical to within $\frac{1}{8}°$.

Almost as important as the gyro itself, in determining the ultimate accuracy of a vertical gyro, is the type of pickoff. There are numerous types of pickoffs, some of the more common being synchros, resolvers, potentiometers, and differential pressure pickoffs. The ultimate choice depends upon the desired linearity and accuracy of the pickoff signal and the amount of torque, if any, produced by the pickoff (or signal generator, as it is sometimes called).

2-7 GYRO STABILIZED PLATFORM AS THE BASIC ATTITUDE REFERENCE

Some military aircraft, especially long-range bombers of the B-52 and B-58 type, are equipped with an inertial navigation system, the heart of which is a gyro stabilized platform that is maintained in a level attitude. The ability of either two two-degree-of-freedom or three single-degree-of-freedom gyros to provide the basic gyro stabilization of the platform is discussed first, followed by a discussion of the technique used to provide the proper signals to the gyros to keep the platform level in the presence of aircraft motion.

The general configuration for the use of the two-degree-of-freedom gyro or the single-degree-of-freedom gyro to stabilize the platform is shown in Figure 2-57. As the single-degree-of-freedom gyro is easier to balance than the two-degree-of-freedom gyro, three single-degree-of-freedom integrating gyros are usually used for platform stabilization. For this application, if any one of the integrating gyros senses an angular velocity about its input axis, an output voltage is generated (the technique used to accomplish this is discussed later in this section) by the gyro, which, after being amplified, is used to rotate the gimbals relative to the base so the platform remains fixed, relative to inertial space. One complication that arises is that the platform axis, as indicated by the input axes of the three gyros, may not be aligned with the gimbal axes at all times; thus, the signals from the gyros must be sent

(a)   (b)
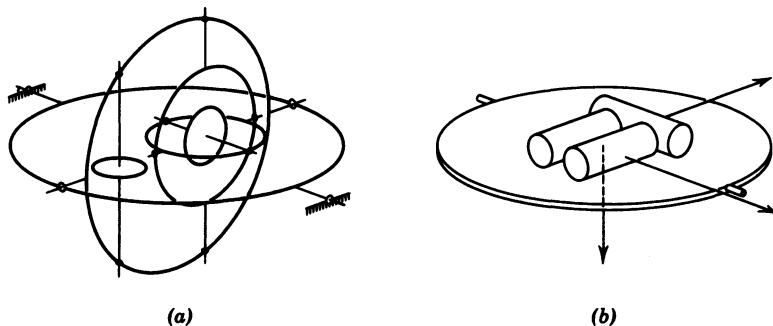
Figure 2-57 (a) Stable platform utilizing two two-degree-of-freedom gyros; (b) stable platform utilizing three single-degree-of-freedom gyros.
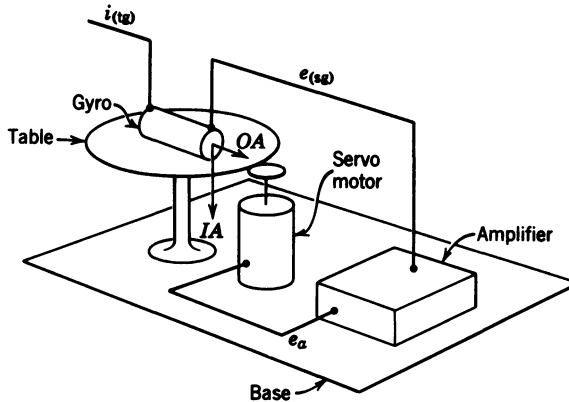
Figure 2-58 *Single-axis space integrator.*

through resolvers so that the proper signal is sent to the proper gimbal axis. However, to study the operation and analyze the performance of the stable platform, it is necessary to consider only one axis. Thus, the rest of this discussion deals with an analysis of a single-axis stabilized platform utilizing an integrating gyro with the associated amplifier and servo drive.

A single-axis stabilized platform has been referred to by personnel of the Instrumentation Laboratory, MIT, as a "single-axis space integrator."[3] The reason for this becomes more obvious later; however, for brevity, the term space integrator will be used when referring to the single-axis stabilized platform. Figure 2-58 illustrates the components of a single-axis space integrator. The integrating gyro is oriented so that its input axis is parallel to the axis of rotation of the table. If the base starts to rotate, the table is carried along with it. This causes the gyro to be rotated about its input axis, generating a gimbal angle, which is sensed by the signal generator. The voltage from the signal generator, $e_{(sg)}$, is then amplified and applied to the servo motor to drive the table in the opposite direction to the base. The net result is that the table remains nonrotating in inertial space. The table can be rotated at a desired rate by feeding a current $i_{(tg)}$ to the torque generator. The operation of the space integrator is explained in detail in the following paragraphs.

Figure 2-59 illustrates the sequence of events that results when the base starts to rotate with respect to inertial space, and the platform, represented by the gyro, remains nonrotating with respect to inertial space. This action is referred to as "base motion isolation," that is, the platform is isolated from the motion of the base about the axis indicated. As the base starts to rotate about the IA with respect to inertial space, ω_{IB}, the gyro is rotated at the same angular velocity, since the motor and gear train allow no motion of the gyro relative to the base as long as the voltage to the motor, e_a, is zero. The rotation of the gyro about its IA results in a gyroscopic output torque, $\mathbf{M_g}$,

which is absorbed by the viscous damping torque, M_{vd}. M_{vd} can result only from a rate of change of the gimbal angle, $\dot{A}_g$; thus, a gimbal angle, A_g, is developed and increases with time. As the gimbal angle increases, the voltage out of the signal generator, $e_{(sg)}$, which is proportional to A_g, increases from a null, is amplified, and is applied to the servo motor, causing the gyro to be rotated relative to the base (ω_{BG}). For proper operation ω_{BG} must be opposite to ω_{IB}; the resulting angular velocity of the gyro about its input axis is $\omega_{IB} + \omega_{BG}$. As A_g increases, ω_{BG} increases and ω_{IA} decreases, causing $\dot{A}_g$ to decrease until the steady-state condition is reached, in which $\omega_{IB} = -\omega_{BG}$ and ω_{IA} goes to zero. With $\omega_{IA} = 0$, $\dot{A}_g = 0$ and A_g remains constant. The steady-state value of A_g is dependent upon the amplifier and servo motor gain. The higher the gain, the smaller the gimbal angle for a given value of ω_{IB}. During the transient period while $\dot{A}_g \neq 0$, there is some net rotation of the gyro about its input axis, which results in an angular orientation error in the platform; however, when ω_{IB} goes to zero, the gimbal angle must return to zero so that ω_{BG} will be zero. This necessitates an ω_{IA} in the same direction as ω_{BG}, which eliminates the angular orientation error that was developed during the presence of ω_{IB}. Thus, for an ideal gyro, the platform has no net angular motion with respect to inertial space.

So far it has been assumed that it is desirable to maintain the platform nonrotating with respect to inertial space; however, there are times when it is desirable to command the platform to rotate relative to inertial space. If an earth reference is desired, the platform should be nonrotating relative to the earth; if the platform is to remain normal to the gravity vector while carried in a vehicle (vertical indicator, to be discussed later in this section), the platform must be rotated relative to the earth. Both of these requirements dictate that the platform rotate in some manner relative to inertial space.

Figure 2-60 illustrates how this is accomplished. If it is desired to cause the platform, and thus the gyro, to rotate about its input axis, a command current is fed to the torque generator, which develops a torque about the OA, $M_{(comm)}$. From here on the sequence of events is the same as those described for the base motion isolation mode of operation. However, in this case the steady-state condition is reached when the gyroscopic output torque M_g developed by the ω_{IA} of the gyro is equal and opposite to the $M_{(comm)}$ developed by the current into the torque generator. Through this technique the platform can be commanded to rotate at any desired angular rate relative to inertial space. Although the two modes of operation have been discussed individually, in practice they can occur simultaneously.

Without a signal to the torque generator the space integrator remains nonrotating with respect to inertial space except for gyro drift, which causes a small rotation of the platform. If it is desired that the platform remain nonrotating with respect to the earth and thus remain level (normal to the gravity vector), the platform must be rotated at an angular velocity, with respect to inertial space, equal to the horizontal component of earth's rate (the total average angular velocity of the earth with respect to the sun, which
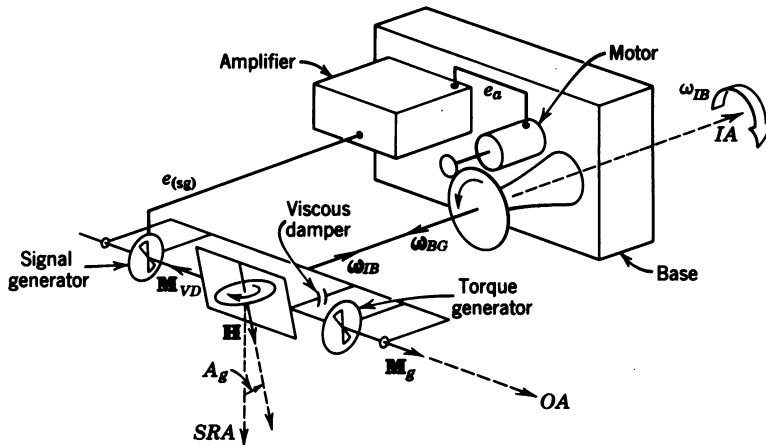
Figure 2-59 Single-axis space integrator, base motion isolation mode.

is $0.07292115 \times 10^{-3}$ rad/sec, is usually used) for the latitude at which the gyro is located. In addition, if the platform is then mounted in an aircraft and the aircraft is in motion, for the platform to remain level it must be rotated at an angular velocity, with respect to the earth, equal to the velocity of the aircraft with respect to the earth (ground speed) divided by the radius of the earth. A signal therefore must be generated and fed as a torquing signal to the integrating gyro to rotate the platform at the required rate.
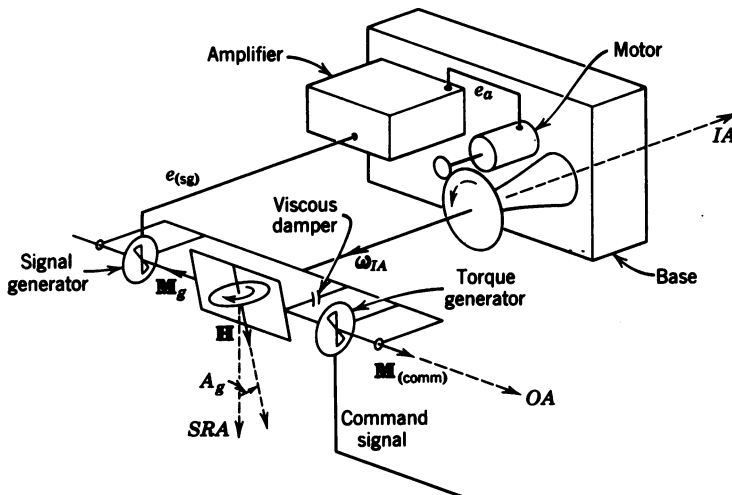
Figure 2-60 Single-axis space integrator, commanded angular velocity input mode.

The portion of the signal required to compensate for the earth's rate is computed from the latitude of the aircraft as indicated by the navigation system. The remainder of the signal is usually supplied from the output of integrating accelerometers corrected for the Coriolis acceleration resulting from the earth's angular velocity.

For this operation, two integrating accelerometers are used, with their sensitive axes aligned with the two horizontal platform axes. The platform axes are usually pointed north (X axis) and east or west (Y axis) with the Z axis along the vertical, so as to form a right-handed system. The X axis integrating accelerometer provides the torquing signal for the Y axis gyro and vice versa.

By properly adjusting the dynamics of each loop of the vertical indicator (Schuler tuning, which results in an undamped period of approximately 84 min) it can be made to track the vertical very accurately, even under the influence of sustained horizontal accelerations. Such a system is usually at least an order of magnitude more accurate than the vertical gyro for indication of the vertical.

2-8 EFFECTS OF NONLINEARITIES

In all the analyses thus far presented in this chapter, no mention has been made of the nonlinearities that are usually present in any physical system. These nonlinearities include such things as amplifier saturation, backlash in gear trains or mechanical linkage, control cable stretch, hysteresis in electromagnetic devices, and dead space in actuators and sensors. If any of these nonlinearities are severe enough, the system may be completely unstable. Thus in the physical design of the hardware all nonlinearities should be kept to a minimum. The analytic analysis of a complete autopilot including nonlinearities is usually impractical, if not impossible. Describing function techniques can be used to determine whether or not a limit cycle will exist, but that is about all. However, if there are known or suspected nonlinearities in the system, they can be included in the computer simulation and thus their effects determined during early design phases. Wherever possible it is always advisable to include any physical hardware available in the analog computer simulation. If the simulation indicates that the existing nonlinearities will make the performance of the system unacceptable, the equipment must be redesigned to reduce the nonlinearities to an acceptable level. In some cases a lead compensator can be used to offset some of the effects of backlash.

2-9 SUMMARY

In this chapter a technique for improving the damping of the short-period oscillation has been discussed. This pitch damper was used as the inner loop

for some typical basic autopilot configurations. This discussion was followed by the analysis of an automatic glide slope and flare control system and the altitude and Mach hold modes of a complete longitudinal flight control system. The chapter concluded with a discussion of the use of a vertical gyro or stabilized platform as a vertical reference.

REFERENCES

1. J. Bicknell, E. E. Larrabee, R. C. Seamans, Jr., and H. P. Whitaker, "Automatic Control of Aircraft," presented at Journées Internationales de Sciences Aéronautiques, J.I.S.A., 57, Paris, May 27–29, 1957.

2. *Automatic Pilot for High Performance Aircraft*, Project MX-1137, Final Report, TR-54A031, General Electric Co., 1954.

3. C. S. Draper, W. Wrigley, and L. R. Grohe, "The Floating Integrating Gyro and Its Application to Geometrical Stabilization Problems on Moving Bases," presented at the 23rd Annual Meeting of the Institute of Aeronautical Sciences, January 1955 (published as *Sherman M. Fairchild Fund Paper* FF-13).

<div align="right">

3

</div>

<div align="right">

Lateral Dynamics

</div>

3-1 LATERAL EQUATIONS OF MOTION

In Chapter 1 the six-degree-of-freedom rigid body equations were separated into three longitudinal and three lateral equations. In this chapter the three lateral equations are linearized and combined with the aerodynamic terms to yield the lateral equations of motion for the rigid aircraft. From these equations, the lateral modes can be determined and the various transfer functions for both rudder and aileron input derived and analyzed. The chapter concludes with a study of the effects of changes in airspeed and altitude on the lateral dynamics in addition to the study of the effects of variations of the stability derivatives.

Before deriving the lateral equations of motion, it is necessary to define the sideslip angle. As in the longitudinal case, stability axes are used. If during the perturbations from equilibrium the aircraft X axis is displaced about the Z axis from the aircraft velocity vector, a sideslip angle will be generated. The positive direction of this angle is indicated in Figure 3-1. The sideslip angle β should not be confused with the yaw angle ψ. An aircraft can have a yaw angle and a yaw rate with zero sideslip. However, if there is an angle of sideslip there must be a yaw angle. In general ψ and β are not equal, but if the flight path of the aircraft is straight and the aircraft is slipping with its wings level, then $\beta = -\psi$.

As mentioned in Section 1-5, there are certain assumptions which, if employed, permit the decoupling of the six equations of motion. The three

Figure 3-1   (a) Disturbed aircraft stability axes showing yaw angle ψ and sideslip angle β;
(b) aircraft slipping with wings level, $\beta = -\psi$.

$Eq. 1-32$

lateral equations can be obtained from Eq. 1-33 and are

$$\sum \Delta F_y = m(\dot{V} + UR - WP)$$

$$\sum \Delta \mathscr{L} = \dot{P}I_x - \dot{R}J_{xz} + QR(I_z - I_y) - PQJ_{xz}$$

$$\sum \Delta \mathscr{N} = \dot{R}I_z - \dot{P}J_{xz} + PQ(I_y - I_x) + QRJ_{xz} \qquad (3\text{-}1)$$

The pitching moment equation that is neglected is also rewritten here from
Eq. 1-32: $\sum \Delta \mathscr{M} = \dot{Q}I_y + PR(I_x - I_z) + (P^2 - R^2)J_{xz}$. This equation contains
both P and R, but if the perturbations are small, and it is assumed that P
and R are so small that their products and squares can be neglected, the
equations can be decoupled. This assumption was made in Section 1-5, and it
applies here. As the equations have been decoupled, Q is assumed zero. By
requiring that the equilibrium direction of the X axis be along the flight path
and that there be no sideslip while in equilibrium, then $V_0 = W = 0$ and
$U = U_0 + u$. Then $\dot{V} = \dot{v}$, $\dot{W} = 0$, $\dot{U} = \dot{u}$. As the aircraft initially is in unaccel-

erated flight, P_0 and R_0 must be zero. Then $P = p$ and $R = r$. Making these substitutions, Eq. 3-1 becomes

$$\sum \Delta F_y = m(\dot{v} + U_0 r + ur)$$

$$\sum \Delta \mathcal{L} = \dot{p} I_x - \dot{r} J_{xz}$$

$$\sum \Delta \mathcal{N} = \dot{r} I_z - \dot{p} J_{xz} \qquad (3\text{-}2)$$

However, since the perturbations are assumed small, the products of the perturbations can be neglected. Equation 3-2 then reduces to

$$\sum \Delta F_y = m(\dot{v} + U_0 r)$$

$$\sum \Delta \mathcal{L} = \dot{p} I_x - \dot{r} J_{xz}$$

$$\sum \Delta \mathcal{N} = \dot{r} I_z - \dot{p} J_{xz} \qquad (3\text{-}3)$$

Factoring U_0 from the right hand side of the $\sum \Delta F_y$ equation, the equation becomes $\sum \Delta F_y = m U_0 (\dot{v} / U_0 + r)$, but $\dot{v} / U_0 \simeq \dot{\beta}$, as $U_0 \simeq U$ for small perturbations. After substituting for p and r, using the above relation, Eq. 3-3 becomes

$$\sum \Delta F_y = m U_0 (\dot{\beta} + \dot{\psi}) = m a_y$$

$$\sum \Delta \mathcal{L} = \ddot{\phi} I_x - \ddot{\psi} J_{xz}$$

$$\sum \Delta \mathcal{N} = \ddot{\psi} I_z - \ddot{\phi} J_{xz} \qquad (3\text{-}4)$$

It is necessary to expand the forces and moments in terms of the changes in them resulting from the perturbations in the linear and angular velocities. The forces in the Y direction are functions of β, ψ, ϕ, $\dot{\phi}$, and $\dot{\psi}$. Then $\sum F_y$ can be written as the total derivative

$$\sum dF_y = \frac{\partial F_y}{\partial \beta} d\beta + \frac{\partial F_y}{\partial \psi} d\psi + \frac{\partial F_y}{\partial \phi} d\phi + \frac{\partial F_y}{\partial \dot{\phi}} d\dot{\phi} + \frac{\partial F_y}{\partial \dot{\psi}} d\dot{\psi} \qquad (3\text{-}5)$$

If the partial derivatives are assumed linear over the range of the perturbations, the differentials can be replaced by actual increments. Thus Eq. 3-5 becomes

$$\sum \Delta F_y = \frac{\partial F_y}{\partial \beta} \Delta\beta + \frac{\partial F_y}{\partial \psi} \Delta\psi + \frac{\partial F_y}{\partial \phi} \Delta\phi + \frac{\partial F_y}{\partial \dot{\phi}} \Delta\dot{\phi} + \frac{\partial F_y}{\partial \dot{\psi}} \Delta\dot{\psi} \qquad (3\text{-}6)$$

Two of these partial derivatives result from the change in the component of gravity along the Y axis as the aircraft attitude is changed. From Eq. 1-35 the
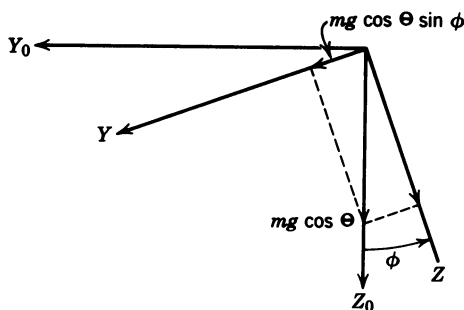
Figure 3-2 *Component of gravity along the disturbed Y axis due to ϕ.*

components of gravity along the equilibrium X and Z axes with $\Phi = 0$ are

$$F_{g_x} = - mg \sin \Theta$$

$$F_{g_z} = mg \cos \Theta \tag{3-7}$$

If the aircraft is disturbed by rolling about the X axis, there is a component of gravity along the Y axis as shown in Figure 3-2. From Figure 3-2,

$$F_{g_y} = mg \cos \Theta \sin \phi \tag{3-8}$$

and

$$\frac{\partial F_{g_y}}{\partial \phi} = mg \cos \Theta \cos \phi \tag{3-9}$$

Similarly, if there is a perturbation about the Z axis, there is a component of gravity along the Y axis, as illustrated in Figure 3-3. From Figure 3-3,

$$F_{g_y} = mg \sin \Theta \sin \psi \tag{3-10}$$

and

$$\frac{\partial F_{g_y}}{\partial \psi} = mg \sin \Theta \cos \psi \tag{3-11}$$

There will be no other forces in the Y direction due to ψ and ϕ. If either of these angles results in a sideslip angle, it will be included in $\partial F_y / \partial \beta$. Thus Eqs. 3-9 and 3-11 can be rewritten using the small-angle assumption for the
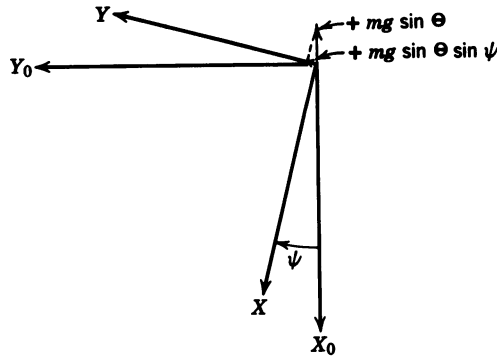
Figure 3-3 Component of gravity along the disturbed Y axis due to ψ.

$\cos \phi$ and $\cos \psi$:

$$\frac{\partial F_y}{\partial \psi} = mg \sin \Theta$$

$$\frac{\partial F_y}{\partial \phi} = mg \cos \Theta \tag{3-12}$$

Since, in Eq. 3-6, the initial values of β, ψ, and ϕ are zero, the Δ's may be dropped. Dropping the Δ's and substituting Eq. 3-6 into the $\Sigma \Delta F_y$ equation of Eq. 3-4 yields

$$mU_0\dot{\beta} + \frac{-\partial F_y}{\partial \beta}\beta + \left(mU_0 - \frac{\partial F_y}{\partial \dot{\psi}}\right)\dot{\psi} - \frac{\partial F_y}{\partial \psi}\psi - \frac{\partial F_y}{\partial \dot{\phi}}\dot{\phi} - \frac{\partial F_y}{\partial \phi}\phi = F_{y_a} \tag{3-13}$$

where F_{y_a} is an aerodynamic force of unspecified origin, and is explained in Section 3-2. As in the derivation of the longitudinal equations, since $U_0 \simeq U$, the subscript zero is dropped (see pp. 21 and 26). Dividing Eq. 3-13 by Sq, substituting from Eq. 3-12, and using the definitions of the stability derivatives in Table 3-1, Eq. 3-13 becomes

$$\frac{mU}{Sq}\dot{\beta} - C_{y_\beta}\beta + \left(\frac{mU}{Sq} - \frac{b}{2U}C_{y_r}\right)\dot{\psi} - C_{y_\psi}\psi - \frac{b}{2U}C_{y_p}\dot{\phi} - C_{y_\phi}\phi$$

$$= \frac{F_{y_a}}{Sq} = C_{y_a} \tag{3-14}$$

The $\mathscr{L}$ and $\mathscr{N}$ equations can be expanded in like manner; however, the

TABLE 3-1 Definitions and Equations for Lateral Stability Derivatives

Symbol	Definition	Origin	Equation	Typical Values
C_{l_β}	$\dfrac{1}{Sqb}\dfrac{\partial \mathscr{L}}{\partial \beta}$	Dihedral and vertical tail	Ref. 1, Chapter 9 Ref. 2, Section 3.10	−0.06
C_{l_p}	$\dfrac{1}{Sqb}\left(\dfrac{2U}{b}\right)\dfrac{\partial \mathscr{L}}{\partial p}$	Wing damping	Ref. 1, Chapter 9	−0.4
C_{l_r}	$\dfrac{1}{Sqb}\left(\dfrac{2U}{b}\right)\dfrac{\partial \mathscr{L}}{\partial r}$	Differential wing normal force	$\dfrac{C_L^w}{4}$	0.06
C_{n_β}	$\dfrac{1}{Sqb}\dfrac{\partial \mathscr{N}}{\partial \beta}$	Directional stability	Ref. 1, Chapter 8 Ref. 2, Section 3.9	0.11
C_{n_p}	$\dfrac{1}{Sqb}\left(\dfrac{2U}{b}\right)\dfrac{\partial \mathscr{N}}{\partial p}$	Differential wing chord force	$-\dfrac{C_L^w}{8}\left(1-\dfrac{d\epsilon}{d\alpha}\right)$	−0.015
C_{n_r}	$\dfrac{1}{Sqb}\left(\dfrac{2U}{b}\right)\dfrac{\partial \mathscr{N}}{\partial r}$	Damping in yaw	$-\dfrac{C_D^w}{4}-2\eta_v\dfrac{S_v}{S}\left(\dfrac{l_v}{b}\right)^2\left(\dfrac{dC_L}{d\alpha}\right)^v$	−0.12
C_{y_β}	$\dfrac{1}{Sq}\dfrac{\partial F_y}{\partial \beta}$	Fuselage and vertical tail	No simple equation	−0.6
C_{y_ϕ}	$\dfrac{1}{Sq}\dfrac{\partial F_y}{\partial \phi}$	Gravity	$\dfrac{mg}{Sq}\cos\Theta$	
C_{y_p}	$\dfrac{1}{Sq}\left(\dfrac{2U}{b}\right)\dfrac{\partial F_y}{\partial p}$	Vertical tail	Neglect	
C_{y_ψ}	$\dfrac{1}{Sq}\left(\dfrac{\partial F_y}{\partial \psi}\right)$	Gravity	$\dfrac{mg}{Sq}\sin\Theta$	
C_{y_r}	$\dfrac{1}{Sq}\left(\dfrac{2U}{b}\right)\dfrac{\partial F_y}{\partial r}$	Vertical tail	Neglect	

partial derivatives of $\mathscr{L}$ and $\mathscr{N}$ with respect to ϕ and ψ are zero. Thus expanding $\Sigma\Delta\mathscr{L}$ and $\Sigma\Delta\mathscr{N}$ and substituting the results into Eq. 3-4 yields

$$\ddot{\phi}I_x - \frac{\partial \mathscr{L}}{\partial \dot{\phi}}\dot{\phi} - \ddot{\psi}J_{xz} - \frac{\partial \mathscr{L}}{\partial \dot{\psi}}\dot{\psi} - \frac{\partial \mathscr{L}}{\partial \beta}\beta = \mathscr{L}_a$$

$$-\ddot{\phi}J_{xz} - \frac{\partial \mathscr{N}}{\partial \dot{\phi}}\dot{\phi} + \ddot{\psi}I_z - \frac{\partial \mathscr{N}}{\partial \dot{\psi}}\dot{\psi} - \frac{\partial \mathscr{N}}{\partial \beta}\beta = \mathscr{N}_a \qquad (3\text{-}15)$$

Dividing through by Sqb, where b is the wingspan, and going to coefficient

form Eq. 3-15 becomes

$$\frac{I_x}{Sqb}\ddot{\phi} - \frac{b}{2U}C_{l_p}\dot{\phi} - \frac{J_{xz}}{Sqb}\ddot{\psi} - \frac{b}{2U}C_{l_r}\dot{\psi} - C_{l_\beta}\beta = \frac{\mathcal{L}_a}{Sqb} = C_{l_a}$$

$$-\frac{J_{xz}}{Sqb}\ddot{\phi} - \frac{b}{2U}C_{n_p}\dot{\phi} + \frac{I_z}{Sqb}\ddot{\psi} - \frac{b}{2U}C_{n_r}\dot{\psi} - C_{n_\beta}\beta = \frac{\mathcal{N}_a}{Sqb} = C_{n_a} \quad (3\text{-}16)$$

It should be noted that the same assumptions used in the derivation of the longitudinal equations apply to the derivation of the lateral equations. Equations 3-14 and 3-15 are rewritten here for convenience:

$$-\frac{b}{2U}C_{y_p}\dot{\phi} - C_{y_\phi}\phi + \left(\frac{mU}{Sq} - \frac{b}{2U}C_{y_r}\right)\dot{\psi} - C_{y_\psi}\psi + \frac{mU}{Sq}\dot{\beta} - C_{y_\beta}\beta = C_{y_a}$$

$$\frac{I_x}{Sqb}\ddot{\phi} - \frac{b}{2U}C_{l_p}\dot{\phi} - \frac{J_{xz}}{Sqb}\ddot{\psi} - \frac{b}{2U}C_{l_r}\dot{\psi} - C_{l_\beta}\beta = C_{l_a}$$

$$-\frac{J_{xz}}{Sqb}\ddot{\phi} - \frac{b}{2U}C_{n_p}\dot{\phi} + \frac{I_z}{Sqb}\ddot{\psi} - \frac{b}{2U}C_{n_r}\dot{\psi} - C_{n_\beta}\beta = C_{n_a} \quad (3\text{-}17)$$

These equations are the uncoupled, linearized, lateral equations of motion. As in the case of the longitudinal equations, they are nondimensional.

3-2 DERIVATION OF EQUATIONS FOR THE LATERAL STABILITY DERIVATIVES

The explanation for the indication in Table 3-1 that C_{y_p} and C_{y_r} can be neglected is that C_{y_p} results from the side force on the vertical tail caused by a rolling velocity. This rolling velocity causes lift to be produced by the vertical tail causing a force in the Y direction; however, this force is small, since the rolling velocity must be small in order to decouple the equations. Similarly, C_{y_r} results from the lift generated by the vertical tail due to a yawing velocity. C_{y_r} is, in general, larger than C_{y_p}, and the magnitudes of both should be checked before neglecting them. The evaluation of the rest of the stability derivatives follows:

C_{l_β}, the change in the rolling moment due to sideslip, results from the lift produced by the vertical tail due to the sideslip and the effective dihedral of the wing. There is no simple relation for this stability derivative, mainly because of the contribution of the dihedral effect of the wing. The effect of this dihedral is to produce a rolling moment to the left if the aircraft is sideslipping to the right and the aircraft has positive dihedral. This point is discussed in detail in Chapter 9 of Ref. 1, where it is referred to as C_{l_ψ}, and in Section 3-10 of Ref. 2.

C_{n_β}, the change in the yawing moment due to sideslip, results from the yawing moment produced by the vertical tail, wing, fuselage, and nacelles in the presence of sideslip. There is also some effect due to the sidewash created by the wing–fuselage combination.

The wing contribution is very small; it is greater for swept wings and approaches zero for zero sweep of the quarter chord points. The fuselage and nacelles usually have a destabilizing effect which must be overcome by the vertical tail. The combination of these various effects is covered in detail in Chapter 8 of Ref. 1, and in Section 3-9 of Ref. 2. In general, C_{n_β} can best be obtained from actual wind tunnel tests. This stability derivative determines the static directional stability of the aircraft, and it must be positive for a stable aircraft. In Ref. 1, C_{n_β} is referred to as C_{n_ψ}, and as $\psi = -\beta$ for pure sideslip, C_{n_ψ} is negative for an aircraft with directional stability.

C_{y_β}, the change in the force in the Y direction due to sideslip, is the force that, if multiplied by the proper moment arm, generates C_{n_β}; as in the case of C_{n_β}, there is no simple relation.

C_{l_p}, the change in the rolling moment due to a rolling velocity, arises from the change in the angle of attack on the wings caused by a rolling velocity. The down-going wing experiences an increase in angle of attack while the up-going wing is subjected to a decrease in angle of attack. These changes in angle of attack cause changes in the lift and drag of the up- and down-going wings. The amounts of the changes in the angle of attack in relation to the rolling velocity are shown in Figure 3-4.

If the new lift and drag vectors are resolved along the equilibrium X and Z axes, it can be seen that the Z components produce a moment opposing the rolling velocity. Normally the Z component of drag is neglected and only the change in lift considered; however, no simple expression can be obtained for C_{l_p}. This subject is discussed in Chapter 9 of Ref. 1 and also in NACA TR 635.
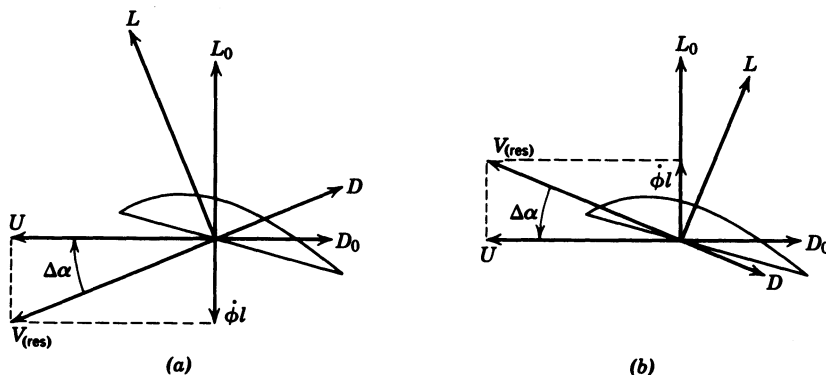
Figure 3-4 *Change in lift and drag on a section of the down-going wing (a) and the up-going wing (b) at a distance I from the center of gravity due to $\dot{\phi}$.*

C_{n_p} is the change in the yawing moment due to a rolling velocity. Its cause is the same as that for C_{l_p}. As can be seen from Figure 3-4, the lift vector is tilted forward on the down-going wing and rearward on the up-going wing. The components of these lift vectors when resolved into the X axis are greater than the change in the X component of drag, thus producing a negative yawing moment for a positive roll rate. This is referred to as "adverse yaw," and is the reason rudder is required to keep an aircraft coordinated while rolling into or out of a steady-state turn. For supersonic flight (wing leading edge supersonic) the lift vector remains normal to the chord; therefore the difference in the drag produces a positive C_{n_p}. As seen from Table 3-1, assuming an elliptical lift distribution,

$$C_{n_p} = -\frac{C_L^w}{8}\left(1 - \frac{d\epsilon}{d\alpha}\right) \tag{3-18}$$

where $d\epsilon/d\alpha$ is the rate of change of the downwash angle with angle of attack, and can be approximated (see NACA TR 648) by

$$\frac{d\epsilon}{d\alpha} = \frac{2}{\pi e \mathcal{R}} \frac{dC_L^w}{d\alpha} \tag{3-19}$$

where e is an efficiency factor varying from 0.8 to 0.9, and $\mathcal{R}$ is the aspect ratio of the wing (see Appendix D).

C_{l_r}, the change in the rolling moment due to a yawing velocity, arises from the changes in the lift on the wings resulting from a yawing velocity. If the aircraft is subject to a yawing velocity, the relative velocity of the left and right wing panels changes, with respect to the air mass. The forward-going wing experiences an increase in lift while the lift on the rearward-going wing decreases. This factor causes a positive rolling moment for a positive yawing velocity. By strip integration over the wing, and assuming an elliptical lift distribution,

$$C_{l_r} = \frac{C_L^w}{4} \tag{3-20}$$

Both C_{n_p} and C_{l_r} are extremely difficult to obtain from wind tunnel tests and are usually evaluated analytically.

C_{n_r}, the change in the yawing moment due to a yawing velocity, is caused partly by the same phenomenon as that for C_{l_r} and partly by the lift generated by the vertical stabilizer. This moment opposes the yawing velocity, is therefore negative, and is the damping in yaw. The contribution from the vertical tail can be derived as follows.

The change in the angle of attack of the vertical tail due to a yawing velocity r is $\Delta\alpha_v = r l_v / U$, where l_v is the distance from the center of gravity

to the aerodynamic center of the vertical tail. The lift generated by this $\Delta\alpha_v$ is

$$L_v = \left(\frac{rl_v}{U}\right)qS_v\left(\frac{dC_L}{d\alpha}\right)^v\eta_v \tag{3-21}$$

where η_v is the vertical stabilizer efficiency factor to compensate for the interference between the vertical tail and the fuselage. The yawing moment caused by this lift is

$$\mathcal{N}_v = -l_vL_v = -\left(\frac{rl_v^2}{U}\right)qS_v\left(\frac{dC_L}{d\alpha}\right)^v\eta_v \tag{3-22}$$

Differentiating with respect to r, Eq. 3-22 becomes

$$\left(\frac{\partial\mathcal{N}}{\partial r}\right)^v = -\frac{l_v^2}{U}qS_v\left(\frac{dC_L}{d\alpha}\right)^v\eta_v \tag{3-23}$$

But

$$(C_{n_r})^v = \frac{1}{Sqb}\left(\frac{2U}{b}\right)\left(\frac{\partial\mathcal{N}}{\partial r}\right)^v = -2\frac{S_v}{S}\left(\frac{l_v}{b}\right)^2\left(\frac{dC_L}{d\alpha}\right)^v\eta_v \tag{3-24}$$

The contribution of the wing to C_{n_r} is usually taken as $-C_D^w/4$. Therefore

$$C_{n_r} = -\frac{C_D^w}{4} - 2\frac{S_v}{S}\left(\frac{l_v}{b}\right)^2\left(\frac{dC_L}{d\alpha}\right)^v\eta_v \tag{3-25}$$

The external applied aerodynamic forces and moments arise from aileron or rudder deflection. Thus

$$C_{y_a} = C_{y_{\delta_a}}\delta_a + C_{y_{\delta_r}}\delta_r$$

$$C_{l_a} = C_{l_{\delta_a}}\delta_a + C_{l_{\delta_r}}\delta_r$$

$$C_{n_a} = C_{n_{\delta_a}}\delta_a + C_{n_{\delta_r}}\delta_r \tag{3-26}$$

3-3   SOLUTION OF LATERAL EQUATIONS (STICK FIXED)

As in the case of the longitudinal equations, the homogeneous equation is obtained first. Taking the Laplace transform of Eq. 3-17 and neglecting C_{y_p}

and C_{y_r}, we obtain

$$\left(\frac{I_x}{Sqb}s^2 - \frac{b}{2U}C_{l_p}s\right)\phi(s) + \left(-\frac{J_{xz}}{Sqb}s^2 - \frac{b}{2U}C_{l_r}s\right)\psi(s) - C_{l_\beta}\beta(s) = 0$$

$$\left(-\frac{J_{xz}}{Sqb}s^2 - \frac{b}{2U}C_{n_p}s\right)\phi(s) + \left(\frac{I_z}{Sqb}s^2 - \frac{b}{2U}C_{n_r}s\right)\psi(s) - C_{n_\beta}\beta(s) = 0$$

$$-C_{y_\phi}\phi(s) + \left(\frac{mU}{Sq}s - C_{y_\psi}\right)\psi(s) + \left(\frac{mU}{Sq}s - C_{y_\beta}\right)\beta(s) = 0 \quad (3\text{-}27)$$

For this example, the stability derivatives for a jet transport flying straight and level at 300 mph at sea level are used. For this aircraft the values are as follows:

$$\Theta = 0$$
$$\text{Mach} = 0.394$$
$$m = 5900 \text{ slugs}$$
$$U = 440 \text{ ft/sec}$$
$$S = 2400 \text{ sq ft}$$
$$I_x = 1.955 \times 10^6 \text{ slug ft}^2$$
$$I_z = 4.2 \times 10^6 \text{ slug ft}^2$$
$$J_{xz} = 0 \text{ by assumption}$$
$$C_{l_p} = -0.38$$
$$C_{l_r} = \frac{C_L}{4} = \frac{0.344}{4} = 0.086$$
$$b = 130 \text{ ft}$$
$$C_{n_p} = -0.0228$$
$$C_{n_\beta} = 0.096$$
$$C_{n_r} = -0.107$$
$$C_{y_\beta} \approx -0.6$$
$$C_{y_\phi} = \frac{mg}{Sq} = C_L = 0.344$$
$$C_{y_\psi} = 0$$
$$C_{l_\beta} = -0.057$$
$$\frac{b}{2U} = \frac{130}{2(440)} = 0.148 \text{ sec}$$
$$\frac{b}{2U}C_{l_p} = -0.0553 \text{ sec}$$
$$\frac{b}{2U}C_{l_r} = 0.0128 \text{ sec}$$

$$\frac{b}{2U}C_{n_p} = -0.00338 \text{ sec}$$

$$\frac{b}{2U}C_{n_r} = -0.0158 \text{ sec}$$

$$q = \frac{\rho}{2}U^2 = \frac{(0.002378)(440)^2}{2} = 230 \text{ lb/sq ft}$$

$$\frac{I_x}{Sqb} = \frac{1.955 \times 10^6}{(2400)(230)(130)} = 0.02725 \text{ sec}^2$$

$$\frac{I_z}{Sqb} = \frac{4.2 \times 10^6}{(2400)(230)(130)} = 0.0585 \text{ sec}^2$$

$$\frac{mU}{Sq} = \frac{(5900)(440)}{(2400)(230)} = 4.71 \text{ sec}$$

Substituting these values into Eq. 3-27 and writing the equations in determinant form yields

$$\begin{vmatrix} 0.02725s^2 + 0.0553s & -0.0128s & 0.057 \\ 0.00338s & 0.058s^2 + 0.0158s & -0.096 \\ -0.344 & 4.71s & 4.71s + 0.6 \end{vmatrix} = 0 \quad (3\text{-}28)$$

Expanding,

$$0.00748s^5 + 0.01827s^4 + 0.01876s^3 + 0.0275s^2 - 0.0001135s = 0 \quad (3\text{-}29)$$

The fact that one root of the equation is zero indicates that the aircraft is insensitive to heading. This means that once disturbed, there is no moment trying to return the aircraft to its original heading. Dividing Eq. 3-29 by 0.00748 yields

$$s^5 + 2.44s^4 + 2.51s^3 + 3.68s^2 - 0.0152s = 0 \quad (3\text{-}30)$$

Factoring,

$$s(s^2 + 0.380s + 1.813)(s + 2.09)(s - 0.004) = 0 \quad (3\text{-}31)$$

The modes are identified as follows: $s^2 + 0.380s + 1.813$ is the Dutch roll, and in this case $\zeta_D = 0.14$, $\omega_{nD} = 1.345$ rad/sec, $s + 2.09$ is the roll subsidence, and $s - 0.004$ is the spiral divergence. These modes are typical of

present-day aircraft. The damping and natural frequency of the Dutch roll vary with aircraft and flight conditions and may become objectionable due to light damping. It is also possible for the natural frequency to become high enough, combined with light damping, to require artificial damping of the Dutch roll mode. The roll subsidence is the rolling response of the aircraft to an aileron input. The spiral divergence is not usually objectionable, since its time constant is so large that the pilot has little trouble controlling it. The resulting motion consists of a combination of an increase in yaw angle and in roll angle, and the aircraft eventually falls into a high-speed spiral dive if uncorrected. The condition for spiral stability and its effect on the Dutch roll mode is discussed in Section 3-8.

3-4   LATERAL TRANSFER FUNCTION FOR RUDDER DISPLACEMENT

Before evaluating the transfer function it is necessary to define positive rudder deflection. Left rudder, which produces a force in the positive Y direction and a negative yawing moment, is defined as "positive rudder." Then let $C_{y_{\delta_r}} = 0.171$, $C_{n_{\delta_r}} = -0.08$, $C_{l_{\delta_r}} = 0.0131$, and $\delta_a = 0$. Taking the Laplace transform of Eq. 3-17 with the initial conditions equal to zero, and substituting the proper values yields

$$(0.02725s^2 + 0.0553s)\phi(s) - (0.0128s)\psi(s) + 0.057\beta(s) = 0.0131\delta_r(s)$$

$$(0.00338s)\phi(s) + (0.0585s^2 + 0.0158s)\psi(s) - 0.096\beta(s) = -0.08\delta_r(s)$$

$$-0.344\phi(s) + (4.71s)\psi(s) + (4.71s + 0.6)\beta(s) = 0.171\delta_r(s)$$

$$(3\text{-}32)$$

Then the transfer function for δ_r input and ϕ output in determinant form can be written

$$\frac{\phi(s)}{\delta_r(s)} = \frac{\begin{vmatrix} 0.0131 & -0.0128s & 0.057 \\ -0.08 & 0.0585s^2 + 0.0158s & -0.096 \\ 0.171 & 4.71s & 4.71s + 0.6 \end{vmatrix}}{\nabla} \qquad (3\text{-}33)$$

where

$$\nabla = 0.00748s(s^2 + 0.380s + 1.813)(s + 2.09)(s - 0.004) \qquad (3\text{-}34)$$

Expanding the numerator, Eq. 3-33 becomes

$$\frac{\phi(s)}{\delta_r(s)} = \frac{0.00362s(s^2 - 1.1s - 4.42)}{\nabla}$$

Factoring,

$$\frac{\phi(s)}{\delta_r(s)} = \frac{0.485(s+1.53)(s-2.73)}{(s^2+0.380s+1.813)(s+2.09)(s-0.004)} \tag{3-35}$$

Going to the alternative form,

$$\frac{\phi(s)}{\delta_r(s)} = \frac{134\left(\frac{s}{1.53}+1\right)\left(\frac{s}{2.73}-1\right)}{\left[\left(\frac{s}{1.345}\right)^2+\frac{2(0.14)}{1.345}s+1\right]\left(\frac{s}{2.09}+1\right)\left(\frac{s}{0.004}-1\right)} \tag{3-36}$$

The transfer function for ψ output δ_r input in determinant form is

$$\frac{\psi(s)}{\delta_r(s)} = \frac{\begin{vmatrix} 0.02725s^2+0.0553s & 0.0131 & 0.057 \\ 0.00338s & -0.08 & -0.096 \\ -0.344 & 0.171 & 4.71s+0.6 \end{vmatrix}}{\nabla} \tag{3-37}$$

Expanding,

$$\frac{\psi(s)}{\delta_r(s)} = \frac{-0.0103(s^3+2.12s^2+0.169s+0.128)}{\nabla} $$

Factoring,

$$\frac{\psi(s)}{\delta_r(s)} = \frac{-1.38(s+2.07)(s^2+0.05s+0.066)}{s(s^2+0.380s+1.813)(s+2.09)(s-0.004)} \tag{3-38}$$

In the alternative form

$$\frac{\psi(s)}{\delta_r(s)} = \frac{-12.4\left(\frac{s}{2.07}+1\right)\left[\left(\frac{s}{0.257}\right)^2+\frac{2(0.097)}{0.257}s+1\right]}{s\left[\left(\frac{s}{1.345}\right)^2+\frac{2(0.14)}{1.345}s+1\right]\left(\frac{s}{2.09}+1\right)\left(\frac{s}{0.004}-1\right)} \tag{3-39}$$

The transfer function for β output δ_r input in determinant form is

$$\frac{\beta(s)}{\delta_r(s)} = \frac{\begin{vmatrix} 0.02725s^2+0.0553s & -0.0128s & 0.0131 \\ 0.00338s & 0.0585s^2+0.0158s & -0.08 \\ -0.344 & 4.71s & 0.171 \end{vmatrix}}{\nabla} \tag{3-40}$$

Expanding,

$$\frac{\beta(s)}{\delta_r(s)} = \frac{0.0002725s(s^3 + 39.8s^2 + 77.2s - 1.03)}{\nabla}$$

Factoring,

$$\frac{\beta(s)}{\delta_r(s)} = \frac{0.0364(s - 0.01)(s + 2.06)(s + 37.75)}{(s^2 + 0.380s + 1.813)(s + 2.09)(s - 0.004)} \qquad (3\text{-}41)$$

In the alternative form

$$\frac{\beta(s)}{\delta_r(s)} = \frac{1.87\left(\dfrac{s}{0.01} - 1\right)\left(\dfrac{s}{2.06} + 1\right)\left(\dfrac{s}{37.75} + 1\right)}{\left[\left(\dfrac{s}{1.345}\right)^2 + \dfrac{2(0.14)}{1.345}s + 1\right]\left(\dfrac{s}{2.09} + 1\right)\left(\dfrac{s}{0.004} - 1\right)} \qquad (3\text{-}42)$$

Figures 3-5, 3-6, and 3-7 are amplitude ratio plots of Eqs. 3-36, 3-39, and 3-42 against ω for $s = j\omega$.

3-5   LATERAL TRANSFER FUNCTION FOR AILERON DISPLACEMENT

It is first necessary to define positive aileron deflection. Right aileron as seen by the pilot (wheel to the right or stick to the right), which produces a positive rolling moment, is defined as positive aileron. Then let $C_{l_{\delta_a}} = 0.6$, $C_{n_{\delta_a}} = -0.01$, $C_{y_{\delta_a}} = 0$, and $\delta_r = 0$. The Laplace transform of Eq. 3-17 with the initial conditions equal to zero and substitution of the proper values yields

$$(0.02725s^2 + 0.0553s)\phi(s) - (0.0128s)\psi(s) + 0.057\beta(s) = 0.6\delta_a(s)$$

$$(0.00338s)\phi(s) + (0.0585s^2 + 0.0158s)\psi(s) - 0.096\beta(s) = -0.01\delta_a(s)$$

$$-0.344\phi(s) + (4.71s)\psi(s) + (4.71s + 0.6)\beta(s) = 0 \qquad (3\text{-}43)$$

Then the transfer function for δ_a input and ϕ output in determinant form can be written

$$\frac{\phi(s)}{\delta_a(s)} = \frac{\begin{vmatrix} 0.6 & -0.0128s & 0.057 \\ -0.01 & 0.0585s^2 + 0.0158s & -0.096 \\ 0 & 4.71s & 4.71s + 0.6 \end{vmatrix}}{\nabla} \qquad (3\text{-}44)$$
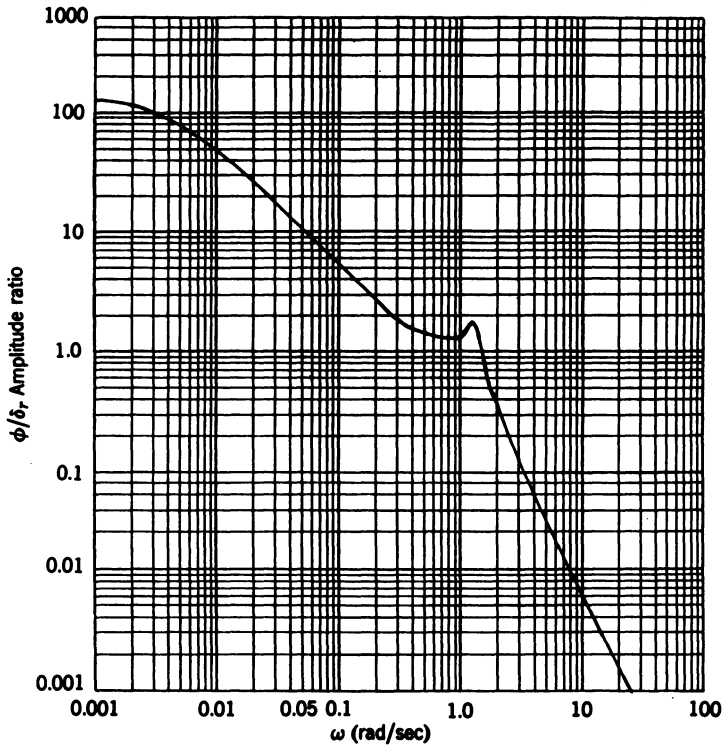
Figure 3-5 *Magnitude plot for ϕ/δ_r transfer function versus ω for $s = j\omega$.*

Expanding,

$$\frac{\phi(s)}{\delta_a(s)} = \frac{0.165s(s^2 + 0.4s + 1.67)}{\nabla}$$

Factoring,

$$\frac{\phi(s)}{\delta_a(s)} = \frac{22.1(s^2 + 0.4s + 1.67)}{(s^2 + 0.380s + 1.813)(s + 2.09)(s - 0.004)} \qquad (3\text{-}45)$$

Going to the alternative form,

$$\frac{\phi(s)}{\delta_a(s)} = \frac{2440\left[\left(\frac{s}{1.3}\right)^2 + \frac{2(0.154)}{1.3}s + 1\right]}{\left[\left(\frac{s}{1.345}\right)^2 + \frac{2(0.14)}{1.345}s + 1\right]\left(\frac{s}{2.09} + 1\right)\left(\frac{s}{0.004} - 1\right)} \qquad (3\text{-}46)$$
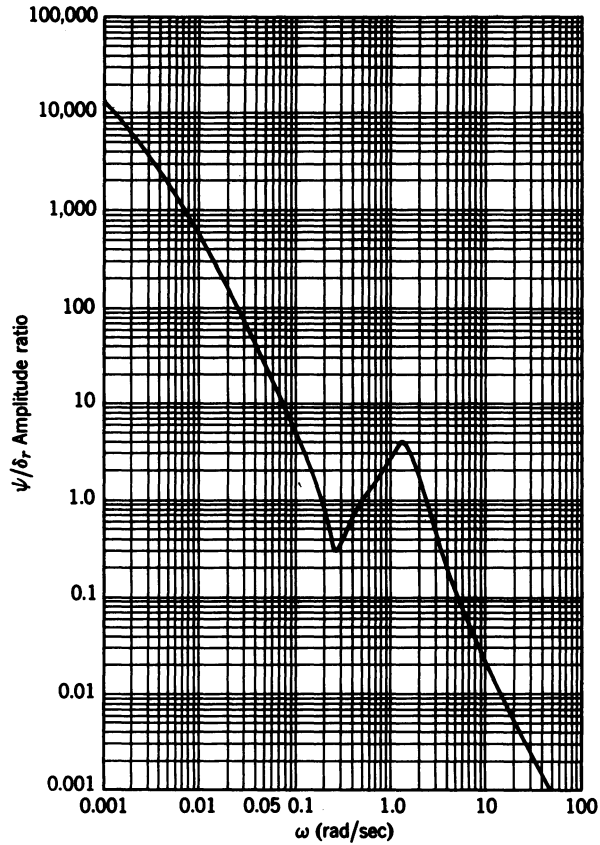
Figure 3-6   *Magnitude plot for ψ/δ_r transfer function versus ω for $s = j\omega$.*

The transfer function for ψ output and δ_a input in determinant form is

$$\frac{\psi(s)}{\delta_a(s)} = \frac{\begin{vmatrix} 0.02725s^2 + 0.0553s & 0.6 & 0.057 \\ 0.00338s & -0.01 & -0.096 \\ -0.344 & 0 & 4.71s + 0.6 \end{vmatrix}}{\nabla} \qquad (3\text{-}47)$$

Expanding,

$$\frac{\psi(s)}{\delta_a(s)} = \frac{-0.00128(s^3 + 9.6s^2 + 1.2s - 15.3)}{\nabla}$$
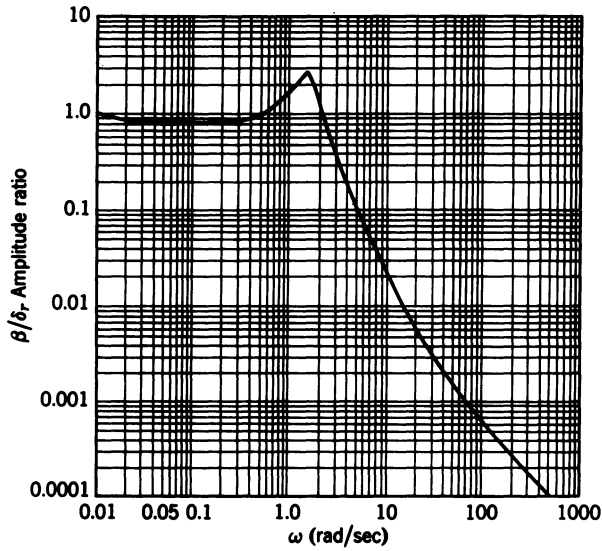
Figure 3-7 *Magnitude plot for β/δ_r transfer function versus ω for $s = j\omega$.*

Factoring,

$$\frac{\psi(s)}{\delta_a(s)} = \frac{-0.171(s-1.14)(s+9.29)(s+1.45)}{s(s^2+0.380s+1.813)(s+2.09)(s-0.004)} \quad (3\text{-}48)$$

Going to the alternative form,

$$\frac{\psi(s)}{\delta_a(s)} = \frac{-173\left(\dfrac{s}{1.14}-1\right)\left(\dfrac{s}{9.29}+1\right)\left(\dfrac{s}{1.45}+1\right)}{s\left[\left(\dfrac{s}{1.345}\right)^2+\dfrac{2(0.14)}{1.345}s+1\right]\left(\dfrac{s}{2.09}+1\right)\left(\dfrac{s}{0.004}-1\right)} \quad (3\text{-}49)$$

The transfer function for β output and δ_a input in determinant form is

$$\frac{\beta(s)}{\delta_a(s)} = \frac{\begin{vmatrix} 0.02725s^2+0.0553s & -0.0128s & 0.6 \\ 0.00338s & 0.0585s^2+0.0158s & -0.01 \\ -0.344 & 4.71s & 0 \end{vmatrix}}{\nabla} \quad (3\text{-}50)$$

Expanding,

$$\frac{\beta(s)}{\delta_a(s)} = \frac{0.00128s(s^2 + 18.9s + 2.51)}{\nabla}$$

Factoring,

$$\frac{\beta(s)}{\delta_a(s)} = \frac{0.171(s + 18.75)(s + 0.15)}{(s^2 + 0.380s + 1.813)(s + 2.09)(s - 0.004)} \tag{3-51}$$
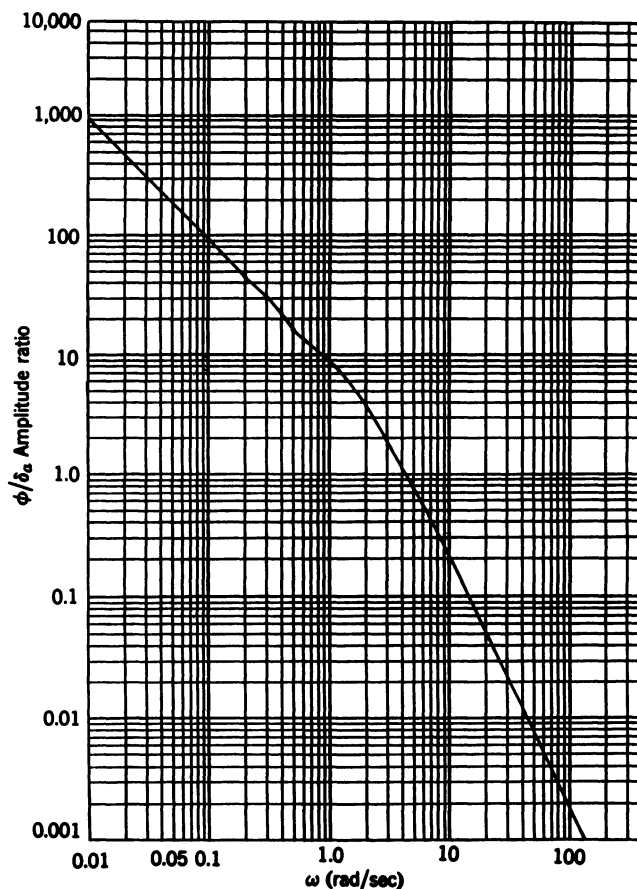
Figure 3-8   *Magnitude plot for ϕ/δ_a transfer function versus ω for $s = j\omega$.*
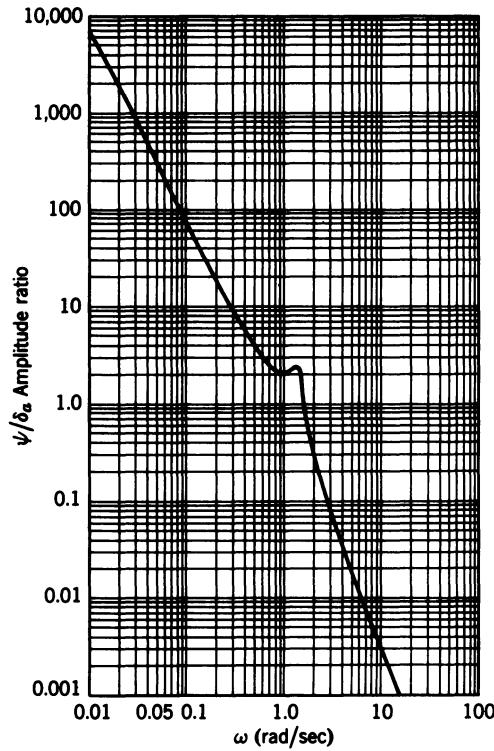
Figure 3-9 *Magnitude plot for ψ/δ_a transfer function versus ω for $s = j\omega$.*

Going to the alternative form,

$$\frac{\beta(s)}{\delta_a(s)} = \frac{31.7\left(\dfrac{s}{18.75}+1\right)\left(\dfrac{s}{0.15}+1\right)}{\left[\left(\dfrac{s}{1.345}\right)^2 + \dfrac{2(0.14)}{1.345}s + 1\right]\left(\dfrac{s}{2.09}+1\right)\left(\dfrac{s}{0.004}-1\right)} \quad (3\text{-}52)$$

Figures 3-8, 3-9, and 3-10 are amplitude ratio plots of Eqs. 3-46, 3-49, and 3-52 against ω for $s = j\omega$.

3-6 APPROXIMATE TRANSFER FUNCTIONS

As in the case of the longitudinal equations, there are some approximations to the lateral modes. They are as follows:
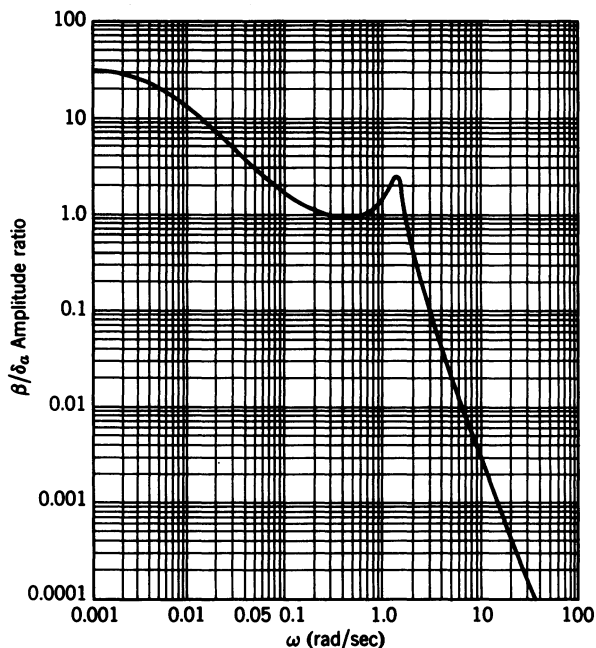
Figure 3-10   *Magnitude plot for β/δ_a transfer function versus ω for $s = j\omega$.*

One-Degree-of-Freedom Dutch Roll Mode. An examination of the transfer functions for ψ and β output and δ_r input shows that the roll subsidence pole is effectively canceled by the zero in the numerator. Thus it is considered that, although the rudder does generate some roll, the major effect of the rudder deflection is the generation of the Dutch roll mode. It is therefore assumed that the Dutch roll mode consists of only sideslip and yaw. If pure sideslip exists, then $\beta = -\psi$, and ϕ and its derivatives can be assumed zero. Considering only a δ_r input with $\Theta = 0$ and neglecting C_{y_r}, Eq. 3-17 in operator form becomes

$$\frac{mU}{Sq}\dot{\psi}(s) + \left(\frac{mU}{Sq}s - C_{y_\beta}\right)\beta(s) = C_{y_{\delta_r}}\delta_r(s)$$

$$\left(-\frac{J_{xz}}{Sqb}s - \frac{b}{2U}C_{l_r}\right)\dot{\psi}(s) - C_{l_\beta}\beta(s) = C_{l_{\delta_r}}\delta_r(s)$$

$$\left(\frac{I_z}{Sqb}s - \frac{b}{2U}C_{n_r}\right)\dot{\psi}(s) - C_{n_\beta}\beta(s) = C_{n_{\delta_r}}\delta_r(s) \qquad (3\text{-}53)$$

Since ϕ and its derivatives are equal to zero, $\Sigma\mathscr{L}$ must equal zero, and the rolling moment equation can be eliminated. With $\beta = -\psi$ the Y equation

reduces to $-C_{y_\beta}\beta = C_{y_{\delta_r}}\delta_r$; thus the yawing moment equation must be used. The yawing moment equation with $\psi = -\beta$ becomes

$$\left(-\frac{I_z}{Sqb}s^2 + \frac{b}{2U}C_{n_r}s - C_{n_\beta}\right)\beta(s) = C_{n_{\delta_r}}\delta_r(s) \tag{3-54}$$

Taking the characteristic equation and dividing through by $-I_z/Sqb$, Eq. 3-54 becomes

$$\left[s^2 - \left(\frac{Sqb}{I_z}\right)\left(\frac{b}{2U}\right)C_{n_r}s + \frac{Sqb}{I_z}C_{n_\beta}\right]\beta(s) = 0$$

Then

$$\omega_n = \left(\frac{C_{n_\beta}Sqb}{I_z}\right)^{1/2} = U\left(\frac{C_{n_\beta}S\rho b}{2I_z}\right)^{1/2} \quad \alpha \; U\sqrt{\rho} \tag{3-55}$$

and

$$2\zeta\omega_n = -\left(\frac{Sqb}{I_z}\right)\left(\frac{b}{2U}\right)C_{n_r} = -\frac{S\rho Ub^2}{4I_z}C_{n_r}$$

Then

$$\zeta = -\left[\frac{S\rho Ub^2}{2(4I_z)}\left(\frac{2I_z}{C_{n_\beta}S\rho b}\right)^{1/2}\right]\frac{C_{n_r}}{U} = \frac{-C_{n_r}}{8}\left(\frac{2S\rho b^3}{I_z C_{n_\beta}}\right)^{1/2} \quad \alpha \; \sqrt{\rho} \tag{3-56}$$

From an examination of Eqs. 3-55 and 3-56 it can be seen that for a given altitude the natural frequency is proportional to U while the damping ratio is constant. However, both the natural frequency and the damping ratio are proportional to the $\sqrt{\rho}$ for a given U. This is the same effect as observed for the short-period mode. Equation 3-54 is evaluated to compare the natural frequency and damping ratio with those obtained from the complete equations. Equation 3-54 in transfer function form is

$$\frac{\beta(s)}{\delta_r(s)} = \frac{-C_{n_{\delta_r}}}{\dfrac{I_z}{Sqb}s^2 - \dfrac{b}{2U}C_{n_r}s + C_{n_\beta}} \tag{3-57}$$

Evaluating, it becomes

$$\frac{\beta(s)}{\delta_r(s)} = \frac{0.08}{0.0585s^2 + 0.0158s + 0.096}$$

$$= \frac{1.37}{s^2 + 0.27s + 1.64} \tag{3-58}$$

Going to the alternative form,

$$\frac{\beta(s)}{\delta_r(s)} = \frac{0.835}{\left(\dfrac{s}{1.28}\right)^2 + \dfrac{2(0.114)}{1.28}s + 1} \tag{3-59}$$

Comparing this with the values of ζ and ω_n obtained from the complete equations shows good agreement. From the complete equations, $\zeta = 0.14$ and $\omega_n = 1.345$.

The one-degree-of-freedom Dutch roll approximation is then very useful for obtaining the damping ratio and natural frequency of the Dutch roll.

One-Degree-of-Freedom Rolling Mode. Because the rolling mode consists almost entirely of rolling motion, only the rolling moment equation is needed. Since sideslip and yaw angle are being neglected, these may be set equal to zero; then the rolling moment equation from Eq. 3-17 in operator form with $\delta_r = 0$ reduces to

$$\left(\frac{I_x}{Sqb}s - \frac{b}{2U}C_{l_p}\right)\dot{\phi}(s) = C_{l_{\delta_a}}\delta_a(s)$$

Then

$$\frac{\dot{\phi}(s)}{\delta_a(s)} = \frac{C_{l_{\delta_a}}}{\dfrac{I_x}{Sqb}s - \dfrac{b}{2U}C_{l_p}} \tag{3-60}$$

The time constant is

$$\tau = -\left(\frac{I_x}{Sqb}\right)\left(\frac{2U}{bC_{l_p}}\right) = -\frac{4I_x}{S\rho Ub^2 C_{l_p}} \alpha \frac{1}{U\rho} \tag{3-61}$$

Evaluating, $\tau = 0.493$ sec. From the complete equations, $\tau = 1/2.09 = 0.479$ sec, which gives good agreement. The ϕ/δ_a transfer function can be

written as

$$\frac{\phi(s)}{\delta_a(s)} = \frac{0.6}{s(0.02725s + 0.0553)}$$

In the alternative form

$$\frac{\phi(s)}{\delta_a(s)} = \frac{10.84}{s\left(\dfrac{s}{2.03} + 1\right)} \tag{3-62}$$
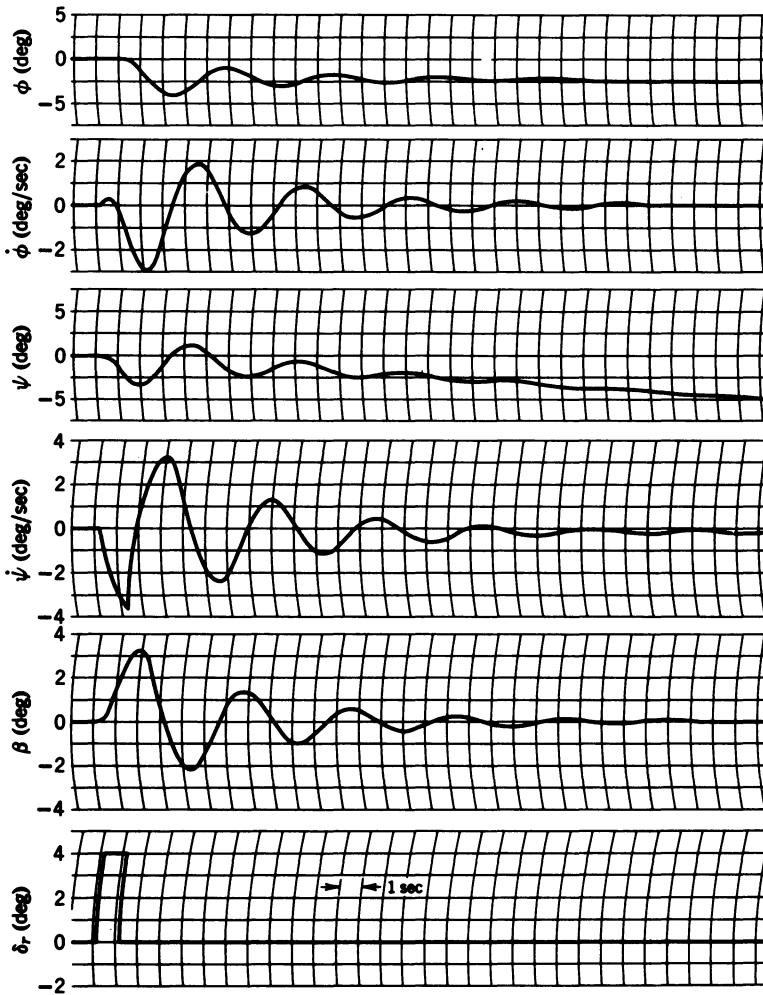
Figure 3-11   *Transient response of the aircraft for a pulse rudder deflection (complete lateral equations for 440 ft / sec at sea level).*

In Chapter 4 it is seen that the one-degree-of-freedom rolling mode is an excellent approximation for the transfer function of the coordinated aircraft defined there.

3-7 TRANSIENT RESPONSE OF THE AIRCRAFT

In this section the transient response of the aircraft for various airspeeds and altitudes, as obtained by use of the analog computer, is discussed. For the computer simulation, the stability derivatives C_{l_p}, C_{l_β}, C_{n_r}, C_{y_β} are assumed constant, which is a valid assumption for the lower Mach numbers. The other stability derivatives are calculated using the equations previously given in
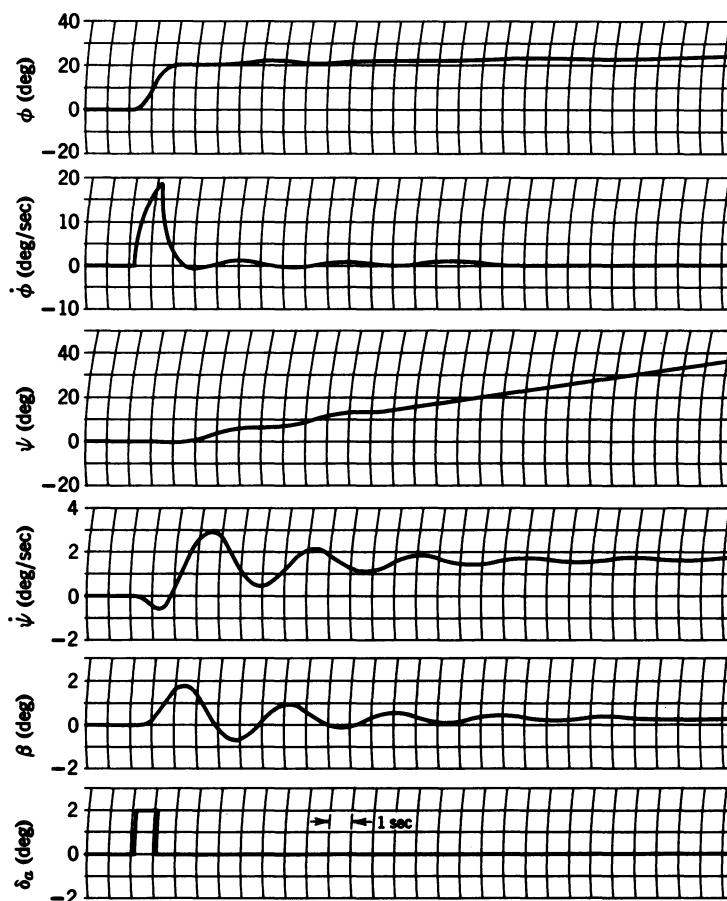
Figure 3-12 *Transient response of the aircraft for a pulse aileron deflection (complete lateral equations for 440 ft / sec at sea level).*
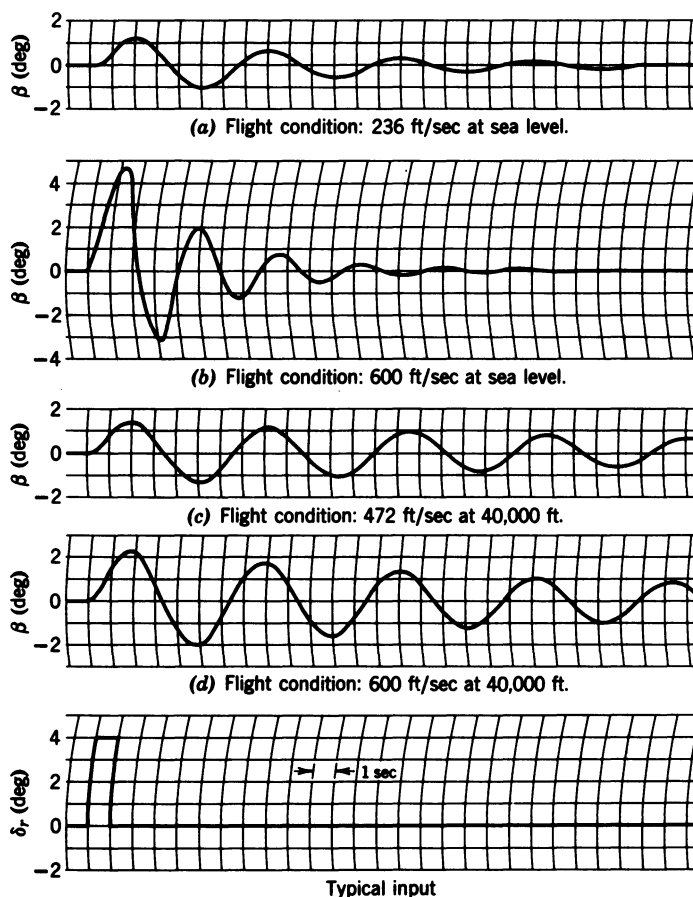
Figure 3-13 Computer results showing the effects of changes in airspeed and altitude on the Dutch roll mode (complete lateral equations).

Table 3-1. The stability derivatives for the forces and moments caused by rudder and aileron deflection are assumed constant, as are the mass and the moments of inertia of the aircraft. The rudder and aileron inputs are applied separately; both consist of pulses 1 sec in duration, with the amplitude of the rudder pulse equal to 4° and that of the aileron equal to 2°. Two different altitudes and four different airspeeds were studied; the results are presented in Figures 3-11 through 3-15.

In the discussion of the one-degree-of-freedom Dutch roll mode it was deduced that the damping ratio was proportional to $\sqrt{\rho}$ and that the natural frequency was proportional to $U\sqrt{\rho}$. The computer study only partially verifies this. The effects of air speed and altitude on the Dutch roll mode are shown in Figure 3-13 and summarized in Table 3-2(a), where Eqs. 3-56 and
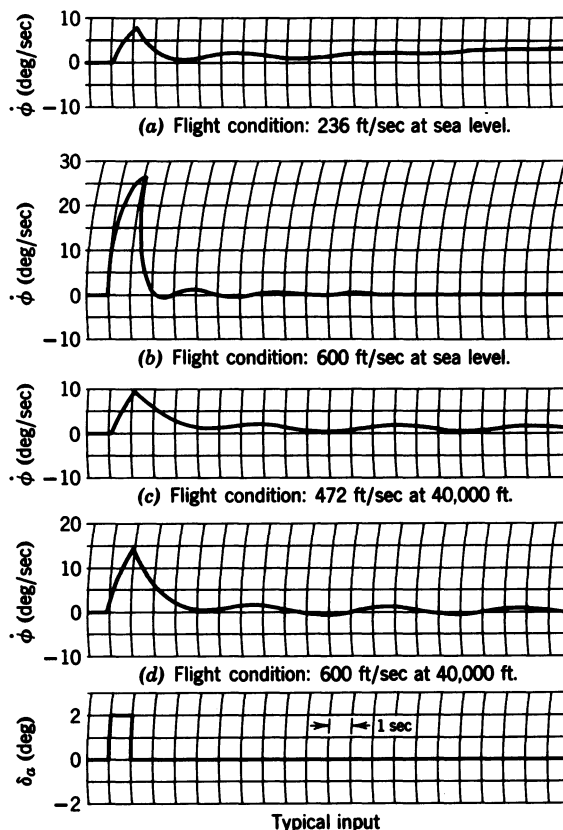
Figure 3-14 *Computer results showing the effects of changes in airspeed and altitude on the roll subsidence time constant (complete lateral equations).*

3-55 are used to determine the expected values of the damping ratios and natural frequencies, respectively. The predicted and actual values compare quite well. The unpredicted variation of the damping ratio with U is caused by the fact that C_{n_β} is dependent upon airspeed.

In the discussion of the one-degree-of-freedom rolling mode, Eq. 3-61 shows that the roll subsidence time constant is inversely proportional to $U\rho$. These effects are shown in Figure 3-14 and summarized in Table 3-2(b). The agreement is considered excellent considering the difficulty of measuring the time constant from the computer traces.

The effects of changes in altitude and airspeed on the spiral divergence are graphically illustrated in Figure 3-15. As the airspeed or air density (and thus the dynamic pressure) is decreased, the divergence becomes more severe; however, at 600 ft/sec at sea level the aircraft is slightly spirally stable. (This phenomenon is explained in Section 3-8.) The adverse yaw
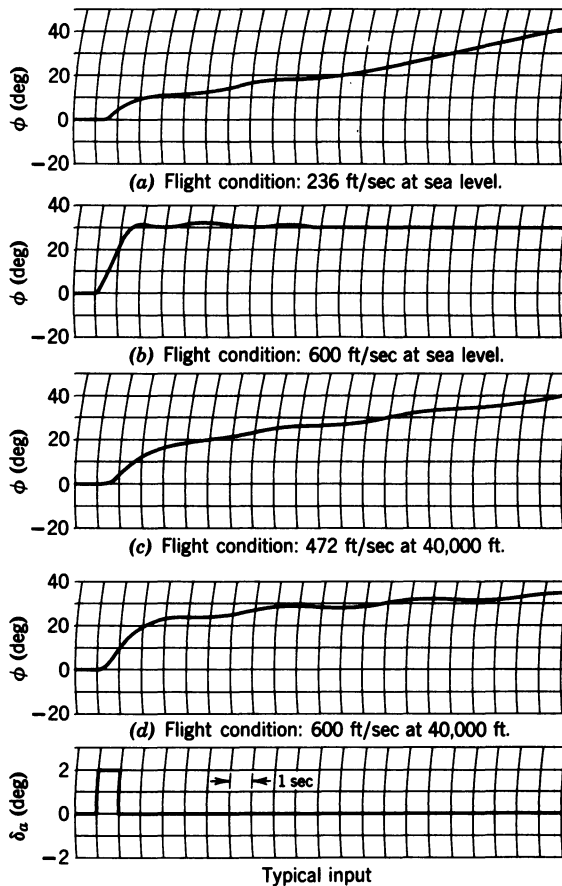
Figure 3-15 *Computer results showing the effects of changes in airspeed and altitude on the spiral mode (complete lateral equations).*

resulting from the aileron deflection and roll rate is clearly shown in the yaw rate trace of Figure 3-12.

From a study of the computer results, it can be said in general that the rudder excites the Dutch roll mode primarily, while aileron deflection produces mostly roll rate and roll angle, with some Dutch roll oscillation superimposed on this basic motion. However, considerable Dutch roll does show up in the yaw rate and sideslip response. Further use will be made of the foregoing observations in the chapter on lateral autopilots.

3-8 EFFECT OF STABILITY DERIVATIVE VARIATION

Before investigating the effect of stability derivative variation, the requirements for spiral stability will be studied. An expansion of the determinant of

TABLE 3-2   Comparison of the Predicted and Actual Effects of the Variation of Airspeed and Altitude on the Lateral Dynamic Response

(a) Dutch Roll Mode

Flight Condition		ζ		ω_n (rad / sec)	
Altitude (ft)	U_0 (ft / sec)	Predicted from Eq. 3-56	Actual	Predicted from Eq. 3-55	Actual
Sea level	236	0.072	0.1	0.98	1.05
Sea level	600	0.109	0.14	1.7	1.74
40,000	472	0.036	0.035	1.01	1.05
40,000	600	0.045	0.04	0.98	1.03

(b) Roll Subsidence Mode

Flight Condition		τ_r (sec)	
Altitude (ft)	U_0 (ft / sec)	Predicted from Eq. 3-61	Actual
Sea level	236	0.91	0.8
Sea level	600	0.353	0.35
40,000	472	1.82	1.6
40,000	600	1.43	1.3

the lateral equation yields the following for the constant term:

$$C_{y_\phi}\left(C_{l_\beta}\frac{b}{2U}C_{n_r} - C_{n_\beta}\frac{b}{2U}C_{l_r}\right)$$

or

$$\frac{b}{2U}C_{y_\phi}\left(C_{l_\beta}C_{n_r} - C_{n_\beta}C_{l_r}\right)$$

For an aircraft to be spirally stable, the product $C_{l_\beta}C_{n_r}$ must be greater than the product $C_{n_\beta}C_{l_r}$. From the data listed for the jet transport in Section 3-3,

$$C_{l_\beta}C_{n_r} - C_{n_\beta}C_{l_r} = (-0.057)(-0.107) - (0.096)(0.086)$$

or

$$C_{l_\beta}C_{n_r} - C_{n_\beta}C_{l_r} = 0.0061 - 0.00825$$

C_{n_r} and C_{n_β} are both affected by the size of the vertical tail, so that one cannot be increased without increasing the other. However, C_{l_β} is mainly a

TABLE 3-3   Effects of Variation of the Stability Derivatives on the Damping Ratio, Natural Frequency, and Time Constants of the Lateral Modes

Stability Derivative	Basic Value	Change	Dutch Roll ζ	Dutch Roll ω_n	Roll Subsidence $1/\tau_r$	Spiral Divergence* $1/\tau_s$
C_{l_p}	-0.38	$\times 4$	0.13	1.32	-8	$+0.00105$
		$\times 2$			-4	$+0.0021$
		$\times \frac{1}{2}$			-1.0	$+0.0084$
		$\times \frac{1}{4}$			-0.5	$+0.0168$
C_{l_r}	0.086	$\times 4$		1.38	-2	$+0.0535$
		$\times 2$		1.35		$+0.0206$
		$\times \frac{1}{2}$		1.32		-0.00406
		$\times \frac{1}{4}$				-0.0082
C_{n_r}	-0.107	$\times 4$	0.4			-0.0327
		$\times 2$	0.22			-0.008
		$\times \frac{1}{2}$	0.06			$+0.0103$
		$\times \frac{1}{4}$	0.04			$+0.0134$
C_{n_β}	0.096	$\times 4$	0.05	2.42		$+0.0133$
		$\times 2$	0.13	1.87		$+0.0103$
		$\times \frac{1}{2}$	0.16	0.994		-0.0081
		$\times \frac{1}{4}$	0.25	0.738		-0.0328
C_{y_β}	-0.6	$\times 4$	0.275	1.36		$+0.0042$
		$\times 2$	0.16	1.33		
		$\times \frac{1}{4}$	0.094	1.316		
C_{l_β}	-0.057	$\times 4$	0.03	1.32	-2.5	-0.034
		$\times 2$	0.1		-2.1	-0.008
		$\times \frac{1}{4}$	0.16		-1.7	$+0.0134$
C_{n_p}	-0.0228	$\times 4$	0.11	1.41	-2.2	$+0.0042$
		$\times \frac{1}{4}$	0.13	1.32	-2.0	$+0.0042$

* + sign indicates divergence; − sign indicates convergence.

function of the effective dihedral of the wing and can be increased by increasing the dihedral. Since $C_{l_r} = C_L^w / 4$, spiral stability can be obtained by decreasing C_L, which can be accomplished by flying faster, thus decreasing the wing angle of attack. This fact indicates that an aircraft can be spirally stable at low angles of attack (high speed) and spirally unstable at low airspeed, as shown in Section 3-7. On examining the effects of obtaining spiral stability by changing C_{l_β} by increasing the dihedral, it can be seen that the damping ratio of the Dutch roll mode is decreased (see Table 3-3). If C_{l_β} is increased sufficiently, the Dutch roll oscillations can go unstable. Thus in most aircraft a slight amount of spiral instability is permitted in order to obtain other, more important flying qualities, such as better damping of the Dutch roll.

The effects of varying the individual stability derivatives on the lateral modes are studied next. The data for Table 3-3 was obtained for an airspeed

TABLE 3-4   The Stability Derivatives Having the Largest Effects on the Lateral Modes

Stability Derivative	Quantity Most Affected	How Affected
C_{n_r}	Damping of the Dutch roll	Increase C_{n_r} to increase the damping
C_{n_β}	Natural frequency of the Dutch roll	Increase C_{n_β} to increase the natural frequency
C_{l_p}	Roll subsidence	Increase C_{l_p} to increase $1/\tau_r$
C_{l_β}*	Spiral divergence	Increase C_{l_β} for spiral stability

*C_{l_β} was selected for the reasons stated at the beginning of Section 3-8.

of 440 ft/sec at sea level through the use of the analog computer by varying each stability derivative individually and then determining the damping ratio and natural frequency of the Dutch roll and the two time constants from the time recordings. In the analysis of the recordings it proves difficult to evaluate the spiral divergence time constant; therefore, this time constant is calculated from the following equation:

$$\tau_s = \frac{mU}{Sq}\left[\frac{C_{l_p}C_{n_\beta}}{C_{y_\phi}(C_{l_\beta}C_{n_r} - C_{n_\beta}C_{l_r})}\right] \tag{3-63}$$

As mentioned in Section 1-11, the varying of the stability derivatives individually is an artificial situation, but it is included to give the reader some feel for the relative importance of the various stability derivatives.

It must be remembered that the data presented in Table 3-3 was obtained from the analog computer traces; thus extremely small changes in the characteristics of the modes cannot be detected. The basic values of the modes as measured from the computer traces are given here for reference. Dutch roll: $\zeta_D = 0.13$, $\omega_{n_D} = 1.32$; roll subsidence: $1/\tau_r = -2$; spiral divergence: $1/\tau_s = +0.0042$. From Table 3-3 it can be concluded that the stability derivatives in Table 3-4 have the most effect on the lateral modes.

REFERENCES

1. C. D. Perkins, and R. E. Hage, *Airplane Performance, Stability, and Control*, John Wiley and Sons, New York, 1949.

2. B. Etkin, *Dynamics of Flight: Stability and Control*, 2nd ed., John Wiley and Sons, New York, 1982.

4

Lateral Autopilots

4-1 INTRODUCTION

As most aircraft are spirally unstable, there is no tendency for the aircraft to return to its initial heading and roll angle after it has been disturbed from equilibrium by either a control surface deflection or a gust. Thus the pilot must continually make corrections to maintain a given heading. The early lateral autopilots were designed primarily to keep the wings level and hold the aircraft on a desired heading. A vertical gyro was used for the purpose of keeping the wings level, and a directional gyro was used for the heading reference. Figure 4-1 is a block diagram of such an autopilot. This autopilot had only very limited maneuvering capabilities. Once the references were aligned and the autopilot engaged, only small heading changes could be made. This was generally accomplished by changing the heading reference and thus yawing the aircraft through the use of the rudders to the new heading. Obviously such a maneuver was uncoordinated and practical only for small heading changes. Due to the lack of maneuverability and the light damping characteristic of the Dutch roll oscillation in high-performance aircraft, this autopilot is not satisfactory for our present-day aircraft. Present-day lateral autopilots are much more complex. In most cases it is necessary to provide artificial damping of the Dutch roll. Also, to add maneuverability, provisions are provided for turn control through the deflection of the aileron, and coordination is achieved by proper signals to the rudder. In this discussion of lateral autopilots the damping of the Dutch roll is discussed first, followed by methods of obtaining coordination, and then the complete autopilot is examined.

143
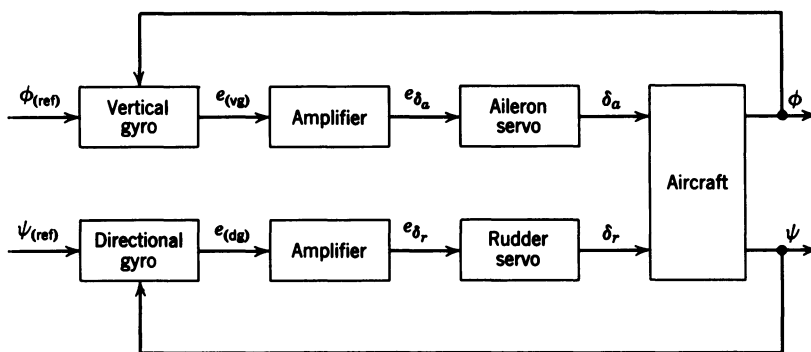
Figure 4-1   *Basic lateral autopilot.*

4-2   DAMPING OF THE DUTCH ROLL

In the derivation of the lateral equations of motion $\dot{\phi}$ and $\dot{\psi}$ were substituted for p and r, respectively. This was done on the assumption that the perturbations from equilibrium were small. However, $\dot{\psi}$ is an angular velocity about the vertical, while r is measured with respect to the Z axis of the aircraft. For small roll angles $\dot{\psi}$ and r are approximately equal, but for larger roll angles this is not true. In the study of lateral autopilots, especially in the analysis of methods of obtaining coordination, the roll angle is not necessarily small; therefore, it is more correct to use r instead of $\dot{\psi}$ when referring to angular velocities about the aircraft Z axis; that is, the angular velocity measured by a yaw rate gyro is r not $\dot{\psi}$. With reference to p and $\dot{\phi}$, both are angular velocities about the aircraft X axis and are therefore always identical as long as Θ is zero. Thus for the remainder of this chapter, r is used instead of $\dot{\psi}$, but $\dot{\phi}$ and ϕ are used for the roll rate and roll angle.

In the discussion of the transient response in Section 3-7 it was stated that the rudder excites primarily the Dutch roll mode; the Dutch roll that is observed in the yaw rate and sideslip response from an aileron deflection is caused by the yawing moment resulting from the aileron deflection. For these reasons the usual method of damping the Dutch roll is to detect the yaw rate with a rate gyro and use this signal to deflect the rudder. Figure 4-2 is a block diagram of the Dutch roll damper. The washout circuit produces an output only during the transient period. If the yaw rate signal did not go to zero in the steady state, then for a positive yaw rate, for instance, the output of the yaw rate gyro would produce a positive rudder deflection. This would result in an uncoordinated maneuver and require a larger pilot's rudder input to achieve coordination. The transfer function of the washout circuit is $\tau s/(\tau s + 1)$.

The best way to illustrate the effect of different values of the time constant for the washout circuit is to draw the root locus for two different values of
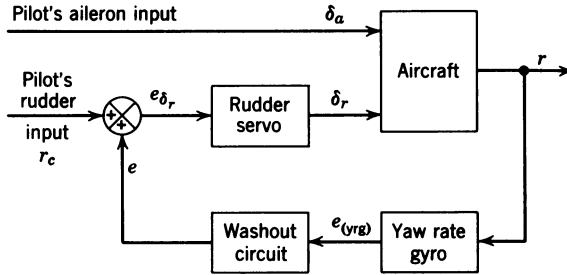
Figure 4-2 Block diagram of Dutch roll damper.

the time constant. First, Figure 4-2 is redrawn with the transfer functions of the various blocks indicated (see Figure 4-3). Since the root locus is drawn for a rudder input only, the aileron input is not indicated in Figure 4-3. The transfer function of the aircraft is obtained from Eq. 3-38 after canceling the rolling mode pole with the appropriate zero. Figures 4-4 and 4-5 are the root loci of the Dutch roll damper as the yaw rate gyro sensitivity is increased from zero for a time constant of the washout circuit of 3 sec and $\frac{1}{2}$ sec, respectively. As can be seen from the root loci, if the time constant is not large enough, very little increase in the damping ratio can be obtained. If the time constant is larger, then considerable improvement of the damping ratio can be obtained as the rate gyro sensitivity is increased. The location of the closed loop poles for a yaw rate gyro sensitivity of 1.04 volt/(deg/sec) is indicated in Figure 4-4. These closed loop poles are used in the subsequent lateral autopilot analysis. Figure 4-6 shows the results of a computer simulation of the aircraft with the Dutch roll damper. The effectiveness of the Dutch roll damper is evident; however, some sideslip is present, especially during the transient period. This is due to the adverse yawing moment caused by the roll rate. It should be noted that the rudder deflection goes to zero shortly after the yaw rate reaches a steady state. Now that the Dutch roll has
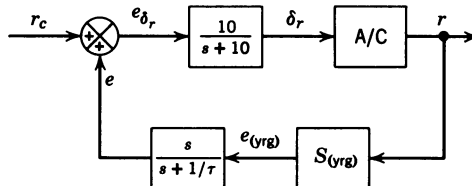
Figure 4-3 Block diagram of the Dutch roll damper for the root locus study;

$$[\text{TF}]_{(\text{A/C})[\delta_r;r]} = \frac{-1.38(s^2 + 0.05s + 0.066)}{(s - 0.004)(s^2 + 0.38s + 1.813)}$$
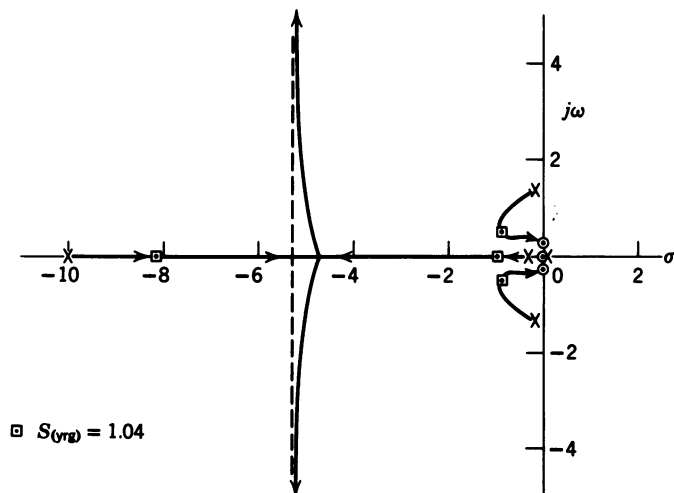
Figure 4-4   Root locus for the Dutch roll damper for τ of the washout circuit equal to 3 sec.
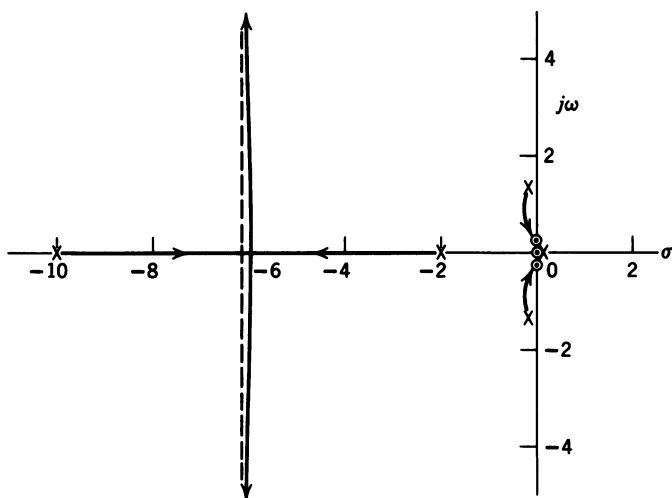
Figure 4-5   Root locus for the Dutch roll damper for τ of the washout circuit equal to 0.5 sec.
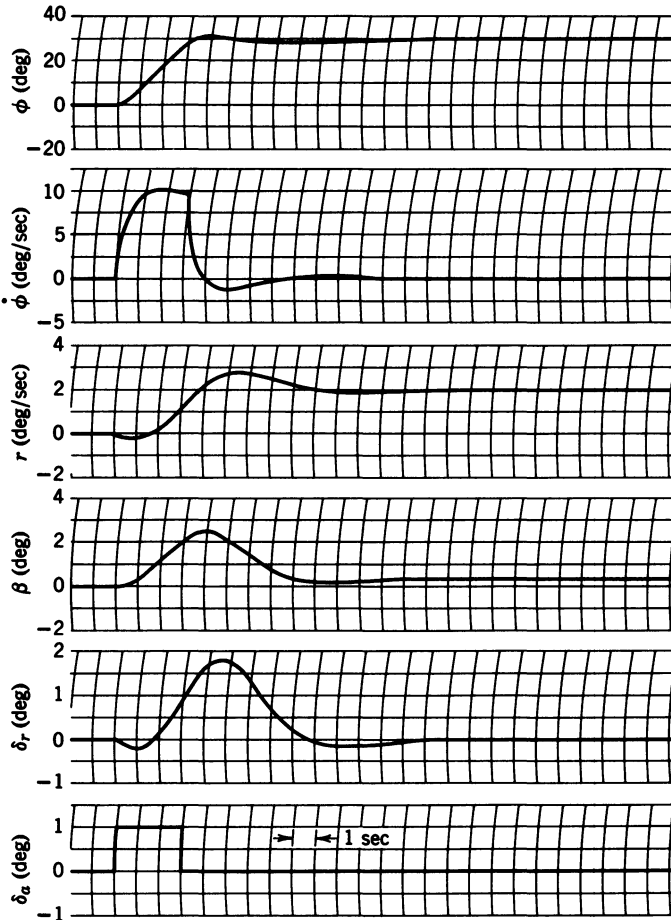
Figure 4-6 *Response of the aircraft with Dutch roll damping for $S_{(yrg)} = 1.04$ volt / (deg / sec) for a pulse aileron deflection (sea level at 440 ft / sec).*

been adequately damped, it is necessary to eliminate the sideslip to achieve a coordinated turn. Section 4-3 discusses several different methods for achieving coordination, and the advantages and disadvantages of each.

4-3 METHODS OF OBTAINING COORDINATION

1. The most logical method of eliminating sideslip is to feed back a signal proportional to sideslip. Figure 4-7 is a block diagram of this system. The inner loop of the system shown in Figure 4-7 is the Dutch roll damper.
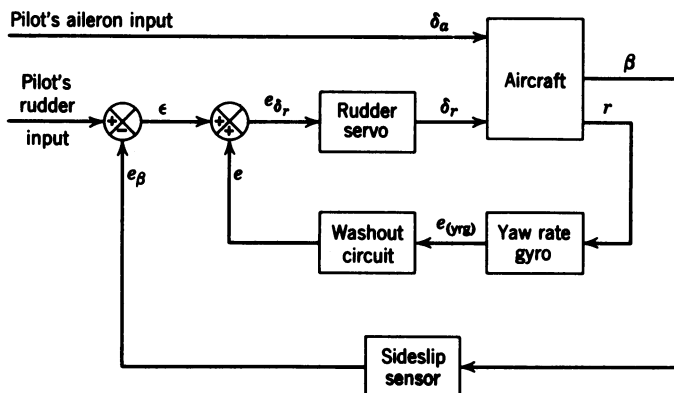
Figure 4-7 *Block diagram of system using sideslip to obtain coordination.*

Selection of the yaw rate gyro sensitivity determines the closed loop poles of the inner loop; these are in turn the open loop poles of the outer loop. However, there is one additional zero introduced into the closed loop transfer function of the inner loop by the washout circuit.

Figure 4-7 is redrawn in Figure 4-8, replacing the inner loop with its appropriate transfer function. The block containing $\beta(s)/r(s)$ is the ratio of the transfer functions of the aircraft for rudder input to sideslip and yaw rate output, respectively. The $\beta(s)/r(s)$ transfer function is required to convert the output of the closed loop transfer function of the inner loop from r to β. Because the sideslip and yaw rate transfer functions have the same denominator, their ratio is the ratio of their numerators. Thus

$$\frac{\beta(s)}{r(s)} = \frac{-0.0364(s-0.01)(s+2.06)(s+37.75)}{1.38(s+2.07)(s^2+0.05s+0.066)} \text{ sec} \qquad (4\text{-}1)$$

When the forward transfer function shown in Figure 4-8 is multiplied by Eq. 4-1 after canceling the factor $s+2.06$ in the numerator with the factor $s+2.07$ in the denominator and canceling the zero at 0.01 with the pole at
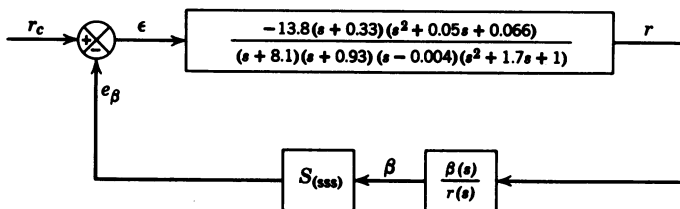
Figure 4-8 *Simplified block diagram of coordination system.*
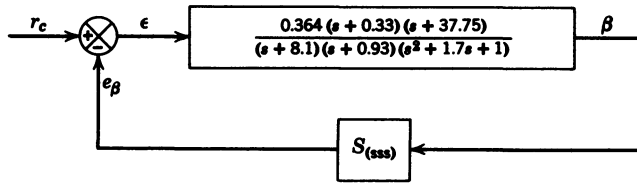
Figure 4-9 *Block diagram for root locus study of system using sideslip to obtain coordination.*

0.004, Figure 4-8 can be redrawn as shown in Figure 4-9. The poles and zeros that are canceled are so close together that they do not influence the root locus. The plotting of this root locus will be left as an exercise for the student.

Before going on to the next method, some problems associated with measurement of the sideslip angle are discussed. In general, it is easier to measure sideslip than to measure angle of attack. In both cases it is not difficult to measure the direction of the local air flow. The problem arises in determining whether the direction of the local air flow measured is the direction of the undisturbed air. Since sideslip is measured with respect to the plane of symmetry, there is less distortion of the local air flow and thus the local air flow is more nearly aligned with the undisturbed air flow ahead of the aircraft. This is not true for the angle of attack, due to the upwash in front of the wing and the downwash behind the wing. Another problem is the noise produced by the sideslip sensor. This noise can arise either in the signal generator or from disturbances in the air flow. The sensitivity of the sideslip sensor must be kept low or the loop will be too sensitive and the damping too low. The low sensitivity also minimizes the effects of the noise. In spite of the apparent disadvantages, the use of sideslip to achieve coordination is quite extensive.

Although sideslip feedback has been shown to be effective, the use of $\beta - \dot{\beta}$ feedback had proved so effective in a study[1] on the F-106 that it was
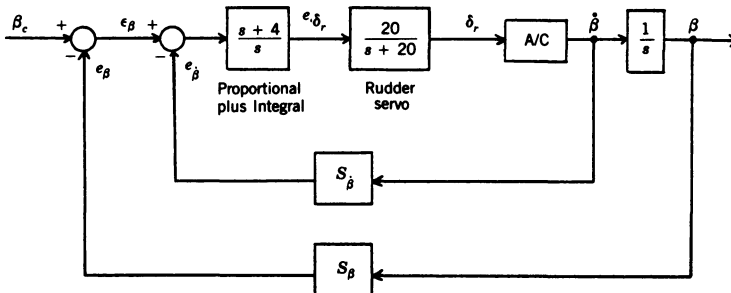
Figure 4-10 *Block diagram of $\beta - \dot{\beta}$ SAS.*
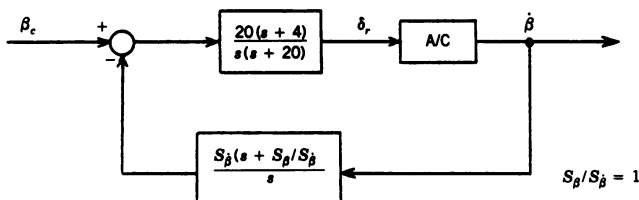
Figure 4-11   *Single loop block diagram of β-β̇ SAS.*

used in the design of the autopilot for the F-15 integrated flight/fire control system presented in Chapter 9 from Ref. 2. The block diagram for the $\beta-\dot{\beta}$ feedback stability augmentation system (SAS) is shown in Figure 4-10. The transfer function of the F-15 for Mach 0.8 at 20,000 ft is

$$\frac{\dot{\beta}(s)}{\delta_r(s)} = \frac{0.0573s(s-0.0061)(s+2.783)(s+79.77)}{(s+0.024)(s+2.95)(s^2+0.492s+7.46)} \tag{4-2}$$

For the root locus analysis the block diagram shown in Figure 4-10 was simplified to a single feedback loop. The resulting block diagram is shown in Figure 4-11. The root locus is shown in Figure 4-12 with the location of the closed loop poles for $S_\beta = S_{\dot{\beta}} = 3$ indicated.
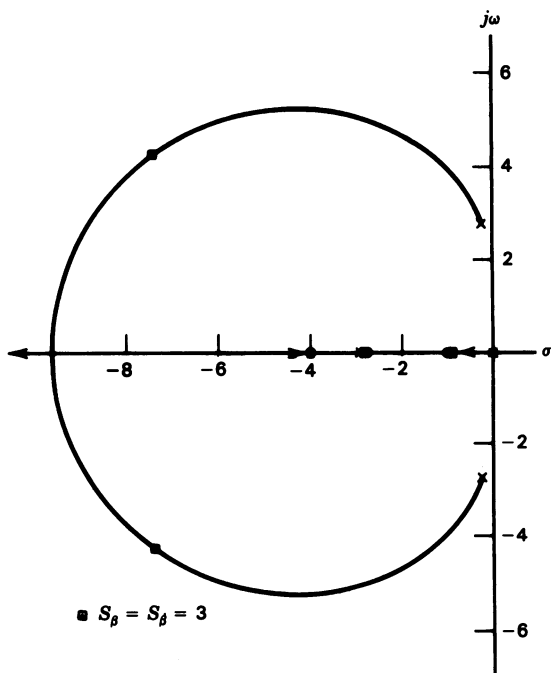
Figure 4-12   *Root locus for β-β̇ SAS.*

Although β can be measured with a vane or other similar sensor, $\dot{\beta}$ cannot, and differentiating the β signal would only amplify the noise in an already noisy signal. Therefore $\dot{\beta}$ must be calculated from measurable parameters using the following equation, which is derived in Appendix G:

$$\dot{\beta} = P \sin \alpha - R \cos \alpha$$

$$+ 57.3g \frac{a_{(\text{lat})} + \cos \Theta \cos \Phi}{V_T} \text{ deg/sec} \qquad (4\text{-}3)$$

2. The second method for obtaining coordination arises from the definition of a "coordinated turn." A coordinated turn is one in which the resulting acceleration lies in the plane of symmetry. This means that there is no lateral acceleration; thus if an accelerometer is used to sense lateral acceleration and its output is fed to the rudder so that the rudder will be deflected in such a direction as to null the output of the accelerometer, coordination can be obtained. Figure 4-13 is a block diagram of the system. To analyze this system, it is first necessary to obtain a transfer function for the aircraft for a rudder input to lateral acceleration output. An expression for the lateral acceleration can be obtained from Eq. 3-14 for $\Theta = 0$, neglecting C_{y_p}. Thus, as $C_{y_\psi} = (mg/Sq)\sin \Theta = 0$,

$$\frac{mU}{Sq}\dot{\beta} - C_{y_\beta}\beta + \left(\frac{mU}{Sq} - \frac{b}{2U}C_{y_r}\right)r - C_{y_\phi}\phi = C_{y_a} \qquad (4\text{-}4)$$

For the lateral acceleration to be zero the summation of the terms in Eq. 4-4 must be zero. As will be shown in Eq. 4-5, all the terms on the left hand side of Eq. 4-4, except the term $(b/2U)C_{y_r}r$, add to zero for $\beta = 0$, that is, a steady-state coordinated turn. This means that for the steady-state coordination $C_{y_a} = -(b/2U)C_{y_r}r$. Since $C_{y_a} = C_{y_{\delta_r}}\delta_r$, during a coordinated turn the
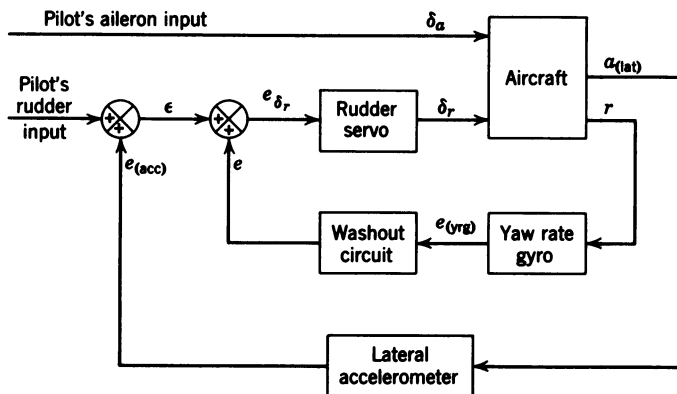
Figure 4-13 Block diagram of system using lateral acceleration to obtain coordination.
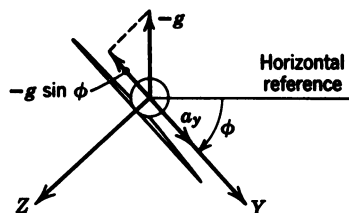
Figure 4-14 *Components of acceleration along the Y axis during a turn.*

rudder deflection is such that the side force produced by the turning angular velocity is zero. These terms are then eliminated from the rest of the analysis, and Eq. 4-4 reduces to

$$\frac{Sq}{m}C_{y_\beta}\beta = U(\dot{\beta}+r)-\frac{Sq}{m}C_{y_\phi}\phi = a_{(\text{lat})} \tag{4-5}$$

after multiplying throughout by Sq/m. From Eq. 3-4 it can be seen that $U(\dot{\beta}+r)=a_y$, and from Table 3-1, $C_{y_\phi}=mg/Sq$ for $\Theta=0$. Then $(Sq/m)C_{y_\phi}\phi$ is the small-angle approximation of $g\sin\phi$, which is the component of gravity along the Y axis as shown in Figure 4-14. Therefore the right hand side of Eq. 4-5 yields the total lateral acceleration that would be detected by a lateral accelerometer (the kinematic acceleration a_y, and the gravitational acceleration $-g\sin\phi$). The lateral acceleration transfer function can be obtained from the sideslip transfer function as

$$\frac{a_{(\text{lat})}(s)}{\delta_r(s)}=\frac{Sq}{m}C_{y_\beta}\frac{\beta(s)}{\delta_r(s)}\frac{\text{ft/sec}^2}{\text{rad}}=\frac{Sq}{(32.2)(57.3)m}C_{y_\beta}\frac{\beta(s)}{\delta_r(s)}\frac{g}{\text{deg}} \tag{4-6}$$

The simplified block diagram for the system using lateral acceleration to obtain coordination is shown in Figure 4-15. The reason for the positive sign at the summer for the feedback signal is the sign of C_{y_β}, which is negative (see Table 3-1). This means that positive sideslip results in a negative lateral acceleration. From this analysis it can be seen that the use of a lateral
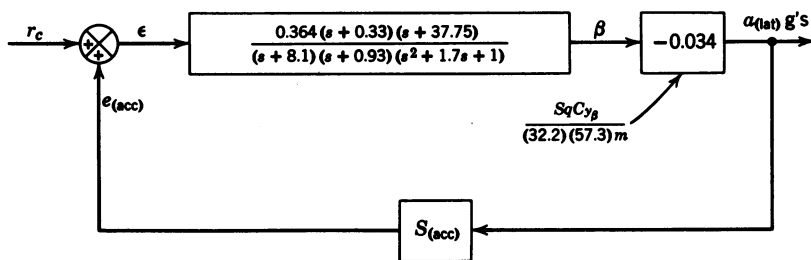
Figure 4-15 *Block diagram for root locus study of system using lateral acceleration for coordination.*

accelerometer is effectively the same as use of a sideslip sensor; but because the ratio acceleration to β is only $0.034g/\text{deg}$, the lateral accelerometer is much less sensitive and is not as effective. The root locus is the same as for the sideslip sensor and therefore is not drawn here.

Some of the problems associated with the use of the lateral accelerometer are discussed in the following paragraphs. As in the case of the sideslip sensor, the output of the accelerometer may be noisy, thus necessitating a low sensitivity. In practice, a sensitivity of 10 volt/g would probably be satisfactory, and flight test might show that a higher gain could be used. Another problem that faces the engineer is determining the minimum acceleration that the accelerometer should be capable of detecting. If the accelerometer is extremely sensitive, say $10^{-3}g$ or lower, the accelerometer, if used in a high-performance fighter, could possibly sense the Coriolis acceleration resulting from the craft's velocity. Normally an accelerometer capable of sensing $0.1g$ is adequate. The location of the accelerometer is another factor to be considered. In general, the accelerometer should be placed as close to the center of gravity of the aircraft as possible. The farther the accelerometer is removed from the center of gravity of the aircraft, the larger will be the tangential acceleration that the accelerometer is subjected to due to yaw angular accelerations of the aircraft. There is one condition that may dictate a location that is not close to the center of gravity. This is the case in which the aircraft cannot be assumed rigid. If there is considerable fuselage bending, the accelerometer should be located closer to the node of the first body bending mode. (This problem is discussed further in Chapter 11.) If body bending is a problem, the final location of the accelerometer will probably be a compromise between locating it near the center of gravity and close to the node of the first body bending mode.

To achieve coordination the use of the lateral accelerometer, like the use of sideslip, is popular. In fact in some cases both have been used together successfully. However, both techniques require that the sensitivities of the closed loop be scheduled as a function of the dynamic pressure, or possibly the Mach number, if the aircraft is to operate over a wide range of air speeds and altitudes.

3. The third method of obtaining coordination is based on the fact that for a certain bank angle and true air speed, there is only one value of yaw rate for which coordination can be achieved. This can be seen by referring to Figure 4-16. For a coordinated turn the lift vector must be perpendicular to the aircraft Y axis. The lift vector is the vector sum of the weight vector (mg) and the centripetal acceleration times the aircraft mass ($m\dot{\Psi}^2 R$), where R is the radius of curvature of the circular flight path of the aircraft.

Now $m\dot{\Psi}^2 R = mV_T\dot{\Psi}$, as $\dot{\Psi}R$ is the tangential velocity of a point moving in a circle. From Figure 4-16 the horizontal component of lift must be equal to $mV_T\dot{\Psi}$, or in equation form,

$$L \sin \phi = mV_T\dot{\Psi} \qquad (4\text{-}7)$$
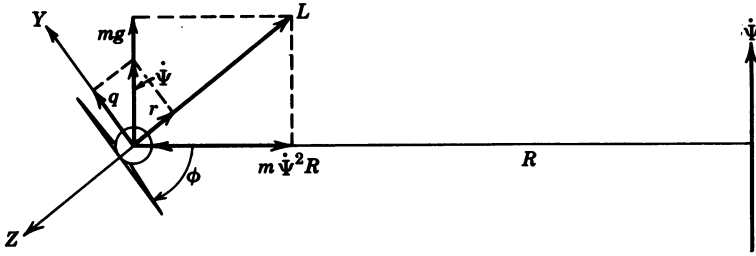
Figure 4-16 *Geometry of an aircraft in a coordinated level turn.*

The vertical component of the lift must equal mg; thus

$$L \cos \phi = mg \tag{4-8}$$

Dividing Eq. 4-7 by Eq. 4-8, we obtain

$$\tan \phi = \frac{V_T \dot{\Psi}}{g} \quad \text{or} \quad \dot{\Psi} = \frac{g}{V_T} \tan \phi \tag{4-9}$$

From Figure 4-16 for $\Theta = 0$

$$r = \dot{\Psi} \cos \phi \tag{4-10}$$

and

$$q = \dot{\Psi} \sin \phi \tag{4-11}$$

It should be noted that ϕ is actually a negative angle. Substituting Eq. 4-9 into Eq. 4-10, Eq. 4-10 becomes

$$r = \frac{g}{V_T} \sin \phi \tag{4-12}$$

If Eq. 4-9 is substituted into Eq. 4-11, the following equation is obtained:

$$q = \frac{g}{V_T} \tan \phi \sin \phi \tag{4-13}$$

Equation 4-12 is of immediate interest; the usefulness of Eq. 4-13 is discussed in Section 4-7. From Eq. 4-12 it can be seen that if V_T and ϕ are known, the proper value of r can be determined. This can then be the command signal to the rudder. Figure 4-17 is a block diagram of this system. The output of the yaw rate gyro is multiplied by the inverse sensitivity of the yaw rate gyro so that the voltage corresponding to the actual yaw rate, $e_{r(act)}$, just equals r, that is, unity feedback. The variation in gain for this loop is
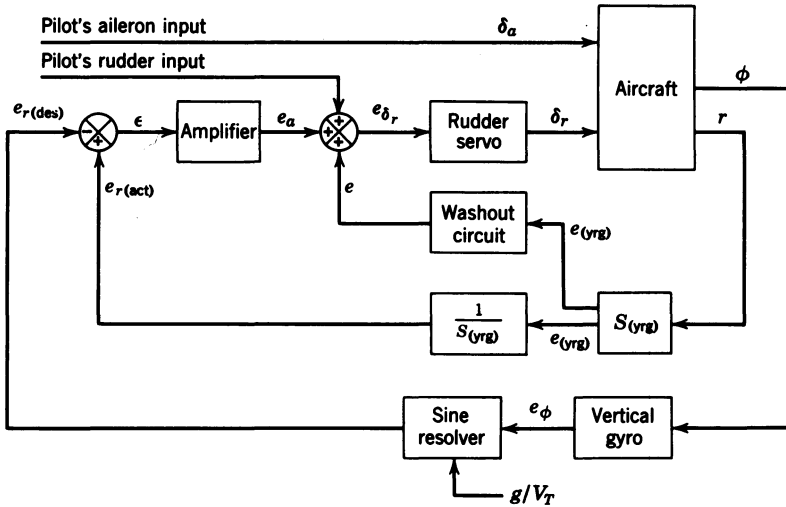
Figure 4-17   Block diagram of system using computed yaw rate to obtain coordination.

obtained by changing the gain of the amplifier. From an inspection of Figure 4-17 it might be concluded that two new feedback loops have been added; however, this is not the case. The apparent feedback through the vertical gyro and the sine resolver is simply to generate the command signal $e_{r(\text{des})}$. Thus for analysis, Figure 4-17 can be redrawn as shown in Figure 4-18, after replacing the Dutch roll damping loop by its closed loop transfer function. Figure 4-19 is the root locus for the block diagram shown in Figure 4-18. As the gain of the amplifier is increased, the complex poles move toward the complex zeros and the spiral divergent pole moves into the left half plane toward the real zero. The closer the poles approach these zeros, the less effect they have on the transient response. By the time the gain has been increased sufficiently to move the complex poles into the proximity of the zeros, the poles on the real axis have come together and moved out along the 90° asymptotes and off the graph. These new complex poles are then the dominant roots and determine the characteristics of the transient response. In general, the gain should be as high as possible consistent with good
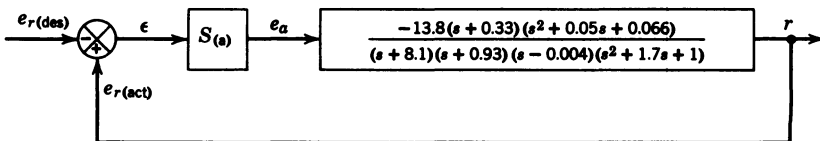
Figure 4-18   Block diagram for root locus study of system using computed yaw rate to obtain coordination.
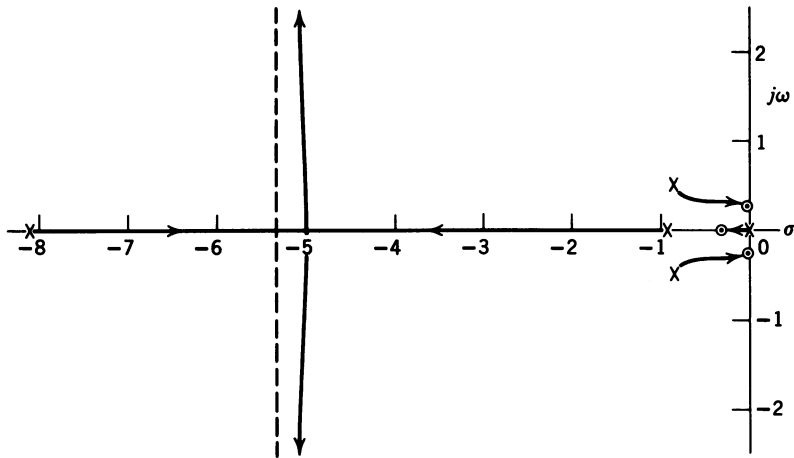
Figure 4-19 *Root locus of system using computed yaw rate to obtain coordination.*

response. In this case a gain of 10 volt/volt yields a damped natural frequency of about 11 rad/sec with a damping ratio of about 0.5. This system is obviously more complicated than the first two systems for achieving coordination, and for this reason it is not as popular. As with the other systems, the gains must be changed as the flight conditions vary. Besides, the velocity being fed into the sine resolver (see Figure 4-17) must be the true airspeed if the value of the desired yaw rate is to be correct. This requires a voltage proportional to g/V_T to be continuously generated and fed to the sine resolver along with the signal from the vertical gyro. If the quantity g/V_T is not correct, or if the sine resolver is not positioned to an angle equal to the roll angle, the value of $e_{r(\text{des})}$ will be incorrect, thus calling for the incorrect amount of rudder and will cause the turn to be uncoordinated. If the value of $e_{r(\text{des})}$ is too large, too much rudder will be called for, resulting in "bottom" rudder being held in the turn. If $e_{r(\text{des})}$ is too low, "top" rudder will be held in a steady-state turn. These situations are demonstrated by the computer traces in Section 4-4, along with the effects of holding "top" and "bottom" rudder. The lack of coordination resulting from such a situation is very objectionable to the pilot. This is probably the main reason for the lack of popularity of this system.

4. The last method to be discussed utilizes a component referred to as the "rudder coordination computer," which computes the amount of rudder required for a given amount of aileron. Figure 4-20 is a block diagram of this system. The transfer function of the rudder coordination computer is now derived. The total sideslip experienced by the aircraft is equal to the sideslip resulting from the rudder and the aileron, or in equation form,

$$\beta_{\text{total}} = [\text{TF}]_{(A/C)[\delta_r;\,\beta]}\delta_r + [\text{TF}]_{(A/C)[\delta_a;\,\beta]}\delta_a \qquad (4\text{-}14)$$
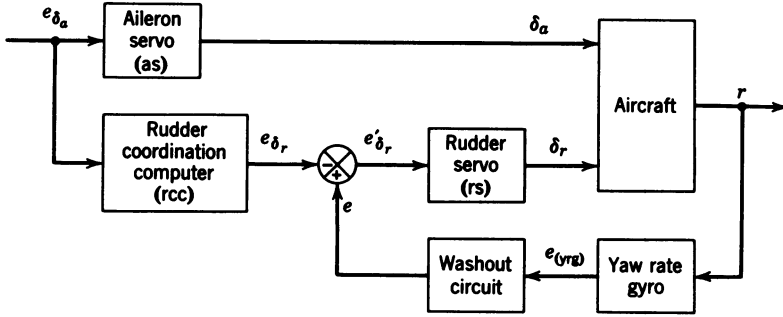
Figure 4-20 *Block diagram of system using a rudder coordination computer to achieve coordination.*

But if the coordination is perfect, the total sideslip is zero; then from Eq. 4-14

$$\frac{\delta_r}{\delta_a} = \frac{-[\text{TF}]_{(A/C)[\delta_a;\beta]}}{[\text{TF}]_{(A/C)[\delta_r;\beta]}} \qquad (4\text{-}15)$$

But from Figure 4-20

$$\delta_r = -e_{\delta_a}[\text{TF}]_{(\text{rcc})}[\text{TF}]_{(\text{rs})} \qquad (4\text{-}16)$$

and

$$\delta_a = e_{\delta_a}[\text{TF}]_{(\text{as})} \qquad (4\text{-}17)$$

where the minus sign in Eq. 4-16 comes from the summer and arises from the fact that for positive aileron negative rudder is required. Dividing Eq. 4-16 by Eq. 4-17, we obtain

$$\frac{\delta_r}{\delta_a} = -[\text{TF}]_{(\text{rcc})} \qquad (4\text{-}18)$$

as the transfer functions for the aileron and rudder servos are the same. The transfer function for the rudder coordination computer can be obtained by equating Eq. 4-18 and 4-15. Therefore

$$[\text{TF}]_{(\text{rcc})} = \frac{[\text{TF}]_{(A/C)[\delta_a;\beta]}}{[\text{TF}]_{(A/C)[\delta_r;\beta]}} \qquad (4\text{-}19)$$

The transfer function for the rudder coordination computer can be obtained
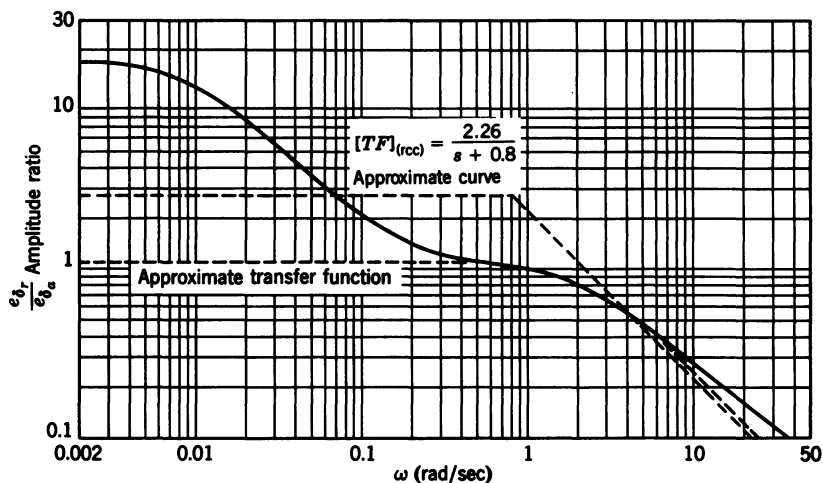
Figure 4-21   *Amplitude ratio plot for the rudder coordination computer for s = jω.*

by dividing Eq. 3-51 by Eq. 3-41, yielding

$$[\text{TF}]_{(\text{rcc})} = \frac{0.171(s+18.75)(s+0.15)}{0.0364(s-0.01)(s+2.06)(s+37.75)} \tag{4-20}$$

or in the alternative form,

$$[\text{TF}]_{(\text{rcc})} = \frac{17\left(\dfrac{s}{18.75}+1\right)\left(\dfrac{s}{0.15}+1\right)}{\left(\dfrac{s}{0.01}-1\right)\left(\dfrac{s}{2.06}+1\right)\left(\dfrac{s}{37.75}+1\right)} \tag{4-21}$$

An amplitude ratio plot of Eq. 4-21 is shown in Figure 4-21, and the phase angle plot in Figure 4-22. The transfer function given in Eq. 4-20 is comparatively complex; however, it is not usually necessary to design a circuit that gives the complete transfer function. Normally, the desired transfer function can be approximated by a first-order time lag. For this case the approximate transfer function is

$$[\text{TF}]_{(\text{rcc})} \simeq \frac{1.1}{\dfrac{s}{2.06}+1} = \frac{2.26}{s+2.06} \tag{4-22}$$

The amplitude ratio and phase angle of the approximate transfer function are also plotted in Figures 4-21 and 4-22 (see dashed lines). As long as the frequencies of the input lie between about 0.5 and 10 rad/sec the approxi-
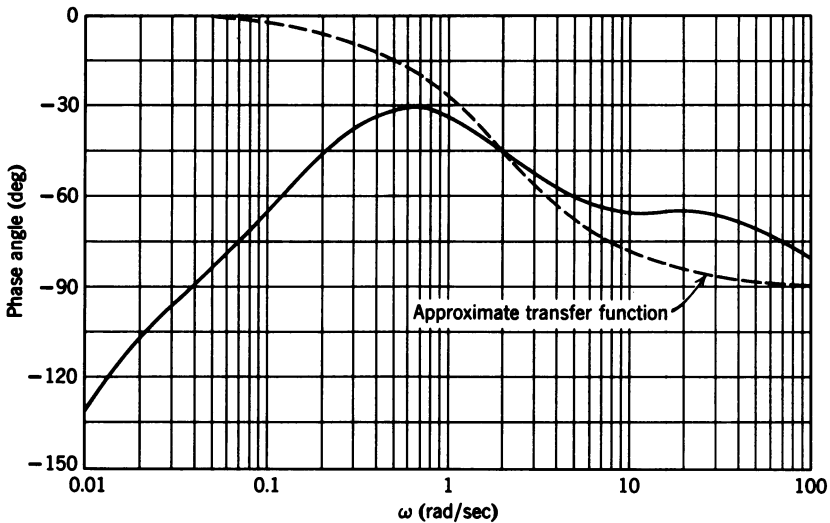
Figure 4-22 *Phase angle plot for the rudder coordination computer for s = jω.*

mation is quite good. However, at low frequencies, that is, below 0.5 rad/sec, the first-order time lag does not adequately represent the complete transfer function; thus it might be reasoned that the steady-state coordination would be poor. This is not necessarily true, for present-day aircraft, especially jet aircraft, require very little aileron to maintain a desired bank angle, and the amount of rudder required for coordination is often negligible.

There is, however, one serious drawback if this system is to be used on high-performance aircraft. It is well known that the various transfer functions for high-performance aircraft vary considerably with altitude and airspeed; thus the transfer function of the rudder coordination computer has to be programmed as a function of airspeed, altitude, dynamic pressure, or Mach number. This situation is even more complicated than gain scheduling, because the time constant of the first-order time lag has to be varied also. One practical use for this system is a conventional aircraft that flies at one normal cruise airspeed, within limited ranges of altitudes. For this case a transfer function for the normal cruise condition can be calculated and used for all cruise conditions. The coordination system can be turned off for takeoff and landing and other low-speed flying. This system is therefore the least practical of the four systems discussed.

In this section several methods of obtaining coordination have been discussed. Of these, the systems utilizing sideslip and lateral acceleration are the most straightforward and simple. Of these two, the system probably most used is the one utilizing the lateral accelerometer. The use of $\beta - \dot{\beta}$ feedback was also discussed, and its effectiveness will be illustrated in the next section.

One feature of the $\beta - \dot{\beta}$ SAS is that it provides damping for the Dutch roll as well as sideslip control. The calculation of $\dot{\beta}$ using Eq. 4-3 would not be difficult with the modern digital autopilots. The main disadvantage of the sideslip sensor is the difficulty often encountered in properly installing the instrument, as mentioned early in this section.

4-4 DISCUSSION OF COORDINATION TECHNIQUES

Figure 4-23 shows some computer results of the simulation of the system using sideslip feedback to achieve coordination. The sensitivity of the sideslip sensor is 1 volt/deg. A higher gain would be preferred; however, a further increase in the gain leads to a lightly damped oscillatory response which is objectional. This response is confirmed if the root locus of the system shown
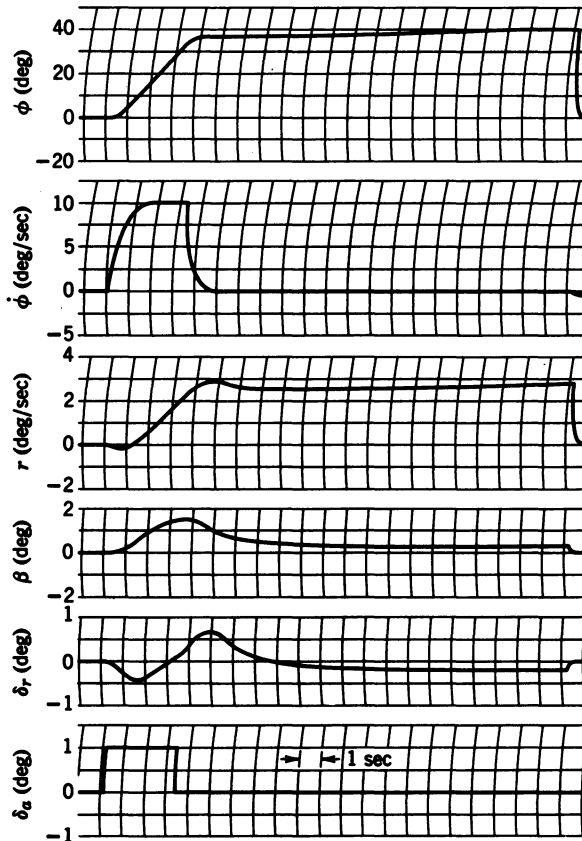
Figure 4-23 *Response of the aircraft with sideslip feedback to achieve coordination for a pulse aileron deflection.* $S_{(sss)} = 1$ *volt / deg.*

in the block diagram of Figure 4-9 is drawn. From the root locus it can be seen that 90° asymptotes lie in the right half plane and the complex poles move outward from the real axis toward the imaginary axis, leading to a lightly damped oscillatory response at the higher values of gain. A lead compensator can be added to cause the complex poles to move farther into the left half plane as they move out from the real axis. This procedure allows the use of a higher gain and maintains sufficient damping. If a gain as high as 10 volt/deg could be used, the maximum sideslip would be only 0.3° instead of 1.4°, as shown in Figure 4-23.

Another form of compensation that could be used is a lag compensator such as $(s+0.1)/(s+0.01)$, which would have little effect on the shape of the root locus, but would increase the error coefficient by a factor of 10 approximately. This would reduce the steady-state sideslip by the same factor. However, a lag compensator would not decrease the maximum sideslip experienced while rolling into or out of a turn. Therefore, the best results are achieved by the use of both a lead and a lag compensator. A suggested lead compensator is $(s+0.93)/(s+9.3)$.
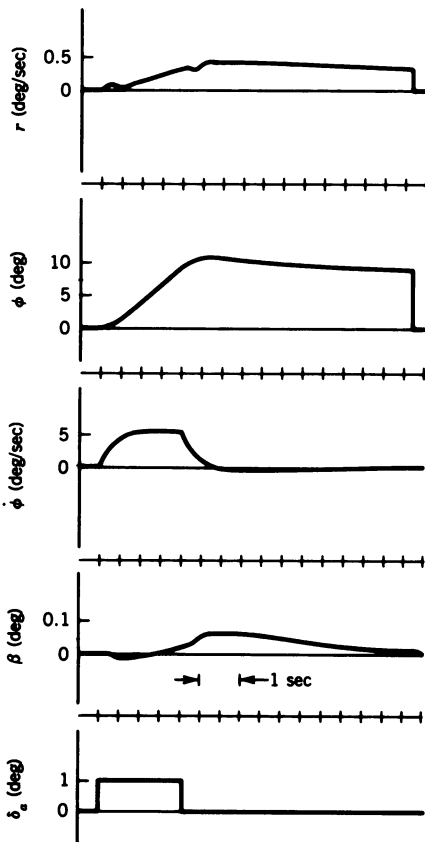
Figure 4-24 *Response of the F-15 with yaw damper and sideslip control to achieve coordination for a pulse aileron deflection.* $S_{(yrg)} = 0.68$ *volt / (deg / sec) and* $S_{(sss)} = 1.4$ *volt / deg.*
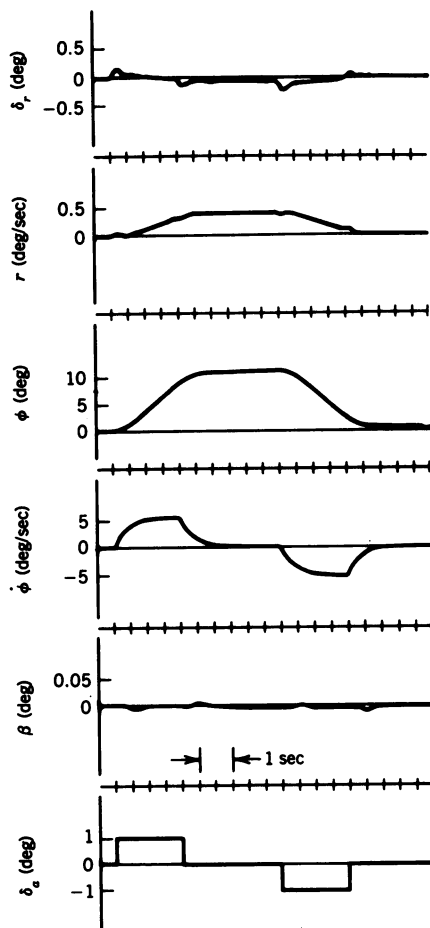
Figure 4-25   *Response of the F-15 with β–β̇ SAS to achieve coordination for a pulse aileron deflection.*

$S_\beta = 3$ volt / deg and

$S_{\dot\beta} = 3$ volt / (deg / sec).

The computer results illustrated in Figure 4-23 also apply to the system using lateral acceleration feedback to achieve coordination for an accelerometer sensitivity of 30.6 volt/g. Thus it can be seen that the use of sideslip feedback leads to a more sensitive system for the control of sideslip than the use of lateral acceleration.

Figures 4-24 and 4-25 show the results of a computer simulation of the F-15 for Mach 0.8 at 20,000 ft (lateral equations only). The results of a six-degree-of-freedom (six-DOF) hybrid simulation are shown in Section 9-11. The responses in Figure 4-24 are for the aircraft with Dutch roll damping and sideslip feedback as depicted in Figure 4-7. The time constant of the washout circuit was 5 sec. The reduction of the transient sideslip achieved by the β–β̇ SAS is quite dramatic, as can be seen in Figure 4-25. The discussion of the next three coordination techniques refers to the original jet transport with the Dutch roll damper.
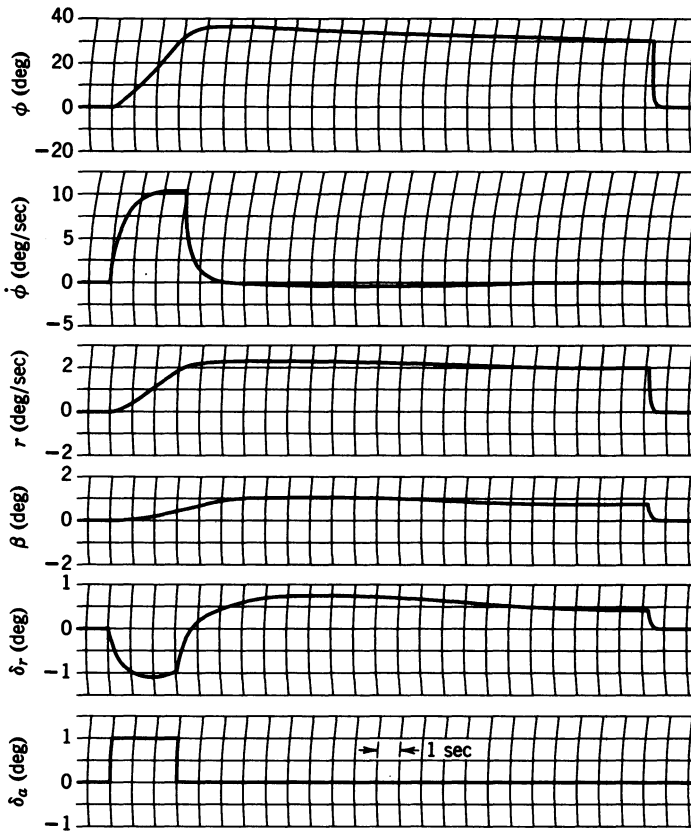
Figure 4-26 *Response of the aircraft using computed yaw rate to achieve coordination for a pulse aileron deflection. Top rudder held in the steady state.*

The results of the computer simulation of the system using the computed yaw rate are shown in Figures 4-26 and 4-27. The gain used for both cases is 10 volt/volt. In Figure 4-26 the actual yaw rate is greater than the computed desired yaw rate, resulting in top rudder being held, which causes the aircraft to slowly decrease its angle of bank. In Figure 4-27 the actual yaw rate is less than the computed desired yaw rate, resulting in bottom rudder being held, causing the aircraft to increase its angle of bank. The value of the computed desired yaw rate is dependent upon the value of g/V_T that is fed into the sine resolver. Thus the performance of this system depends on the proper value of g/V_T being available, as mentioned in Section 4-3. However, the system is very effective for controlling sideslip during a turn.

Figures 4-28 and 4-29 are the computer results of the simulation of the system using the rudder coordination computer to achieve coordination. Two different transfer functions are used: for Figure 4-28, $[TF]_{(rcc)} = 2.26/$
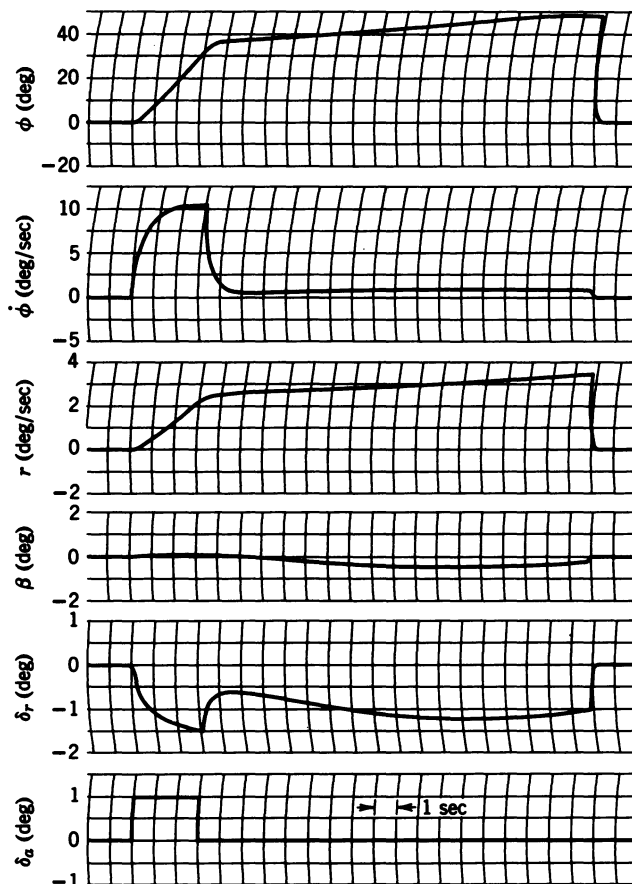
Figure 4-27   *Response of the aircraft using computed yaw rate to achieve coordination for a pulse aileron deflection. Bottom rudder held in the steady state.*

$(s + 2.06)$; for Figure 4-29, $[\text{TF}]_{(\text{rcc})} = 2.26/(s + 0.8)$. The transfer function used in Figure 4-28 has the same time constant as that derived in Section 4-3; however, there is not much reduction in the maximum value of sideslip from the case of no sideslip control (see Figure 4-6). The best control is obtained by using the transfer function with $1/\tau = 0.8$, which leads to some negative sideslip but lowers the maximum sideslip to 1.2°. For both transfer functions the steady-state value of sideslip is about 0.5°.

As can be seen from the computer analysis, the use of sideslip to achieve coordination is very effective, and even with a compensator to allow for a higher gain this system is simple and straightforward. However, especially for high-performance aircraft, the use of $\beta - \dot{\beta}$ feedback is much superior. All of the methods studied do decrease the maximum amount of sideslip during a turn and can be used, but the use of sideslip or lateral acceleration yields the
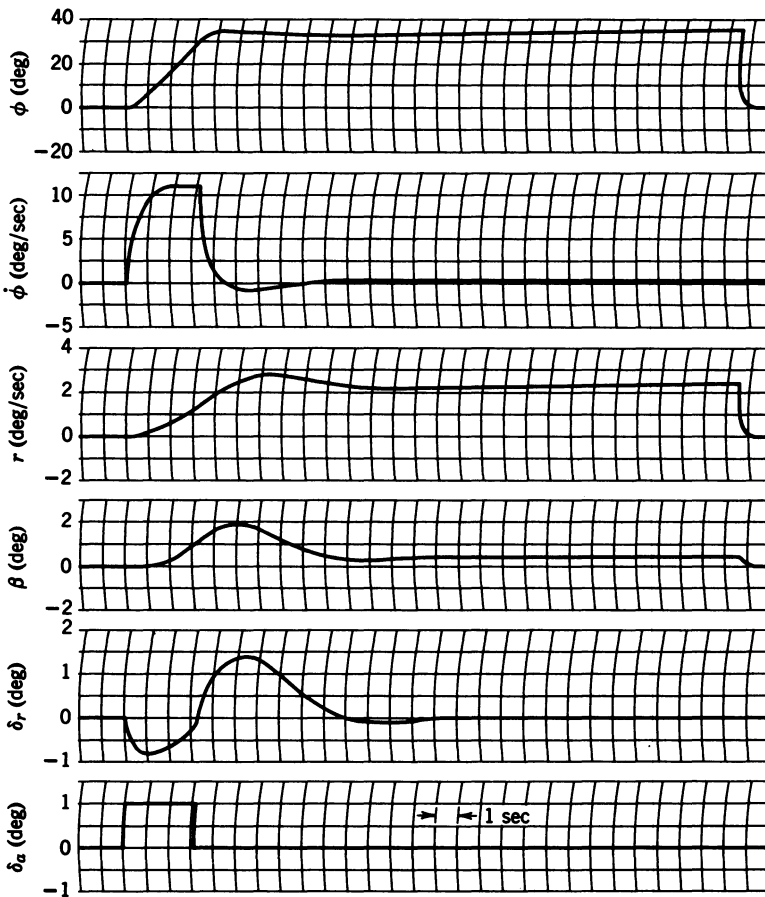
Figure 4-28 Response of the aircraft using the rudder coordination computer to achieve coordination for a pulse aileron deflection. $[TF]_{(rcc)} = 2.26 / (s + 2.06)$.

simpler systems, and thus they are probably to be preferred. In the study of the yaw orientational control system in Section 4-5, sideslip will be used to achieve coordination.

4-5 YAW ORIENTATIONAL CONTROL SYSTEM

Figure 4-30 is the block diagram for the yaw orientational control system including the Dutch roll damper and sideslip feedback for coordination. In addition, a yaw rate integrating gyro is used so that heading changes can be obtained by commanding a desired yaw rate. In this case an additional loop is used for stabilization. The need for this is shown in Figure 4-33 below. For
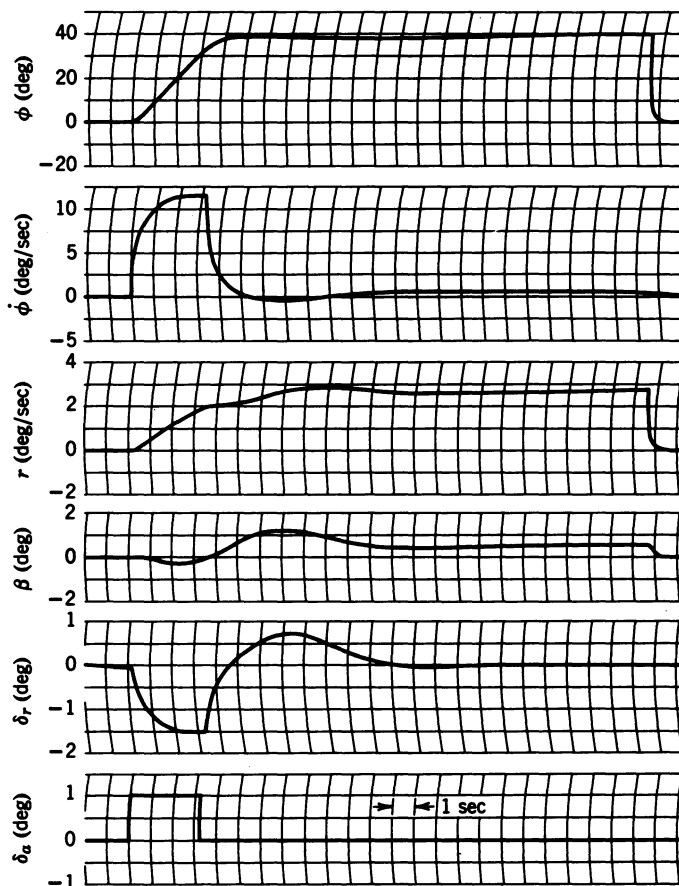
Figure 4-29   *Response of the aircraft using the rudder coordination computer to achieve coordination for a pulse aileron deflection.* $[TF]_{(rcc)} = 2.26 / (s + 0.8)$.

this stabilization a roll rate signal is fed back and summed with the yaw rate command signal. The result is fed as the torquing current to the yaw rate integrating gyro. In a steady turn this signal goes to zero, so that the signal to the yaw rate integrating gyro is the commanded yaw rate. In Section 3-4 the aircraft with sideslip feedback was analyzed. With the results of this analysis the root locus study could be continued to analyze the two new loops that have been added; however, the closed loop transfer function of the two inner loops can be greatly simplified. An examination of the roll rate trace of Figure 4-23 shows that this response is similar to the step response of a first-order system. This is indeed the case. Thus the two inner loops (Dutch roll damper and sideslip feedback) of the aircraft–autopilot combination can be replaced with one block, referred to as the coordinated aircraft. From an
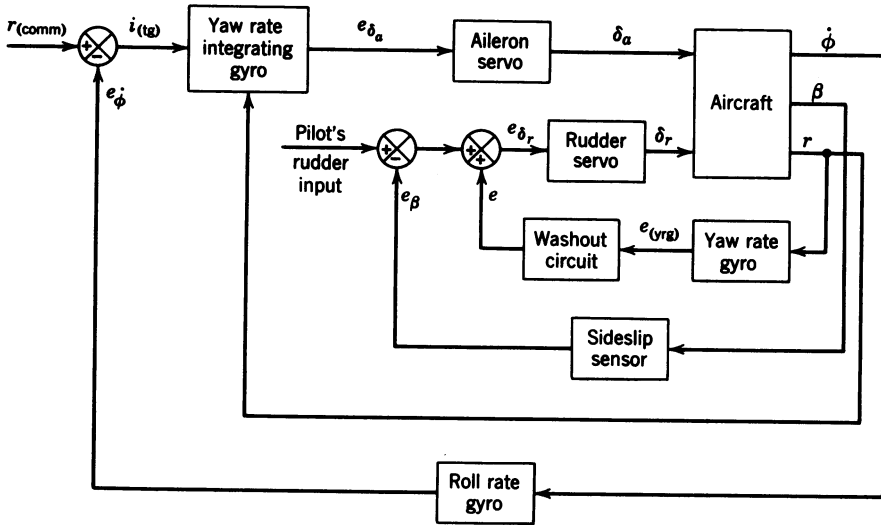
Figure 4-30   Block diagram of yaw orientational control system.

analysis of the roll rate trace of Figure 4-23 we have

$$[TF]_{(coord \ A/C)[\delta_a; \dot\phi]} = \frac{23}{s + 2.3} \qquad (4\text{-}23)$$

The validity of representing the coordinated aircraft for aileron input to roll rate output by a first-order time lag has been verified by flight test and will be demonstrated in Section 9-5 from the results of the F-15 six-DOF hybrid simulation. Now Figure 4-30 can be redrawn to include the coordinated aircraft block as shown in Figure 4-31. A root locus analysis is performed on this simplified system. The inner loop is analyzed first. To do this, the transfer function for the coordinated aircraft for aileron input to yaw rate output is required. Equation 4-23 represented the transfer function for the
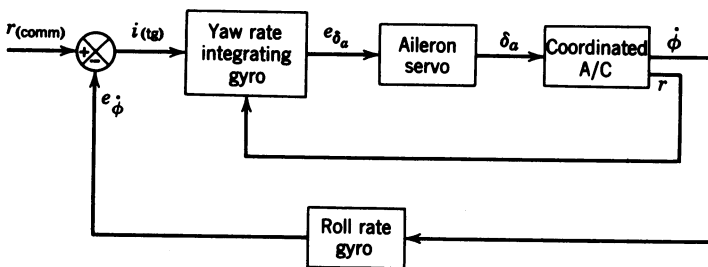
Figure 4-31   Simplified block diagram of yaw orientational control system.
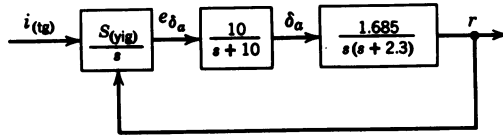
Figure 4-32 Block diagram of inner loop of Figure 4-31 for root locus study.

coordinated aircraft for aileron input to roll rate output. Then

$$[TF]_{(coord\ A/C)[\delta_a;\phi]} = \frac{23}{s(s+2.3)} \qquad (4\text{-}24)$$

and

$$[TF]_{(coord\ A/C)[\delta_a;r]} = \frac{g}{V_T}[TF]_{(coord\ A/C)[\delta_a;\phi]} \qquad (4\text{-}25)$$

because at a given airspeed there is only one rate of turn corresponding to a particular bank angle for a coordinated turn. Therefore $[TF]_{(coord\ A/C)[\delta_a;r]} = 1.685/s(s+2.3)$ for $V_T = 440$ ft/sec. The block diagram of the inner loop used for the root locus analysis is shown in Figure 4-32. Figure 4-33 is the root locus for the inner loop of the yaw orientational control system, with the location of the closed loop poles shown for a yaw rate integrating gyro sensitivity of 0.4 volt/(deg/sec). The reason the roll rate feedback loop is
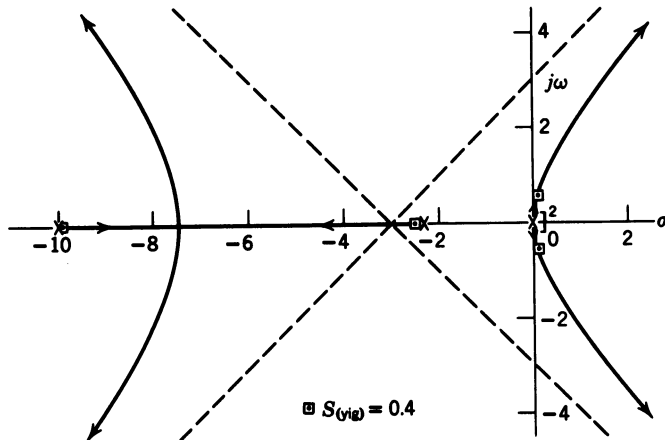
Figure 4-33 Root locus for block diagram shown in Figure 4-32.
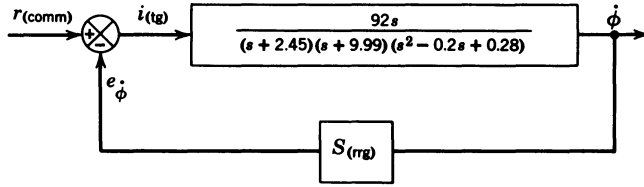
Figure 4-34 *Block diagram of outer loop of the yaw orientational control system for root locus analysis.*

required for stabilization is now evident. From the root locus,

$$[\text{TF}]_{(\text{CL})(i_{(\text{tg})}; r)} = \frac{6.74}{(s+2.45)(s+9.99)(s^2-0.2s+0.28)} \quad (4\text{-}26)$$

To obtain the transfer function required for the analysis of the outer loop it is necessary to reverse the steps followed when proceeding from Eq. 4-23 to Eq. 4-25. Then

$$[\text{TF}]_{(\text{OL})(i_{(\text{tg})}; \dot{\phi})} = s\frac{V_T}{g}[\text{TF}]_{(\text{CL})(i_{(\text{tg})}; r)} \quad (4\text{-}27)$$

Therefore

$$[\text{TF}]_{(\text{OL})(i_{(\text{tg})}; \dot{\phi})} = \frac{92s}{(s+2.45)(s+9.99)(s^2-0.2s+0.28)} \quad (4\text{-}28)$$

and the block diagram for the outer loop to be used for the final root locus analysis is shown in Figure 4-34. The root locus for the outer loop is shown in Figure 4-35. The locations of the closed loop poles for a roll rate gyro sensitivity of 0.31 volt/(deg/sec) are shown. Since the inner loop is unstable, its gain on the computer cannot be adjusted without having the outer loop closed. Therefore, after selecting initial values for the sensitivity of the yaw rate integrating gyro and the roll rate gyro from the root locus, the system is optimized by adjusting the sensitivities of the two gyros on the computer simulation. The criterion used is the fastest response of yaw rate for a commanded step input without oscillations. No attempt has been made here to completely optimize the system. By adding compensation the response could probably be improved further. The main purpose here is to show the validity of assuming that the two inner loops of the yaw orientational control system can be approximated by a simple first-order system, and that using this simplified model in the subsequent root locus analysis gives sufficiently accurate predictions of the behavior of the complete system. Figure 4-36 shows the result of the computer run of the yaw orientational control system
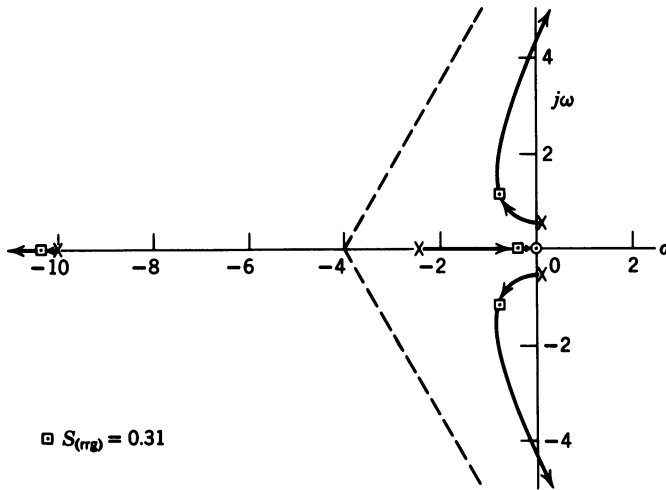
Figure 4-35   *Root locus for the block diagram shown in Figure 4-34.*

for a commanded yaw rate. For the computer simulation, the linearized lateral three-degree-of-freedom equations are used, with no further simplifying assumptions. The yaw rate integrating gyro sensitivity is 0.4 volt/(deg/sec), and the roll rate gyro sensitivity is 0.31 volt/(deg/sec). Although Figure 4-36 might not convince the reader that the root loci shown in Figures 4-33 and 4-35 do accurately predict the final response, checks made at other values of the gyro sensitivities indicated excellent agreement between the computer results and the root locus analysis. The use of the coordinated aircraft transfer function for the analysis of the outer loops of lateral flight control systems is further validated in Section 9-5 using a six-degree-of-freedom hybrid simulation and in Section 10-4 using a multivariable design technique.

Until now no mention has been made of the origin of the yaw rate command signal. One source of input could be a control stick steering autopilot in which the signal results from a lateral deflection of the stick in the same manner as that described in Chapter 2. There is one big difference between aileron input for a turn and an elevator input for a pitch rate. Under manual control, elevator stick force must be continuously applied to maintain a desired pitch rate; however, if lateral (aileron) stick force is continuously applied, the result is a sustained roll rate. Thus stick pressure need only be applied during the entry into a turn and the roll out. However, the yaw orientational control system needs a constant yaw rate command to maintain a sustained rate of turn, which can be accomplished by feeding the force stick output to an integrator. Thus the constant voltage required for the commanded input yaw rate signal is the integral of the output of the force stick sensor. In this discussion the control stick was referred to; however, the same
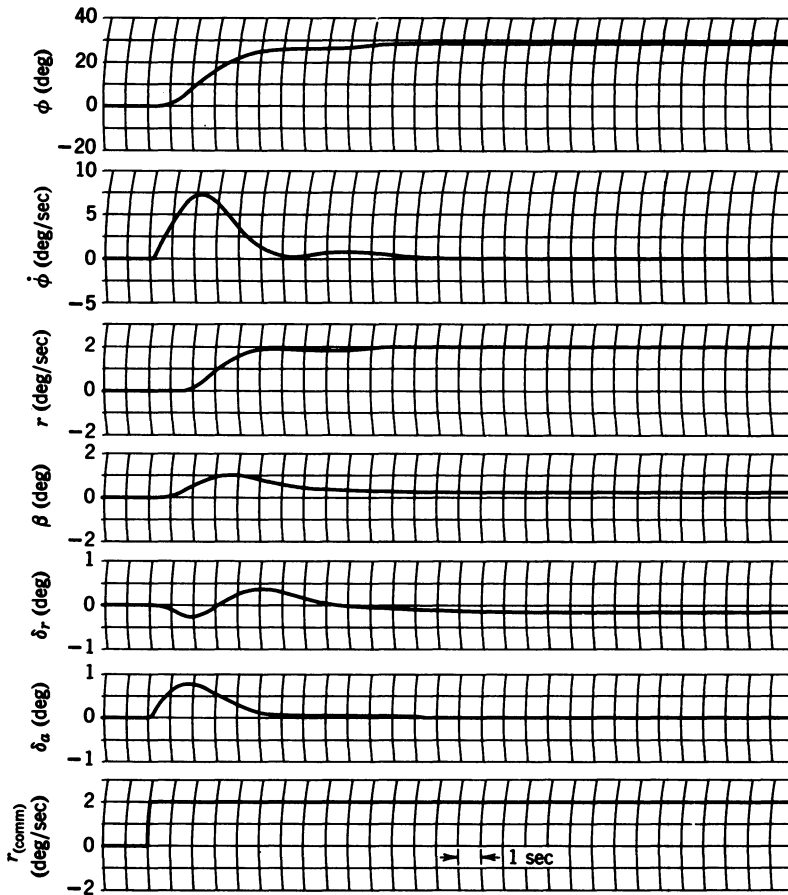
Figure 4-36 *Response of the yaw orientational control system for a step input of commanded yaw rate.*

technique is applicable to the control column using a wheel for the aileron input.

Another source of input could be a heading reference, which would result in completely automatic flight. For this source another loop would be closed through a directional gyro. Thus any deviation from the desired heading would result in a commanded yaw rate to bring the aircraft back to the desired heading. Turns to new headings could be accomplished by use of a turn control or by resetting the heading reference. Operation of the turn control would disengage the heading reference and command a yaw rate. Upon recentering the turn control the commanded yaw rate returns to zero and the heading reference automatically reengages at the new heading.

Still another source of input could be the instrument landing and approach system (ILAS) course coupler, which, together with the glide slope
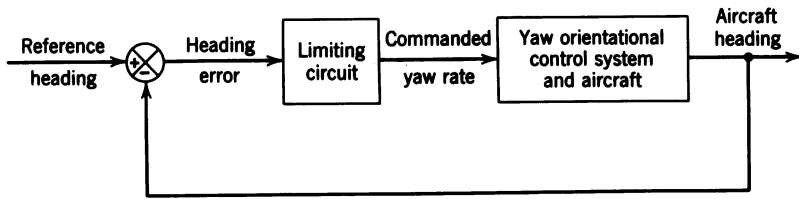
Figure 4-37   *Block diagram of lateral autopilot with yaw rate limiting.*
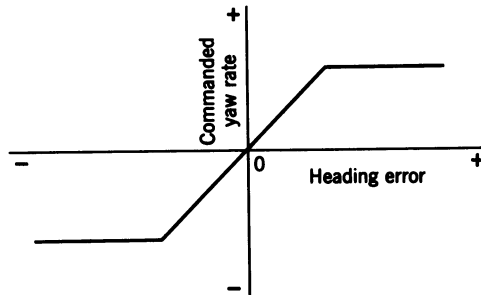
Figure 4-38   *Input – output characteristics of limiting circuit.*

coupled into the longitudinal autopilot, would result in a completely automatic approach.

The use of the heading error to generate the yaw rate command can lead to a commanded yaw rate that overstresses the aircraft. For this reason a limiting circuit must be placed in the system as shown in Figure 4-37. The input–output characteristics of the limiting circuit are shown in Figure 4-38. The maximum value of the commanded yaw rate is dictated by the maximum airspeed at which the autopilot is used and the maximum allowable acceleration for which the aircraft is stressed.

This concludes the discussion of the yaw orientational control system.

4-6   OTHER LATERAL AUTOPILOT CONFIGURATIONS

In Section 4-5 a yaw orientational control system was analyzed. In this section some other possible lateral autopilot configurations are discussed. In the case of the yaw orientational control system a turn was obtained by commanding a desired yaw rate; however, it may be desirable to command a desired bank angle, which necessitates the use of a vertical gyro. Figure 4-39 is a block diagram of a roll angle control system. The reader probably wonders why the roll rate feedback is necessary (this could have been added to the yaw orientational control system). A look at a sketch of the root locus
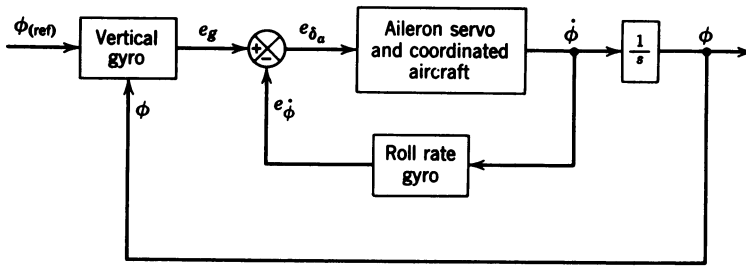
Figure 4-39   *Block diagram of roll angle control system.*

for the system without roll rate feedback shows why it is needed. As can be seen from Figure 4-40, even a low gain drives the system unstable, and unity feedback results in a too lightly damped response. Figure 4-41 shows the effect of roll rate gyro feedback. By adding the inner loop with the roll rate feedback, a higher outer loop sensitivity can be used without producing instability. To provide a heading reference a third loop can be added to Figure 4-39 by feeding the heading back through a directional gyro. With this configuration, a heading error provides a commanded roll angle to the roll angle control system. Then it is possible to command an excessive roll angle when the heading error is large. Thus, as in the case of the yaw orientational control system, it is necessary to limit the maximum commanded roll angle to prevent exceeding the acceleration limits of the aircraft. With respect to the limiting required, the roll angle control system is superior to the yaw orientational control system. This can be seen by looking at the equations for the horizontal accelerations resulting from a turn. From Figure 4-16, the horizontal acceleration during a coordinated turn is given by

$$a_{(hor)} = V_T \dot{\Psi} \tag{4-29}$$
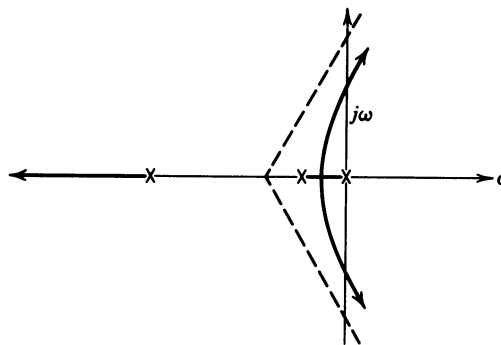
Figure 4-40   *Sketch of root locus of roll angle control system without roll rate feedback.*

(a) Inner loop   (b) Outer loop
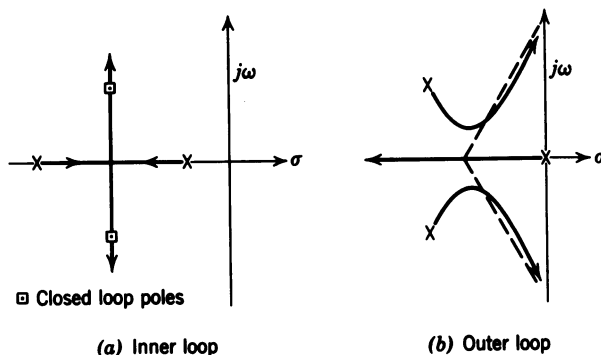
Figure 4-41   *Sketch of root locus of roll angle control system with roll rate feedback.*

From Eq. 4-10 $r = \dot{\Psi} \cos \phi$. Thus

$$a_{(hor)} = \frac{V_T r}{\cos \phi} \qquad (4\text{-}30)$$

but from Eq. 4-9 $\dot{\Psi} = (g / V_T)\tan \phi$; then substituting for $\dot{\Psi}$ in Eq. 4-29 yields

$$a_{(hor)} = g \tan \phi \qquad (4\text{-}31)$$

The total acceleration experienced by the aircraft is the vector sum of the acceleration of gravity and $a_{(hor)}$ (see Figure 4-16). Thus, it can be seen from Eq. 4-31 that the maximum acceleration will be experienced at the same bank angle regardless of velocity. However, for the yaw orientational control system, a limit on the value of r would provide acceleration limiting at the maximum value for only one value of V_T (see Eq. 4-30). Therefore, at lower airspeeds the aircraft would experience less acceleration than the maximum allowable. Another source of actuating signal to the roll angle control system can be the pilot in the form of an aileron control stick steering signal. For this source the block diagram shown in Figure 4-39 would be altered by removing the vertical gyro loop and feeding in the control stick steering signal in place of e_g (see Figure 4-42).
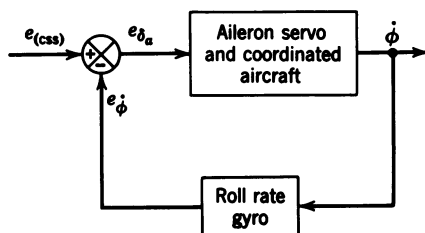
Figure 4-42   *Control stick steering mode for roll angle control system.*
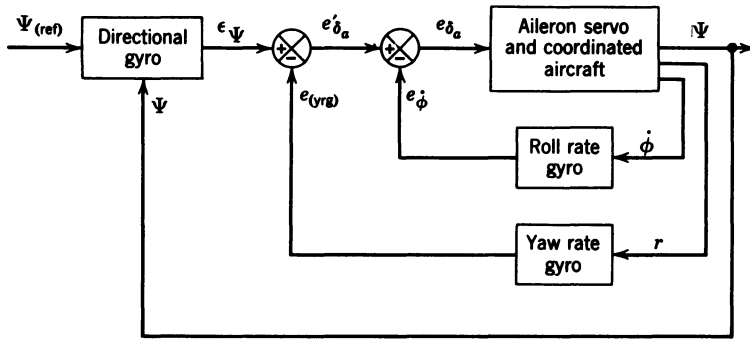
Figure 4-43 *Block diagram of a rate stabilized lateral autopilot.*

A third lateral autopilot configuration is shown in Figure 4-43. This autopilot is similar to the yaw orientational control system in that a heading error commands a yaw rate. However, the integration resulting from the yaw rate integrating gyro used in the yaw orientational control system is lacking.

This concludes the discussion of some of the different types of lateral autopilots, which was not intended to be exhaustive but only to illustrate some of the more common configurations. The analysis methods discussed in this chapter are applicable to these and any other configurations that might be encountered. There is, however, one problem that is common to all autopilots, and that is the generation of the proper signal to the elevator during turns. This problem is discussed in Section 4-7.

4-7 TURN COMPENSATION

When an aircraft enters a steady-state turn, the vertical component of lift must still support the weight of the aircraft (see Figure 4-16). Thus the lift must be increased by increasing the angle of attack. This requires an elevator displacement, the amount of which depends on the bank angle and the elevator effectiveness. The problem, therefore, for completely automatic flight, is to apply the correct amount of elevator to maintain altitude in a turn. One possible technique arises from Eq. 4-13, which was derived in Section 4-3 and is repeated here for convenience:

$$q = \frac{g}{V_T} \tan \phi \sin \phi \qquad (4\text{-}32)$$

Also in the same section, from Eq. 4-12,

$$r = \frac{g}{V_T} \sin \phi \qquad (4\text{-}33)$$

If Eq. 4-33 is substituted into Eq. 4-32, an expression for the pitch rate required during a turn is obtained, which is

$$q = r \tan \phi \qquad (4\text{-}34)$$

Thus, if the roll angle ϕ and the yaw rate r are known, the pitch rate can be calculated. If the longitudinal autopilot is a pitch orientational control system, the required pitch rate can be fed to the longitudinal autopilot. This technique requires a vertical gyro to measure the roll angle, a yaw rate gyro to measure r, and a computer to solve Eq. 4-34 for q. Two of the three lateral autopilot configurations studied did not use a vertical gyro, and not all longitudinal autopilots can accept a commanded pitch rate. Thus, this simple scheme does not work in many cases, and the equation must be approximated. If the signal is applied directly to the elevator servo, the amount of pitch rate per volt of signal must be known; this, of course, varies with airspeed. If the longitudinal autopilot has an altitude hold mode, then this feature can be used to provide the necessary elevator signal.

4-8 AUTOMATIC LATERAL BEAM GUIDANCE

It is often desirable to be able to couple the output of an Omni or localizer receiver to the lateral autopilot in order to obtain automatic following of either of these beams. A localizer receiver can provide an automatic landing system. The problems of coupling either the Omni or localizer signals to the lateral autopilot are similar, the only difference being in the width of the beams. For Omni tracking, full-scale deflection of the course indicator represents an angle of 10° with respect to the centerline, while for the localizer full-scale indication represents $2\frac{1}{2}$°. Thus a different gain may be required for the two cases. In both cases the systems become more sensitive as the aircraft nears the station, because a given lateral distance off course corresponds to a larger angle off course as the station is approached. This situation normally requires some gain scheduling as a function of range to the station. The major question to be answered then is the type of command signal that is to be sent to the lateral autopilot as a function of the error signals from the Omni or localizer receivers. If the lateral autopilot is already constructed or designed, this may dictate the type of signal required. If not, the choice can be based on the type of command that provides the best response with the simplest coupler. The basic choices are a heading command, a yaw rate command, or a bank angle command. The last two are similar in that they both result in a yaw rate; however, the mechanization would be different and one choice might yield a simpler coupler. Another factor to be considered is the requirement for an integration in the forward loop so the aircraft remains on course in the presence of a steady crosswind. With these points in mind, different configurations are analyzed here to
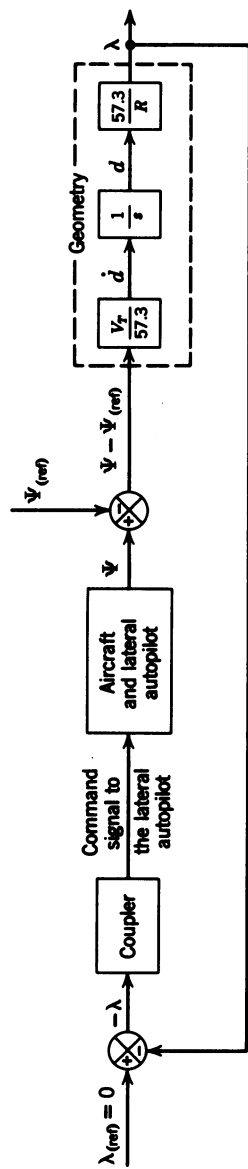
Figure 4-44 Generalized block diagram of lateral beam guidance system.
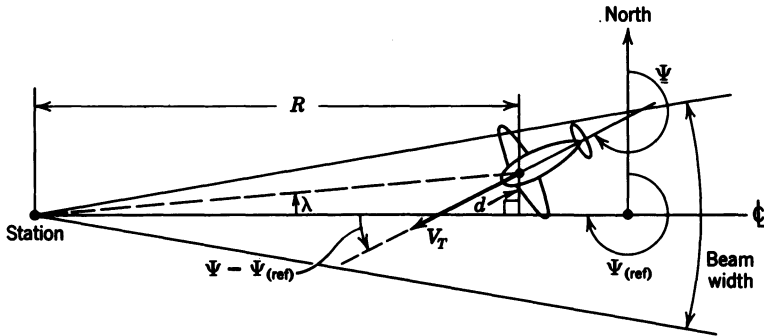
Figure 4-45 *Geometry of lateral beam guidance. R = distance from the station to the aircraft; d = lateral distance of the aircraft off course; λ = angular error represented by d (λ and d are positive as shown); Ψ − Ψ(ref) = interception angle is negative when λ and d are positive.*

determine the type of coupler that is required. Figure 4-44 is a generalized block diagram that fits all systems and is used to show how the geometry of the problem is introduced for purposes of analysis and simulation. Figure 4-45 shows this geometry and defines the variables introduced. From Figure 4-45 $\tan \lambda = d/R$; then $57.3d/R \simeq \lambda$ deg (using small-angle assumptions). Also $\dot{d} = V_T \sin(\Psi - \Psi_{(ref)}) \simeq V_T(\Psi - \Psi_{(ref)})$ for small angles. If Ψ and $\Psi_{(ref)}$ are to be measured in degrees, then $\dot{d} \simeq (V_T/57.3)(\Psi - \Psi_{(ref)})$; and $\dot{d}$ is negative for the case shown in Figure 4-45. In the generalized block diagram shown in Figure 4-44, $\Psi_{(ref)}$, which represents the heading of the beam to be followed, would be set in by the pilot. To simplify the following explanations, $\Psi_{(ref)}$ is taken as zero.

It is now necessary to select a specific lateral autopilot in order to analyze the system. The first system studied is the roll angle control system shown in Figure 4-39, with a heading feedback loop added. Figure 4-44 is redrawn to include more of the details of the system to be studied (see Figure 4-46). The gain of the coupler (S_c) is set at 10° of commanded Ψ per degree of λ; this may sound high, but it proves very satisfactory, as will be seen in Figure 4-56. The $0.1/s$ path provides the slow integration necessary to cope with a steady crosswind. The value 0.1 is selected somewhat arbitrarily, but proves to be a good selection. A detailed analysis of the system, starting with the roll angle control system, follows.

Figure 4-47 is a detailed block diagram of the roll angle control system used, complete with heading feedback. The innermost loop of Figure 4-47 is redrawn for the root locus analysis to determine the sensitivity of the roll rate gyro (see Figure 4-48). Figure 4-50 below is the root locus for the inner loop. It should be noted that the steady-state gain of the aileron servo is reduced from that previously used. This is found necessary because the response of
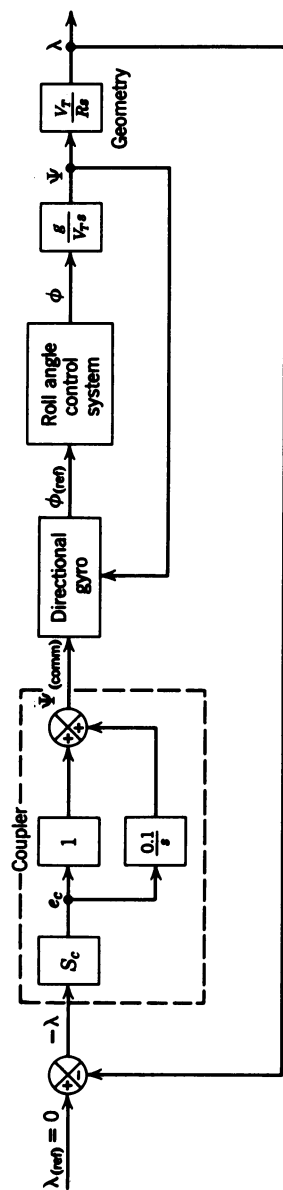
Figure 4-46 More detailed block diagram of lateral beam guidance system. Note: S_c = coupler gain in degrees of Ψ per degree of λ.
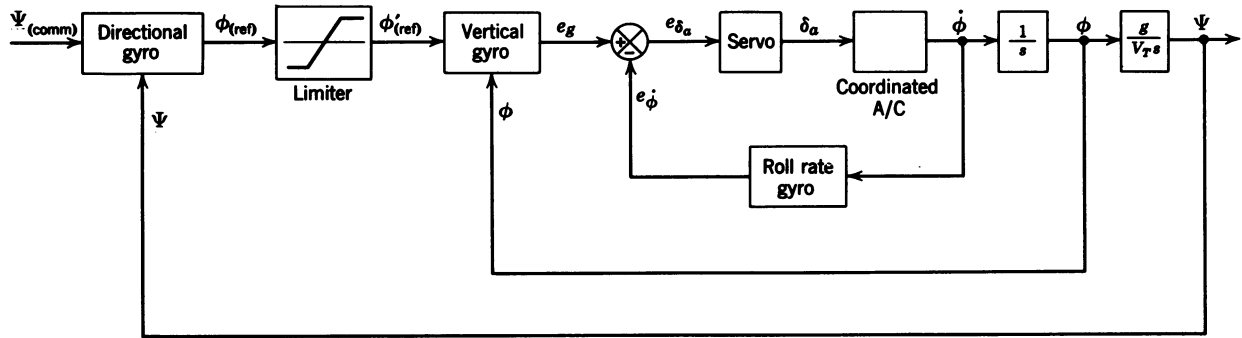
Figure 4-47 Block diagram of lateral autopilot used for the lateral beam guidance study:

$$[TF]_{(servo)[e_{\delta_a};\delta_a]} = \frac{4}{s + 10} \text{ deg / volt}$$

$$[TF]_{(coord\ A/C)[\delta_a;\phi]} = \frac{23}{s + 2.3} \text{ sec}$$

Limits on limiter $= \pm 30°$ of $\phi'_{(ref)}$
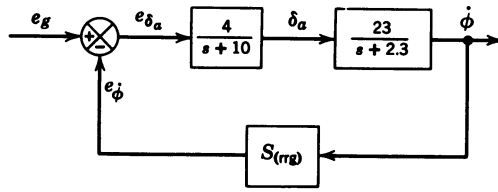
Figure 4-48 *Block diagram of inner loop of Figure 4-47 for root locus analysis.*

the lateral autopilot to a step heading command results in excessive aileron displacements and roll rates. This is discovered from the simulation, not the root locus; however, the root locus does predict the rapid response times, which would be an indication to the designer that the loop gains may be too high. The locations of the closed loop poles for the inner loop are taken to provide a damping ratio of 0.7. This results in a roll rate gyro sensitivity of 0.564 volt/(deg/sec). Using the closed loop poles from Figure 4-50, the block diagram for the root locus analysis of the vertical gyro loop can now be drawn (see Figure 4-49). The root locus for Figure 4-49 is shown in Figure 4-51. The reason for the choice of the vertical gyro sensitivity is not obvious from Figure 4-51. It results from the fact that the initial root locus analysis is performed for

$$[TF]_{(servo)[e_{\delta_a};\delta_a]} = \frac{10}{s+10}$$

For both the high- and low-gain servos the same inner loop closed loop poles are used. Thus, Figures 4-50 and 4-51 are valid for both cases (the rate gyro sensitivity is different for the two cases). The vertical gyro sensitivity is then selected using the higher-gain servo, which yielded a damping ratio of 0.5 for the complex roots in Figure 4-51. This gives a value of 1 volt/deg for the vertical gyro sensitivity. When the lower-gain servo is introduced, the vertical gyro gain is unchanged, since an increase in this gain will offset the decrease in the servo gain. Using the closed loop poles from Figure 4-51, the block diagram for the heading feedback loop for root locus analysis can be drawn (see Figure 4-52). In Figure 4-52 the limiter is eliminated, and $\dot{\Psi}$ and r are considered equal. This restricts the analysis to small roll angles, but is necessary because the root locus is valid only for linear systems. This
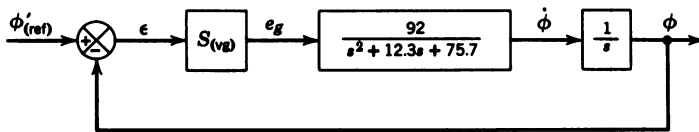
Figure 4-49 *Block diagram of vertical gyro loop for root locus analysis.*
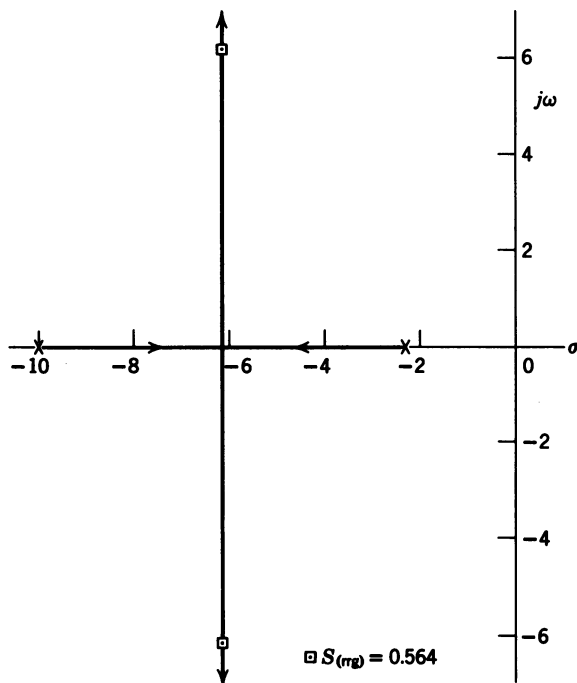
Figure 4-50   *Root locus for Figure 4-48, the inner loop of the roll angle control system.*

restriction need be imposed only during the analytic analysis and may be removed later in the computer simulation. Figure 4-53 is the root locus of Figure 4-52. The next problem is to decide on a sensitivity for the directional gyro. As the system will be nonlinear for large input signals, the root locus is used only as a guide, and a value is selected for the directional gyro sensitivity from observation of the computer response. This procedure results in a directional gyro sensitivity of 6 volt/deg. Any higher value results in an oscillatory response and, finally, in instability. The optimization is accomplished using a 10° heading step command. The locations of the closed loop poles for the selected directional gyro sensitivity are indicated in Figure 4-53.

Another factor that should be considered in selecting the directional gyro sensitivity is shown in the root locus analysis of the final loop. Using the closed loop poles from Figure 4-53, the final block diagram can be drawn (see Figure 4-54). The root locus for Figure 4-54 is shown in Figure 4-55. As can be seen from Figure 4-54, the geometry loop adds two poles at the origin: one from the geometry and one from the integration introduced by the coupler. The motion of these two poles is very critical; they must move into the left half plane for at least some value of closed loop gain. The two complex poles near the origin have a large effect on the movement of the two poles at the origin. If the complex poles are too close to the origin, they may cause the
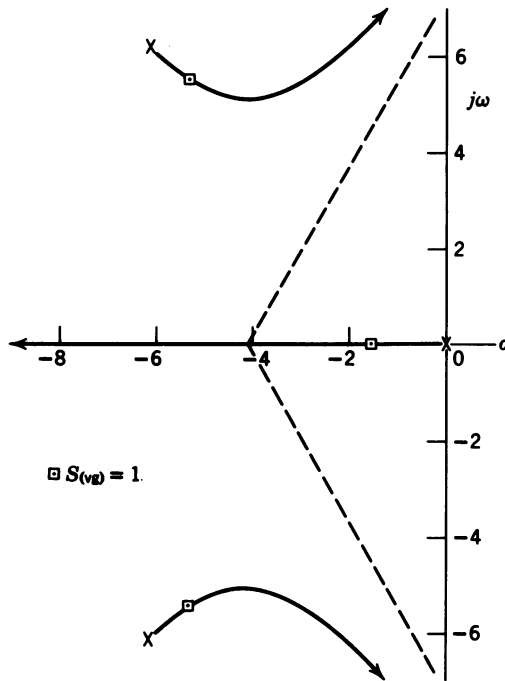
Figure 4-51 Root locus for Figure 4-49, the vertical gyro loop of the roll angle control system.

two poles at the origin to move rapidly into the right half plane, thus resulting in a completely unstable system. Therefore, in closing the directional gyro loop the sensitivity of the directional gyro should be such that the complex poles are as far from the origin as possible, but not too close to the imaginary axis. After obtaining the best value for the sensitivity of the directional gyro, the root locus of the outer loop enables the designer to determine whether a compensating network should be added to the coupler. A lead network of the form of $(1 + \alpha \tau s)/(1 + \tau s)$ could be used with a zero close to the origin and an α of 10 or larger. In order not to attenuate the error signal, an active network must be used with a gain of α. Such a network
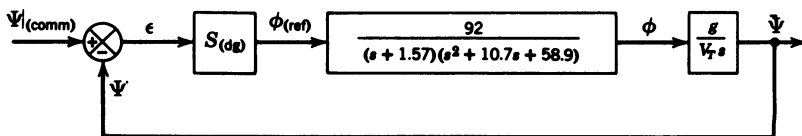
Figure 4-52 Block diagram of heading feedback loop for root locus analysis. $V_T = 440$ ft / sec.
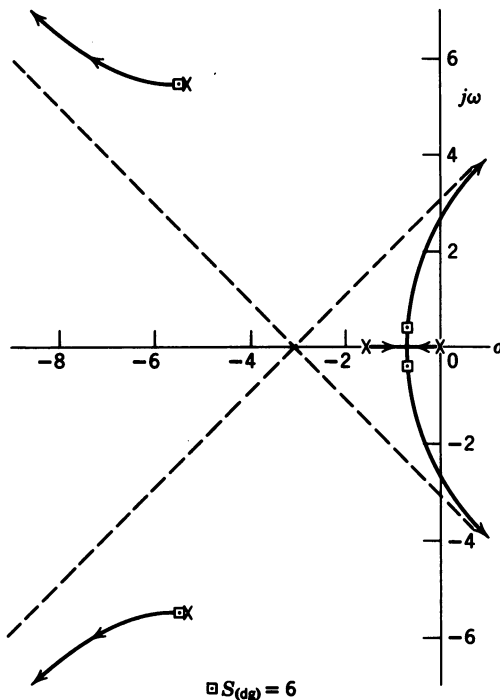
Figure 4-53 Root locus for Figure 4-52, the heading feedback loop of the lateral autopilot.

usually causes the two poles at the origin to circle around and break into the real axis between the two zeros. The complex poles near the origin are thus the ones to move into the right half plane, which may provide a better response for the system or a smaller minimum range to the station for instability; however, it may just add to the complexity of the system with no real significant improvement in performance.

Figure 4-54 illustrates that the loop gain is a function of V_T and R as well as of S_c. Normally, a value of S_c that will not result in excessive interception angles is selected. The coupler sensitivity used in the simulation is 10° of Ψ for each degree of λ off course. Having selected a value of S_c and V_T for a particular simulation, the root locus can be used to determine at what range the system will go unstable. It is usually necessary to decrease the coupler
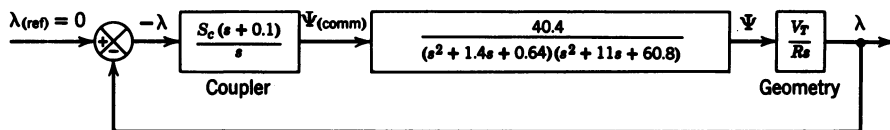
Figure 4-54 Block diagram for geometry loop.
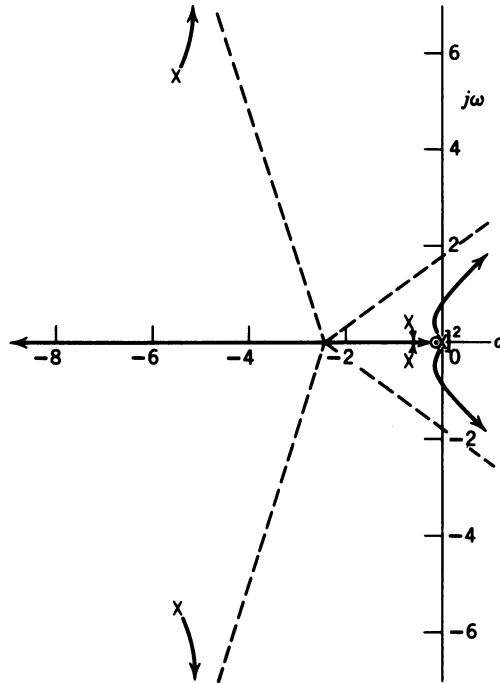
Figure 4-55 Root locus for Figure 4-54, the geometry loop for the lateral beam guidance system.

sensitivity as the range decreases; however, as the range goes to zero, the loop gain goes to infinity for any finite coupler sensitivity; thus there is always a minimum range for satisfactory operation. In actual operation, if it is desired to fly across an Omni station, the system must be disengaged at some minimum range and then reengaged after passing the station by the same minimum range. If the system is to be used in conjunction with a localizer beam for an automatic approach system, the range need not go to zero, since normally the localizer transmitter is located at the far end of the landing runway. Thus, if the minimum range for stability is less than the length of the runway, the system should perform satisfactorily. From Figure 4-55 the calculated value of the minimum range for $V_T = 440$ ft/sec and $S_c = 10$ is 3720 ft. This figure is very accurately verified by the computer simulation.

Figure 4-56 shows the results of the computer simulation. Figure 4-56(a) shows the response of the system for an initial displacement of the aircraft from the centerline of the beam but on the beam heading. The values of d_0 were 100 and 500 ft. The first overshoot is largely caused by the integration introduced by the coupler. Figure 4-56(b) shows the response of the system to a step crosswind, with the aircraft initially on course and on the beam heading. The values of the crosswinds were 25 and 100 ft/sec, 90° to the
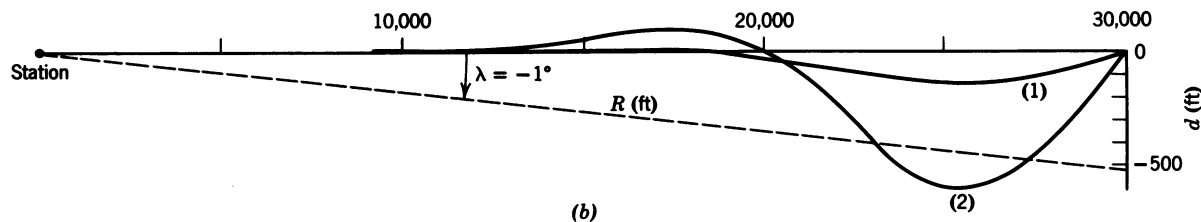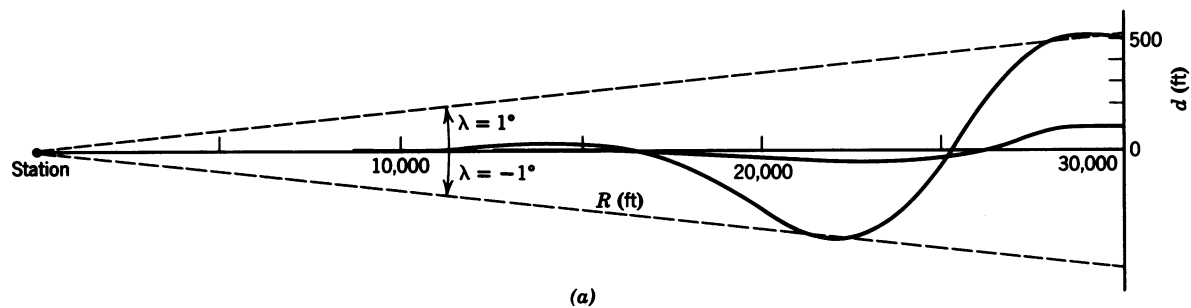
Figure 4-56 (a) Response of the lateral beam guidance system for $d_0 = 100$ and 500 ft and $\Psi_0 = \Psi_{(ref)}$. (b) Response of the lateral beam guidance system with $d_0 = 0$ and $\Psi_0 = \Psi_{(ref)}$, for a $90°$ crosswind of (1) 25 ft / sec; (2) 100 ft / sec.

course. In all cases the aircraft was back on course by the time the range had decreased to 10,000 ft. For all cases the aircraft was well within the $\pm 2\frac{1}{2}°$ beam width of the localizer beam. The initial conditions imposed in the simulation were probably more severe than would be encountered in practice, as normally the aircraft would be lined up with the centerline of the beam before engaging the coupler.

This discussion concludes the analysis of the lateral beam coupler for this particular autopilot. The same analysis can be applied to any of the other lateral autopilots discussed here or encountered in the field. The final root locus is always the most critical and indicates whether some compensating networks are required to insure system stability for the overall system.

An examination of the rate stabilized lateral autopilot (see Figure 4-43) shows that it yields the same pole configuration as the roll angle control system and that the same coupler as was developed for the roll angle control system should be satisfactory for the rate stabilized system.

This technique can be used for the design and analysis of the coupler required for the yaw orientational control system studied in Section 4-5; however, roll rate feedback should be added around the coordinated aircraft as the inner loop.

Figure 4-57 is a block diagram of the proposed system. A detailed analysis is not presented here, but is left as a design problem for the student; however, some suggestions are offered. In selecting the roll rate gyro sensitivity for the innermost loop, it is recommended that the complex poles have a damping ratio of 0.7. The next loop through the yaw rate integrating gyro is very critical. As shown in Section 4-5, the yaw integrating gyro loop adds two poles at the origin (see Figure 4-33) that move into the right half plane as the integrating gyro sensitivity is increased. The roll rate feedback into the summing amplifier then brings these poles back into the left half plane (see Figure 4-35). If the yaw rate integrating gyro sensitivity is selected properly, when these poles move into the left half plane, they will break into the real axis. Above some critical value the poles will behave as shown in Figure 4-35. The selected value for the sensitivity of the yaw rate integrating gyro should be equal to or less than this critical value. The summing amplifier gain should then be selected to give a damping ratio for these complex poles of between 0.7 and 0.8. The heading feedback loop adds another pole at the origin. The directional gyro sensitivity should then be selected using the same criterion as discussed earlier in this section for the roll angle control system. A limiter will probably be required, after the directional gyro, to limit the commanded yaw rate. The final root locus can then be used to determine if a compensator is required as part of the coupler.

This concludes the analysis of the automatic lateral beam guidance system. It should be mentioned, however, that although the first-order time lag was used to approximate the coordinated aircraft, excellent correlation was obtained between the computer results and the root locus.
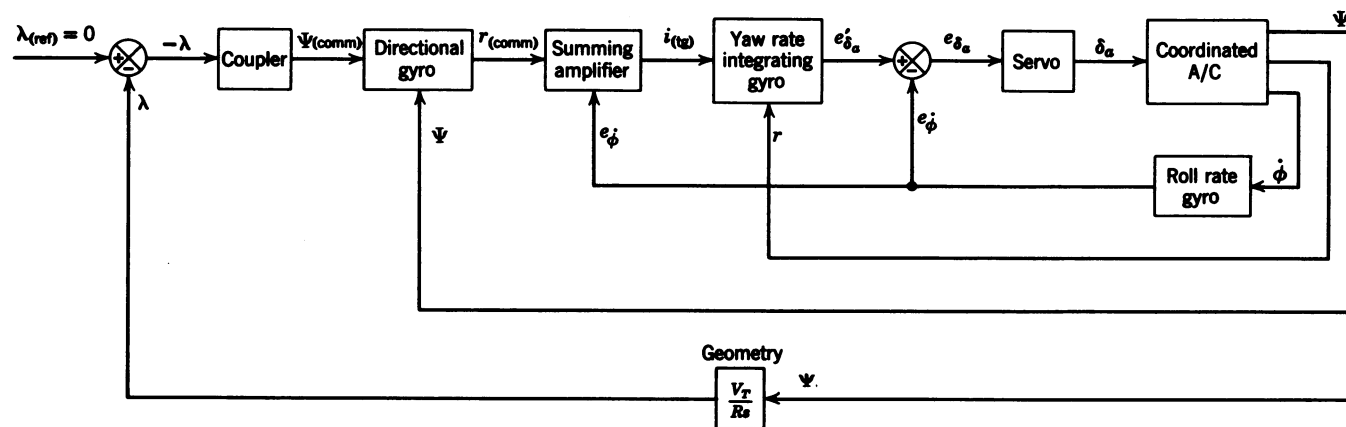
Figure 4-57 Block diagram of lateral beam guidance system using a yaw orientational control system:

$$[\text{TF}]_{(\text{servo})[e_{\delta_a}:\delta_a]} = \frac{10}{s+10}$$

$$[\text{TF}]_{(\text{coord A/C})[\delta_a:\dot{\phi}]} = \frac{23}{s+2.3}$$

4-9 NONLINEAR EFFECTS

So far, in all the analyses on the lateral autopilot, except for the effect of the limiter, it has been assumed that the system was linear. This is seldom the case for the actual system. Phenomena such as saturation, backlash, deadspot, and cable stretching introduce nonlinearities. These nonlinearities may result in a limit cycle roll oscillation or, if severe enough, in system instability. However, if they are known or suspected, these effects can be simulated during the computer simulation. By adjusting the severity of these nonlinearities during the computer simulation, the allowable limits on the nonlinearities can be determined. This information can then be used in specifying the tolerances on the actual hardware. Normally, very little backlash and deadspot can be tolerated, and every effort should be made to eliminate or minimize them. This can best be effected by installing close tolerance bolts in all linkages, using close tolerance gears or antibacklash gears, and maintaining maximum allowable tension in all cables and minimum deadspot in all hydraulic control valves.

4-10 SUMMARY

In this chapter some of the techniques for artificially improving the lateral transient response of the aircraft have been presented and analyzed. The Dutch roll oscillation was first damped, then the coordination improved, and then the complete lateral autopilot studied. The problems involved in providing automatic lateral beam guidance were demonstrated by means of the design and analysis of the lateral beam guidance coupler. After coordination was obtained, the transfer function of the lateral aircraft for aileron input to roll rate output was reduced to a first-order time lag, and the validity of this simplification was evidenced. All the paper analyses were substantiated by an analog computer simulation to show the actual improvements provided by each of the systems added.

Section 3-7 showed that the transient response of the aircraft varies considerably with changes in airspeed and altitude. This indicates changes in the roots of the characteristic equation and changes in the location of the aircraft poles and zeros when plotted in the complex plane. Thus, the root locus for each flight condition will vary, as well as the optimum loop gain for any particular loop. Therefore, for the best operation the gains must be varied as the flight conditions change. This situation is discussed in more detail in Chapter 6.

There is one more aspect of autopilot design that may still be bothering the reader. How well does the computer simulation predict the actual behavior of the aircraft? It has been found that, in general, the computer simulation enables the designer to determine all the system gains quite accurately before the aircraft flies. Normally, some small changes in gains are

required for optimum performance, but on the first model that flies there are provisions made for making such final adjustments. If the system does not perform as expected, the cause is probably either nonlinearities in the system that were overlooked or inaccuracies in the values of the stability derivatives used. Simulation of the basic equations should yield excellent results if the values of the stability derivatives themselves are accurate. If the assumption of quasisteady flow is considered invalid, its effects may be included by introducing the proper stability derivatives if they are available. The other assumptions may also be eliminated or modified by introducing the proper terms into the equations. This procedure may result in nonlinear equations which cannot be studied analytically, but the equations can still be solved and the system analyzed on the computer. This subject is discussed further in Chapter 6.

REFERENCES

1. R. D. Holdridge, *A Design of a Lateral Stability Augmentation System for the F-106 to Improve Lateral Handling Qualities During Tracking*, Unpublished Report, Aerospace Engineering Department, School of Engineering, University of Dayton, Dayton, Ohio, April 1978.
2. J. H. Blakelock, *Design of an Integrated Flight / Fire Control System Including Movable Gun and Line-of-Sight Tracker*, UDR-TR-79-84, University of Dayton, Dayton, Ohio, December 1979.

5

Inertial Cross-Coupling

5-1 INTRODUCTION

The problem of inertial cross-coupling did not manifest itself until the introduction of the century-series aircraft. As the fighter plane evolved from the conventional fighter, such as the F-51 and F-47, through the first jet fighter, the F-80, and then to the F-100 and the other century-series aircraft, there was a slow but steady change in the weight distribution. During this evolution more and more weight became concentrated in the fuselage as the aircraft's wings became thinner and shorter. This shift of weight caused relations between the moments of inertia to change. As more weight is concentrated along the longitudinal axis, the moment of inertia about the X axis decreases while the moments of inertia about the Y and Z axes increase. This phenomenon increases the coupling between the lateral and longitudinal equations, and can best be seen by examining the basic moment equations, which, from Eq. 1-32, are

$$\sum \Delta \mathcal{L} = \dot{P}I_x - \dot{R}J_{xz} + QR(I_z - I_y) - PQJ_{xz}$$

$$\sum \Delta \mathcal{M} = \dot{Q}I_y + PR(I_x - I_z) + (P^2 - R^2)J_{xz}$$

$$\sum \Delta \mathcal{N} = \dot{R}I_z - \dot{P}J_{xz} + PQ(I_y - I_x) + QRJ_{xz} \qquad (5\text{-}1)$$

As I_x becomes much smaller than I_y and I_z, the moment of inertia differences $I_x - I_z$ and $I_y - I_x$ become large. If a rolling moment is introduced, this results in some yawing moment, and the term $PR(I_x - I_z)$ may become large enough to cause an uncontrollable pitching moment.

Another factor that must be considered is the aerodynamic effect which results if the aircraft is rolled about an axis other than the instantaneous

191

stability axis, that is, the aircraft's velocity vector. If an aircraft rolls about its longitudinal axis at some angle of attack, the angle of attack after 90° of roll is now a sideslip angle; after 180° of roll it is a negative angle of attack, and after 270° it is again a sideslip angle. This interchange of angle of attack and sideslip angle causes the aerodynamic moments to alternate between pitching and yawing moments, which, coupled with the moment of inertia effects, further aggravates the inertial cross-coupling.

5-2 EFFECTS OF HIGH ROLL RATES

The design changes that have increased the coupling between the lateral and longitudinal equations were discussed in the Introduction. As a result of these design changes, some aircraft are completely unstable at high roll rates. A mathematical analysis of this phenomenon would generally be considered impossible, since the coupled equations involve products of the dependent variables. However, by making certain simplifying assumptions and with the proper combining of the equations, a linear analysis is possible. This linear analysis predicts the susceptibility of the aircraft to inertial cross-coupling, which is verified to some extent in this chapter, and has been verified in the past by actual flight test. For the purpose of this discussion, an aircraft is considered as being susceptible to inertial cross-coupling if the aircraft goes unstable at high roll rates. After using the simplified linear analysis to predict the susceptibility of the aircraft to inertial cross-coupling, the analysis is continued to determine the required loop gains for a control system to stabilize the inertially cross-coupled aircraft. The predicted results are compared with the results of an analog computer simulation of the inertially cross-coupled aircraft complete with the control system. The reader may find it difficult to accept some of the assumptions made; however, they are necessary in order to obtain the desired linear equations. The justification stems mainly from the fact that the predicted results are valid, not that the assumptions themselves are normally considered valid.

To show mathematically that some aircraft are completely unstable at high roll rates, the Y and Z force equations are combined so as to yield two oscillatory modes, which at zero roll rate represent the short-period and Dutch roll modes. It is shown mathematically that as the roll rate is increased, the natural frequency and damping ratio of the two oscillations vary and the lateral oscillations may eventually become divergent.

For this analysis, U is considered constant, so that the X force equation can be eliminated. This leaves only the Y and Z force equations, which, from Eq. 1-33, are

$$\sum \Delta F_y = m(\dot{V} + UR - WP)$$

$$\sum \Delta F_z = m(\dot{W} + VP - UQ) \tag{5-2}$$

As it is desired to study the effects of high roll rates, P is assumed to be equal to P_0; and since only the steady-state condition is to be evaluated, P_0 is assumed to exist instantaneously. How it is developed or what happens during the transient period is of no interest at this time. As the roll rate has been assumed constant, the changes in the rolling moments must be zero, and the rolling moment equation may be eliminated. Also, if $V_0 = W_0 = Q_0 = R_0 = 0$, then Eqs. 5-1 and 5-2 become

$$\sum \Delta \mathcal{M} = \dot{q}I_y + P_0 r(I_x - I_z) + (P_0^2 - r^2)J_{xz}$$

$$\sum \Delta \mathcal{N} = \dot{r}I_z + P_0 q(I_y - I_x) + qrJ_{xz}$$

$$\sum \Delta F_y = m(\dot{v} + U_0 r - wP_0)$$

$$\sum \Delta F_z = m(\dot{w} + vP_0 - U_0 q) \tag{5-3}$$

If the stability axes are also considered as principle axes, and if $\sum \Delta \mathcal{M} = \sum \Delta \mathcal{N} = \sum \Delta F_y = \sum \Delta F_z = 0$, then Eq. 5-3 reduces to

$$\dot{q}I_y + P_0 r(I_x - I_z) = 0$$

$$\dot{r}I_z + P_0 q(I_y - I_x) = 0$$

$$\dot{\beta} + r - P_0{}'\alpha = 0$$

$${}'\dot{\alpha} + P_0 \beta - q = 0 \tag{5-4}$$

because $\beta \simeq v/U_0$ and ${}'\alpha \simeq w/U_0$.

Combining the moment equations from Eq. 5-4 with the aerodynamic moments including all the stability derivatives retained in Chapters 1 and 3 yields

$$\frac{I_z}{Sqb}\dot{r} - \frac{b}{2U}C_{n_r}r - C_{n_\beta}\beta + \frac{I_y - I_x}{Sqb}P_0 q = \frac{b}{2U}C_{n_p}P_0$$

$$\frac{I_y}{Sqc}\dot{q} - \frac{c}{2U}C_{m_q}q - \frac{c}{2U}C_{m_{\dot{\alpha}}}{}'\dot{\alpha} - C_{m_\alpha}{}'\alpha + \frac{I_x - I_z}{Sqc}P_0 r = 0 \tag{5-5}$$

Solving the force equations of Eq. 5-4 for r and q yields

$$r = P_0{}'\alpha - \dot{\beta} \quad \text{and} \quad q = P_0\beta + {}'\dot{\alpha} \tag{5-6}$$

Differentiating,

$$\dot{r} = P_0{}'\dot{\alpha} - \ddot{\beta} \quad \text{and} \quad \dot{q} = P_0\dot{\beta} + {}'\ddot{\alpha} \tag{5-7}$$

Substituting Eqs. 5-6 and 5-7 into Eq. 5-5 yields

$$\frac{I_z}{Sqb}(P_0'\dot{\alpha} - \ddot{\beta}) - \frac{b}{2U}C_{n_r}(P_0'\alpha - \dot{\beta}) - C_{n_\beta}\beta + \frac{I_y - I_x}{Sqb}P_0(P_0\beta + '\dot{\alpha})$$

$$= \frac{b}{2U}C_{n_p}P_0$$

$$\frac{I_y}{Sqc}(P_0\dot{\beta} + '\ddot{\alpha}) - \frac{c}{2U}C_{m_q}(P_0\beta + '\dot{\alpha}) - \frac{c}{2U}C_{m_{\dot{\alpha}}}'\dot{\alpha} - C_{m_\alpha}'\alpha$$

$$+ \frac{I_x - I_z}{Sqc}P_0(P_0'\alpha - \dot{\beta}) = 0 \tag{5-8}$$

The roots of the characteristic equation determine the stability of the system; thus only the characteristic equation will be considered in the subsequent analysis. Regrouping and taking the Laplace transformation of the characteristic equation, Eq. 5-8 becomes

$$\left[\frac{I_z}{Sqb}s^2 - \frac{b}{2U}C_{n_r}s + C_{n_\beta} - \left(\frac{I_y - I_x}{Sqb}\right)P_0^2\right]\beta(s)$$

$$+ \left[-\left(\frac{I_y - I_x + I_z}{Sqb}\right)P_0s + \frac{b}{2U}C_{n_r}P_0\right]'\alpha(s) = 0$$

$$\left[\left(\frac{I_y - I_x + I_z}{Sqc}\right)P_0s - \frac{c}{2U}C_{m_q}P_0\right]\beta(s)$$

$$+ \left[\frac{I_y}{Sqc}s^2 - \frac{c}{2U}(C_{m_q} + C_{m_{\dot{\alpha}}})s - C_{m_\alpha} + \left(\frac{I_x - I_z}{Sqc}\right)P_0^2\right]'\alpha(s) = 0 \tag{5-9}$$

An examination of Eq. 5-9 shows that for $P_0 = 0$, the coupled equations reduced to two uncoupled equations which are the same as Eq. 3-54 (the one-degree-of-freedom Dutch roll mode) and Eq. 1-130, after eliminating the C_{z_α} terms (the short-period approximation). For $P_0 \neq 0$, Eq. 5-9 has the form

$$(a_2s^2 + a_1s + a_0)\beta(s) + (c_1s + c_0)'\alpha(s) = 0$$

$$(d_1s + d_0)\beta(s) + (b_2s^2 + b_1s + b_0)'\alpha(s) = 0 \tag{5-10}$$

which yields a fourth-order characteristic equation, the roots of which are a function of P_0. These roots can then be plotted in the complex plane as a function of P_0. The values used in evaluating Eq. 5-9 are listed in Table 5-1. After substitution of these values into Eq. 5-9 the characteristic equations for

TABLE 5-1   Values Used to Evaluate Eq. 5-9

Parameter	Aircraft A	Aircraft B
C_{m_α}	-1	-0.6
C_{n_β}	0.4	0.1
$\dfrac{I_x - I_z}{Sqc}$	0.121	-0.21
$\dfrac{I_y - I_x}{Sqb}$	0.05	0.056
$\dfrac{I_y + I_z - I_x}{Sqb}$	0.11	0.126
$\dfrac{I_y + I_z - I_x}{Sqc}$	0.25	0.44
$\dfrac{I_y}{Sqc}$	0.13	0.23
$\dfrac{I_z}{Sqb}$	0.057	0.07
$\dfrac{c}{2U}C_{m_q}$	-0.04	-0.02
$\dfrac{c}{2U}\left(C_{m_q} + C_{m_{\dot\alpha}}\right)$	-0.06	-0.026
$\dfrac{b}{2U}C_{n_r}$	-0.007	-0.0034

the two aircraft are

Aircraft A:

$$s^4 + 0.585s^3 + \left(14.7 + 1.92P_0^2\right)s^2 + \left(4.2 + 0.3P_0^2\right)s$$
$$+ \left(54 - 13.24P_0^2 + 0.817P_0^4\right) = 0 \qquad (5\text{-}11)$$

Aircraft B:

$$s^4 + 0.16s^3 + \left(4 + 1.7P_0^2\right)s^2 + \left(0.3 + 0.115P_0^2\right)s$$
$$+ \left(3.7 - 3.4P_0^2 + 0.73P_0^4\right) = 0 \qquad (5\text{-}12)$$

The locus of the roots for Eq. 5-11 is plotted in Figure 5-1. As P_0 is increased from zero, the locus of the roots is similar to Figure 5-2 with the exception that the real root does not move into the right half plane and thus the aircraft remains stable. The locus of the roots of Eq. 5-12, as P_0 is varied, is plotted in Figure 5-2.* As P_0 is increased from zero, the natural frequency

*As the curve is symmetrical about the real axis, only the upper half of the plot is shown.
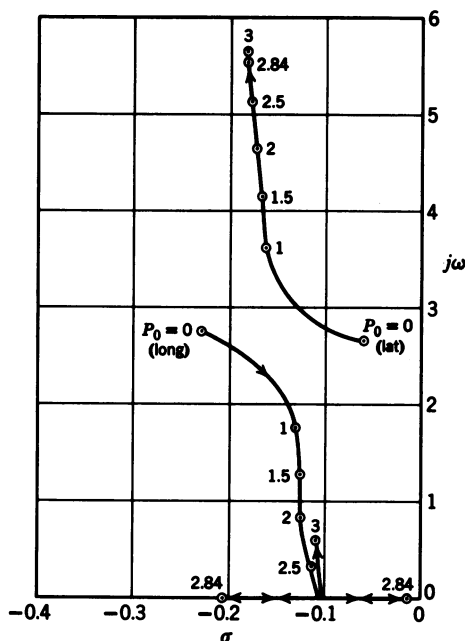
Figure 5-1 *The locus of the roots of Eq. 5-11, Aircraft A, as a function of the steady-state roll rate P_0.*

of one set of roots increases and the damping ratio decreases, while the opposite is true for the other roots. The latter set of roots then breaks into the real axis, forming two real roots, one of which moves into the right half plane and becomes divergent. The neutral stability point occurs at $P_0 = 1.33$ rad/sec (97.4 deg/sec). At the higher value of P_0 the divergent root moves into the left half plane, and the aircraft is again stable. A further increase in P_0 results in the two real roots becoming oscillatory again. An examination of the coefficient of the s^0 term shows whether the aircraft will go unstable. These expressions, for both aircraft, are presented here for comparison:

Aircraft A: $\qquad\qquad 54 - 13.24 P_0^2 + 0.817 P_0^4$

Aircraft B: $\qquad\qquad 3.7 - 3.4 P_0^2 + 0.73 P_0^4$ $\qquad\qquad$ (5-13)

Since the algebraic signs of the rest of the terms in the characteristic equation are positive, the sign of the term represented by Eq. 5-13 determines the stability or instability of the system. A characteristic equation can have roots in the right half plane even though all the coefficients are positive (see Routh's stability criterion, Ref. 1, pp. 185–191). If this did occur, the value of P_0 would be so large that it would be of academic interest only. Because the coefficients of P_0^2 in Eq. 5-13 are negative, it is possible for
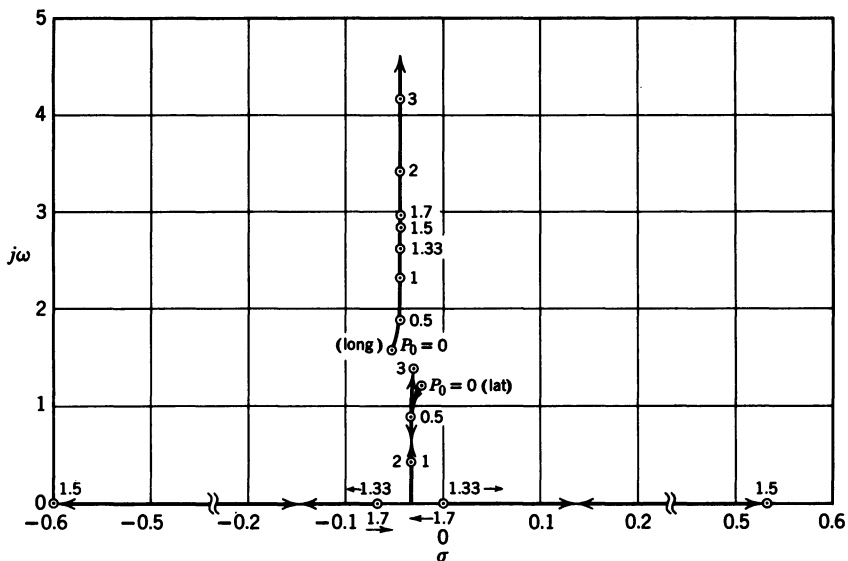
Figure 5-2 *The locus of the roots of Eq. 5-12, Aircraft B, as a function of the steady-state roll rate P_0.*

these expressions to become negative. The points of neutral stability can be determined by equating Eq. 5-13 to zero and solving for P_0. This operation yields the values 1.33 and 1.7 rad/sec for aircraft B, and imaginary roots for aircraft A. The imaginary roots indicate there is no real value of the roll rate that makes the coefficient of the s^0 term go to zero; therefore the term cannot change sign, and aircraft A is stable for all roll rates.

5-3 DETERMINATION OF THE AIRCRAFT PARAMETERS THAT AFFECT STABILITY

In Section 5-2 it was shown that the sign of the coefficient of the s^0 term of the characteristic equation for steady rolling determined the stability of the aircraft at high roll rates. The s^0 term is examined here in its general form to determine which of the aircraft parameters have the largest effect on its sign. This term can be obtained from the expansion of the determinant formed from Eq. 5-9; the s^0 term is then

$$-\left(C_{n_\beta}C_{m_\alpha}\right)+\left\{\left[C_{m_\alpha}\left(\frac{I_y-I_x}{Sqb}\right)+C_{n_\beta}\left(\frac{I_x-I_z}{Sqc}\right)\right]+\left(\frac{bc}{4U^2}C_{n_r}C_{m_q}\right)\right\}P_0^2$$

$$-\left(\frac{I_y-I_x}{Sqb}\right)\left(\frac{I_x-I_z}{Sqc}\right)P_0^4 \tag{5-14}$$

From Eq. 5-13 it can be seen that it is the coefficient of the P_0^2 term that is negative; thus, this term of Eq. 5-14 is examined first. Referring to Table 5-1, it can be seen that the portion of the coefficient of the P_0^2 term of Eq. 5-14 that is in brackets is negative, while the portion in parentheses is positive. Since the negative portion is larger than the positive portion, the net sign of the term is negative. If the moments of inertia of the aircraft about each of the three axes were equal, the coefficient of the P_0^2 term would be positive, and there would be no inertial cross-coupling. As I_y and I_z increase and I_x decreases (which has been the trend in modern jet fighters) the negative portion of the P_0^2 term increases; eventually the sign of the P_0^2 term goes negative as I_y and I_z become increasingly larger than I_x, and the possibility of inertial cross-coupling increases. There is little that can be done about the relative magnitude of the moments of inertia of the present-day high-performance fighters; thus, to offset the effects of the increase in the magnitude of the negative portion of the P_0^2 term, the term in parentheses which contains the product of C_{n_r} and C_{m_q} should be increased. This can be done by increasing the size and lift curve slope of the vertical stabilizer for C_{n_r} and the size and lift curve slope of the horizontal stabilizer for C_{m_q}. However, this operation would require extensive modification of the aircraft and would be expensive. The quantities C_{n_r} and C_{m_q} can be increased artificially by adding yaw and pitch rate feedback. It is first necessary to determine how much the product of C_{n_r} and C_{m_q} must be increased so that Eq. 5-14 will be positive for all values of P_0. By examining Eq. 5-13 for aircraft B, which is repeated here for convenience,

$$3.7 - 3.4P_0^2 + 0.73P_0^4 \tag{5-15}$$

it can be seen that if the coefficient of the P_0^2 term of Eq. 5-15 is decreased to 3.27, the equation will be positive for all values of P_0. This means that

$$\frac{\left[C_{m_\alpha}\left(\dfrac{I_y - I_x}{Sqb}\right) + C_{n_\beta}\left(\dfrac{I_x - I_z}{Sqc}\right) \right] + \dfrac{bc}{4U^2}C_{n_r}C_{m_q}}{\left(\dfrac{I_z}{Sqb}\right)\left(\dfrac{I_y}{Sqc}\right)} = -3.27 \tag{5-16}$$

Equation 5-16 is divided by $(I_z/Sqb)(I_y/Sqc)$ just as Eq. 5-12 was normalized by dividing by the coefficient of the s^4 term. Substituting the values from Table 5-1 into Eq. 5-16, it is found that $(bc/4U^2)C_{n_r}C_{m_q}$ must be equal to 0.002. The original value of $(bc/4U^2)C_{n_r}C_{m_q}$ was 0.000068; therefore, $C_{n_r}C_{m_q}$ must be increased by a factor of 29.4. This means that if C_{n_r} and C_{m_q} are each increased by a factor of 5.42, the desired results will be obtained. From Eq. 3-56 it can be seen that the damping ratio of the Dutch roll is proportional to C_{n_r}, and Eq. 1-136 shows that the damping ratio of the short period

is proportional to the $\sqrt{C_{m_q}}$. Thus, to obtain the desired increase in C_{n_r} and C_{m_q}, the damping of the Dutch roll should be increased by a factor of 5.42 and the damping ratio of the short period by a factor of 2.33. In Section 5-4 a control system to achieve the desired increase in the damping ratios of the Dutch roll and short-period oscillations is presented and analyzed to determine its effectiveness in stabilizing the aircraft at high roll rates.

5-4   SYSTEM FOR CONTROLLING AN AIRCRAFT SUBJECT TO INERTIAL CROSS-COUPLING

Figure 5-3 is a block diagram of the system for controlling an aircraft that is subject to inertial cross-coupling. To analyze the system, each of the two loops in Figure 5-3 is studied separately to determine the sensitivities of the two rate gyros required to achieve the required increase in the damping ratios of the short-period and Dutch roll modes. Figure 5-4 is the block diagram for the pitch rate feedback loop with the transfer functions of each block indicated. From the aircraft transfer function it can be seen that the
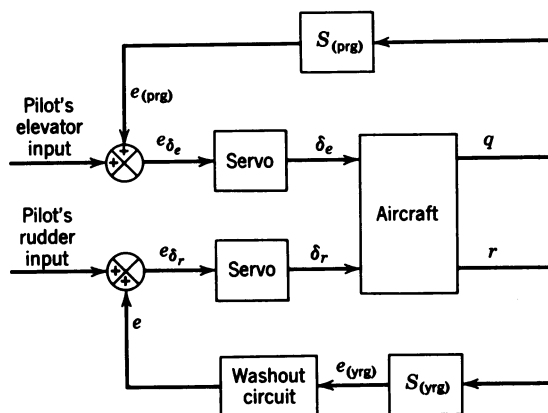
Figure 5-3   *System for controlling an aircraft subject to inertial cross-coupling.*
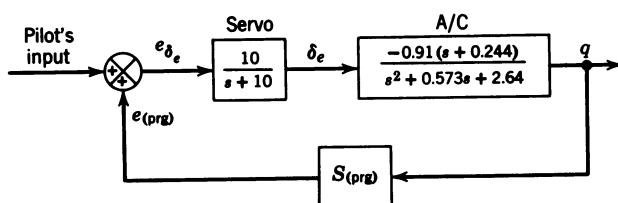
Figure 5-4   *Pitch rate feedback loop.*
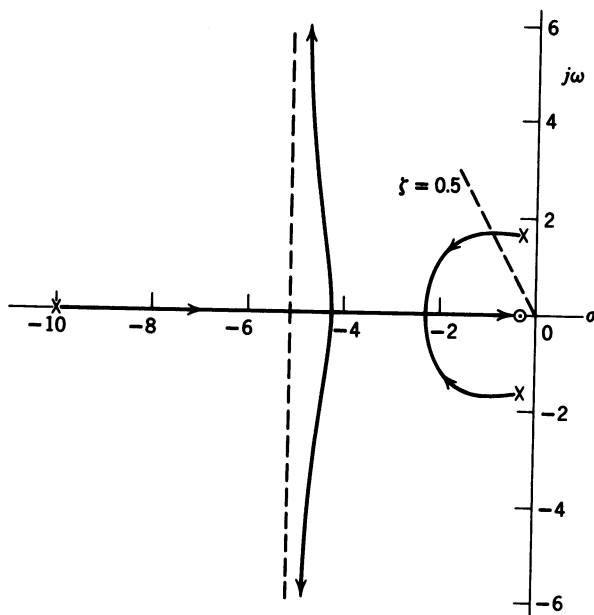
Figure 5-5 Root locus for the pitch rate feedback loop.

damping ratio of the short period is 0.176. As developed in Section 5-3, this amount should be increased by a factor of 2.33, which means a minimum value of 0.41. Figure 5-5 is a root locus for the pitch rate feedback loop. To provide for a margin of safety, a minimum damping ratio of 0.5 is selected. This results in a $S_{(prg)}$ of 1.28 volt/(deg/sec). Figure 5-6 is the block diagram for the yaw rate feedback loop, again with the transfer functions indicated. From the aircraft transfer function it can be seen that the damping ratio of the Dutch roll is 0.066. To increase this amount by a factor of 5.42 (as indicated in Section 5-4) means that the minimum value of the damping ratio must be 0.358; to provide a margin of safety, use 0.4. Figure 5-7 is the root
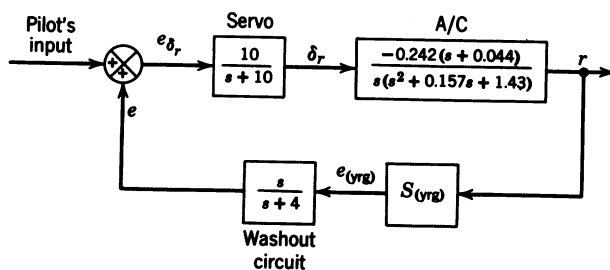
Figure 5-6 Yaw rate feedback loop.
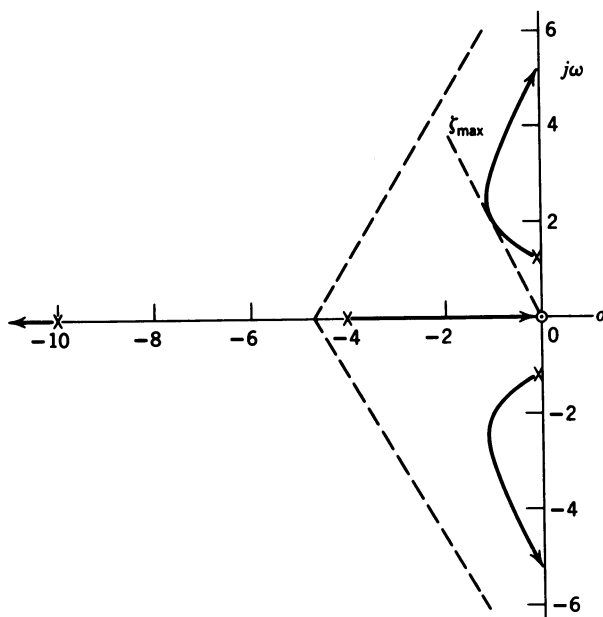
Figure 5-7 *Root locus for the yaw rate feedback loop.*

locus for the yaw rate feedback loop. The value of the yaw rate gyro sensitivity for maximum damping is 26 volt/(deg/sec), which yields a damping ratio of 0.45. These values are used in the computer simulation, the results of which are shown in Figures 5-8 and 5-9. Figure 5-8 shows the response of the basic aircraft for a commanded roll rate of 1.5 rad/sec. The effects of inertial cross-coupling are obvious. Figure 5-9 shows the response of the basic aircraft and the control system. The improvement in the response is apparent; however, the response is still not optimum, as unacceptably large values of sideslip and angle of attack still exist. The sideslip could be eliminated by one of the coordination techniques discussed in Chapter 4. The steady-state angle of attack is required to balance the Z components of acceleration resulting from the pitch rate and the product βP.

5-5 IMPROVED SYSTEM FOR CONTROLLING AN AIRCRAFT SUBJECT TO INERTIAL CROSS-COUPLING

The pitch orientational control system is used to reduce the pitch rate to zero so that the steady-state angle of attack is reduced; if necessary a sideslip sensor is used to reduce sideslip. The block diagram of the proposed system is shown in Figure 5-10. Since the pole at the origin introduced by the
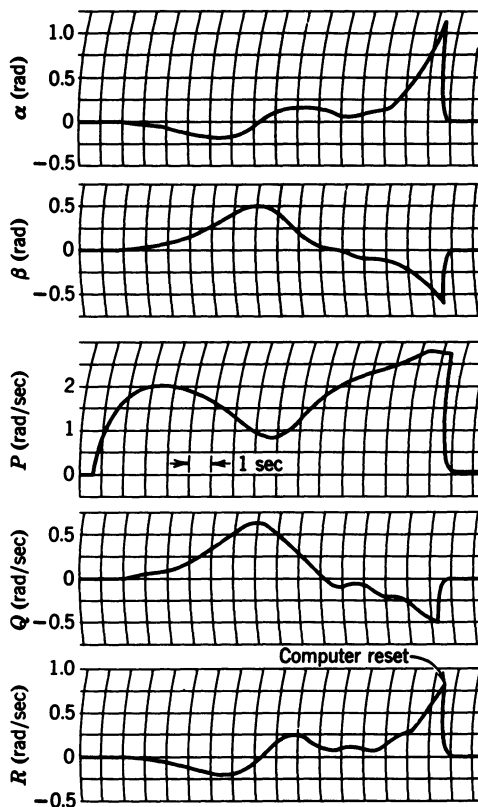
Figure 5-8   *Response of the basic aircraft to a commanded roll rate of 1.5 rad / sec.*

integrating gyro causes the closed loop complex poles resulting from the inner loop to move toward the imaginary axis, the gain of the inner loop is increased from 1.28 to 2.37 volt/(deg/sec). This increase in gain increases the damping ratio of the complex pole to 0.8 and results in the following closed loop transfer function for the inner loop:

$$[TF]_{(CL)(e_{(ig)}; q]} = \frac{-9.1(s+0.244)}{(s+6.9)(s^2+3.6s+5.3)}$$

The block diagram for the outer loop is shown in Figure 5-11. The root locus for the outer loop is shown in Figure 5-12 with the location of the closed loop complex poles for an integrating gyro gain of 10 volt/(deg/sec). This gain was determined from the simulation because the validity of the root locus for the outer loop was questionable. Several other gains were used to determine the best integrating gyro sensitivity. An integrating gyro sensitivity of 0.62 volt/(deg/sec), which should have yielded a damping ratio of 0.7 for
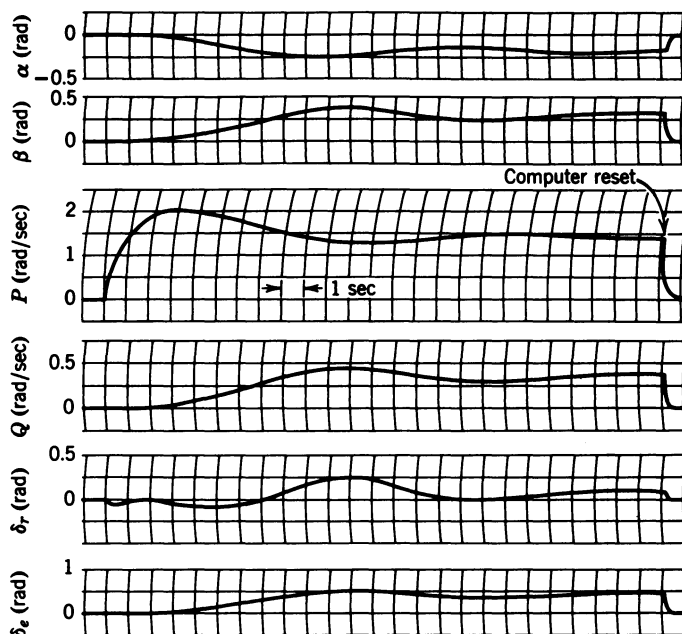
Figure 5-9 Response of the basic aircraft and the control system to a commanded roll rate of 1.5 rad / sec.
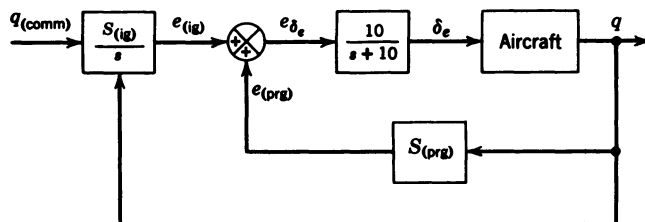
Figure 5-10 Pitch orientational control system for controlling an aircraft subject to inertial cross-coupling.
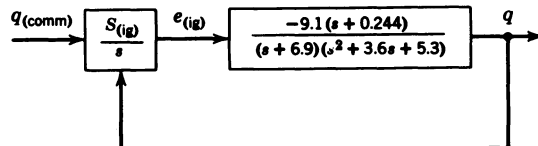
Figure 5-11 Block diagram of outer loop for the inertial cross-coupling control system.
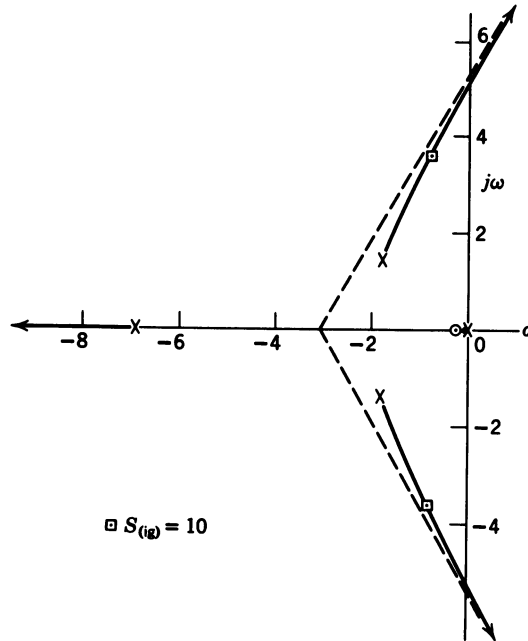
Figure 5-12 Root locus for the outer loop of the inertial cross-coupling control system.

the complex roots, resulted in a rapid divergence after about 19 sec. This is really not surprising when one considers the assumptions made for the linear analysis. However, the root locus did predict the integrating gyro gain for instability very accurately, as can be seen in Table 5-2. The results of the computer simulation are shown in Figure 5-13. The effects of the integrating gyro are apparent: not only has the steady-state pitch rate been reduced to zero, but the sideslip also has been greatly reduced. The maximum sideslip is 1.25°, with a steady-state value of 0.75°. It is doubtful that a sideslip sensor would be very effective in reducing the remaining sideslip. An examination of the roll rate response shows that it has the characteristics of a first-order

TABLE 5-2   Comparison of Actual and Predicted Values for Instability

Quantity	Value	
	Predicted	Actual
$S_{(Ig)}$ for $\zeta = 0$ [volt / (deg / sec)]	27.7	26.2
ω_n for $\zeta = 0$ (rad / sec)	5.2	5.23
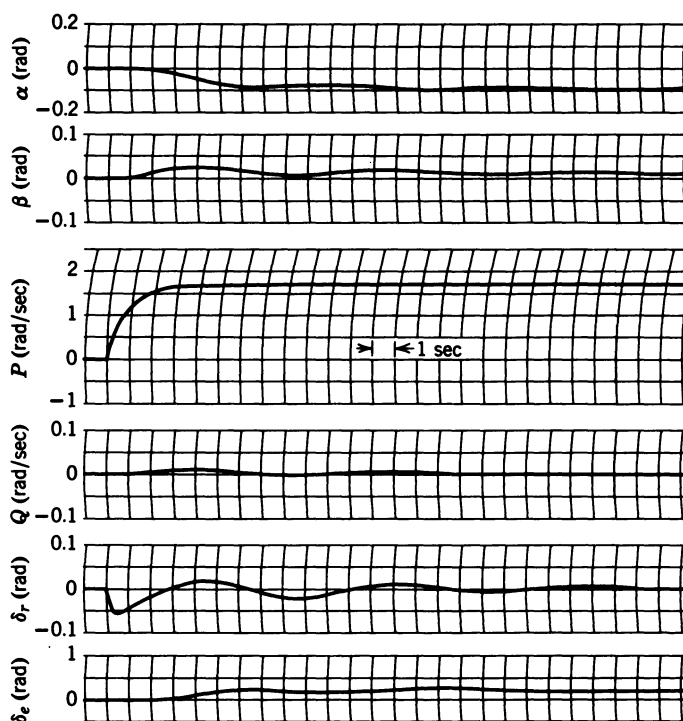
Figure 5-13 *Response of the basic aircraft and complete control system to an aileron step command of 0.2 rad.*

response. The one-degree-of-freedom rolling mode transfer function can be obtained by using Eq. 3-60 and is

$$\frac{P(s)}{\delta_a(s)} = \frac{10}{s + 1.2} \qquad (5\text{-}17)$$

For the computer simulation an aileron step input of 0.2 rad is used. Then from Eq. 5-17 the steady-state roll rate should be 1.67 rad/sec, which checks perfectly with the computer results. From Eq. 5-17 the roll subsidence time constant is 0.833 sec. The measured value of the time constant from the computer trace is 0.8 sec, which provides excellent agreement. Thus, now that the effects of inertial cross-coupling have been overcome, the coordinated aircraft transfer functions can be used for any further lateral autopilot analysis for this aircraft, as was done in Chapter 4 for the jet transport.

This concludes the analysis of an inertially cross-coupled aircraft and a control system to stabilize such an aircraft. Although the simplified linear

analysis was used to study the effects of inertial cross-coupling and to determine the minimum values of the pitch and yaw rate gyro sensitivities, the complete coupled five-degree-of-freedom equations were used in the computer simulation (the airspeed was assumed constant).

REFERENCE

1. J. J. D'Azzo and C. H. Houpis, *Linear Control System Analysis and Design: Conventional and Modern*, 3rd ed., McGraw-Hill Book Co., New York, 1988.

6

Self-Adaptive Autopilots

6-1 INTRODUCTION

As discussed in Chapters 1 and 3, the transient response of an aircraft varies considerably with changes in airspeed and altitude. This means that the roots of the characteristic equation, and thus the location in the complex plane, of the poles and zeros of the aircraft transfer functions change widely. Thus, the root locus for each flight condition and the optimum gain for each loop vary. For this reason, until recently, the gains of all autopilots were scheduled as a function of Mach number or dynamic pressure. This required extensive system analysis on the ground to determine the gains for the various flight conditions. To perform this analysis the stability derivatives for the entire flight regime had to be known accurately. These figures were usually obtained from wind tunnel tests of scale models of the aircraft. After the aircraft was built, provisions had to be made for changing the autopilot gains in flight. This procedure was then followed by extensive flight testing to determine the final optimum gain settings. All this analysis was time consuming and expensive. Also, any changes in airplane configuration probably would require more autopilot testing and adjustment.

For these reasons, the Air Research and Development Command initiated a program to determine methods of adjusting the loop gains of the flight control systems without the necessity of sensing any air data. This program led to a closed loop system for automatic gain adjustment by constantly monitoring the performance of the system. In January 1949 a symposium was held at Wright-Patterson AFB to present to industry the results of this program and to encourage applications of the techniques developed. The
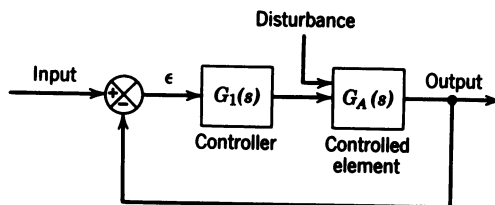
Figure 6-1   Block diagram of a generalized control system.

proceedings of this symposium were published in the form of a WADC Technical Report.[1] This report defines a self-adaptive system as one "which has the capability of changing its parameters through an internal process of measurement, evaluation, and adjustment to adapt to a changing environment, either external or internal, to the vehicle under control."

With this introduction as background, the general philosophy of the operation of self-adaptive control systems is discussed, followed by a description of three of the systems presented at the Wright-Patterson symposium.

6-2   GENERAL PHILOSOPHY OF THE SELF-ADAPTIVE CONTROL SYSTEM

To better understand the action of the self-adaptive control system, the effects of very high forward loop gain are discussed. Figure 6-1 is the block diagram of a generalized control system. The controller contains the dynamics of the systems necessary to drive the controlled element (including compensators, if required) and a variable gain. The controlled element consists of the dynamics of the unit being controlled, in this case, the aircraft. The closed loop transfer function relating the output to the input is

$$\frac{\text{output}}{\text{input}} = \frac{G_1(s)G_A(s)}{1 + G_1(s)G_A(s)} \simeq 1 \quad \text{for} \quad G_1(s)G_A(s) \gg 1 \quad (6\text{-}1)$$

The transfer function of the system for a disturbance input is

$$\frac{\text{output}}{\text{disturbance}} = \frac{G_A(s)}{1 + G_1(s)G_A(s)} \simeq \frac{1}{G_1(s)} \quad \text{for} \quad G_1(s)G_A(s) \gg 1 \quad (6\text{-}2)$$

Thus, Eq. 6-1 shows that if the gain is very high, the ratio of the output to the input is approximately 1, so that the output always follows the input. Equation 6-2 shows that the response of the system to an external disturbance is approximately equal to $1/G_1(s)$, which, if $G_1(s)$ is very large, means that the response of the system to a disturbance is negligible. The basic
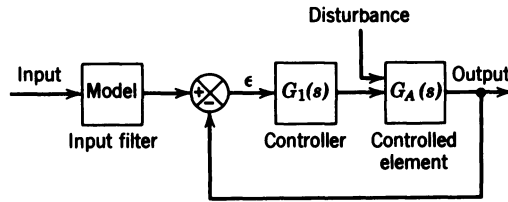
Figure 6-2 *Block diagram of basic system with input filter added.*

system can be improved by adding an input filter ahead of the summer. This input filter, when used with self-adaptive control systems, is usually referred to as a "model." The revised block diagram is shown in Figure 6-2. Now the input to the summer is the output of the model, and as the closed loop transfer function for the basic system is approximately 1, the output approximates the output of the model. The dynamics of the model can therefore be adjusted to yield an optimum response; thus the system always behaves in an optimum fashion. All this theory would be fine if the extremely high gain required could be realized at all times; however, as seen in Chapters 2 and 4, there is usually a practical limitation on the gain if the system is to remain stable. In spite of this problem, the idea of high forward loop gain is used in most of the self-adaptive systems. For systems of this type various schemes are used to obtain the maximum gain and still maintain stability. There is one precaution that must be taken when utilizing this principle: The poles that move toward the imaginary axis are the poles of the controller and not those of the controlled element. This often requires the addition of a compensator to assure that the controlled element poles break into and remain on the negative real axis. With this introduction complete, Sections 6-3, 6-4, and 6-5 describe three different self-adaptive control systems.

6-3   SPERRY SELF-ADAPTIVE CONTROL SYSTEM[1,2]

The Sperry self-adaptive control system relies on maintaining the maximum gain possible with light damping of the servo poles. Figure 6-3 is a block diagram of the basic system without the automatic gain changer. The basic autopilot employs both pitch rate and pitch attitude feedback, with K_R the ratio of the rate gain $K_{\dot{\theta}}$ to the displacement gain K_θ. Figure 6-4 shows the form of the root locus as K_θ is increased with K_R held constant. If the gain is high enough, the aircraft poles will be driven into the real axis, one moving out along the real axis to infinity and the other three moving into close proximity of the three zeros. Thus the servo poles become the dominant ones. For a given damping ratio, the higher the natural frequency of the servo poles, the higher the gain possible before instability. Therefore, it would be desirable to have the natural frequency of the servo as high as
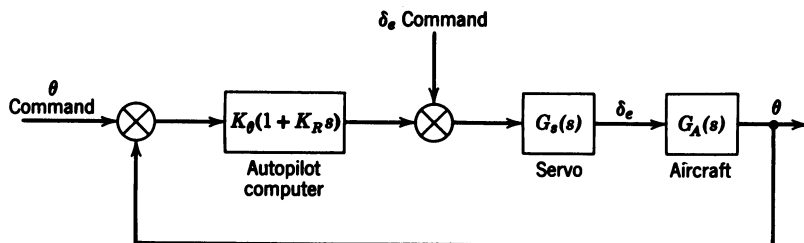
Figure 6-3 *Basic pitch attitude system.*

possible with a damping ratio of about 0.7. In Section 6-2 it was shown that the higher the forward loop gain, the more nearly the closed loop transfer function approximated unity. Thus, it is desirable to increase the gain to move the servo poles as close to the imaginary axis as possible without decreasing the damping ratio too much. The Sperry system was designed to keep the damping ratio of the servo poles between about 0.11 and 0.23.

Figure 6-5 is a block diagram of the Sperry self-adaptive control system. To determine the location of the servo poles, small-amplitude narrow pulses are fed to the servo actuator and the response of the servo measured. The amplitude and duration of the pulses is such that they mainly excite the oscillatory mode associated with the lightly damped high-frequency servo poles. The output of the pulse shaper is a series of constant-amplitude pulses, with the number of pulses corresponding to the number of reversals of δ_e. The pulses are counted by the counter that controls the switching logic that adjusts the system gain. Since the number of pulses is a measure of the damping, the switching logic is able, by sensing the output of the counter, to control the gain and maintain the damping of the servo poles between the
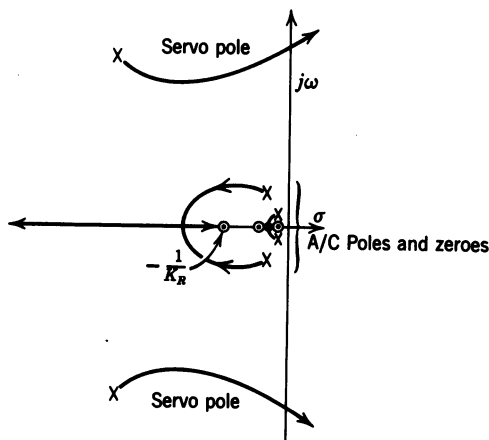
Figure 6-4 *Typical root locus for the basic attitude system. Note: This figure is not to scale.*
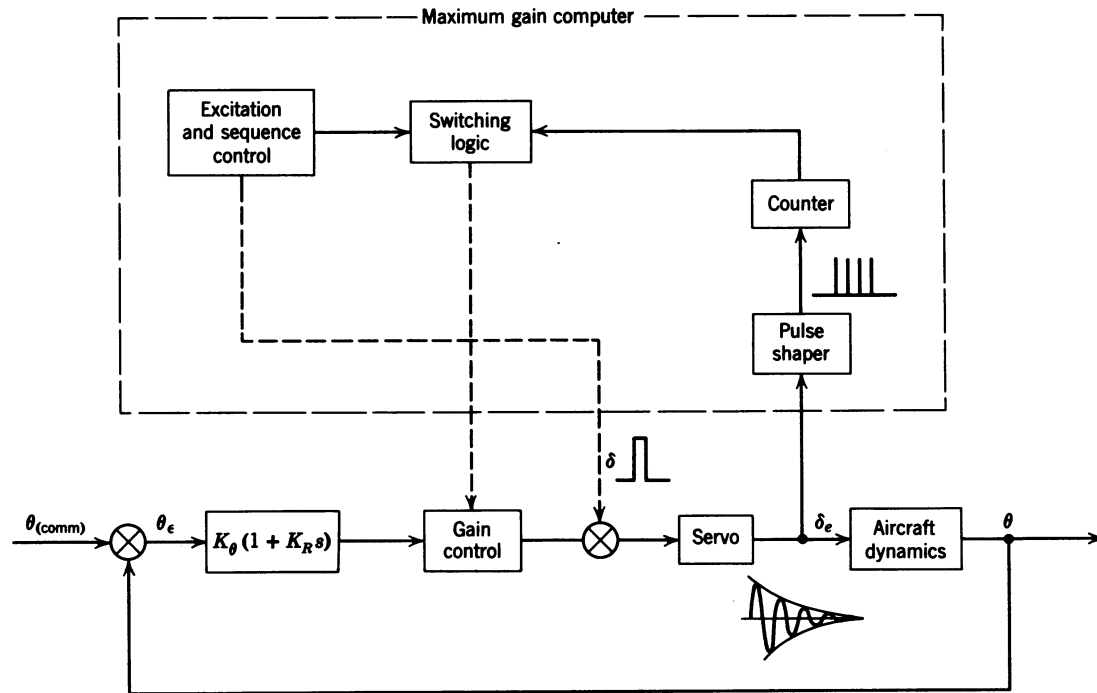
Figure 6-5 Block diagram of the Sperry self-adaptive control system.

desired bounds (sometimes referred to as process identification). The sampling period and the amplitude and shape of the excitation pulse are established by the excitation sequence control. With the aircraft flying in still air, the pilot will probably be able to detect the tremors of the aircraft resulting from the pulsing. The repetition rate of the pulse is made a function of the changing environment, with a higher repetition rate occurring when the environment is changing rapidly. The period between pulses was varied from 3 to 30 sec. This was accomplished by sensing vertical rate and forward acceleration.

Figure 6-6 is a block diagram of the logic circuit of the maximum gain computer. The output of the Schmitt trigger is a series of pulses, the number of which is equal to the number of control surface reversals which exceed the threshold sensitivity of the Schmitt trigger. The number of pulses from the Schmitt trigger controls the gain control motor through the decade counter. If the count of the counter is three, four, or five, the gain is decreased at a slow, medium, or fast rate, respectively. A slow increase in gain is commanded if a count of zero or one is obtained from two successive sampling periods. If the count is two, no change in gain occurs. The 3-second pulse from the monostable binary stage or circuit allows the counter and motor gate to remain open for 3 seconds. Thus, after the 3-second pulse from the monostable binary circuit, no change in gain is effected until the next pulse is generated by the astable binary circuit. This prevents gain changes due to random disturbances during the period between pulses.

The system was simulated by Sperry on an analog computer using a hypothetical aircraft, the physical equipment for the maximum gain control, and the servo actuator. For this simulation K_θ was held constant and also varied as a function of the error (θ_e). The latter method, referred to as "nonlinear error control," resulted in tighter control of the aircraft.

A self-adaptive system is ideally suited to determine the switchover point from aerodynamic control to reaction controls for vehicle exit and vice versa for reentry. As the vehicle reaches the less-dense atmosphere, the system gains continue to increase to compensate for the reduction in elevator effectiveness. By designing the system to switch to reaction controls when the gain reaches a certain value, successful control of the vehicle during exit and reentry is possible. This was also demonstrated by analog simulation. Thus, the Sperry system demonstrated the practicality of the self-adaptive control system utilizing a maximum forward gain controlled by a self-contained process of measurement, evaluation, and adjustment.

6-4 MINNEAPOLIS-HONEYWELL SELF-ADAPTIVE CONTROL SYSTEM[1,3]

The desirability of using a model as an input filter was discussed in Section 6-2. This concept was utilized by Minneapolis-Honeywell for their self-adaptive control system, the block diagram of which is shown in Figure 6-7. In
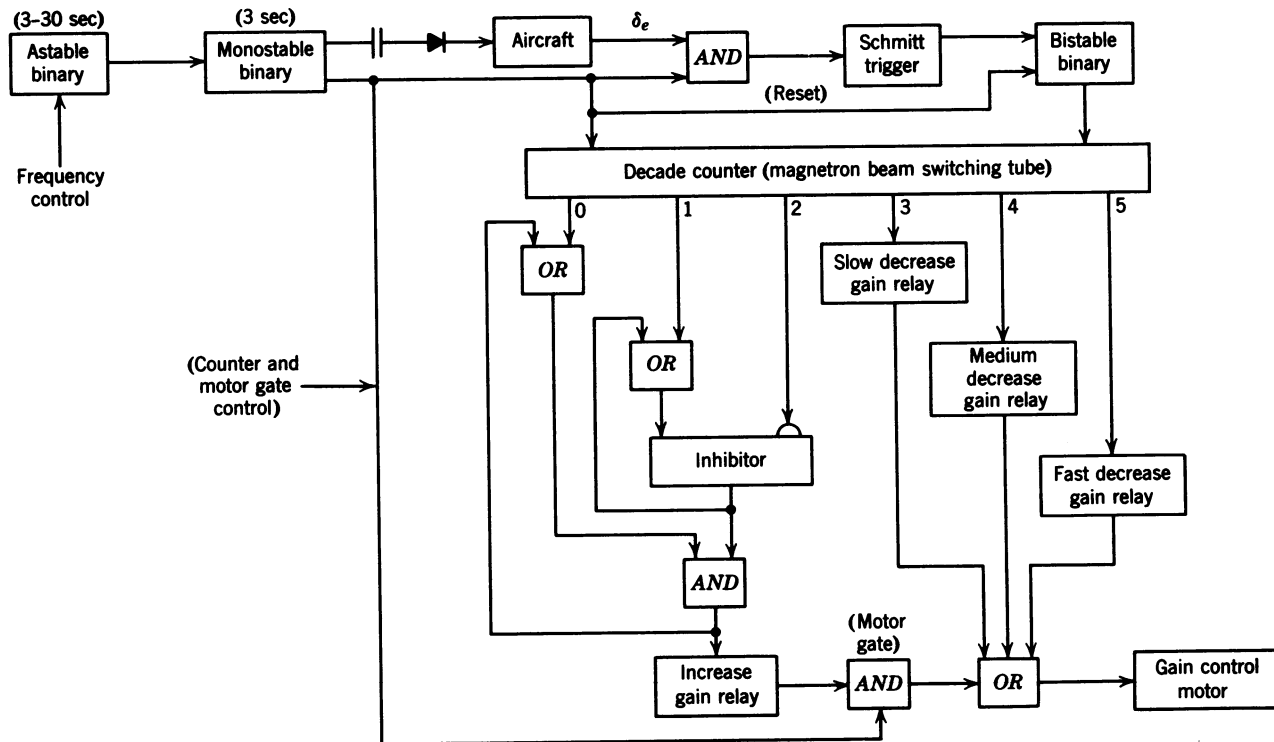
Figure 6-6 *Block diagram of the logic circuit of the maximum-gain computer.*
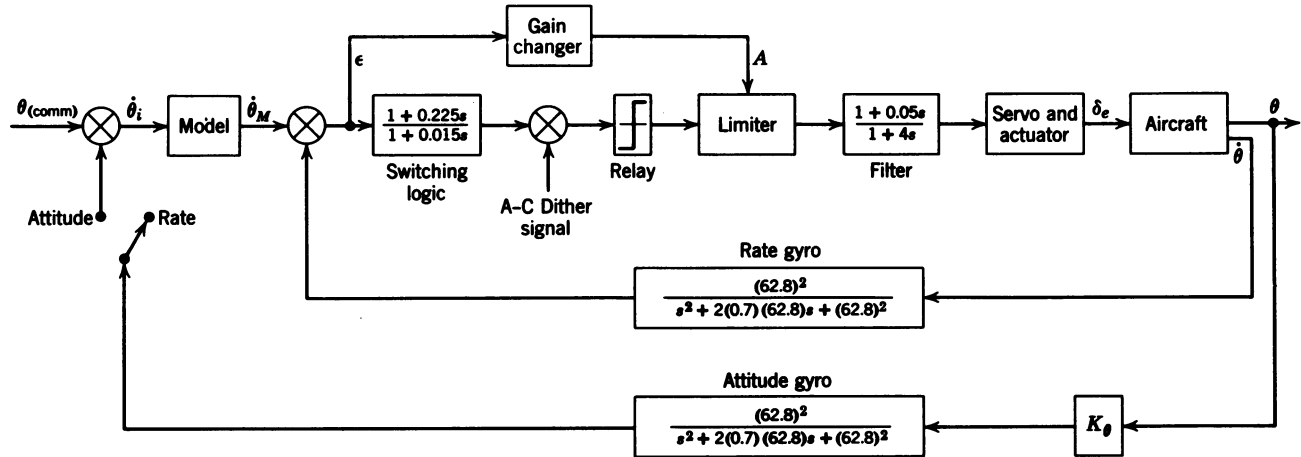
Figure 6-7 Block diagram of the Minneapolis-Honeywell self-adaptive control system. Gain changer operation:

$$A = \begin{cases} A_1 & \text{if } |\epsilon| > B \\ A_2 + (A_1 - A_2)e^{-t/2} & \text{if } |\epsilon| \le B \end{cases}$$

$$A_1 = 9.2, \qquad A_2 = 2.3° / (\sec \delta_e)$$

$$B = \text{a preselected constant}$$

$$[\text{TF}]_{(\text{model})} = \frac{10}{s^2 + 2(0.63)(3.17)s + 10}$$

$$[\text{TF}]_{(\text{servo and actuator})} = \frac{(1 + 2s)(37)^2}{2s\left[s^2 + 52s + (37)^2\right]}$$

$$[\text{TF}]_{(A/C)(\delta_e;\dot\theta)} = \text{short-period approximation}$$

order for the response of the aircraft to be equal to that of the model, the forward loop gain must be very high. As the gain required is usually larger than can be achieved by a linear servo system, a nonlinear system of the bang–bang type was used. In order to eliminate the limit cycle oscillations characteristic of a bang–bang system, an AC dither signal was introduced. The effect of the dither signal on the apparent output of the relay is explained later in this section.

Figure 6-7 indicates that the system can operate as a pitch rate command system or a pitch attitude command system. The operation as a pitch rate command system is discussed first.

The commanded pitch rate is fed to the model, the dynamics of which were selected from values established by NACA and Cornell Aeronautical Laboratories as acceptable for this type of aircraft. The output of the model is summed with the actual pitch rate of the aircraft, which is detected by a rate gyro. The output of the summer is the error between the aircraft's response and the model's. This error signal (ϵ) is fed to the switching logic circuit and the gain changer. The denominator time constant of the switching logic circuit is ideally zero, thus yielding a proportional plus derivative circuit. Also included in the switching logic block, but not shown, is an isolation amplifier. The output of the switching logic circuit is summed with the AC dither signal, which is a 2000-cps sine wave, and fed to the electronic relay. Obviously the servo and the aircraft cannot follow the 2000-cps dither signal; thus, the effective result is an averaging of the actual output of the relay so that the system responds as if the output of the relay were the arc sine characteristic shown in Figure 6-8.

The output of the relay is a commanded elevator rate. The limiter is designed to control the output of the relay as a function of the absolute magnitude of the error (see Figure 6-7). As long as the magnitude of the error is greater than some fixed quantity B, the output of the limiter is at its maximum value of 9.2 deg/sec of commanded elevator rate. When the
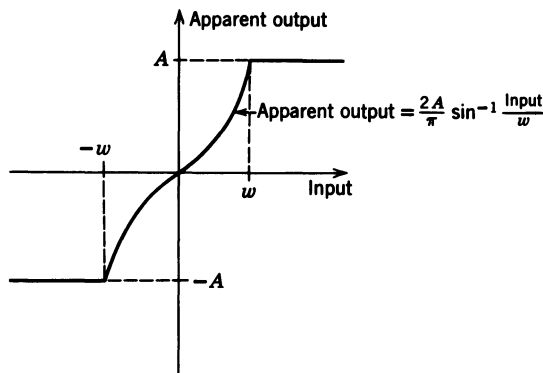
Figure 6-8 *Apparent output of an ideal relay with sinusoidal dither.*

magnitude of the error decreases to B, the gain changer starts decreasing the limits of the limiter at an exponential rate, with a time constant of 2 sec, to the minimum value of 2.3 deg/sec of commanded elevator rate. The output of the limiter is fed through a filter before being applied to the servo. The pole of the filter was selected to cancel approximately the zero of the servo and actuator. The zero or lead of the filter is introduced to compensate for the backlash of the control gearing. This operation is an example of compensation required to counteract the nonlinear effects and would not be predicted by any linear analysis. The servo is represented by a second-order system with a natural frequency of 37 rad/sec and a damping ratio of 0.7. The $(1+2s)/s$ in the servo transfer function results from a proportional plus integral network in the forward loop ahead of the servo and actuator. The aircraft is represented by the short-period approximation. By maintaining a very high forward loop gain, the actual pitch rate is made to follow the output of the model with an acceptable error; thus, the aircraft's response is effectively that of the model at all operating conditions.

The system was flight tested in an F-94C. The first set of tests were conducted with the limiter set at 4.6 deg/sec of commanded elevator rate. For this condition the performance was excellent except for the extreme ranges of the flight envelope. At low dynamic pressure the damping was lower than that of the model, while at high dynamic pressure the system followed the model, but there was a low-amplitude limit cycle that was only marginally acceptable. Introduction of the variable gain improved the performance at both extremes of the flight envelope by increasing the gain at conditions of low dynamic pressure and decreasing it at conditions of high dynamic pressure. The gain limits 9.2 and 2.3 deg/sec of elevator rate were found to be completely adequate to provide acceptable performance throughout the flight envelope.

For the attitude control mode the switch is moved to the attitude position. Since the closed loop transfer function for $\dot{\theta}_M$ in to $\dot{\theta}$ out is effectively unity, the closed loop transfer function for $\theta_{(comm)}$ in to θ out is simply a third-order system, consisting of the two complex poles from the model and the $1/s$ necessary to go from $\dot{\theta}$ out to θ out. The closed loop poles for the attitude control system for $K_\theta = 1$ are a real pole at -1.63 and two complex poles with a natural frequency of 2.48 rad/sec and a damping ratio of 0.48. The flight test of this configuration substantiated the assumption that the inner loop transfer function can be assumed to be unity. Thus, this system is also self-adaptive and adjusts the forward loop gain as a function of the error between the model response and the system response.

6-5 MIT MODEL-REFERENCE ADAPTIVE CONTROL SYSTEM FOR AIRCRAFT[1,4]

As the name implies, the MIT system also uses a model, but not as an input filter as in the case of the Minneapolis-Honeywell system. The output of the

model is compared with the output of the system, and the gains of the system are adjusted as a function of the system error. However, the gains are not kept at the highest possible level consistent with a certain stability level, but are adjusted so that certain error criteria are satisfied. These error criteria and the operation of the system are discussed in detail in the following paragraphs.

Figure 6-9 is the block diagram of the system. An examination of Figure 6-9 shows that the basic control system is the same as the yaw orientational control system discussed in Chapter 4, with the addition of the roll damping loop. The three loop gains are varied by the output of the error criteria logic system through the three rate servos that drive the three potentiometers. To better understand the error criteria used to control each loop gain and the necessity for the roll damping loop, the effects of the loop gains are illustrated by examining the root locus of each loop.

The root loci of the system are first drawn using the optimum gains as selected by the adaptive system for the F-94A at 22,000 ft and Mach 0.6, and then drawn for the system without the roll damping loop. Figure 6-10 is the block diagram of the roll damping loop. Figure 6-11 is the root locus for the roll damping loop with the location of the closed loop poles for an $S_{(rd)}$ of 0.352. Using the closed loop poles from Figure 6-11, the block diagram for the yaw orientational control loop is shown in Figure 6-12. The root locus for the yaw orientational control loop is shown in Figure 6-13 with the location of the closed loop poles for $S_{(yoc)} = 11.75$. Figure 6-14 is the block diagram of the roll stabilizing loop using the closed loop poles from Figure 6-13. Figure 6-15 is the root locus for the roll stabilization loop with the location of the closed loop poles for $S_{(rs)} = 0.086$. Figures 6-16 and 6-17 are the root loci for the yaw orientational control and roll stabilization loops for $S_{(rd)} = 0$ and $S_{(yoc)} = 11.75$.

A comparison of Figures 6-15 and 6-17 shows the effect of the roll damping loop on the overall system response. From Figure 6-15 it can be seen that a roll damping loop gain of only 0.352 volt/volt makes it possible to achieve any damping ratio desired in the final roll stabilization loop; whereas Figure 6-17 indicates that when the gain of the roll damping loop is zero, the maximum damping ratio obtainable by the roll stabilization loop is about 0.22. This illustration graphically demonstrates the effect of the roll damping loop.

Having discussed the root loci of the three loops and demonstrated the necessity for the roll damping loop, the error criteria used to set the three loop gains can now be discussed. The yaw orientational control loop gain is in the forward loop; therefore, it affects the magnitude of the signal being fed to the aileron servo and thence to the aileron. This gain has a large effect on the initial response of the aircraft. For this reason the error criterion used for the yaw orientational control loop is to make the integral of the yaw rate error signal zero, over a period starting with the initiation of the input signal and ending at the time at which the model output reached 70 percent of the input. Thus, if the gain is too low, the aircraft lags the model, and the signal
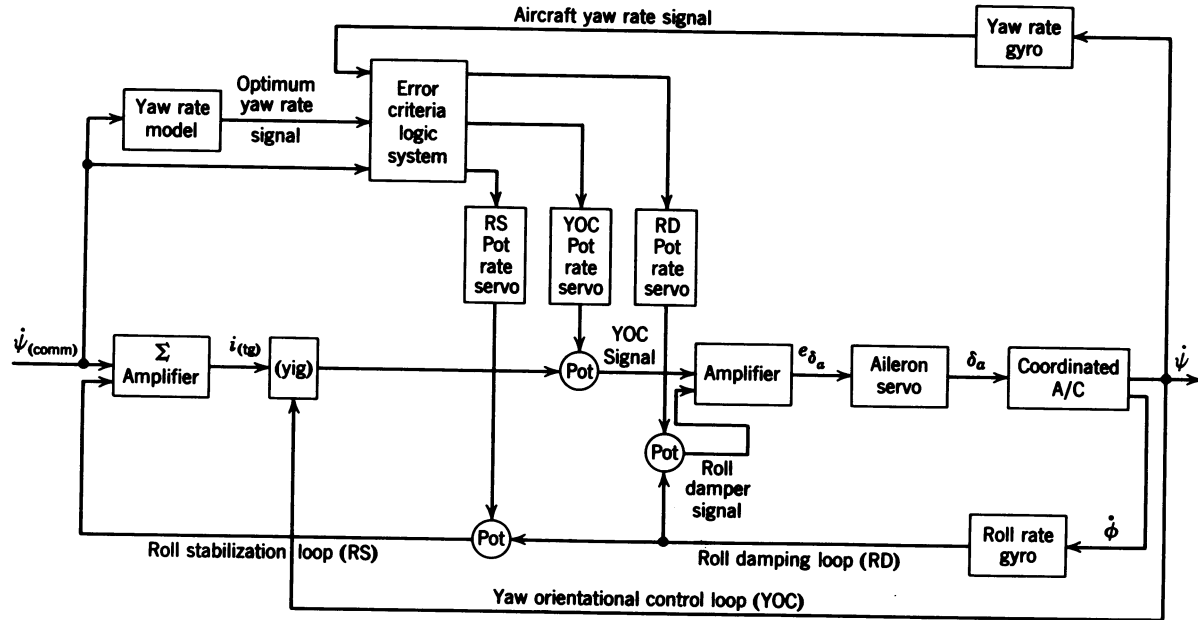
Figure 6-9 *Block diagram of the MIT model-reference adaptive control system.*

$$[TF]_{m[\varphi;\varphi]} = \cfrac{1}{(1+0.7s)\left[1 + \cfrac{2(0.8)}{1.65}s + \left(\cfrac{s}{1.65}\right)^2\right]}$$
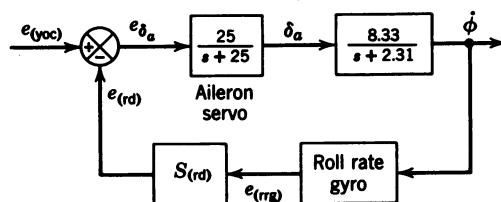
Figure 6-10 Block diagram of the roll damping loop. $[\text{TF}]_{(\text{rrg})[\dot{\phi};\,\theta]} = 1$.
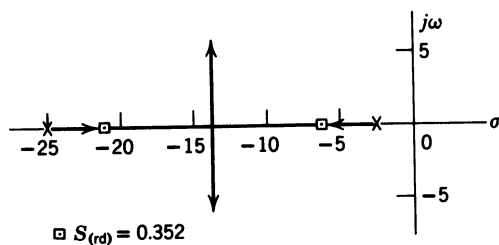
$\boxdot\ S_{(\text{rd})} = 0.352$

Figure 6-11 Root locus for the roll damping loop.
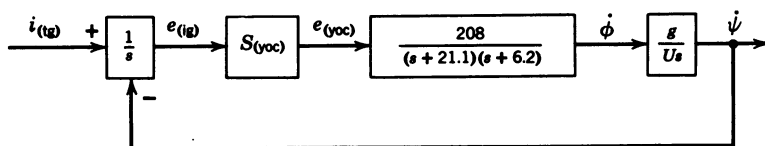
Figure 6-12 Block diagram of the yaw orientational control loop, where $g\,/\,U = 0.0524\ sec^{-1}$.

$\boxdot\ S_{(\text{yoc})} = 11.75$
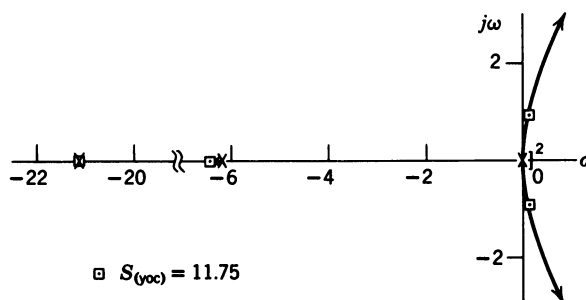
Figure 6-13 Root locus for the yaw orientational control loop for $S_{(\text{rd})} = 0.352$.
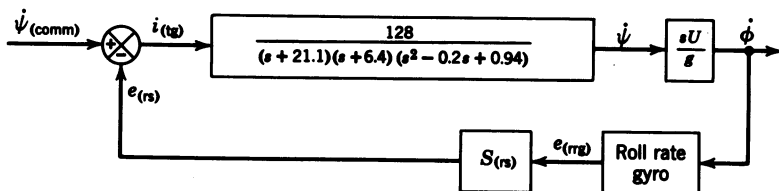
Figure 6-14 Block diagram of the roll stabilization loop. $[TF]_{(rrg)[\dot{\phi};\,e]} = 1$.

□ $S_{(rs)} = 0.086$
△   Model poles
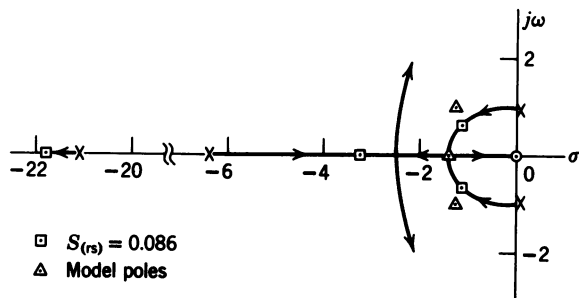
Figure 6-15 Root locus for the roll stabilization loop for $S_{(rd)} = 0.352$.

from the error logic criteria system commands an increase in the gain. The opposite will be true if the gain is too high. As the aircraft enters flight conditions resulting in low dynamic pressures, the response of the aircraft in roll will be slower (see Eq. 3-61); thus, the system tries to compensate for this by increasing the yaw orientational loop gain. If this gain is driven too high, the other two loop gains may be driven to excessively large values in trying to optimize the system, with detrimental results on the system response. For this reason an upper limit must be placed on the yaw orientational control loop

□ $S_{(yoc)} = 11.75$
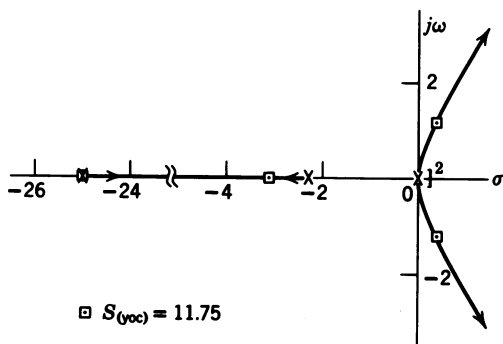
Figure 6-16 Root locus for the yaw orientational control loop for $S_{(rd)} = 0$.
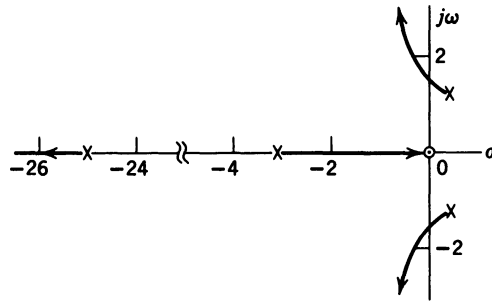
Figure 6-17 *Root locus for the roll stabilization loop for $S_{(rd)} = 0$.*

gain, but this alone is not the solution. If the yaw orientational control loop gain is limited, the error criterion used to control that gain will not be satisfied. This fact, plus the idea that for the flight conditions yielding low dynamic pressures it might be desirable to slow down the response of the model, led to the idea of adjusting the time constant of the model under these conditions. Thus, the gain of the yaw orientational control loop was varied linearly from its minimum value of about 3.5 to a maximum value of 7.5. At this point the time constant of the first-order term of the model was increased linearly from 0.7 until the error criterion was satisfied. The maximum value of the time constant used was 1.2 sec. In this manner both the system and the model were made self-adaptive.

As seen from the root loci, the roll stabilization loop is responsible for stabilizing the overall system and determining the final closed loop poles of the system. Since the location of the closed loop poles determines the response time of the system, the integral of the error sampled over the response time was used to vary the roll stabilization loop gain. The response time was taken as the time between the initiation of an input signal and the time for the output of the model to reach 95 percent of the input. However, for this loop the integral of the error was nulled rather than made equal to zero, as for the case of the yaw orientational control loop.

As was shown in Section 4-6, the roll damping loop determines the amount of damping possible in the overall system. The system may be underdamped with its response oscillating about the desired response, yet the other two error criteria may be satisfied; thus the integral of the absolute value of the error was chosen as this criterion. The integral of the absolute value of the error is large if the system is underdamped or so overdamped that the system response is sluggish. However, using the absolute value of the error introduces the problem of which direction to adjust the gain of the roll damping loop. In order to solve this problem, each successive value of the integral of the absolute value of the error is compared with the previous value. As long as each successive value of the error is less, the gain is adjusted in the same direction. If the value of the error is greater than the

previous value, the adjustment of the gain is reversed. In this manner the gain of the roll damping loop is adjusted to minimize the integral of the absolute value of the error.

Having discussed the various error criteria, the effectiveness of the optimum values of the various gains can now be discussed. As mentioned in the preceding paragraphs, Figures 6-11, 6-13, and 6-15 are the root loci for the three autopilot loops, and the closed loop poles indicated are for the optimum values of each loop gain as determined by the system. For this case there was no limiting of the yaw orientational control loop gain. Figure 6-15 shows the location of the outer loop closed loop poles as well as the model poles. From an examination of Figure 6-15 it can be seen that the closed loop complex system poles are very close to the model's complex poles, while the real closed loop system pole is much farther to the left of the model pole. From a comparison of the system and model poles it is not evident that the error criteria have been satisfied. To check this, the inverse Laplace transforms of the system and the model for a step input of $\dot{\psi}_{(comm)}$ were taken. A comparison of the two responses showed that the error between the aircraft and the model varied from 0.08 to 2.6 percent, with the system response leading the model slightly. This was caused by the real system pole; however, if the complex system poles had been slightly closer to the imaginary axis the results would have been better. The difference between the two responses is probably due to the inaccuracies in the root locus plots. However, it is evident from Figure 6-15 that, for this flight condition, the real pole at -6.4 can never move to the location of the model real pole if the system's complex poles are to remain in the vicinity of the model's complex poles. This will probably be the case for most of the flight conditions; thus this system is in general incapable of forcing the dominant system poles to become identical with the model poles. This means that complete optimization is impossible for all flight conditions; however, the system is apparently capable of positioning the closed loop poles of the system in such a manner that the error criteria are satisfied. The capabilities of this system were demonstrated by actual flight test using an F-94C, the results of which are shown in Ref. 4.

6-6 MH-90 ADAPTIVE CONTROL SYSTEM

Since the writing of the references listed at the end of the chapter, new and improved systems have been developed; however, the same basic idea of using the highest forward loop gain consistent with some set stability criterion is still prevalent. A good example of this is the MH-90 flight control system developed by Minneapolis-Honeywell for the F-101. This system is an outgrowth of the Minneapolis-Honeywell system discussed in Section 6-4. The maximum possible forward loop gain is still used, so that the closed loop transfer function of the system will be approximately 1; thus the output of the system theoretically will follow the output of the model. However, the
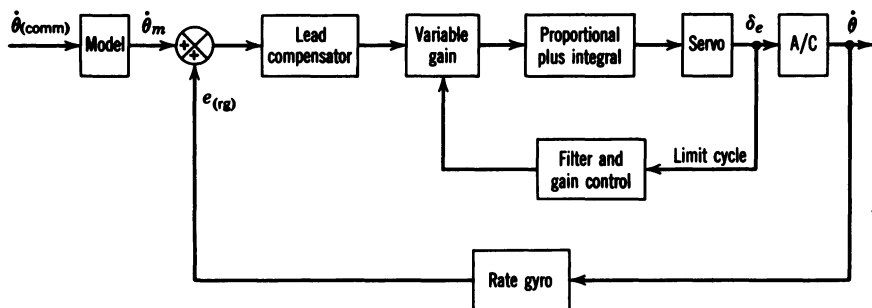
Figure 6-18 *General block diagram of the MH-90 adaptive control system.*

technique for controlling the maximum allowable gain is different. The MH-90 system maintains the forward loop gain at a sufficient level to keep the complex servo poles on the imaginary axis. This results in a limit cycle, the frequency of which is the natural frequency of the servo poles where they cross the imaginary axis. To control the forward loop gain, the limit cycle is fed through a narrow-band filter which is tuned to 25 rad/sec, the ideal limit-cycle frequency. The output of the filter is rectified and compared with a limit-cycle amplitude "set point." The difference between the set point and the limit cycle is used to adjust the variable forward loop gain. As the operation of the gain changer is not pertinent to the discussion to follow, it will not be explained further. The basic system is shown in Figure 6-18. Several Master of Science theses have been written under the author's supervision by students of the Graduate Guidance and Control course of the Air Force Institute of Technology, under the sponsorship of the Flight Control Laboratory, Aeronautical Systems Division at Wright-Patterson AFB, Ohio (Refs. 5, 6, 7). These theses have disclosed some very interesting operating characteristics of the MH-90 adaptive control system. The main results of these theses are discussed in the following paragraphs.

An investigation performed by Lt. Blum[5] shows the effect of noise on the operation of the MH-90 adaptive control system. In the investigation, white noise, in the form of an electrical signal, was fed to the input of the servo, which was simulated along with the aircraft and the rest of the system on an analog computer. With the forward loop gain at the proper level to assure a limit cycle with no noise present, the input to the filter in the presence of noise would be the limit cycle plus the noise response of the servo. The output of the filter and rectifier of the gain control would then be larger than the set point. This situation would result in a decrease in the forward loop gain, and with sufficient noise present the limit cycle would disappear completely, being replaced by the noise signal passed by the filter, and the system operation would deteriorate rapidly. For a limit cycle with a peak-to-peak amplitude of 0.1 volt, the maximum allowable RMS noise response of the servo was found to be 0.34°.

Lt. Johannes in his thesis[6] investigated the effects of using a low-frequency servo on the performance of the MH-90 adaptive control system. Figure 6-19 is the block diagram of the system as analyzed by Lt. Johannes. At the request of the Flight Control Laboratory, he used a simple second-order system as the controlled element and added a compensator between the servo and the controlled element. The results of this study would still be valid if the controlled element were the short-period dynamics of an aircraft. The natural frequency of the servo was varied from 40 to 15 rad/sec with the damping ratio held constant at 0.8. Figure 6-20 shows the form of the root locus for the system with the natural frequency of the servo equal to 40 rad/sec. From Figure 6-20 it can be seen that for high natural frequencies of the servo, the branch that crosses the imaginary axis originated from the two real poles of the two compensators. The frequency of the limit cycle was 33 rad/sec. If the natural frequency of the servo is reduced to 35 rad/sec, the branches from the servo poles cross the imaginary axis. Finally, for a servo natural frequency of 15 rad/sec the servo poles break into the two real zeros, and the branches from the controlled element poles cross the imaginary axis. For this condition the limit-cycle frequency has decreased to about 19 rad/sec. The fact that the controlled element poles cross the imaginary axis makes the operation of the MH-90 system, with a servo having a natural frequency of 15 rad/sec, unsatisfactory. This is because, as the dynamics of the controlled element change, the natural frequency at which they cross the imaginary axis changes excessively and degrades the operation of the system.

Captains Christiansen and Fleming in their thesis[7] investigated, among other things, the improvement gained by introducing a variable compensator when using a low-frequency servo ($\omega_n = 12$ rad/sec). In this investigation the damping ratio of the controlled element was varied from 0.2 to 0.9, while the natural frequency was varied from 4 to 10 rad/sec. A total of nine combinations were used. With the compensator as shown in Figure 6-19, the imaginary axis crossing frequency varied from 9.7 to 18.4 rad/sec. The two extreme cases were caused by a ζ of 0.2 and ω_n of 4 for the lower value of imaginary axis crossing frequency, and a ζ of 0.9 and ω_n of 10 for the higher value. Since the band-pass filter at the input to the gain control has a very narrow pass band, centered on 25 rad/sec, the operation of the adaptive loop is unsatisfactory unless the limit cycle remains near 25 rad/sec. It was found that by moving the pole of the compensator to the left, the imaginary axis crossing frequency was increased. A system was then devised by these two students to control the location of the compensator pole as a function of the limit-cycle frequency. The location of the pole was varied from -10 to -95 automatically, to assure a limit-cycle frequency of 25 rad/sec. Through the use of the dynamic compensator the MH-90 system performed adequately with the low-natural-frequency servo.

As mentioned in Section 6-2, proper operation of an adaptive control system similar to the MH-90 depends on a very high forward loop gain so that the closed loop transfer function of the system, exclusive of the model,
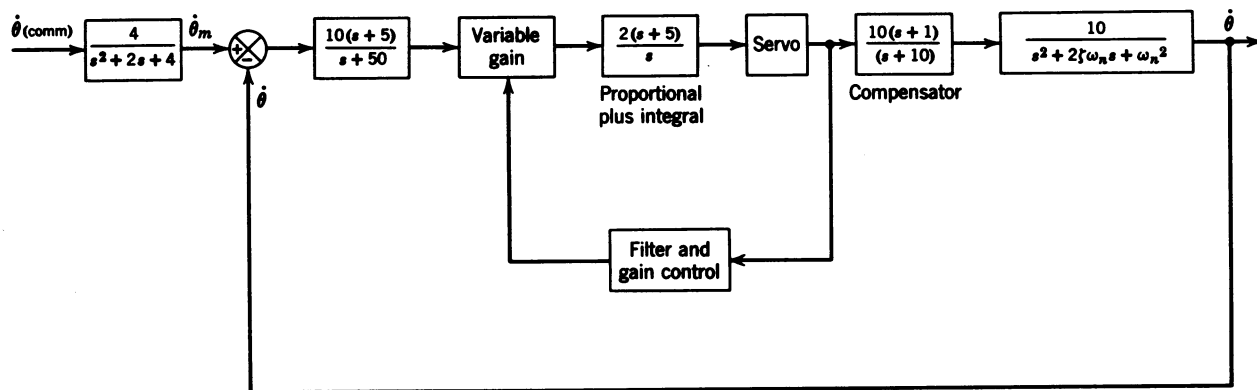
Figure 6-19 *Block diagram for analysis of MH-90 adaptive control system (Ref. 6).*
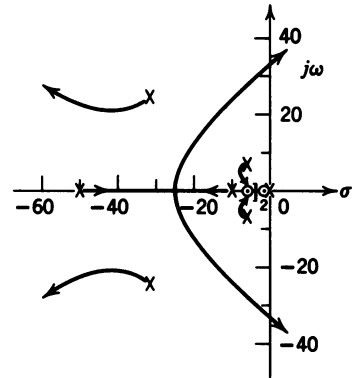
Figure 6-20 Sketch of root locus for system with the
natural frequency of the servo equal to 40 rad / sec.
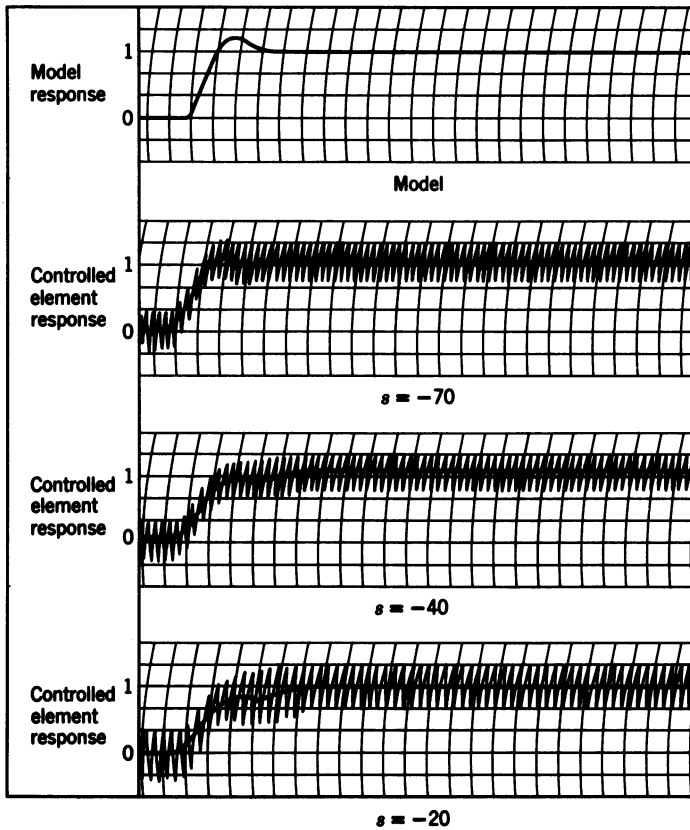
Figure 6-21 System response with $\zeta_{ce} = 0.4$, $\omega_{nce} = 10$ rad / sec for four compensator pole
locations, for a unit step input (Ref. 7).

can be considered to be 1. The high gain required cannot in all cases be obtained without driving the system completely unstable. This is especially true for the MH-90 system when used with a low-frequency servo. Referring to Figure 6-20, it can be seen that there is a pole at the origin that moves toward the zero at -1. The closed loop location of this pole relative to the zero determines the effect of this large time constant on the overall system response. The transient resulting from this pole persists the longest and is of the form $Ae^{-t/\tau}$. If A is large, the slow decay of this term prevents the system from following the model. The value of A is dependent upon the distance from this closed loop pole to the zero. The closer the pole is to the zero, the smaller A becomes and the less effect this large time constant has on the behavior of the system. With the compensator pole at -10, the gain of the system cannot be raised sufficiently to drive the pole at the origin close enough to the zero to prevent this adverse performance; however, the addition of the dynamic compensator permits a larger gain and decreases the effect of this troublesome pole. This effect is illustrated in Figure 6-21 from Ref. 7.

In addition to the problems introduced by noise, structural flexibility can result in unsatisfactory operation if one of the body bending modes is near the limit-cycle frequency. If the amplitude of the body bending mode oscillation that appears at the input to the filter of the adaptive control is of sufficient amplitude, then the gain changer reduces the loop gain and system operation deteriorates. This effect has been investigated by Cornell Aeronautical Laboratory, and is reported in Refs. 8 and 9. This subject is discussed in more detail in Chapter 11.

6-7 SUMMARY

In this chapter the basic concept of the self-adaptive autopilot was discussed, and several examples were examined. In all cases, except the MIT system, adaptation was accomplished by maintaining the maximum forward loop gain consistent with some set margin of stability. The MIT system, however, adjusted the loop gains by satisfying certain error criteria, and in this respect may be considered more truly self-adaptive. One fact that should be remembered is that no system will be able to maintain optimum system performance for all flight conditions. In most cases some form of compensation will be required to obtain the best adaptation possible, and as shown in Section 6-6, the compensator may be dynamic.

The introduction of the self-adaptive control system has been a great step forward in the field of automatic control systems. Self-adaptive control systems are playing an important role in the conquest of space as evidenced by Refs. 10, 11, and 12. Reference 10 describes an adaptive algorithm for the space shuttle that varies the longitudinal stick gearing in order to reduce the tendency for pilot-induced oscillations during approach and landing. Refer-

ences 11 and 12 discuss the use of adaptive techniques to achieve control of the dynamics of large structural systems such as space stations.

REFERENCES

1. *Proceedings of the Self-Adaptive Flight Control Systems Symposium*, WADC-TR-59-49, Sperry Gyroscope Company, March 1959.

2. *Final Technical Report Feasibility Study Automatic Optimizing Stabilization System*, Part I, WADC-TR-58-243, Sperry Gyroscope Company, June 1958.

3. *A Study to Determine an Automatic Flight Control Configuration to Provide a Stability Augmentation Capability for a High-Performance Supersonic Aircraft*, WADC-TR-57-349 (Final), Minneapolis-Honeywell Regulator Company, Aeronautical Division, May 1958.

4. H. P. Whitaker, J. Yarmon, and A. Kezer, *Design of Model-Reference Adaptive Control Systems for Aircraft*, Report R-164, Instrumentation Laboratory, Massachusetts Institute of Technology, September 1958.

5. J. J. Blum, *A Study to Determine the Effects of Random Disturbances in an Adaptive Flight Control System*, M.S. Thesis, Air Force Institute of Technology, Wright-Patterson AFB, Ohio, March 1961.

6. R. P. Johannes, *Study of a Self-Adaptive Control System Including Simulation and Effects of Variation of the System Dynamics*, M.S. Thesis, Air Force Institute of Technology, Wright-Patterson AFB, Ohio, March 1961.

7. R. H. Christiansen, and R. J. Fleming, *Variable Compensator Loop Application to a Self-Adaptive Flight Control System*, M.S. Thesis, Air Force Institute of Technology, Wright-Patterson AFB, Ohio, March 1962.

8. *Application of Self-Adaptive Control Techniques to the Flexible Transport*, First Quarterly Technical Report, CAL Report No. IH-1696-F-1, AF33(657)8540, Cornell Aeronautical Laboratory, October 1, 1962.

9. Clark, Notess, Pritchard, Reynolds, and Schuler, *Application of Self-Adaptive Control Techniques to the Flexible Supersonic Transport*, CAL Report No. IH-1696-F-5, Vol. I, Cornell Aeronautical Laboratory, July 1, 1963.

10. B. G. Powers, "An Adaptive Stick-Gain to Reduce Pilot-Induced Oscillation Tendencies," *Journal of Guidance, Control, and Dynamics*, March-April 1982, Vol. 5, No. 2.

11. N. Sundararajan, J. P. Williams, and R. C. Montgomery, "Adaptive Modal Control of Structural Dynamic Systems Using Recursive Lattice Filters," *Journal of Guidance, Control, and Dynamics*, March-April 1985, Vol. 8, No. 2.

12. I. Bar-Kana, H. Kaufman, and M. Balas, "Model Reference Adaptive Control of Large Structural Systems," *Journal of Guidance, Control, and Dynamics*, March-April 1983, Vol. 6, No. 2.

7

Missile Control Systems

7-1 INTRODUCTION

The control systems for aircraft having been discussed in the preceding chapters, this chapter deals with the discussion of control systems for guided missiles. The name "guided missile" implies that the missile is controlled either by an internal guidance system or by commands transmitted to the missile by radio from the ground or launching vehicle.

Before discussing some typical guidance systems, the terms "navigation system," "guidance system," and "control system" are defined. A navigation system is one that automatically determines the position of the vehicle with respect to some reference frame, for example, the earth, and displays this to an operator. If the vehicle is off course, it is up to the operator to make the necessary correction. A guidance system, on the other hand, automatically makes the necessary correction to keep the vehicle on course by sending the proper signal to the control system or autopilot. The guidance system then performs all the functions of a navigation system plus generating the required correction signal to be sent to the control system. The control system controls the direction of the motion of the vehicle or simply the orientation of the velocity vector.

The type of guidance system used depends upon the type and mission of the missile being controlled, and they can vary in complexity from an inertial guidance system for long-range surface-to-surface or air-to-surface winged missiles to a simple system where the operator visually observes the missile and sends guidance commands via a radio link. In any case, the guidance command serves as the input to the missile control system. The command

may be in the form of a heading or attitude command, a pitching or turning rate command, or a pitch or yaw acceleration command, depending upon the type of guidance scheme used. This chapter deals with the control system in the missile that receives the signal from the guidance system and not with the guidance system itself. Guidance systems for aerodynamic missiles will be discussed in Chapter 8. For details of inertial guidance systems the reader is referred to the references at the end of this chapter.

Of the various types of guided missiles, those that are flown in the same manner as manned aircraft (that is, missiles that are banked to turn, such as cruise missiles and remotely piloted vehicles) will not be discussed. Control systems and methods of analysis previously discussed can be used for these types of missiles. Of interest in this chapter are other "aerodynamic missiles" (which use aerodynamic lift to control the direction of flight), such as the Sidewinder, Patriot, etc., and "ballistic missiles" (which are guided during powered flight by deflecting the thrust vector and become free-falling bodies after engine cutoff). One feature of these missiles is that they are roll stabilized; thus there is no coupling between the longitudinal and the lateral modes, which simplifies the analysis. The basic assumptions made in Chapter 1 are still valid for studying the control systems; however, for analyzing the guidance system for ballistic missiles, the rotating earth cannot be assumed as an inertial reference. Additional assumptions will be made as required. Since the missiles to be studied in this chapter are roll stabilized, a system for accomplishing this is discussed first.

7-2 ROLL STABILIZATION

Roll stabilization can be accomplished by different means, depending on the type of missile. For aerodynamic missiles, the required rolling moment is achieved by differential movement of the control surfaces. For ballistic missiles, the rolling moment can be obtained by differential swiveling of small rockets mounted on the side of the missile, as is done on the Atlas, or by differential swiveling of the two main rocket engines if more than one engine is used. The next problem is the detection of the rolling motion so that it can be controlled, and the reduction of roll rate to zero or maintenance of the roll angle equal to some specified reference. The use of a roll rate gyro would not be satisfactory unless it was desirable only to reduce the roll rate considerably. The use of the roll rate gyro would result in a Type 0 system, which would further result in a steady-state error in roll rate in the presence of a constant disturbing rolling moment. To maintain a desired roll angle, some form of an attitude reference must be used. This can be a vertical gyro for air-to-air or surface-to-air missiles. In either case the feedback would be a signal proportional to the roll angle about the longitudinal axis of the missile. Still another possible method is the use of an integrating gyro with its input axis along the longitudinal axis of the missile. Figure 7-1 is the block diagram
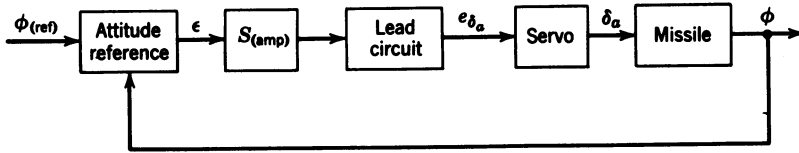
Figure 7-1 *General block diagram of a roll stabilization system.*

$$[TF]_{(lead\ circuit)} = \frac{1}{\alpha}\left(\frac{1 + \alpha \tau s}{1 + \tau s}\right)$$

of a possible roll stabilization control system. The servo might be represented by a first-order time lag or a second-order system. The transfer function of the missile for δ_a input to roll angle output would be the same as the one-degree-of-freedom rolling mode derived in Section 3-6 for aircraft, which is repeated here:

$$\frac{\phi(s)}{\delta_a(s)} = \frac{C_{l_{\delta_a}}}{s\left(\dfrac{I_x}{Sqd}s - \dfrac{d}{2U}C_{l_p}\right)} \tag{7-1}$$

where $C_{l_{\delta_a}}$ is the rolling moment generated by the aerodynamic controls or the reaction controls divided by Sqd, and d is the diameter of the missile. The reference area, S, is usually taken as the cross-sectional area of the missile. C_{l_p} for the aerodynamic missile results from the same cause as discussed in Section 3-2; for the ballistic missile C_{l_p} is due mostly to aerodynamic friction and thus is negligible. The requirement for the lead network is demonstrated by drawing the root locus of the system for the worst condition, that is, $C_{l_p} = 0$ (roll rate feedback could also be used for stabilization). Figure 7-2 shows the block diagram used for the root locus. The root locus of the system is shown in Figure 7-3. Without the lead circuit
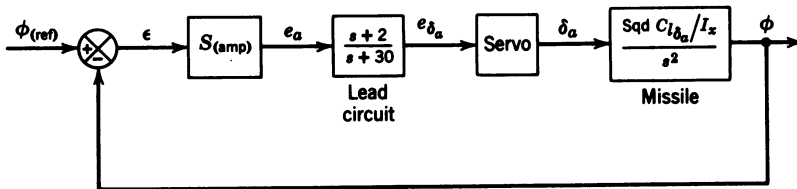
Figure 7-2 *Block diagram of roll stabilization system for root locus analysis.*

$$[TF]_{(servo)(e_{\delta_a}\colon \delta_a)} = \frac{2750}{s^2 + 84s + (52.5)^2}$$
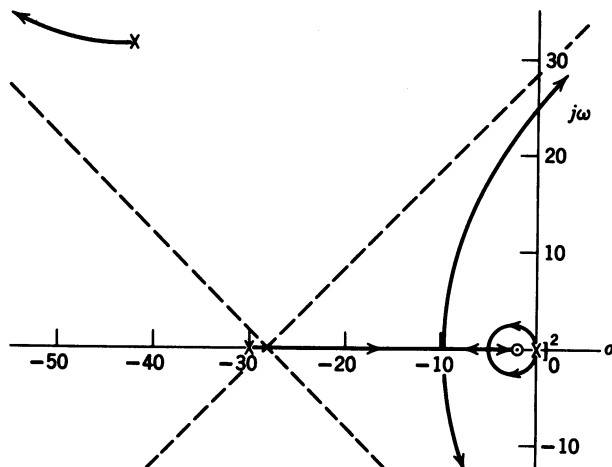
Figure 7-3 Root locus for the roll stabilization system shown in Figure 7-2.

the two poles at the origin would move directly into the right half plane; the effect of the lead circuit is evident. If C_{l_p} is not zero, the transfer function of the missile consists of a pole at the origin and a pole at $s = -1/\tau = -(Sqd^2/2UI_x)C_{l_p}$. The larger C_{l_p}, the larger $1/\tau$, and the less is the requirement for the lead circuit.

An alternate control system could consist of an integrating gyro with its input axis parallel to the longitudinal axis of the missile. This would provide the same quality of control as the attitude reference system as long as the drift rate of the gyro were low enough. The root locus for this system would be the same as Figure 7-3.

Some aerodynamic missiles such as the Sidewinder use control surfaces referred to as rollerons to reduce the roll rate. This technique is illustrated in Figure 7-4 which shows a small gyro wheel attached to the movable control surface on the missile tail fin. The gyro wheels can be spun up using exhaust gases vented from the rocket engine or by a short lanyard wrapped around
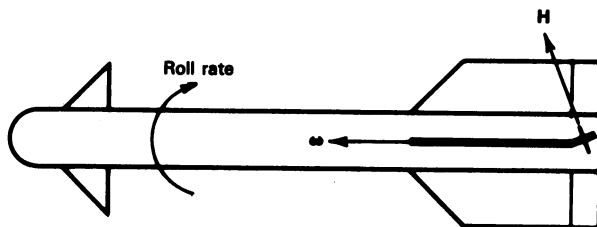
Figure 7-4 Sketch of rolleron action for an aerodynamic missile.

the shaft of the gyro wheel and attached to the missile launcher. As illustrated in Figure 7-4, the **H** vector of the gyro wheel is to the right, and if the missile is rolling to the right, the ω vector is toward the nose of the missile, resulting in a gyroscopic output torque $\mathbf{M}_g$ coming out of the page (see Appendix B, Eq. B-11). This torque will cause the control surface to be deflected to the right, thus slowing down the roll rate.

7-3 CONTROL OF AERODYNAMIC MISSILES

Figure 7-5 is a sketch of a typical aerodynamic missile showing the orientation of the axis system. By using a body axis system the product of inertia term J_{xz} is zero and $I_z = I_y$. Thus for $P = 0$ there is no coupling between the longitudinal and lateral equations. Control can be accomplished either by conventional control surfaces with the canards stationary or absent, or by use of the canards with no control surfaces on the main lifting surfaces.

Missiles such as the one shown in Figure 7-5 are often referred to as cruciform missiles due to the Y and Z symmetry of the lifting surfaces, and are usually flown with a roll angle of 45°. As these missiles use direct side force to turn, they are referred to as skid-to-turn missiles, and by flying with a roll angle of 45° (referred to as the $\times$ configuration) all four lifting surfaces are used for pitch and yaw control. If the missile is flown with zero roll angle as shown in Figure 7-5, it is said to be in the $+$ configuration. The aerodynamic data for these missiles may be given for either of the configurations; the engineer must check to determine which configuration was used to evaluate the data. A majority of the data is obtained from wind tunnel test using the $+$ configuration. To convert the stability derivatives and/or force and moment coefficients from the $+$ to the $\times$ configuration it is only necessary to multiply the values by 1.414 ($2\cos 45°$). In the analysis to follow and the missile simulation the missile was assumed to be flown in the $+$ configuration. The guidance systems used to generate the command inputs to the control systems covered in this chapter are discussed in Chapter 8 along with the control of a bank-to-turn missile.

As a result of the Y and Z symmetry, the pitch axis short-period approximation transfer functions can be used for both the pitch and the yaw axis
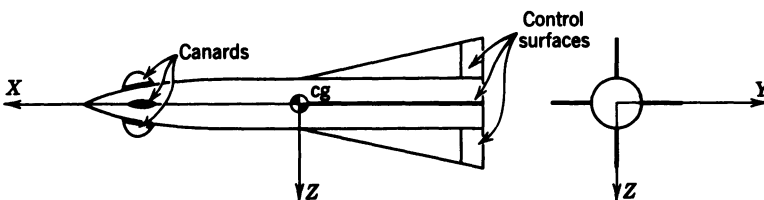
Figure 7-5 Sketch of an aerodynamic missile and axis system.

TABLE 7-1   List of Missile Parameters for Dynamic Analysis

t (sec)	h (m)	V (m / sec)	Mach	m (kg)	I_y (kg m^2)	C_{m_α} (1 / rad) (ref.)	C_{z_α} (1 / rad)	$C_{m_{\delta_t}}$ (1 / rad) (ref.)	$C_{z_{\delta_t}}$ (1 / rad)	cg (m)
3	159	387.67	1.14	908.8	2334.4	−123.8	−19.22	−120.88	−8.3	−3.578
5	464	652.37	1.928	798	2050	−61.2	−15.25	−97.98	−6.72	−3.49
12	2400	829.8	2.508	623	1767.69	−36.78	−13.1	−78.99	−5.41	−3.336
20*	5819	1139.62	3.59	423	1445	−9.04	−10.78	−58.79	−4.03	−3.16
26	8524	884.12	2.89	423	1445	−27.07	−11.39	−70.24	−4.82	−3.16
27	8927	851.87	2.802	423	1445	−29.3	−11.79	−72.05	−4.94	−3.16

*Sustainer burnout and point of maximum dynamic pressure, ref. cg = −3.16 m, d = 0.203 m, S = 0.13 m^2.

analysis; however, the analysis need only be accomplished about one of the axes, due to the symmetry just mentioned. The two channels are the same except for the signs at the various summers due to the sign conventions used for the two axes. Unlike the calculation of the transfer functions for aircraft, the calculation of the missile transfer functions is complicated by the need to determine a consistent set of physical properties and flight conditions. The physical properties of interest are the mass, moment of inertia, and cg location, which are functions of the fuel used. The flight conditions (altitude and velocity) determine the Mach number, which is needed to calculate the missile stability derivatives; the latter can also be functions of angle of attack and control surface deflection. During the early design phase, flyouts can be run at different launch conditions by developing and running a point mass missile simulation, using the design thrust profile with the corresponding mass and the estimated drag coefficient variation with Mach number. Using the data from selected points from the point mass flyouts, a preliminary dynamic analysis can be performed. Using the results from the initial dynamic analysis, a full missile simulation can be developed to obtain data for the final autopilot and guidance system design. This was the procedure followed in the development of this autopilot, and the analysis using data from the final missile simulation will be presented. From the missile flyout described in Section 8-2 the missile parameters listed in Table 7-1 for six points in the trajectory were obtained and used to calculate the corresponding missile transfer functions.

For the aerodynamic analysis of missiles, body axis rather than stability axis stability derivatives are used; thus from Table 7-1 $C_{z_\alpha} = - C_{N_\alpha}$, where $C_{N_\alpha} = \partial C_N / \partial \alpha$ and C_N is the normal force coefficient (perpendicular to the X axis and positive up). For drag the axial force coefficient C_A (positive along the negative X axis) is used rather than C_D. The moment stability derivatives C_{m_α} and $C_{m_{\delta_t}}$ are taken with respect to the reference cg and must be corrected for the location of the actual cg relative to the reference cg. This is shown in Figure 7-6 where the distances shown measured from the nose of
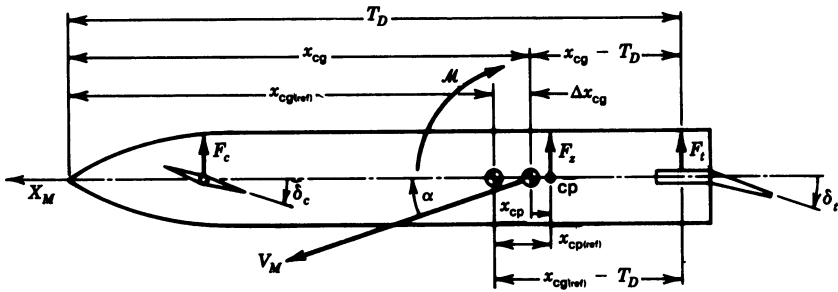
Figure 7-6 *Generation of pitching moment.* $\Delta x_{cg} = x_{cg} - x_{cg(ref)}$; x_{cg} *and* $x_{cg(ref)}$ *are negative distances from the nose; T_D is distance from the nose to $c/4$ of MAC of tail — a negative distance.*

the missile are considered negative (measured in the negative X direction). The aerodynamic forces acting on the missile for tail control ($\delta_c = 0$) are F_z, acting at the center of pressure (cp), and F_t, assumed to be acting at the quarter chord point of the mean aerodynamic chord (MAC). The moments generated by these forces are

$$\mathcal{M} = x_{cp}F_z + (x_{cg} - T_D)F_t \tag{7-2}$$

where

$$F_z = SqC_{z_\alpha}\alpha$$

$$F_t = SqC_{z_{\delta_t}}\delta_t \tag{7-3}$$

Substituting Eq. 7-3 into Eq. 7-2 yields

$$\mathcal{M} = x_{cp}SqC_{z_\alpha}\alpha + (x_{cg} - T_D)SqC_{z_{\delta_t}}\delta_t \tag{7-4}$$

Going to the coefficient form by dividing by Sqd yields

$$C_m = \frac{x_{cp}}{d}C_{z_\alpha}\alpha + \frac{x_{cg} - T_D}{d}C_{z_{\delta_t}}\delta_t \tag{7-5}$$

In like manner

$$C_{m(ref)} = \frac{x_{cp(ref)}}{d}C_{z_\alpha}\alpha + \frac{x_{cg(ref)} - T_D}{d}C_{z_{\delta_t}}\delta_t \tag{7-6}$$

Subtracting Eq. 7-6 from Eq. 7-5 and solving for C_m yields

$$C_m = C_{m(\text{ref})} + \frac{\Delta x_{cg}}{d} C_{z_\alpha} \alpha + \frac{\Delta x_{cg}}{d} C_{z_{\delta_t}} \delta_t \tag{7-7}$$

But

$$C_{m(\text{ref})} = C_{m_\alpha(\text{ref})} \alpha + C_{m_{\delta_t}(\text{ref})} \delta_t \tag{7-8}$$

Substituting Eq. 7-8 into Eq. 7-7 yields

$$C_m = \left(C_{m_\alpha(\text{ref})} + \frac{\Delta x_{cg}}{d} C_{z_\alpha} \right) \alpha + \left(C_{m_{\delta_t}(\text{ref})} + \frac{\Delta x_{cg}}{d} C_{z_{\delta_t}} \right) \delta_t \tag{7-9}$$

But

$$C_m = C_{m_\alpha} \alpha + C_{m_{\delta_t}} \delta_t \tag{7-10}$$

Comparing like terms between Eq. 7-9 and Eq. 7-10 yields the equations for C_{m_α} and $C_{m_{\delta_t}}$ in terms of the reference values and the correction for the location of the cg relative to the reference cg. Thus

$$C_{m_\alpha} = C_{m_\alpha(\text{ref})} + \frac{\Delta x_{cg}}{d} C_{z_\alpha}$$

$$C_{m_{\delta_t}} = C_{m_{\delta_t}(\text{ref})} + \frac{\Delta x_{cg}}{d} C_{z_{\delta_t}} \tag{7-11}$$

For the case of canard control with $\delta_t = 0$, the moment correction for the canard is

$$C_{m_{\delta_c}} = C_{m_{\delta_c}(\text{ref})} + \frac{\Delta x_{cg}}{d} C_{z_{\delta_c}} \tag{7-12}$$

To check the correctness of Eqs. 7-11 and 7-12 the signs of the terms will be examined. For the C_{m_α} equation, $C_{m_\alpha(\text{ref})}$, C_{z_α}, and Δx_{cg} are all negative thus the magnitude of C_{m_α} will be reduced which is consistent with the figure (actual cg closer to cp than the reference cg is). The same is true for the case of $C_{m_{\delta_t}}$, where again all the terms are negative, thus reducing the magnitude of $C_{m_{\delta_t}}$, which is again consistent with Figure 7-6. In the case of Eq. 7-12, $C_{m_{\delta_c}(\text{ref})}$ is positive while Δx_{cg} and $C_{z_{\delta_c}}$ are negative, resulting in an increase in $C_{m_{\delta_c}}$ as expected.

From Table 7-1 it can be seen that C_{m_q} and $C_{m_{\dot\alpha}}$ were neglected, as is often the case with missiles. Most missiles will have some pitch damping from the main wing if they are similar to the one shown in Figure 7-5 without the canards. If the missile has a fixed wing plus a tail surface, then C_{m_q} will be

larger. As $C_{m_{\dot{\alpha}}}$ results from the time required for the downwash generated by the wing to reach the tail, unless the missile has a wing and tail there will be no downwash effect. This would be true of the missile sketched in Figure 7-5 without the canards. Such a configuration is assumed for the missile being studied here. However, if either C_{m_q} or $C_{m_{\dot{\alpha}}}$ is nonzero, then the reference values of these stability derivatives must be corrected for the actual cg location. The correction equation can be derived from Eq. 1-97, which is repeated here:

$$C_{m_q} = \frac{1}{Sqd}\left(\frac{2V_M}{d}\right)\frac{\partial \mathcal{M}}{\partial \dot{\theta}} \tag{7-13}$$

The pitching moment due to the pitch rate of the missile results from the change in the lift of the tail caused by a change in the angle of attack of the tail. Then from Eq. 1-94

$$\Delta \alpha_t = (x_{cg} - T_D)\dot{\theta}/V_M \tag{7-14}$$

Thus the resulting change in F_t is

$$\Delta F_t = SqC_{z_{\alpha_t}}\Delta \alpha_t \tag{7-15}$$

where

$$C_{z_{\alpha_t}} = -C_{L_{\alpha_t}}$$

with $\delta_t = 0$.

The moment due to the pitch rate is

$$\mathcal{M} = \Delta F_t(x_{cg} - T_D) \tag{7-16}$$

Substituting Eq. 7-14 into Eq. 7-15 and the results into Eq. 7-16 yields

$$\mathcal{M} = SqC_{z_{\alpha_t}}(x_{cg} - T_D)^2\dot{\theta}/V_M \tag{7-17}$$

Differentiating,

$$\frac{\partial \mathcal{M}}{\partial \dot{\theta}} = SqC_{z_{\alpha_t}}(x_{cg} - T_D)^2/V_M \tag{7-18}$$

Substituting Eq. 7-18 into Eq. 7-13 yields

$$C_{m_q} = 2C_{z_{\alpha_t}}\left(\frac{x_{cg} - T_D}{d}\right)^2 \tag{7-19}$$

TABLE 7-2   Missile Transfer Functions for the Dynamic Analysis

Case	t (sec)	$\dot{\theta}(s)\,/\,\delta_t(s)$ (1 / sec)
1	3	$\dfrac{-106.47(s+0.418)}{s^2+0.644s+86.4}$
2	5	$\dfrac{-279.61(s+0.775)}{s^2+0.95s+116.87}$
3	12	$\dfrac{-369.4(s+0.94)}{s^2+1.098s+126.4}$
4	20	$\dfrac{-469.6(s+1.2)}{s^2+1.27s+72.25}$
5	26	$\dfrac{-247.7(s+0.64)}{s^2+0.764s+95.46}$
6	27	$\dfrac{-224.75(s+0.603)}{s^2+0.726s+91.4}$

Now

$$C_{m_q(\text{ref})} = 2C_{z_{a_t}}\left(\frac{x_{\text{cg(ref)}} - T_D}{d}\right)^2 \tag{7-20}$$

Dividing Eq. 7-19 by Eq. 7-20 and solving for C_{m_q} yields

$$C_{m_q} = C_{m_q(\text{ref})}\left(\frac{x_{\text{cg}} - T_D}{x_{\text{cg(ref)}} - T_D}\right)^2 \; 1/\text{rad} \tag{7-21}$$

The same equation can be used for $C_{m_{\dot{\alpha}}}$ by replacing C_{m_q} with $C_{m_{\dot{\alpha}}}$. From Eq. 7-21 it can be seen that if the reference cg is ahead of the actual cg, as shown in Figure 7-6, the correction will result in a reduction in the magnitude of C_{m_q} from its reference value. The opposite will be the case if the reference cg is behind the actual cg.

This completes the discussion of the stability derivatives used to calculate the missile transfer functions. The transfer functions for the data contained in Table 7-1 are given in Table 7-2.

Figure 7-7 is a block diagram of a typical missile autopilot found in present day air-to-air and surface-to-air missiles. As the missile is symmetrical with respect to the Y and Z axes, the pitch and yaw autopilots are the same. The pitch autopilot is shown in Figure 7-7, which employs rate feedback to damp the short-period oscillations. There are two paths shown
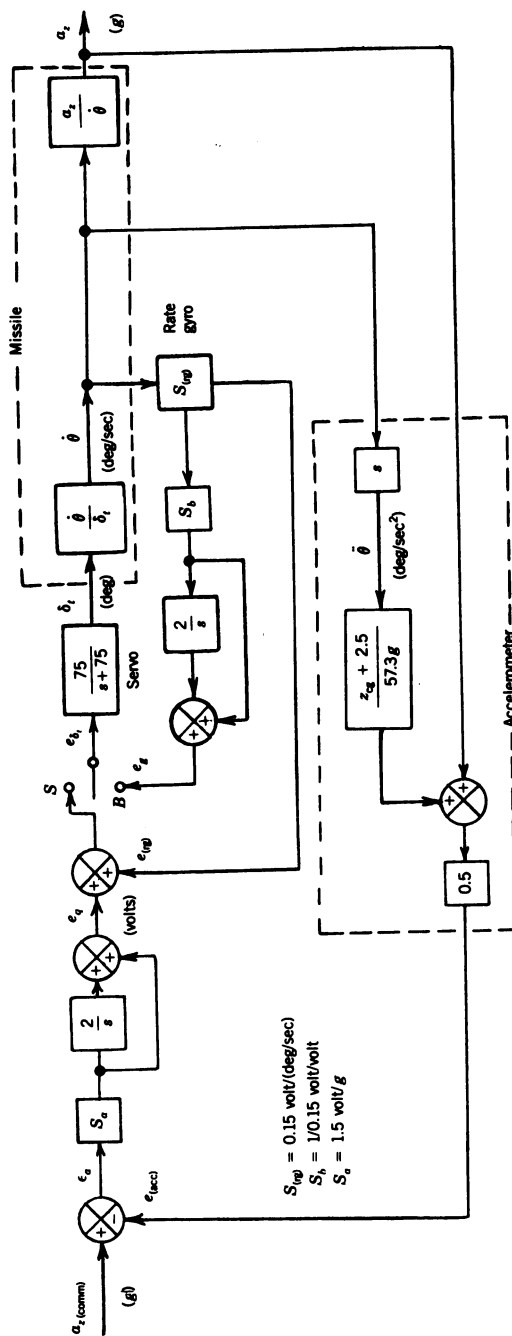
Figure 7-7 Block diagram of missile autopilot.

$S_{(rg)} = 0.15$ volt/(deg/sec)
$S_b = 1/0.15$ volt/volt
$S_a = 1.5$ volt/g
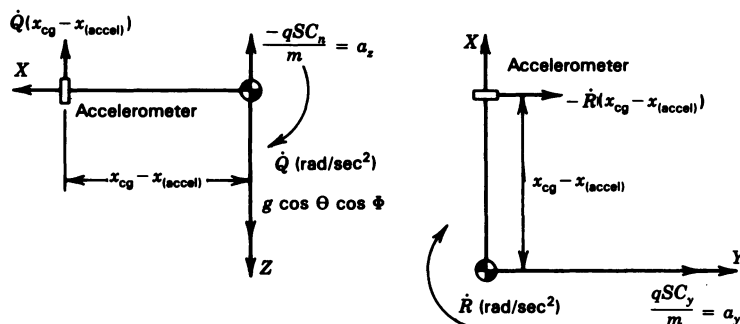
Figure 7-8 *Accelerations sensed by accelerometer located forward of missile cg.*

for the rate feedback signal: one is for the boost phase (B), the other for the sustainer and coast phases (S). As the missile is not guided during the boost phase, the integration in the boost phase loop attempts to zero out the missile pitch rate, thus providing pitch control during boost (no control required in yaw). At the termination of boost the acceleration loop and alternate rate feedback loop are engaged (switch in S position). As the accelerometer is not located at the missile center of gravity (cg), the accelerometer will sense both the normal acceleration of the missile cg (a_z) and the tangential acceleration due to a pitch angular acceleration ($\ddot{\theta}$). To understand the choice of signs at the summer in the accelerometer block it is necessary to examine Figure 7-8 which shows the accelerations sensed by an accelerometer located ahead of the missile cg. In the figure x_{cg} and $x_{(accel)}$ are the distances from the nose of the missile to the missile cg and accelerometer respectively, with both distances taken as negative. For this example $x_{(accel)} = -2.5$ m. Then for the pitch loop, a positive pitch rate (positive angle of attack) resulting from a negative pitch tail deflection will generate a negative a_z. This fin deflection will also generate a positive pitch angular acceleration, resulting in a negative output from the accelerometer. The sign of $x_{cg} + 2.5$ will be negative, as the magnitude of x_{cg} is greater than 2.5. As both acceleration terms have the same sign, they are summed positively at the summer. This is not true for the yaw channel, where both a positive yaw rate (negative sideslip angle) and yaw angular acceleration result in a positive accelerometer output. But as the sign of $x_{cg} + 2.5$ is negative, the angular acceleration term must be subtracted from a_y to obtain the proper accelerometer output. Since the cg of the missile moves forward as the rocket fuel is burned, the distance between the missile cg and the accelerometer decreases, thus reducing the magnitude of the tangential acceleration sensed by the accelerometer. The equations for the outputs of
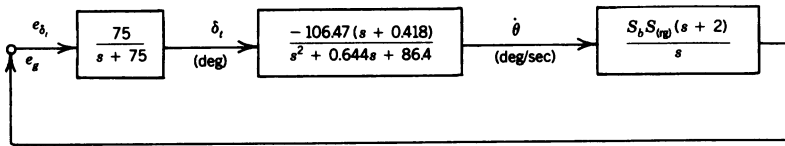
Figure 7-9 Block diagram for the boost autopilot.

the two accelerometers are

$$a_{z_a} = \frac{-qSC_n}{m} + \dot{Q}(x_{cg} + 2.5) \text{ m/sec}^2$$

$$a_{y_a} = \frac{qSC_y}{m} - \dot{R}(x_{cg} + 2.5) \text{ m/sec}^2 \tag{7-22}$$

after substituting for the accelerometer location.

Using the missile transfer function for case 1, the block diagram for the boost autopilot can be redrawn as shown in Figure 7-9. The root locus is shown in Figure 7-10 with the closed loop poles indicated for $S_b S_{(rg)} = 1$. The closed loop transfer function is

$$\frac{\dot{\theta}(s)}{e_g(s)} = \frac{-7985.25(s+2)(s+0.418)}{(s+0.284)(s+2.98)(s^2+72.38s+7882)} \tag{7-23}$$

From Eq. 7-23 it can be determined that the damping ratio for the complex closed loop poles is 0.41 with a damped natural frequency of 81.07 rad/sec; thus the real pole at -0.284 is dominant. The boost autopilot proved quite
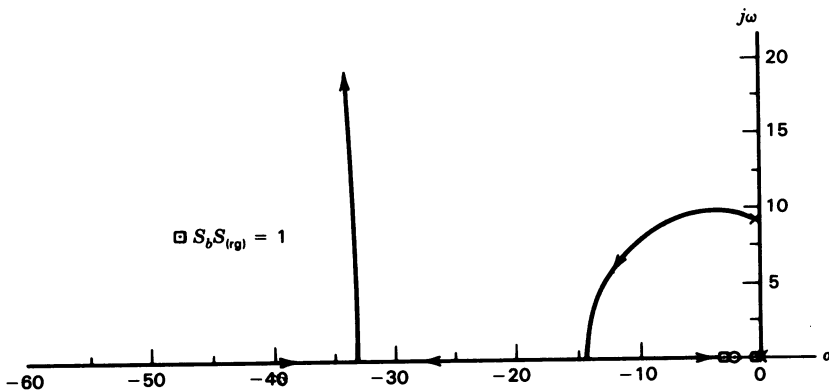
Figure 7-10 Root locus for the boost autopilot.
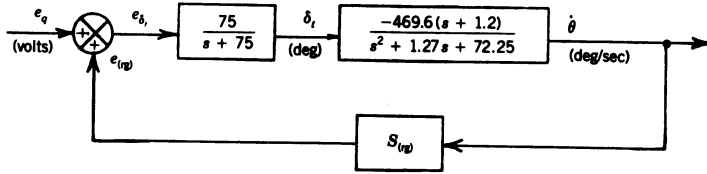
Figure 7-11   Block diagram of the rate loop for the complete missile autopilot.

adequate, as the missile pitch angle decreased by only 0.5° from the launch angle of 19.8°.

The block diagram for the inner loop of the complete autopilot for case 4 (maximum dynamic pressure) is shown in Figure 7-11 and the closed loop transfer function for $S_{(rg)} = 0.15$ volt/(deg/sec) is

$$\frac{\dot{\theta}(s)}{e_q(s)} = \frac{-35220(s+1.2)}{(s+2.22)(s^2+74.04s+5285.5)} \qquad (7\text{-}24)$$

The root locus is not drawn, as it is typical of pitch rate feedback plots (see Figure 2-8). Using the closed loop transfer function from Eq. 7-24, the block diagram for the acceleration feedback loop from Figure 7.7 can be drawn and is shown in Figure 7-12. The $a_z(s)/\dot{\theta}(s)$ transfer function is the ratio of the $a_z(s)/\delta_t(s)$ transfer function to the $\theta(s)/\delta_t(s)$ transfer function. The a_z transfer function for case 4 is

$$\frac{a_z(s)}{\delta_t(s)} = \frac{-0.964(s+34.41)(s-34.41)}{s^2+1.27s+72.25} \quad \frac{g}{\text{deg}} \qquad (7\text{-}25)$$

then using the $\dot{\theta}$ transfer function for case 4 from Table 7-2, the $a_z(s)/\dot{\theta}(s)$ transfer function is

$$\frac{a_z(s)}{\dot{\theta}(s)} = \frac{0.00205(s+34.41)(s-34.41)}{s+1.2} \quad \frac{g}{\text{deg/sec}} \qquad (7\text{-}26)$$

From Figure 7-12

$$\frac{a_{z_a}(s)}{\dot{\theta}(s)} = \frac{(x_{cg}+2.5)s}{57.3g} + \frac{a_z(s)}{\dot{\theta}(s)} \qquad (7\text{-}27)$$

From Table 7-1, $x_{cg} = -3.16$ m; then for $g = 9.81$ m/sec^2

$$\frac{x_{cg}+2.5}{57.3g} = -0.001174g \qquad (7\text{-}28)$$
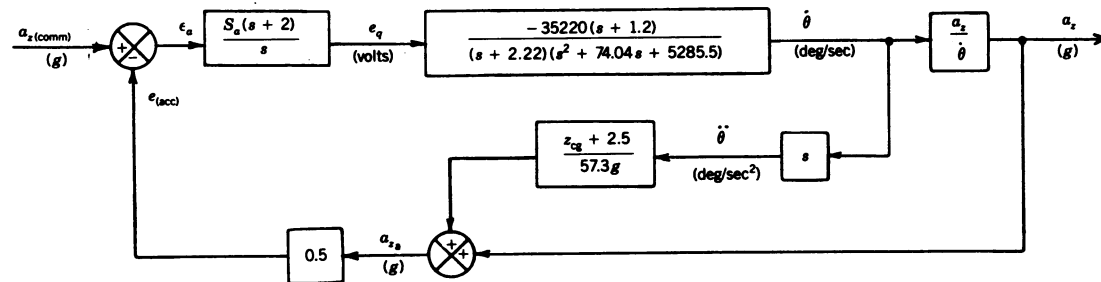
$$\frac{a_z(s)}{\dot{\theta}(s)} = \frac{55.22\,(s + 34.41)\,(s - 34.41)}{-\,(57.3)\,(469.6)\,(s + 1.2)}\;\frac{g}{\text{deg/sec}}$$

Figure 7-12 Block diagram of acceleration loop of the complete missile autopilot.
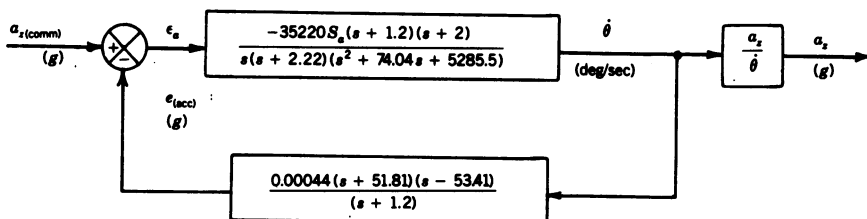
Figure 7-13 *Simplified block diagram of the accelerometer loop for root locus analysis.*

Substituting Eqs. 7-26 and 7-28 into Eq. 7-27 yields

$$\frac{a_{z_a}(s)}{\dot{\theta}(s)} = \frac{0.00088(s+51.81)(s-53.41)}{s+1.2} \quad \frac{g}{deg/sec} \qquad (7\text{-}29)$$

Using Eq. 7-29, Figure 7-12 can be redrawn as shown in Figure 7-13.

Figure 7-14 is the zero-angle root locus for the acceleration loop shown in Figure 7-13, and the Bodé root locus (see Section C-9) is shown in Figure 7-15. The locations of the closed loop poles for $S_a = 1.5$ are indicated in both figures. The closed loop transfer function is

$$\frac{\dot{\theta}(s)}{a_{z(comm)}(s)} = \frac{-52830(s+1.2)(s+2)}{(s+1.96)(s+13.58)(s^2+37.48s+4830.81)} \quad \frac{deg/sec}{g}$$

$$(7\text{-}30)$$

From Figure 7-15 the phase margin is 85°, and the gain margin is 3.16. The gain margin frequency can be obtained from either figure and is 73.56
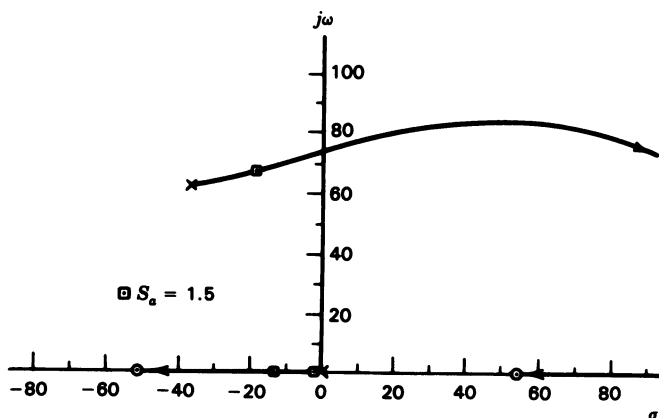
Figure 7-14 *Root locus for acceleration loop of the missile autopilot (zero-angle root locus).*
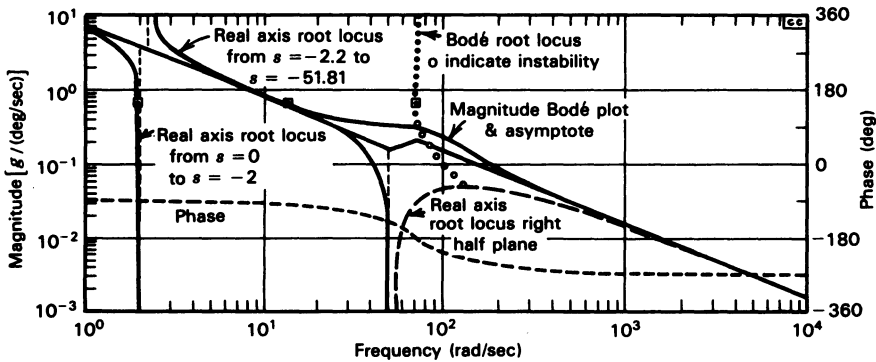
Figure 7-15 *Bodé root locus for acceleration loop of the missile autopilot.*

rad/sec. As a result of the logarithmic scale used for the Bodé root locus, the portion of the root locus in the vicinity of the origin is enlarged. Thus the root locus from the origin to the pole at $s = -2$ is much expanded. From Figure 7-15 the break-in point in the right half plane occurs at $s = 106$. Multiplying Eq. 7-30 by Eq. 7-26 yields the final closed loop transfer function for an acceleration input command to a missile output acceleration:

$$\frac{a_z(s)}{a_{z(\text{comm})}(s)} = \frac{-108.3(s+2)(s+34.41)(s-34.41)}{(s+1.96)(s+13.58)(s^2+37.48s+4830.81)} \quad (7\text{-}31)$$

Equation 7-31 will be used in Chapter 8 for the root locus analysis of the guidance schemes studied. An application of the final value theorem to Eq. 7-31 for a unit step input shows that the steady-state value of a_z is $2g$. This results from the gain of 0.5 in the feedback loop and the integration in the forward loop resulting in a Type 1 system.

This concludes the analysis of this missile autopilot. However, there is another type of control frequently employed for aerodynamic missiles, and that is the use of hinge moment commands to the canards. This type of control will be discussed next.

Figure 7-16 is the block diagram of an air-to-air missile autopilot employing torque or hinge moment commands to the canards. The $e_{\theta(\text{comm})}$ would come from one of the types of guidance systems discussed in Chapter 8. The canard command e_{δ_c} is compared with the actual canard position, and the error signal is converted to a torque command T_c by the $750(s+5)/(s+50)$ transfer function, which combines a torque generator and lead compensator. The torque command is compared with the hinge moment feedback T_h (the hinge moment coefficients are negative), and the resulting torque drives the canard. The 100 gain in the feedback path of the inner loop represents the inverse motor time constant. The $H_A(s)/\delta(s)$ transfer function for Mach
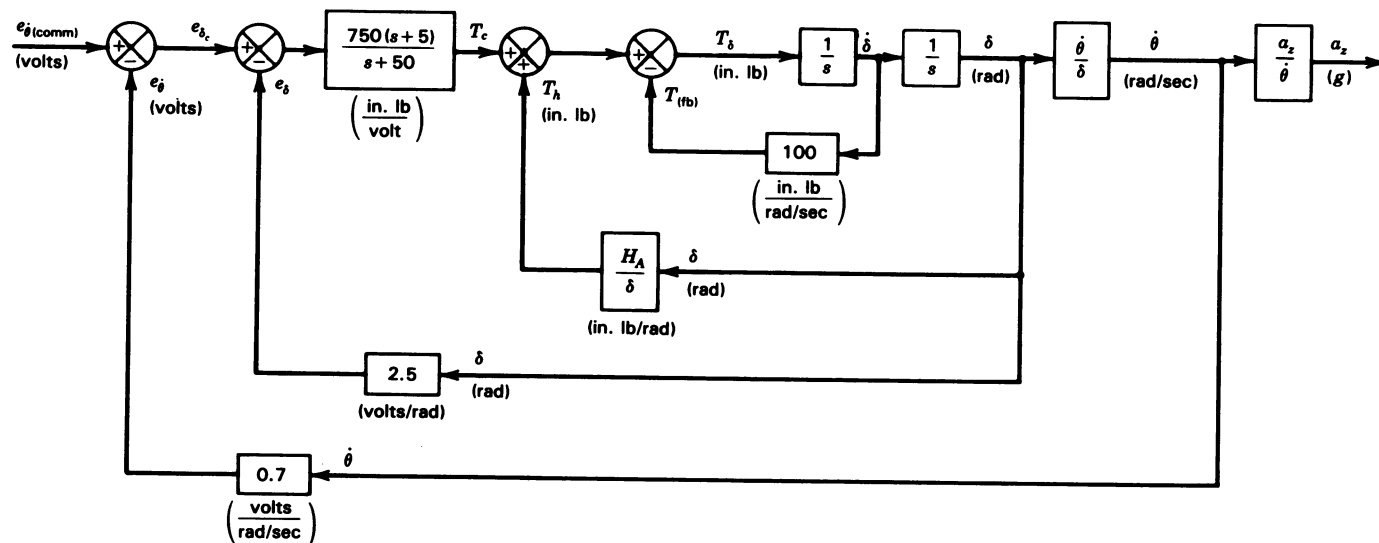
Figure 7-16 Block diagram for canard control, hinge moment control autopilot.

2.44 at 6096 m is

$$\frac{H_A(s)}{\delta(s)} = Sqd\left(C_{H_\delta} + C_{H_\alpha}\frac{\alpha(s)}{\delta(s)}\right) \text{ in. lb/rad}$$

where

$C_{H_\delta} = -0.034$ 1/rad is the slope of the curve of hinge moment coefficient versus canard deflection,

$C_{H_\alpha} = -0.04$ 1/rad is the slope of the hinge moment coefficient curve versus missile angle of attack, and

$$\frac{\alpha(s)}{\delta(s)} = \frac{-0.066(s - 4591.3)}{s^2 + 1.652s + 424.63} \tag{7-32}$$

Substituting the values into the hinge moment equation yields

$$\frac{H_A(s)}{\delta(s)} = \frac{-116.8(s^2 + 1.56s + 811.72)}{s^2 + 1.652s + 424.63} \quad \frac{\text{in. lb}}{\text{rad}} \tag{7-33}$$

Using the closed loop transfer function of the inner loop and Eq. 7-33, the block diagram for the torque loop for the root locus analysis is shown in Figure 7-17 and the corresponding root locus in Figure 7-18 with the location of the closed loop poles indicated. Although the paths of the complex poles as they move to the complex zeros cross into the right half plane, the torque loop is stable. The closed loop transfer function for the poles shown in Figure 7-18 is

$$\frac{\delta(s)}{T_c(s)} = \frac{s^2 + 1.652s + 424.63}{(s + 2.28)(s + 98.77)(s^2 + 0.6s + 420.75)} \quad \frac{\text{rad}}{\text{in. lb}} \tag{7-34}$$

Using Eq. 7-34, the block diagram of the δ feedback loop of Figure 7-16 can be drawn as shown in Figure 7-19. The corresponding root locus is shown in Figure 7-20 with the location of the closed loop poles indicated. The closed
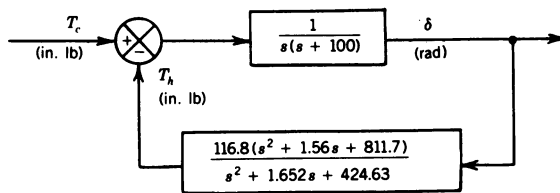
Figure 7-17   Block diagram for torque loop of Figure 7-16 for root locus analysis.
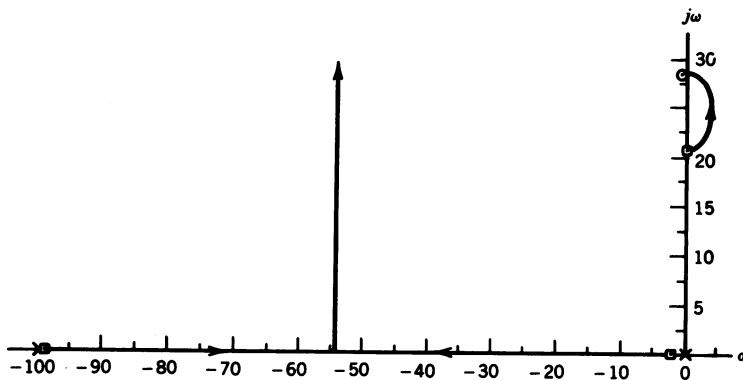
Figure 7-18   *Root locus for torque loop shown in Figure 7-17.*
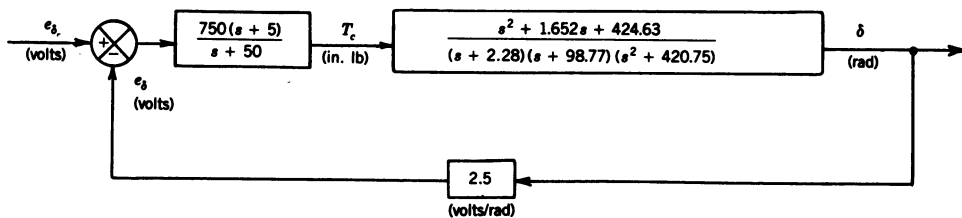
Figure 7-19   *Block diagram for δ loop of Figure 7-16 for root locus analysis.*
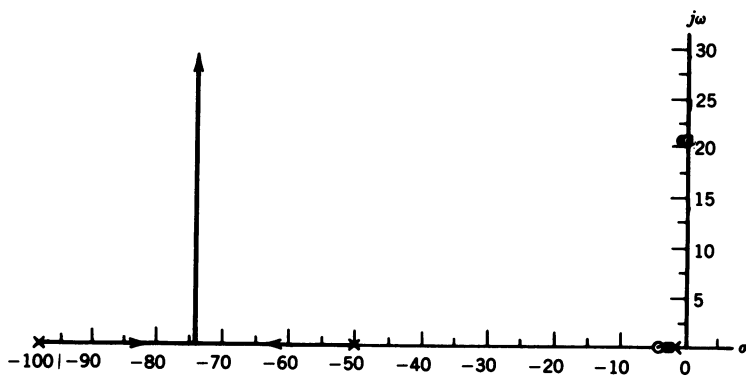
Figure 7-20   *Root locus for δ loop shown in Figure 7-19.*
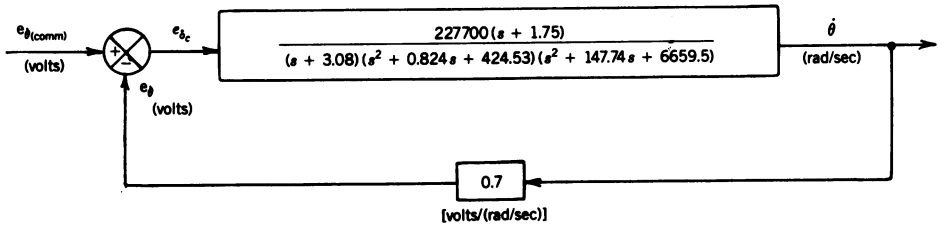
Figure 7-21 Block diagram of outer loop of Figure 7-16 for root locus analysis.

loop transfer function for the δ feedback loop is

$$\frac{\delta(s)}{e_{\delta_c}(s)} = \frac{750(s^2 + 1.652s + 424.63)}{(s + 3.08)(s^2 + 0.824s + 424.53)}$$

$$\times \frac{s + 5}{s^2 + 147.74s + 6659.48} \frac{\text{rad}}{\text{volt}} \quad (7\text{-}35)$$

The missile transfer function is

$$\frac{\dot{\theta}(s)}{\delta(s)} = \frac{303.6(s + 1.75)}{s^2 + 1.652s + 424.63} \quad (7\text{-}36)$$

Multiplying Eq. 7-35 by Eq. 7-36 yields the forward transfer function for the outer loop of Figure 7-16. The block diagram for this loop is shown in Figure 7-21; the corresponding root locus is shown in Figure 7-22 and the Bodé root locus in Figure 7-23, with the locations of the closed loop poles indicated in both figures. As a result of the two zeros in the forward transfer function of Figure 7-21, the phase angle swings positive before going negative at the
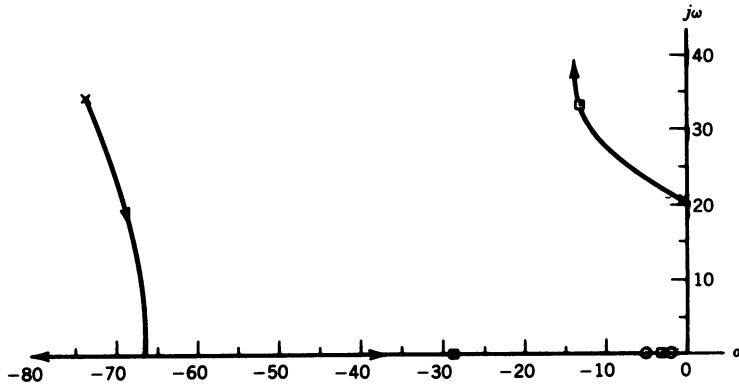
Figure 7-22 Root locus for the outer loop shown in Figure 7-21.
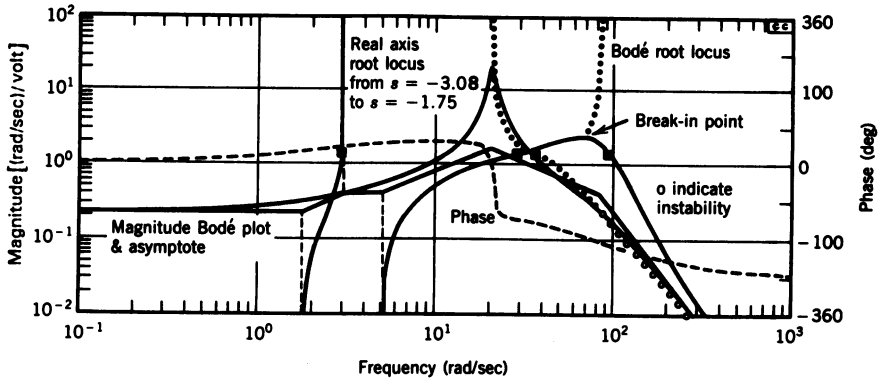
Figure 7-23   *Bodé root locus for the outer loop shown in Figure 7-21.*

missile natural frequency of 20.6 rad/sec. The phase margin is 37.15° with a gain margin of 3.75. From Figure 7-23 it can be seen that the branch of the root locus emanating from the missile poles crosses into the right half plane at $j\omega = 78.76$ rad/sec. The final closed loop transfer function is

$$\frac{\dot{\theta}(s)}{e_{\dot{\theta}(comm)}(s)} = \frac{227700(s+1.75)(s+5)}{(s+2.94)(s+28.68)(s+93.26)}$$

$$\times \frac{1}{s^2 + 26.78s + 1287.5} \quad \frac{rad/sec}{volt} \qquad (7\text{-}37)$$

The damping ratio for the closed loop complex poles is 0.37. Without the lead compensator the open loop complex poles originating near the imaginary axis move directly into the right half plane. The analysis also showed that the compensator resulted in better damping of these dominant poles by being placed in the forward path of the δ feedback loop rather than in the forward path of the outer loop.

To obtain the acceleration step response the $a_z/\dot{\theta}$ transfer function

$$\frac{a_z(s)}{\dot{\theta}(s)} = \frac{-0.056(s^2 + 8.7s + 8050)}{s + 1.75} \quad \frac{g}{rad/sec} \qquad (7\text{-}38)$$

is required. The acceleration response for a unit step input of $e_{\dot{\theta}(comm)}$ is shown in Figure 7-24. The response is considered excellent: the steady-state condition is reached in 1.2 sec. The steady value of about $-50g$ for a 1-volt input command would have to be compensated for in the scaling and sign of the input guidance command.

This concludes the discussion of the control of aerodynamic missiles.
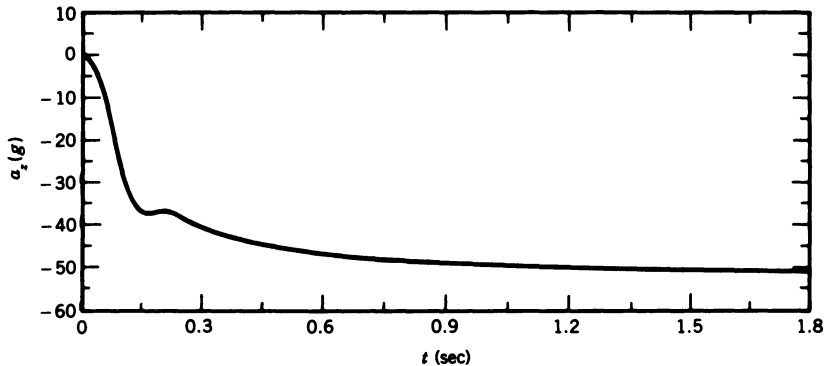
Figure 7-24   *Acceleration step response for canard hinge moment controlled missile.*

7-4   TRANSFER FUNCTION FOR A BALLISTIC-TYPE MISSILE

Because all detailed information on ballistic missiles is classified, the Van-guard missile is used here to illustrate the control problems associated with ballistic missiles. The stability derivatives for the rigid missile, the structural transfer function, and the block diagram of the autopilot were furnished through the courtesy of the Martin Company, Baltimore, Maryland.

To derive the transfer function of the missile, it is necessary to orient the missile axis system. The trajectory of ballistic-type missiles is planned to maintain the missile at a zero angle of attack. This is normally attempted by programming the pitch attitude or pitch rate to yield a zero-g trajectory. This, of course, assumes a certain velocity profile, which may or may not be realized due to variations in the fuel flow rate. This condition and the presence of gusts result in the angle of attack not being zero at all times; however, the angle of attack must be kept small to avoid excessive loading of the structure. Therefore the assumption of zero angle of attack for the equilibrium condition is quite valid, and any changes in angle of attack can be considered perturbations from the equilibrium condition. With this assump-tion, if the X axis of the missile is along the longitudinal axis of the missile, this body axis system becomes a stability axis system. By placing the Z axis in the trajectory plane, all pitch motion is about the Y axis (see Figure 7-25). Basically the axis system is the same as the one used for the pitching motion for the aircraft (see Figure 1-3). Assuming that the angle of attack is zero for the equilibrium condition, then α for the missile is the same as $'\alpha$ for the aircraft. For the missile to fly a zero-angle-of-attack trajectory, the centripetal acceleration resulting from the curved trajectory $(-V_T\dot{\gamma})$ must equal the component of weight normal to the X axis, which establishes the equilibrium condition. The dynamic analysis to follow is based on perturbations from this equilibrium condition. It should be noted from Figure 7-25 that if an angle of

Figure 7-25 *Ballistic missile axis system.*

attack is generated, the lift vector acting at the center of pressure (cp) has a destabilizing effect. This factor is one of the major control problems of the missile.

In the derivation of the aircraft's equations of motion, certain assumptions were made, which are reviewed here for their applicability to the missile control problem. These assumptions are listed on p. 25, and are repeated here for reference with the word missile replacing the word aircraft. The assumptions are

1. The X and Z axes lie in the plane of symmetry, and the origin of the axis system is located at the center of gravity of the missile. (Actually the X and Y axes also lie in a plane of symmetry.)
2. The mass of the missile is constant.
3. The missile is a rigid body.
4. The earth is an inertial reference.
5. The perturbations from equilibrium are small.

All these assumptions are still valid. Although the missile is consuming fuel

at a terrific rate, if the instantaneous mass is used, the mass may be assumed constant during the period of analysis. The ballistic missile in general cannot be considered a rigid body; however, the missile is first analyzed as a rigid body and then the effect of body bending is studied in Chapter 11.

The assumption that the earth is an inertial reference is satisfactory for the analysis of the control system but not of the inertial guidance system that would be sending the command signals to the control system. The assumption of small perturbations is even more valid for the ballistic missile than for the aircraft. Because the perturbations have been assumed small, and as the duration of the disturbance is short, the velocity can be assumed constant during the period of the dynamic analysis. Thus the equations for the short-period approximation of the aircraft may be used for the longitudinal analysis. From Eq. 1-128 these equations are

$$\left(\frac{mU}{Sq}s - C_{z_\alpha}\right)\alpha(s) + \left(-\frac{mU}{Sq}s - C_w\sin\Theta\right)\theta(s) = C_{z_\delta}\delta$$

$$\left(-\frac{d}{2U}C_{m_{\dot{\alpha}}}s - C_{m_\alpha}\right)\alpha(s) + \left(\frac{I_y}{Sqd}s^2 - \frac{d}{2U}C_{m_q}s\right)\theta(s) = C_{m_\delta}\delta \quad (7\text{-}39)$$

where c has been replaced by d, the diameter of the missile. In the case of the aircraft, $C_{m_{\dot{\alpha}}}$ arose from the time lag for the downwash created by the wing to reach the tail. As there is neither a wing nor a horizontal stabilizer for this missile, $C_{m_{\dot{\alpha}}} = 0$. The actuating signal δ is the deflection of the thrust chamber, with the same sign convention as was used for the conventional aircraft. The component of thrust normal to the X axis is proportional to $\sin\delta$; however, if δ is small, $\sin\delta$ can be replaced by δ in radians. The values of the rest of the quantities in Eq. 7-39 are given for the time of maximum dynamic pressure, which occurred at 75 sec after launch, at an altitude of 36,000 ft, a velocity of 1285 ft/sec, and a mass of 445 slugs. Then

$$C_{m_\delta} = -\frac{Tl}{Sqd} = -34.25$$

$$C_{z_\delta} = -\frac{T}{Sq} = -4.63$$

$$C_{z_\alpha} = -3.13$$

$$C_{m_\alpha} = +11.27 \qquad (\text{as the cp is ahead of the cg})$$

$$l = 27 \text{ ft}$$

$$\Theta_0 = 68.5°$$

$$d = 3.75 \text{ ft}$$

$$q = 585 \text{ lb/sq ft}$$

$$S = 11.04 \text{ sq ft}$$

$$\frac{d}{2U} C_{m_q} = -0.321 \text{ sec}$$

$$\frac{mU}{Sq} = 88.5 \text{ sec}$$

$$\frac{mg}{Sq} = -C_w = 2.22$$

$$I_y = 115{,}000 \text{ slug ft}^2$$

$$\frac{I_y}{Sqd} = 4.75 \text{ sec}^2$$

Substituting these values, Eq. 7-39 becomes

$$(88.5s + 3.13)\alpha(s) + (-88.5s + 2.06)\theta(s) = -4.63\delta(s)$$

$$-11.27\alpha(s) + (4.75s^2 + 0.321s)\theta(s) = -34.25\delta(s) \quad (7\text{-}40)$$

Then the transfer function for δ input to θ output is

$$\frac{\theta(s)}{\delta(s)} = \frac{-7.21(s + 0.0526)}{(s + 1.6)(s - 1.48)(s - 0.023)} \quad (7\text{-}41)$$

Equation 7-41 shows that the missile is unstable with a pole at $+1.48$. The pole at $+0.023$ arises from the fact that Θ_0 is not zero.

7-5 VANGUARD CONTROL SYSTEM (RIGID MISSILE)

One of the main functions of the control system is to stabilize the otherwise unstable missile. To accomplish this, the Martin Company added a lead compensator to the forward loop. Figure 7-26 is the block diagram for the Vanguard rigid body control system. The transfer function of the servo is

$$[\text{TF}]_{(\text{servo})(\delta_i;\,\delta)} = \frac{2750}{s^2 + 42.3s + 2750} \quad (7\text{-}42)$$
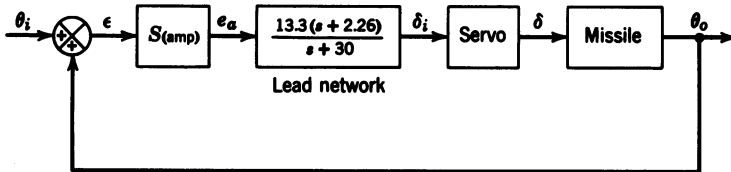
Figure 7-26 Vanguard control system (rigid missile).
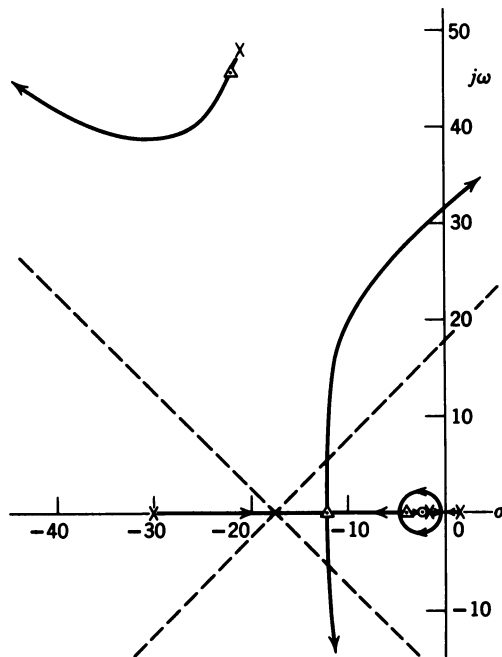
$\triangle\ S_{(amp)} = 2.3$ volt/volt

Figure 7-27 *Root locus for the Vanguard rigid body control system.*

After canceling the zero at -0.0526 with the pole at 0.023, the missile transfer function is

$$[\text{TF}]_{(\text{missile})(\delta:\theta)} \simeq \frac{-7.21}{(s+1.6)(s-1.48)} \qquad (7\text{-}43)$$

The root locus for the Vanguard control system is plotted in Figure 7-27. The stabilizing action of the lead network is apparent.

The student is probably wondering about the pole and zero that were canceled in the missile transfer function. Figure 7-28 is an exploded view of the root locus in the vicinity of the origin. From Figure 7-28 it can be seen that only the portion of the root locus near the origin is modified by the addition of the canceled pole and zero. The angle contribution of the canceled pole and zero to the rest of the root locus is negligible. Actually the missile pole at -1.6 can be canceled by the zero of the lead compensator without significantly changing the root locus.

Another control system that is capable of controlling the Vanguard or similar missiles is discussed in Section 7-6.
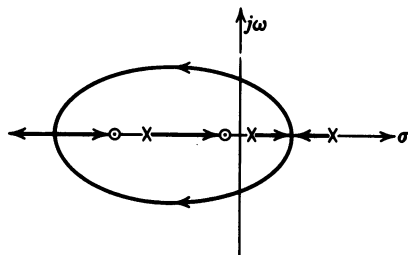
Figure 7-28 *Root locus in the vicinity of the origin with the complete missile transfer function. Note: This figure is not to scale.*

7-6 ALTERNATE MISSILE CONTROL SYSTEM (RIGID MISSILE)

In Chapter 2 it was found that the pitch orientational control system was capable of controlling an aircraft that was unstable in pitch. This same basic autopilot then should be capable of controlling a ballistic missile. Some guidance systems also require that the control system be capable of accepting a commanded pitch rate. Thus a system of the same configuration as the pitch orientational control system should be very useful for ballistic missiles. Figure 7-29 is the block diagram for this system. The transfer function for the Vanguard is again used, and the same servo with the damping ratio increased to 0.8. Thus

$$[\text{TF}]_{(\text{servo})[\delta_i;\delta]} = \frac{2750}{s^2 + 84s + 2750} \qquad (7\text{-}44)$$
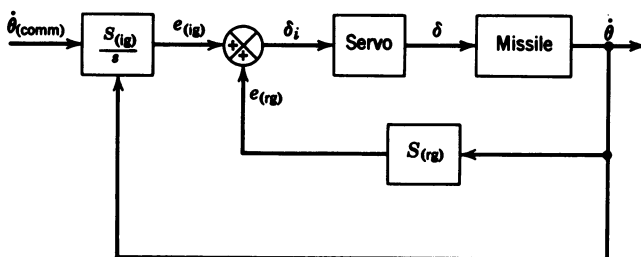
Figure 7-29 *Alternate missile control system (rigid missile).*
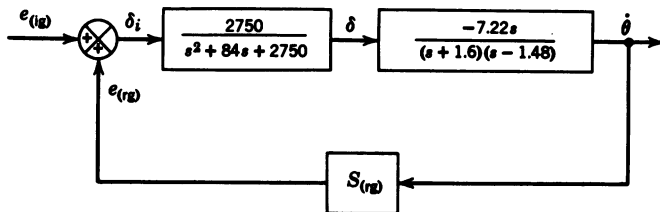
Figure 7-30 *Block diagram of inner loop of the alternate control system.*

$\square$ $S_{(rg)} = 1.58$ volt/rad/sec
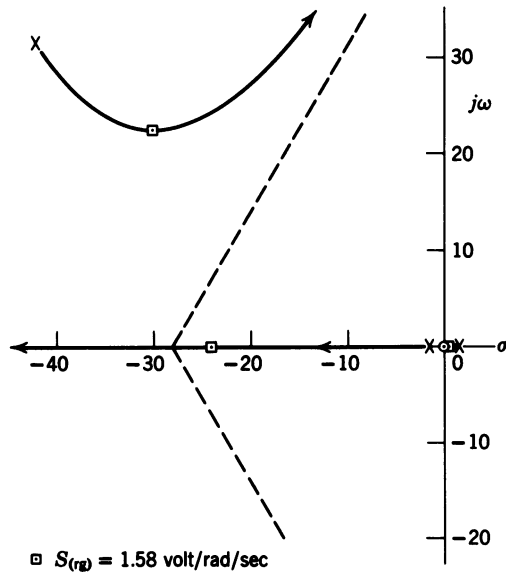
Figure 7-31   Root locus of the inner loop of the alternate control system.
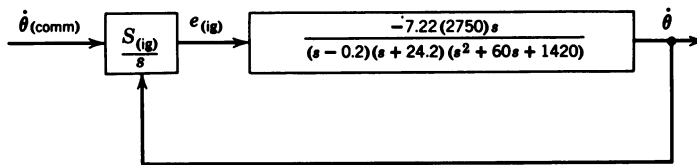
Figure 7-32   Block diagram for outer loop root locus.

$\square$ $S_{(ig)} = 10.2$ volt/rad/sec
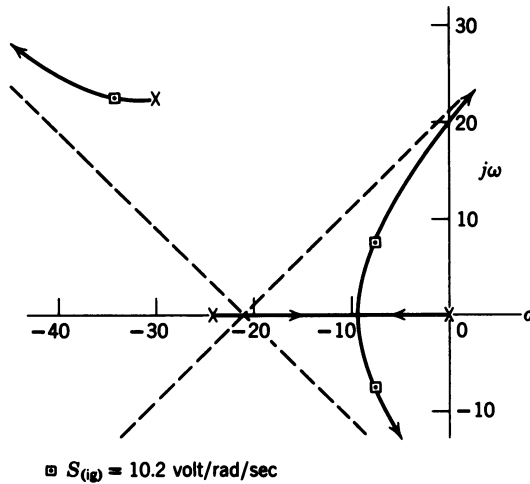
Figure 7-33   Root locus of the outer loop of the alternate control system.

TABLE 7-3 Aerodynamic Coefficients for the Vanguard Missile (Rigid Missile)

t (sec)	h (ft)	V (ft / sec)	M	q (lb / ft^2)	m (slugs)	Θ (deg)	C_{m_α}	C_{z_α}	$\dfrac{d}{2U}C_{m_q}$ (sec)	C_{m_δ}	C_{z_δ}	I_y (slug ft^2)
48	12,200	604	0.57	300	547	81.7	10.55	-3.08	-0.683	-60.83	-8.69	121,400
75	36,000	1285	1.26	585	445	68.5	11.27	-3.13	-0.321	-34.25	-4.63	115,000
100.4	76,000	2400	2.41 ·	300	354	57.2	16.59	-2.88	-0.172	-70.15	-9.17	104,000
139*	185,000	5600	5.02	12	218	46.5	8.32	-2.3	-0.0736	-2140	-229	75,400

*First-stage burnout, $l = 27$ ft, $S = 11.04$ ft^2, $d = 3.75$ ft.

Figure 7-30 is the block diagram for the inner loop showing the transfer functions of the servo and missile, and Figure 7-31 is the root locus for the inner loop. The locations of the closed loop poles of the inner loop are shown for a $S_{(rg)} = 1.58$ volt/(rad/sec). The rate gyro sensitivity is selected so that the missile pole at -1.6 will be driven well into the left half plane without excessively decreasing the damping of the servo.

The need for a higher value of the initial damping ratio of the servo is now evident. Figure 7-32 is the block diagram for the outer loop of the alternate control system using the closed loop poles from Figure 7-31. The root locus for the outer loop is shown in Figure 7-33 with the location of the closed loop poles for $S_{(ig)} = 10.2$ volt/(rad/sec). From Figure 7-33 it can be seen that this system is capable of controlling the instability of the ballistic missile or large booster rockets.

In order for the student to determine the control requirements for other portions of the power trajectory, Table 7-3 lists the aerodynamic coefficients for three other flight conditions in addition to the one already used.

7-7 SUMMARY

In this chapter the control of both aerodynamic and ballistic-type missiles has been discussed. It was shown that the analysis of missiles is simpler than the analysis of aircraft, since there is no coupling between the lateral and longitudinal modes, because the missiles are roll stabilized and turning is accomplished by yawing the missile. Thus the short-period approximation can be used for analyzing both the longitudinal and the lateral dynamics. Two control systems for aerodynamic missiles and two techniques for stabilizing ballistic type missiles were discussed.

REFERENCES

1. A. S. Locke, *Guidance*, D. Van Nostrand Company, Princeton, New Jersey, 1955.
2. C. Broxmeyer, *Inertial Navigation Systems*, McGraw-Hill Book Co., New York, 1964.
3. C. S. Draper, W. Wrigley, and J. Hovorka, *Inertial Guidance*, Pergamon Press, New York, 1960.
4. M. Fernandez and G. R. Macomber, *Inertial Guidance Engineering*, Prentice-Hall, Englewood Cliffs, New Jersey, 1962.
5. R. H. Parvin, *Inertial Navigation*, D. Van Nostrand Co., Princeton, New Jersey, 1962.
6. G. R. Pitman, Jr., *Inertial Guidance*, John Wiley and Sons, New York, 1962.

<div style="text-align: right;">

8

</div>

Guidance Systems

8-1   INTRODUCTION

In Chapter 7 an acceleration autopilot for an aerodynamic missile was examined and it was stated that the acceleration command would be provided by an appropriate guidance system. In this chapter two such guidance systems will be described and analyzed and their performance compared, using a digital simulation of the missile, autopilot, guidance system, and intercept geometry. The important parameters of the missile–target intercept are shown in Figure 8-1. An earth reference axis system (X_E, Y_E, Z_E), the same as the fixed axis system shown in Figure 1-2, is located at the missile M and target T. The headings of the missile Ψ_M and the target Ψ_T as well as the azimuth angle Ψ_R of the LOS from the missile to the target R are measured from the X_E axis as described in Section 1-4. As shown in Figure 8-1, Ψ_T is measured in the negative direction. The elevation angles of the missile, the target, and R are Θ_M, Θ_T, and Θ_R respectively. To simplify the figure the missile angle of attack has been taken as zero. In order to familiarize the reader with the metric system, which is becoming more popular, it will be used for the analysis in this chapter. Special conversion factors that are sometimes not found in standard conversion tables are listed in Table 8-1. The guidance systems will be analyzed using the generic surface-to-air missile analyzed in Section 7-3.

The two missile guidance systems to be analyzed are proportional navigation and line-of-sight command guidance. For proportional navigation the missile is guided by either the reflected radio frequency (RF) or the radiant infrared (IR) energy from the target. The reflected RF energy can result
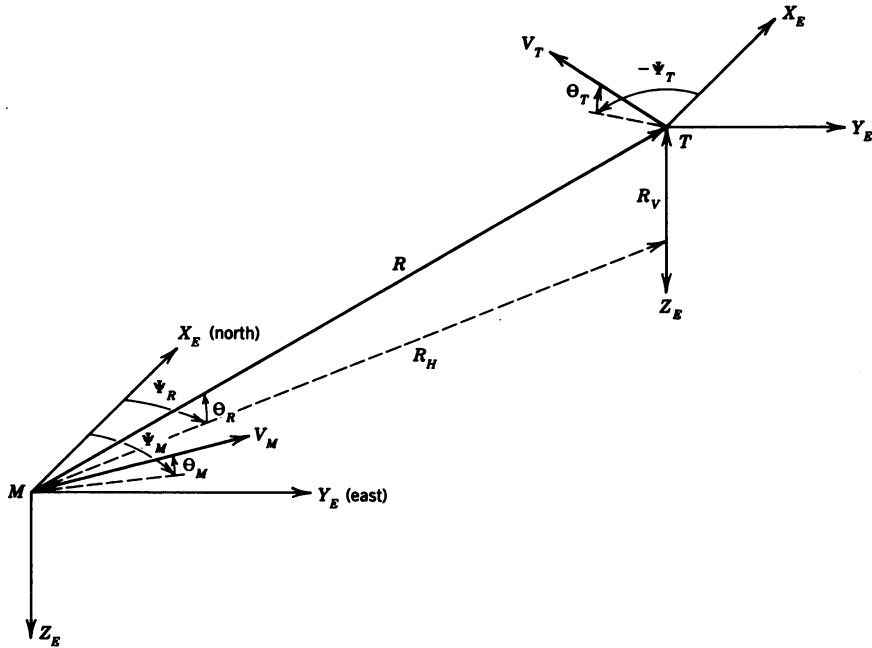
Figure 8-1   *Missile – target intercept geometry.*

from a separate illuminating radar or an active radar in the missile itself. The illuminating radar for air-to-air missiles is normally the fire control radar of the launch aircraft. For surface-to-air missiles the illuminating radar is a ground radar at the launch sight. Missiles that use the reflected RF energy from an illuminating radar are referred to as passive RF missiles, while missiles that have their own radar transmitters are called active RF missiles. In both cases the reflected energy (RF or IR) is received by an appropriate tracking device referred to as the seeker. The dynamics of the seeker and its role in the generation of the guidance command will be discussed in the next

TABLE 8-1   Special English-to-Metric Conversion Factors

Multiply	By	To obtain
Dynamic pressure, lb / ft^2	47.88085	N / m^2
Air density ρ, slugs / ft^3	515.46756	kg / m^3
Weight, lb	4.448	N
Mass, slugs	14.59	kg
Moment of inertia, slug ft^2	1.3557	kg m^2

section along with the incorporation of the geometry of proportional navigation guidance into the dynamic analysis. For command guidance of surface-to-air missiles two tracking radars are located at the launch sight, one to track the target the other the missile. How the outputs of the two radars are used to generate the guidance commands and how the geometry of command guidance is introduced into the dynamic analysis will be covered in Section 8-3.

In Section 8-4 the launch envelopes and missile trajectories for the guidance modes analyzed are compared and the relative merits of the guidance systems discussed.

Recently there has been renewed interest in exploring bank-to-turn (BTT) missiles[1]; therefore the design of a flight control system for such a missile is included in Sections 8-5 and 8-6, along with a guidance law and the results of a digital simulation of the missile and guidance system.

8-2   PROPORTIONAL NAVIGATION GUIDANCE[2]

For proportional navigation guidance the missile is commanded to turn at a rate proportional to the angular velocity of the line of sight (LOS). This ratio of the missile turning rate to the angular velocity of the LOS is called the proportional navigation constant. The letter N will be used to represent this quantity. In proportional navigation guidance N is greater than 1 and usually ranges from 2 to 6. This means that the missile will be turning faster than the LOS, and thus the missile will build up a lead angle with respect to the LOS. For a constant velocity missile and target (target not maneuvering) the generation of this lead angle can put the missile on a collision course with the target (zero angular velocity of the line of sight). If $N = 1$, then the missile is turning at the same rate as the LOS, or simply homing on the target. If $N < 1$, then the missile will be turning slower than the LOS, thus continuously falling behind the target, making an intercept impossible. This instability will be shown in the root locus analysis that follows.

The LOS is defined as an imaginary line from the missile to the target. The seeker, by tracking the target, establishes the direction of the LOS, and the output of the seeker is the angular velocity of the LOS with respect to inertial space as measured by rate gyros mounted on the seeker. For the missile guidance being discussed, an axis system fixed with respect to the earth can be considered an inertial reference. In order to completely analyze proportional navigation guidance it is necessary to consider the guidance geometry shown in Figure 8-2. The magnitude of the angular velocity of the LOS which generates the angular velocity of the seeker, $\omega_{(SK)I}$, is determined by the components of missile and target velocity perpendicular to the LOS, which for simplicity is shown in the vertical plane in Figure 8-2. The
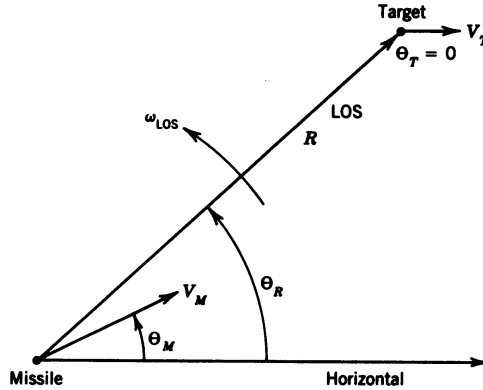
Figure 8-2   *Generation of the angular velocity of the LOS.*

component of missile velocity perpendicular to the LOS is

$$V_{M(\perp \text{LOS})} = V_M \sin(\Theta_R - \Theta_M) \tag{8-1}$$

which generates a positive LOS rotation. The component of target velocity perpendicular to the LOS is

$$V_{T(\perp \text{LOS})} = V_T \sin(\Theta_R - \Theta_T) \tag{8-2}$$

which generates a negative LOS rotation. The magnitude of the angular velocity is then the difference between the components of missile and target velocity perpendicular to the LOS divided by the distance between the target and the missile R. If the perpendicular components of missile and target velocity are equal and unchanging, there will be no rotation of the LOS and the missile will be on a collision course with the target. For the general case the angular velocity of the LOS is

$$\omega_{\text{LOS}} = \frac{V_M \sin(\Theta_R - \Theta_M) - V_T \sin(\Theta_R - \Theta_T)}{R} \; \text{rad/sec} \tag{8-3}$$

If Θ_T, Θ_M, and Θ_R can be assumed to be small angles, then Eq. 8-3 can be linearized. Then

$$\omega_{\text{LOS}} \approx \frac{V_M(\Theta_R - \Theta_M)}{R} - \frac{V_T(\Theta_R - \Theta_T)}{R} \; \text{rad/sec} \tag{8-4}$$

From Figure 8-2, $\omega_{\text{LOS}} = \dot{\Theta}_R$; then using Laplace notation and transposing

the V_M term to the left hand side of the equation, Eq. 8-4 becomes

$$\left(s - \frac{V_M(s)}{R(s)}\right)\Theta_R(s) + \frac{V_M(s)\Theta_M(s)}{R(s)} = \frac{V_T(s)[\Theta_T(s) - \Theta_R(s)]}{R(s)} \quad (8\text{-}5)$$

Solving Eq. 8-5 for Θ_R and dropping the (s)'s yields

$$\Theta_R = \frac{V_T(\Theta_T - \Theta_R)/R}{s - V_M/R} - \frac{V_M\Theta_M/R}{s - V_M/R} \text{ rad} \quad (8\text{-}6)$$

Using Eq. 8-6, the block diagram for the analysis of proportional navigation guidance can be drawn as shown in Figure 8-3 where $\Theta_R]_T$ is the LOS direction due to target motion and thus the input to the seeker. The output of the seeker is the input to the guidance computer (discussed later) which generates the missile acceleration command. For the purpose of this discussion the acceleration command is assumed proportional to the missile velocity (rather than the closing velocity) times the angular velocity of the LOS. The missile acceleration in g's times $9.81/V_M$ is equal to the missile pitch rate, which integrated yields Θ_M. The output of the transfer function in the feedback path is the rotation of the LOS due to the missile $\Theta_R]_M$, which provides the feedback. From Eq. 8-6 and Figure 8-3 it can be seen that the geometry of proportional navigation guidance introduces a pole in the right half s plane. It will be shown in the root locus analysis that as N is increased from zero the geometry pole in the right half plane moves to the left and crosses the imaginary axis at $N = 1$.

A simplified block diagram of a typical passive RF seeker is shown in Figure 8-4. The angular tracking error between the true LOS and the indicated LOS as represented by the angular orientation of the radar antenna is converted into a voltage by the demodulator. The low-pass noise filter smooths the output of the demodulator and provides the signal to drive the seeker pitch and yaw gimbals. The dynamics of the gimbals and their drives are usually at least second-order; however, as a result of studying actual seeker dynamics it has been found that these higher-order dynamics can be approximated by a simple gain. This has been verified by modeling the complete seeker dynamics in a hybrid simulation. The angular velocities of the gimbals, $\omega_{(SK)I}$, are the measured angular velocities of the LOS, which integrated yield the indicated LOS. Rate gyros mounted on these gimbals sense the gimbal rates and provide the input to the guidance computer. In many cases the gyros are also used to isolate the gimbals from the pitch and yaw motions of the missile (see Section 2-7). The guidance computer contains the guidance gain S_g, a lead compensator, and a final low-pass filter. The guidance gain will now be examined in detail.

As mentioned earlier for proportional navigation guidance, the missile is commanded to turn at a rate proportional to the angular velocity of the LOS.
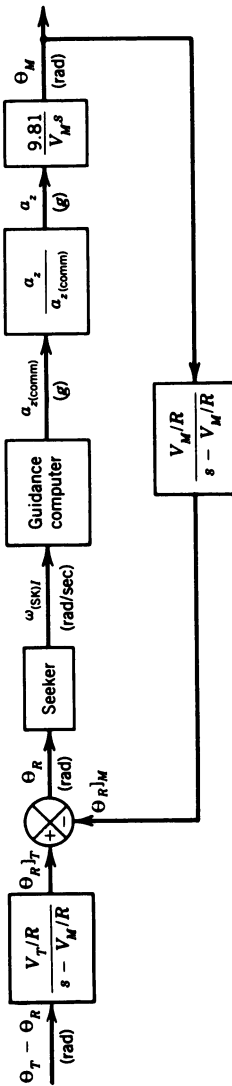
Figure 8-3 Block diagram for proportional navigation guidance including geometry.
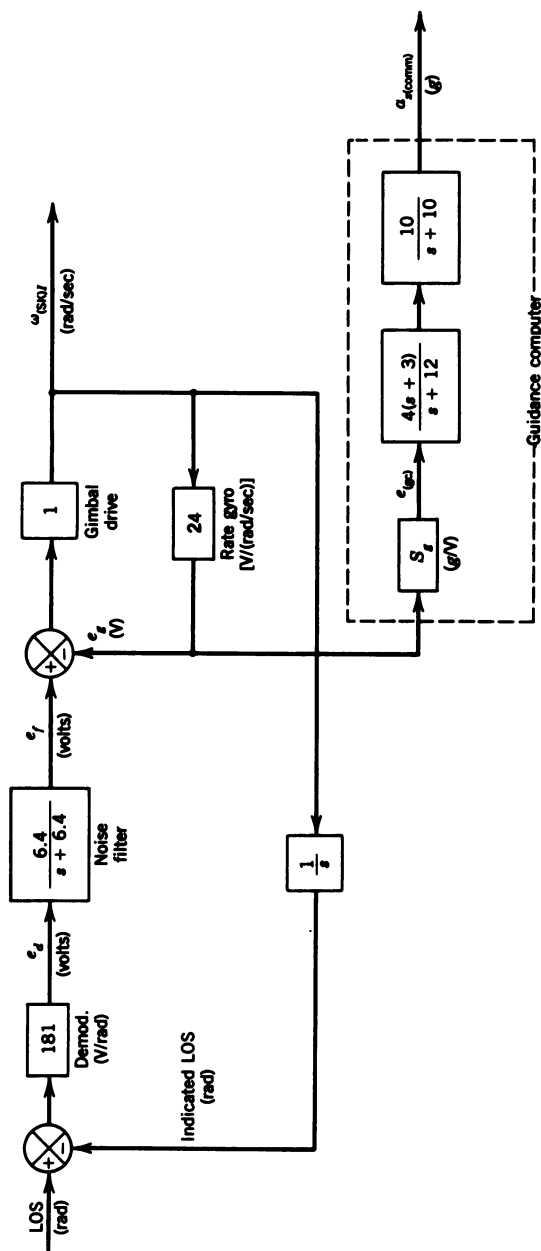
Figure 8-4 *Simplified seeker block diagram.*

$$S_g = \frac{NV_M}{2(24)g} \ g \ / \ \text{volt}$$

$$N = 5$$

Thus in the steady state

$$\omega_M = N\omega_{(LOS)} \text{ rad/sec} \tag{8-7}$$

and the missile acceleration (in g's) resulting from ω_M is

$$a_M = \frac{V_M\omega_M}{g} \tag{8-8}$$

From Figure 8-4 the steady-state missile acceleration (in g's) resulting from the angular velocity of the seeker is

$$a_M = 24S_g \times 2\omega_{(SK)} \tag{8-9}$$

where the 2 results from the gain of 2 through the missile autopilot as a result of the 0.5 feedback in the acceleration feedback loop (see Figure 7-12). Substituting Eq. 8-7 into Eq. 8-8 and equating the resulting equation to Eq. 8-9 yields

$$24S_g \times 2\omega_{(SK)} = V_M N\omega_{(LOS)}/g \tag{8-10}$$

Assuming that in the steady state $\omega_{(SK)} = \omega_{(LOS)}$, then solving Eq. 8-10 for S_g yields (normally closing velocity is used in Eq. 8-11 rather than V_M)

$$S_g = \frac{NV_M}{24(2)g}\ g/\text{volt} \tag{8-11}$$

If N and V_M are known, then Eq. 8-11 can be used to calculate a value of S_g for the root locus analysis. In order to perform a root locus analysis, the closed loop transfer function for the seeker is required. From Figure 8-4 the closed loop gain for the gimbal rate loop is 0.04. This gain combined with the filter transfer function and the integration in the feedback path yields

$$\frac{\omega_{(SK)I}}{LOS} = \frac{46.336s}{s^2 + 6.4s + 46.336}\ \frac{\text{rad/sec}}{\text{rad}} \tag{8-12}$$

Using Eq. 8-12 and the transfer function for the guidance computer from Figure 8-4, the block diagram for the root locus analysis of proportional navigation guidance can be drawn as shown in Figure 8-5. The missile and autopilot transfer function from Eq. 7-31 is repeated here for convenience:

$$\frac{a_z(s)}{a_{z(comm)}(s)} = \frac{-108.3(s+2)(s+34.41)(s-34.41)}{(s+1.96)(s+13.58)(s^2+37.48s+4830.81)} \tag{8-13}$$

For case 4, studied in Section 7-3, $V_M = 1139.62$ m/sec, and $R = 8350$ meters.
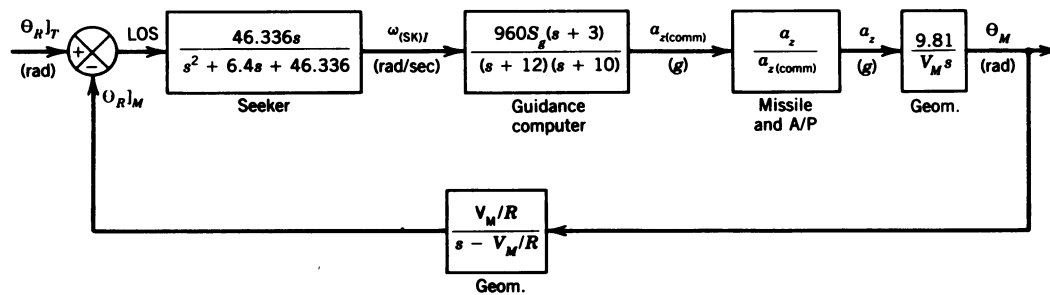
Figure 8-5 Block diagram for the root locus analysis of proportional navigation guidance.
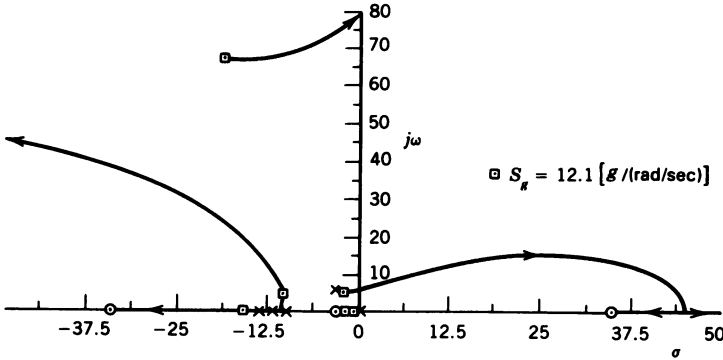
Figure 8-6 Root locus for geometry loop of proportional navigation guidance (zero-angle root locus).

Then $V_M/R = 0.136$ and $S_g = 12.1$ for $N = 5$. The zero-angle root locus for the block diagram in Figure 8-5 is shown in Figure 8-6 with the location of the closed loop poles indicated for $S_g = 12.1$ ($N = 5$). The corresponding closed loop transfer function is

$$\frac{\Theta_M(s)}{\Theta_R]_T(s)} = \frac{-501779.1(s-0.136)(s+2)(s+3)}{(s+0.515)(s+1.95)(s+15.908)(s^2+4.68s+35.91)}$$

$$\times \frac{(s+34.41)(s-34.41)}{(s^2+20.752s+128.64)(s^2+37.476s+4830.74)} \quad (8\text{-}14)$$

Multiplying Eq. 8-14 by $(V_T/R)/(s - V_M/R)$, where $V_T = 243$ m/sec (see Figure 8-3), yields the final closed loop transfer function

$$\frac{\Theta_M(s)}{(\Theta_T - \Theta_R)(s)} = \frac{-14602.67(s+2)(s+3)}{(s+0.515)(s+1.95)(s+15.908)}$$

$$\times \frac{(s+34.41)(s-34.41)}{(s^2+20.752s+128.64)(s^2+37.476s+4830.74)}$$

$$\times \frac{1}{(s^2+4.68s+35.91)} \quad (8\text{-}15)$$

As mentioned earlier in this section, the geometry pole in the right half plane moves to the origin for $N = 1$ ($S_g = 2.42$). This can be seen in the Bodé root locus shown in Figure 8-7 for the guidance loop shown in Figure 8-5. For Figure 8-7 the variable gain has been changed from S_g to N; thus the real axis root locus originating from the geometry pole at $s = 0.136$ (dashed line) becomes asymptotic to the unity magnitude line as N is increased to 1. For N
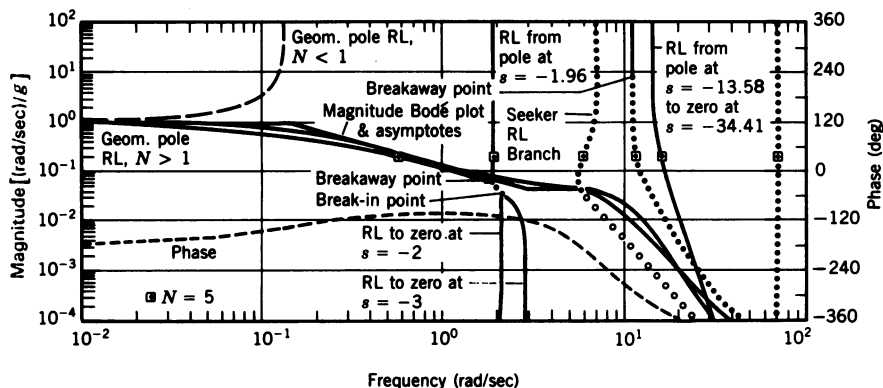
Figure 8-7 Bodé root locus for geometry loop of proportional navigation guidance.

greater than 1 the pole, now in the left half plane (solid line), heads toward the pole moving to the right from $s = -1.96$. The two poles break away and then break in between the zeros at $s = -2$ and $s = -3$. The complex seeker poles cross into the right half plane at $N = 22$. The real axis root locus from the poles at $s = -10$ and -12 breaks away and becomes complex and asymptotic to the Bodé magnitude plot. The real pole at $s = -13.58$ moves toward the zero at $s = -34.41$. The missile complex poles are still stable for $N = 10,000$.

This same root locus analysis was performed for cases 2 through 6 in Table 7-2. The results of the analysis are summarized in Table 8-2. The dominant real pole for cases 2, 3, and 4 results from the closed loop location of the geometry pole as it moves into the left half plane. For case 5 the geometry pole and the dominant real missile autopilot pole have come together and broken away from the real axis to yield complex poles. The reciprocal of the real part of these complex poles is 0.53 (equivalent to the time constant of a

TABLE 8-2 Closed Loop Dynamic Characteristics from the Root Locus Analysis of Proportional Navigation Guidance

Case	Time Constant of Dominant Real Pole (sec)	Seeker Closed Loop Poles
2	8.33	$-3.16 \pm j5.86$
3	4.55	$-3.02 \pm j5.7$
4	1.79	$-2.28 \pm j5.5$
5	Complex	$-0.096 \pm j4.6$
6	System unstable	
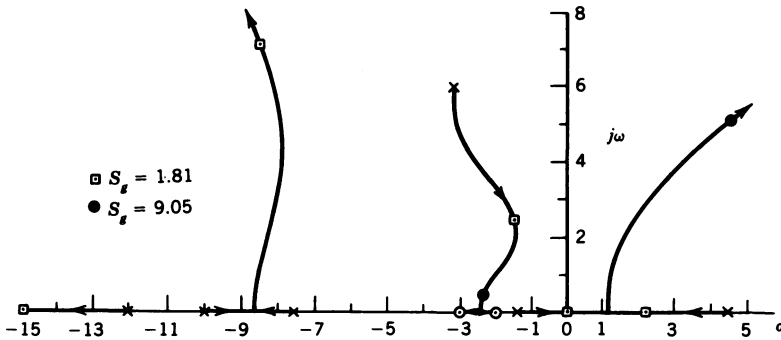
Figure 8-8 Root locus for geometry loop of proportional navigation guidance for case 6 (zero-angle root locus).

real pole). Thus the missile response time decreases as the missile moves toward the target. As S_g increases from zero, the open loop seeker poles move toward the imaginary axis and finally break into the real axis to the right of the missile zero in the right half plane. For all cases except 5 the damping of these poles is still satisfactory. For case 5 these poles are barely stable, and if it were not for the fact that the missile is so very close to the target, it would have been necessary to reduce the gain. However, the point of closest approach, or miss distance, was 1.036 meters, and values of 4 and 6 for N resulted in greater miss distances; therefore the value 5 was selected. As the missile approaches the target, the geometry pole moves farther into the right half plane. For case 6 the open loop geometry pole is at $s = 4.46$, and as shown in Figure 8-8 this pole never leaves the right half plane. At this point the missile is only 0.19 sec from the point of closest approach and 191 meters from the target; thus this terminal instability, which can not be avoided, has little effect on the missile performance.

To evaluate the effectiveness of the modes of guidance studied and to provide for a quantitative comparison between proportional navigation and command guided systems, intercept envelopes were generated. For command guidance, envelopes were generated for both the three-point and lead angle guidance modes discussed in the next section. To establish a starting point for the evaluation, a standard run was set up. For the standard intercept the target was at Mach 0.8 (243 m/sec) at 9000 meters with $\Psi_T = -90°$ and $\Theta_T = 0°$. The initial coordinates of the target were 21,650 meters east and 12,500 meters north of the missile launch point. The value of Θ_M at launch was set equal to the initial value of Θ_R, but rather than set $\Psi_M = \Psi_R$ at launch, an initial lead angle was calculated using

$$\text{lead} = 0.05(733)\omega_{(\text{LOS})} \text{ rad} \tag{8-16}$$
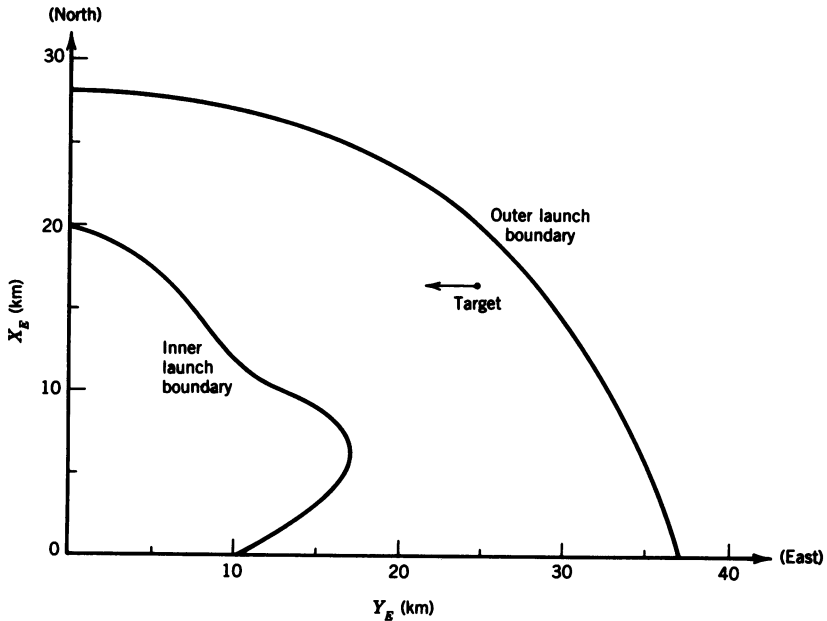
Figure 8-9 *Missile intercept envelope using proportional navigation guidance (N = 5) against an incoming target ($\Psi_T = -90°$) flying at Mach 0.8 at 9000 meters.*

where

$\omega_{(LOS)}$ is the initial angular velocity of the LOS due to target motion, rad/sec,

733 is the calculated average missile velocity for the standard run, m/sec,

0.05 is the required proportionality constant, rad/(m/sec²).

The standard intercept was also used to obtain the data required for the missile control system analysis presented in Section 7-3.

For the intercept geometry used, the initial value of $\omega_{(LOS)}$ is negative, thus making the lead angle negative. The value of 0.05 was selected so that the missile was aimed at the final missile–target intercept point for the standard run. This resulted in a lead angle of $-10.2°$. A check of intercepts at other target initial conditions (coordinates and speed) showed that the lead angle calculation was accurate to within a few degrees. The introduction of the initial lead angle allows the missile to fly a straighter intercept trajectory and improves the missile performance, especially against close in targets. The intercept envelope for an incoming target flying at Mach 0.8 at 9000 meters is shown in Figure 8-9. The outer launch boundary results from the missile Mach falling below the minimum value of 1.1 set in the simula-

tion. Some of these long-range shots had times of flight of 35 to 40 sec with missile sustainer burnout occurring at 20 sec. The inner launch boundary results from the missile dynamics and the maximum acceleration the missile can withstand. The maximum acceleration command was limited to $10g$, which would result in the missile pulling $20g$ in the steady state.

This concludes the discussion of proportional navigation guidance. Command guidance will be covered in the next section, as well as a comparison of the two guidance techniques.

8-3 COMMAND GUIDANCE

The most commonly employed form of command guidance is called three-point guidance, referred to in Ref. 2 as line-of-sight trajectory (beam-rider missile). For three-point guidance the missile is guided so as to remain on the LOS, or tracking line, between the launch point and the target. A variation of three-point guidance is lead angle guidance, in which the missile is commanded to fly ahead of the LOS a distance that is a function of the difference between the range from the launch point to the target and to the missile. Thus this commanded distance approaches zero as the missile nears the target. These types of guidance are normally used for surface-to-air missiles and require two tracking radars at the launch site. One radar tracks the target while the other tracks the missile. For three-point guidance the missile-tracking radar acquires the missile shortly after launch and then guides the missile into the beam of the target-tracking radar. The missile normally has a transponder in the rear of the missile to facilitate the tracking of the missile and to distinguish the missile return from that of the target. As soon as the missile is stabilized in the beam of the target-tracking radar, the missile-tracking radar is free to track another missile. In this way two missiles can be fired at a given target, with three-point guidance used for the first missile and lead angle guidance for the second. For lead angle guidance the missile-tracking radar tracks the missile all the way to intercept. The dynamic analysis of the two forms of command guidance is the same except that the missile-tracking radar pedestal dynamics must be included for lead angle guidance analysis.

The geometry for both three-point and lead angle guidance is shown in Figure 8-10. In the figure R_M and R_T are the tracking lines to the missile and the target, respectively, established by the missile- and/or target-tracking radars. The azimuth angles of the missile and target tracking lines are Ψ_{RM} and Ψ_{RT} respectively, with the corresponding elevation angles Θ_{RM} and Θ_{RT}. The angular differences between the two tracking lines are

$$\Delta\Psi = \Psi_{RT} - \Psi_{RM}$$

$$\Delta\Theta = \Theta_{RT} - \Theta_{RM} \qquad (8\text{-}17)$$

Figure 8-10   *Missile – target geometry for three-point and lead angle guidance.*

For the guidance command the actual distance from the tracking line to the missile is required. In the vertical plane this distance is the length of the chord subtended by the arc $\Delta\Theta$ at the missile range; thus for $\Delta\Theta$ in radians,

$$h_\theta = \Delta\Theta\, R_M \text{ meters} \tag{8-18}$$

To obtain the lateral distance from the tracking line it is necessary to project the missile position into the horizontal plane, which yields $R_M \cos\Theta_{RM}$. The lateral distance is then the length of the chord subtended at this range by the arc $\Delta\Psi$; thus

$$h_\psi = \Delta\Psi\, R_M \cos\Theta_{RM} \text{ meters} \tag{8-19}$$

Using Eqs. 8-17 and 8-18, the block diagram for three-point guidance including geometry can be drawn as shown in Figure 8-11. The $a_z/a_{z(\text{comm})}$ transfer function was given in Eq. 8-13, which is repeated here for convenience:

$$\frac{a_z(s)}{a_{z(\text{comm})}(s)} = \frac{-108.3(s+2)(s+34.41)(s-34.41)}{(s+1.96)(s+13.58)(s^2+37.48s+4830.81)} \tag{8-20}$$
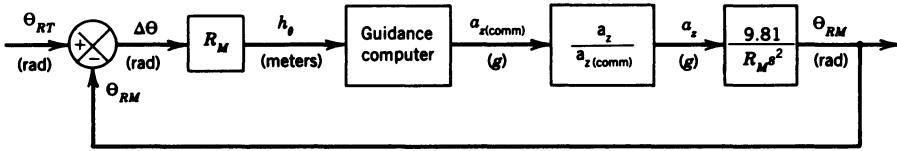
Figure 8-11 *Block diagram for three-point guidance including geometry.*
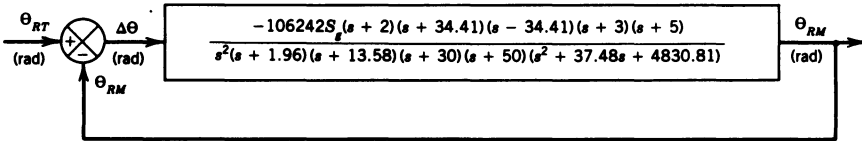
Figure 8-12 *Block diagram for root locus analysis of three-point guidance including geometry.*

As two integrations are required to go from an acceleration to a distance, the double lead compensator shown in Eq. 8-21 is required for stability:

$$[\text{TF}]_{(\text{comp})} = \frac{100 S_g (s+3)(s+5)}{(s+30)(s+50)} \frac{g}{\text{meter}} \qquad (8\text{-}21)$$

The distance resulting from the double integration of missile normal acceleration divided by R_M yields the required feedback quantity Θ_{RM}, thus closing the loop. Using Eqs. 8-20 and 8-21 and Figure 8-11, the block diagram for the root locus analysis of three-point guidance can be drawn as shown in Figure 8-12. The zero-angle root locus for three-point guidance is shown in Figure 8-13 and the Bodé root locus in Figure 8-14 with the location of the closed loop poles for $S_g = 0.6$ indicated in both figures. From the Bodé root locus,
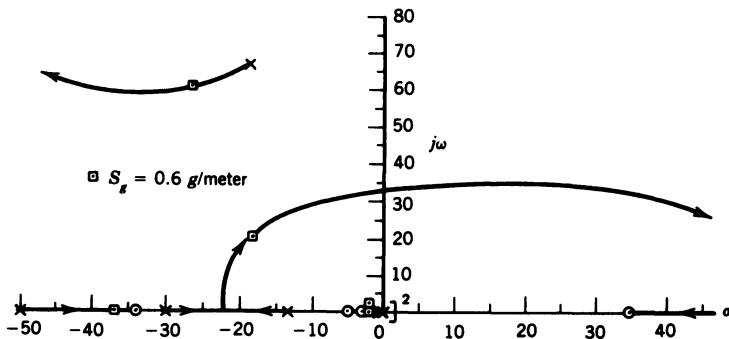
Figure 8-13 *Root locus for three-point guidance including geometry (zero-angle root locus).*
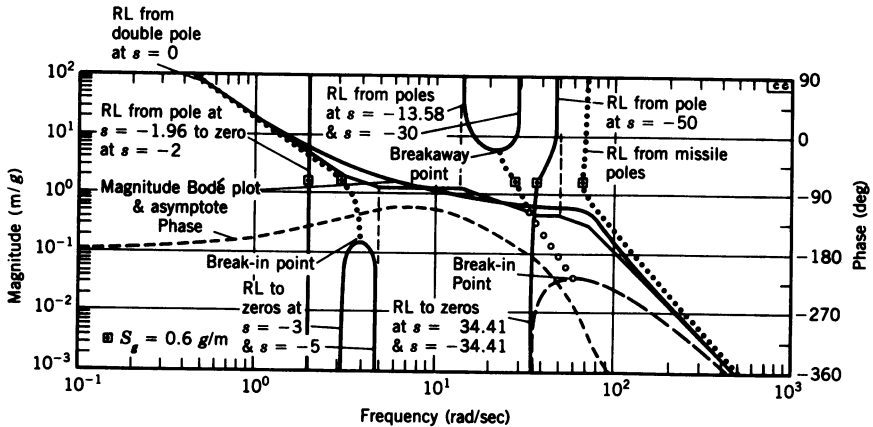
Figure 8-14   Bodé root locus for three-point guidance including geometry.

the action of the compensator zeros in controlling the loci of the double poles at the origin is evident. Without the compensator the double poles at the origin move directly into the right half plane and break into the real axis to the right of the missile zero. From Figure 8-14 the gain margin is 1.53. The closed loop transfer function for $S_g = 0.6$ is

$$\frac{\Theta_{RM}(s)}{\Theta_{RT}(s)} = \frac{-63768(s+2)(s+3)(s+5)(s+34.41)(s-34.41)}{(s+1.98)(s^2+4.06s+9.18)(s^2+36.84s+772.77)}$$

$$\times \frac{1}{(s+36.91)(s^2+53.22s+4378.03)} \tag{8-22}$$

From Eq. 8-22 it can be seen that the pole at -1.98 is very close to the zero at -2 from the missile and autopilot transfer function; thus the complex poles at $-2.03 \pm j2.25$ are the dominant closed loop poles. This should provide good performance for the three-point guidance system. Before examining the intercept capabilities of a missile using three-point guidance the dynamics of lead angle guidance will be analyzed.

As mentioned earlier, for the analysis of lead angle guidance the pedestal dynamics of the missile tracking radar must be considered. The dynamics of the missile-tracking radar (MTR) affect not only the stability but also the overall performance of the system. The effect of the MTR dynamics on the performance of the system can only be determined by using a full-scale simulation as was done in this case. Before discussing the effects of the MTR dynamics, the generation of the lead angle term will be covered.

As mentioned earlier in this section, for lead angle guidance the missile is commanded to fly ahead of the LOS a distance that is a function of the difference between the ranges from the launch point to the target and to the

missile. For this study, the lead was programmed to start out at zero, increase linearly to a maximum at the midpoint of the trajectory, and then decrease linearly to zero as the missile approached the target. A variable ΔR was generated as shown in the following equation:

$$\Delta R = \frac{RT - R}{RT} \text{ meters} \qquad (8\text{-}23)$$

where RT and R are the ranges from the launch point to the target and missile respectively. For $\Delta R \geq 0.5$ then

$$\text{DLEAD} = \text{CGLEAD} \times (1 - \Delta R) \text{ meters} \qquad (8\text{-}24)$$

And for $\Delta R < 0.5$

$$\text{DLEAD} = \text{CGLEAD} \, \Delta R \text{ meters} \qquad (8\text{-}25)$$

where

$$\text{CGLEAD} = 2500 \cos \Psi_{RT_0} \qquad (8\text{-}26)$$

and Ψ_{RT_0} is the initial azimuth angle of the LOS from the launch point to the target. The value of 2500 in Eq. 8-26 was selected because it yielded the smallest miss distance for the standard intercept. With CGLEAD a function of Ψ_{RT_0}, then CGLEAD is zero for a target flying along the reference Y axis. To be more general CGLEAD could have been made a function of the initial angular velocity of the LOS due to target motion.

Having discussed the generation of the lead-angle term, the dynamic analysis of lead angle guidance will now be presented. The general block diagram for lead angle guidance is shown in Figure 8-15. The selection of the MTR pedestal dynamics will be discussed first. If the dynamics of the MTR are assumed to be second-order, then the effect of the addition of a pair of complex poles on the root locus must be investigated. For the MTR dynamics given by

$$[\text{TF}]_{(\text{MTR})} = \frac{9.34}{s^2 + 5.64s + 9.34} \qquad (8\text{-}27)$$
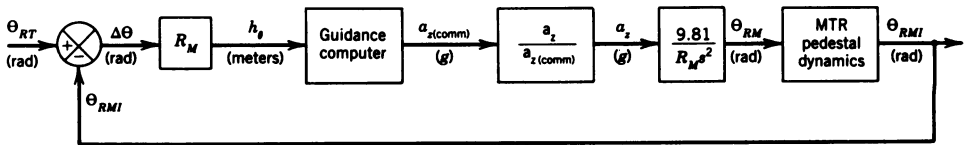
Figure 8-15   Block diagram for lead angle guidance including geometry.

the compensator given in Eq. 8-21 would not stabilize the lead angle guidance system. For that compensator the two poles at the origin move directly into the right half plane. In order to adequately stabilize the system an additional double lead compensator with a gain of 10 is required. As a lead compensator amplifies noise, the introduction of four cascade lead compensators into an actual system with a gain of 1000 at $t = 0$ is impractical. An alternative would be the MTR transfer function shown in Eq. 8-28.

$$[TF]_{(MTR)} = \frac{5.14(s + 1.75)}{s^2 + 5.64s + 8.99} \qquad (8\text{-}28)$$

The MTR transfer function in Eq. 8-28 could be achieved by using a compensator transfer function of $(s + 1.75)/(s + 0.5)$ with a motor gain of 5.14 followed by $1/s$. This MTR transfer function with the compensator

$$[TF]_{(comp)} = \frac{10(s + 1)(s + 3)}{(s + 10)(s + 30)} \qquad (8\text{-}29)$$

resulted in a well-stabilized guidance loop and was used in the simulation with good results; however, the miss distances varied from 17.94 to 21.2 meters as the guidance gain and lead angle constant in Eq. 8-26 were varied. Using the first-order lag

$$[TF]_{(MTR)} = \frac{10}{s + 10} \qquad (8\text{-}30)$$

for the MTR transfer function reduced the miss distance to 3.84 meters. Thus Eq. 8-30 was used to represent the MTR dynamics in the root locus analysis that follows. Using Eqs. 8-20, 8-29, and 8-30 and Figure 8-15, the block diagram for the root locus analysis of lead angle guidance can be drawn as shown in Figure 8-16. The zero-angle root locus for lead angle guidance is shown in Figure 8-17 and the Bodé root locus in Figure 8-18, with the location of the closed loop poles for $S_g = 1$ indicated in both figures. The action of the compensator zeros in controlling the loci of the double poles at the origin is evident. From Figure 8-18 the gain margin is 4.08 at a crossover
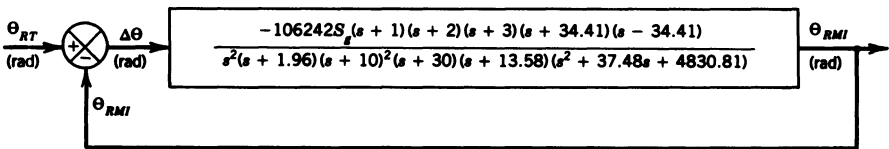
Figure 8-16 *Block diagram for root locus of lead angle guidance including geometry.*
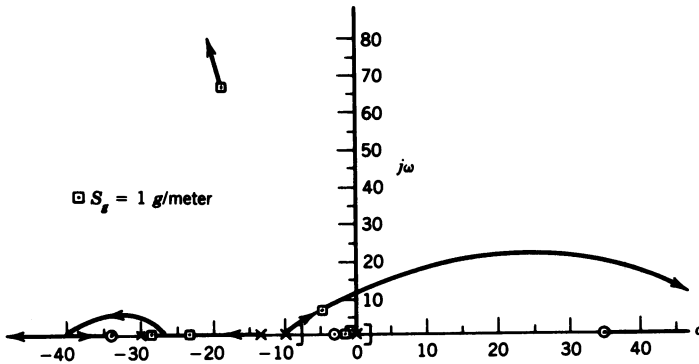
Figure 8-17 Root locus for lead angle guidance including geometry (zero-angle root locus).

frequency of 11.08 rad/sec. The closed loop transfer function for $S_g = 1$ is

$$\frac{\Theta_{RMI}(s)}{\Theta_{RT}(s)} = \frac{-106242(s+1)(s+2)(s+3)(s+34.41)}{(s+1.94)(s^2+1.97s+1.8)(s^2+9.1s+65.19)}$$

$$\times \frac{s-34.41}{(s+23.58)(s+28.74)(s^2+37.78s+4903.64)} \quad (8\text{-}31)$$

As in the case for three-point guidance, the complex poles at $-0.985 \pm j0.91$ are the dominant closed loop poles. A comparison of these poles with the dominant closed loop poles from Eq. 8-22 indicates that the lead angle guidance response time will be about twice that of three-point guidance.
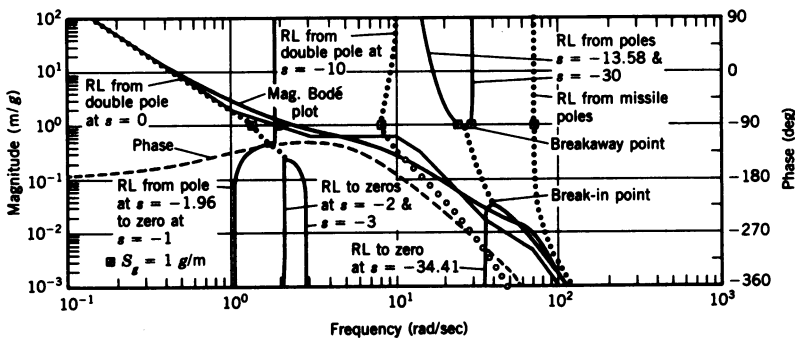
Figure 8-18 Bodé root locus for lead angle guidance including geometry.

8-4 COMPARISON OF GUIDANCE SYSTEM PERFORMANCE

A comparison of the intercept envelopes for the three guidance modes studied is shown in Figure 8-19. As can be seen, the outer launch boundaries are very similar for initial LOS azimuth angles of less than about 35°; however, there is considerable difference in the inner launch boundaries. This can best be explained by looking at Figures 8-20 and 8-21. From the horizontal missile trajectories shown in Figure 8-20, it can be seen that with proportional navigation guidance the missile flies a fairly straight path. This is substantiated by the correspondingly small heading changes shown in Figure 8-21. For three-point guidance the missile flies a smooth curved trajectory with a large but rather steady heading change. From the LOS line to the target for 20 sec after launch it can be seen that the missile is almost on the LOS, indicating good guidance. For lead angle guidance the missile initially turns to the left (heading angle decreasing) to establish its lead, then makes a hard turn back to the right to eliminate the built-in lead, and then makes a final large turn to the left. The lateral accelerations resulting from these maneuvers slow the command guided missiles down and result in the observed degradation in their inner launch boundaries. Some of the additional degradation for lead angle as compared to three-point guidance is probably due to the slower response for lead angle guidance mentioned
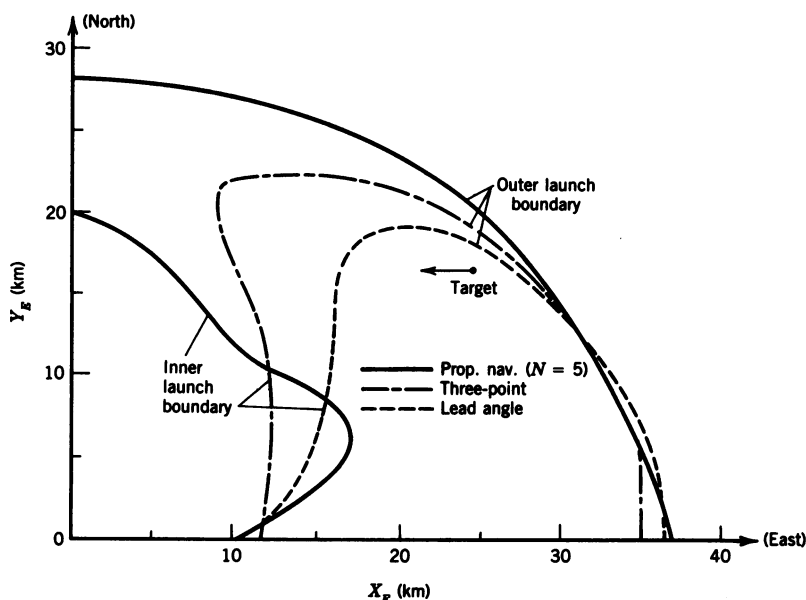
Figure 8-19 *Comparison of intercept envelopes for the three types of guidance analyzed against an incoming target ($\Psi_T = -90°$) flying at 9000 meters.*
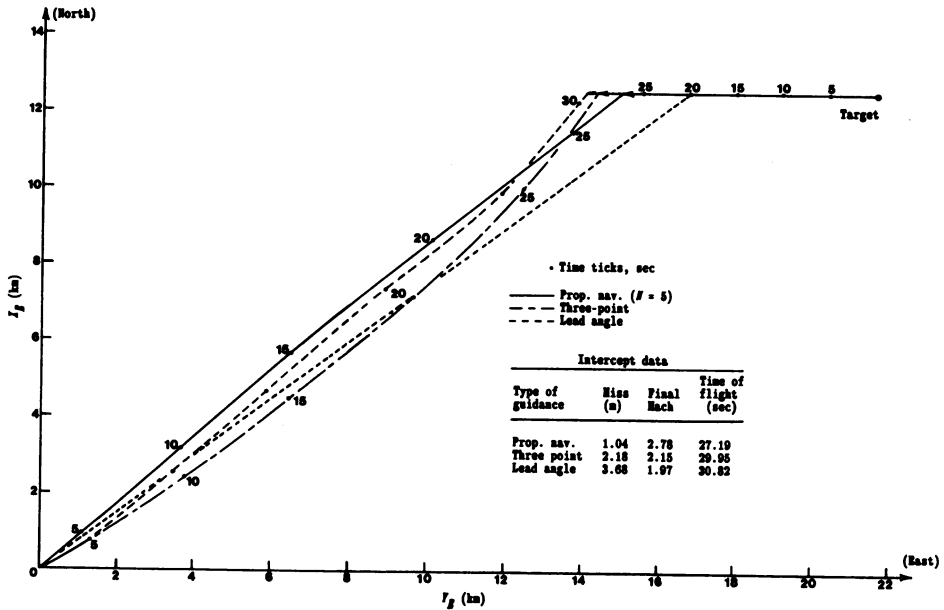
Figure 8-20   Comparison of horizontal missile trajectories against a Mach 0.8 target at 9000 meters for the three types of guidance analyzed.
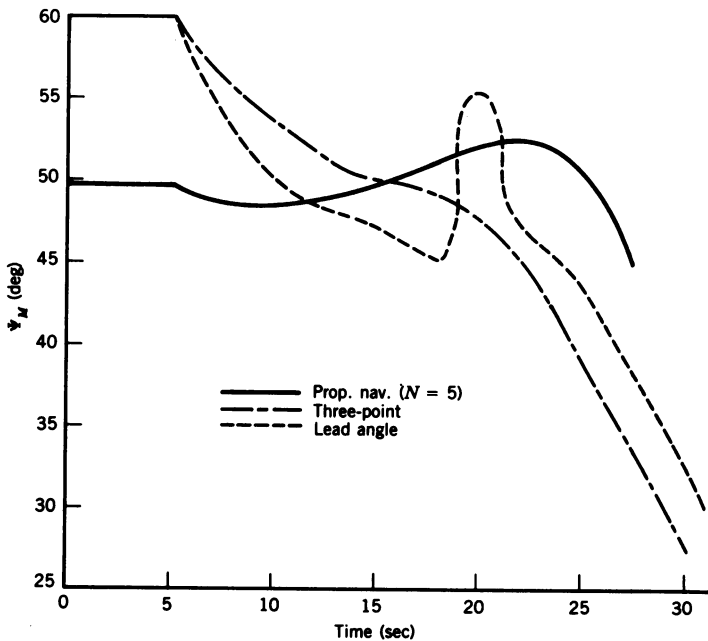
Figure 8-21   Comparison of missile headings for the missile trajectories shown in Figure 8-20.
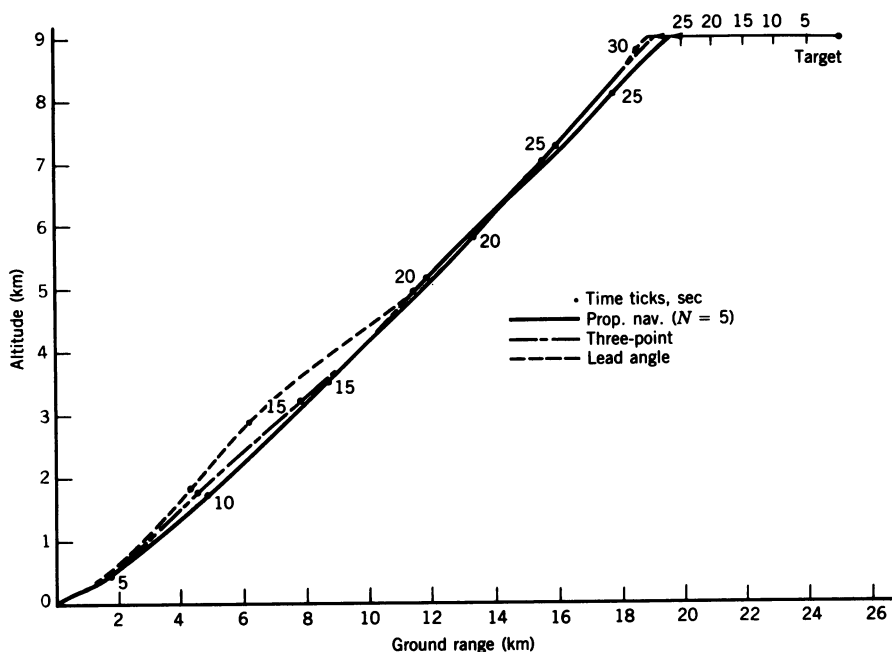
Figure 8-22 *Comparison of vertical missile trajectories against a Mach 0.8 target at 9000 meters for the three types of guidance analyzed.*

earlier. From Figures 8-22 and 8-23 it can be seen that there is less variation in the vertical missile trajectories and pitch angle changes for the three guidance modes than observed in Figures 8-20 and 8-21 for the horizontal trajectories and heading changes. From this analysis the superiority of proportional navigation guidance is obvious. In addition, the double pole at the origin, resulting from the geometry of the command guidance modes, makes the design for these systems more difficult and adds to the attractiveness of proportional navigation guidance. If command guidance is used, then three-point guidance is the preferred mode, with lead angle guidance used only for the second missile in a two-missile salvo.

A check of Figures 8-11 and 8-15 shows that the range from the missile to the target R does not appear in the guidance loop block diagrams for command guidance. Thus the instability, as the missile approaches the target, inherent in proportional navigation guidance does not exist in command guided missiles. However, the terminal accuracy of command guided missiles decreases as the range from the launch point to the target increases. This results from the fact that the missile- and target-tracking radars have a finite angular tracking error that is a function of the antenna beam width. Thus for a given angular tracking error, the error in the indicated position of the
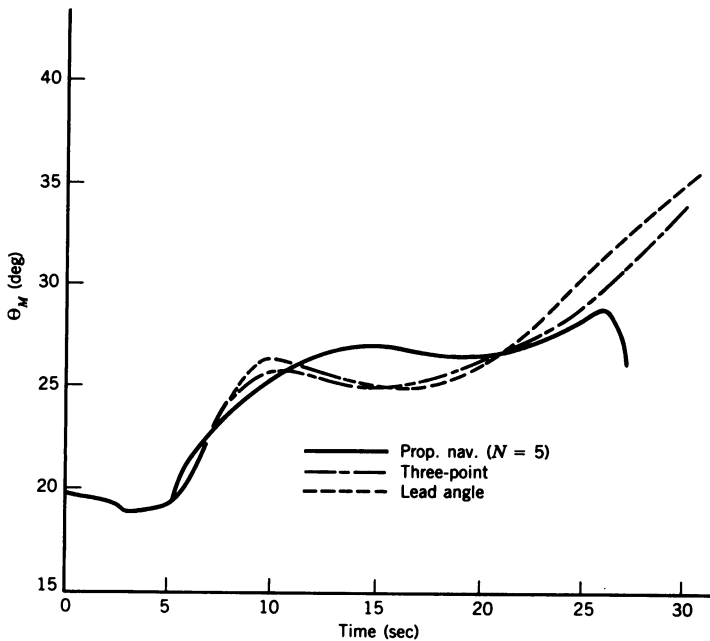
Figure 8-23 *Comparison of missile pitch angles for the missile trajectories shown in Figure 8-22.*

target is directly proportional to the range from the radar to the target. For this reason, proportional navigation guided rather than command guided missiles are used for long-range intercepts. In fact for very long-range intercepts, command guidance could be used for the initial phase, switching to proportional navigation for terminal guidance with an active radar in the missile. In summary, proportional navigation guidance is more accurate than command guidance and does not have the double pole at the origin to compensate for, resulting in a simpler control system.

The comparison of the horizontal trajectories for a missile using proportional navigation guidance fired with and without an initial lead angle against a close-in target is shown in Figure 8-24. Although the missile was launched with about 5° more lead than required, the performance of the missile launched with a lead angle was superior to that of the missile launched directly at the target. This improvement in missile performance, achieved by the use of an initial lead angle, enhances the capability of the missile against close-in targets.

This concludes the discussion of guidance systems for so-called aerodynamic controlled skid-to-turn missiles. A guidance system for an aerodynamic controlled bank-to-turn missile will be analyzed in the next two sections.
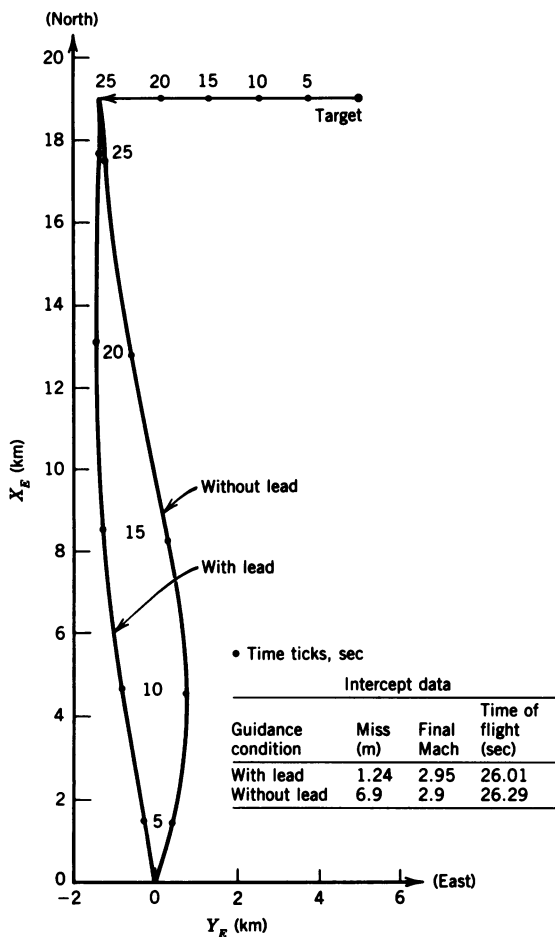
Figure 8-24 *Comparison of proportional navigation guidance trajectories with and without an initial lead angle against a Mach 0.8 target at 9000 meters.*

8-5 BANK-TO-TURN MISSILE GUIDANCE

Reference 1 provides a good summary of the status of bank-to-turn missile technology. In his report Arrow uses the term preferred orientation control (POC) rather than bank-to-turn (BTT); the latter term will be used here. As stated in Ref. 1, skid-to-turn (STT) missile technology, as discussed in Sections 8-2 and 8-3, has dominated in both surface-to-air and air-to-air missile applications. However, recently the U.S. Navy has established mission objectives that rely on the successful application of ramjet propulsion technology. In general, ramjet missile propulsion requires positive angles of attack and minimal sideslip angles, which can best be achieved with BTT

missiles. As pointed out by Arrow, BTT missile control is made more difficult by the high roll rates required to achieve the short response time necessary for a high-performance missile. The high roll rates increase the aerodynamic coupling, which will be discussed here, and can lead to inertial cross-coupling problems as described in Chapter 5.

The aerodynamic coupling can be seen by looking at the $\dot{\alpha}$ and $\dot{\beta}$ wind axis equations of motion, which are repeated here from Eq. G-13, using the small-angle approximations for the sine and cosine of α and β and neglecting the product of α and β:

$$\dot{\alpha} = \frac{A_{ZW}}{V_M} + Q - P\beta$$

$$\dot{\beta} = \frac{A_{YW}}{V_M} + P\alpha - R \tag{8-32}$$

where

$$\frac{A_{ZW}}{V_M} = \frac{Sq}{mV_M}\left(C_{z_\alpha}\alpha + C_{z_{\delta_e}}\delta_e\right) \text{ rad/sec}$$

$$\frac{A_{YW}}{V_M} = \frac{Sq}{mV_M}\left(C_{y_\beta}\beta + C_{y_{\delta_r}}\delta_r\right) \text{ rad/sec} \tag{8-33}$$

and V_M is the total missile velocity. From Eq. 8-32 it can be seen that the roll rate P couples the Y and Z force equations through α and β. Using the dimensional stability derivatives from Ref. 3 for a missile velocity of 1509.27 ft/sec (Mach 1.38) at 10,000 ft, the short-period missile equations of motion are

$$\dot{\alpha} = \dot{\theta} - 3.0286\alpha - P\beta - 0.7785\delta_e + \frac{G_z\cos\alpha - G_x\sin\alpha}{V_M} \text{ rad/sec}$$

$$\ddot{\theta} = -0.028\dot{\theta} + 149\alpha - 701\delta_e \text{ rad/sec}^2 \tag{8-34}$$

where G_z and G_x are the gravity terms defined in Eq. 8-36. As a ramjet engine can be partially throttled, it can be assumed that, for small variations in altitude, the velocity is constant. In addition the aerodynamic data in Ref. 3 included neither thrust nor drag values. Thus the short-period equations are used. As the sign of the coefficient of the α term in the $\ddot{\theta}$ equation of Eq. 8-34 is positive, the missile is statically unstable (positive C_{m_α}). Again using

the data from Ref. 3, the lateral equations of motion are

$$\dot{\beta} = -\dot{\psi} - 0.853\beta + P\alpha + 0.8\delta_r + \frac{G_y \cos\beta}{V_M} \text{ rad/sec}$$

$$\ddot{\phi} = -2.61\dot{\phi} + 0.014\dot{\psi} - 6438\beta + 11113\delta_a \text{ rad/sec}^2$$

$$\ddot{\psi} = -0.0028\dot{\phi} - 0.028\dot{\psi} + 295\beta - 85\delta_a - 695\delta_r \text{ rad/sec}^2 \qquad (8\text{-}35)$$

The gravity terms are

$$G_x = -32.2 \sin\Theta \text{ ft/sec}^2$$

$$G_y = 32.2 \cos\Theta \sin\Phi \text{ ft/sec}^2$$

$$G_z = 32.2 \cos\Theta \cos\Phi \text{ ft/sec}^2 \qquad (8\text{-}36)$$

The control of a BTT missile requires a roll angle and pitch command rather than the less complex yaw and pitch acceleration commands required for the STT missile. Using the seeker described in Section 8-2, it was initially considered that the LOS yaw rate could be used to command a roll angle and the LOS pitch rate used to provide a pitch rate command to a pitch orientational control system (see Section 2-2). However, this did not prove to be the case. Thus the guidance law given by Eq. 19 of Ref. 3 (to be discussed later in this section) was used, the resulting pitch and yaw acceleration commands (in g's) are

$$a_{z(\text{comm})} = N\frac{R_{MTZ} + V_{MTZ}t_{go}}{gt_{go}^2} - g_{z(\text{bias})}$$

$$a_{y(\text{comm})} = N\frac{R_{MTY} + V_{MTY}t_{go}}{gt_{go}^2} - g_{y(\text{bias})} \qquad (8\text{-}37)$$

where

R_{MTY} and R_{MTZ} are the Y and Z components of the missile-to-target range vector in missile coordinates, ft,

V_{MTY} and V_{MTZ} are the Y and Z components of the missile-to-target relative velocity vector in missile coordinates (negative quantities if the missile is closing on the target), ft/sec,

N is the navigation constant,

t_{go} is the time to go, sec,

$g_{y(\text{bias})}$ and $g_{z(\text{bias})}$ are the Y and Z gravity bias terms, in g's.

The time-to-go equation is

$$t_{go} = \frac{R_{MT}}{V_{cl}} \text{ sec} \tag{8-38}$$

where

R_{MT} is the magnitude of the missile to target range vector, ft,

V_{cl} is the closing velocity between the missile and the target (a positive quantity if the missile is closing on the target), ft/sec.

Equation 8-38 is valid because the missile and target velocities are considered constant. For the general case a more complex equation is required, usually incorporating an acceleration term; such an equation is used in the next section. It was assumed in Ref. 3 that all the quantities required in Eqs. 8-37 and 8-38 were known exactly. This implies an active radar in the missile. The same assumption will be made here. The gravity bias terms are

$$g_{y(bias)} = (\cos \Theta \sin \Phi \cos \beta) g$$

$$g_{z(bias)} = (\cos \Theta \cos \Phi \cos \alpha + \sin \Theta \sin \alpha) g \tag{8-39}$$

The roll angle error is calculated using

$$\epsilon_\phi = -\arctan(a_{y(comm)} / a_{z(comm)}) \text{ deg} \tag{8-40}$$

The choice of the sign in the equation will be explained later in this section.

Having presented the governing equations and the guidance law, the design of the pitch acceleration control system and the roll angle control system (RACS) will now be discussed. The block diagram for the pitch acceleration control system is shown in Figure 8-25. The signs at the summers result from the fact that a positive δ_e generates a negative $\dot{\theta}$ and a positive a_z; thus a positive $a_{z(comm)}$ results in a positive a_z. The steady-state gain of
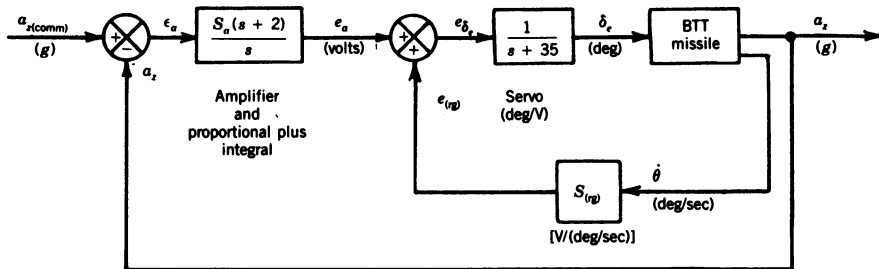
Figure 8-25   *Block diagram of acceleration control system for BTT missile.*
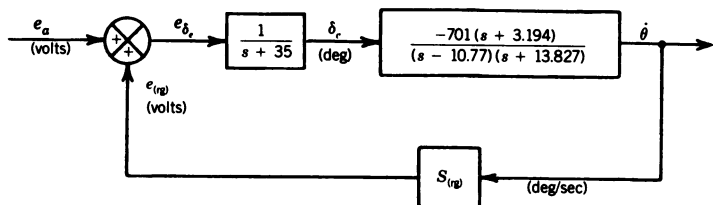
Figure 8-26 Block diagram for the inner loop of the acceleration control system.

the servo has been reduced from unity to compensate for the high gain of the $\dot{\theta}$ transfer function, which is

$$\frac{\dot{\theta}(s)}{\delta_e(s)} = \frac{-701(s+3.194)}{(s-10.77)(s+13.827)} \quad \frac{deg/sec}{deg} \tag{8-41}$$

The proportional plus integral network is required to stabilize the outer acceleration feedback loop.

The inner rate feedback loop will now be analyzed. The block diagram for this loop is shown in Figure 8-26 and the corresponding root locus in Figure 8-27. The closed loop poles are indicated for an $S_{(rg)}$ of 1.25 volts/(deg/sec), and the corresponding closed loop transfer function is

$$\frac{\dot{\theta}(s)}{e_a(s)} = \frac{-701(s+3.194)}{(s-2.57)(s^2+40.62s+938.74)} \quad \frac{deg/sec}{volt} \tag{8-42}$$

The block diagram of the outer loop of the acceleration control system is
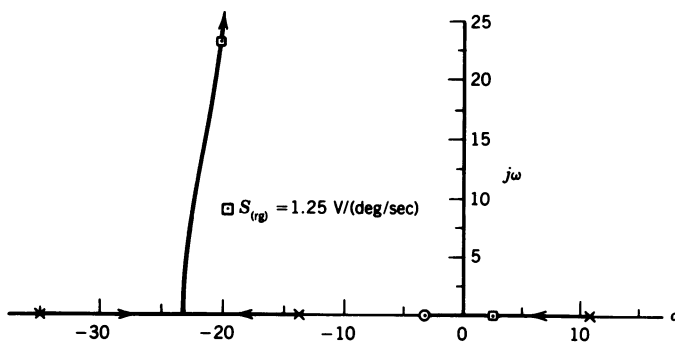
Figure 8-27 Root locus for the inner loop of the acceleration control system.
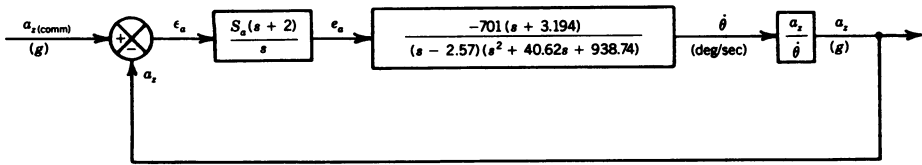
Figure 8-28 *Block diagram for the outer loop of the acceleration control system.*

shown in Figure 8-28, and the $a_z(s)/\dot{\theta}(s)$ transfer function is

$$\frac{a_z(s)}{\dot{\theta}(s)} = \frac{-0.6368(s-47.318)(s+47.329)}{-701(s+3.194)} \quad \frac{g}{\text{deg/sec}} \quad (8\text{-}43)$$

Using the block diagram in Figure 8-28 and Eq. 8-43, the zero-angle root locus for the outer loop can be drawn and is shown in Figure 8-29. The locations of the closed loop poles are indicated for $S_a = 5$ volts/g, and the corresponding closed loop transfer function is

$$\frac{a_z(s)}{a_{z(\text{comm})}(s)} = \frac{-3.184(s+2)(s-47.318)(s+47.329)}{(s^2+6.56s+23.01)(s^2+28.3s+619.08)} \quad (8\text{-}44)$$

From the root locus in Figure 8-29, the stabilizing action of the zero of the proportional plus integral circuit is very apparent. Without this zero the locus of the pole at the origin and the pole at $s = 2.57$ would not move into the left half plane.

This completes the analysis of the pitch acceleration control system; the design of the roll angle control system (RACS) will be discussed next.
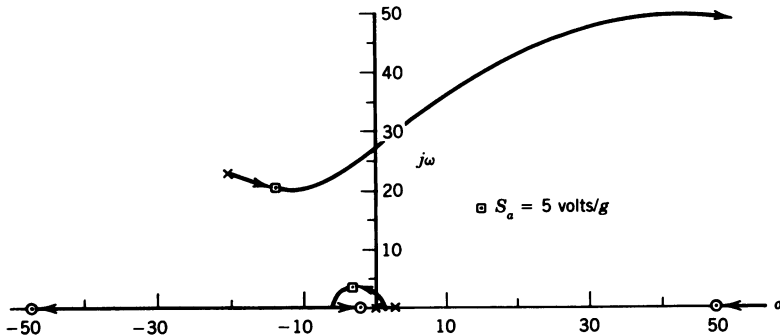
Figure 8-29 *Root locus of the outer loop of the acceleration control system (zero-angle root locus).*
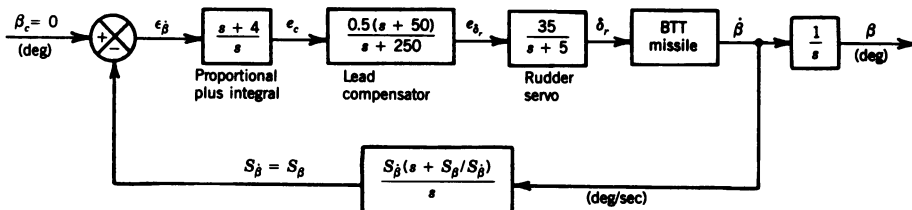
Figure 8-30 Block diagram of $\beta - \dot{\beta}$ SAS.

To control the BTT missile in roll, a RACS similar to the one discussed in Section 4-6 is used, along with the $\beta - \dot{\beta}$ SAS covered in Section 4-2 for Dutch roll damping and sideslip control. The block diagram of the $\beta - \dot{\beta}$ SAS is shown in Figure 8-30. The $\dot{\beta}$ transfer function is

$$\frac{\dot{\beta}(s)}{\delta_r(s)} = \frac{0.8s(s - 0.000114)(s + 2.61)(s + 869.06)}{(s + 0.0242)(s + 3.04)(s^2 + 0.414s + 295.88)} \tag{8-45}$$

The root locus for the $\beta - \dot{\beta}$ SAS is shown in Figure 8-31. Without the lead compensator the missile Dutch roll poles move up along the imaginary axis with no significant increase in damping until the damped natural frequency is greater than 600 rad/sec with a corresponding high gain. The action of the lead compensator in shaping the root locus is very evident. The movement of the real poles in the vicinity of the origin, with the exception of the path of the pole from $s = 0$ to the zero at $s = 0.000114$, can be seen in Figure 32. The locations of the closed loop poles for $S_\beta = S_{\dot{\beta}} = 4$ are indicated in both figures, and the locations of the complex poles for $S_\beta = S_{\dot{\beta}} = 2$ are also shown in Figure 8-31.

Initially the lower gain was selected, as it provided the best damping for the complex poles. Later the gain was raised to 4 after observing the
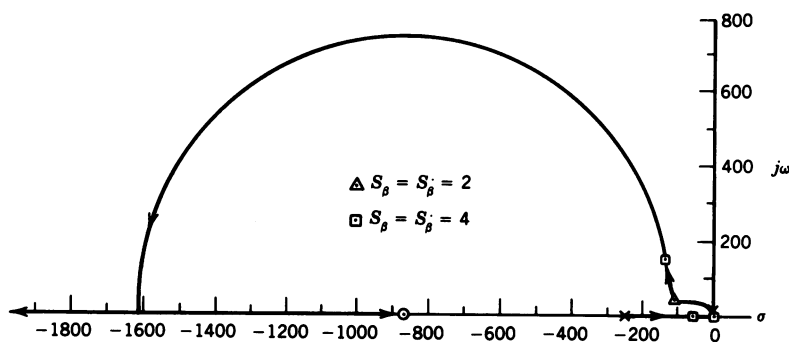
Figure 8-31 Root locus for $\beta - \dot{\beta}$ SAS.
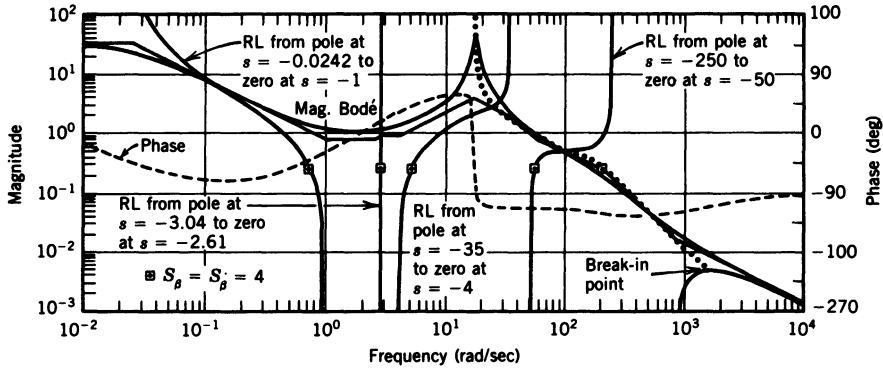
Figure 8-32 Bodé root locus for $\beta - \dot{\beta}$ SAS.

transient sideslip while rolling from $+85$ to -85 degrees of roll angle, as shown later in this section. The closed loop transfer function for $S_\beta = S_{\dot{\beta}} = 2$ is

$$\frac{\beta(s)}{\beta_c(s)} = \frac{14(s - 0.000114)(s + 2.61)(s + 869.06)}{(s - 0.0001127)(s + 0.58)(s + 2.93)(s + 6.31)}$$

$$\times \frac{(s + 4)(s + 50)}{(s + 84.61)(s^2 + 222.05s + 14156.7)} \qquad (8\text{-}46)$$

and for $S_\beta = S_{\dot{\beta}} = 4$ is

$$\frac{\beta(s)}{\beta_c(s)} = \frac{14(s - 0.000114)(s + 2.61)(s + 869.06)}{(s - 0.000113)(s + 0.723)(s + 2.86)(s + 5.1)}$$

$$\times \frac{(s + 4)(s + 50)}{(s + 55.88)(s^2 + 279.9s + 43352.4)} \qquad (8\text{-}47)$$

The damping provided by the $\beta - \dot{\beta}$ SAS is illustrated in Figure 8-33, which shows the response of the missile to a 2-sec pulse aileron deflection of $0.01°$ for $S_\beta = S_{\dot{\beta}} = 2$.

Following the design procedure used in Chapter 4, the coordinated missile transfer function is required in order to perform the root locus analysis of the RACS. The inverse time constant for the coordinated missile transfer function can be obtained from the value of the closed loop roll subsidence pole ($s = -2.93$) from Eq. 8-46. For the coordinated missile transfer function the value from Eq. 8-46 was rounded off to 3. From Figure 8-33, $40°$ was selected as the steady-state value of the roll angle which resulted from an aileron
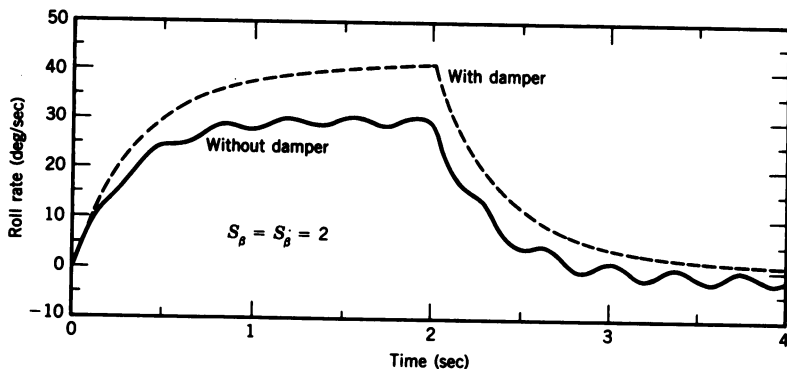
Figure 8-33 *Missile roll rate response for a 2-sec 0.01-deg aileron pulse, with and without* $\beta - \dot{\beta}$ *SAS.*

input of 0.01°. Thus the coordinated missile transfer function is

$$\frac{\dot{\phi}(s)}{\delta_a(s)} = \frac{12,000}{s+3} \frac{\text{deg/sec}}{\text{deg}} \tag{8-48}$$

A comparison of the roll rate response of the coordinated missile transfer function to a 0.01° aileron step input with the roll rate response of the 3-DOF lateral simulation of the missile to a 2-sec 0.01° aileron pulse input is shown in Figure 8-34. The agreement between the two responses is excellent, further testifying to the validity of this design technique.

The block diagram of the RACS is shown in Figure 8-35. Although the roll angle error ϵ_ϕ in Figure 8-35 is shown as the difference between the commanded and actual roll angle, in the simulation ϵ_ϕ was generated using
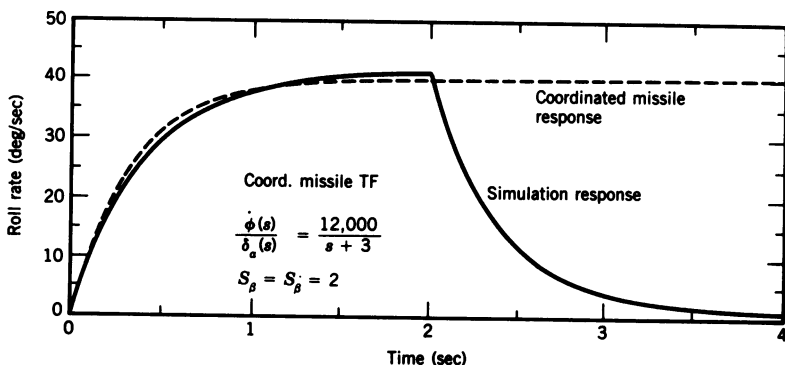
Figure 8-34 *Comparison of the roll rate responses of the coordinated missile to a step aileron input and the missile simulation to a 2-sec aileron pulse input —* $\delta_a = 0.01°$.
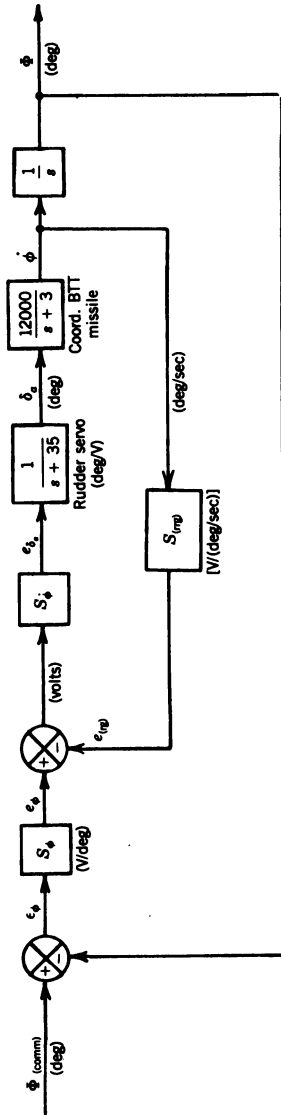
Figure 8-35   Block diagram of RACS.
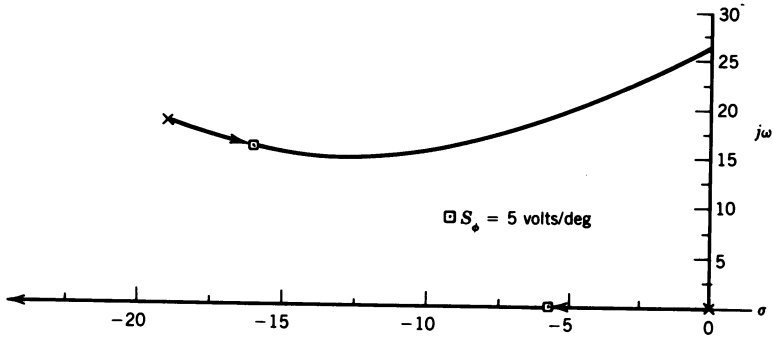
Figure 8-36   Root locus for the outer roll angle loop of the RACS.

Eq. 8-40. The closed loop transfer function for the inner roll rate loop for $S_{\dot\phi} = 0.05$ and $S_{(rrg)} = 1$ volt/(deg/sec) is

$$\frac{\dot\phi(s)}{e_\phi(s)} = \frac{600}{s^2 + 38s + 705} \quad \frac{\text{deg/sec}}{\text{volt}} \tag{8-49}$$

The root locus for the outer roll angle loop of the RACS is shown in Figure 8-36 with the location of the closed loop poles for $S_\phi = 5$ indicated. The corresponding closed loop transfer function is

$$\frac{\Phi(s)}{\Phi_{(comm)}(s)} = \frac{3000}{(s + 5.78)(s^2 + 32.216s + 518.68)} \tag{8-50}$$

To check out the RACS a 5-DOF digital simulation was developed and runs were made with and without the aerodynamic coupling terms contained in Eqs. 8-34 and 8-35. A POCS was used for pitch control. The POCS was later replaced by the acceleration control system discussed earlier in this section. A $\pm 85°$ roll angle command that switched at 2 sec was used for the input. The results are shown in Figures 8-37 through 8-39. It can be seen from the roll angle response shown in Figure 8-37 and the roll rate response shown in Figure 8-38 that the aerodynamic coupling terms have little effect on the missile rolling response. However, the terms do have more effect on the sideslip response as shown in Figure 8-39. From Figure 8-39 it can be seen that doubling S_β and $S_{\dot\beta}$ cuts the maximum sideslip during the roll reversal by approximately 50 percent. It was felt that a further increase in the gain was not necessary. The effects of inertial cross-coupling will be discussed in the next section.

With the design of the pitch acceleration control system and the RACS complete, the missile and the control systems can be integrated with the air-to-air missile–target geometry and the guidance law to develop a com-
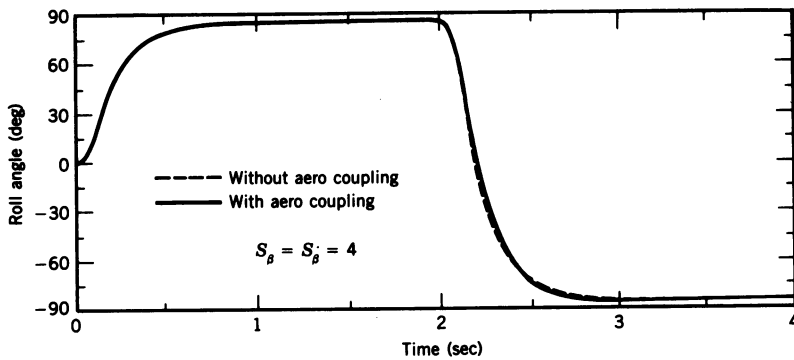
Figure 8-37 Roll angle response of the RACS to a ±85° roll angle command switching at 2 sec, with and without aero coupling terms.
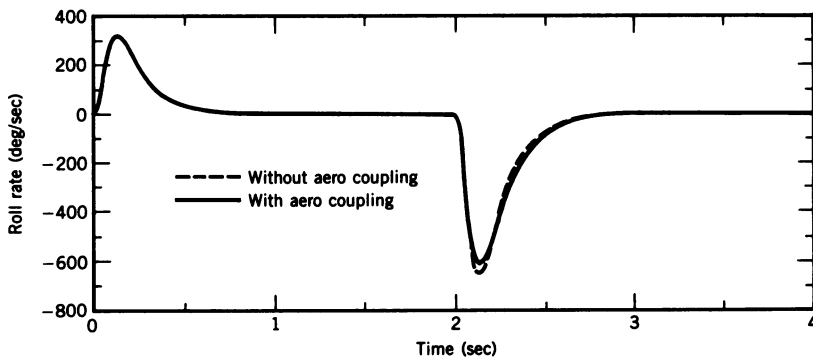
Figure 8-38 Roll rate response for the roll angle response shown in Figure 8-37.
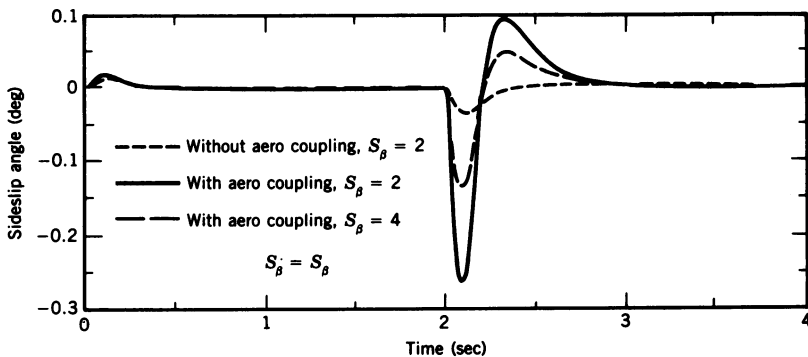
Figure 8-39 Effect of aero coupling terms and β–$\dot{\beta}$ SAS gain on the sideslip response for the roll angle response shown in Figure 8-37.

plete intercept simulation. For the air-to-air intercept the missile was assumed to be at the beginning of its terminal guidance phase heading toward the target and at the target altitude. The missile would have just completed an inertially guided mid-course phase. The pitch and yaw commanded accelerations for the missile guidance were given in Eq. 8-37, which is repeated here for convenience:

$$a_{z(\text{comm})} = N\frac{R_{MTZ} + V_{MTZ}t_{go}}{gt_{go}^2} - g_{z(\text{bias})}$$

$$a_{y(\text{comm})} = N\frac{R_{MTY} + V_{MTY}t_{go}}{gt_{go}^2} - g_{y(\text{bias})} \qquad (8\text{-}51)$$

In the simulation R_{MTZ} and R_{MTY} were calculated by resolving the components of the missile-to-target range vector from the reference coordinates into the missile coordinates through the missile Euler angles. The components of the range vector in the reference coordinates were calculated from the known position of the missile and target. In the actual missile, assuming that the missile had an active radar, these components of the range vector could be calculated from the magnitude of the range vector available from the radar and the radar gimbal angles, as shown in Figure 8-40. Also, in the simulation the velocity components V_{MTZ} and V_{MTY} were calculated by resolving the components of the target velocity minus the missile velocity from the reference coordinates into missile coordinates through the missile Euler angles. In the actual missile the range rate (a negative quantity while the missile is closing on the target) from the radar, resolved through the radar gimbal angles, would provide the component of the vector difference between the missile and target velocities parallel to the LOS. The component perpendicular to the LOS would be equal to the angular velocity of the LOS times the magnitude of the range vector. The R_{MTY} and $V_{MTY}t_{go}$ terms of Eq. 8-51, for a zero roll angle, are shown graphically in Figure 8-41. For a constant-speed missile and target, if the magnitudes of the two terms are equal, then the missile is on a collision course with the target and $a_{y(\text{comm})}$ and $\omega_{(\text{LOS})_z}$ are zero. If the range term R_{MTY} is less than the velocity term $V_{MTY}t_{go}$, then $\omega_{(\text{LOS})_z}$ will be negative (counterclockwise) and the lead angle γ_M must be increased, requiring a negative Y acceleration command and a negative roll angle command. Under these conditions Eq. 8-51 will yield the required negative Y acceleration command. For the missile angle of attack to be positive the pitch acceleration command must be negative (positive Z is down); thus a minus sign is required in Eq. 8-40 to yield a negative roll angle error.

A block diagram showing how the roll angle error signal was introduced into the BTT missile simulation is shown in Figure 8-42. To simplify the block diagram the roll rate feedback loop shown in Figure 8-35 has been replaced
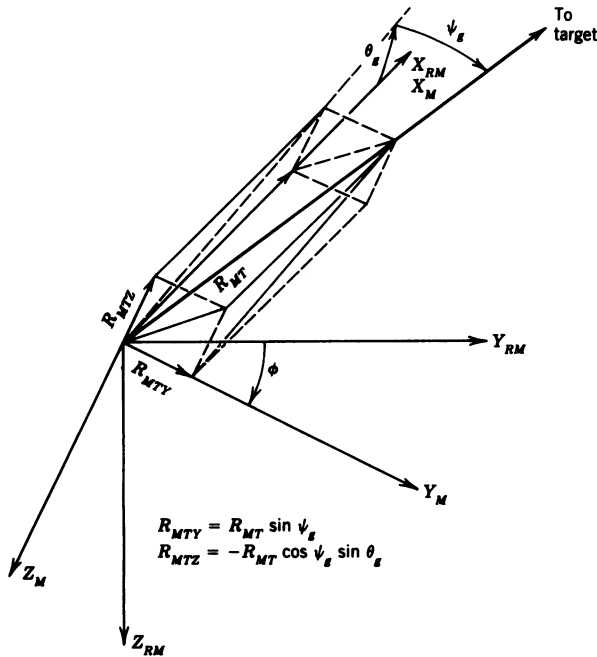
Figure 8-40 *Resolution of missile-to-target range vector from radar tracker axis to missile coordinates.*

by its closed loop transfer function from Eq. 8-49. However, none of these simplifications were made in the 5-DOF missile simulation. For the roll angle loop root locus previously discussed and the corresponding closed loop transfer function it is assumed that the roll angle loop is closed in the conventional manner. The simulation results to be shown next certainly seem to substantiate this assumption.
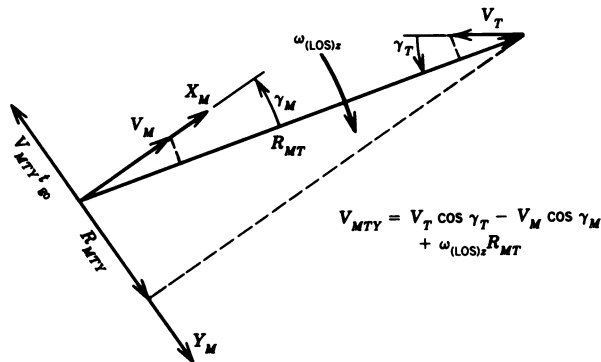
Figure 8-41 *Graphic representation of the components of the yaw acceleration command.*

$$\xrightarrow{\underset{\text{(deg)}}{\epsilon_\phi}} \boxed{\underset{\text{(V/deg)}}{S_\phi}} \xrightarrow{\underset{\text{(volts)}}{e_\phi}} \boxed{\frac{600}{s^2 + 38s + 705}} \xrightarrow{\underset{\text{(deg/sec)}}{\dot{\phi}}} \boxed{\frac{1}{s}} \xrightarrow{\underset{\text{(deg)}}{\Phi}}$$
$$\text{[(deg/sec)/V]}$$
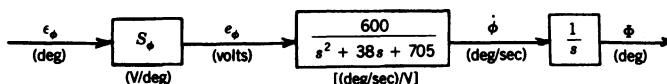
Figure 8-42 Block diagram showing how the input to the RACS was modeled in the BTT missile simulation.

To evaluate the capability of the BTT missile and the guidance laws used, several missile intercepts were run. A navigation constant of 3 (N in Eq. 8-51) was used for all the runs. The initial geometry places the missile and target at 10,000 ft with the missile 30° off the nose of the target and pointed at the target with an initial range of 15,000 ft. The missile velocity is 1509.27 ft/sec and the target velocity 800 ft/sec with the target heading west. The horizontal trajectories of the missile and target for this standard intercept are shown in Figure 8-43. Note how straight the final portion of the missile trajectory is, indicating that the missile is approaching a collision course. The miss distance as used here represents the point of closest approach between the missile and the target. The variation in the missile altitude from the initial altitude of 10,000 ft during the standard run is shown in Figure 8-44. The variation is considered acceptable, especially in view of the miss distance of only 0.45 ft. Successful intercepts were also run with the same initial geometry but with target velocities of 1200 and 1500 ft/sec. The miss distances are included in Table 8-3 at the end of this section, which summarizes the miss distances for all of the intercept scenarios run.

The horizontal missile and target trajectories for a maneuvering target are shown in Figures 8-45 and 8-46. In Figure 8-45 the target starts a 9g turn (20.76 deg/sec) to the right or away from the missile at 2-sec time to go. In Figure 8-46 the target makes a 9g turn to the left or into the missile at 2-sec time to go. The time responses for the intercept shown in Figure 8-46 are
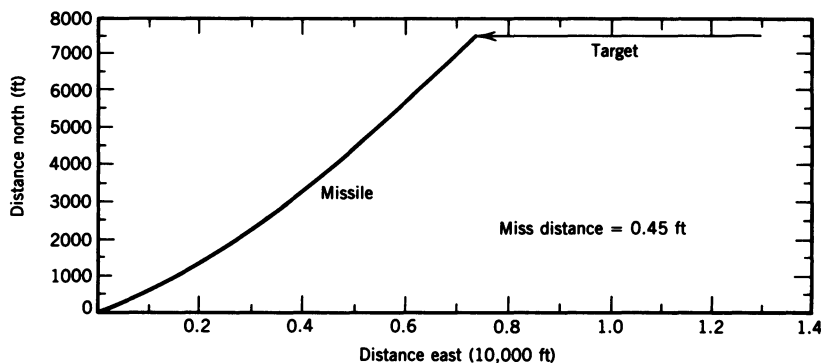
Figure 8-43 Horizontal missile and target trajectories for standard intercept (R_0 = 15,000 ft; target velocity 800 ft / sec at 10,000 ft; missile velocity 1509.27 ft / sec at 10,000 ft).
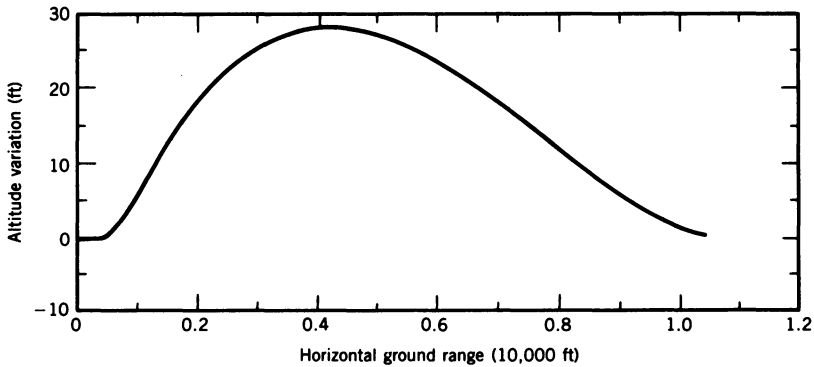
Figure 8-44   *Variation of missile altitude from 10,000 ft during standard intercept.*

shown in Figures 8-47 through 8-50. The roll angle error and related responses are shown in Figure 8-47. The initial value of the roll angle error is due to the component of target velocity normal to the LOS limited to $-80°$. As the initial missile pitch angle is zero (see Figure 8-48), the initial pitch axis acceleration command is the initial Z axis acceleration bias of $-g$, as can also be seen in Figure 8-48. From Figure 8-47 it can be seen that as the roll angle builds up, the roll angle error rapidly decays and goes slightly positive and the roll angle bleeds off, resulting in a slow decrease in the magnitude of the turn rate as the missile approaches a collision course. At about 5 sec the target starts its turn and the missile rapidly rolls to the right to complete the intercept. Figure 8-48 shows the pitch acceleration command following a similar pattern with the sign of the acceleration command always negative. The acceleration command reaches its $-20g$ limit at the end of the run. The
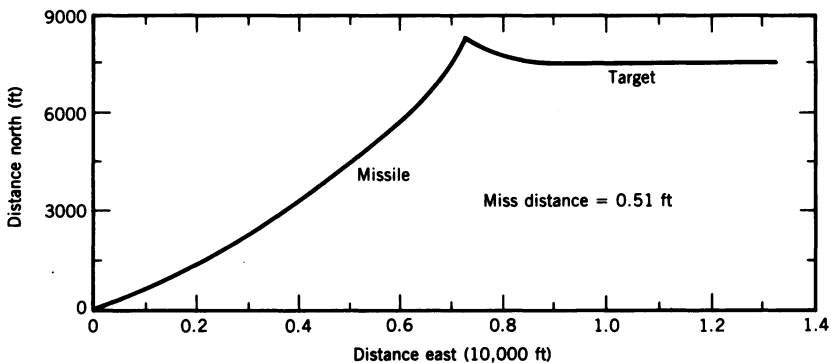
Figure 8-45   *Horizontal missile and target trajectories for target starting a 9g turn (20.76 deg / sec) away from the missile at 2-sec time to go — other conditions same as for standard intercept.*
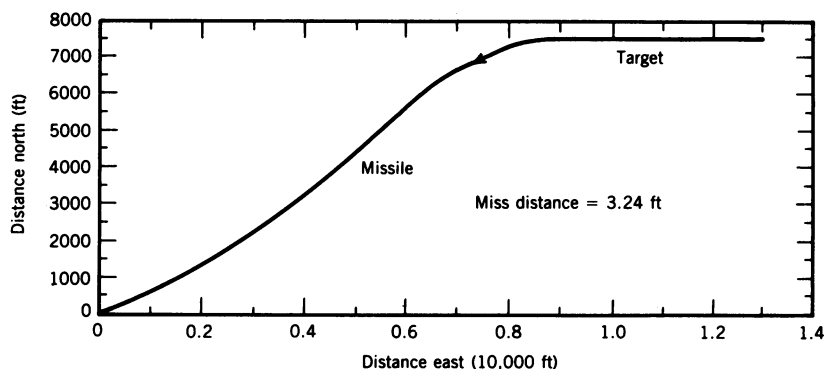
Figure 8-46 *Horizontal missile and target trajectories for target starting a 9g turn into the missile at 3-sec time to go — other conditions same as for standard intercept.*

angles of attack and sideslip experienced by the missile during the intercept are shown in Figure 8-49, with a blowup of the angle of sideslip shown in Figure 8-50. From the results shown here, it can be concluded that the performance of the guidance law coupled with the control system designed provides an exceptional intercept capability for the BTT missile.

Arrow in Ref. 1 comments that a major shortcoming of the BTT missile is its slower response than that of STT missiles. His report shows that a typical air-to-air STT missile has a maneuver plane time constant of about 0.25 sec for a dynamic pressure of 2000 lb/ft^2 (the dynamic pressure of this engagement). The missile time constant is defined in Ref. 4 as the time for the response due to a step input to reach 63 percent of its final value. Using this definition, then in 4 time constants (4τ) the response will reach 98 percent of its final value. This is often referred to as the response time. An examination
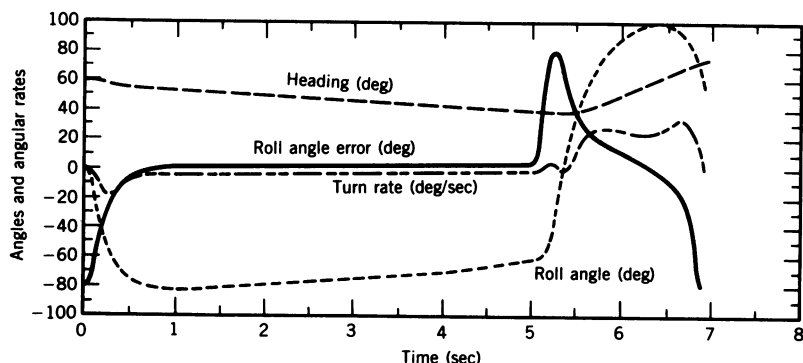
Figure 8-47 *Roll angle error and indicated missile responses for intercept shown in Figure 8-46.*
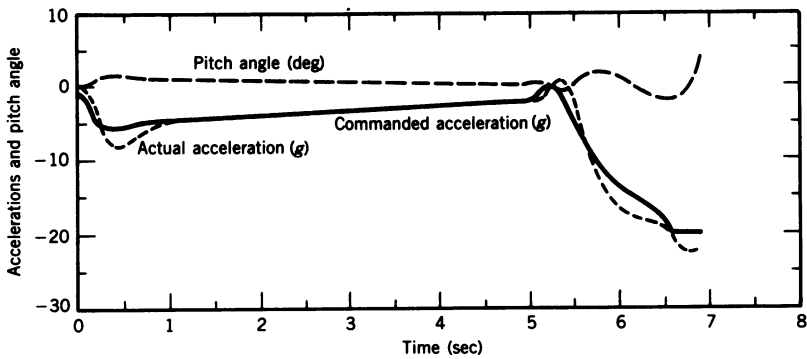
Figure 8-48 Pitch acceleration command and indicated missile responses for intercept shown in Figure 8-46.
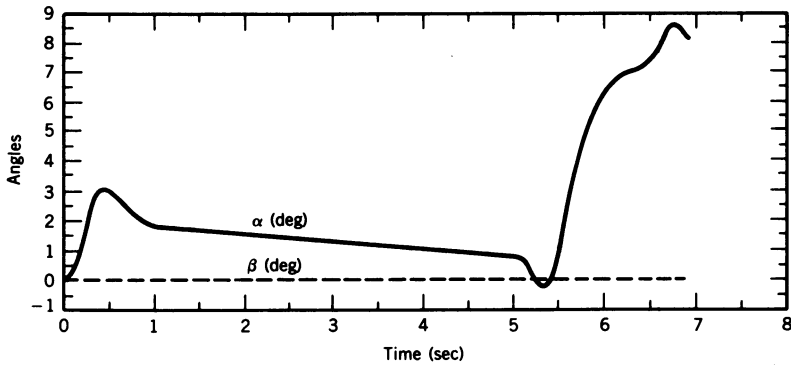
Figure 8-49 Missile angles of attack and sideslip during intercept shown in Figure 8-46.
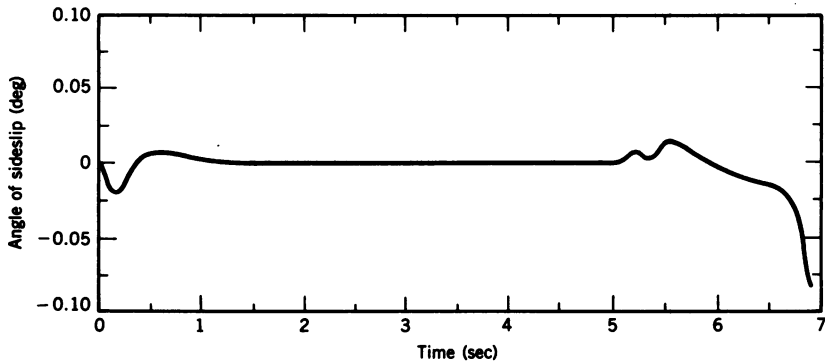
Figure 8-50 Blowup of missile angle of sideslip shown in Figure 8-49.

TABLE 8-3 Summary of Miss Distances for Different Intercept Scenarios*

Angle Off Nose of Target (deg)	Maneuvering Target			Miss Distance (ft)
	Target Velocity (ft / sec)	Direction[†] of 9g Turn	Time to go at Start of Turn (sec)	
30	800	None	—	0.45
30	1200	None	—	0.96
30	1500	None	—	0.83
60	800	None	—	0.4
30	800	Right	2	0.41
30	800	Left	2	3.24
30	800	Left	3	2.2

*R_0 = 15,000 ft; missile velocity 1509.27 ft / sec; missile and target at 10,000 ft.
[†]Right turn is a turn away from the missile; left turn is a turn toward the missile.

of Figures 8-47 and 8-48 shows that the missile has rolled to its maximum roll angle and the missile acceleration has reached the commanded value within 1 sec. If 1 sec is taken for 4τ, then the missile time constant is 0.25 sec, making the response of this BTT missile model equal to that of the STT missile cited in Ref. 1.

This completes the design and analysis of an autopilot and guidance system for a ramjet propelled BTT air-to-air missile. The same autopilot and guidance system will be used for a study of a short- to medium-range BTT missile in the next section.

8-6 SHORT/MEDIUM-RANGE BTT MISSILE

Using the thrust, drag, and weight data from Ref. 5 as a basis, estimates were made for the moments of inertia of the missile in order to develop a 6-DOF missile simulation. The missile used in Ref. 5 was a short-range missile with a burnout time of 2.6 sec and a thrust of 4700 lb. In order to model a medium-range missile the weight was increased and the burn time doubled to 5.2 sec with the thrust unchanged. Assuming that the majority of the weight was concentrated in the cylindrical body, the three moments of inertia were estimated by using the equations for the moment of inertia for a right circular cylinder from mechanics. It was also assumed that I_y and I_z were equal and that all the products of inertia were zero. The mass and moments of inertia were reduced as fuel was burned. With estimates of the mass and moments of inertia, the nondimensional stability derivatives were calculated from the dimensional stability derivatives from Ref. 3. With the exception of C_{L_α}, the stability derivatives were assumed not to be a function of Mach number. The lift curve slope was assumed to decrease linearly with increasing

Mach number for Mach > 1.1. With the introduction of thrust and drag, including drag due to lift, the dynamics of the missile vary during the intercept due to the changes in velocity and dynamic pressure. To check out the 6-DOF simulation, the standard intercept described in the last section was run using the control system gains determined from that root locus analysis. Although the intercept was successful, a fairly well-damped low-frequency oscillation was evident during the first 2 sec of the run, and several cycles of a high-frequency oscillation at about 4.7 sec. As a result, a root locus analysis for the conditions at 1, 3, and 4.5 sec was carried out. The corresponding dynamic pressures were 1509, 3217.3, and 4840 lb/sq ft. Initially only the accelerometer loop gain S_a was varied; however, as this did not eliminate the high-frequency oscillation at 4.5 sec, both gains in the acceleration control system were scheduled. The resulting initial gain schedules are

$$S_a = 85{,}849/q^{1.3} \qquad (8\text{-}52)$$

For $q > 1880$ lb/sq ft,

$$S_{(rg)} = 1.25 - 0.000254(q - 1880) \qquad (8\text{-}52a)$$

with $S_{(rg)} = 1.25$ for $q \leq 1880$ lb/sq ft.

A similar root locus analysis of the $\beta - \dot{\beta}$ SAS and the RACS was performed using data from the standard intercept at 0.5, 3, and 4.5 sec of flight time, which resulted in dynamic pressures of 1087.08, 3217.3, and 4831.4 lb/sq ft respectively. The resulting gain schedules for S_β ($S_{\dot{\beta}} = S_\beta$) and S_ϕ are shown in Figures 8-51 and 8-52 respectively. The feedback gain ($S_{(rrg)} = 1$) in the roll damping loop (see Figure 8-35) and the forward gain ($S_\phi = 5$) in the roll angle loop of the RACS were not scheduled. The
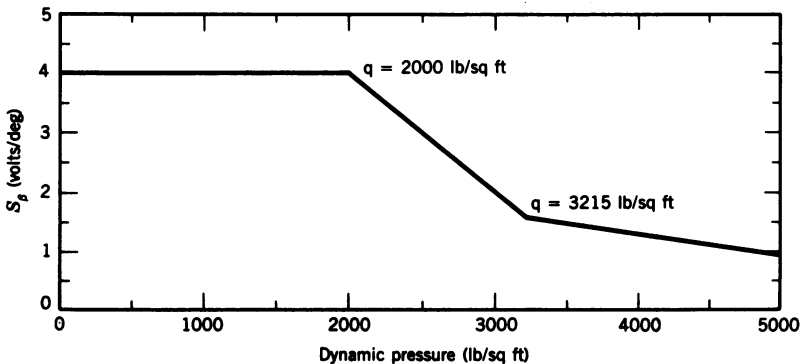
Figure 8-51 Gain schedule for the $\beta - \dot{\beta}$ SAS.
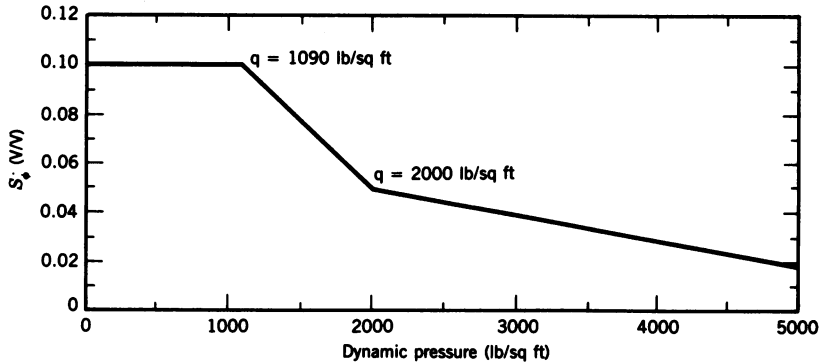
Figure 8-52   Gain schedule for S_ϕ in the roll damping loop of the RACS.

equation for S_β is

For $q > 2000$ and $q \leq 3215$ lb/sq ft:

$$S_\beta = 4 - 0.002(q - 2000) \qquad (8\text{-}53)$$

For $q > 3215$ lb/sq ft:

$$S_\beta = 1.57 - 0.000353(q - 3215) \qquad (8\text{-}53\text{a})$$

with the minimum value limited to 0.5 and with $S_{\dot\beta} = S_\beta$.

The equation for S_ϕ is

For $q > 1090$ and $q \leq 2000$ lb/sq ft:

$$S_{\dot\phi} = 0.1 - 5.5 \times 10^{-5}(q - 1090) \qquad (8\text{-}54)$$

For $q > 2000$ lb/sq ft:

$$S_{\dot\phi} = 0.05 - 1.06 \times 10^{-5}(q - 2000) \qquad (8\text{-}54\text{a})$$

with the minimum value limited to 0.01.

Using these gain schedules, a series of intercepts were run to evaluate the capability of this design of the BTT missile. The missile and target were at an altitude of 10,000 ft, with the target heading west at 800 ft/sec (Mach 0.74) 7500 ft north of the missile launch point. The missile was launched directly at the target with an initial velocity of 1000 ft/sec (Mach 0.93). The target was

TABLE 8-4   Summary of Miss Distances for the Listed Target Distances East of the Missile Launch Point*

Distance East (ft)	Miss Distance (ft)	Time of Flight (sec)	Final Mach No.
55,000	0.11	21.3	1.27
10,000	1.38	5.31	2.33
5,000	2.05	4.59	2.18
2,500	7.19	4.6	2.18
0	7.88	4.97	2.27
−2,500	0.99	5.68	2.28
−10,000	1.68	9.63	1.9
−20,000	0.75	19.91	1.32

*Target: $M = 0.74$ at 10,000 ft, heading west, 7500 ft north of the missile launch point. Missile: 10,000 ft, launched at $M = 0.93$, heading at the target.

placed at the distances east of the missile launch point as shown in Table 8-4 (a negative distance indicates a retreating target).

From Table 8-4 it can be seen that the beam shot (target directly north of the missile launch point) resulted in the greatest miss distance and thus presented the most difficult missile–target geometry for this series of runs. Thus intercepts were made using this initial geometry, but with increased altitudes. An intercept made with this geometry, but with both the missile and target at 30,000 ft, resulted in a 2.62-ft miss distance after a time of flight of 4.92 sec with a final Mach number of 2.56. A similar run at 40,000-ft altitude terminated at 1.64 sec when the missile went unstable. The reason for this can be seen by examining the root loci shown in Figures 8-53 and 8-54 for the accelerometer loop of the acceleration control system (see Figure 8-25) for two values of the rate damping loop gain $S_{(rg)}$. The flight condition
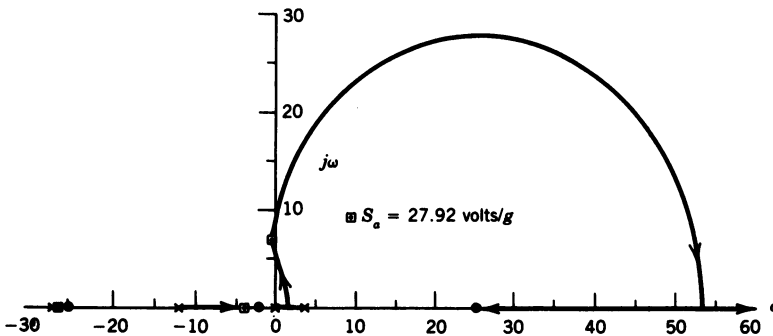
Figure 8-53 *Accelerometer loop root locus for $V_M = 1280.52$ ft / sec at 40,000 ft for $S_{(rg)} = 1.25$.*
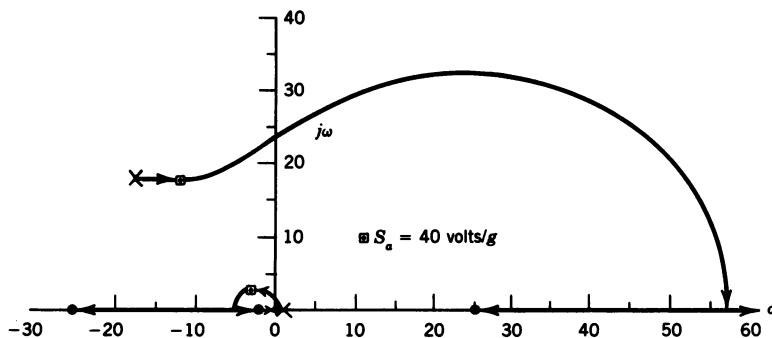
Figure 8-54 *Accelerometer loop root locus for $V_M = 1280.52$ ft / sec at 40,000 ft for $S_{(rg)} = 4$.*

for the root loci is a missile velocity of 1280.52 ft/sec at 40,000-ft altitude (Mach 1.32) for a dynamic pressure of 481.917 lb/sq ft. Figure 8-53 is the accelerometer loop root locus for $S_{(rg)} = 1.25$, which resulted in the following closed loop transfer function for the rate damping loop:

$$\frac{\dot{\theta}(s)}{e_a(s)} = \frac{-157.325(s + 0.854)}{(s - 3.175)(s + 11.465)(s + 27.526)} \quad \frac{\text{deg/sec}}{\text{volt}} \quad (8\text{-}55)$$

From Eq. 8-55 it can be seen that all of the closed loop poles are real, and from Figure 8-53 it can be seen that the branch of the root locus generated by the unstable missile pole and the pole at the origin barely cross into the left half plane. The closed loop poles are indicated for $S_a = 27.92$ (calculated from Eq. 8-52), which results in a damping ratio of 0.06 for the complex poles. As will be seen later in this section, closing the geometry loop drives these poles unstable. Increasing the value of $S_{(rg)}$ to 4 results in the following closed loop transfer function for the rate damping loop:

$$\frac{\dot{\theta}(s)}{e_a(s)} = \frac{-157.325(s + 0.854)}{(s - 0.959)(s^2 + 36.776s + 659.711)} \quad \frac{\text{deg/sec}}{\text{volt}} \quad (8\text{-}56)$$

The root locus for the accelerometer loop for $S_{(rg)} = 4$ is shown in Figure 8-54 with the location of the closed loop poles indicated for $S_a = 40$. The damping ratio for the missile complex poles in Eq. 8-56 is 0.72. It was found in the analysis of the different flight conditions studied that setting the rate damping loop gain so that the damping of these complex poles was approximately 0.7 resulted, for all cases considered, in the root locus configuration for the accelerometer loop shown in Figure 8-54. If the damping of the complex poles is much greater than 0.7, then the complex poles break into the real axis and the branch coming from the right half plane has the configuration shown in Figure 8-53, with the exception that the path moves further into the
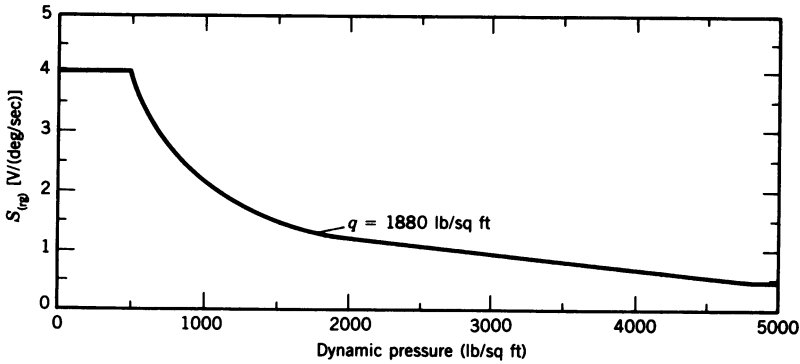
Figure 8-55   *Gain schedule for rate damping loop gain for the acceleration control system.*

left half plane before going unstable. As a result of this analysis, the gain schedules for both the rate damping and acceleration loops of the acceleration control system were changed to the schedules shown in Figures 8-55 and 8-56:

For $q \leq 1880$ lb/sq ft (original gain schedule),

$$S_{(rg)} = 784.62/q^{0.8545}$$

$$S_a = 628389/q^{1.564} \tag{8-57}$$

For $q > 1880$ lb/sq ft,

$$S_{(rg)} = 1.25 - 0.000254(q - 1880)$$

$$S_a = 85849/q^{1.3} \tag{8-58}$$
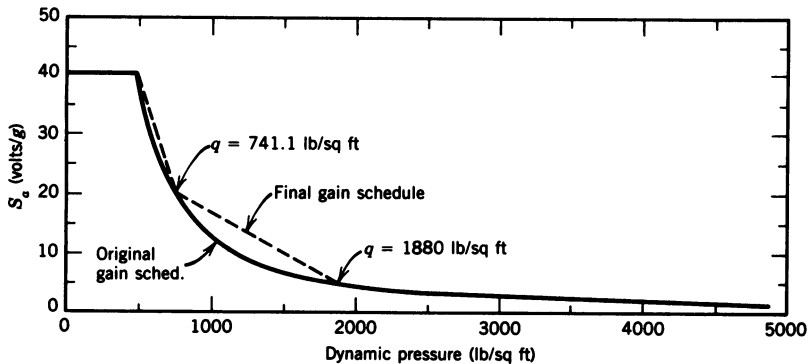
Figure 8-56   *Gain schedule for the acceleration loop gain for the acceleration control system.*

with the minimum value of $S_{(rg)}$ equal to 0.5. The original gain schedule for S_a was modified as shown in Figure 8-56 after a root locus analysis for 50,000 ft showed that the slightly higher gain provided by the linear gain schedule shown in the figure and given in Eq. 8-59 for $q \leq 1880$ lb/sq ft provided better results:

For $q > 741.1$ lb/sq ft,

$$S_a = 22 - 0.0151(q - 741.1) \tag{8-59}$$

For $q \leq 741.1$ lb/sq ft,

$$S_a = 40 - 0.0695(q - 481.9) \tag{8-59a}$$

It has been found that the form of Eq. 8-58 for S_a is very useful for scheduling gains as a function of dynamic pressure, and stability derivatives as a function of Mach number for supersonic Mach numbers. The numerator constant and the power of q can normally be calculated by solving the two equations generated using the values of the variables at the end points of the curve. Although the resulting curve will not match the desired curve exactly, it has been found that the variation from the desired curve is usually acceptable.

In Section 8-2 it was shown that the geometry loop for proportional navigation guidance added a real pole in the right half s plane (see Figure 8-3). It seemed that a similar analysis of the geometry loop for the BTT missile should be possible using the guidance law for the BTT missile, which is repeated here from Eq. 8-37 for the pitch acceleration command:

$$a_{z(\text{comm})} = N \frac{R_{MTZ} + V_{MTZ} t_{\text{go}}}{g t_{\text{go}}^2} - g_{z(\text{bias})} \tag{8-60}$$

The resulting block diagram is shown in Figure 8-57 which gave reasonable correlation between the root locus analysis and the simulation results. The differences between the block diagram shown in Figure 8-57 and the one in Figure 8-3 will now be explained. For a co-altitude attack, almost all the maneuvering is in the horizontal plane; thus Θ in Figure 8-3 has been replaced by Ψ in Figure 8-57. The $V_M s/(g \sin \Phi)$ block performs the function of the seeker in Figure 8-3 and generates the commanded missile turning rate in rad/sec. The commanded turn rate is converted to a horizontal acceleration command in g's by the factor V_M/g. The horizontal acceleration command is converted to a missile pitch acceleration command by dividing by $\sin \Phi$. The gain block is the magnitude of Eq. 8-60. The magnitude alone is used, as the sign of Φ determines the direction of the turn. The values for all the variables in the gain block are taken from the printout of the run at the time selected for analysis. The next block is the missile closed

Figure 8-57 Block diagram for BTT missile guidance including geometry.

loop transfer function for the flight condition being analyzed. The $(g \sin \Phi)/V_M s$ block converts the missile acceleration a_z in g's to a missile pitch rate $\dot{\Theta}$ in rad/sec. Multiplying the pitch rate by $\sin \Phi$ yields the missile turning rate $\dot{\Psi}_M$, which when integrated gives the missile heading Ψ_M the required feedback quantity.

The root locus analysis for the 40,000-ft intercept at $t = 1$ sec shown in Figures 8-53 and 8-54 will now be continued using the geometry loop block diagram from Figure 8-57. For the case shown by the root locus in Figure 8-53, the required variables are

$$N = 3$$

$$R_{MTZ} = 1069.72 \text{ ft}$$

$$V_{MTZ} = -60.2 \text{ ft/sec}$$

$$t_{go} = 3.41 \text{ sec}$$

$$V_M = 1280.52 \text{ ft/sec}$$

$$R = 6407.8 \text{ ft}$$

$$\text{gain} = \left| \frac{N(R_{MTZ} + V_{MTZ} t_{go})}{g t_{go}^2} \right| = 6.926$$

$$V_M / R = 0.2$$

The root locus for the geometry loop is shown in Figure 8-58 and the Bodé root locus in Figure 8-59 with the closed loop poles indicated for gain = 6.926. From Figure 8-59 it can be seen that the geometry pole crosses into the left half plane at a value of gain = 1, as was seen in Section 8-2 for proportional navigation guidance. The closed loop transfer function for gain = 6.926, after
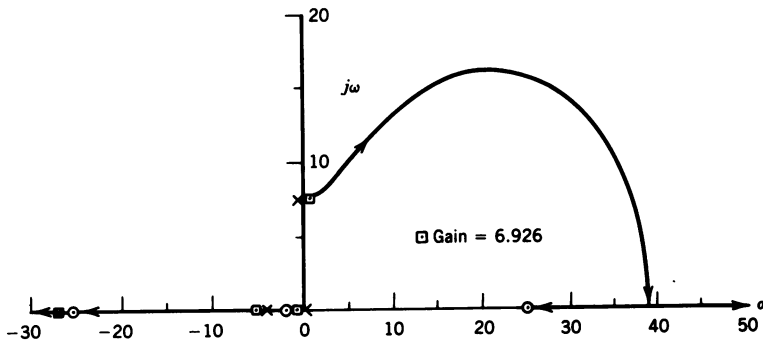
Figure 8-58 Root locus for the geometry loop for 40,000 ft, $S_{(rg)} = 1.25$, $S_a = 27.92$ (zero-angle root locus).
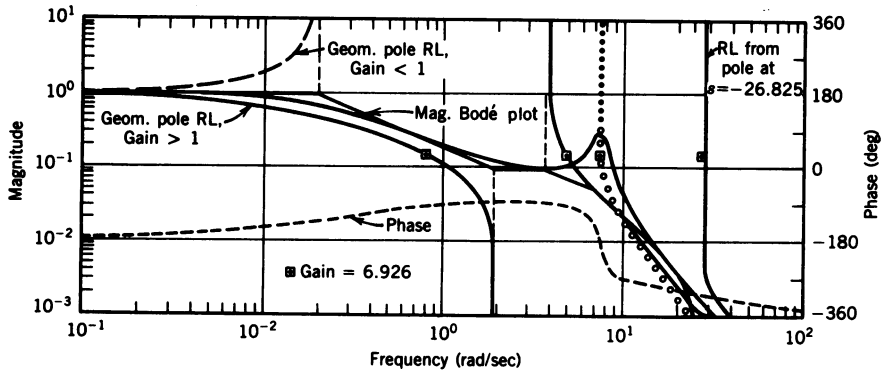
Figure 8-59 *Bodé root locus for the geometry loop for 40,000 ft, $S_{(rg)} = 1.25$, $S_a = 27.92$.*

multiplying by $(V_T/R)/(s - V_M/R)$, where $V_T = 800$ ft/sec, is

$$\frac{\Psi_M(s)}{(\Psi_T - \Psi_R)(s)} = \frac{-3.53(s+2)(s-25.285)(s+25.292)}{(s+0.812)(s+4.936)(s+26.85)(s^2 - 1.35s + 56.7)}$$

$$(8-61)$$

For the case shown by the root locus in Figure 8-54, the required variables are:

$$N = 3$$
$$R_{MTZ} = 2338.1 \text{ ft}$$
$$V_{MTZ} = -996.17 \text{ ft/sec}$$
$$t_{go} = 4.19 \text{ sec}$$
$$V_M = 1301.36 \text{ ft/sec}$$
$$R = 6397.71 \text{ ft}$$
$$\text{gain} = \left| \frac{N(R_{MTZ} + V_{MTZ}t_{go})}{gt_{go}^2} \right| = 9.74$$
$$V_M/R = 0.2$$

The value of the gain here is different from the one used for the unstable case (though that gain could have been used), as the values of the variables were taken from the run at 40,000 ft after the new gain schedule had been introduced into the simulation. The root locus for the geometry loop is shown in Figure 8-60 and the Bodé root locus in Figure 8-61. Again from Figure 8-61 it can be seen that the geometry pole moves into the left half plane at a gain of one. The gain margin from Figure 8-61 is 37.6, and the closed loop
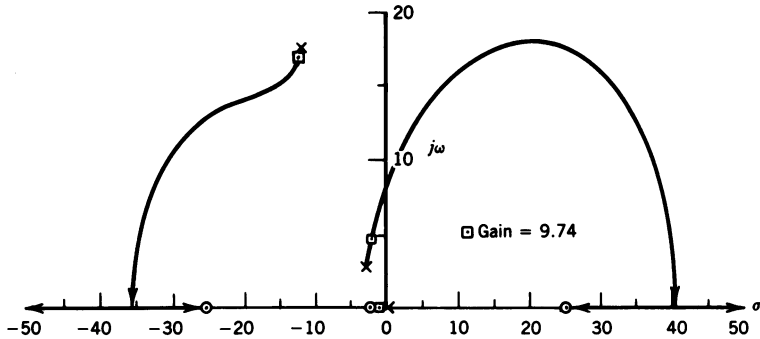
Figure 8-60 *Root locus for the geometry loop for 40,000 ft, $S_{(rg)} = 4$, $S_a = 40$ (zero-angle root locus).*

transfer function after multiplying by $(V_T/R)/(s - V_M/R)$ is

$$\frac{\Psi_M(s)}{(\Psi_T - \Psi_R)(s)} = \frac{-7.11(s+2)(s-25.285)(s+25.292)}{(s+1.136)(s^2+3.78s+25.945)(s^2+26.86s+442.825)}$$

$$(8\text{-}62)$$

The missile responses for the 40,000-ft intercept for the gain schedule from Eq. 8-52 (old gain schedule) and Eqs. 8-57 and 8-58 (new gain schedule) are shown in Figures 8-62 through 8-65. Figure 8-62 shows the Z axis acceleration command, and Figure 8-63 the resulting missile acceleration. The roll angle error response is shown in Figure 8-64 and the resulting missile roll angle in Figure 8-65. The improvement provided by the new gain schedule is obvious. The step response for the closed loop transfer function given in Eq. 8-61 is shown in Figure 8-66, and that for the closed loop
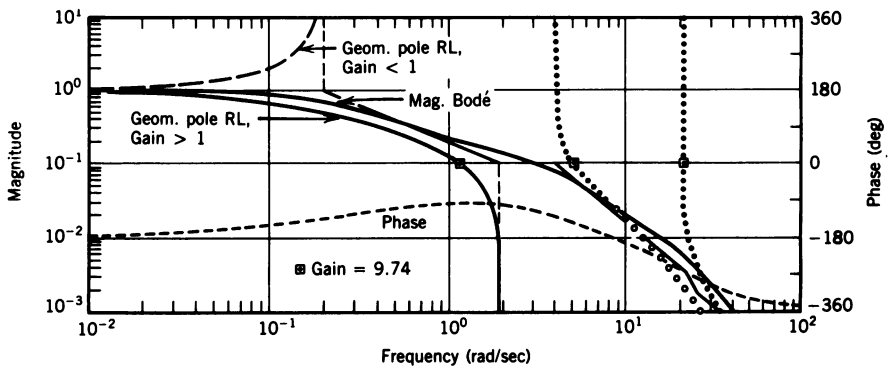
Figure 8-61 *Bodé root locus for the geometry loop for 40,000 ft, $S_{(rg)} = 4$, $S_a = 40$.*
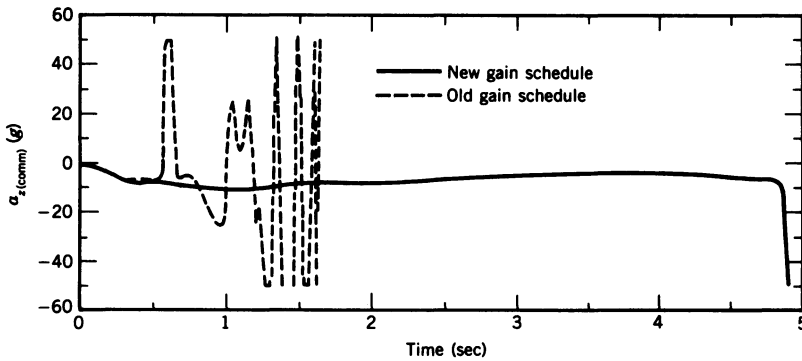
Figure 8-62   *Comparison of the $a_{z(comm)}$ responses for the 40,000-ft intercept for the old and new gain schedules.*

transfer function given in Eq. 8-62 is shown in Figure 8-67. These responses can best be compared with the missile acceleration response shown in Figure 8-63. However, the comparison is difficult in that the acceleration command in the simulation is not a step, but more like a ramp that levels off at about $-10g$. The frequency of the response shown in Figure 8-66 is certainly lower than that shown in Figure 8-63 at 1 sec; however, it is very close to the frequency of the response in Figure 8-63 at 0.5 sec. It must be remembered that the missile dynamics are changing very rapidly as the missile is accelerating at about 180 ft/sec^2. Even if the frequencies are off, the analysis certainly predicts the stability or instability accurately. This was further substantiated by a similar analysis for the close-in beam attack at 50,000 ft.

This completes the discussion of the analysis required to obtain the required gain schedules. The effects of inertial cross-coupling will be discussed next, followed by some intercept results against a maneuvering target.
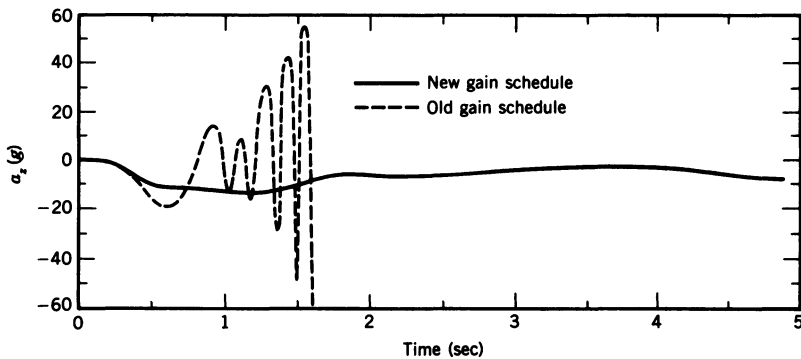
Figure 8-63   *Comparison of the missile a_z responses for the 40,000-ft intercept for the old and new gain schedules.*
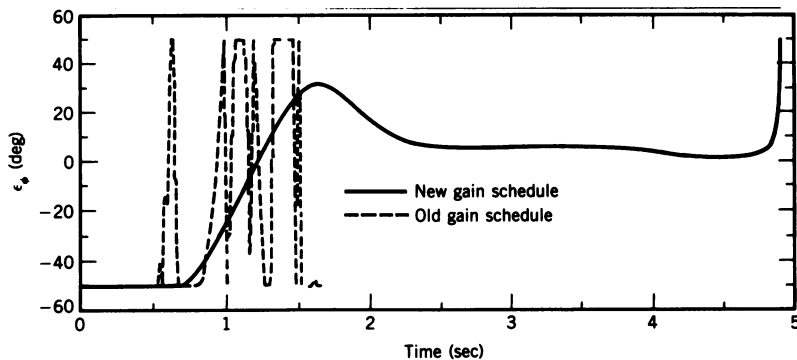
Figure 8-64 Comparison of the roll angle error responses for the 40,000-ft intercept for the old and new gain schedules.
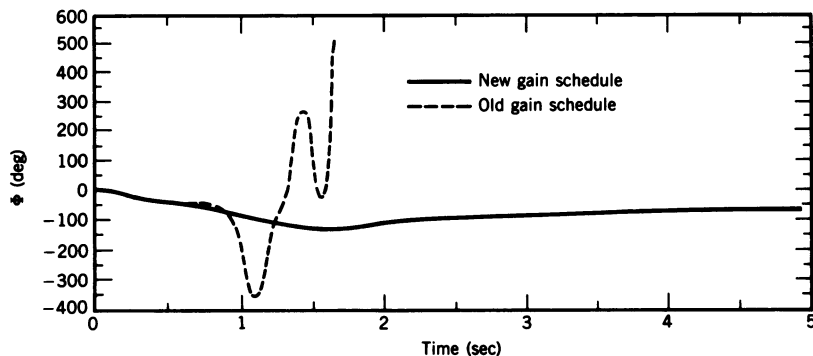
Figure 8-65 Comparison of the missile roll angle responses for the 40,000-ft intercept for the old and new gain schedules.
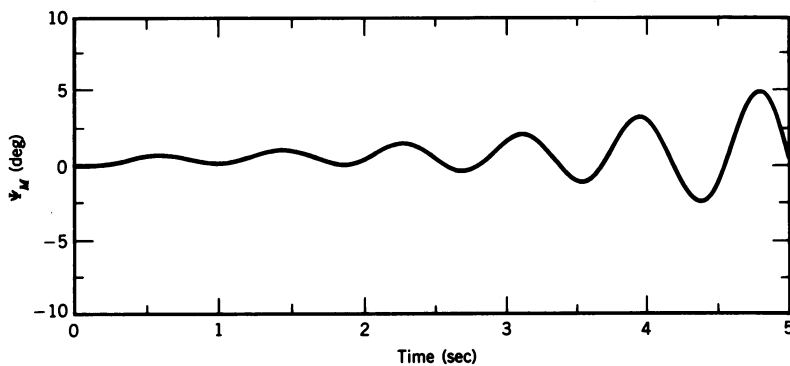
Figure 8-66 Step response for the closed loop transfer function given in Eq. 8-61.
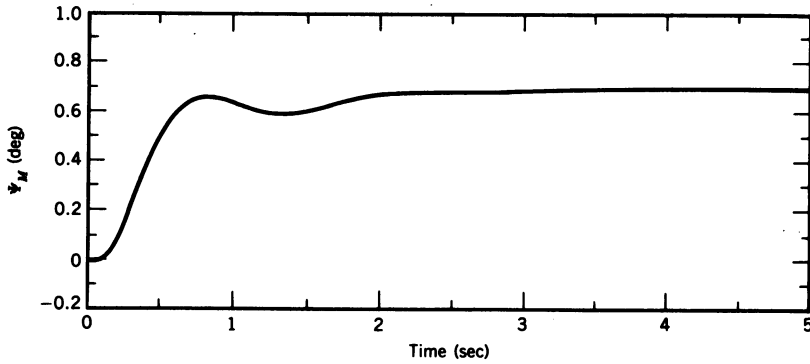
Figure 8-67 *Step response for the closed loop transfer function given in Eq. 8-62.*

The 6-DOF equations of motion used in the simulation to model the missile, including the inertial cross-coupling terms, can be obtained from Eqs. G-15, G-8, 1-59, and 3-17 with the addition of the moment of inertia terms from Eq. 1-32 (assuming that the products of inertia are zero and that $I_y = I_z$). They are

$$\dot{V}_M = A_{XS} \cos \beta + A_{YS} \sin \beta \text{ ft/sec}^2$$

$$\dot{\alpha} = \frac{A_{ZS}}{V_M \cos \beta} + Q - \frac{P_S \sin \beta}{\cos \beta} \text{ sec}^{-1}$$

$$\dot{Q} = \frac{Sqd}{I_y} \left(\frac{d}{2V_M} C_{m_q} Q + C_{m_\alpha} \alpha + C_{m_{\delta_e}} \delta_e \right) + \frac{I_z - I_x}{I_y} PR \text{ sec}^{-2}$$

$$\dot{\beta} = \frac{-A_{XS} \sin \beta + A_{YS} \cos \beta}{V_M} - R_S \text{ sec}^{-1}$$

$$\dot{R} = \frac{Sqb}{I_z} \left(\frac{b}{2V_M} (C_{n_p} P + C_{n_r} R) + C_{n_\beta} \beta + C_{n_{\delta_a}} \delta_a + C_{n_{\delta_r}} \delta_r \right)$$

$$+ \frac{I_x - I_y}{I_z} PQ \text{ sec}^{-2}$$

$$\dot{P} = \frac{Sqb}{I_x} \left(\frac{b}{2V_M} (C_{l_p} P + C_{l_r} R) + C_{l_b} b + C_{l_{d_a}} d_a \right) \text{ sec}^{-2} \tag{8-63}$$

where, from Eq. G-14,

$$P_S = R \sin \alpha + P \cos \alpha$$

$$R_S = R \cos \alpha - P \sin \alpha \tag{8-64}$$
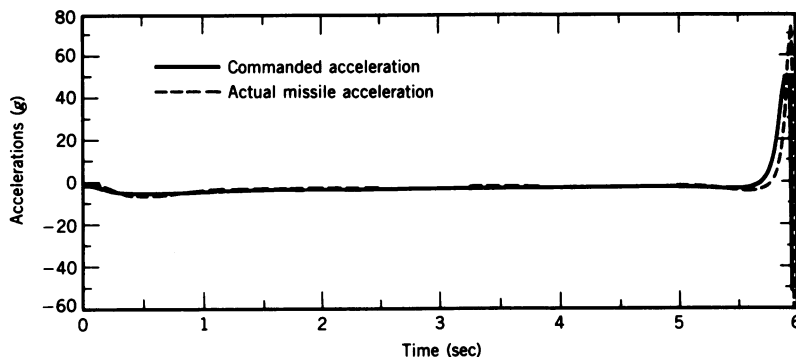
Figure 8-68 *Commanded and actual missile normal accelerations for the standard run with inertial cross-coupling.*

and from Eq. G-16 (see Eq. 8-36 for G_x, G_y, and G_z)

$$A_{XS} = \left(\frac{T}{m} + G_x\right)\cos\alpha + G_z\sin\alpha - \frac{Sq}{m}C_D \text{ ft/sec}^2$$

$$A_{YS} = G_y + \frac{Sq}{m}\left(C_{y_\beta}\beta + C_{y_{\delta_r}}\delta_r\right) \text{ ft/sec}^2$$

$$A_{ZS} = -\left(\frac{T}{m} + G_x\right)\sin\alpha + G_z\cos\alpha - \frac{Sq}{m}\left(C_{L_\alpha}\alpha + C_{L_{\delta_e}}\delta_e\right) \text{ ft/sec}^2 \quad (8\text{-}65)$$

As shown in Section 5-1, the inertial cross-coupling terms are $PR(I_z - I_x)/I_y$ and $PQ(I_x - I_y)/I_z$, which couple the rolling angular velocity P into the pitching and yawing moment equations. To determine the effect of inertial cross-coupling on the BTT missile, the standard intercept was run with and without the inertial cross-coupling terms. As can be seen in Figures 8-68 through 8-71, most of the effect occurred just prior to intercept and resulted in the miss distance increasing from 1.27 ft to 4.4 ft. The normal acceleration command and the actual missile normal acceleration are shown in Figure 8-68 for the case with inertial cross-coupling. The addition of the inertial cross-coupling terms had no effect on the normal acceleration command. The effect on the normal acceleration had the same pattern as that shown for the angle of attack in Figure 8-69 just prior to intercept. The effect of inertial cross-coupling on the roll angle error and the missile roll angle is shown in Figure 8-70, and on the roll rate in Figure 8-71. The large increase in the roll angle error at engine burnout results from the change in the calculated time to go as the missile starts to decelerate, causing both the normal and lateral commanded accelerations to change (see Eq. 8-37). The lateral acceleration command goes from $0.24g$ at 5 sec to $-1.73g$ at 5.25 sec; the normal acceleration command goes from $-1.5g$ to $-2.02g$ during the same period.
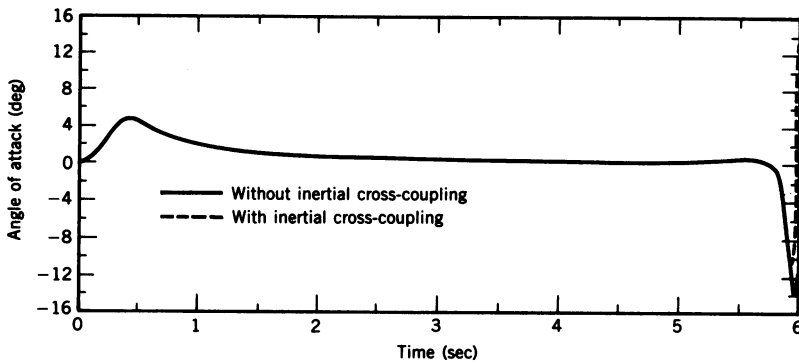
Figure 8-69 *Comparison of missile angle of attack for the standard run with and without inertial cross-coupling.*
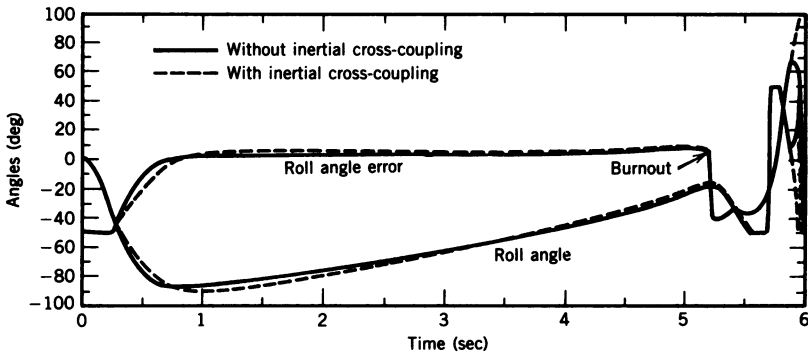
Figure 8-70 *Comparison of roll angle error and missile roll angle for the standard run with and without inertial cross-coupling.*
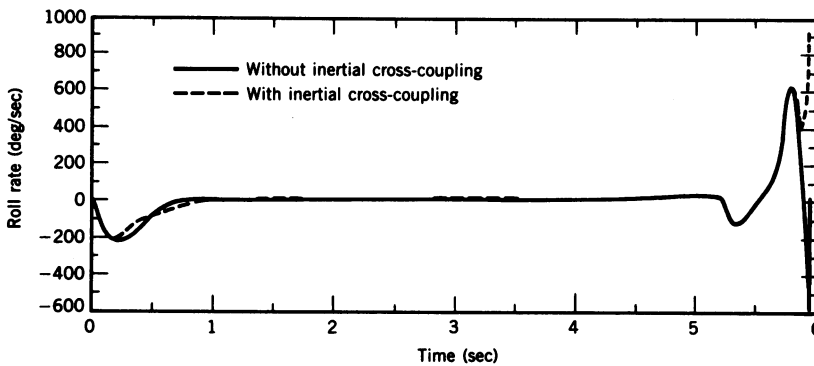
Figure 8-71 *Comparison of missile roll rate for the standard run with and without inertial cross-coupling.*

This results in a roll angle error change of from 9.05 to -40.6 deg. From the results shown in these figures it can be seen that the inclusion of the inertial cross-coupling terms had minimal effect on the performance of the BTT missile. The performance of the missile against a maneuvering target will now be presented.

The BTT missile was evaluated by making a series of intercepts against a target performing a $9g$ chandelle, turning toward and away from the missile, at 1-, 2-, and 3-sec time to go. The chandelle was performed by putting the target into a 45° bank angle (with no target dynamics) and introducing the required pitch rate for $9g$ as a function of the target velocity (20.74 deg/sec for 800 ft/sec). The target was thus pitching in a 45° plane with zero body yaw rate. A summary of the miss distances for the different engagement scenarios is contained in Table 8-5. For runs 1 through 14, runs were made at all three times to go. However, all of the runs are not included in the table. The runs not included had miss distances of less than 4 ft. The last four runs listed in the table were only run with the target turning toward the missile at 3-sec time to go. With the exception of runs 3, 5, and 17, the miss distances were either less than 16.4 ft or greater than 50 ft. An examination of the miss distances shows no real pattern, except that turning away from the missile (right turn) seemed to be more effective than turning toward the missile. The cause of the large miss distances was generally missile instability, to be discussed later in this section. Time histories for run 1 in Table 8-5 are shown in Figures 8-72 through 8-74. The three-dimensional missile and target trajectories are shown in Figure 8-72, the roll angle error and resulting lateral responses in Figure 8-73, and the normal acceleration command and result-ing pitch axis responses in Figure 8-74. From Figure 8-74 it can be seen that the normal acceleration command remains negative and goes off scale at the end of the run, resulting in a positive angle of attack for the entire run. The roll angle error is also very smooth, as can be seen from Figure 8-73. The roll angle error goes more negative at burnout, as observed in Figure 8-70, and then decays rapidly as the roll angle builds up. The large positive swing just after 6 sec is in response to the target starting its turn into the missile. The time responses for run 5 from Table 8-5 are shown in Figures 8-75 and 8-76. From Figure 8-75 it can be seen that the roll angle error starts diverging at just past 9 sec and hits the positive limit at 9.34 sec. Figure 8-76 shows that the normal acceleration command starts swinging in the positive direction slightly later than the roll angle error, and reaches its positive limit at 9.48 sec. The variables that enter into the acceleration command equations are listed in Table 8-6 for run 5 for 9 and 9.5 sec times of flight. From Eq. 8-60 it can be seen that the sign of the normal acceleration command is determined by the sign of $R_{MTZ} + V_{MTZ}t_{go}$. For the lateral acceleration replace Z by Y. From Table 8-6 at 9 sec (run 5) $V_{MTZ}t_{go} = -496.19$, which results in a negative normal acceleration command, but at 9.5 sec $V_{MTZ}t_{go} = -55.03$, resulting in a positive normal acceleration command. At this range $N = 1.5$, as N is scaled to decrease linearly from 3 starting at a range of 4000 ft to 1.5

TABLE 8-5   Summary of Miss Distances Against a Target Performing a 9g Chandelle in the Direction Indicated*

Run	Initial Target Position Dist. North (ft)	Initial Target Position Dist. East (ft)	Engagement Altitude at Launch (ft)	Target Velocity (ft / sec)	Direction[†] of Turn	Time to go at Start of Turn (sec)	Miss Distance (ft)	Time of Flight (sec)
1	7,500	24,000	10,000	800	Left	3	2.42	9.26
2					Left	1	5.69	9.15
3					Right	1	37.8	9.18
4						2	10.14	9.31
5						3	41.95	9.61
6		20,000			Left	1	10.2	7.9
7					Right	1	15.4	7.93
8						2	14.3	8.06
9						3	50.4	8.55
10		16,000			Left	3	3.77	6.79
11					Left	1	131.8	6.74
12					Right	1	87.0	6.78
13					Right	2	96.5	6.94
14					Right	3	83.0	7.28
15		24,000	10,000	1200[‡]	Left	3	1.95	8.18
16		24,000	30,000	800			3.17	8.85
17	24,000	7,500	10,000	800			16.4	11.9
18	7,500	24,000	50,000	1200			5.01	7.75

*Target initially heading west; missile launch velocity 1000 ft / sec, heading at the target.
[†]Right turn is a turn away from the missile; Left turn is a turn toward the missile.
[‡]Pitch rate is 13.84 deg / sec.
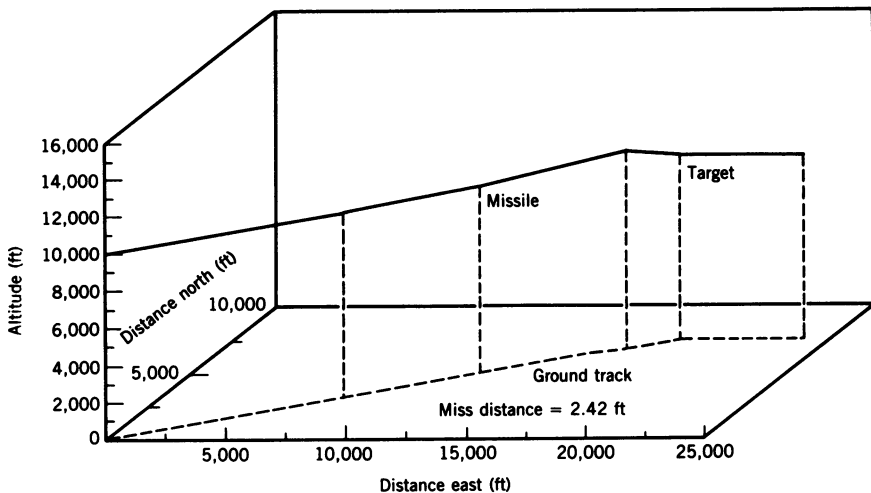
Figure 8-72   *Missile and target trajectories for run 1 Table 8-5.*

at a range of 2000 ft. For the lateral acceleration command at 9.5 sec, both R_{MTY} and V_{MTY} have changed sign and $V_{MTY}t_{go} = 54.1$, resulting in a positive command. With both acceleration commands positive, the sign of the roll angle error command is negative (see Eq. 8-40), and the final roll angle is $-391.09°$. There is no doubt that the missile has gone unstable. From Table 8-6 for run 1, it can be seen that there is no change in the sign of the range or velocity terms that are used in the acceleration command equations, and that the normal acceleration command becomes more negative as intercept is approached. Also the lateral acceleration and the roll angle error commands
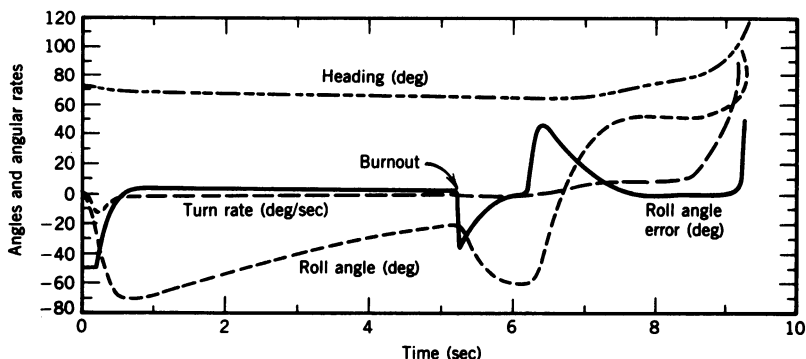
Figure 8-73   *Roll angle error and indicated missile responses for the intercept shown in Figure 8-72.*
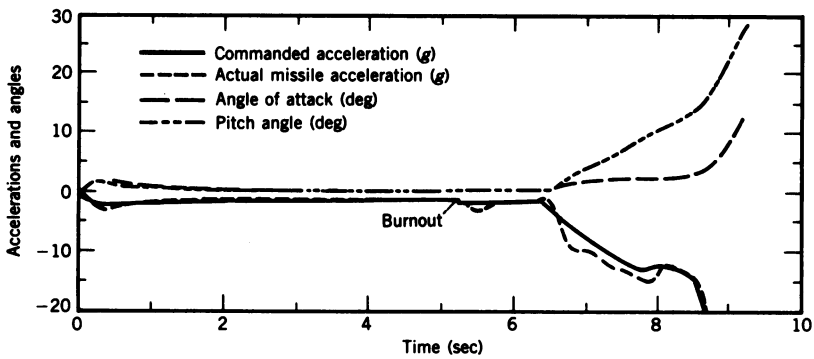
Figure 8-74 *Normal acceleration command and indicated missile responses for the intercept shown in Figure 8-72.*
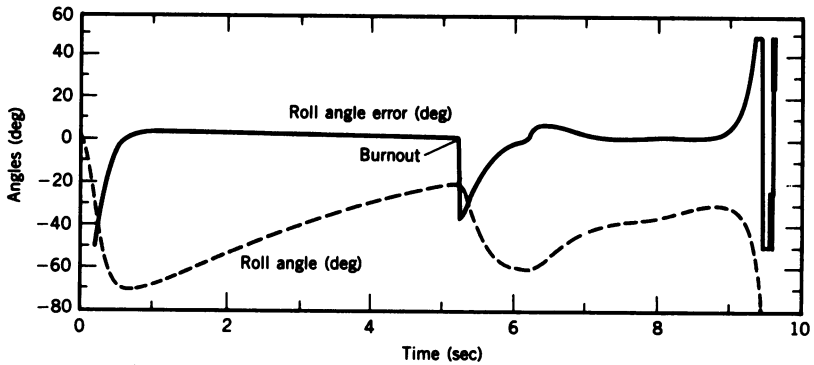
Figure 8-75 *Roll angle error and missile roll angle response for run 5, Table 8-5.*
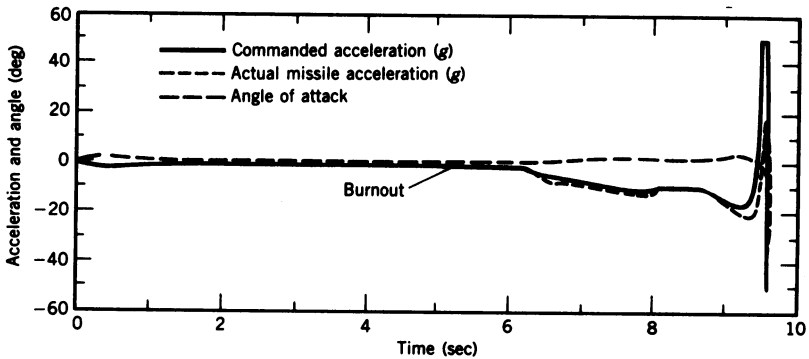
Figure 8-76 *Commanded normal acceleration and actual missile acceleration response for run 5, Table 8-5.*

TABLE 8-6   Variables Affecting Acceleration Commands and the Roll Angle Error for the Intercept Geometry Shown in Figure 8-72 with the Target Turning Away from the Missile at 3-sec Time to Go

Run	Time (sec)	Range (ft)	R_{MTZ} (ft)	R_{MTY} (ft)	V_{MTZ} (ft / sec)	V_{MTY} (ft / sec)	Time to go (sec)	$a_{z(comm)}$ (g)	$a_{y(comm)}$ (g)	ϵ_ϕ (deg)
5	9.0	1208.45	392.2	188.64	−841	−306.8	0.59	−14.74	1.53	5.91
	9.5	212.1	81.59	−24.6	−487	478.8	0.113	50.0	108.5	−50.0
1	8.5	1915.	346.	177.6	−693	−234.2	0.726	−14.5	−0.09	−0.36
	9.0	608.7	214.6	63.	−1032	−242.	0.26	−35.8	−0.03	−0.05

become less negative, resulting in the smooth responses seen in Figures 8-73 and 8-74.

For the standard intercept (see Figure 8-43) a $9g$ chandelle into the missile proved ineffective (miss distances of 2.14, 8.75, and 1.59 ft for the maneuver starting at 1-, 2-, and 3-sec time to go respectively), while turning away from the missile proved very effective (miss distances of 62.3, 33.7, and 70.4 ft for the maneuver starting at 1-, 2-, and 3-sec time to go respectively). Thus in general the $9g$ chandelle turning away from the missile was the most effective evasive maneuver. This completes the discussion of BTT missile guidance.

REFERENCES

1. A. Arrow, "Status and Concerns for Bank-to-Turn Control of Tactical Missiles," *Journal of Guidance, Control, and Dynamics*, March–April 1985, Vol. 8.

2. A. S. Locke, *Guidance*, D. Van Nostrand Company, Princeton, New Jersey, 1955.

3. D. E. Williams, B. Friedland, and A. N. Madiwale, "Modern Control Theory for Design of Autopilots for Bank-to-Turn Missiles," *Journal of Guidance, Control, and Dynamics*, July–August 1987, Vol. 10.

4. A. Arrow and D. E. Williams, "Comparison of Classical and Modern Autopilot Design and Analysis Techniques," *Journal of Guidance, Control, and Dynamics*, March–April 1989, Vol. 12.

5. B. Sridhar and N. K. Gupta, "Missile Guidance Laws Based on Singular Perturbation Methodology," *Journal of Guidance, Control, and Dynamics*, March–April 1980, Vol. 3.

9

Integrated Flight / Fire Control System

9-1 INTRODUCTION

The fire control problem has existed since the early days of air combat in World War I. During the Korean conflict the F-86 aircraft were equipped with the A-1 and A-4 gun–bomb–rocket sights with radar ranging (see Appendix J). The lead computing optical sight (LCOS) presently used in the F-15 and F-16 aircraft differs from the A-1 and A-4 gunsights in that the two single-degree-of-freedom rate gyros have been replaced by a 2-DOF gyro. The computation of the lead angle, which compensates for target motion, and the superelevation, which compensates for curvature of the projectile trajectory due to the force of gravity, still utilizes analog components. This chapter presents the design of an alternative system.

The major component of the prediction angle λ is the lead angle, which compensates for target motion during the time of flight of the projectile. A measure of target motion is the angular velocity of the aircraft-to-target line of sight, ω_{LS}. In the case of the LCOS, the body mounted gyro gives a measure of the angular velocity of the weapon line, ω_{WL}, rather than ω_{LS}, which results in tracking stability problems.[1] The tracking instability results from the fact that the gyro used to compute the prediction angle is mounted on the aircraft. For proper tracking the pilot must keep the reticle or pipper, which is displayed on the head-up display (HUD), on the target. The pipper

is displaced from the bore-sight line by the amount of the prediction angle. Now assume that the pipper is behind the target, which means that the attacking aircraft must increase its rate of turn to bring the pipper into alignment with the target. As the gyro which is used to measure the prediction angle is mounted on the aircraft, if the rate of turn of the aircraft or angular velocity of the weapon line, ω_{WL}, is increased, then the magnitude of the prediction angle will increase instantly and the pipper will move further behind the target, resulting in tracking instability. Thus some damping is required, the amount being a compromise between the speed of response of the aircraft–pilot combination and the time required to generate a new prediction angle based on new values of ω_{WL}.

Dr. Draper,[1] former Director of the Instrumentation Laboratory at M.I.T., was probably the first person to completely understand the tracking instability phenomenon and was thus able to solve this troublesome problem. The solution of the tracking stability problem led to the development, under Dr. Draper's leadership, of the famous Mark 14 naval gunsight for 20-mm antiaircraft guns, and its successors the A-1 and A-4 gun–bomb–rocket sights for fighter aircraft. Theoretically, direct ω_{LS} data would make it possible to implement the director gunsight described in Section 9-2 without the tracking stability problems inherent in the LCOS configuration. Although automatic radar trackers are available, the short ranges for air-to-air gunnery and relatively large target area result in noisy line-of-sight (LOS) information due to glint (directional changes in the LOS) and scintillation (variations in the strength of the signal) as the aspect angle of the LOS relative to the target changes. An electro-optical tracker, as typified by the adaptive scan optical tracker (ASCOT), has the desirable quality of low tracking noise. Although the ASCOT provides good LOS information, it is very susceptible to background clutter.[2] It has been shown that the ASCOT, aided by a Kalman-type estimator and digital control logic, can track through the clutter to provide an accurate measure of ω_{LS} for the director gunsight application.[3]

A movable gun servo system designed to move $\pm 3°$ in elevation and azimuth relative to the boresight line has been developed by the Delco Electronics Division of General Motors Corporation for the F-15 aircraft.[4] A drawing of the proposed installation in the F-15 is shown in Figure 9-1. This gun and proposed servo control system have been tested at Eglin Air Force Base.

With an improved LOS tracker making a director fire control system possible—by utilizing an onboard digital computer to compute the prediction angle, thus eliminating the simplifying assumptions necessary for analog computation, and by employing a movable gun—the pilot is then the main source of tracking error. It is believed that the movable gun with only $\pm 3°$ of motion can compensate for most, if not all, of the tracking errors introduced by the pilot. However, there are tracking encounters, such as high angles off and high crossing rates, which can result in prediction angles large enough
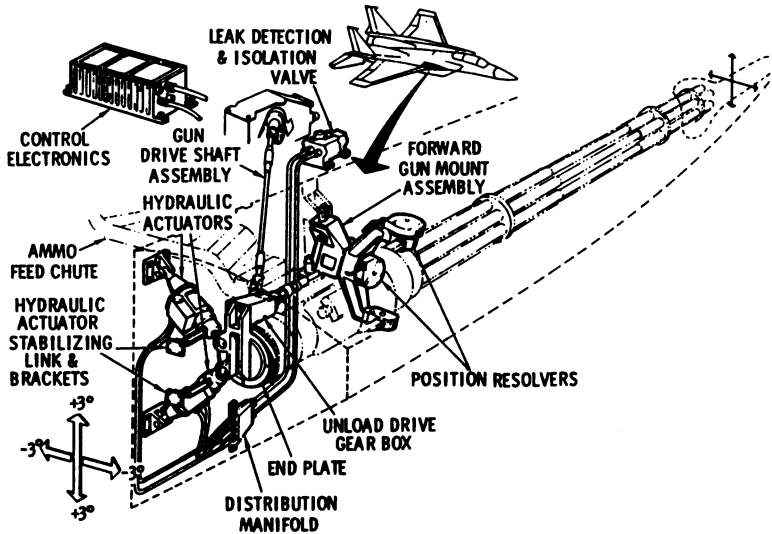
Figure 9-1   *M61A1 movable gun servo system.*

that they exceed the HUD field-of-view and/or over-the-nose vision angle, thus making it impossible for the pilot to track the target visually.[2] One possible solution is an integrated flight/fire control (IFFC) system, in which the aircraft is commanded through the flight control system (FCS) by the output of the fire control system.

This chapter presents the design and integration of a gimbaled LOS tracker, movable gun, and flight control system so as to yield an IFFC system that is stable and capable of directing the gun to score a hit for a wide range of target scenarios. This requires the design of (1) the gimbaled LOS tracker drive system, (2) the flight control system, (3) the gun control laws, and (4) the tracking control laws. As the prediction angle is computed digitally, the outer control loops represent sampled-data systems requiring discrete analysis techniques to determine the gains and sampling rates necessary for stable operation over the large range of dynamic pressures. It will be shown that by the use of the Padé approximation to represent the e^{-Ts} of the zero-order hold of the sampling process, the discrete analysis can be performed in the s plane.[5] The predicted gains for neutral stability for various sampling frequencies determined by this analysis are shown to correlate very well with the gains predicted using the conventional z transform method and with those obtained from the hybrid simulation of the complete system. Selected results from the 6-DOF hybrid simulation of the complete system are included to illustrate the tracking capabilities of the designed IFFC system, including automatic inverted flight.

The results of runs made with the 6-DOF hybrid simulation, verifying the use of the coordinated aircraft transfer function for the analysis of the outer loops of the lateral autopilot after Dutch roll damping and sideslip control have been achieved, are contained in Section 9-5.

9-2 DIRECTOR FIRE CONTROL SYSTEM

The block diagram of a director fire control system is shown in Figure 9-2. The direction of the LOS as determined by the relative geometry between the two aircraft provides the input to the automatic tracker and the HUD. The output of the tracking correction indicator (TCI) is the tracking error that provides the inputs to the two rate integrating gyros that are used to stabilize the gimbaled tracker described in Section 9-8. The output of the tracker is the commanded angular velocity of the tracking line, $\omega_{(TL)comm}$, which is the major input to the prediction computer for calculation of the prediction angle λ_c (see Appendix I) and to the flight control system to provide a rate aid command to the pitch attitude control system as described in Section 9-9. The commanded prediction angle is added to the indicated tracking line $(TL)_i$ to provide the commanded direction of the weapon line $(WL)_c$, that is, the direction in space that the gun must point to score a hit. The commanded direction of the weapon line is compared with WL, the actual direction of the weapon line, to provide the input $C(WL)_{ci}$, in earth coordinates, to the tracking control laws, which, as described in Section 9-9, resolve the commands into aircraft coordinates for input to the flight control system. The longitudinal and lateral control systems are analyzed in Sections 9-3 and 9-4 respectively, and the velocity control system in Section 9-6. The movable gun control is covered in Section 9-7. The prediction angle is also subtracted from WL to generate the computed tracking line $(TL)_c$ for input to the HUD to position the pipper. For pilot control the switch is in the manual position, and the pilot, by controlling the aircraft so as to keep the pipper on the target, provides the control inputs to the aircraft.

As shown here, a director fire control system with the gyros mounted on the tracker measures the angular velocity of the LOS, not of the weapon line as in the case of the LCOS. The Mark 51 naval gunsight employed a director fire control system, with the tracker completely separate from the guns. Thus the tracker was isolated from the gun motion. With the gyros mounted on the weapon line as in the LCOS, there is direct feedback from the weapon line to the gunsight, resulting in the stability problem mentioned in Section 9-1. In mounting the tracker on the aircraft as in the IFFC system, the angular motion of the aircraft does, to some extent, feed back into the tracker. This is, however, a secondary effect as compared to the LCOS case, and it might be assumed that the tracking stability problem associated with the LCOS would not be found in the IFFC system. However, as shown in Section 9-11, some stability problems may still exist.

Figure 9-2 *Director fire control system.*

LOS = Line of sight
TCI = Tracking correction indicator
C(TL) = Correction to tracking line
$\omega_{(TL)comm}$ = Commanded angular velocity of TL
SI = Space integrator
TL = Tracking line
PC = Prediction computer
λ_c = Computed prediction angle

$(TL)_c$ = Computed tracking line
$(TL)_i$ = Indicated tracking line
$C(TL)_{ci}$ = Correction from computed to
indicated TL
WL = Direction of weapon line
➡ = Mechanical feedback
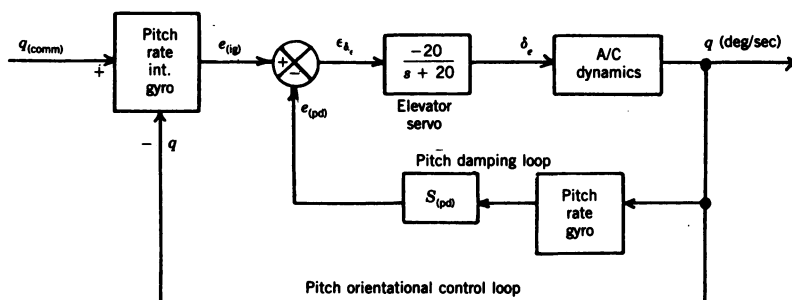
Figure 9-3   Block diagram of the pitch orientational control system.

9-3   LONGITUDINAL FLIGHT CONTROL SYSTEM

The longitudinal flight control system consists of a pitch orientational control system (POCS) and an outer pitch attitude control loop. A block diagram of the POCS is shown in Figure 9-3. The gains of the pitch damping loop $S_{(pd)}$ and the pitch orientational control loop $S_{(ig)}$ were determined by performing a root locus analysis of the system followed by a 2-DOF simulation using the short-period equations of motion. The four flight conditions selected for the analysis and hybrid simulation are shown in Table 9-1 along with the selected gains. Both gains were scheduled as a function of dynamic pressure as shown in the table. The flight conditions chosen provided a range of dynamic pressures from a low of 176.3 to a high of 786.9 psf. The $\dot{\theta}(s)/\delta_e(s)$ transfer function for the F-15 for Mach 0.8 at 20,000 ft is given by

$$\frac{\dot{\theta}(s)}{\delta_e(s)} = \frac{-11.41(s+1.126)}{s^2+2.18s+10.49} \tag{9-1}$$

The aerodynamic data for the transfer function given in Eq. 9-1 and for all of the analysis to follow, as well as for the hybrid simulation, was obtained from

TABLE 9-1   POCS Loop Gains for the Four Flight Conditions used for Control System Design and Simulation

Flight Condition		Dynamic Pressure q (psf)	Airspeed U (fps)	$S_{(pd)} = 782/q$ [volt / (deg / sec)]	$S_{(ig)} = 2063/q$ [volt / (deg / sec)]
Mach No.	Altitude (ft)				
0.6	20,000	245.2	622.14	3.19	8.41
0.8	5,000	786.9	877.68	0.994	2.62
	20,000	439.9	829.52	1.78	4.69
	40,000	176.1	774.8	4.44	10*

*$S_{(ig)}$ limited to maximum value of 10.
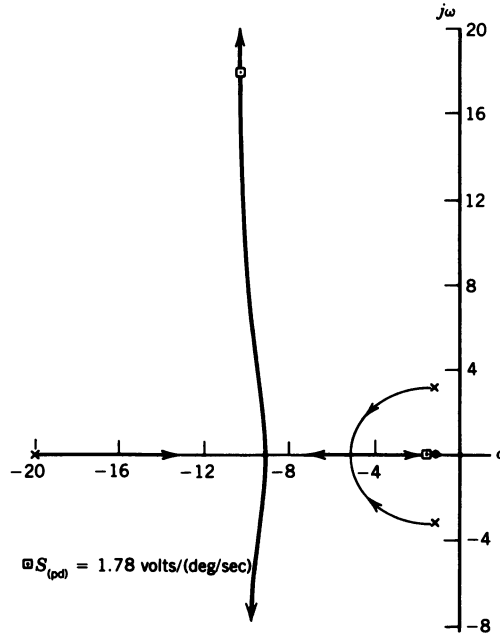
Figure 9-4 *Root locus for the pitch damping loop of the POCS.*

Ref. 6. The longitudinal and lateral aerodynamic data for the four flight conditions studied are contained in Appendix F. The root locus for the pitch damping loop of the POCS is shown in Figure 9-4 with the location of the closed loop poles indicated for $S_{(pd)} = 1.78$. For this gain the closed loop transfer function for the pitch damping loop is

$$\frac{q(s)}{e_{(ig)}(s)} = \frac{228.2(s+1.126)}{(s+1.558)(s^2+20.62s+428.14)} \quad \frac{deg/sec}{volt} \qquad (9\text{-}2)$$

Then from Figure 9-3 the open loop transfer function for the outer loop of the POCS is

$$[TF]_{(OL)(q_{(comm)};q]} = \frac{228.2S_{(ig)}(s+1.126)}{s(s+1.558)(s^2+20.62s+428.14)} \qquad (9\text{-}3)$$

The root locus is shown in Figure 9-5 with the location of the closed loop poles indicated for $S_{(ig)} = 4.69$; the corresponding closed loop transfer

□ $S_{(i\varphi)}$ = 4.69 volts/(deg/sec)
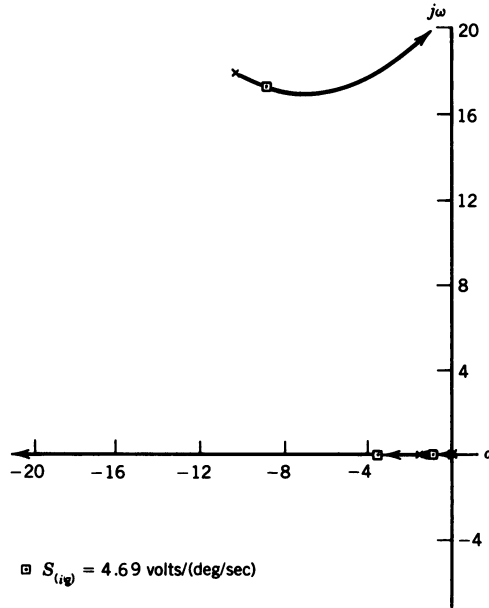
Figure 9-5   *Root locus for the pitch orientational control loop of the POCS.*

function is

$$\frac{q(s)}{q_{(comm)}(s)} = \frac{1070.26(s+1.126)}{(s+0.9)(s+3.54)(s^2+17.74s+378.313)} \tag{9-4}$$

The responses for the POCS for a 10-deg/sec pitch rate step input for the four flight conditions and corresponding gains listed in Table 9-1 are shown in Figure 9-6. The final gains shown in Table 9-1 were raised from those initially selected from the root locus analysis in order to obtain the excellent responses shown in Figure 9-6. The responses shown in Figure 9-6 will be compared in Section 9-6 with those from the 6-DOF hybrid simulation for the same input with and without velocity control.

When the F-15 is tracking a moving target, the direction of the LOS is continuously changing; thus the input to the outer pitch attitude control loop will be at least a ramp. This means that the pitch attitude loop should be a Type 2 system as described in Section C-3. However, it was found that adding a rate aid command to a Type 1 control system resulted in a simpler system with better performance. As shown in Section 9-9, the rate aid signal is the angular velocity of the LOS obtained from the tracker drive system. The block diagram of the Type 1 pitch attitude control loop is shown in Figure
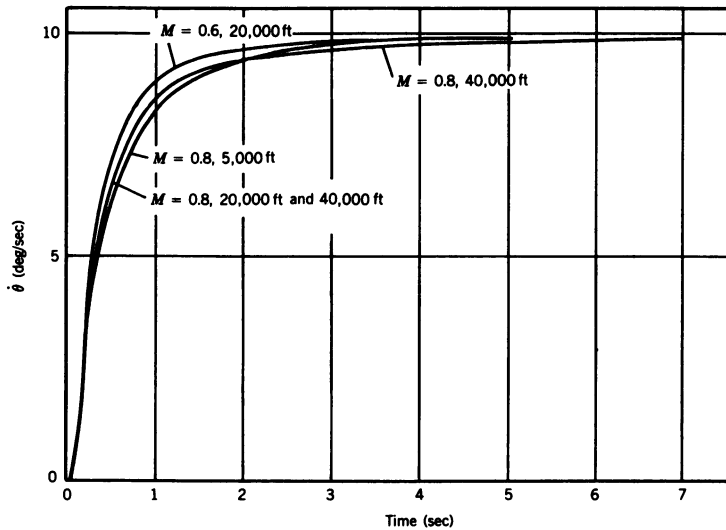
Figure 9-6 *Response of the POCS to a 10-deg / sec step input with the gains as listed in Table 9-1.*

9-7. The forward transfer function for the root locus analysis is

$$\frac{(\mathrm{WL})_\theta(s)}{C(\mathrm{WL})_\theta(s)} = \frac{10702.6K_\theta(s+1.126)}{s(s+0.9)(s+3.54)(s+25)}$$

$$\times \frac{s+2.5}{s^2+17.74s+378.313} \qquad (9\text{-}5)$$

The root locus is shown in Figure 9-8 with the location of the closed loop poles indicated for $K_\theta = 5$. An exploded view of the root locus in Figure 9-8 in the vicinity of the origin is shown in Figure 9-9. The two real closed loop poles shown are the dominant poles for the pitch attitude control loop. The
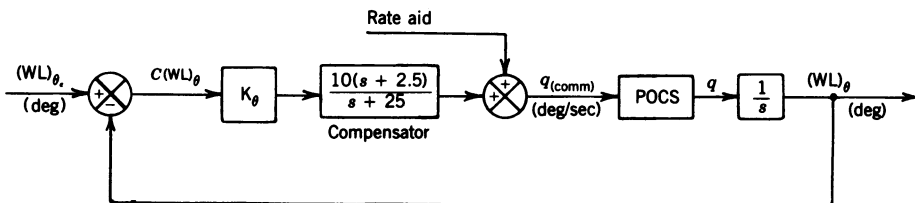
Figure 9-7 *Block diagram of the Type 1 pitch attitude control loop.*
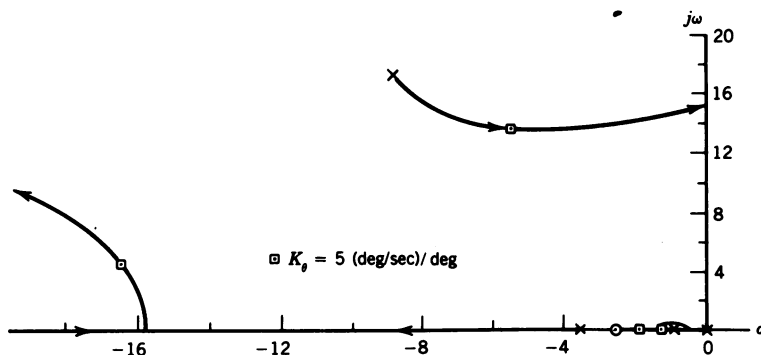
Figure 9-8   *Root locus for the pitch attitude control loop.*

closed loop transfer function for $K_\theta = 5$ is

$$\frac{(\text{WL})_\theta(s)}{(\text{WL})_{\theta_c}(s)} = \frac{53513(s+1.126)(s+2.5)}{(s+1.257)(s+1.89)(s^2+11.07s+217.16)}$$

$$\times \frac{1}{s^2+32.96s+291.66} \tag{9-6}$$

The step responses for the pitch attitude control system for all four flight conditions using the 2-DOF simulation are shown in Figure 9-10. The Type 2 pitch attitude control loop, besides being more complex, experienced a 30 to 40 percent overshoot and a 1.5-sec settling time for a unit step input. Thus
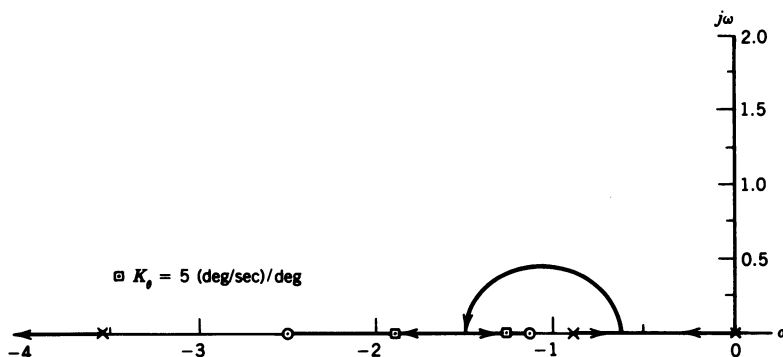
Figure 9-9   *Exploded view of root locus shown in Figure 9-8 in the vicinity of the origin.*
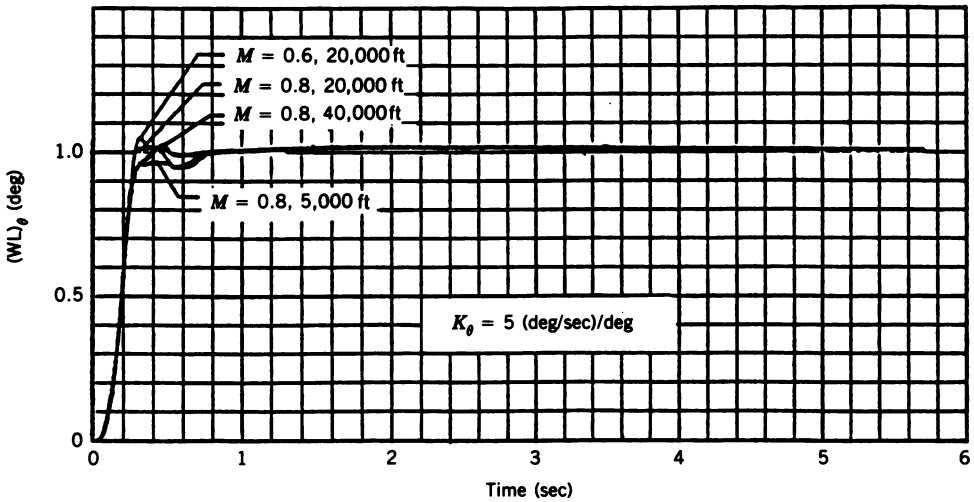
Figure 9-10   *Step response for the pitch attitude control system for all four flight conditions.*

the Type 1 system with the rate aid command was selected for the final pitch attitude control system.

9-4   LATERAL FLIGHT CONTROL SYSTEM

Following the pattern of the longitudinal flight control system (FCS), it was originally planned to use a yaw rate damper, a sideslip control system, and a yaw orientational control system (YOCS) for the lateral FCS. The YOCS was initially selected because it would provide a Type 1 system for a commanded yaw rate similar to the POCS discussed in the last section. However, the YOCS was later replaced by a roll angle control system (RACS) to improve the lateral tracking response. Also the yaw damper and sideslip control system were replaced by the $\beta - \dot{\beta}$ feedback system described in Section 4-3. In the final RACS a commanded yaw rate loop was added to the $\beta - \dot{\beta}$ feedback system.

The block diagram of the RACS, including the $\beta - \dot{\beta}$ stability augmentation system (SAS), is shown in Figure 9-11. The superiority of the $\beta - \dot{\beta}$ SAS over the yaw damper with sideslip control was demonstrated in Section 4-4. The commanded yaw rate (CYR) loop around the $\beta - \dot{\beta}$ SAS was added to reduce a large opposite swing of yaw rate when rolling out of a turn. The CYR loop consists of yaw rate feedback r and the commanded yaw rate r_c as described in Section 4-3. Besides adding the CYR loop, the gains of the $\beta - \dot{\beta}$ SAS were increased as shown in Figure 9-11. In order to increase these gains
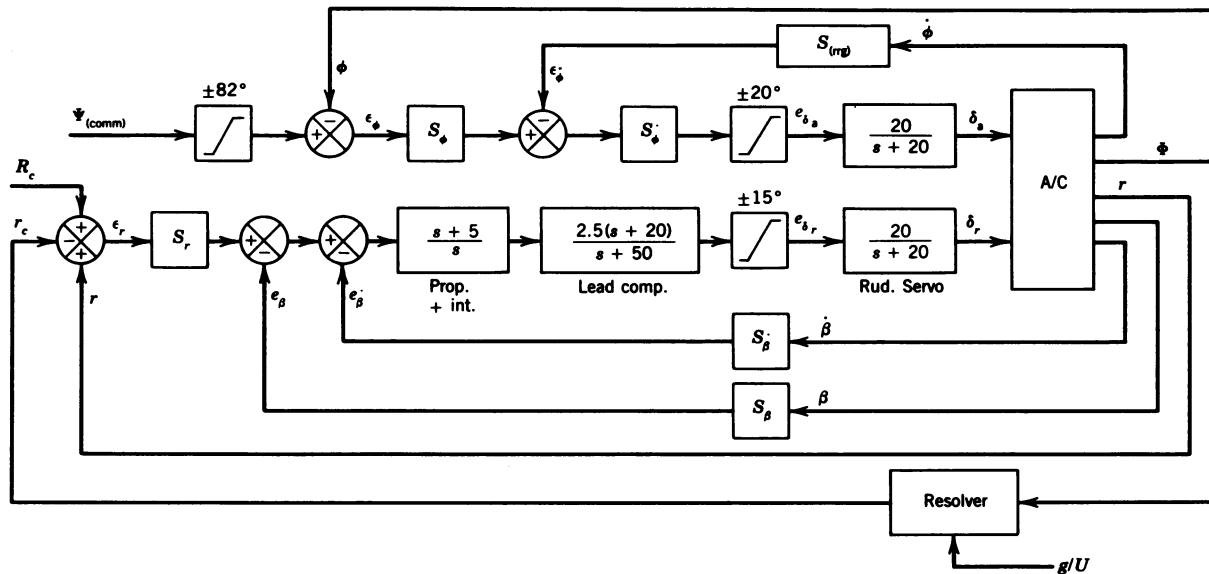
Figure 9-11 *Block diagram of RACS with* β-$\dot{\beta}$ *SAS with commanded yaw rate.* $r_c = (57.3g \, / \, U)\sin \Phi$ *deg / sec;* $S_{\dot{\beta}} = 5$ *V / (deg / sec);* $S_{\dot{\phi}} = (10 \, / \, \sqrt{q})$ *V / V;* $S_{\beta} = 7.5$ *V / deg;* $S_{(rrg)} = 1.5$ *V / (deg / sec);* $S_r = 30$ *V / V;* $S_{\phi} = 4.17$ *V / V.*
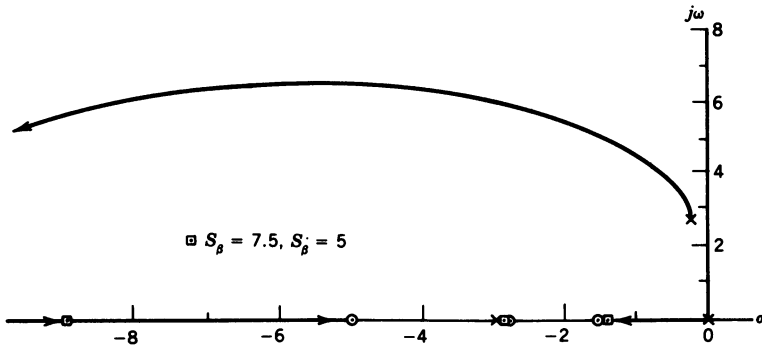
Figure 9-12 Root locus for β–$\dot{\beta}$ feedback, S_β = 7.5, $S_{\dot{\beta}}$ = 5.

it was necessary to add a lead compensator and increase the integrator gain to 5. The R_c term will be discussed in Section 9-9.

The open loop transfer function as defined in Section C-2 for the root locus of the revised β–$\dot{\beta}$ SAS is (see Section 4-3)

$$[TF]_{OL} = \frac{-2.865 S_{\dot{\beta}}(s+1.5)(s+5)(s+2.783)(s+79.8)}{s(s+0.024)(s+2.95)(s^2+0.492s+7.46)}$$

$$\times \frac{s-0.0061}{s+50} \tag{9-7}$$

The root locus is shown in Figure 9-12 with the location of the closed loop poles indicated for $S_{\dot{\beta}} = 5$. The corresponding closed loop transfer function is

$$[TF]_{CL} = \frac{2.865s(s+5)(s+2.783)(s+79.8)}{(s-0.006)(s+1.346)(s+2.85)(s+8.9)}$$

$$\times \frac{s-0.0061}{s+34.285} \tag{9-8}$$

To obtain the transfer function for the CYR loop root locus it is necessary to multiply Eq. 9-8 by the $r(s)/\dot{\beta}(s)$ transfer function

$$\frac{r(s)}{\dot{\beta}(s)} = \frac{-4.56(s+2.93)(s^2+0.007s+0.476)}{0.0573s(s-0.0061)(s+2.783)(s+79.8)} \tag{9-9}$$
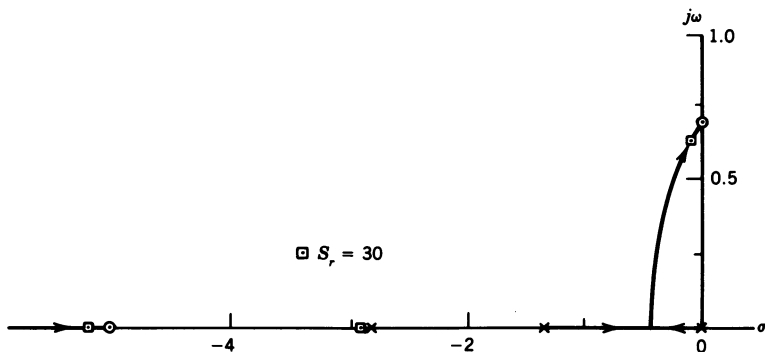
Figure 9-13   *Root locus for CYR system with β–β̇ feedback.*

Multiplying Eq. 9-8 by Eq. 9-9 yields

$$[TF]_{OL} = \frac{-228 S_r (s + 2.93)(s^2 + 0.007s + 0.476)}{(s - 0.006)(s + 1.346)(s + 2.85)(s + 8.9)}$$

$$\times \frac{s + 5}{(s + 20.39)(s + 34.285)} \tag{9-10}$$

The root locus is shown in Figure 9-13 with the location of the closed loop poles for $S_r = 30$ indicated. In order to show more detail the real pole at $s = -8.9$ has not been shown. The corresponding closed loop transfer function is

$$\frac{r(s)}{r_c(s)} = \frac{6834(s + 2.93)(s^2 + 0.007s + 0.476)}{(s + 2.89)(s + 5.18)(s^2 + 0.21s + 0.404)}$$

$$\times \frac{s + 5}{s^2 + 59.46s + 7779} \tag{9-11}$$

As was done in Section 4-5, the coordinated aircraft transfer function will be used for the analysis of the RACS. From Figure 4-25 it can be seen that a 1° aileron step input resulted in about a 5.6-deg/sec roll rate. From Eq. 9-11 it can be seen that the location of the roll subsidence pole has moved from $s = -2.95$ as shown in Eq. 4-2 to $s = -2.89$. From Figure 9-11, using the steady-state gain of 5.6 and the final location of the roll subsidence pole, the block diagram for the root locus analysis of the RACS can be drawn as shown in Figure 9-14. From Figure 9-14 the open loop transfer function for
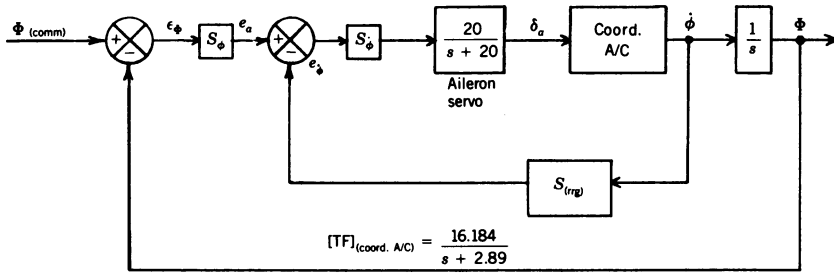
Figure 9-14 *Block diagram of RACS for root locus analysis.*

the roll rate feedback loop is

$$[\text{TF}]_{\text{OL}} = \frac{-323.68 S_{\dot{\phi}} S_{(\text{rrg})}}{(s+2.89)(s+20)} \tag{9-12}$$

The root locus is shown in Figure 9-15 with the location of the closed poles for $S_{\dot{\phi}} = 0.479$ and $S_{(\text{rrg})} = 1.5$ indicated. The corresponding closed loop
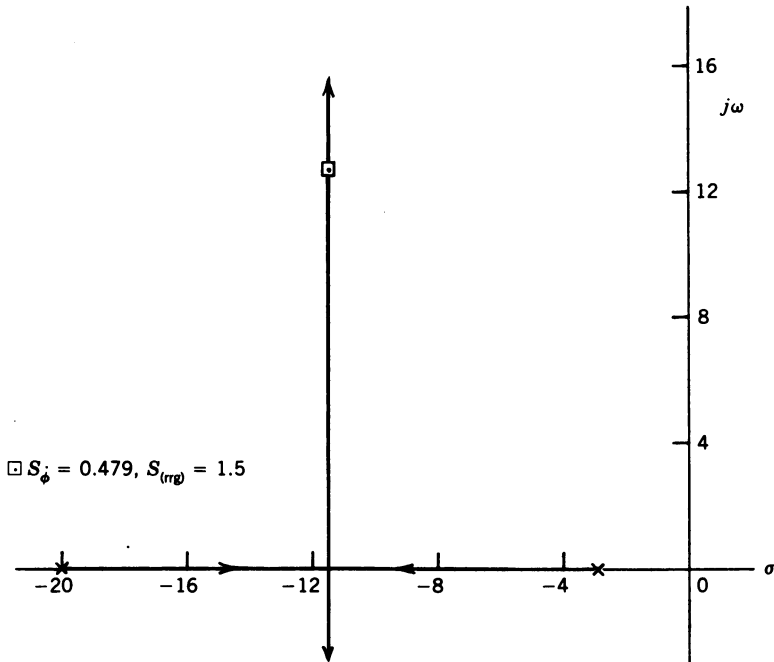
Figure 9-15 *Root locus for roll damping loop of RACS.*
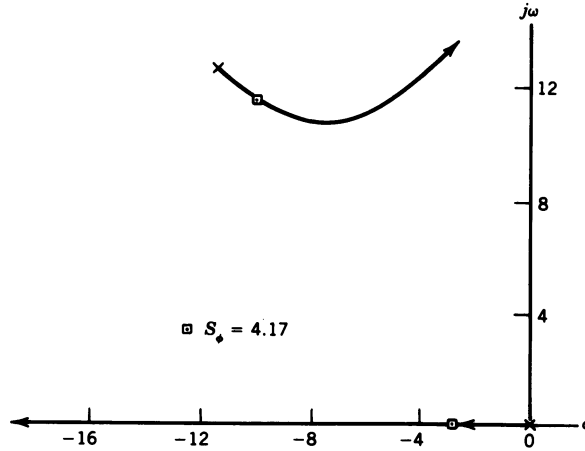
Figure 9-16   *Root locus for outer loop of RACS.*

transfer function is

$$\frac{\dot{\phi}(s)}{e_a(s)} = \frac{155}{s^2 + 22.89s + 290.36} \tag{9-13}$$

The outer roll angle feedback loop adds a pole at the origin; thus

$$[\text{TF}]_{\text{OL}} = \frac{-155S_\phi}{s(s^2 + 22.89s + 290.36)} \tag{9-14}$$

The root locus for the outer loop of the RACS is shown in Figure 9-16 with the location of the closed loop poles for $S_\phi = 4.17$ indicated. The corresponding closed loop transfer function is

$$\frac{\Phi(s)}{\Phi_{(\text{comm})}(s)} = \frac{646.35}{(s + 2.75)(s^2 + 20.14s + 235)} \tag{9-15}$$

The response of the RACS for a 60° roll angle step command is shown in Figure 9-17. The response was obtained using a coupled 5-DOF analog simulation (X force equation neglected) with the POCS and the RACS. The pitch rate command for input to the POCS was calculated using Eq. 4-34, which is repeated here:

$$q = r \tan \phi \tag{9-16}$$

The rates of change of the Euler angles were calculated using Eq. 1-34a. For the simulation the initial angle of attack was set at the trim value for 1g
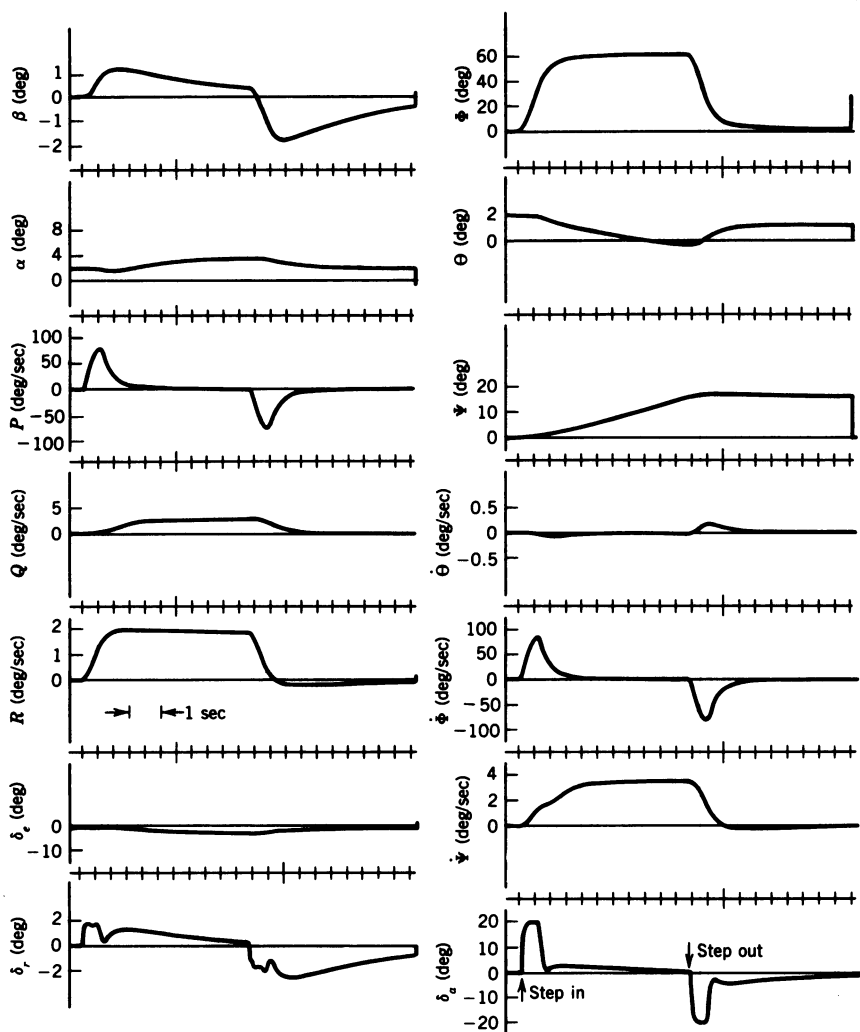
Figure 9-17   Response of the RACS to a 60° roll angle step (in and out).

(straight and level) flight. As the roll angle increases and the aircraft enters the turn, the pitch rate and the angle of attack increase as required to maintain a level turn. A 60° roll angle results in a 2*g* turn.

The final loop for the lateral flight control system is the Type 2 yaw attitude loop shown in Figure 9-18. As shown in the block diagram, the roll angle command is limited to 82°, which would result in an acceleration limit of 7.33*g*. The limit was later removed to provide for inverted flight when the tracking control system was introduced. The root locus for the yaw attitude control system is shown in Figure 9-19 with the location of the closed loop
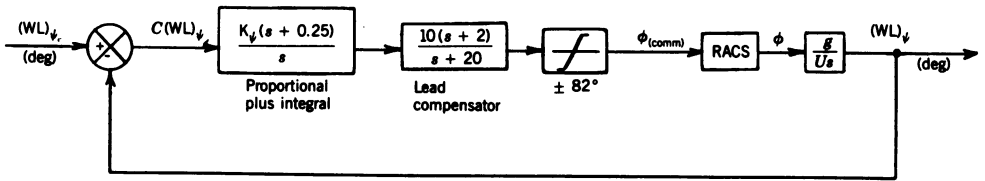
Figure 9-18   *Block diagram of the Type 2 yaw attitude control system.*
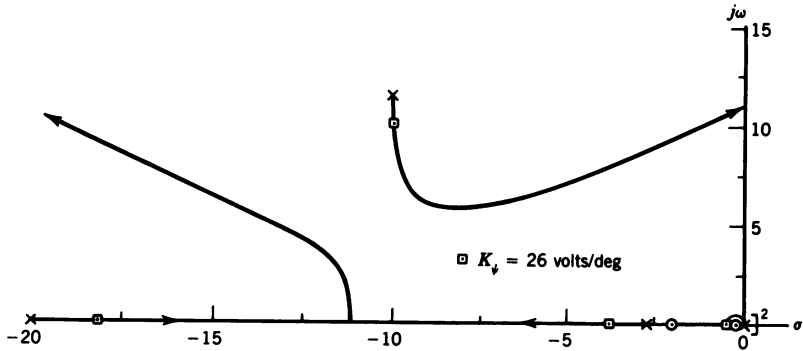
Figure 9-19   *Root locus for the Type 2 yaw attitude control system.*

poles indicated for $K_\psi = 26$. A blowup of the area near the origin of Figure 9-19 is shown in Figure 9-20. The closed loop transfer function for the yaw attitude control system for $K_\psi = 26$ is

$$\frac{(\text{WL})_\psi(s)}{(\text{WL})_{\psi_c}(s)} = \frac{6523.4(s+0.25)(s+2)}{(s+3.764)(s+18.12)(s^2+0.972s+0.2384)}$$

$$\times \frac{1}{s^2+20.03s+200.557} \tag{9-17}$$

The gain of 26 was selected, as it minimized the tracking error as discussed in Section 9-9. A K_ψ value of 60 results in a damping ratio of 0.72 for the complex poles on the path of the root locus moving toward the $j\omega$ axis, thus providing a wide range of acceptable gains. From Figure 9-20 it can be seen that a gain of 26 results in the fastest response for the yaw attitude control system. This is consistent with the results from the system optimization. Looking back at Figure 9-11, it can be seen that only one gain, S_ϕ, is scheduled as a function of dynamic pressure. The other five gains are constant for all four of the flight conditions analyzed, thus attesting to the robustness of the complete yaw attitude control system.
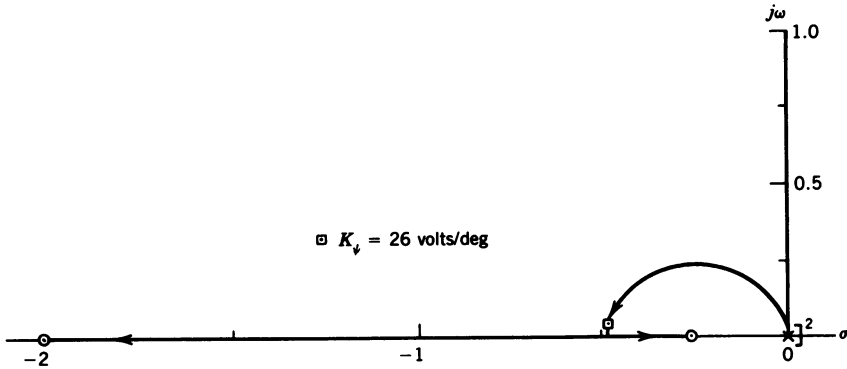
Figure 9-20 *Root locus for the Type 2 yaw attitude control system in the vicinity of the origin.*

9-5 VERIFICATION OF LATERAL CONTROL SYSTEM ANALYSIS

In the last section and in Section 4-5 the coordinated aircraft transfer function was used for the analysis of the outer control loops through the aileron after the design of the SAS was completed. The validity of this will now be shown. From the block diagram of the RACS in Figure 9-14, by multiplying Eq. 9-12 by $1/s$, the open loop transfer function for the roll angle loop without roll rate feedback and with $S_{\dot{\phi}} = 1$ is

$$[\text{TF}]_{\text{OL}} = \frac{-323.68 S_{\phi}}{s(s+2.89)(s+20)} \tag{9-18}$$

The root locus has the shape shown in Figure 9-21. The value of S_{ϕ} for $\zeta = 0$ is 3.93, and for $\zeta = 0.3$ is 0.789. The coupled 6-DOF hybrid simulation was run with these values of the gain, and the results are shown in Figure 9-22(a) and (b). The calculated and measured frequencies and damping ratios are summarized in Table 9-2. The rate gyro loop was then closed; for $S_{(\text{rrg})} = 0.4$ and $S_{\dot{\phi}} = 0.479$, the closed loop transfer function for the roll rate loop is

$$\frac{\dot{\phi}(s)}{e_a(s)} = \frac{155}{(s+8.1)(s+14.8)} \tag{9-19}$$

The open loop transfer function for the outer loop is

$$[\text{TF}]_{\text{OL}} = \frac{-155 S_{\phi}}{s(s+8.1)(s+14.8)} \tag{9-20}$$

and for $\zeta = 0.3$, $S_{\phi} = 5.44$. The response of the RACS for these gains is shown in Figure 9-22(c), and the measured and calculated values of the
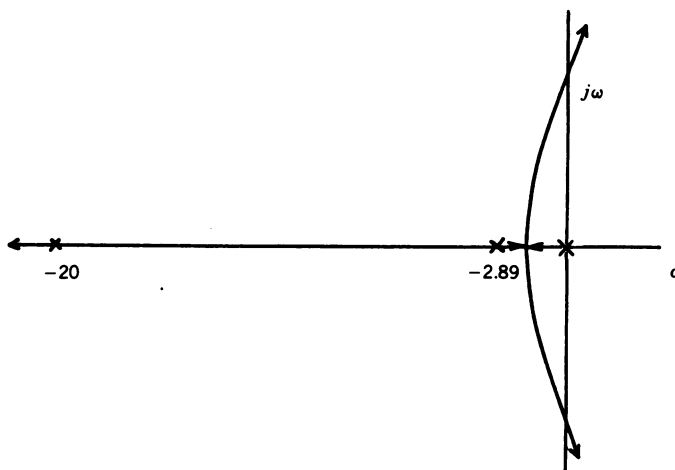
Figure 9-21 *Sketch of root locus of RACS without roll rate feedback.*
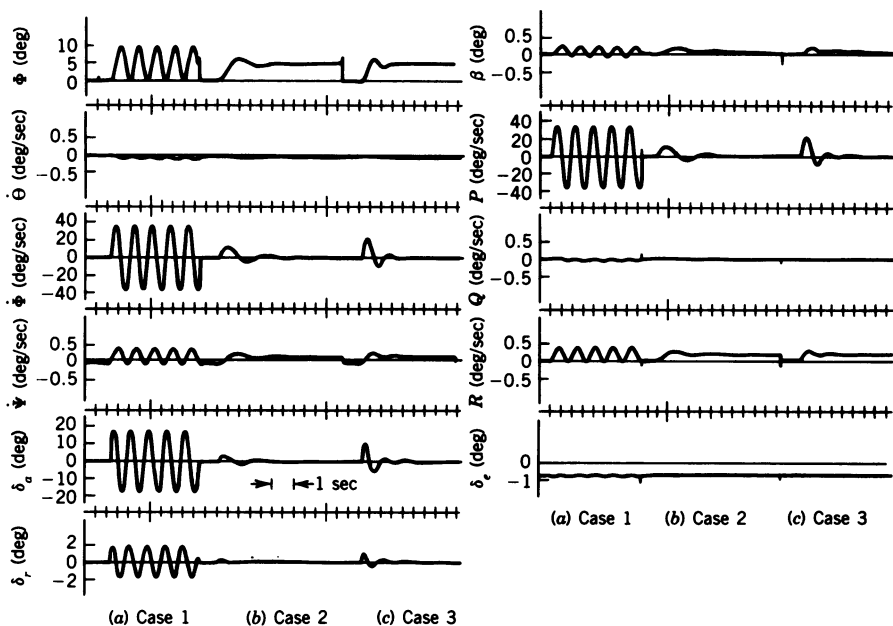
Figure 9-22 *Response of RACS for different loop gains.*

TABLE 9-2   Measured and Calculated Values of ζ and ω_d for Various RACS Gains

Case	S_ϕ	$S_{\dot\phi}$	$S_{(rrg)}$	Calculated ζ	Calculated ω_d	Measured ζ	Measured ω_d
1	3.93	1	0	0	7.45	0.001	7.48
2	0.789	1	0	0.3	3.35	0.3	3.38
3	5.44	0.479	0.4	0.3	6.3	0.3	6.28

damping ratios and frequencies are also included in Table 9-2. Considering the measurement inaccuracies, the correlation is exceptional. Thus the lateral FCS including the lateral SAS, which is a two-input multiple-output control system, can be reduced to a simple single-input single-output control system for analysis. Runs were made with and without the POCS engaged, with no discernible difference in the lateral response. For these runs a roll angle command of 5° was used so that there would be no aileron limiting.

This concludes the analysis of the lateral FCS; the velocity control system will be discussed next.

9-6   VELOCITY CONTROL SYSTEM

The same velocity control system studied in Section 2-4 (see Figure 2-32) will be used for this application. The block diagram is shown in Figure 9-23. The value of the engine sensitivity S_e is equal to the maximum thrust in full afterburner divided by 100, with 100 corresponding to full throttle. Full military power occurs at a throttle setting of 50 and is, for the Mach numbers considered in this study, approximately 50 percent of full afterburner. Thus thrust is considered to vary linearly with throttle position. The values of K_T and S_e for the four flight conditions considered are given in Table 9-3. The aircraft transfer function for Mach 0.8 at 20,000 ft for the change in airspeed
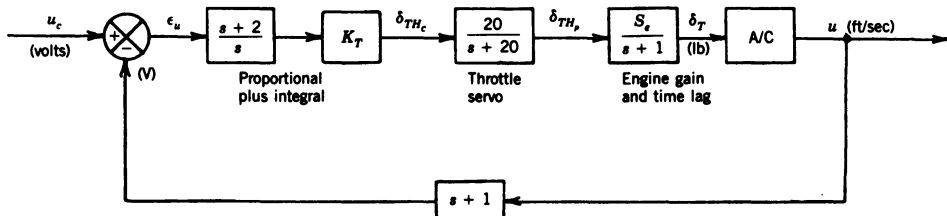
Figure 9-23   *Block diagram of velocity control system.*

TABLE 9-3   Engine Sensitivity and Gain for Velocity Control System

| Flight Condition | | | |
Mach No.	Altitude (ft)	$S_e = \dfrac{\text{Max. Thrust (lb)}}{100}$	$K_T = \dfrac{654}{\sqrt{q}}$
0.6	20,000	307.58	41.79
0.8	5,000	505.06	23.33
0.8	20,000	355.44	31.32
0.8	40,000	190.83	49.27

u per unit change in thrust δ_T is

$$\frac{u(s)}{\delta_T(s)} = \frac{9 \times 10^{-4} s}{s^2 + 0.028s + 0.0027} \; \text{(ft/sec)/lb} \qquad (9\text{-}21)$$

The units of Eq. 9-21 can be reduced from (ft/sec)/lb to sec/slug, as 1 lb = 1 slug ft/sec^2, and s has units of 1/sec. Then the numerator constant has units of 1/slug, and indeed the mass of the aircraft is $1/(9 \times 10^{-4})$. The transfer functions for the other three flight conditions had the same numerator constant. As the maximum thrust is a function of altitude and Mach number, then K_T must compensate for these changes. It was found that $654/\sqrt{q}$ gave good values of K_T. The values of K_T and S_e for the four flight conditions considered are given in Table 9-3. Both velocity and longitudinal acceleration are fed back equally, so that the $s + 1$ in the feedback path cancels the engine time lag. The engine time lag is equal to 1 second as long as the commanded throttle position minus the current throttle position is less than 25, which would normally be the case, as the aircraft is initially in trimmed flight for each run.

From Figure 9-23 the open loop transfer function for the root locus analysis is

$$[\text{TF}]_{\text{OL}} = \frac{-6.4 K_T (s + 2)}{(s + 20)(s^2 + 0.028s + 0.0027)} \qquad (9\text{-}22)$$

The root locus for the velocity control system is shown in Figure 9-24 with the location of the closed loop poles indicated for $K_T = 31.32$, which yields a damping ratio of 0.7 for the complex poles. The corresponding closed loop transfer function is

$$\frac{u(s)}{u_c(s)} = \frac{200(s + 2)}{(s + 1)(s + 2.57)(s^2 + 17.45s + 155.3)} \qquad (9\text{-}23)$$
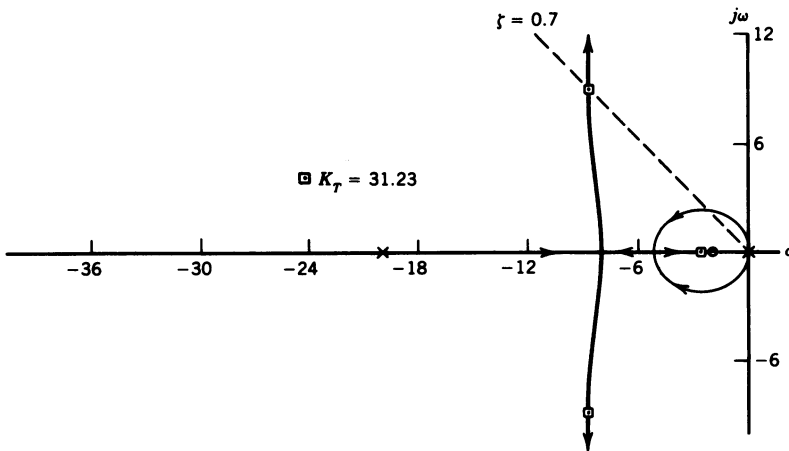
Figure 9-24 Root locus for the velocity control system.
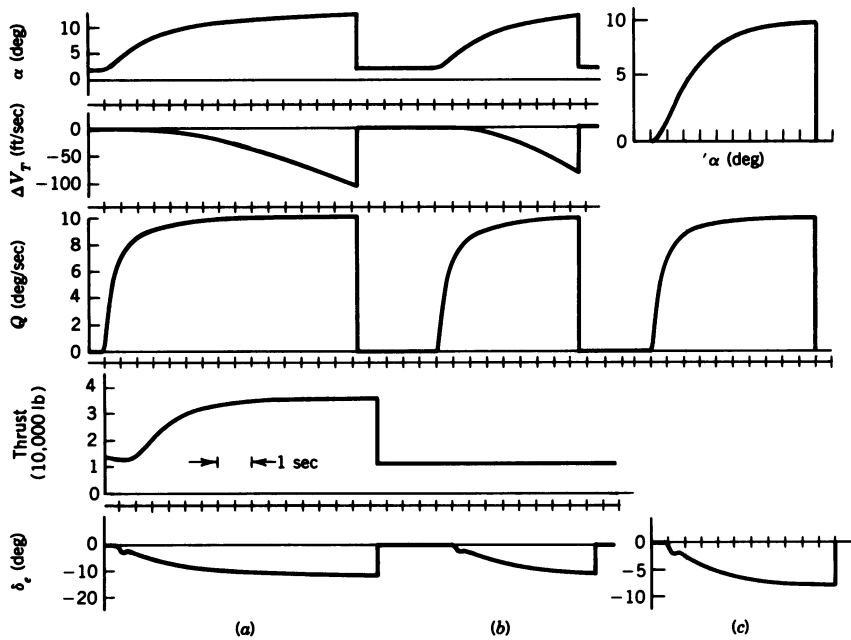
Figure 9-25 Response of POCS to a 10-deg / sec step input of pitch rate (a) with and (b) without velocity control; (c) short-period approximation.

As the factor $s+1$ that cancels the $s+1$ of the engine transfer function is in the feedback path, the engine time constant remains unchanged. Had the feedback factor been $0.5(s+2)$, then the pole at -1 from the engine would have moved toward the double zero at -2. At first it might seem that this would yield a faster response; however, for a gain that resulted in a damping ratio of 0.7 for the complex poles, the engine pole would move only to -1.07, no real improvement. Thus the engine time constant governs the system response time, provided the zero associated with the proportional plus integral is to the left of the engine pole.

The responses of the POCS hybrid simulation to a 10-deg/sec step input of pitch rate for Mach 0.8 at 20,000 ft with and without velocity control are shown in Figure 9-25(a) and (b). Although the thrust has reached its maximum value for this flight condition of 35,964 lb, it is less than the component of weight along the thrust axis (34,676 for $\Theta = 74°$) plus the drag (29,565). This results in a calculated deceleration of 25.3 ft/sec^2. From the slope of the ΔV_T trace at the end of the run the measured value of deceleration is 27 ft/sec^2. This agreement is excellent. The initial velocity for this flight condition is 829.52 ft/sec. The same response from the 2-DOF (short-period approximation) simulation is shown in Figure 9-25(c). For the three cases the pitch rate responses are identical. For the short-period case $'\alpha$, the change in angle of attack, reaches 4° at 1 sec. The α trace with velocity control shows 6° ($\alpha_0 = 2°$), thus further substantiating the comments made in Section 2-4 with respect to the use of the short-period approximation for the longitudinal control system analysis when velocity control is assumed. The effects of the 1-second time constant of the engine can be seen in the thrust trace in Figure 9-25(a).

9-7 MOVABLE GUN CONTROL

The aircraft movable gun configuration is shown in Figure 9-26. The complete block diagram and transfer functions for the gun drive came from Ref.

Figure 9-26 *Block diagram of aircraft – movable gun configuration — pitch axis (for yaw axis replace θ with ψ).*
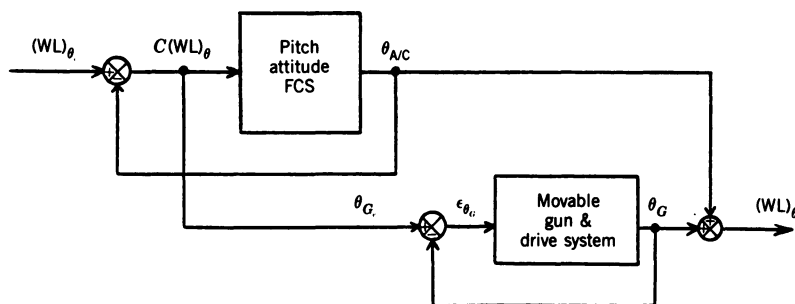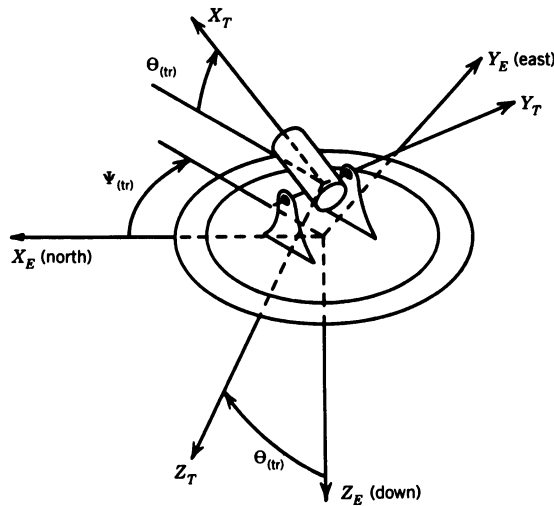
Figure 9-27 Earth stabilized tracker axes.

4. A root locus analysis was performed and the closed loop step response obtained using an Air Force Institute of Technology computer program TOTAL. From the step response of the complete closed loop transfer function (five zeros and nine poles) it was determined that the movable gun dynamics could be adequately represented by a first-order lag with a time constant of 0.004 sec and unity gain. As can be seen in Figure 9-26, the gun is driven by the tracking error; thus the gun angle is a measure of the tracking error as long as the error is less than 3°. The final orientation of the weapon line (WL) is the aircraft orientation plus the gun displacement, which is not fed back. This was done so that the system would always be trying to drive the aircraft into alignment with the commanded weapon line, with the movable gun taking care of small tracking errors.

9-8 GIMBALED TRACKER DESIGN

The configuration of the two-axis tracker mounted on an earth referenced stabilized platform is shown in Figure 9-27. The two tracker gimbal angles are the azimuth angle $\Psi_{(tr)}$ and the elevation angle (measured in the vertical plane) $\Theta_{(tr)}$. Notice that the gimbal angles are defined in the same manner as the Euler angles in Section 1-4. The direction X_T is the indicated direction of the line of sight (LOS). The heart of the tracker is the integrating gyro unit (IGU) described in Sections 2-7 and B-4. The azimuth gyro would have its input axis along, and drive the tracker about, the Z_E axis, and the elevation gyro would have its input axis along the Y_T axis. The block diagram of the
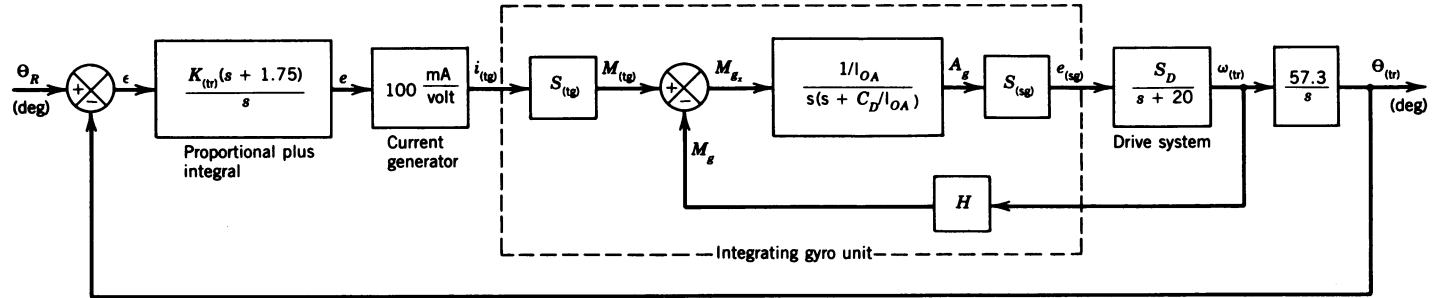
Figure 9-28 *Block diagram of the elevation axis of the tracker.*

$S_{(tg)}$ = sensitivity of torque generator = 2.5 $\left(g \text{ cm}^2 / \text{sec}^2 \right)$ / mA

I_{OA} = moment of inertia of gyro gimbal and wheel about gyro output axis

= 35 g cm^2

C_D = coefficient of damping of viscous fluid between gyro gimbal and case

= 10^4 g cm^2 / sec

H = angular momentum of gyro wheel = 10^4 g cm^2 / sec

$S_{(sg)}$ = sensitivity of signal generator = 25 mV / mrad

A_g = gimbal angle, ±5° maximum

$K_{(tr)}$ = tracker gain = 2.848 V / deg

S_D = sensitivity of drive system = 6 $\left(\text{rad} / \text{sec} \right)$ / volt
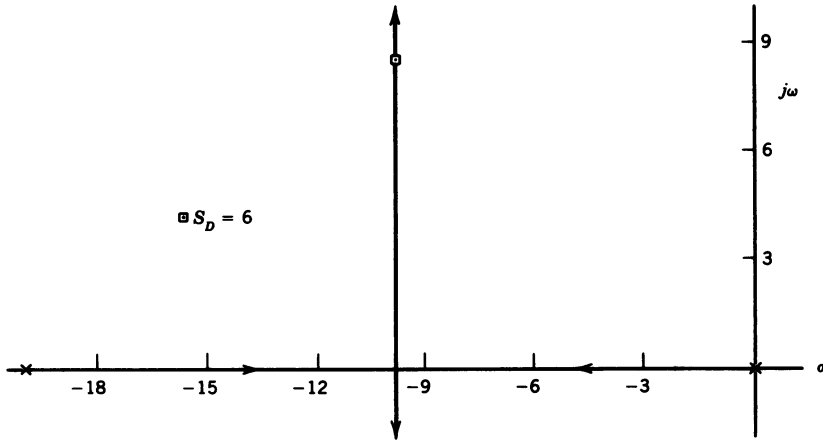
Figure 9-29 *Root locus of the IGU and drive system of the tracker.*

elevation axis is shown in Figure 9-28. The block diagram of the azimuth axis of the tracker is the same. From the block diagram, the forward transfer function of the inner loop (IGU and drive system) is

$$\frac{\omega_{(tr)}(s)}{M_{g_x}(s)} = \frac{4.2857}{s(s+20)(s+258.7)} \frac{rad/sec}{g\,cm^2/sec^2} \tag{9-24}$$

The root locus is shown in Figure 9-29 with the location of the closed loop poles for $S_D = 6$ (rad/sec)/volt indicated. The corresponding closed loop transfer function is

$$\frac{\omega_{(tr)}(s)}{M_{(tg)}(s)} = \frac{4.2857}{(s+259.39)(s^2+19.3s+165)} \frac{rad/sec}{g\,cm^2/sec^2} \tag{9-25}$$

The forward transfer function for the outer loop is

$$\frac{\Theta_{(tr)}(s)}{\epsilon(s)} = \frac{61392.65 K_{(tr)}(s+1.75)}{s^2(s+259.39)(s^2+19.3s+165)} \frac{deg}{deg} \tag{9-26}$$

The root locus for the outer loop of the tracker is shown in Figure 9-30 with the location of the closed loop poles for $K_{(tr)} = 2.848$ volts/deg indicated.
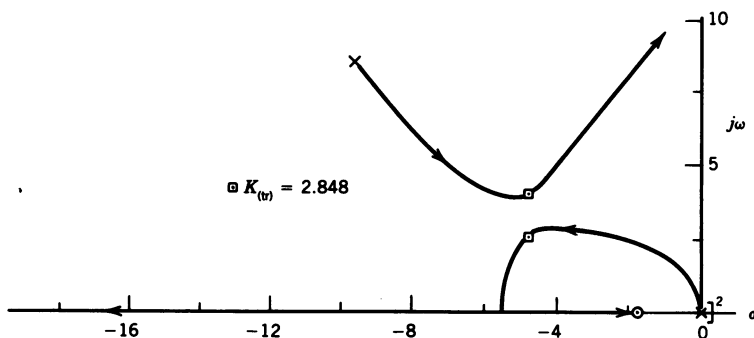
Figure 9-30   Root locus of the outer loop of the tracker.

The corresponding closed loop transfer function is

$$\frac{\Theta_{(tr)}(s)}{\Theta_R(s)} = \frac{1.75 \times 10^5 (s + 1.75)}{(s + 259.38)(s^2 + 9.64s + 30)}$$

$$\times \frac{1}{s^2 + 9.66s + 39.33} \frac{deg}{deg} \qquad (9\text{-}27)$$

9-9 TRACKING CONTROL LAWS (TCL)

With the design of the longitudinal and lateral flight control systems, the gimbaled tracker, and the movable gun control completed, it is necessary to integrate these subsystems into the complete IFFC. This is the role of the TCL; however, before looking at the TCL the generation of the commanded orientation of the weapon line will be reviewed. The schematic of the director fire control system presented in Section 9-2 is repeated here in Figure 9-31 for convenience. As shown in the figure and discussed in Section 9-2, the commanded orientation of the weapon line is obtained by adding the prediction angle to the indicated LOS. This is done in earth coordinates, and the azimuth and elevation components of the commanded weapon line are

$$(WL)_{\psi_c} = \Psi_{(tr)} + \lambda_\psi$$

$$(WL)_{\theta_c} = \Theta_{(tr)} + \lambda_\theta \qquad (9\text{-}28)$$

where λ_ψ and λ_θ are the azimuth and elevation components of the prediction angle computed from the equations developed in Appendix I. The basic tracking control laws are shown in Figure 9-32, and the azimuth and

LOS = Line of sight
TCI = Tracking correction indicator
C(TL) = Correction to tracking line
$\omega_{(TL)comm}$ = Commanded angular velocity of TL
SI = Space integrator
TL = Tracking line
PC = Prediction computer
λ_c = Computed prediction angle

$(TL)_c$ = Computed tracking line
$(TL)_i$ = Indicated tracking line
$C(TL)_{ci}$ = Correction from computed to indicated TL
WL = Direction of weapon line
➤ = Mechanical feedback

Figure 9-31   *Director fire control system.*

Figure 9-32 *Tracking control laws with movable gun.*

elevation components of the tracking error in earth axis are

$$C(\text{WL})_\psi = (\text{WL})_{\psi_c} - \Psi_{A/C}$$
$$C(\text{WL})_\theta = (\text{WL})_{\theta_c} - \Theta_{A/C} \tag{9-29}$$

The TCL perform the following functions: (1) resolve the tracking error signals from earth axis to aircraft axis for input to the longitudinal and lateral FCS, (2) provide a tracking aid R_c for input to the RACS and SAS (see Figure 9-11), and (3) provide the rate aid command q_c to the POCS. The TCL are summarized as follows:

Coordinate axis transformation:

$$\theta_c = \theta_{G_c} = C(\text{WL})_\theta \cos \Phi + C(\text{WL})_\psi \cos \Theta \sin \Phi$$
$$\psi_c = \psi_{G_c} = -C(\text{WL})_\theta \sin \Phi + C(\text{WL})_\psi \cos \Theta \cos \Phi$$

Tracking aid:

$$R_c = S_{(r,\theta)}C(\text{WL})_\theta \sin \Phi - S_{(r,\psi)}C(\text{WL})_\psi \cos \Phi$$

Rate aid:

$$q_c = \dot{\Psi}_{(\text{tr})} \sin \Phi \cos \Theta + \dot{\Theta}_{(\text{tr})} \cos \Phi \tag{9-30}$$

Note that the coordinate axis transformation and the q_c equations use the same transformation as for the Q and R terms in Eq. 1-34 in Section 1-4. The final values for the gains for the PACS, for the YACS, and for the tracking aid are

$$K_\psi = 26$$
$$K_\theta = K_{\theta_0} + K_{\theta_p}|\Phi| = 0.4 + 0.13|\Phi|$$
$$S_{(r,\theta)} = S_{(r,\psi)} = 1 \tag{9-31}$$

with K_θ limited to 5.

The optimization method used to obtain the values of the gains in Eq. 9-31 will be discussed later in this section. The evolution of the TCL will be discussed first. The original TCL consisted of the coordinate axis transformation and rate aid. Referring to Figure 9-32, the θ_c and ψ_c commands from the coordinate axis transformation control law provide the inputs to the PACS and YACS respectively (see Figures 9-7 and 9-18). The rate aid inputs, as an additional pitch rate command, directly into the POCS. This signal enables the Type 1 PACS to track a ramp input. The first term of the tracking aid was introduced as the result of early co-altitude tracking runs to correct for

elevation tracking errors at roll angles near 90°. At these roll angles a yaw rate about the aircraft's Z axis corrects for elevation tracking errors. The gain K_θ was made variable for the same reason. It was found that a value of 1 for K_θ during the first second of the run resulted in a 5° overshoot in Θ; however, a value of up to 5 was required at roll angles near 90° for good terminal tracking. The second term of the tracking aid for the TCL was introduced to improve the azimuth tracking when the attacker is in inverted flight (Φ near 180°) while tracking a target performing a split S.

Using the gains given in Eq. 9-31, it was found that the co-altitude attacks at an angle off the tail of 90° or greater resulted in excessive acceleration at about one second into the run. This resulted from the combination of the θ_c pitch command and the rate aid q_c. The solution was twofold. First, θ_c was limited to the value that would result in 7.33g, assuming that the aircraft had achieved the commanded pitch rate. The limiting value was computed using

$$\theta_{c(\text{max})} = \frac{7.33(57.3)g}{V_T K_\theta} \tag{9-32}$$

where

$\quad V_T$ is the total velocity of the attacker, and
$\quad K_\theta$ is given by Eq. 9-31.

Second, the rate aid command q_c was made zero for the first 3 sec and then increased linearly to its final value during the next 3 sec to minimize the transient resulting from introducing q_c after the run had started. In equation form,

$$q_c = \begin{cases} 0 & \text{for} \quad t \le 3 \text{ sec} \\ q_c \dfrac{t-3}{3} & \text{for} \quad 3 < t \le 6 \text{ sec} \\ q_c & \text{for} \quad t > 6 \text{ sec} \end{cases} \tag{9-33}$$

With these limits on θ_c and q_c, co-altitude attacks and attacks with the attacker initially 1500 ft below the target at angles off the tail of up to 150° were possible. However, attacks with the attacker initially 1500 ft above the target resulted in the aircraft pulling about $-5g$ due to the initial negative pitch command. To prevent this θ_c was set to zero if *all* of the following statements were true:

$$t < 1 \text{ sec}$$
$$C(\text{WL})_\theta < -5°$$
$$\theta_c < 0 \tag{9-34}$$

The second condition was included so that θ_c would not be restricted for co-altitude attacks. For these conditions, due to Θ_0 being equal to the trim angle of attack, there was always a small initial pitch down command that caused no problem. With θ_c restricted by Eq. 9-34, the aircraft rolls past 90° during the first second. By this time, although $C(\text{WL}) < -5°$, we have $\theta_c > 0$, as $C(\text{WL})_\theta \cos \Phi$ is positive because $\Phi > 90°$. Thus a positive pitch rate is commanded and the aircraft pulls through, maintaining positive acceleration as would be done under manual control. This scenario proved to be the most difficult one attempted.

The values of the five gains given in Eq. 9-31 were obtained by optimizing the system performance. The optimization was accomplished by adjusting the gains so as to minimize SUMI, the sum of the integrals of the magnitudes of the tracking errors $C(\text{WL})_\psi$ and $C(\text{WL})_\theta$ over the first 10 sec of the test run. The test run was a co-altitude attack with the attacker 30° off the tail of the target. The target was flying at Mach 0.65 in a 10° climb. The initial range was 5000 ft with the F-15 flying at Mach 0.8. Both aircraft were at 20,000 ft.

The optimization technique was designed to approximate the method of steepest descent. This was done by adjusting each gain up and down by a fixed amount Δ, the amplitude of which depended on the initial magnitude of the gain. After all the gains had been varied, those gains that resulted in a reduction of SUMI were incremented by Δ. If a change of gain resulted in a large reduction in SUMI compared to the other gains, that gain was incremented by 2Δ. The process was continued until the minimum value of SUMI was obtained. The optimization was accomplished for all four of the flight conditions, and the resulting gains are listed in Table 9-4, which shows that except for the value of 17 for K_ψ for Mach 0.8 at 5000 ft and the value of 1.7 for $S_{(r,\psi)}$ for Mach 0.8 at 40,000 ft, there are only minor variations in the optimum gains. As it is unlikely that many actual encounters using guns will occur at 40,000 ft, no scheduling was introduced to vary $S_{(r,\psi)}$. However, K_ψ was reduced linearly from 26 down to 17 as a function of dynamic pressure for $q > 440 \text{ lb/ft}^2$ so that $K_\psi = 17$ for $q = 786.9$. Thus, except for the variation in K_ψ, the optimum gains for Mach 0.8 at 20,000 ft were used for the other flight conditions.

TABLE 9-4 Optimum Gains for the Four Flight Conditions

Flight Condition		Optimum Gains					Dyn. Press. (lb / ft²)
M	Alt. (ft)	K_ψ	K_{θ_0}	K_{θ_p}	$S_{(r,\theta)}$	$S_{(r,\psi)}$	
0.6	20,000	27	0.5	0.14	1.1	1.0	245.2
0.8	5,000	17	0.35	0.12	0.9	0.9	786.9
0.8	20,000	26	0.4	0.13	1.0	1.0	439.9
0.8	40,000	26	0.4	0.13	1.0	1.7	176.1

9-10   DISCRETE ANALYSIS

As the pitch and yaw and attitude loops shown in Figure 9-32 are closed through the digital computer, the resulting system will be a digital or sampled-data control system. For such a system the rate at which the states of the continuous system are sampled as well as the loop gains determine the overall system stability. The discrete analysis of the sampled-data control system can be accomplished by two methods:[5] (1) the direct digital control design technique uses the z transform method and performs all the analysis in the z plane; and (2) the digitization, or discrete, digital control design technique uses the Padé approximation and performs all the analysis in the s plane. Here these methods will be referred to simply as the direct and digitization methods. For the digitization method the Laplace transform of the zero-order hold (ZOH) is

$$\mathscr{L}[\text{ZOH}] = \frac{1 - e^{-Ts}}{s} \tag{9-35}$$

where T is the time between samples. The first-order Padé approximation of e^{-Ts} from Section 13-2 is

$$e^{-Ts} = -\frac{s - 2/T}{s + 2/T} \tag{9-36}$$

Substituting Eq. 9-36 into Eq. 9-35 and simplifying yields

$$\mathscr{L}[\text{ZOH}] = \frac{2}{s + 2/T} \tag{9-37}$$

Thus it can be seen that the effect of digitizing the control system is equivalent to adding a lag to the continuous system. As shown in Ref. 7 and 8, Eq. 9-37 can be considered as representing the ZOH, but a factor of $1/T$ must be included to represent the sampler. Thus the sampler and ZOH are replaced by $(2/T)/(s + 2/T)$. This expression has a steady-state gain of 1 for a step input, which is consistent with the purpose of the sampler and ZOH, whereas the steady-state value from Eq. 9-37 is T. The validity of this approximation of the sampler and ZOH will be shown later in this section.

For the direct method the transformation from the s domain to the z domain is accomplished by the use of the z transform

$$z \equiv e^{sT} \tag{9-38}$$

But as $s = \sigma \pm j\omega$, then

$$|z| = e^{\sigma T} \tag{9-39}$$

and

$$\angle z = \pm \omega T \text{ rad} \tag{9-40}$$

Now the fundamental theorem of sampling states[9,10] that in order to reconstruct the continuous signal it must be sampled at a rate that is at least twice the highest frequency of the signal being sampled. If ω_s is the sampling angular frequency, then $T = 2\pi / \omega_s$, and substituting this for T in Eq. 9-40 yields

$$\angle z = \frac{2\pi\omega}{\omega_s} \text{ rad} \tag{9-41}$$

If ω is the highest frequency in the system, then from the sampling theorem the minimum value of ω_s is 2ω. Substituting 2ω for ω_s in Eq. 9-41 yields

$$\angle z = \pi = 180°$$

This value of ω_s defines the boundary of the primary strip as shown in Figure 9-33. For $\omega_s = 2\omega/3$, $\angle z = 3\pi = 540°$, which is the upper boundary of the first complementary strip, etc. If ω_s is such that the complex poles in the s plane lie in the first complementary strip, then folding occurs. This will be illustrated by using the open loop complex poles of the PACS.

From Eq. 9-5, $s = -8.87 \pm j17.31$; substituting this into Eq. 9-38 yields

$$z = e^{-(8.87 \pm j17.31)T}$$
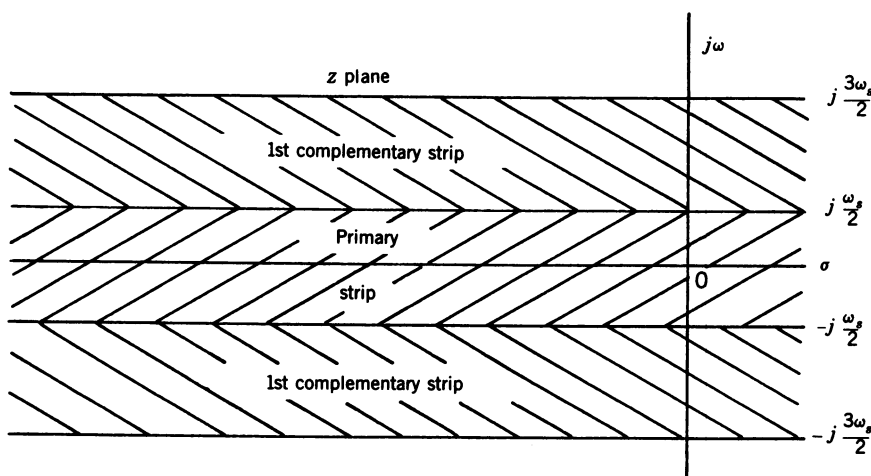
Figure 9-33   *Periodic strips determined by sampling period.*
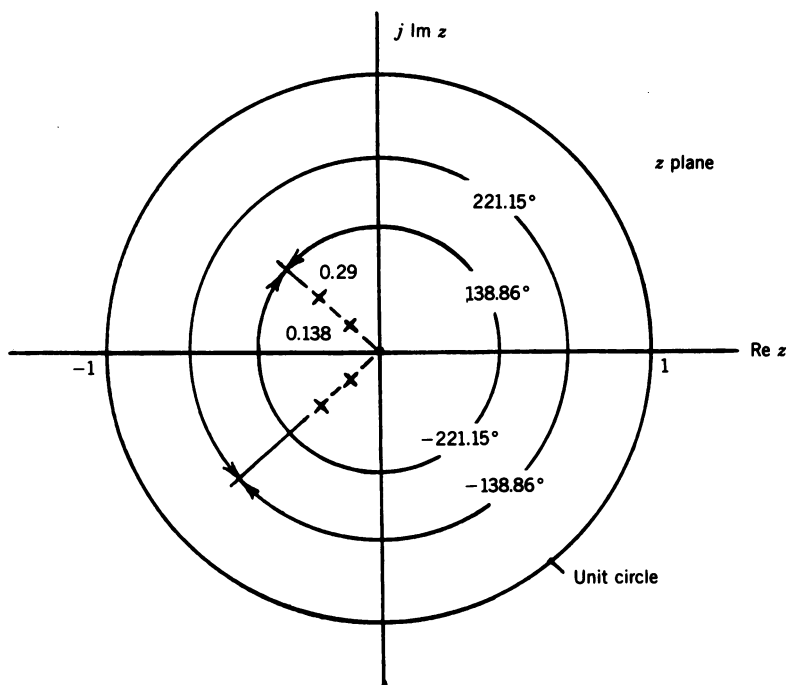
Figure 9-34   *Location of s plane poles, s = −8.87 ± j17.31, in the z plane for T = 0.14 and 0.223 sec.*

For $T = 0.14$ sec then

$$z = 0.29 \underline{/\pm 138.86°} \tag{9-42}$$

and for $T = 0.223$ then

$$z = 0.138 \underline{/\pm 221.15°} \tag{9-43}$$

As $+138.86° \simeq -221.15°$, the only difference in the plotting of the two values of z would be in the magnitude. This is illustrated in Figure 9-34.

Now if it were not known that the pole at 0.138 in the z plane was in the first complementary strip in the s plane (an open loop pole in the s plane could move into the first complementary strip as the gain is increased), then it would be assumed that the pole was located at $z = 0.138 \underline{/\pm 138.86°}$. The inverse z transform can be taken using

$$\sigma = \frac{1}{T} \ln|z|$$

$$\omega = \frac{1}{T} \angle z \tag{9-44}$$

Then for $T = 0.223$, we have $\sigma = -8.88$ and $\omega = 10.87$, and the location of the complex poles in the s plane is

$$s = -8.88 \pm j10.87$$

while the actual location is

$$s = -8.88 \pm j17.31$$

Thus the magnitude checks, but the damped natural frequency puts the pole in the primary strip, as would be expected. To continue, if $T = 0.503$ then

$$z = 0.0115 \underline{/\pm 498.91°} = 0.0115 \underline{/\pm 138.91°}$$

which is referred to as folding, as the angle is approximately the value of the angle for $T = 0.14$ plus 360°. Thus even though the open loop complex poles are in the primary strip, the closed loop complex poles could be in the first complementary strip. If this were the case, then the value of ω for these poles when transformed from the z plane back to the s plane would be incorrect. The utilization of the digitization method (Padé approximation) avoids this problem. The discrete analysis of the PACS will now be presented.

A simplified block diagram of the sampled-data configuration of the PACS from Figure 9-32 is shown in Figure 9-35 with the closed loop transfer function for the POCS from Eq. 9-4 included. In the hybrid simulation, which will be discussed in the next section, there are actually two sampling periods: (1) the frame time of 15 msec allocated for all of the digital calculations required for the simulation, which is considered fixed; and (2) the variable sampling time, which determines how frequently the command is calculated for input to the PACS. As the shortest variable sampling time is 0.05 sec, it is more than three times the frame time; thus for the discrete analysis only the variable sampling time needs to be considered. The discrete analyses for both the PACS and YACS that follow were accomplished with and without the lead compensators. The analysis without the lead compensators was used for the comparison of the predicted gains from the analysis with the gains from the hybrid simulation for zero damping at low sampling rates. This was necessary because as the period between the samples increases, the change in the amplitude of the output of the ZOH (lead compensator input), which is a series of steps, increases. The resulting output of the lead compensator is a series of decaying exponentials, which are then input to the POCS and RACS. The pitch integrating gyro of the POCS has a smoothing effect on these inputs; however, they are simply amplified in the RACS, resulting in 20° aileron pulses (the ailerons are limited to $\pm 20°$) with the corresponding aircraft roll rate and roll angle responses. The system's response to these pulses makes it difficult to determine if the resulting oscillations are due to the pulses or to system instability. For this reason the lead compensators were omitted when the analysis involved comparing analytical results with simulation results.
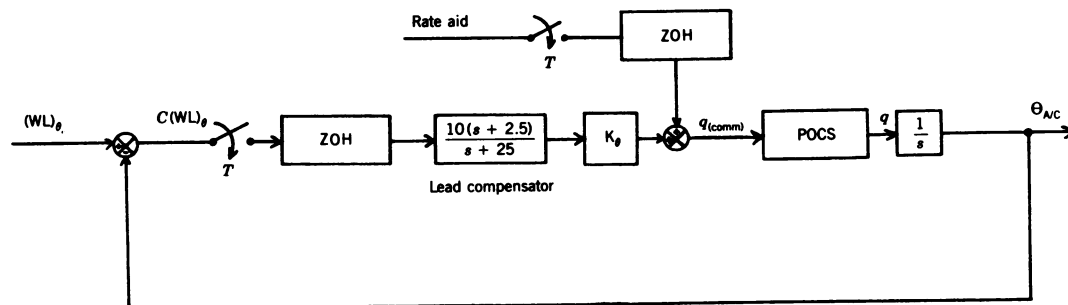
Figure 9-35 *Sampled-data configuration of the PACS for discrete analysis. As $\Phi = 0$, $\theta_c = C(\text{WL})_\theta$, and $(\text{WL})_\theta = \Theta_{A/C} + \theta_g$,*

$$\frac{q(s)}{q_{(comm)}(s)} = \frac{1070.26\,(s + 1.126)}{(s + 0.9)\,(s + 3.54)\,(s^2 + 17.74s + 378.313)}$$
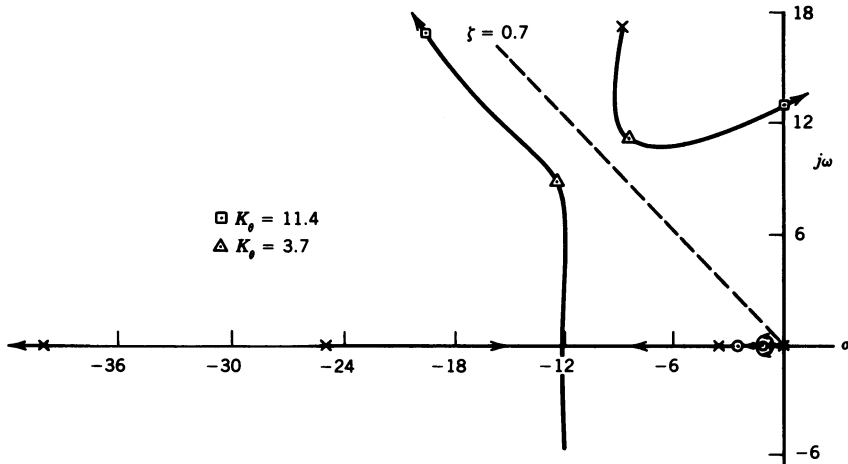
Figure 9-36 Root locus of discrete PACS — digitization method, $1/T = 20$ sps.

To continue, using the digitization method, we find that the forward transfer function for the PACS with the lead compensator, the sampler, and ZOH from Figure 9-35 is

$$\frac{\Theta_{A/C}(s)}{C(WL)_{\theta}(s)} = \frac{428,104 K_{\theta}(s + 1.126)}{s(s + 0.9)(s + 3.54)(s + 25)(s + 40)}$$

$$\times \frac{s + 2.5}{s + 8.87 \pm j17.31} \qquad (9\text{-}45)$$

where the function for the sampler and ZOH for $T = 0.05$ sec is

$$\frac{2/T}{s + 2/T} = \frac{40}{s + 40}$$

The root locus is shown in Figure 9-36, which can be compared to the root locus of the PACS without sampling shown in Figure 9-8. The complex closed loop poles for $K_{\theta} = 11.4$ and 3.7 are indicated in Figure 9-36. The higher gain yields a damping ratio of approximately zero. The closed loop transfer function for $K_{\theta} = 11.4$ is

$$\frac{\Theta_{A/C}(s)}{(WL)_{\theta_c}(s)} = \frac{4.88 \times 10^6 (s + 1.126)}{(s + 2.29)(s + 1.16)(s + 43.9)}$$

$$\times \frac{s + 2.5}{(s + 0.0015 \pm j13)(s + 19.9 \pm j17.2)} \qquad (9\text{-}46)$$

and the closed loop transfer function for $K_\theta = 3.7$ is

$$\frac{\Theta_{A/C}(s)}{(WL)_{\theta_c}(s)} = \frac{1.58 \times 10^6 (s + 1.126)}{(s + 1.43)(s + 1.55)(s + 41.69)}$$

$$\times \frac{s + 2.5}{(s + 8.617 \pm j11.21)(s + 12.64 \pm j9.01)} \qquad (9\text{-}47)$$

For the direct method it is necessary to take the z transform of the ZOH times Eq. 9-45. But the z transform of e^{Ts} is z; then from Eq. 9-35

$$\mathscr{Z}[1 - e^{-Ts}] = 1 - z^{-1} = \frac{z - 1}{z} \qquad (9\text{-}48)$$

This still leaves the $1/s$ in Eq. 9-35; therefore, Eq. 9-45 must be multiplied by $1/s$ before taking the z transform. Taking the z transform of $1/s$ times Eq. 9-45 and then multiplying the results by $(z-1)/z$ yields

$$\frac{\Theta_{A/C}(z)}{C(WL)_\theta(z)} = \frac{0.0018 K_\theta (z - 0.88)(z - 0.945)(z + 0.65)}{(z - 1)(z - 0.945)(z - 0.84)(z - 0.286)}$$

$$\times \frac{(z + 0.066)(z + 6.3)}{z - 0.416 \pm j0.489} \qquad (9\text{-}49)$$

It should be noted that taking the z transform introduces additional zeros into the transfer function. The z plane root locus for Eq. 9-49 is shown in Figure 9-37. In going from the s plane to the z plane the imaginary axis maps into the unit circle. Poles inside the unit circle are stable, and for the damping ratio to be zero the corresponding complex poles must lie on the unit circle. In this case, for zero damping $K_\theta = 11$, which agrees very well with the value of 11.4 obtained using the digitization method. The closed loop poles for $K_\theta = 11$ are indicated in Figure 9-37 as well as the closed loop
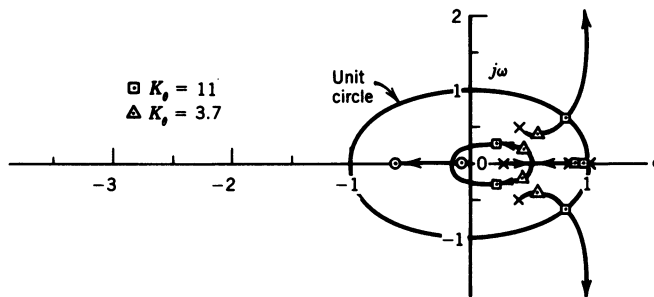
Figure 9-37   *Root locus of discrete PACS — direct method, 1 / T = 20 sps.*
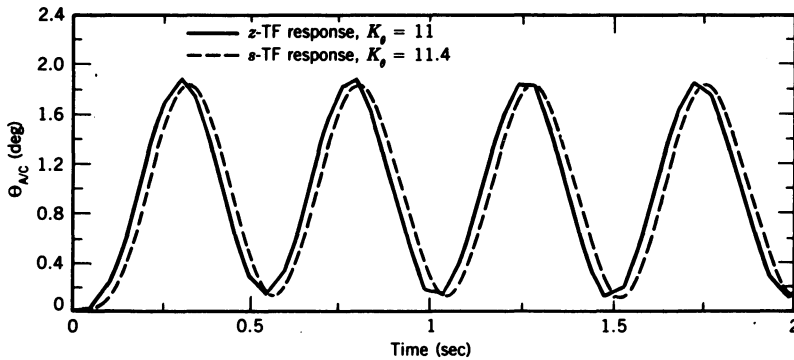
Figure 9-38 *Comparison of step responses from CLTF obtained using the direct method (z-TF) and digitization method (s-TF) for indicated K_θ, $1/T = 20$ sps.*

complex poles for $K_\theta = 3.7$. The closed loop transfer function for $K_\theta = 11$ is

$$\frac{\Theta_{A/C}(z)}{(WL)_{\theta_c}(z)} = \frac{0.01967(z+0.066)(z+0.648)(z-0.88)}{(z-0.892)(z-0.94)(z-0.2306\pm j0.2536)}$$

$$\times \frac{(z-0.945)(z+6.3)}{z-0.798\pm j0.6035} \tag{9-50}$$

and for $K_\theta = 3.7$ is

$$\frac{\Theta_{A/C}(z)}{(WL)_{\theta_c}(z)} = \frac{0.0066(z+0.066)(z+0.648)(z-0.88)}{(z-0.926)(z-0.931)(z-0.457\pm j0.1874)}$$

$$\times \frac{(z-0.945)(z+6.3)}{z-0.5676\pm j0.367} \tag{9-51}$$

The step responses obtained from the closed loop transfer functions for the gains selected for zero damping are shown in Figure 9-38. The discontinuities in the z transform plot, most notable near the peaks of the oscillations, occur at the sampling times. Similarly the step responses for $K_\theta = 3.7$ are shown in Figure 9-39. The excellent agreement of the step responses attests to the validity of using the digitization method for the discrete analysis of sampled-data control systems. As an additional check, using the forward transfer function from Figure 9-35 without the lead compensator, the values of K_θ for zero damping and the corresponding natural frequencies for sampling rates from 1.837 to 20 sps were determined by both methods using the program TOTAL. The resulting calculated values were then compared with the values obtained from the hybrid simulation. For these runs the target was climbing at a 30° angle at a constant speed, with both aircraft on
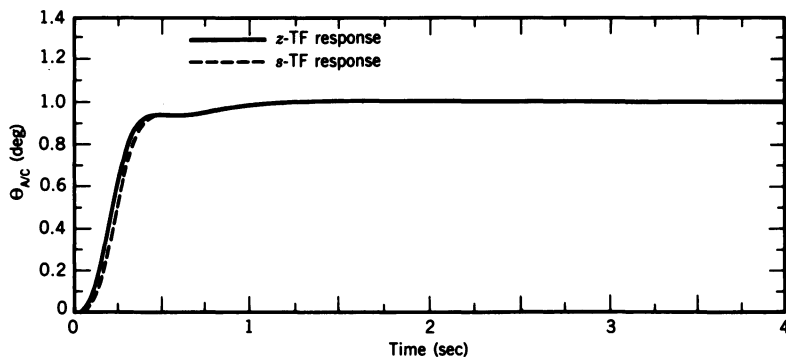
Figure 9-39 *Comparison of step responses from CLTF obtained using the direct method (z-TF) and digitization method (s-TF) for $K_\theta = 3.7$, $1 / T = 20$ sps.*

the same heading. The input was the LOS generated by the tracker plus a constant-pitch lead angle of 4°. The value of K_θ was adjusted to obtain zero damping of the $C(WL)_\theta$ trace. The frequency of the resulting sustained oscillation was measured from the recording. The results are summarized in Table 9-5. Referring to Table 9-5 for $1/T > 7.14$ sps ($\omega_s/2 = 22.43$), the open loop complex poles ($\omega = 17.31$) are in the primary strip. For $1/T < 7.14$ sps they are in the first complementary strip. The value $1/T = 2.81$ ($\omega_s/2 = 8.83$) puts the poles about in the middle of the complementary strip, and the value 1.837 ($3\omega_s/2 = 17.31$) puts them at the upper boundary of the first complementary strip. A comparison of the calculated and measured values in Table 9-5 shows very good agreement, with no consistent trends. The main conclusion is that the digitization method gives very good to excellent results and makes it possible to do all the analysis in the s plane. A recording for a sampling rate of 1.837 sps is shown in Figure 9-40 for $K_\theta = 5.2$ and 0.764. The

TABLE 9-5 Comparison of Calculated and Measured Values of Gain and Natural Frequency for Zero Damping for PACS without Lead Compensator*

Sampling Rate (sps)	K_θ for $\zeta = 0$			ω_n(rad / sec)		
	Digitization Method	Direct Method	Meas. Value	Digitization Method	Direct Method	Meas. Value
1.837	5.848	5.313	5.2	2.92	2.83	2.67
2.81	7.079	6.676	6.5	3.52	3.46	3.31
4.485	8.776	8.31	8.6	4.23	4.2	4.25
7.14	10.77	11.05	10.77	4.95	5.07	4.65
10	12.31	12.8	12.9	5.45	5.59	5.53
20	15.33	17.4	15.51	6.31	6.78	6.28

*Mach 0.8 at 20,000 ft.
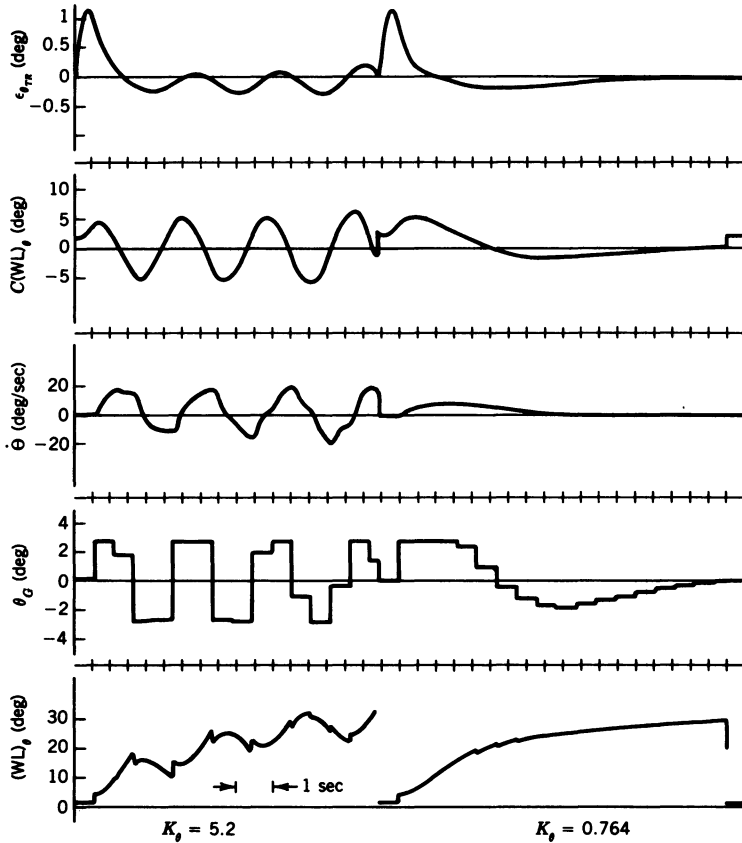
Figure 9-40 *Tracking response of PACS without lead compensator for a sampling rate of 1.837 sps, Mach 0.8 at 20,000 ft.*

latter value is the calculated value for a damping ratio of 0.7 using the digitization method. It is important to note that although the lowest sampling rate is lower than the frequency of the open loop complex poles, it is still more than four times the frequency of the dominant closed loop poles, as can be seen from Figure 9-40. Thus the damped response of $(WL)_\theta$ is relatively smooth. The characteristic stairstep due to the sampling does not show up in the $C(WL)_\theta$ trace, as the sampling takes place after the summer as shown in Figure 9-35. As the output of the ZOH goes to both the POCS and the movable gun, the gun response, being much faster than that of the POCS, is in fact a sampled version of $C(WL)_\theta$.

A simplified block diagram of the sampled-data configuration of the YACS from Figure 9-32 is shown in Figure 9-41, including the closed loop transfer function for the RACS for a roll command input to a yaw rate output. The RACS transfer function is equal to g / V_T times Eq. 9-15. As the
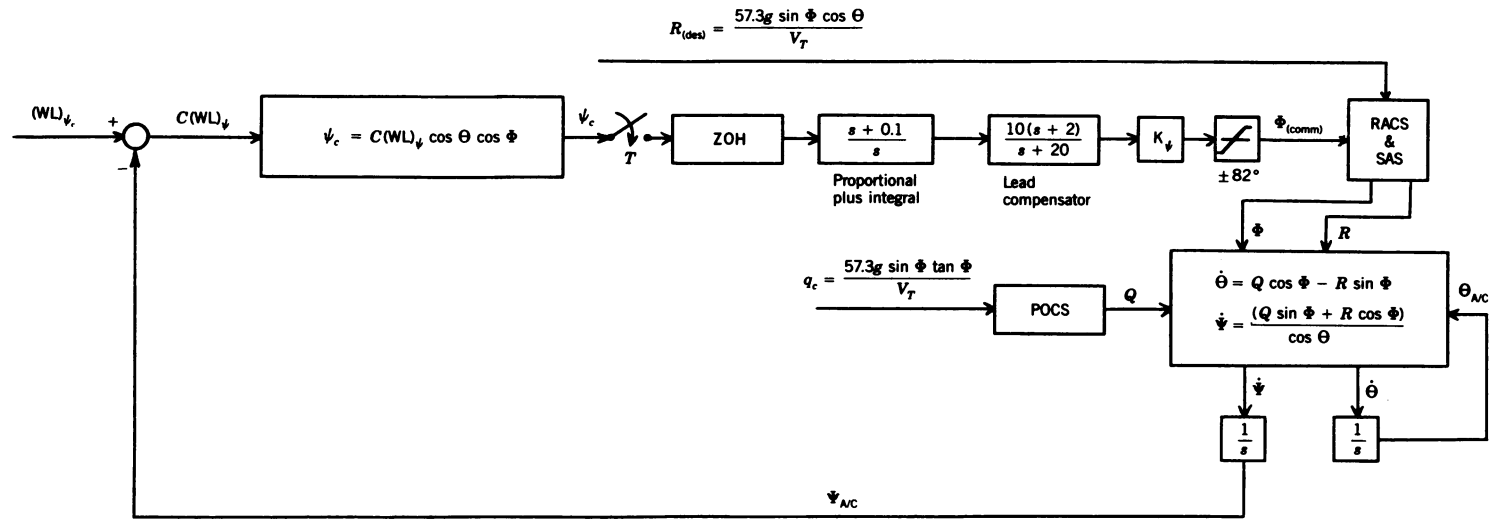
Figure 9-41 *Sampled-data configuration of YACS for discrete analysis.*

$$\frac{R(s)}{\Phi_{(comm)}(s)} = \frac{g}{V_T} \left(\frac{\Phi(s)}{\Phi_{(comm)}(s)} \right)$$

$$= \frac{25.1}{(s+2.75)(s^2+20.14s+235)} \frac{deg/sec}{deg}$$

aircraft must bank to turn, there must be a pitch rate as well as a yaw rate; thus the pitching and yawing motions cannot be decoupled as they could for a pitch rate command alone. In order to reduce the coupling, the PACS loop was not closed. To generate the required pitch rate a command q_c, the required pitch rate for a coordinated turn, was input to the POCS. The tracking aid input to the rudder R_c was also disconnected.

Following the pattern used for the PACS, the forward transfer function for the YACS with the lead compensator from Figure 9-41 is

$$\frac{\Psi_{A/C}(s)}{C(WL)_\psi(s)} = \frac{251 K_\psi(s+0.1)(s+2)}{s^2(s+20)(s+2.75)(s^2+20.14s+235)} \qquad (9\text{-}52)$$

For $T = 0.05$ sec, using the digitization method, the transfer function for the s plane root locus is

$$\frac{\Psi_{A/C}(s)}{C(WL)_\psi(s)} = \frac{10040 K_\psi(s+0.1)(s+2)}{s^2(s+2.75)(s+20)(s+40)(s+10.07\pm j11.56)} \qquad (9\text{-}53)$$

The root locus is shown in Figure 9-42 which can be compared with Figure 9-19. The closed loop poles are indicated for $K_\psi = 216.4$ ($\zeta = 0$) and for $K_\psi = 53.59$ ($\zeta = 0.7$, complex poles only). The closed loop transfer function for $K_\psi = 216.4$ is

$$\frac{\Psi_{A/C}(s)}{(WL)_{\psi_c}(s)} = \frac{2.17 \times 10^6 (s+0.1)(s+2)}{(s+0.1)(s+1.89)(s+42)}$$

$$\times \frac{1}{(s+0.00017 \pm j9.7)(s+19.4 \pm j14.1)} \qquad (9\text{-}54)$$
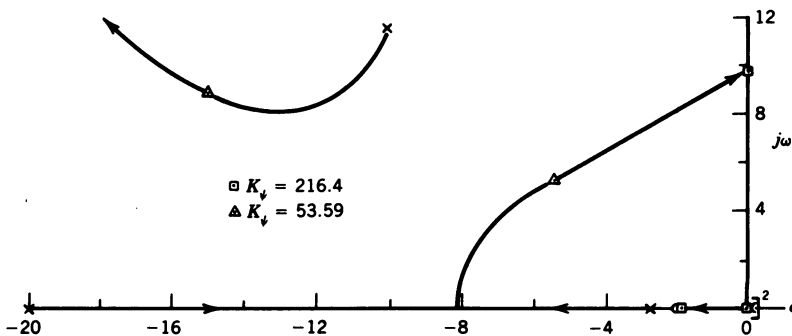
Figure 9-42 Root locus of discrete YACS — digitization method, 1 / T = 20 sps.
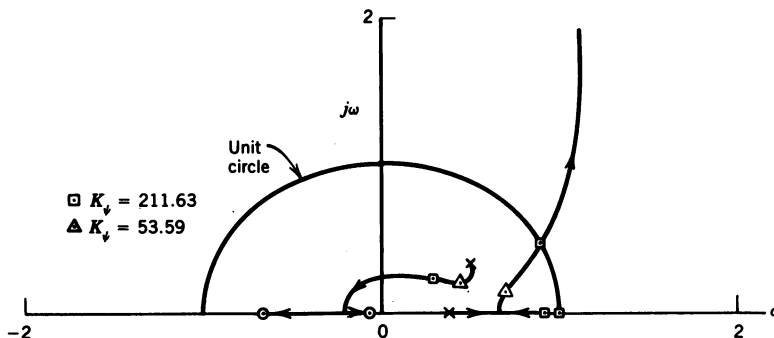
Figure 9-43 Root locus of discrete YACS — direct method, $1/T = 20$ sps.

and the closed loop transfer function for $K_\psi = 53.59$ is

$$\frac{\Psi_{A/C}(s)}{(WL)_{\psi_c}(s)} = \frac{538043.6(s+0.1)(s+2)}{(s+0.105)(s+1.44)(s+5.367\pm j5.354)}$$

$$\times \frac{1}{(s+15\pm j8.904)(s+40.6)} \tag{9-55}$$

For the direct method, taking the z transform of $1/s$ times Eq. 9-52 and multiplying the results by $(z-1)/z$ yields

$$\frac{\Psi_{A/C}(z)}{C(WL)_\psi(z)} = \frac{0.00004349 K_\psi(z-0.905)(z-0.995)}{(z-1)^2(z-0.8715)(z-0.368)}$$

$$\times \frac{(z+0.0672)(z+0.6645)(z+6.587)}{z-0.506\pm j0.33} \tag{9-56}$$

The root locus is shown in Figure 9-43 with the location of the closed loop poles indicated for $K_\psi = 211.63$ ($\zeta = 0$) and for $K_\psi = 53.59$ ($\zeta = 0.7$, complex poles only). The value 211.63 for K_ψ is in excellent agreement with the value of 216.4 obtained using the digitization method. For the continuous system K_ψ for zero damping is 259.3. The closed loop transfer function for $K_\psi = 211.63$ is

$$\frac{\Psi_{A/C}(z)}{(WL)_{\psi_c}(z)} = \frac{0.0092(z-0.905)(z-0.995)(z+0.0672)}{(z-0.91)(z-0.995)(z-0.283\pm j0.227)}$$

$$\times \frac{(z+0.6645)(z+6.587)}{z-0.89\pm j0.4646} \tag{9-57}$$
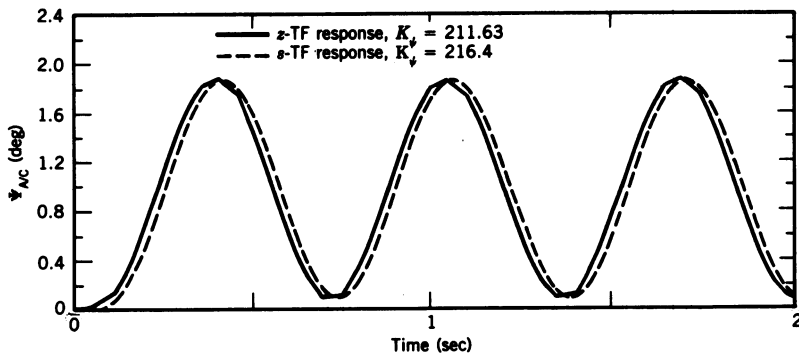
Figure 9-44 *Comparison of step responses from CLTF obtained using the direct method (z-TF) and digitization method (s-TF) for indicated K_ψ, $1/T = 20$ sps.*

and the closed loop transfer function for $K_\psi = 53.59$ is

$$\frac{\Psi_{A/C}(z)}{(WL)_{\psi_c}(z)} = \frac{0.00233(z+0.06718)(z+0.6645)(z-0.995)}{(z-0.93)(z-0.995)(z-0.4277\pm j0.189)}$$

$$\times \frac{(z-0.9048)(z+6.587)}{(z-0.734\pm j0.205)} \qquad (9\text{-}58)$$

The step responses obtained from the closed loop transfer functions for the gains selected for zero damping are shown in Figure 9-44, and for $K_\psi = 53.59$ in Figure 9-45. Again the agreement is excellent, further attesting to the validity of using the digitization method for the analysis of sampled-data control systems.
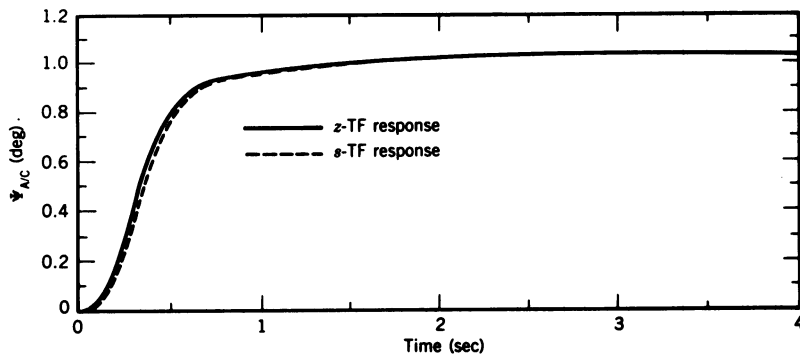
Figure 9-45 *Comparison of step responses from CLTF obtained using the direct method (z-TF) and digitization method (s-TF) for $K_\psi = 53.59$, $1/T = 20$ sps.*

TABLE 9-6   Comparison of Calculated and Measured Values of Gain and Natural Frequency for Zero Damping and Calculated Values of Gain for 0.7 Damping, without Lead Compensator*

	K_ψ for $\zeta = 0$			ω_n for $\zeta = 0$ (rad / sec)			K_ψ for $\zeta = 0.7$	
1 / T (sps)	Digitization Method	Direct Method	Meas. Value	Digitization Method	Direct Method	Meas. Value	Digitization Method	Direct Method
1.227	86.5	69.37	60	2.064	1.90	1.95	15.3	15.82
1.84	101.7	84.25	86	2.459	2.3	2.36	18.13	19.04
3	124.4	108.6	135	2.96	2.84	3.14	21.29	22.14
4.77	149.0	145.9	174	3.43	3.43	3.7	23.73	24.46
10	193.3	189.3	228	4.117	4.1	3.93	26.4	27.62
20	228.5	225.0	254	4.58	4.55	4.83	27.78	28.44
∞ (cont.)	252.4			5.2			30	

*Mach 0.8 at 20,000 ft.

A comparison of the calculated and measured values of K_ψ and the natural frequencies for zero damping and the calculated values of K_ψ for 0.7 damping using the digitization and direct method are listed in Table 9-6. To obtain the measured values for the table, the simulation was run with the target on a heading of from 1 to 4° with zero lead angle to keep the roll angle command less than the limiting value of 82°. As mentioned earlier in this section, a pitch rate command q_c was input to the POCS rather than closing the PACS loop. An examination of the gains for zero damping reveals that for sampling rates of 3 sps and higher the values computed by both methods are in close agreement, but consistently lower than the measured values. The opposite is true for sampling rates below 3 sps, with the exception of the value 84.25 for the direct method for $1/T = 1.84$.

The calculated values of gain for 0.7 damping are of more practical interest, as they are the gains that would probably be used in the control system. The agreement between the two calculated values is excellent, and although no measured values of gain are included, the results of runs made at sampling rates of 1.227 and 20 sps are shown in Figure 9-46. For these runs the target heading was 30° with zero lead and without pitch control through the PACS. With the target on a heading of 30° and no lead, the attacking aircraft should settle out on a heading of 30°. For $1/T = 1.227$ there is a 20 percent overshoot in the (WL)$_\psi$ trace, which would indicate a damping ratio of approximately 0.45. For the other case the damping ratio is probably greater than 0.7; however, the correlation is still very good.

All of the analysis in this section indicates excellent agreement between the two methods for analyzing sampled-data control systems, and with the results of the simulation, thus justifying the use of the simpler digitization method for the discrete analysis. It should be remembered that all of the lateral analysis was accomplished using the coordinated aircraft transfer
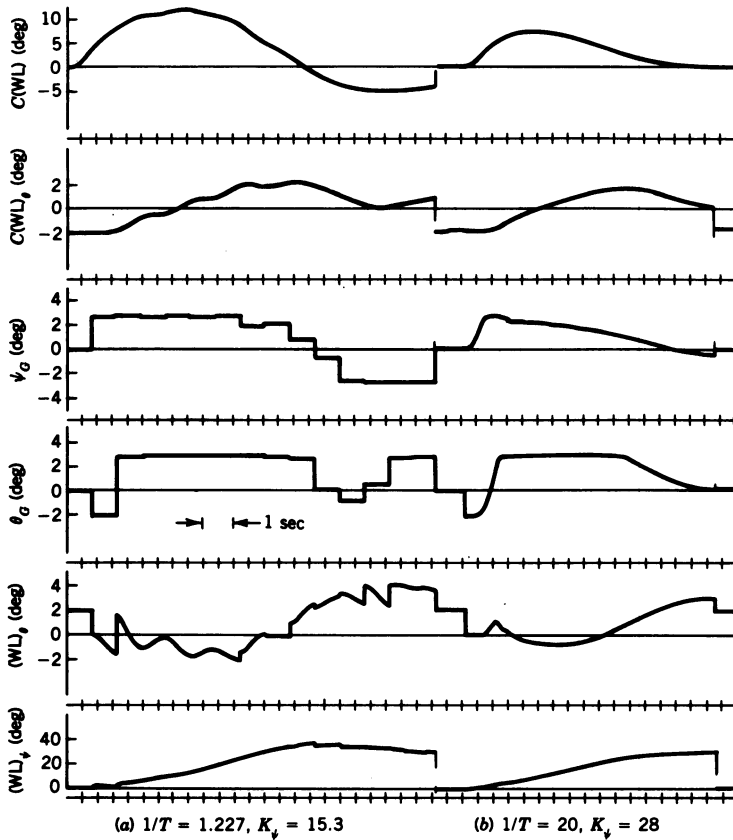
Figure 9-46 *Tracking response of the YACS without the lead compensator for different sampling rates, Mach 0.8 at 20,000 ft.*

function used in Section 9-4. This concludes the discussion of the discrete analysis; the simulation results will be presented in the next section.

9-11 SIMULATION RESULTS

Before discussing the simulation results, a brief description of the hybrid simulation will be presented. A block diagram of the hybrid simulation of the IFFC system, showing the division of the simulation and the flow of the parameters between the analog and digital computers, is contained in Figure 9-47. As can be seen from the figure, the high-frequency calculations, such as the solution of the aircraft equations of motion and the simulation of the system dynamics (blocks 3, 4, 6, 9), are accomplished on the analog computer. The analog outputs are passed to the digital computer by ADCs (analog-to-

1. Relative geometry calculations
Inputs: problem initial conditions and output of ADCs
Output: earth axis velocity components of both A/C and inputs to DACs

V_{T_0}

$\alpha, \beta, \dot{\gamma}, V_T, \Psi, \Theta, \Phi, C_L, T/m$

3. Solution of six-degree-of-freedom equations of motion of attacker A/C
Inputs: from DACs
Outputs: to recorders and ADCs

ρ, V_T, C_L

2. Dynamic pressure calculations

$\dfrac{D}{m}, \dfrac{qcS}{I_y}, \dfrac{qbS}{I_x}, \dfrac{qbS}{I_z}, \dfrac{qS}{57.3\,m}$

T, δ_e
δ_r, δ_a

Ψ_R, Θ_R

4. Gimbaled tracker simulation

ρ, α, β
$R, \dot{R}$

$\Theta_{(tr)}, \Psi_{(tr)}, \Theta_{(tr)}$

Ψ, Θ, Φ

5. ω_{LOS}, prediction angle, time of flight of projectile, future range calculations

ψ_G, θ_G

6. 2-axis movable gun simulation

$(WL)_\theta$
$(WL)_\psi$

$\Psi_{(tr)}, \Theta_{(tr)}$

Ψ, Θ

$\lambda_\psi, \lambda_\theta$

$\Psi_{(tr)} - \Psi$
$\Theta_{(tr)} - \Theta$

V_T, Φ, Θ

7. Command signals
$C(WL)_\psi = \Psi_{(tr)} + \lambda_\psi - \Psi$
$C(WL)_\theta = \Theta_{(tr)} + \lambda_\theta - \Theta$
$R_{(DES)} = (57.3g \sin \Phi \cos \Theta)/V_T$
$R_c = S_{(r,\theta)} C(WL)_\theta \sin \Phi - S_{(r,\psi)} C(WL)_\psi \cos \Phi$
$K_\phi = 0.4 + 0.13|\Phi|$

θ_{G_c}
ψ_{G_c}

P, Q, R
β, Φ
$V_{T_0}, V_T, \dot{V}_T$

$1/T$ $\dot{\Psi}_{(tr)}, \dot{\Theta}_{(tr)}$

$1/T$ $C(WL)_\psi$
$C(WL)_\theta$

Φ, Θ

$S_{(rg)}, S_{(ig)}, S_\phi, K_\psi, S_\beta \dot{\beta}$

8. Control system inputs
$\theta_c = C(WL)_\psi \cos \Theta \sin \Phi + C(WL)_\theta \cos \Phi$
$\dot{\psi}_c = C(WL)_\psi \cos \Theta \cos \Phi - C(WL)_\theta \sin \Phi$
$q_c = \dot{\Psi}_{(tr)} \cos \Theta \sin \Phi + \dot{\Theta}_{(tr)} \cos \Phi$

$R_{(DES)}, R_c, K_\phi$

$1/T$

θ_c, ψ_c, q_c

9. Longitudinal and lateral FCS and throttle control simulation

Digital computer

Analog computer

Figure 9-47 Block diagram of hybrid simulation of IFFC system.

digital converters). The command signals (block 7) and control system inputs (block 8) to block 9, as well as the LOS angles to block 4, are passed from the digital computer by DACs (digital-to-analog converters). The inputs that are a function of dynamic pressure are calculated in block 2. These quantities are passed to blocks 3 and 9 via MDACs (multiplying digital-to-analog converters) to be multiplied by the appropriate variable on the analog computer. The wind axis equations of motion used in the 6-DOF aircraft simulation are derived in Appendix G. The $1/T$ switches provide the sampling described in Section 9-10. The 15-msec frame time mentioned in the last section refers to the time allocated for the calculations contained in blocks 1, 2, 5, and 7. At the beginning of the frame time all ADCs are read, the computations in blocks 1, 2, 5, and 7 are executed, and then all DACs and MDACs are written. The calculations in block 8 are executed at the variable sampling rate described in the last section (normal operation was at 20 sps). The complete details of the simulation are contained in Ref. 7, along with the listing for the digital portion of the simulation and the analog computer schematics.

Having briefly described the simulation, the various intercept scenarios investigated will now be described. The scenarios included: a turning target with and without a reversal and a climbing turning target; a target performing a split S plus reversal; the attacker at angles of 30 to 150° off the tail of the target with the target flying a straight line, turning into the attacker; and the target initially 1500 ft above and below the attacker and flying in a straight line. The gains used were the optimum gains given in Eq. 9·31, where R_c is defined in Eq. 9-30. The magnitude of K_θ was limited to 5 and that of R_c to 3.

For runs against a turning target both aircraft are initially on the same heading with the target turning at 10 deg/sec ($3.65g$) and 16.5 deg/sec ($6.03g$). Both aircraft are at 20,000 ft, with the target at Mach 0.65 and the attacker at Mach 0.8. For runs against a turning target plus reversal, the initial conditions and turning rates are the same as for the turning target with the target reversing its rate of turn after turning about 90°. For the target performing a climbing turn (chandelle), the target had a yaw rate of 10 deg/sec with $\Theta_T = 45 \sin \Psi_T$. Runs were made for all four flight conditions. With the exception of the attack against the turning target plus reversal for a turn rate of 16.5 deg/sec and the chandelle for a Mach 0.8 attacker at 40,000 ft against a Mach 0.65 target, the gun was on track during the entire run. For the case of the turning target plus reversal the gun was against the yaw stop for only the last 1.5 sec of the 12.5-sec engagement. For the chandelle the gun was against the pitch stop only during the first second of a 10.5-sec run.

The case of the target performing a split S plus reversal presented slightly more of a challenge. In a split S an aircraft rolls inverted ($\Phi = 180°$) and then pulls through with a positive pitch rate with respect to the aircraft axis system (a negative $\dot{\Theta}$ with respect to an earth axis system). Normally the maneuver ends after 180° of pitch or when the aircraft is again in level flight. For the aircraft simulation division by $\cos \Theta$ is performed, so that the attacker cannot
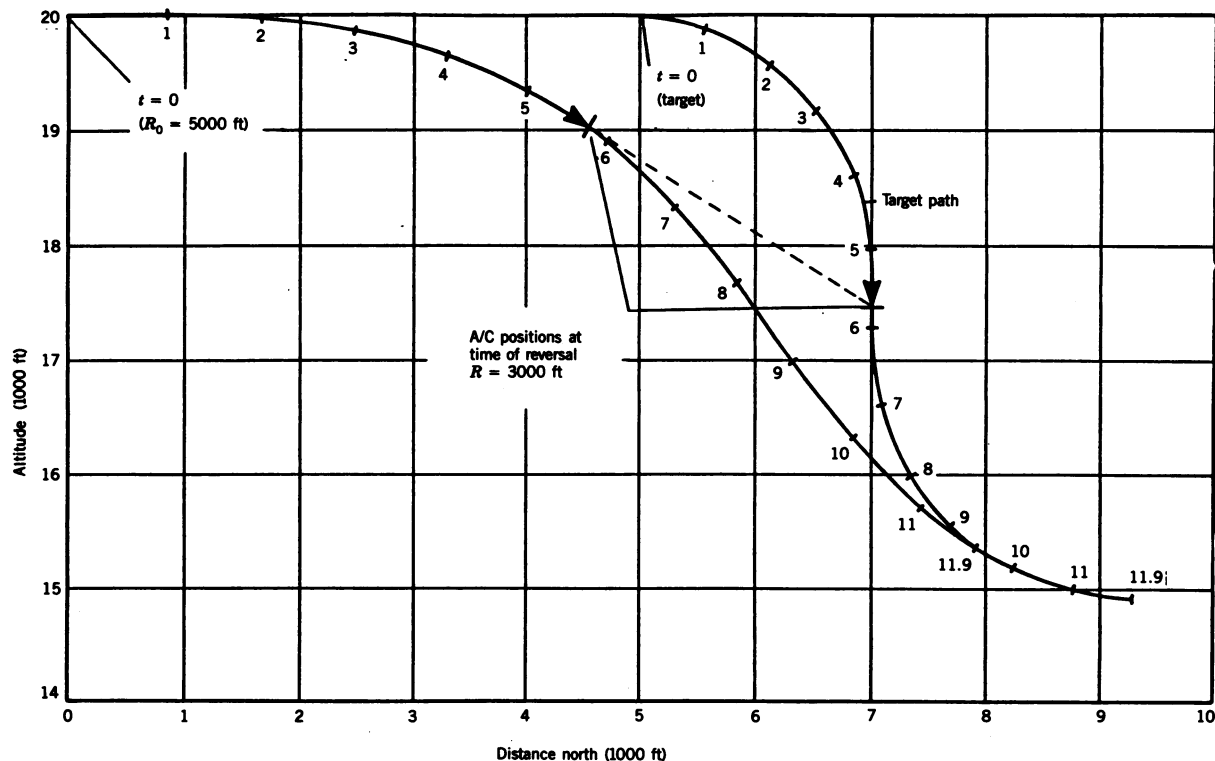
Figure 9-48 *Vertical trajectory tracking response of attacker against a target performing a split S plus reversal ($R_0 = 5000$ ft; target: Mach 0.65 at 20,000 ft, $\Psi_T = 30°$, $\dot{\Theta}_{T_0} = -16.5$ deg / sec; attacker: Mach 0.8 at 20,000 ft).*
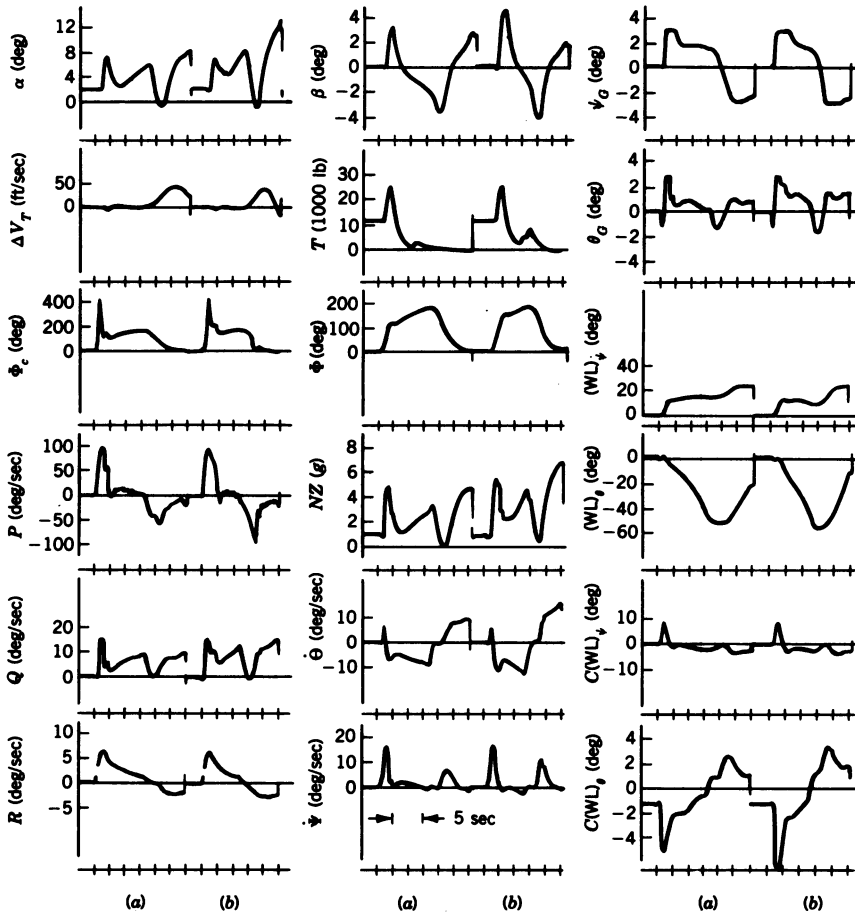
Figure 9-49 Tracking response of attacker against a target performing a split S plus reversal ($R_0 = 5000$ ft; target: Mach 0.65 at 20,000 ft, $\Psi_T = 30°$, (a) $\dot{\Theta}_{T_0} = -10$ deg / sec, (b) $\dot{\Theta}_{T_0} = -16.5$ deg / sec; attacker: Mach 0.8 at 20,000 ft).

pitch through 90°; therefore the maneuver is modified, with the target rolling back 180° and pulling out straight ahead. As the target is considered a point mass, this was accomplished by changing the sign of $\dot{\Theta}_T$ about halfway through the run. Cases were run with $\dot{\Theta}_{T_0}$ equal to -10 and -16.5 deg/sec. The heading of the target, Ψ_T, was 30°. The attacker was initially wings level with $\Psi = 0°$. The vertical trajectory of the two aircraft for $\dot{\Theta}_{T_0} = -16.5$ deg/sec is shown in Figure 9-48. The corresponding time responses for both pitch rates are shown in Figure 9-49. The tracking response is excellent, with the attacker rolling smoothly to about 175° and 180° for the two cases and then rolling back out. For the 10-deg/sec pitch rate case, the gun is off the yaw stop from 2 seconds on, and for the 16.5-deg/sec case the gun is on track

TABLE 9-7   Summary of IFFC System Intercept Capabilities for Various Angles off for Four Intercept Scenarios*

Angle off (deg)	Initial Range (ft)			Time Guns on Track, (sec)				Run Terminated by[†]			
	Inter 1, 2	Inter 3	Inter 4	Inter 1	Inter 2	Inter 3	Inter 4	Inter 1	Inter 2	Inter 3	Inter 4
30	5,000	5,000	5,000	14.25	9.25	13	10	Min R	Min R	Min R	Min R
50	5,000	5,000	5,000	13.25	7	12.5	10	Min R	Min R	Min R	Min R
70	5,000	5,000	6,000	11.25	4.75	11.25	10	Min R	Min R	Min R	Min R
90	6,000	7,000	7,000	9.75	3	12.25	10	Min R	Max NZ	Min R	Min R
110	6,000	7,000	7,000	7.25	1	11.25	0	Min R	Max NZ	Min R	Max NZ
120	7,000	7,000	8,000	4.25	2.5	11.75	7.25	Max NZ	Min R	Min R	Min R
130	7,000	8,000	9,000	2.75	3.25	4.75	4.5	Max NZ	Min R	Max NZ	Max NZ
150	8,000	9,000	10,000	3.75	4	4.5	5	Min R	Min R	Min R	Min R

Target: Mach 0.65 at 20,000 ft, $\Psi_T = \Theta_T = 0°$; attacker: Mach 0.8.
*Inter 1: co-altitude; Inter 2: co-altitude, target turning into attacker at 10 deg / sec; Inter 3: attacker initially 1500 ft below target; Inter 4: attacker initially 1500 ft above target and heading 5° left of the initial LOS.
[†]Min R = 1500 ft; Max NZ = 7.33g.

from 2 to 9 seconds, then loses track for about 1 second, and then regains track.

The performance of the IFFC system, for various angles off the tail of the target for the four intercept scenarios run, is summarized in Table 9-7. As the angle off increases, the initial closing velocity increases, requiring greater initial ranges as shown in the table. Looking at the time that the gun was on track, it would seem that turning into the attacker is a fair evasive maneuver (Inter 2). If it is assumed that the gun must be on track for a minimum of 3 seconds in order to achieve a kill, then from Table 9-7 it can be seen that all but four of the 32 intercepts were successful. The run termination data show that only seven of the 32 runs were terminated prematurely due to the attacker hitting the acceleration limit of 7.33g.

The ground and vertical tracks for runs at various angles off the tail of the target with the attacker initially 1500 ft above the target (Inter 4) are shown in Figure 9-50 with the gun responses in Figure 9-51. The time response traces for 30° angle off are shown in Figure 9-52. In Figure 9-50 one-second time ticks are shown for the target. The points marked F on the attacker tracks indicate the point at which the gun is on track (i.e. against neither stop). The corresponding time for the point F is also indicated. The initial ranges for the various angles off are indicated. For angles off greater than 90° the time at the end of the run is also indicated. For 110° angle off the gun never acquired track before the aircraft exceeded the 7.33g limit. An increase in the initial range might have enabled the attacker to make a successful intercept. With the attacker above the target the aircraft was headed 5° to the left of the direction of the LOS. This would allow the pilot
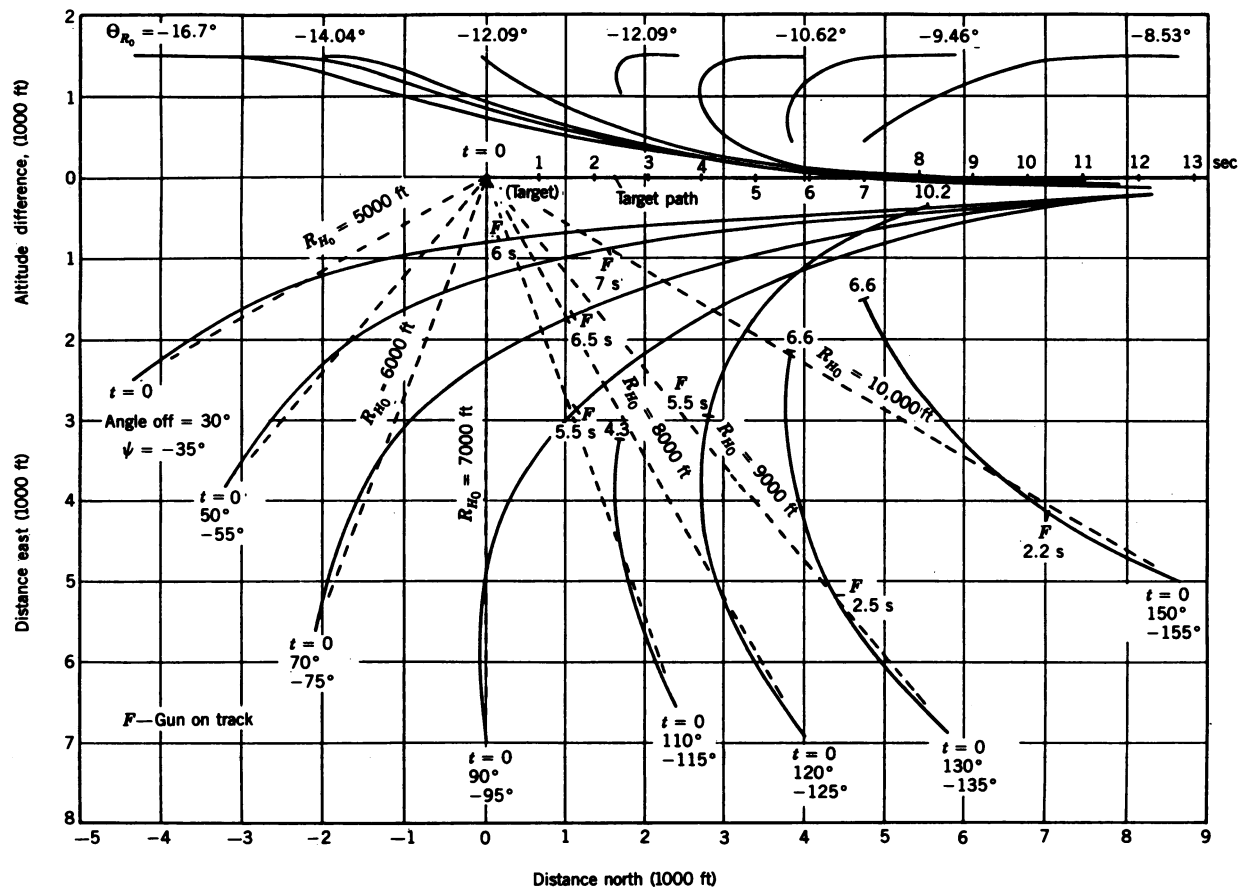
Figure 9-50 Tracking response at various angles off the tail of the target with the attacker initially 1500 ft above the target (target: Mach 0.65 at 20,000 ft, $\Psi_T = \Theta_T = 0°$; attacker: Mach 0.8 at 20,000 ft).
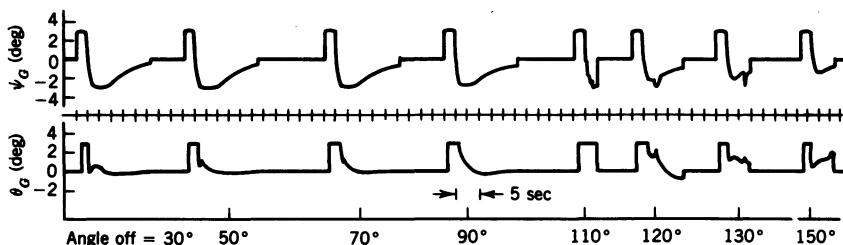
Figure 9-51 Tracking response at various angles off the tail of the target with the attacker initially 1500 ft above the target (conditions same as in Figure 9-50).

to look to the right of the nose to observe the target and hopefully preclude the target from being obscured by the nose of the aircraft. From the roll angle trace in Figure 9-52 it can be seen that the attacker rolls to about 125°; thus a positive pitch rate Q results in a negative $\dot{\Theta}$ and a positive acceleration throughout the maneuver. The response of the velocity control system can be observed from the ΔV_T and thrust (T) traces. No explanation could be found for the aileron oscillation evident in Figure 9-52, which seemed to be more a function of the system input than of the system gains, as the oscillation did not occur for all the runs. For all of the angle-off attacks the initial prediction angle exceeded the estimated maximum HUD field of view of 15° for angles off in the vicinity of 90°.

As mentioned in Section 9-2, with the tracker mounted on the aircraft, the angular motion of the aircraft does, to some extent, feed back into the tracker. It was found in this study that when the prediction angle computations were introduced, a lightly damped roll oscillation was present. The roll oscillation was eliminated by reducing K_ψ from 60 to 18 and $S_{(r,\theta)}$ from 2 to 1 (this was done before the system gains were optimized), with a corresponding degradation in the tracking response. Thus there seemed to be the possibility of a tracking stability problem associated with a director fire control system, when used in a highly maneuverable aircraft. To check this the computed components of the prediction angle were fed through a first-order lag on the digital computer. For the A-1 and A-4 sights the damping was such that the solution time (taken as 3 time constants) was about $\frac{1}{2}$ the time of flight of the projectile.[11] Using this criterion and using a time of flight of 1.5 sec as a base (approximate time of flight for a range of 4000 ft) resulted in a time constant τ_λ of 0.25 sec. Runs were made for different values of τ_λ, and it was found that a value of 0.25 gave the best results and made it possible to increase $S_{(r,\theta)}$ to 2 and K_ψ to 30. This improvement can be seen in Figure 9-53, which shows the effect of τ_λ on the tracking response. For the co-altitude attack the target was on a heading of 30° while the attacker was on a heading of 0°, the equivalent of the attacker being 30° off the tail of the target. Although the introduction of a time lag in the generation of the prediction angle was beneficial in this case, it should be
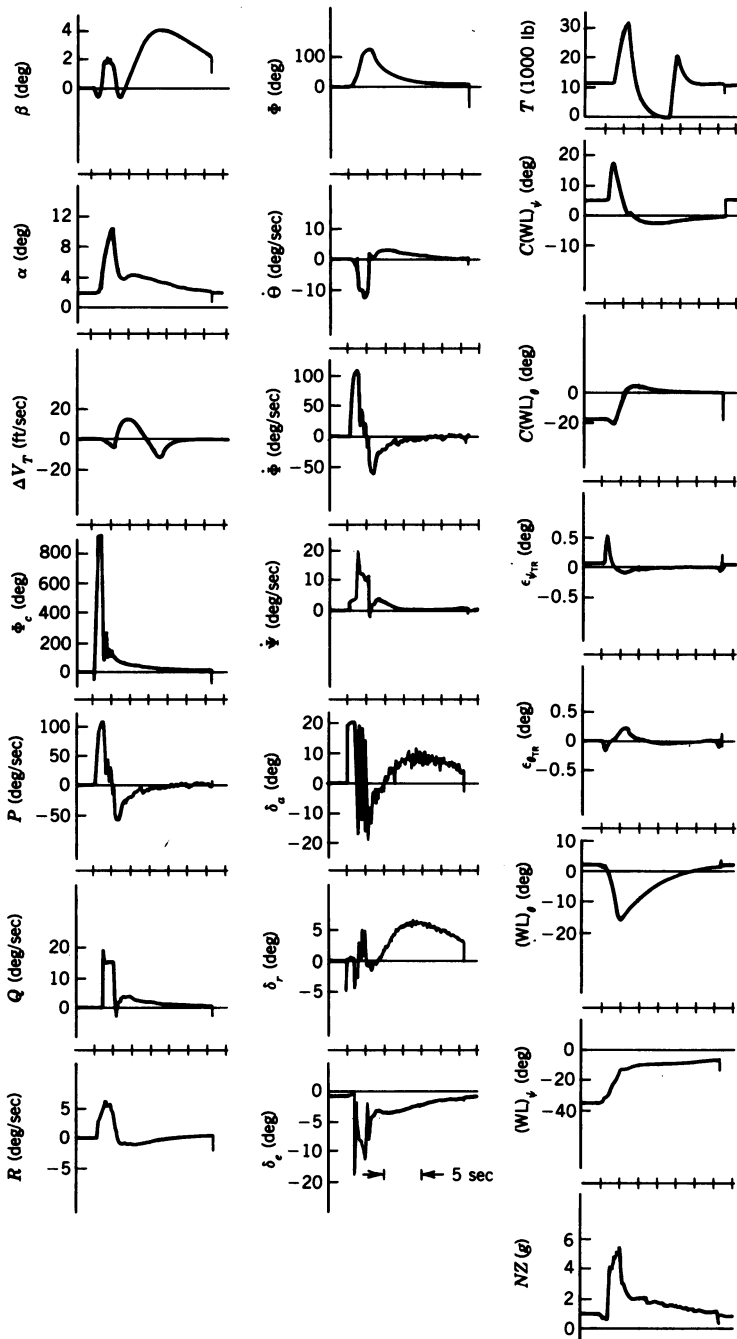
Figure 9-52   *Tracking response for 30° off the tail of the target with the attacker initially 1500 ft above the target (conditions same as in Figure 9-50).*
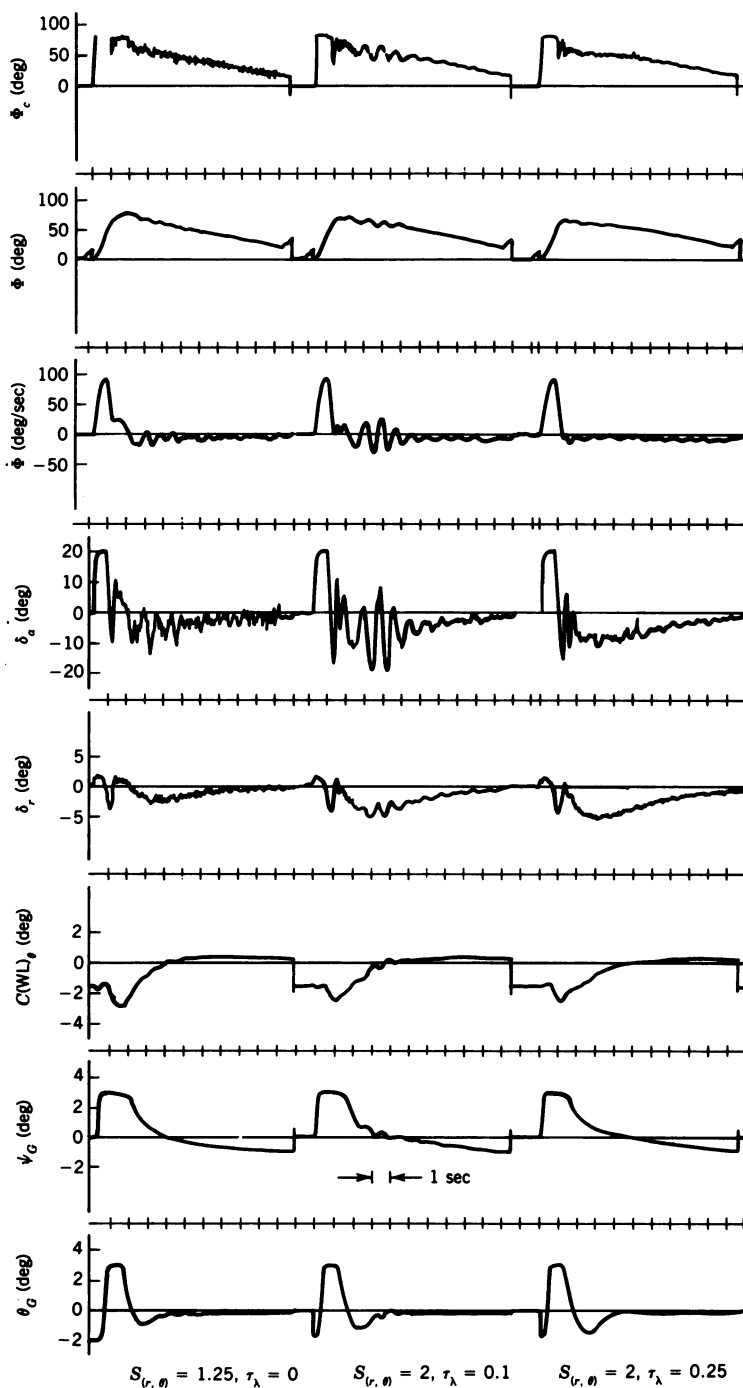
Figure 9-53 Effect of τ_λ on tracking response (target: Mach 0.65 at 20,000 ft, $\Psi_T = 30°$; attacker: Mach 0.8 at 20,000 ft).

investigated in more detail before drawing any definite conclusions.

As demonstrated by the examples presented here, the IFFC system designed provides good to excellent control for all the scenarios examined. In particular this system provides for automatic inverted flight, which was not demonstrated in the first live air-to-air demonstration at White Sands Test Range on August 19, 1982 of the IFFC system under development by the Flight Dynamics and Avionics Laboratories at Wright-Patterson AFB, Ohio. The addition of the movable gun greatly enhances the overall effectiveness of the IFFC system.

REFERENCES

1. S. Lees, *Air, Space, and Instruments*, Draper Anniversary Volume, McGraw-Hill Book Co., New York, 1963.

2. A. L. Leatham, "A New Approach to an Old Problem: Aircraft Gunnery," Paper delivered to the 1978 Air University Airpower Symposium, Air War College, Maxwell Air Force Base, Alabama, February 13–15, 1978.

3. C. E. Fosha, A. L. Leatham, and R. P. Neeland, *A Digital Line of Sight Estimator Employing the ASCOT Electro-optical Sensor for Air-to-Air Gunnery Engagements*, USAFA-TR-77-11, Air Force Avionics Laboratory, Air Force Flight Dynamics Laboratory, Wright-Patterson Air Force Base, June 1977.

4. A. A. Beck, W. F. Probert, and D. M. Reneau, *M61A1 Gun Servo Design, Phase II*, AFATL-TR-77-15, Delco Electronics Division, General Motors Corporation, Goleta, Final Report for July 1 to December 31, 1976.

5. C. H. Houpis and G. B. Lamont, *Digital Control Systems, Theory, Hardware, Software*, McGraw-Hill Book Co., New York, 1985.

6. *F / TF-15 Stability Derivatives, Mass and Inertia Characteristics, Flight Test Data Basis, Part I and II*, MDCA4172, McDonnell Aircraft Company, Missouri, August 1976, revised October 1977.

7. J. H. Blakelock, *Design of an Integrated Flight / Fire Control System Including Movable Gun and Gimbaled Line-of-Sight Tracker*, UDR-TR-79-84, University of Dayton, Dayton, Ohio, December 1979.

8. J. J. D'Azzo and C. H. Houpis, *Linear Control System Analysis and Design: Conventional and Modern*, 3rd ed., McGraw-Hill Book Co., New York, 1988.

9. R. Saucedo and E. E. Schiring, *Introduction to Continuous and Digital Control Systems*, MacMillan Publishing Co., New York, 1968.

10. B. C. Kuo, *Analysis and Synthesis of Sample-Data Control Systems*, Prentice-Hall, Englewood Cliffs, New Jersey, 1963.

11. W. Wrigley and J. Hovorka, *Fire Control Principles*, McGraw-Hill Book Co., New York, 1959.

10

Multivariable
Control Systems

10-1 INTRODUCTION

In the analysis presented in the preceding chapters the control systems have been considered single-input, single-output (SISO) systems. That is, each loop had only one input and one output. The lateral control systems were also considered SISO systems, although the lateral equations of motion have two inputs (rudder and aileron), and outputs such as yaw rate, roll rate, their integrals, and sideslip angle. Such systems are referred to as multiple-input, multiple-output (MIMO) systems. For the analysis of the lateral control systems in Chapters 4, 6, 8, and 9, the Dutch roll damper and sideslip control systems were considered SISO systems with rudder the only input. Then with the Dutch roll damped and sideslip control achieved, the coordinated aircraft or missile transfer function was used for the outer roll control loops with the aileron the only input. This is still the recommended procedure and provides for a straightforward root locus analysis.

The analysis of MIMO systems is more complex than that of SISO systems, and has received considerable attention in the literature during the last several years. Reference 1 is a long (441 pages) and detailed report on the subject of robustness analysis and design techniques for MIMO control systems. It is a set of lecture notes for a course given by the authors at Wright-Patterson Air Force Base to engineers in the Flight Dynamics Laboratory and students at the Air Force Institute of Technology. After presenting the necessary mathematical background, the report concentrates on developing and applying the "linear–quadratic Gaussian with loop transfer recovery" (LQG/LTR) methodology, which is one particular robust control

design technique. The LQG/LTR design technique is used to design several controllers for the lateral attitude control of a drone aircraft. The aircraft dynamics used are the same as those given in Ref. 2, where the authors present a stability margin method that treats the gain and phase changes in all loops of a multiloop system simultaneously. The report analyzes a lateral attitude control system for the drone aircraft as well as a 25th-order SISO flutter suppression system. In Ref. 3 the authors design a MIMO controller which decouples pitch rate and normal acceleration for the AFTI/F-16 aircraft (advanced fighter technology integration). Using a particular linear combination of the state variables, the order of the state space is reduced to yield a controllable state space. The linear–quadratic regulator (LQR) is applied to this final state space, and the gains of both the observer and the filter are obtained using the discrete option of the Stanford LQR Synthesis Program. An observer is required to estimate the required actuator states that are not measurable. Reference 3 contains an extensive list of references on the subject of multivariable control. All these design techniques require the development of more mathematical background than can be covered here, as evidenced by the length of Ref. 1.

However, two other design techniques that are less complex will be presented here. The first is covered in Refs. 4 and 5 and will be applied to decouple the control of the pitch and flight path angles for the F-15, neglecting the servo dynamics. The second technique employs a computer-aided-design package called Program CC developed by Systems Technology, Inc., Hawthorn, Calif., which will be used to analyze the F-15 control system, including the servo dynamics, and the YOCS presented in Section 4-5. The first technique is covered in the next section, and the second technique in Sections 10-3 and 10-4.

10-2 MULTIVARIABLE DESIGN WITHOUT SERVO DYNAMICS

The design problem considered here is to decouple the control of the aircraft's pitch and flight path angles by the combined use of trailing edge wing flaps and canards. Both control surfaces are limited to $\pm 20°$ deflection. The same velocity control system analyzed in Section 9-6 is used to maintain the initial speed of the aircraft. As shown in Sections 2-4 and 9-6, the velocity control loop does not affect the initial portion of the short-period response; thus the velocity control system can be considered as already decoupled and need not be considered in the multivariable analysis. For the F-15 at Mach 0.8 at 20,000 ft the short-period equations of motion are

$$\dot{\alpha} = -1.21'\alpha + \dot{\theta} - 0.717\delta_c - 0.143\delta_f$$

$$\ddot{\theta} = -9.39'\alpha - 0.964\dot{\theta} + 11.42\delta_c - 7.284\delta_f \qquad (10\text{-}1)$$

where δ_c and δ_f are the canard and flap deflections. The sign convention on the canard and flap deflections is the same as that given in Section 1-9 for

elevator deflection, that is, trailing edge down is positive. As the aerodynamic force generated by a flap deflection acts behind the center of gravity of the aircraft; a positive flap deflection generates a force in the negative Z direction and a negative pitching moment. On the other hand, since the canards are ahead of the center of gravity, a positive canard deflection generates a force in the negative Z direction and a positive pitching moment. Since both the flight path angle γ and the pitch angle θ are to be controlled we require

$$\gamma = \theta - \alpha \tag{10-2}$$

The general forms of the state and output equations for a MIMO plant are[5]

$$\dot{x}(t) = Ax(t) + Bu(t)$$

$$y(t) = Cx(t) \tag{10-3}$$

where A is $n \times n$, B is $n \times m$, and C is $l \times n$. The rank of B is m. (The rank of a matrix is the order of its largest square submatrix that has a nonzero determinant. The matrix in question does not have to be square.) Using Eqs. 10-1, 10-2, and 10-3, the state equation is

$$\begin{bmatrix} \dot{\theta} \\ \dot{\alpha} \\ \ddot{\theta} \end{bmatrix} = \begin{bmatrix} 0 & 0 & 1 \\ 0 & -1.21 & 1 \\ 0 & -9.39 & -0.964 \end{bmatrix} \begin{bmatrix} \theta \\ \alpha \\ \dot{\theta} \end{bmatrix} + \begin{bmatrix} 0 & 0 \\ -0.717 & -0.143 \\ 11.42 & -7.284 \end{bmatrix} \begin{bmatrix} \delta_c \\ \delta_f \end{bmatrix} \tag{10-4}$$

and the output equation is

$$\begin{bmatrix} \theta \\ \gamma \end{bmatrix} = \begin{bmatrix} 1 & 0 & 0 \\ 1 & -1 & 0 \end{bmatrix} \begin{bmatrix} \theta \\ \alpha \\ \dot{\theta} \end{bmatrix} \tag{10-5}$$

From Eq. 10-4 it can be seen that A is 3×3 and B is 3×2. The dimension of C from Eq. 10-5 is 2×3. Then $n = 3$, $m = l = 2$, and the rank of B is 2. Equation 10-3 can be put in the form[5]

$$\begin{bmatrix} \dot{x}_1(t) \\ \dot{x}_2(t) \end{bmatrix} = \begin{bmatrix} A_{11} & A_{12} \\ A_{21} & A_{22} \end{bmatrix} \begin{bmatrix} x_1(t) \\ x_2(t) \end{bmatrix} + \begin{bmatrix} 0 \\ B_2 \end{bmatrix} u(t) \tag{10-6}$$

$$y(t) = [C_1 \quad C_2] \begin{bmatrix} x_1(t) \\ x_2(t) \end{bmatrix} \tag{10-7}$$

Comparing Eq. 10-4 with Eq. 10-6, we have $\dot{x}_1(t) = \dot{\theta}(t)$ and

$$A_{22} = \begin{bmatrix} -1.21 & 1 \\ -9.39 & -0.964 \end{bmatrix}$$

and

$$B_2 = \begin{bmatrix} -0.717 & -0.143 \\ 11.42 & -7.284 \end{bmatrix}$$

From Eqs. 10-3, 10-4, and 10-5 the matrix product **CB** is

$$CB = \begin{bmatrix} 1 & 0 & 0 \\ 1 & -1 & 0 \end{bmatrix} \begin{bmatrix} 0 & 0 \\ -0.717 & -0.143 \\ 11.42 & -7.284 \end{bmatrix} = \begin{bmatrix} 0 & 0 \\ 0.717 & 0.143 \end{bmatrix} \qquad (10\text{-}8)$$

As the inverse of the matrix **CB** does not exist, a plant measurement matrix **M** must be added to provide additional output measurements as shown in Eq. 10-9:[5]

$$w(t) = y(t) + M\dot{x}_1(t) \qquad (10\text{-}9)$$

The block diagram of the resulting tracking system containing a proportional plus integral controller to provide a Type 1 system is shown in Figure 10-1.[4,5] From Figure 10-1 the output $w(t)$ is

$$w(t) = Cx + M\dot{x}_1 \qquad (10\text{-}10)$$

Substituting from Eq. 10-7 for **Cx** and from Eq. 10-6 for $\dot{x}_1$, Eq. 10-10
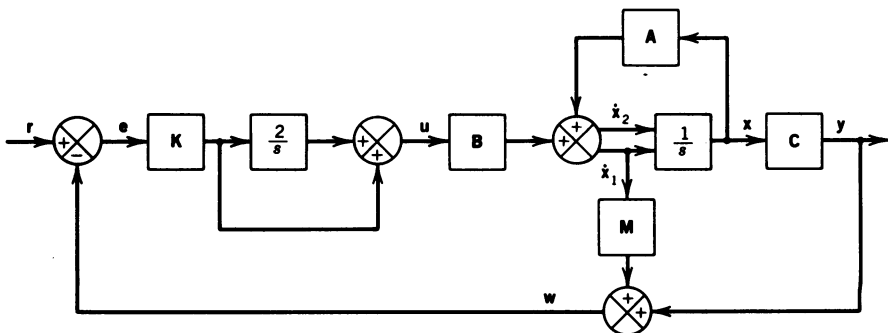
Figure 10-1   State variable block diagram for aircraft tracking system.

becomes

$$w(t) = \begin{bmatrix} C_1 & C_2 \end{bmatrix} \begin{bmatrix} x_1(t) \\ x_2(t) \end{bmatrix} + M \begin{bmatrix} A_{11} & A_{12} \end{bmatrix} \begin{bmatrix} x_1(t) \\ x_2(t) \end{bmatrix}$$

$$= \begin{bmatrix} C_1 + MA_{11} & C_2 + MA_{12} \end{bmatrix} \begin{bmatrix} x_1(t) \\ x_2(t) \end{bmatrix}$$

$$= \begin{bmatrix} F_1 & F_2 \end{bmatrix} \begin{bmatrix} x_1(t) \\ x_2(t) \end{bmatrix} \tag{10-11}$$

From Eq. 10-4 it can be seen that $A_{11} = 0$; therefore M has no effect on F_1, and thus the nonzero terms of M must be such that F_2 has full rank m, where $m = 2$.[5] Then from Eqs. 10-4, 10-5, and 10-11

$$F_2 = \begin{bmatrix} 0 & 0 \\ -1 & 0 \end{bmatrix} + \begin{bmatrix} m_1 \\ m_2 \end{bmatrix} \begin{bmatrix} 0 & 1 \end{bmatrix} = \begin{bmatrix} 0 & m_1 \\ -1 & m_2 \end{bmatrix} \tag{10-12}$$

As shown in Figure 10-1 and Eq. 10-9, the only input to M is $\dot{x}_1$, but from Eqs. 10-4 and 10-6 $\dot{x}_1 = \dot{\theta}$; therefore, $m_2 = 0$. As stated in Ref. 5, the initial value of m_1 is assumed and the final value determined from a complete simulation of the system. However, the value of m_1 can be determined by constructing a root locus of only the pitch angle loop. The block diagram of the pitch angle loop for the canard input from Figure 10-1 is shown in Figure 10-2. From the figure it can be seen that there are two poles at the origin. The integrator gain of 2 was selected to yield a zero close to the aircraft zero. A check of the root locus without the $\dot{\theta}$ feedback shows that the two poles at the origin circle around and break into the real axis between the two zeros; however, the complex poles from the aircraft transfer function cross into the right half plane, making the system unstable. With $m_1 = 0.25$ a feedback transfer function of $0.25(s + 4)$ is introduced for the θ output. The effect of this additional zero can be seen in the root locus shown in Figure 10-3. The locations of the closed loop poles are indicated for $K_{11} = 50$, and the
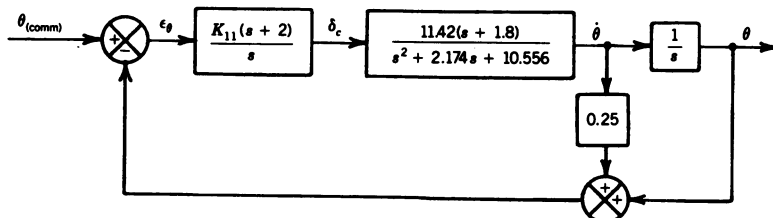
Figure 10-2 Block diagram of the pitch angle loop of Figure 10-1 for canard input for root locus.
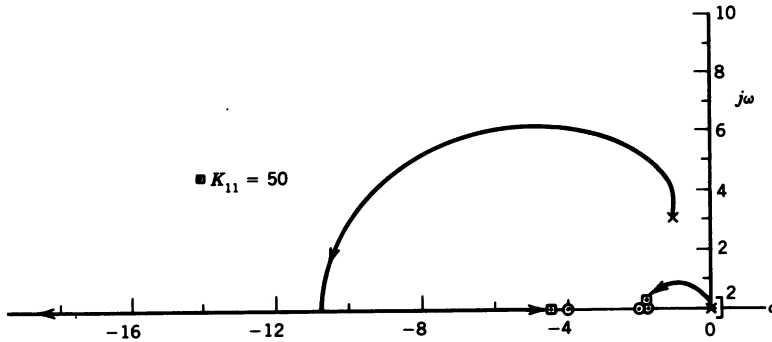
Figure 10-3   Root locus for block diagram shown in Figure 10-2.

corresponding closed loop transfer function is

$$\frac{\theta(s)}{\theta_{(comm)}(s)} = \frac{571(s+1.8)(s+2)}{(s+4.44)(s+136.85)(s^2+3.62s+3.37)} \quad (10\text{-}13)$$

The step response for the system shown in Figure 10-2, obtained using Eq. 10-13, is shown in Figure 10-4. This response will be compared with the θ response from the complete simulation later in this section.

Before evaluating the rest of the elements of the matrix **K**, the relationship between the pitch and flight path angle commands and the flap and canard deflections will be shown. Figure 10-1 is redrawn in Figure 10-5 to show the relationship between the error matrix **e**, each element of **K**, and the control matrix **u**. As shown in Figure 10-5, both error signals drive both of the control surfaces through the elements of **K**.
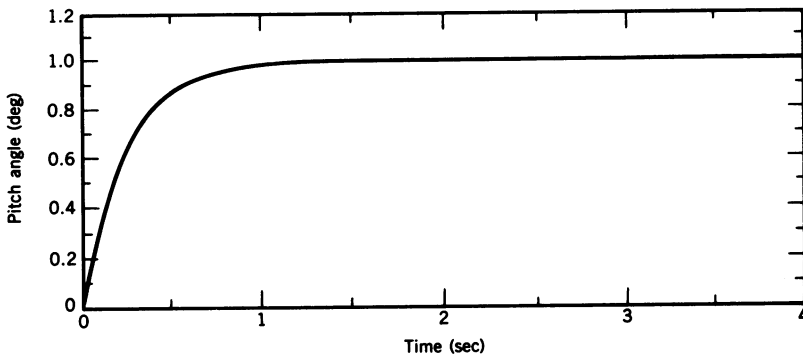
Figure 10-4   Step response for the system shown in Figure 10-2 for $K_{11} = 50$.
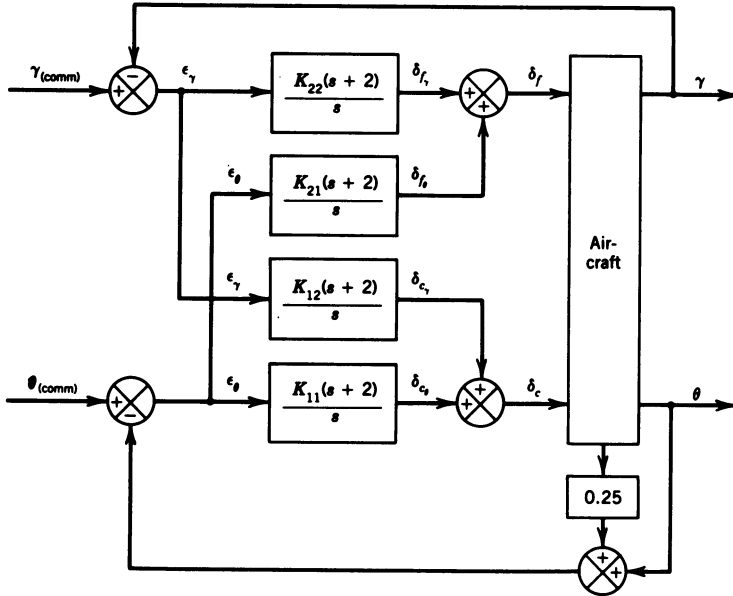
Figure 10-5 Block diagram of tracking system showing elements of K matrix.

With this explanation complete, the magnitudes of the elements of **K** will now be calculated. From Eq. 20.91 of Ref. 5,

$$\mathbf{K} = (\mathbf{F_2 B_2})^{-1} \begin{bmatrix} \sigma_1 & 0 \\ 0 & \sigma_2 \end{bmatrix} \tag{10-14}$$

Substituting for m_1 and m_2 in Eq. 10-12 yields

$$\mathbf{F_2} = \begin{bmatrix} 0 & 0.25 \\ -1 & 0 \end{bmatrix} \tag{10-15}$$

From Eq. 10-4

$$\mathbf{B_2} = \begin{bmatrix} -0.717 & -0.143 \\ 11.42 & -7.284 \end{bmatrix} \tag{10-16}$$

Multiplying Eq. 10-16 by Eq. 10-15 and taking the inverse yields

$$(\mathbf{F_2 B_2})^{-1} = \begin{bmatrix} 0.0834 & 1.062 \\ -0.4183 & 1.666 \end{bmatrix} \tag{10-17}$$

Substituting Eq. 10-17 into Eq. 10-14 and performing the multiplication

yields

$$\mathbf{K} = \begin{bmatrix} 0.0834\sigma_1 & 1.062\sigma_2 \\ -0.4183\sigma_1 & 1.666\sigma_2 \end{bmatrix} \tag{10-18}$$

From the root locus shown in Figure 10-3, $K_{11} = 50$; then

$$0.0834\sigma_1 = 50$$

and

$$\sigma_1 = 599.52$$

Then

$$K_{21} = -0.4183(599.52) = -250.78$$

Let $K_{22} = K_{11} = 50$; then from Eq. 10-18, $\sigma_2 = 30.012$ and $K_{12} = 31.87$. Note that the matrix **K** yields not only the magnitudes of the elements of the matrix but also the associated signs. The resulting matrix is

$$\mathbf{K} = \begin{bmatrix} 50 & 31.87 \\ -250.78 & 50 \end{bmatrix} \tag{10-19}$$

The values of the K's in Eq. 10-19 are referred to later as the design gains.

A digital simulation was designed to model the control system shown in Figure 10-5, the velocity control system from Section 9-6, and the longitudinal equations of motion for the F-15 for Mach 0.8 at 20,000 ft. The equations were modeled to show the perturbations of the parameters from the trim values ($\alpha = \theta = 1.5563°$, $\delta_c = 1.27965°$, $\delta_f = 0°$, thrust = 12,035 lb). The responses of the system to a θ and γ command of 1° for the design gains and for the magnitudes of the gains equal to 50 (K_{21} still negative) are shown in Figure 10-6 and the control requirements in Figure 10-7. From Figures 10-6 and 10-7 it can be seen that there are no significant differences in the performance of the system for the two sets of gains. In fact the angle responses are slightly better with the magnitudes of all the gains set to 50. As a result of these observations, the magnitudes of the gains for the system were set to 50.

From Figure 10-7 it can be seen that for the design gains the flap starts out at $-20°$ (the negative limit). This results from the fact that K_{21} is -250.78 and K_{22} is 50 (see Figure 10-5). With the magnitudes of the gains set to 50, the initial flap deflection is 0°, as K_{21} is negative. As K_{11} and K_{21} are both positive, the initial canard deflection is $+20°$ (the positive limit) for both gain conditions.

A comparison of the pitch response for the complete system with the step response for the closed loop transfer function (CLTF) from Eq. 10-13 is shown in Figure 10-8. The almost perfect match of the two responses
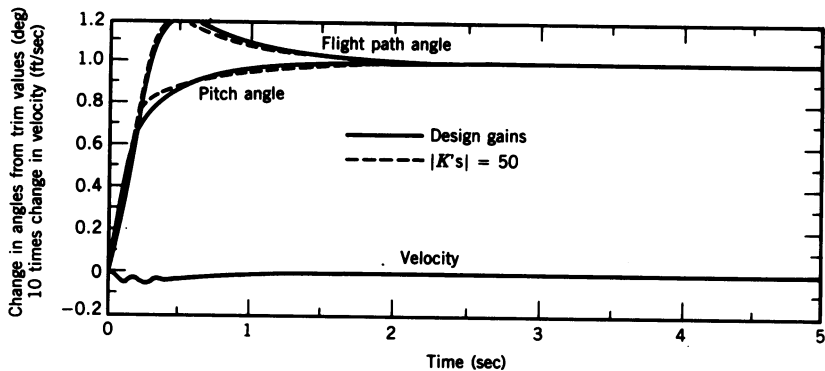
Figure 10-6   *Effect of system gains on aircraft response for straight climb.*
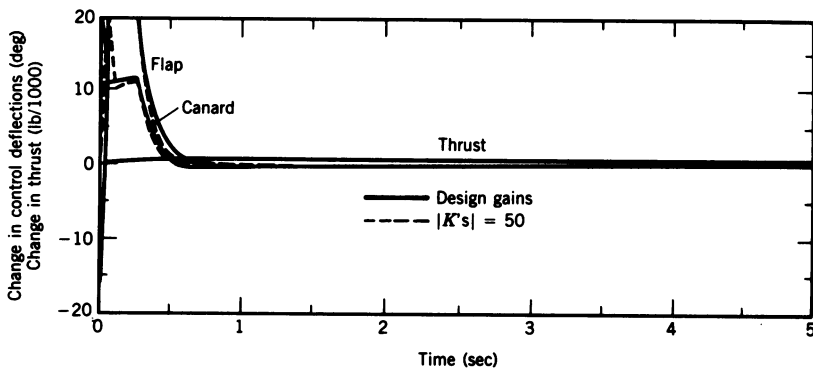
Figure 10-7   *Effect of system gains on control requirements for straight climb.*
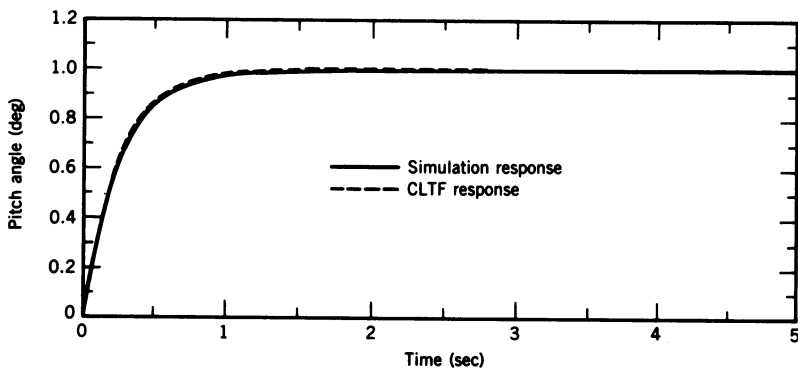
Figure 10-8   *Comparison of simulation and CLTF step responses for pitch only ($|K's| = 50$).*
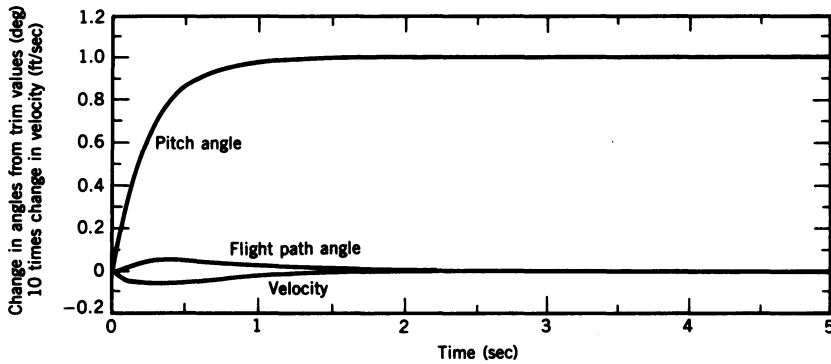
Figure 10-9 *Pitch only, without climb ($|K's| = 50$).*

indicates that the root locus can still be used to advantage in the analysis of MIMO systems. In this case the root locus analysis of the pitch angle loop provided the values of m_1 and K_{11}. With these values a straightforward calculation of the remaining elements of the matrix **K** was possible. The complete system response for a pitch only command of 1° is shown in Figure 10-9 and the corresponding control changes in Figure 10-10. In this case the flight path angle is commanded to be zero. From Figure 10-9 the maximum deviation in γ is about 0.05° and the maximum deviation in velocity is -0.006 ft/sec. As the flight path angle is zero in the steady state, the angle of attack increases by 1° ($\gamma = \theta - \alpha$). This results in a negative (trailing edge up) flap deflection to null out the additional lift created by the increase in angle of attack. The negative flap deflection creates a positive pitching moment, which is balanced by the negative canard deflection.
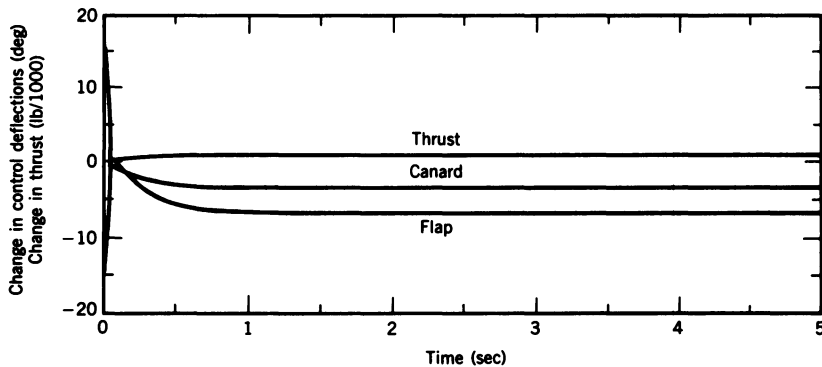
Figure 10-10 *Controls for maneuver shown in Figure 10-9.*
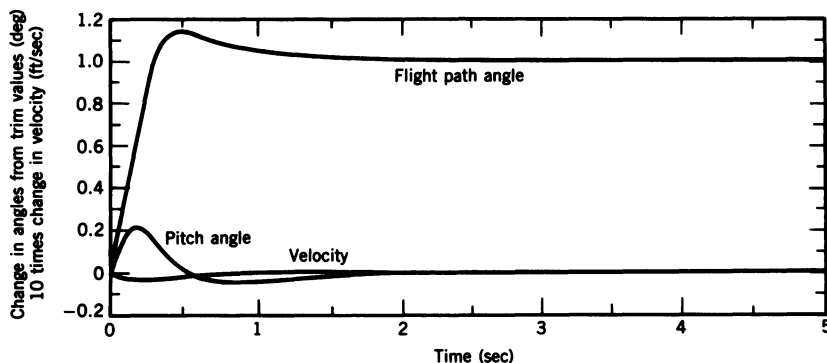
Figure 10-11 *Climb only, without pitch (|K's| = 50).*

The responses for a flight path angle command of 1° with the pitch angle commanded not to change are shown in Figure 10-11 with the required controls shown in Figure 10-12. The overshoot in γ is about 0.15°, and the maximum deviation in θ is about 0.21°. The velocity deviation is less than for the case shown in Figure 10-9. For this case the aircraft is commanded to climb without increasing the wing angle of attack. This requires a positive flap deflection. The resulting negative pitching moment is overcome by the positive canard deflection. All of the responses just discussed are excellent.

This completes the discussion of the design of a MIMO system when the servo dynamics are neglected. In the next section the same system will be analyzed, including the servo dynamics associated with the flap and canard actuators.
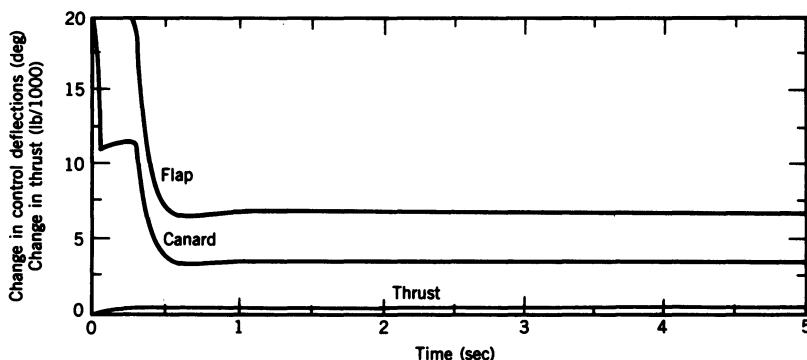
Figure 10-12 *Controls for maneuver shown in Figure 10-11.*

10-3   MULTIVARIABLE DESIGN WITH SERVO DYNAMICS

As mentioned in Section 10-1, the analysis of the MIMO system including the servo dynamics will be accomplished using Program CC (referred to in this section as just CC). To begin the analysis Figure 10-5 is redrawn to include the servo dynamics in Figure 10-13. The figure is also rearranged and a third output $\dot{\theta}$ added. The additional output was required because CC did not allow the use of $0.25(s+4)$ as a feedback transfer function in this type of analysis. Before starting the CC analysis, a root locus analysis of the pitch loop of Figure 10-13 was performed. The block diagram for the root locus is shown in Figure 10-14. The root locus is shown in Figure 10-15, with the location of the closed loop poles for $K_{11} = 5$ indicated. The corresponding closed loop transfer function is

$$\frac{\theta(s)}{\theta_{(comm)}(s)} = \frac{1142(s+1.8)(s+2)}{(s+8.2)(s^2+2.98s+2.65)(s^2+11s+189.5)} \quad (10\text{-}20)$$

The step response for the system for $K_{11} = 5$ is shown in Figure 10-16.

For multivariable analysis Program CC uses a *state space quadruple*, which is a packed set of system matrices representing multivariable state and output equations of the form

$$\dot{x}(t) = Ax(t) + Bu(t)$$

$$y(t) = Cx(t) + Du(t) \quad (10\text{-}21)$$
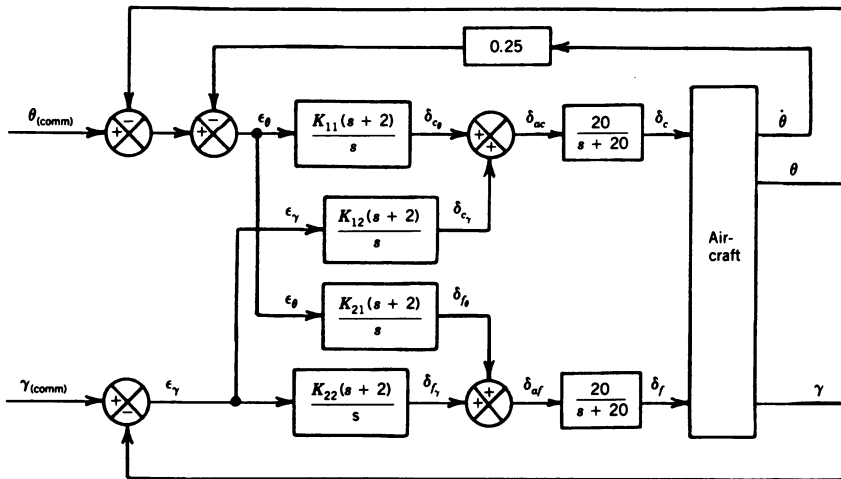
Figure 10-13   Block diagram of tracking system with servo dynamics.
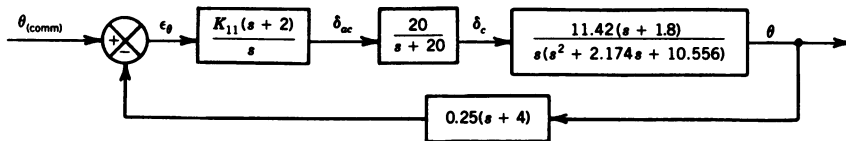
Figure 10-14 *Block diagram of pitch loop of Figure 10-13 for root locus.*

The matrices **A**, **B**, **C**, and **D** are packed into a quadruple

$$P = \left[\begin{array}{c|c} A & B \\ \hline C & D \end{array}\right] \tag{10-22}$$

The solid lines indicate that **P** is a quadruple rather than an ordinary block matrix. The matrices **A** and **B** are given by Eq. 10-4. The new matrix **C** to include the added output is

$$C = \begin{bmatrix} 0 & 0 & 1 \\ 1 & 0 & 0 \\ 1 & -1 & 0 \end{bmatrix} \tag{10-23}$$

The matrix **D** is **0**. The matrices **x**, **u**, and **y** are

$$x = \begin{bmatrix} \theta \\ \alpha \\ \dot\theta \end{bmatrix} \qquad u = \begin{bmatrix} \delta_c \\ \delta_f \end{bmatrix} \qquad y = \begin{bmatrix} \dot\theta \\ \theta \\ \gamma \end{bmatrix} \tag{10-24}$$
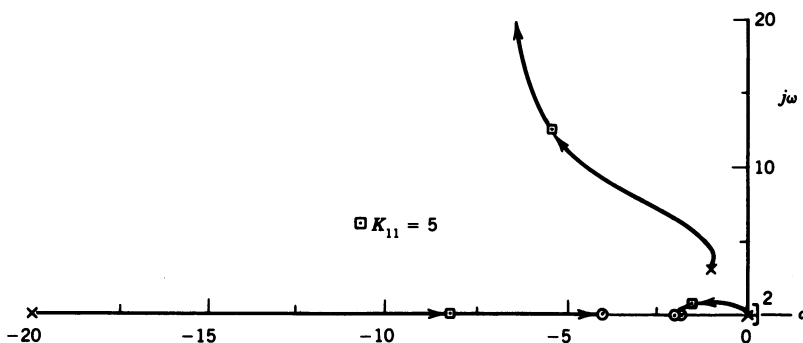
Figure 10-15 *Root locus for block diagram shown in Figure 10-14.*
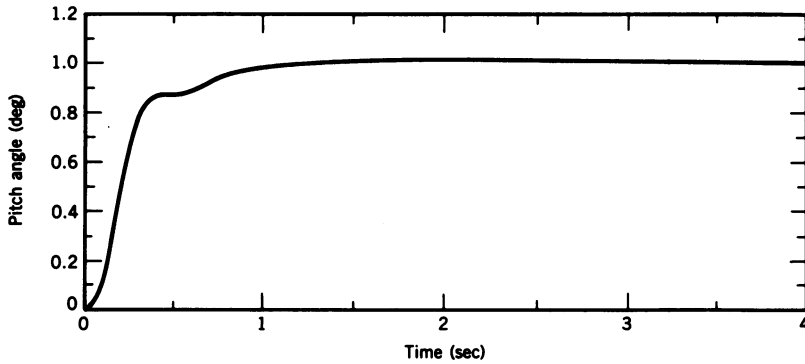
Figure 10-16 *Step response for the system shown in Figure 10-14 for $K_{11} = 5$.*

Substituting for the matrices in Eq. 10-22, the state space quadruple is

$$P = \left[\begin{array}{ccc|cc} 0 & 0 & 1 & 0 & 0 \\ 0 & -1.21 & 1 & -0.717 & -0.143 \\ 0 & -9.39 & -0.964 & 11.42 & -7.284 \\ \hline 0 & 0 & 1 & 0 & 0 \\ 1 & 0 & 0 & 0 & 0 \\ 1 & -1 & 0 & 0 & 0 \end{array}\right] \qquad (10\text{-}25)$$

Figure 10-17 is a matrix block diagram of Figure 10-13 in the form required for Program CC analysis. The aircraft-and-servos block in Figure 10-17 is represented by

$$P_4 = P \left[\begin{array}{cc} G_{(con)} & 0 \\ 0 & G_{(con)} \end{array}\right] \qquad (10\text{-}26)$$
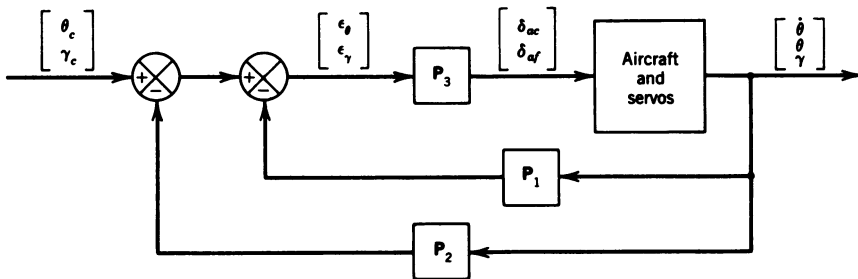
Figure 10-17 *Matrix block diagram of Figure 10-13 for Program CC analysis.*

where $G_{(con)} = 20/(s + 20)$. The matrices $\mathbf{P}_1$, $\mathbf{P}_2$, and $\mathbf{P}_3$ are

$$\mathbf{P}_1 = \begin{bmatrix} 0.25 & 0 & 0 \\ 0 & 0 & 0 \end{bmatrix} \tag{10-27}$$

$$\mathbf{P}_2 = \begin{bmatrix} 0 & 1 & 0 \\ 0 & 0 & 1 \end{bmatrix} \tag{10-28}$$

$$\mathbf{P}_3 = \begin{bmatrix} K_{11}G_{(pi)} & K_{12}G_{(pi)} \\ K_{21}G_{(pi)} & K_{22}G_{(pi)} \end{bmatrix} \tag{10-29}$$

where $G_{(pi)} = (s + 2)/s$. The closed loop system matrix is formed using the following equation, which is written in the form used in CC:

$$P5 = ((P4*P3)|P1)|P2 \tag{10-30}$$

where $|$ indicates feedback and the matrix following the $|$ sign is the feedback matrix. With $K_{11} = 5$ and the remaining K's set to zero, the system shown in Figure 10-17 should reduce to the pitch loop shown in Figure 10-14. The resulting closed loop transfer function $\theta(s)/\theta_{(comm)}(s)$ from CC is identical to Eq. 10-20 and will not be repeated here. A comparison of the pitch angle responses from the 3-DOF digital simulation (FORTRAN simulation), the CC simulation, and the step response using Eq. 10-20 (CLTF response) is shown in Figure 10-18 as well as a comparison of the flight path angle responses from the FORTRAN and CC simulations. Although the flight path angle responses do not compare as well as the pitch angle responses, the agreement is acceptable. With only the pitch loop closed, the steady-state value of the flight path angle in Figure 10-18 is equal to 1 as expected.
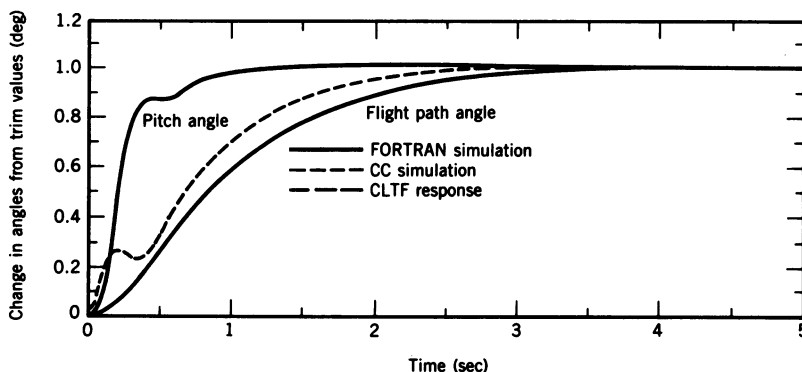
Figure 10-18 *Comparison of both simulation and CLTF responses for pitch only ($K_{11} = 5$, other K's = 0).*

Having selected a value of 5 for K_{11} from the root locus analysis of the pitch loop, the magnitudes of the remaining elements of the matrix **K** were set to 5, resulting in

$$\mathbf{K} = \begin{bmatrix} 5 & 5 \\ -5 & 5 \end{bmatrix} \qquad (10\text{-}31)$$

The negative sign associated with K_{21} results from the fact that the $\theta(s)/\delta_f(s)$ aircraft transfer function is negative. This is also consistent with the sign of K_{21} in Eq. 10-19. The FORTRAN simulation was then run using the gains from Eq. 10-31. With these gains the responses of the system for the different combinations of input commands were found to be stable and well behaved. However, the pitch angle response was a little slow, and for a pitch angle command (zero flight path angle command) using the values of **K** from Eq. 10-31, the flight path angle response was excessive and slow to decay (plots not shown). Runs were then made using different gains to determine the elements of **K** that resulted in the best overall responses. The final gains selected are as follows:

$$\mathbf{K} = \begin{bmatrix} 10 & 10 \\ -10 & 25 \end{bmatrix} \qquad (10\text{-}32)$$

The value of 25 for K_{22} was required to reduce the flight path angle response to a pitch angle only command.

The system responses using the gains shown in Eq. 10-32 are shown in Figures 10-19 through 10-24. Figure 10-19 shows the response for a 1° pitch only command. The maximum value of the flight path angle was reduced from 0.31 to 0.152° as a result of the increase in K_{22} previously mentioned. The small oscillation in the pitch angle response was considered an acceptable compromise in order to achieve a faster overall system response. As
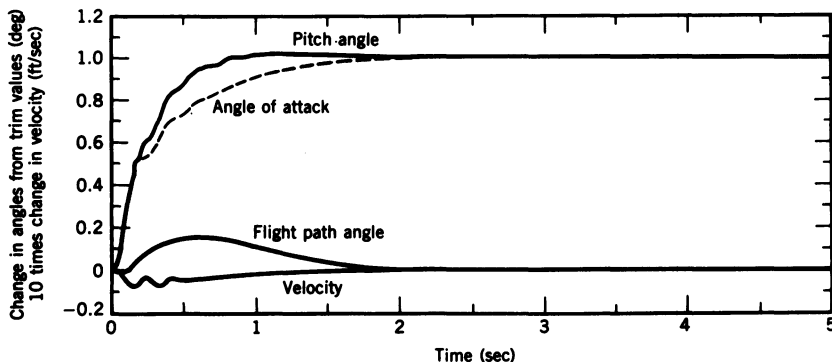
Figure 10-19   *Pitch only, without climb (K's from Eq. 10-32).*
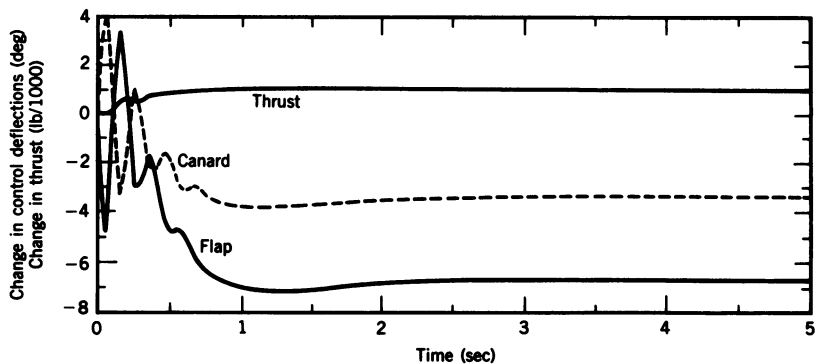
Figure 10-20   *Controls for maneuver shown in Figure 10-19.*
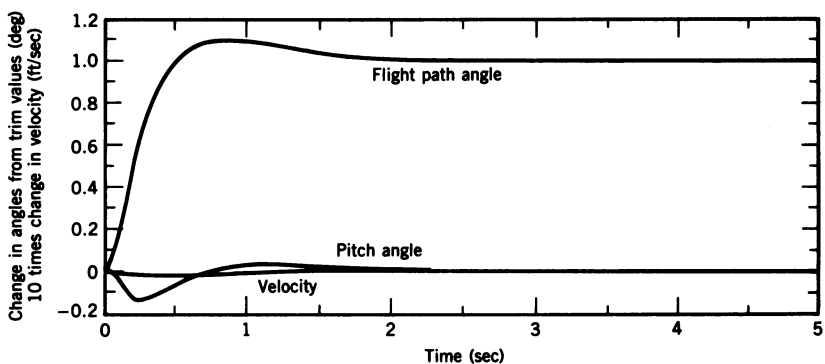
Figure 10-21   *Climb only, without pitch (K's from Eq. 10-32).*
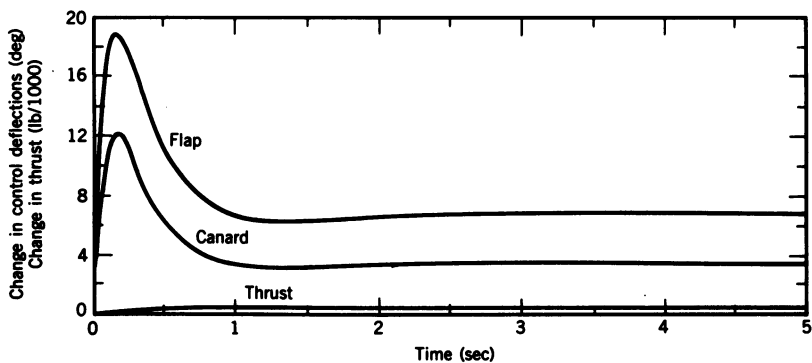
Figure 10-22   *Controls for maneuver shown in Figure 10-21.*
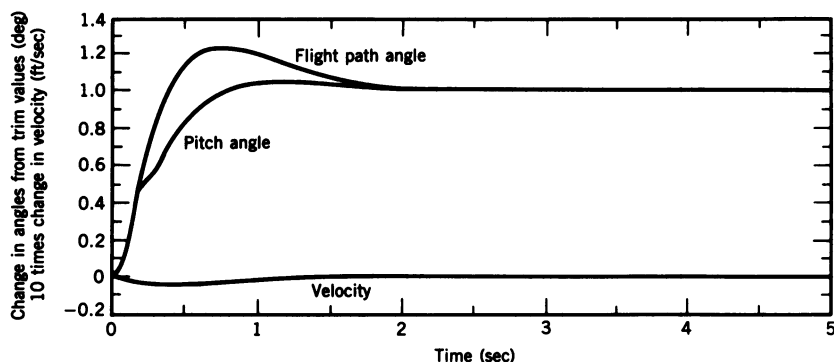
Figure 10-23   *Straight climb (K's from Eq. 10-32).*

seen in the figure, the oscillation also shows up in the angle of attack response. Since the flight path angle is equal to the pitch angle minus the angle of attack, the flight path angle is relatively smooth. The oscillation in the velocity response results from the oscillation in the angle of attack. The canard and flap oscillations in Figure 10-20 reflect the oscillations observed in Figure 10-19. The damping ratio and period of these oscillations are very close to the values obtained from the poles of P_5, which were 0.236 and 0.23 sec respectively. The measured period was found to be 0.225 sec, and the damping appears to be close to the predicted value. The steady-state values of the change in the flap and canard deflections are the same as the values for the response without servo dynamics (Figure 10-10), as expected.

The responses for a 1° flight path only command are shown in Figure 10-21, with the control deflections shown in Figure 10-22. The initial negative swing in the pitch angle shown in Figure 10-21 is due to the large positive flap deflection resulting from the value of 25 for K_{22}. The responses are
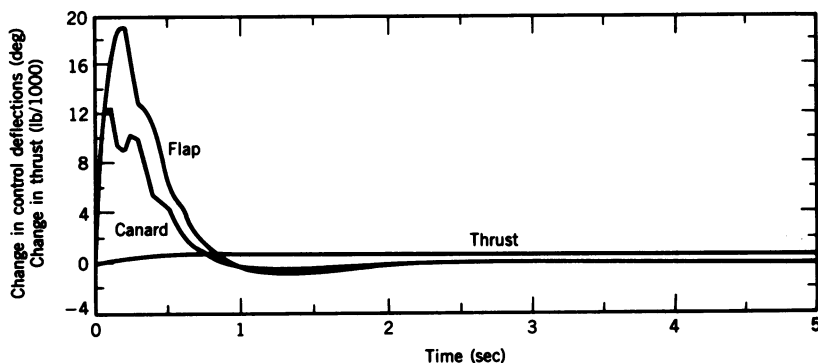
Figure 10-24   *Controls for maneuver shown in Figure 10-23.*

Figure 10-25 *Block diagram of YOCS for multivariable analysis.* $S_{(yrg)} = 1.04$, $S_{(sss)} = 1$, $S_{(rrg)} = 0.31$, $S_{(lg)} = 0.4$.

much smoother than those in Figure 10-19, as the pitch angle deviation is much smaller than the change in the flight path angle. Again the steady-state changes in the flap and canard deflections agree with those shown in Figure 10-12.

Finally, the straight climb maneuver is shown in Figure 10-23 with the required change in the control deflections in Figure 10-24. Notice that the pitch oscillation is again observable in both figures. In Figure 10-24 the steady-state changes in the flap and canard deflections go to zero, since the final value of the change in the angle of attack from the trim is zero. The zero change in angle of attack results from the fact that the changes in both the pitch angle and flight path angle are equal in the steady state.

The YOCS designed in Section 4-5 will now be analyzed using Program CC.

10-4 MULTIVARIABLE DESIGN OF YOCS

The block diagram for the YOCS from Figure 4-30 is redrawn in Figure 10-25 with the transfer functions of the servos and the washout circuit included. The lateral equations of motion from Eqs. 3-32 and 3-43 are

$$\ddot{\phi} = -2.033\dot{\phi} + 0.47\dot{\psi} - 2.096\beta + 22.06\delta_a + 0.48\delta_r$$

$$\ddot{\psi} = -0.058\dot{\phi} - 0.27\dot{\psi} + 1.64\beta - 0.171\delta_a - 1.3675\delta_r$$

$$\dot{\beta} = 0.073\phi - \dot{\psi} - 0.127\beta + 0.036\delta_r \tag{10-33}$$

From Eq. 10-22 the matrix **P** is

$$P = \left[\begin{array}{c|c} A & B \\ \hline C & D \end{array}\right] \tag{10-34}$$

From Eq. 10-33 the matrices **A** and **B** are (see Eq. 10-21)

$$A = \begin{bmatrix} -2.033 & 0.47 & -2.096 & 0 & 0 \\ -0.058 & -0.27 & 1.64 & 0 & 0 \\ 0 & -1 & -0.127 & 0.073 & 0 \\ 1 & 0 & 0 & 0 & 0 \\ 0 & 1 & 0 & 0 & 0 \end{bmatrix} \tag{10-35}$$

$$B = \begin{bmatrix} 22.06 & 0.48 \\ -0.171 & -1.3675 \\ 0 & 0.036 \\ 0 & 0 \\ 0 & 0 \end{bmatrix} \tag{10-36}$$

The matrix **D** is **0**. The matrices **x**, **u**, and **y** are

$$x = \begin{bmatrix} \dot{\phi} \\ \dot{\psi} \\ \beta \\ \phi \\ \psi \end{bmatrix} \qquad u = \begin{bmatrix} \delta_a \\ \delta_r \end{bmatrix} \qquad y = \begin{bmatrix} \dot{\phi} \\ \beta \\ \dot{\psi} \end{bmatrix} \tag{10-37}$$

Then the matrix **C** is

$$C = \begin{bmatrix} 1 & 0 & 0 & 0 & 0 \\ 0 & 0 & 1 & 0 & 0 \\ 0 & 1 & 0 & 0 & 0 \end{bmatrix} \tag{10-38}$$

The matrix block diagram of Figure 10-25 is given in Figure 10-26 where P_4 is

$$P_4 = P \begin{bmatrix} G_{(sig)} & 0 \\ 0 & 1 \end{bmatrix} \begin{bmatrix} G_{(act)} & 0 \\ 0 & G_{(act)} \end{bmatrix} \tag{10-39}$$

where $G_{(sig)} = 0.4/s$ and $G_{(act)} = 10/(s+10)$. The matrices P_1, P_2, and P_3 are

$$P_1 = \begin{bmatrix} 0 & 0 & 1 \\ 0 & 0 & G_{(yrg)} \end{bmatrix} \tag{10-40}$$

$$P_2 = \begin{bmatrix} 0.31 & 0 & 0 \\ 0 & 1 & 0 \end{bmatrix} \tag{10-41}$$

$$P_3 = \begin{bmatrix} 1 & 0 \\ 0 & 1 \end{bmatrix} \tag{10-42}$$
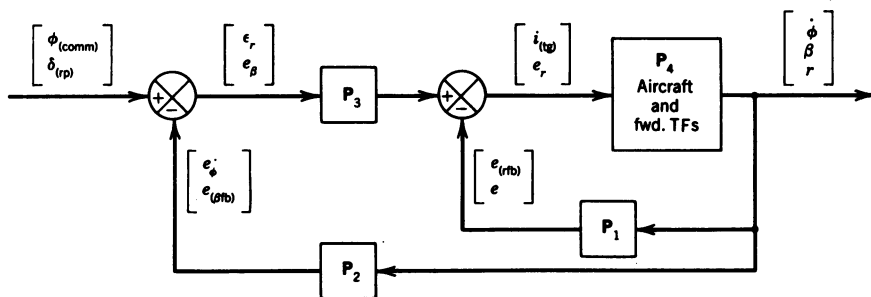
Figure 10-26   *Block diagram of YOCS for Program CC analysis.*

where $G_{(\text{yrg})} = -1.04s/(s + 0.33)$. The minus sign is required, as the r/δ_r transfer function is negative. The closed loop system matrix is formed using the following equation, which is written in the form used in CC:

$$P5 = ((P4|P1)*P3)|P2 \tag{10-43}$$

The step response of the system to a 2-deg/sec yaw rate command is shown in Figure 10-27. The roll rate, yaw rate, and sideslip responses show very close agreement with the corresponding responses shown in Figure 4-36. The similarity of the responses further justifies the use of the coordinated aircraft transfer function for the analysis of the outer loops of a lateral flight control system. If the multivariable analysis method is to be used for the design of a MIMO system such as the YOCS, then the yaw rate and sideslip feedback loops can be closed and analyzed using the SISO method employed in Chapter 4 to obtain the time constant of the washout circuit and the loop gains $S_{(\text{yrg})}$ and $S_{(\text{sss})}$. With these values determined the multivariable design method shown here can be used to determine the values of $S_{(\text{rrg})}$ and $S_{(\text{ig})}$. However, the use of the coordinated aircraft transfer function provides a very
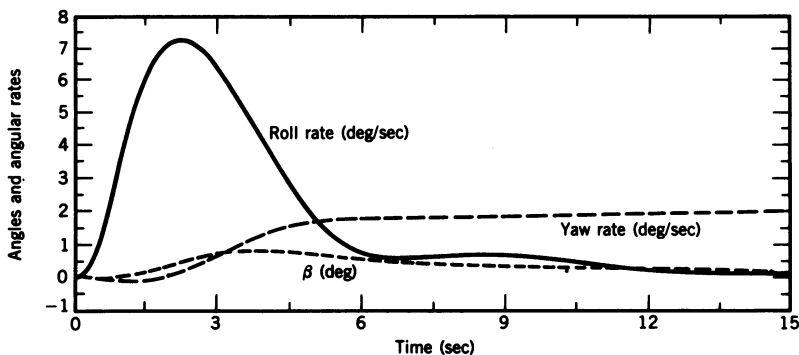
Figure 10-27   *Response of YOCS to a 2-deg/sec yaw rate command.*

straightforward and simple method for the analysis of these kinds of control systems.

This completes the multivariable control system analysis.

10-4 SUMMARY

In this chapter two techniques have been presented for the analysis of a longitudinal MIMO control system. It was shown in both cases that the SISO root locus analysis was still a useful design tool. The adequacy of each design was demonstrated through the use of a complete 3-DOF digital simulation. The multivariable design technique was also used to verify the design of the YOCS presented in Section 4-5.

REFERENCES

1. D. B. Ridgely and S. S. Banda, *Introduction to Robust Multivariable Control*, Air Force Flight Dynamics Laboratory Report AFWAL-TR-85-3102, Wright-Patterson Air Force Base, Ohio, February 1986 (AD-A165 891).
2. V. Mukhopadhyay and J. R. Newsom, "A Multiloop System Stability Margin Study Using Matrix Singular Values," *Journal of Guidance, Control, and Dynamics*, September–October 1984, Vol. 7.
3. J. L. Speyer, J. E. White, R. Douglas, and D. G. Hull, "Multi-input/Multi-output Controller Design for Longitudinal Decoupled Aircraft Motion," *Journal of Guidance, Control, and Dynamics*, November–December 1984, Vol. 7.
4. D. B. Ridgely, S. S. Banda, and J. J. D'Azzo, "Decoupling of High-Gain Multivariable Tracking System," *Journal of Guidance, Control, and Dynamics*, January–February 1985, Vol. 8.
5. J. J. D'Azzo and C. H. Houpis, *Linear Control System Analysis and Design: Conventional and Modern*, 3rd ed., McGraw-Hill Book Co., New York, 1988.

11

Structural Flexibility

11-1 INTRODUCTION

With the introduction of long slender missiles such as the Vanguard, the Redstone, and the various ballistic missiles, the problem of structural flexibility became acute. Due to the limited thrust available from our rocket engines, these missiles had to be as light as possible. This meant a sacrifice in structural rigidity. Missile flexure causes additional aerodynamic loads, which in turn cause additional flexure, etc. Also, coupling occurs between the elastic modes and the control system as the control system gyros and accelerometers sense the flexure motion and the rigid body motion.

In this chapter a method for determining the natural frequencies and mode shapes of the body bending modes is presented, followed by the derivation of the uncoupled body bending equations in normalized coordinates. Next, the transfer function for the flexible missile including the "tail-wags-dog" zero is derived, followed by the derivation of the rigid body transfer function, including the propellant sloshing mode. The chapter concludes with a discussion of the compensation required for body bending to assure stability.

11-2 LAGRANGE'S EQUATION

Lagrange's equation can be derived from Hamilton's principle or the principle of virtual work.[1,2,3] The most general form of Lagrange's equation is

$$\frac{d}{dt}\left(\frac{\partial T}{\partial \dot{q}_j}\right) - \frac{\partial T}{\partial q_j} + \frac{\partial F}{\partial \dot{q}_j} + \frac{\partial U}{\partial q_j} = Q_j \qquad (j = 1, 2, \ldots, n) \qquad (11\text{-}1)$$
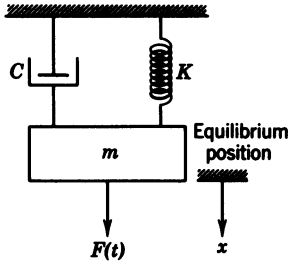
Figure 11-1 Mass, spring, and damper system.

where T is the kinetic energy of the system, U is the potential energy including strain energy, F is the dissipation function equal to one-half the rate at which energy is dissipated, Q_j is the generalized external force acting on the jth station, and q_j is the generalized coordinate of the jth station.

To illustrate the application of Lagrange's equation, the differential equations for two simple mechanical systems are derived. The first system discussed is the simple mass, spring, and damper system shown in Figure 11-1. From Figure 11-1, $q_1 = x$ and $\dot{q}_1 = \dot{x}$; then $T = \frac{1}{2}m\dot{x}^2$, the dissipation function $F = \frac{1}{2}C\dot{x}^2$, and the potential energy stored in the spring is $U = \int_0^x Kx\,dx = Kx^2/2$, and $Q_1 = F(t)$. As T is only a function of $\dot{x}$, then $\partial T/\partial q_1 = \partial T/\partial x = 0$; then $\partial T/\partial \dot{q}_1 = \partial T/\partial \dot{x} = (\partial/\partial \dot{x})(m\dot{x}^2/2) = m\dot{x}$ and $(d/dt)(\partial T/\partial \dot{q}_1) = (d/dt)m\dot{x} = m\ddot{x}$. The dissipation function term is $\partial F/\partial \dot{q}_1 = \partial F/\partial \dot{x} = (\partial/\partial \dot{x})(C\dot{x}^2/2) = C\dot{x}$, and the potential energy term is $\partial U/\partial q_1 = \partial U/\partial x = (\partial/\partial x)(Kx^2/2) = Kx$. Substituting these values into Eq. 11-1, it becomes

$$m\ddot{x} + C\dot{x} + Kx = F(t) \tag{11-2}$$

the standard second-order equation for the mass, spring, and damper system.

The second example is the derivation of the equations of motion for the double pendulum shown in Figure 11-2. For this system, the two generalized coordinates are ϕ_1 and ϕ_2. The lengths of the two pendulums are l_1 and l_2. The expressions for the kinetic and potential energies are expressed in rectangular coordinates and are then transformed into the generalized coor-
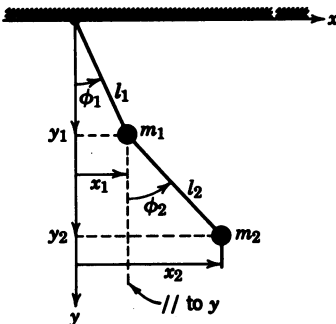
Figure 11-2 Double pendulum.

dinates. Thus, from Figure 11-2, $x_1 = l_1 \sin \phi_1$, $x_2 = l_1 \sin \phi_1 + l_2 \sin \phi_2$, $y_1 = l_1 \cos \phi_1$, and $y_2 = l_1 \cos \phi_1 + l_2 \cos \phi_2$. Differentiating the displacements yields the components of velocity of the two masses; thus $\dot{x}_1 = l_1 \dot{\phi}_1 \cos \phi_1$, $\dot{x}_2 = l_1 \dot{\phi}_1 \cos \phi_1 + l_2 \dot{\phi}_2 \cos \phi_2$, and $\dot{y}_1 = - l_1 \dot{\phi}_1 \sin \phi_1$, $\dot{y}_2 = - l_1 \dot{\phi}_1 \sin \phi_1 - l_2 \dot{\phi}_2 \sin \phi_2$. Then the total kinetic energy of the system is

$$T = \frac{m_1}{2}(\dot{x}_1^2 + \dot{y}_1^2) + \frac{m_2}{2}(\dot{x}_2^2 + \dot{y}_2^2) \tag{11-3}$$

Substituting the values of $\dot{x}_1^2$, $\dot{x}_2^2$, $\dot{y}_1^2$, and $\dot{y}_2^2$ into Eq. 11-3, and then simplifying, yields

$$T = \frac{m_1}{2} l_1^2 \dot{\phi}_1^2 + \frac{m_2}{2} \left[l_1^2 \dot{\phi}_1^2 + l_2^2 \dot{\phi}_2^2 + 2 l_1 l_2 \dot{\phi}_1 \dot{\phi}_2 \cos(\phi_2 - \phi_1) \right] \tag{11-4}$$

The potential energy can be obtained by determining the amount of vertical rise of m_1 and m_2 caused by a rotation ϕ_1 and ϕ_2; thus

$$U = m_1 g (l_1 - y_1) + m_2 g (l_1 + l_2 - y_2) \tag{11-5}$$

Substituting for y_1 and y_2 in Eq. 11-5, and simplifying, yields

$$U = (m_1 + m_2) g l_1 (1 - \cos \phi_1) + m_2 g l_2 (1 - \cos \phi_2) \tag{11-6}$$

Taking the partial derivative of T, Eq. 11-4, with respect to $\dot{q}_j$ yields

$$\frac{\partial T}{\partial \dot{q}_1} = \frac{\partial T}{\partial \dot{\phi}_1} = m_1 l_1^2 \dot{\phi}_1 + m_2 l_1^2 \dot{\phi}_1 + m_2 l_1 l_2 \dot{\phi}_2 \cos(\phi_2 - \phi_1)$$

and

$$\frac{\partial T}{\partial \dot{q}_2} = \frac{\partial T}{\partial \dot{\phi}_2} = m_2 l_2^2 \dot{\phi}_2 + m_2 l_1 l_2 \dot{\phi}_1 \cos(\phi_2 - \phi_1)$$

Differentiating with respect to time,

$$\frac{d}{dt}\left(\frac{\partial T}{\partial \dot{\phi}_1} \right) = (m_1 + m_2) l_1^2 \ddot{\phi}_1$$

$$+ m_2 l_1 l_2 \left[\ddot{\phi}_2 \cos(\phi_2 - \phi_1) - \dot{\phi}_2 (\dot{\phi}_2 - \dot{\phi}_1) \sin(\phi_2 - \phi_1) \right] \tag{11-7}$$

and

$$\frac{d}{dt}\left(\frac{\partial T}{\partial \dot{\phi}_2} \right) = m_2 l_2^2 \ddot{\phi}_2$$

$$+ m_2 l_1 l_2 \left[\ddot{\phi}_1 \cos(\phi_2 - \phi_1) - \dot{\phi}_1 (\dot{\phi}_2 - \dot{\phi}_1) \sin(\phi_2 - \phi_1) \right] \tag{11-8}$$

The partial derivative of T with respect to q_j yields

$$\frac{\partial T}{\partial q_1} = \frac{\partial T}{\partial \phi_1} = m_2 l_1 l_2 \dot{\phi}_1 \dot{\phi}_2 \sin(\phi_2 - \phi_1) \tag{11-9}$$

and

$$\frac{\partial T}{\partial q_2} = \frac{\partial T}{\partial \phi_2} = -m_2 l_1 l_2 \dot{\phi}_1 \dot{\phi}_2 \sin(\phi_2 - \phi_1) \tag{11-10}$$

Taking the partial derivative of U, Eq. 11-6, with respect to q_j, yields

$$\frac{\partial U}{\partial q_1} = \frac{\partial U}{\partial \phi_1} = (m_1 + m_2) g l_1 \sin \phi_1 \tag{11-11}$$

and

$$\frac{\partial U}{\partial q_2} = \frac{\partial U}{\partial \phi_2} = m_2 g l_2 \sin \phi_2 \tag{11-12}$$

Substituting Eqs. 11-7 through 11-12 into Lagrange's equation, Eq. 11-1 provides the equations of motion for the double pendulum:

$$(m_1 + m_2) l_1^2 \ddot{\phi}_1 + m_2 l_1 l_2 \ddot{\phi}_2 \cos(\phi_2 - \phi_1) - m_2 l_1 l_2 \dot{\phi}_2^2 \sin(\phi_2 - \phi_1)$$
$$+ (m_1 + m_2) g l_1 \sin \phi_1 = 0 \tag{11-13}$$

and

$$m_2 l_1 l_2 \ddot{\phi}_1 \cos(\phi_2 - \phi_1) + m_2 l_2^2 \ddot{\phi}_2 + m_2 l_1 l_2 \dot{\phi}_1^2 \sin(\phi_2 - \phi_1)$$
$$+ m_2 g l_2 \sin \phi_2 = 0 \tag{11-14}$$

11-3 LAGRANGE'S EQUATION APPLIED TO A SYSTEM OF LUMPED PARAMETERS

In actuality, a flexible aircraft or missile structure has an infinite number of degrees of freedom, making an exact analysis almost impossible. However, a very accurate approximate analysis can be obtained by reducing the system to one of a finite number of degrees of freedom; the greater the number of degrees of freedom, the greater the accuracy of analysis. To reduce the number of degrees of freedom from an infinite number, the structure is broken down into discrete masses. Thus the total mass of the vehicle is replaced by a number of rigid masses connected by weightless connectors. The connectors are assumed to have the same elastic properties as the physical structure that they replace. The application of this principle is shown in Figure 11-3, which shows the wing of an aircraft reduced to two discrete
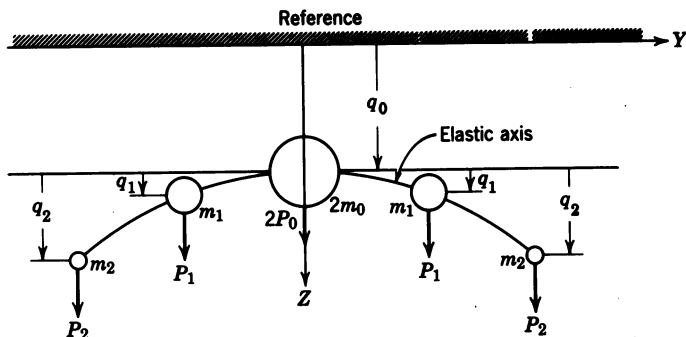
Figure 11-3 *Aircraft wing represented by lumped parameters.*

masses. Also included are the generalized coordinates providing for rigid body motion as well as flexure. Notice that the flexure motion is measured relative to the body, so that the total motion of each element of the wing is the sum of rigid body motion and bending motion. It should also be noted that the moment of inertia effect of an angular rotation of the discrete masses has been neglected, since they are small in comparison to the translation inertia terms. Including them would have doubled the number of degrees of freedom.

The forces represented by the P's are the forces due to gravity and the aerodynamic loads; these forces can be combined as the generalized forces Q_j. To demonstrate this, the P's are broken down into P_g's and P_a's, the gravitational and aerodynamic forces. The gravitational forces are included in the potential energy terms, and the aerodynamic forces in the generalized forces Q_j.

As the system is symmetrical, only half of it need be considered for the analysis. The equation for the kinetic energy of the system can be obtained by taking half the product of each mass in question and the square of its velocity with respect to the reference. Then

$$T = \tfrac{1}{2}\left(m_0 \dot{z}_0^2 + m_1 \dot{z}_1^2 + m_2 \dot{z}_2^2\right) \tag{11-15}$$

but $z_0 = q_0$, $z_1 = q_0 + q_1$, and $z_2 = q_0 + q_2$. Substituting the values of z into Eq. 11-15 and simplifying, the equation for the kinetic energy becomes

$$T = \tfrac{1}{2}\left[m_T \dot{q}_0^2 + m_1 \dot{q}_1^2 + 2m_1 \dot{q}_1 \dot{q}_0 + 2m_2 \dot{q}_0 \dot{q}_2 + m_2 \dot{q}_2^2\right] \tag{11-16}$$

where $m_T = m_0 + m_1 + m_2$. The potential energy is made up of two parts: the internal strain energy U_i, and the potential energy U_g resulting from the

vertical displacement. Thus (see Ref. 3, p. 133)

$$U_i = \frac{1}{2} \sum_{i=1}^{2} \sum_{j=1}^{2} k_{ij} q_i q_j = \frac{1}{2}\left(k_{11}q_1^2 + k_{12}q_1q_2 + k_{21}q_2q_1 + k_{22}q_2^2\right) \quad (11\text{-}17)$$

where the k_{ij}'s are the influence coefficients to be discussed later in this chapter. The gravitational potential energy is

$$U_g = -\left(P_{g_0}\right)q_0 - P_{g_1}(q_0 + q_1) - P_{g_2}(q_0 + q_2) \quad (11\text{-}18)$$

Finally, the aerodynamic forces are

$$Q_0 = P_{a_0} + P_{a_1} + P_{a_2}, \qquad Q_1 = P_{a_1}, \qquad Q_2 = P_{a_2} \quad (11\text{-}19)$$

Taking the partial derivative of Eq. 11-16 with respect to $\dot{q}_0$ yields $\partial T / \partial \dot{q}_0 = m_T \dot{q}_0 + m_1 \dot{q}_1 + m_2 \dot{q}_2$; differentiating with respect to time,

$$\frac{d}{dt}\left(\frac{\partial T}{\partial \dot{q}_0}\right) = m_T \ddot{q}_0 + m_1 \ddot{q}_1 + m_2 \ddot{q}_2 \quad (11\text{-}20)$$

The partial derivatives of Eqs. 11-16 and 11-17 with respect to q_0 are zero; however, the partial derivative of Eq. 11-18 yields

$$\frac{\partial U_g}{\partial q_0} = -\left(P_{g_0} + P_{g_1} + P_{g_2}\right) \quad (11\text{-}21)$$

Substituting the Q_0 term of Eqs. 11-19, 11-20, and 11-21 into Lagrange's equation yields

$$m_T \ddot{q}_0 + m_1 \ddot{q}_1 + m_2 \ddot{q}_2 = P_{a_0} + P_{g_0} + P_{a_1} + P_{g_1} + P_{a_2} + P_{g_2}$$
$$= P_0 + P_1 + P_2 \quad (11\text{-}22)$$

In like manner,

$$\frac{d}{dt}\left(\frac{\partial T}{\partial \dot{q}_1}\right) = m_1 \ddot{q}_0 + m_1 \ddot{q}_1 \quad (11\text{-}23)$$

However, the partial derivative of Eq. 11-17 with respect to q_1 is not zero; thus

$$\frac{\partial U_i}{\partial q_1} = k_{11}q_1 + \tfrac{1}{2}k_{12}q_2 + \tfrac{1}{2}k_{21}q_2 = k_{11}q_1 + k_{12}q_2 \quad (11\text{-}24)$$

as $k_{12} = k_{21}$. The partial derivative of Eq. 11-16 with respect to q_1 is zero;

therefore, substituting Eqs. 11-23 and 11-24 into Lagrange's equation, combining with the partial derivative of Eq. 11-18 with respect to q_1, and adding Q_1 from Eq. 11-19 yields

$$m_1\ddot{q}_0 + m_1\ddot{q}_1 + k_{11}q_1 + k_{12}q_2 = P_1 \qquad (11\text{-}25)$$

The third equation is obtained in the same manner as Eq. 11-25; thus the three equations of motion are

$$
\begin{aligned}
m_T\ddot{q}_0 + m_1\ddot{q}_1 + m_2\ddot{q}_2 &= P_0 + P_1 + P_2 \\
m_1\ddot{q}_0 + m_1\ddot{q}_1 \qquad + k_{11}q_1 + k_{12}q_2 &= P_1 \\
m_2\ddot{q}_0 \qquad + m_2\ddot{q}_2 + k_{21}q_1 + k_{22}q_2 &= P_2
\end{aligned}
\qquad (11\text{-}26)
$$

Equation 11-26 summarizes the three differential equations which describe the behavior of the system shown in Figure 11-3. As just mentioned, the k_{ij}'s are the influence coefficients and can be written in the form of a matrix. The influence coefficient matrix is equal to the inverse, or reciprocal, of the stiffness matrix or $[k_{ij}] = [C_{ij}]^{-1}$, where the C's are the deflections at point i due to a unit load at point j (see Appendix E for a discussion of matrix algebra). Again the stiffness matrix is symmetrical.

11-4 MODE SHAPES AND FREQUENCIES

Before looking at the solution of the simultaneous vibration equations, the technique for determining the shapes and natural frequencies of the vibratory modes is given. First, the vibratory equations are written in matrix form for ease of handling. In matrix form, Eqs. 11-26, or any set of simultaneous equations, can be expressed as

$$[m_{ij}]\{\ddot{q}_j\} + [k_{ij}]\{q_j\} = \{Q_j\} \qquad (11\text{-}27)$$

where $[m_{ij}]$ is the inertial matrix, $[k_{ij}]$ is the stiffness matrix,

$$
\{\ddot{q}_j\} = \begin{bmatrix} \ddot{q}_1 \\ \ddot{q}_2 \\ \vdots \\ \ddot{q}_n \end{bmatrix}
\qquad
\{q_j\} = \begin{bmatrix} q_1 \\ q_2 \\ \vdots \\ q_n \end{bmatrix}
\qquad
\{Q_j\} = \begin{bmatrix} Q_1 \\ Q_2 \\ \vdots \\ Q_n \end{bmatrix}
$$

and n is equal to the number of degrees of freedom. Both the inertial and stiffness matrices are symmetrical, but some of the terms may be zero.

To illustrate, Eq. 11-26 is written in matrix form:

$$
\begin{bmatrix} m_T & m_1 & m_2 \\ m_1 & m_1 & 0 \\ m_2 & 0 & m_2 \end{bmatrix} \begin{bmatrix} \ddot{q}_0 \\ \ddot{q}_1 \\ \ddot{q}_2 \end{bmatrix} + \begin{bmatrix} 0 & 0 & 0 \\ 0 & k_{11} & k_{12} \\ 0 & k_{21} & k_{22} \end{bmatrix} \begin{bmatrix} q_0 \\ q_1 \\ q_2 \end{bmatrix} = \begin{bmatrix} P_0 + P_1 + P_2 \\ P_1 \\ P_2 \end{bmatrix} \quad (11\text{-}28)
$$

Note that if the rigid body motion is neglected, then $q_0 = 0$, and Eq. 11-28 reduces to

$$
\begin{bmatrix} m_1 & 0 \\ 0 & m_2 \end{bmatrix} \begin{bmatrix} \ddot{q}_1 \\ \ddot{q}_2 \end{bmatrix} + \begin{bmatrix} k_{11} & k_{12} \\ k_{21} & k_{22} \end{bmatrix} \begin{bmatrix} q_1 \\ q_2 \end{bmatrix} = \begin{bmatrix} P_1 \\ P_2 \end{bmatrix} \quad (11\text{-}29)
$$

Returning to the determination of the mode shapes and frequencies, Eq. 11-27 is written in general terms for a system with three degrees of freedom:

$$
\begin{bmatrix} m_{11} & m_{12} & m_{13} \\ m_{21} & m_{22} & m_{23} \\ m_{31} & m_{32} & m_{33} \end{bmatrix} \begin{bmatrix} \ddot{q}_1 \\ \ddot{q}_2 \\ \ddot{q}_3 \end{bmatrix} + \begin{bmatrix} k_{11} & k_{12} & k_{13} \\ k_{21} & k_{22} & k_{23} \\ k_{31} & k_{32} & k_{33} \end{bmatrix} \begin{bmatrix} q_1 \\ q_2 \\ q_3 \end{bmatrix} = \begin{bmatrix} Q_1 \\ Q_2 \\ Q_3 \end{bmatrix} \quad (11\text{-}30)
$$

The solution of Eq. 11-30 is assumed to be of the form $q_j = A_j \sin(\omega t + \psi)$; then $\ddot{q}_j = -A_j \omega^2 \sin(\omega t + \psi)$. Substituting these values into Eq. 11-30, and using only the characteristic equation, yields

$$
- \begin{bmatrix} m_{11} & m_{12} & m_{13} \\ m_{21} & m_{22} & m_{23} \\ m_{31} & m_{32} & m_{33} \end{bmatrix} \begin{bmatrix} A_1 \omega^2 \\ A_2 \omega^2 \\ A_3 \omega^2 \end{bmatrix} + \begin{bmatrix} k_{11} & k_{12} & k_{13} \\ k_{21} & k_{22} & k_{23} \\ k_{31} & k_{32} & k_{33} \end{bmatrix} \begin{bmatrix} A_1 \\ A_2 \\ A_3 \end{bmatrix} = 0 \quad (11\text{-}31)
$$

after dividing through by $\sin(\omega t + \psi)$. Simplifying,

$$
\begin{bmatrix} (k_{11} - m_{11}\omega^2) & (k_{12} - m_{12}\omega^2) & (k_{13} - m_{13}\omega^2) \\ (k_{21} - m_{21}\omega^2) & (k_{22} - m_{22}\omega^2) & (k_{23} - m_{23}\omega^2) \\ (k_{31} - m_{31}\omega^2) & (k_{32} - m_{32}\omega^2) & (k_{33} - m_{33}\omega^2) \end{bmatrix} \begin{bmatrix} A_1 \\ A_2 \\ A_3 \end{bmatrix} = 0 \quad (11\text{-}32)
$$

As in the case of the equations of motion of the aircraft, for the solution of Eq. 11-32 to be nontrivial, the determinant of the coefficients of A_j must equal zero. The expansion of the determinant formed by the coefficient matrix of A_j will yield an equation with the highest power of ω equal to $2n$. The factoring of this equation will yield the natural frequencies of the oscillatory modes. These are designated by ω_r, with $r = 1, 2, \ldots, n$ and $\omega_1 < \omega_2 < \cdots < \omega_n$.

The next step is the determination of the mode shapes. To illustrate the required manipulation of the matrix equation, Eq. 11-32 first is expanded,

which yields

$$(k_{11} - m_{11}\omega^2)A_1 + (k_{12} - m_{12}\omega^2)A_2 + (k_{13} - m_{13}\omega^2)A_3 = 0$$
$$(k_{21} - m_{21}\omega^2)A_1 + (k_{22} - m_{22}\omega^2)A_2 + (k_{23} - m_{23}\omega^2)A_3 = 0$$
$$(k_{31} - m_{31}\omega^2)A_1 + (k_{32} - m_{32}\omega^2)A_2 + (k_{33} - m_{33}\omega^2)A_3 = 0 \quad (11\text{-}33)$$

The first two equations of Eq. 11-33 can be written as

$$(k_{11} - m_{11}\omega^2)A_1 + (k_{12} - m_{12}\omega^2)A_2 = -(k_{13} - m_{13}\omega^2)A_3$$
$$(k_{21} - m_{21}\omega^2)A_1 + (k_{22} - m_{22}\omega^2)A_2 = -(k_{23} - m_{23}\omega^2)A_3 \quad (11\text{-}34)$$

Returning to matrix form and dividing both sides by A_3 yields

$$\begin{bmatrix} k_{11} - m_{11}\omega^2 & k_{12} - m_{12}\omega^2 \\ k_{21} - m_{21}\omega^2 & k_{22} - m_{22}\omega^2 \end{bmatrix} \begin{bmatrix} A_1/A_3 \\ A_2/A_3 \end{bmatrix} = - \begin{bmatrix} k_{13} - m_{13}\omega^2 \\ k_{23} - m_{23}\omega^2 \end{bmatrix} \quad (11\text{-}35)$$

The ratios A_1/A_3 and A_2/A_3 are defined as the mode shapes and designated ϕ_j. Previously, the natural frequencies for the n modes of oscillation were determined; thus Eq. 11-35 can be evaluated for each ω_r, yielding a ϕ_j for each natural frequency; these are designated $\phi_j^{(r)}$. Introducing the r notation, Eq. 11-35 becomes

$$\begin{bmatrix} k_{11} - m_{11}\omega_r^2 & k_{12} - m_{12}\omega_r^2 \\ k_{21} - m_{21}\omega_r^2 & k_{22} - m_{22}\omega_r^2 \end{bmatrix} \begin{bmatrix} \phi_1^{(r)} \\ \phi_2^{(r)} \end{bmatrix} = - \begin{bmatrix} k_{13} - m_{13}\omega_r^2 \\ k_{23} - m_{23}\omega_r^2 \end{bmatrix} \quad (11\text{-}36)$$

and $\phi_3^{(r)} = A_3/A_3 = 1$. The mode shapes $\phi_j^{(r)}$ yield the maximum amplitude of each mode of vibration (r) for each station or discrete mass j, as shown in Figure 11-4 for the first mode shape $(r = 1)$. Normally the steps between Eq. 11-33 and Eq. 11-36 can be eliminated, and Eq. 11-36 can be obtained directly from Eq. 11-33. Equation 11-36 then can be solved for the required mode shapes.

To better illustrate this procedure, a simple numerical example is worked. The system analyzed is the same as that shown in Figure 11-3, which is
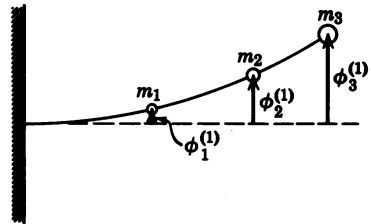
Figure 11-4   *Illustration of mode shapes for the first mode.*
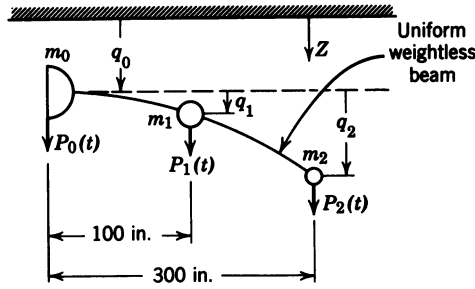
Figure 11-5 System for sample problem.

$EI = 3.6 \times 10^{10}$ lb in.^{2} $m_2 = 12.9$ lb sec^2 / in.

$m_0 = 64.6$ lb sec^2 / in. $m_T = 103.3$ lb sec^2 / in.

$m_1 = 25.8$ lb sec^2 / in. $g = 387$ in / sec^2

redrawn in Figure 11-5 showing only half of the aircraft. The differential equation for this system is given in Eq. 11-28. In comparing Eq. 11-28 with Eq. 11-30, it can be seen that the m's and k's of Eq. 11-28 can be equated to the m's and k's of Eq. 11-30. A prime is used with the k's from Eq. 11-28 to distinguish them from the k's of Eq. 11-30; thus

$$m_{11} = m_T = 103.3 \text{ lb sec}^2/\text{in.}$$

$$m_{12} = m_{21} = m_{22} = m_1 = 25.8 \text{ lb sec}^2/\text{in.}$$

$$m_{13} = m_{31} = m_{33} = m_2 = 12.9 \text{ lb sec}^2/\text{in.}$$

$$m_{23} = m_{32} = 0$$

$$k_{11} = k_{12} = k_{13} = k_{21} = k_{31} = 0$$

$$k_{22} = k'_{11} \qquad k_{23} = k_{32} = k'_{12} \qquad k_{33} = k'_{22}$$

It is now necessary to determine k'_{11}, k'_{12}, and k'_{22}. Since $[k_{ij}] = [C_{ij}]^{-1}$, the stiffness matrix must be determined first. The deflection at point i due to a unit load applied at point j is given by $C_{ij} = (x_i^2/6EI)(3x_j - x_i)$ for $x_i \leq x_j$,[1] where x_i and x_j are the distances from the centerline to the points i and j, respectively, as shown in Figure 11-6. For C_{11} we have $x_i = x_j = 100$
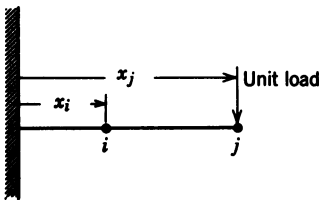
Figure 11-6

in.; then

$$C_{11} = \frac{(100)^2(300-100)}{6(3.6\times10^{10})} = 0.9259\times10^{-5} \text{ in./lb}$$

For C_{12} we have $x_i = 100$ in., $x_j = 300$ in.; then

$$C_{12} = C_{21} = \frac{(100)^2(900-100)}{6(3.6\times10^{10})} = 3.7\times10^{-5} \text{ in./lb}$$

For C_{22} we have $x_i = x_j = 300$ in.; then

$$C_{22} = \frac{(300)^2(900-300)}{6(3.6\times10^{10})} = 25\times10^{-5} \text{ in./lb}$$

Then

$$[C_{ij}] = \begin{bmatrix} 0.9259 & 3.7 \\ 3.7 & 25 \end{bmatrix} \times 10^{-5} \text{ in./lb}$$

But

$$[k'_{ij}] = [C_{ij}]^{-1} = \frac{(-1)^{i+j} \begin{vmatrix} \text{Minor of} \\ [C_{ji}] \end{vmatrix}}{|C_{ij}|}$$

Then,

$$k'_{11} = \frac{(-1)^2(25\times10^{-5})}{\begin{vmatrix} 0.9259\times10^{-5} & 3.7\times10^{-5} \\ 3.7\times10^{-5} & 25\times10^{-5} \end{vmatrix}} = \frac{25\times10^{-5}}{9.4575\times10^{-10}} = 2.64\times10^5 \text{ lb/in.}$$

Similarly,

$$k'_{12} = k'_{21} = \frac{(-1)^3(3.7\times10^{-5})}{9.4575\times10^{-10}} = -0.39\times10^5 \text{ lb/in.}$$

and

$$k'_{22} = \frac{0.925\times10^{-5}}{9.4575\times10^{-10}} = 0.0979\times10^5 \text{ lb/in.}$$

Therefore,

$$[k'_{ij}] = \begin{bmatrix} 2.64 & -0.39 \\ -0.39 & 0.0979 \end{bmatrix} \times 10^5 \text{ lb/in.}$$

The differential equations describing the motion of the wing and fuselage can now be written in matrix form:

$$\begin{bmatrix} 103.3 & 25.8 & 12.9 \\ 25.8 & 25.8 & 0 \\ 12.9 & 0 & 12.9 \end{bmatrix} \begin{bmatrix} \ddot{q}_0 \\ \ddot{q}_1 \\ \ddot{q}_2 \end{bmatrix} + \begin{bmatrix} 0 & 0 & 0 \\ 0 & 2.64 & -0.39 \\ 0 & -0.39 & 0.0979 \end{bmatrix} \begin{bmatrix} q_0 \\ q_1 \\ q_2 \end{bmatrix} \times 10^5$$

$$= \begin{bmatrix} P_0(t) + P_1(t) + P_2(t) \\ P_1(t) \\ P_2(t) \end{bmatrix}$$

Next it is necessary to determine the natural frequencies of oscillation, which can be accomplished by substituting the values of m_{ij} and k_{ij} into Eq. 11-32, which yields

$$\begin{bmatrix} 0 - 103.3\omega^2 & 0 - 25.8\omega^2 & 0 - 12.9\omega^2 \\ 0 - 25.8\omega^2 & 2.64 \times 10^5 - 25.8\omega^2 & -0.39 \times 10^5 - 0 \\ 0 - 12.9\omega^2 & -0.39 \times 10^5 - 0 & 0.0979 \times 10^5 - 12.9\omega^2 \end{bmatrix} \begin{bmatrix} A_1 \\ A_2 \\ A_3 \end{bmatrix} = 0$$

Expanding the determinant and simplifying yields

$$\omega^2(\omega^4 - 14.02 \times 10^3 \omega^2 + 51.1 \times 10^5) = 0$$

Factoring,

$$\omega^2(\omega^2 - 13.65 \times 10^3)(\omega^2 - 374.4) = 0$$

Therefore the natural frequencies of the modes are $\omega_0 = 0$, $\omega_1 = 19.35$ rad/sec, $\omega_2 = 116.8$ rad/sec. The frequency ω_0 is the rigid body mode.

The mode shapes corresponding to the three frequencies of vibration are now evaluated. As the mode shapes represent the eigenfunctions of the solution of the homogeneous equation, each mode shape represents only relative displacements of the portions of the beam; thus the mode shape for the rigid body mode can be obtained by inspection. If the relative displacement of the fuselage is taken as unity, then the mode shape corresponding to ω_0 for the fuselage is $\phi_0^{(0)} = 1$. The mode shapes for the other two stations, m_1 and m_2, are zero, since the displacements of these two stations are measured with respect to the horizontal reference that moves with the fuselage; thus $\phi_1^{(0)} = \phi_2^{(0)} = 0$. The remaining mode shapes can be evaluated

using Eq. 11-36. Substituting for ω_1^2 in Eq. 11-36, it becomes

$$\begin{bmatrix} -(103.3)(374.4) & -(25.8)(374.4) \\ -(25.8)(374.4) & 2.64\times10^5-(25.8)(374.4) \end{bmatrix}\begin{bmatrix} \phi_0^{(1)} \\ \phi_1^{(1)} \end{bmatrix}$$

$$= -\begin{bmatrix} -(12.9)(374.4) \\ -0.39\times10^5 \end{bmatrix}$$

Multiplying through by the inverse of the coefficient matrix yields

$$\begin{bmatrix} \phi_0^{(1)} \\ \phi_1^{(1)} \end{bmatrix}=\begin{bmatrix} -0.0256 & -9.767\times10^{-4} \\ -9.767\times10^{-4} & 0.391\times10^{-2} \end{bmatrix}\begin{bmatrix} 4.83 \\ 39 \end{bmatrix}$$

Solving yields the mode shapes for ω_1, which are $\phi_0^{(1)}=-0.162$, $\phi_1^{(1)}=0.148$, and $\phi_2^{(1)}=1$. In like manner, substituting for ω_2 in Eq. 11-36 and simplifying yields

$$\begin{bmatrix} -141 & -35.217 \\ -35.217 & -8.917 \end{bmatrix}\begin{bmatrix} \phi_0^{(2)} \\ \phi_1^{(2)} \end{bmatrix}=\begin{bmatrix} 17.61 \\ 3.9 \end{bmatrix}$$

Solving for the mode shapes for ω_2 yields $\phi_0^{(2)}=-1.154$, $\phi_1^{(2)}=4.12$, and $\phi_2^{(2)}=1$. Thus the natural frequencies and the mode shapes have been determined.

11-5   NORMAL COORDINATES

So far, the natural frequencies (the eigenvalues) and the mode shapes (the eigenfunctions) for the coupled homogeneous equations have been determined; however, the response of the system to the forcing functions has not been determined. To obtain the so-called particular solution, use is made of the normal coordinates ξ_r, which yield a set of uncoupled second-order equations of the form

$$M_r\ddot{\xi}_r + M_r\omega_r^2\xi_r = \Xi_r \tag{11-37}$$

where $M_r = \lfloor\phi_j^{(r)}\rfloor[m_{ij}]\{\phi_j^{(r)}\}$ are the generalized masses and

$$\Xi_r = \lfloor\phi_j^{(r)}\rfloor\{Q_j\}$$

are the normalized forces. The ω_r's are the natural frequencies of the mode shapes already determined. After solving the uncoupled equations for the ξ_r's, the solution of the original equations in terms of the generalized

coordinates, q_j, can be obtained by using the following equation:

$$\{q_j\} = \left[\phi_j^{(r)}\right]\{\xi_r\} \tag{11-38}$$

The numerical example, started in Section 11-3, is continued here to obtain the uncoupled equations in normal coordinates. Substituting the appropriate values into Eq. 11-37 yields

$$M_0 = \begin{bmatrix} 1 & 0 & 0 \end{bmatrix} \begin{bmatrix} 103.3 & 25.8 & 12.9 \\ 25.8 & 25.8 & 0 \\ 12.9 & 0 & 12.9 \end{bmatrix} \begin{bmatrix} 1 \\ 0 \\ 0 \end{bmatrix}$$

$$= \begin{bmatrix} 103.3 & 25.8 & 12.9 \end{bmatrix} \begin{bmatrix} 1 \\ 0 \\ 0 \end{bmatrix} = 103.3 \ \frac{\text{lb sec}^2}{\text{in.}}$$

Note that the first operation consists of multiplying the square matrix by the row matrix. In like manner

$$M_1 = \begin{bmatrix} -0.162 & 0.148 & 1 \end{bmatrix} \begin{bmatrix} 103.3 & 25.8 & 12.9 \\ 25.8 & 25.8 & 0 \\ 12.9 & 0 & 12.9 \end{bmatrix} \begin{bmatrix} -0.162 \\ 0.148 \\ 1 \end{bmatrix} = 9.76 \ \frac{\text{lb sec}^2}{\text{in.}}$$

and

$$M_2 = \begin{bmatrix} -1.154 & 4.12 & 1 \end{bmatrix} \begin{bmatrix} 103.3 & 25.8 & 12.9 \\ 25.8 & 25.8 & 0 \\ 12.9 & 0 & 12.9 \end{bmatrix} \begin{bmatrix} -1.154 \\ 4.12 \\ 1 \end{bmatrix}$$

$$= 313.3 \ \frac{\text{lb sec}^2}{\text{in.}}$$

Using the equation for the normalized forces,

$$\Xi_0 = \begin{bmatrix} 1 & 0 & 0 \end{bmatrix} \begin{bmatrix} P_0(t) + P_1(t) + P_2(t) \\ P_1(t) \\ P_2(t) \end{bmatrix} = P_0(t) + P_1(t) + P_2(t) \ \text{lb}$$

$$\Xi_1 = \begin{bmatrix} -0.162 & 0.148 & 1 \end{bmatrix} \begin{bmatrix} P_0(t) + P_1(t) + P_2(t) \\ P_1(t) \\ P_2(t) \end{bmatrix}$$

$$= -0.162 P_0(t) - 0.014 P_1(t) + 0.838 P_2(t) \ \text{lb}$$

and

$$\Xi_2 = \begin{bmatrix} -1.154 & 4.12 & 1 \end{bmatrix} \begin{bmatrix} P_0(t) + P_1(t) + P_2(t) \\ P_1(t) \\ P_2(t) \end{bmatrix}$$

$$= -1.154 P_0(t) + 2.966 P_1(t) - 0.154 P_2(t) \text{ lb}$$

Therefore the uncoupled equations in normal coordinates are

$$103.3 \ddot{\xi} = P_0(t) + P_1(t) + P_2(t)$$

$$10.76 \ddot{\xi}_1 + 4028.5 \xi_1 = -0.162 P_0(t) - 0.014 P_1(t) + 0.838 P_2(t)$$

$$313.3 \ddot{\xi}_2 + 4.277 \times 10^6 \xi_2 = -1.154 P_0(t) + 2.966 P_1(t) - 0.154 P_2(t)$$

11-6 SYSTEM TRANSFER FUNCTION, INCLUDING BODY BENDING

The body bending equations have been derived, but to determine the effects of body bending on the control system, the body bending equations must be combined with the rigid body equations. This coupling arises from the fact that the attitude and rate gyros and accelerometers sense both the rigid body changes and the body bending motion. By proper combination of the body bending equations with the rigid body equations, modified as necessary, the transfer function for the combined rigid body and bending modes can be obtained.

For the body bending, the body bending equations in normal coordinate form are used (see Eq. 11-37). The solution of the body bending equations in generalized coordinates (Eq. 11-38) is not generally required; however, as is shown later in this section, the actual displacement of specific stations of the vehicle and the actual slope of the elastic axis at specific points, θ_{B_j}, may be required. These values can be obtained from the following equation:

$$\{\theta_{B_j}\} = \left[\sigma_j^{(r)} \right] \{\xi_r\} \tag{11-39}$$

where $\sigma_j^{(r)}$ is the slope of the rth mode shape at the jth station, and is referred to as the normalized mode slope (rad/ft). See Figure 11-7.

To illustrate the simultaneous solution of the modified rigid body equations and the body bending equations, the equations for the ballistic missile modified for the effects of body bending at the tail are used. This procedure neglects the aerodynamic effects associated with the body bending, which is generally satisfactory for vehicles of this type.[4] Equation 7-39 is rewritten to
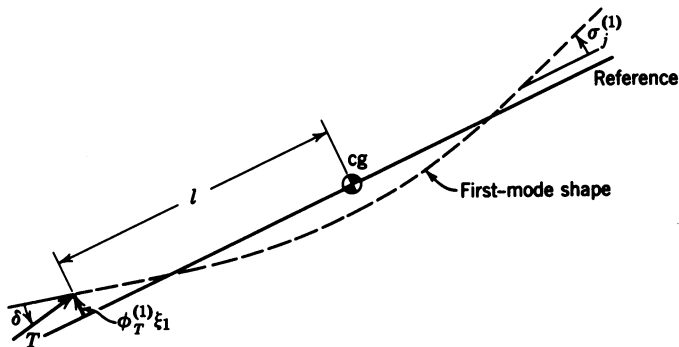
Figure 11-7 *First-mode shape for a missile showing normalized mode slope.*

include the effects of body bending:

$$\left(\frac{mU}{Sq}s - C_{z_\alpha}\right)\alpha(s) + \left[-\frac{mU}{Sq}s - C_w\sin\Theta\right]\theta(s) = C_{z_\delta}\left[\delta(s) + \sigma_T^{(r)}\xi_r(s)\right]$$

$$-C_{m_\alpha}\alpha(s) + \left(\frac{I_y}{Sqd}s^2 - \frac{d}{2U}C_{m_q}s\right)\theta(s) = C_{m_\delta}\left[\delta(s) + \sigma_T^{(r)}\xi_r(s)\right] + \frac{C_{z_\delta}}{d}\phi_T^{(r)}\xi_r(s)$$

$$\left(\frac{M_r}{Sq}s^2 + \frac{M_r\omega_r^2}{Sq}\right)\xi_r(s) = C_{z_\delta}\phi_T^{(r)}\delta(s)\qquad\qquad(11\text{-}40)$$

The expression $\delta(s) + \sigma_T^{(r)}\xi_r(s)$ gives the effective direction of the thrust vector relative to the reference, which is the centerline of the rigid missile; the normalized mode slope is negative at the tail of the missile. The term $(C_{z_\delta}/d)\phi_T^{(r)}\xi_r(s)$ gives the torque resulting from the lateral displacement of the rocket motor gimbal from the reference axis. C_{z_δ} must be divided by the characteristic length to keep the equation nondimensional. The damping of the body bending modes has been neglected. Equation 11-40 is rewritten considering only the first two body bending modes and transcribing the body bending terms in the rigid body equations to the left hand side:

$$A\alpha(s) + B\theta(s) - C_{z_\delta}\sigma_T^{(1)}\xi_1(s) - C_{z_\delta}\sigma_T^{(2)}\xi_2(s) = C_{z_\delta}\delta(s)$$

$$C\alpha(s) + D\theta(s) - \left(C_{m_\delta}\sigma_T^{(1)} + \frac{C_{z_\delta}}{d}\phi_T^{(1)}\right)\xi_1(s) - \left(C_{m_\delta}\sigma_T^{(2)} + \frac{C_{z_\delta}}{d}\phi_T^{(2)}\right)\xi_2(s)$$

$$= C_{m_\delta}\delta(s)$$

$$\left(\frac{M_1}{Sq}s^2 + \frac{M_1\omega_1^2}{Sq}\right)\xi_1(s) = C_{z_\delta}\phi_T^{(1)}\delta(s)$$

$$\left(\frac{M_2}{Sq}s^2 + \frac{M_2}{Sq}\omega_2^2\right)\xi_2(s) = C_{z_\delta}\phi_T^{(2)}\delta(s)\qquad\qquad(11\text{-}41)$$

where

$$A = \frac{mU}{Sq}s - C_{z_\alpha}$$

$$B = -\frac{mU}{Sq}s - C_w \sin \Theta$$

$$C = -C_{m_\alpha}$$

$$D = \frac{I_y}{Sqd}s^2 - \frac{d}{2U}C_{m_q}s$$

The characteristic equation can be obtained by setting the determinant of the coefficients of Eq. 11-41 to zero. Denoting this by ∇, we have

$$\nabla = (AD - BC)\left(\frac{M_1}{Sq}s^2 + \frac{M_1}{Sq}\omega_1^2\right)\left(\frac{M_2}{Sq}s^2 + \frac{M_2}{Sq}\omega_2^2\right) = 0 \quad (11\text{-}42)$$

The factor $AD - BC$ of Eq. 11-42 is equal to the expansion of the determinant formed by the coefficients of Eq. 7-39, and is equivalent to the open loop poles of the rigid body transfer function. Since Eq. 11-42 forms the denominator of the missile transfer functions, including body bending, the roots of Eq. 11-42 yield the poles of the flexible missile transfer function. From Eq. 11-42 it can be seen that the poles of the flexible missile transfer function consist of the rigid body poles and the poles from each of the body bending modes. To obtain the overall flexible missile transfer function, it is first necessary to look at the block diagram of the flexible missile, as shown in Figure 11-8. From Figure 11-8 it can be seen that θ_o, which is the pitch attitude sensed by the attitude gyro or stable platform, consists of θ from the rigid missile plus the attitude resulting from the missile flexure. Thus, the
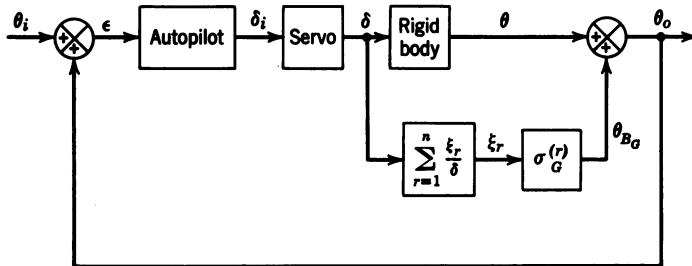
Figure 11-8 Block diagram for the flexible missile. Note: $\sigma_G^{(r)}$ is the normalized mode slope at the gyro or stable platform, used to sense the missile attitude.

overall transfer function is

$$\frac{\theta_o(s)}{\delta(s)} = \frac{\theta(s)}{\delta(s)} + \sigma_G^{(1)}\frac{\xi_1(s)}{\delta(s)} + \sigma_G^{(2)}\frac{\xi_2(s)}{\delta(s)} \tag{11-43}$$

The individual transfer functions can be obtained from Eq. 11-41; they are

$$\frac{\theta(s)}{\delta(s)} = \frac{1}{\nabla}\left[(AC_{m_\delta} - CC_{z_\delta})\left(\frac{M_1 s^2}{Sq} + \frac{M_1 \omega_1^2}{Sq}\right)\left(\frac{M_2 s^2}{Sq} + \frac{M_2 \omega_2^2}{Sq}\right)\right.$$

$$- \phi_T^{(1)}C_{z_\delta}\left\{A\left(C_{m_\delta}\sigma_T^{(1)} + \frac{C_{z_\delta}}{d}\phi_T^{(1)}\right) + CC_{z_\delta}\sigma_T^{(1)}\right\}\left(\frac{M_2 s^2}{Sq} + \frac{M_2 \omega_2^2}{Sq}\right)$$

$$\left. - \phi_T^{(2)}C_{z_\delta}\left\{A\left(C_{m_\delta}\sigma_T^{(2)} + \frac{C_{z_\delta}}{d}\phi_T^{(2)}\right) + CC_{z_\delta}\sigma_T^{(2)}\right\}\left(\frac{M_1 s^2}{Sq} + \frac{M_1 \omega_1^2}{Sq}\right)\right]$$

$$\frac{\sigma_G^{(1)}\xi_1(s)}{\delta(s)} = \frac{\sigma_G^{(1)}C_{z_\delta}\phi_T^{(1)}(AD - BC)\left(\dfrac{M_2 s^2}{Sq} + \dfrac{M_2 \omega_2^2}{Sq}\right)}{\nabla}$$

$$\frac{\sigma_G^{(2)}\xi_2(s)}{\delta(s)} = \frac{\sigma_G^{(2)}C_{z_\delta}\phi_T^{(2)}(AD - BC)\left(\dfrac{M_1 s^2}{Sq} + \dfrac{M_1 \omega_1^2}{Sq}\right)}{\nabla} \tag{11-44}$$

As mentioned earlier in this paragraph, the poles of the flexible missile transfer function are the rigid body poles plus the body bending poles. The zeros of the flexible transfer function in general consist of zeros only slightly different from the rigid body zeros, plus complex zeros near each of the body bending poles. This pattern is normally found when analyzing the flexible missile or aircraft;[5] however, the gyro location influences the location of the zeros, and as will be seen in Section 11-9, other zero locations are possible.

Contained in Ref. 4 is a diagram of the stability boundaries for several flight times. This plot, shown in Figure 11-9, resulted from analog studies and gives the relation between the gyro location and the maximum allowable gain for stability. From this figure it can be seen that the best location for the sensors (gyros) is just to the rear of the center of the missile. This location puts the sensors near the antinode of the first body bending mode.

11-7 THE "TAIL-WAGS-DOG" ZERO

Another factor that must be considered in the missile transfer function is the so-called "tail-wags-dog" (TWD) zero. This zero, actually a pair of complex
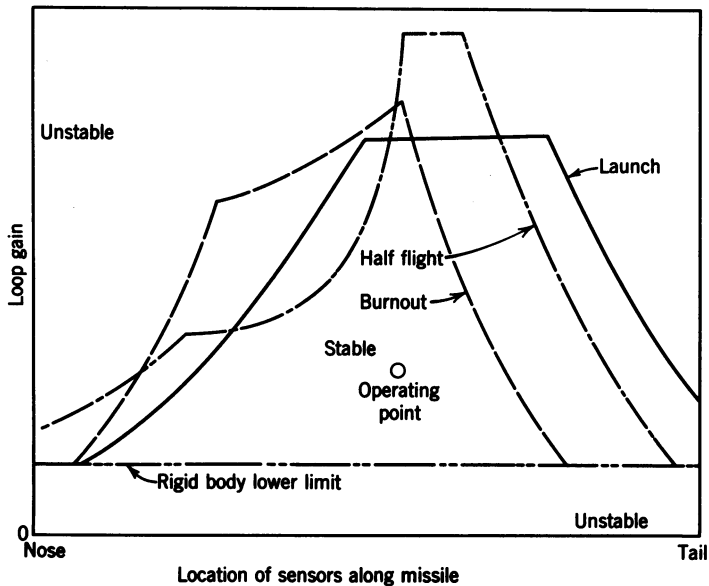
Figure 11-9 *Typical stability boundary plot for several flight times.*

zeros, occurs at the frequency at which the inertial forces resulting from the gimbaling of the rocket engine cancel the component of thrust normal to the missile axis due to deflection of the motor chamber. There are two inertial torques, one resulting from the angular acceleration of the rocket engine about its gimbal pivot, and the other resulting from the translation of the center of gravity of the rocket engine, as shown in Figure 11-10. Due to an angular acceleration of the rocket chamber there will be an inertial reaction torque at the gimbal. This torque can be transferred to the center of gravity of the missile and will be in the direction shown and equal to $I_y \ddot{\delta}$. As a result
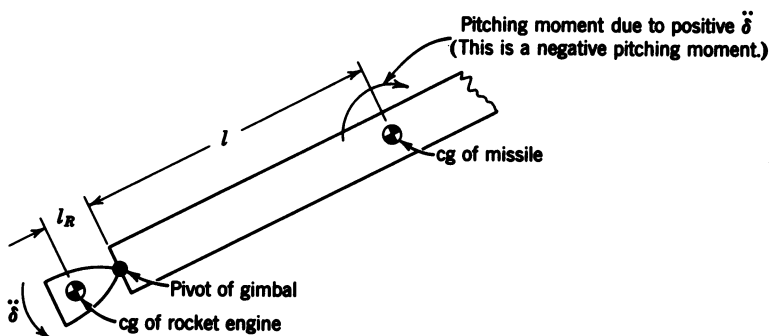
Figure 11-10 *Sketch showing inertial torques resulting from gimbal deflections.*

of the lateral translation of the center of gravity of the chamber, there will be an inertial reaction force equal to $m_R l_R \ddot{\delta}$, where m_R is the mass of the chamber and $l_R \ddot{\delta}$ is the tangential acceleration of the center of mass of the rocket motor. This inertial reaction force multiplied by l gives a torque acting about the missile center of gravity in the direction shown in Figure 11-10. The torque due to engine deflection is equal to $Tl\delta$ as before; the summation of the applied moments is then

$$\sum \text{applied moments} = -\left(Tl\delta + m_R l_R l\ddot{\delta} + I_y \ddot{\delta}\right) \qquad (11\text{-}45)$$

Before Eq. 11-45 can be introduced into the moment equation of Eq. 11-41, it must be nondimensionalized by dividing by Sqd. For the force equation, Eq. 11-45 must be divided by l and then nondimensionalized by dividing by Sq. The right hand side of Eq. 11-41 then becomes

For force equations:

$$\left[C_{z_\delta} - \frac{1}{Sq}\left(m_R l_R + \frac{I_y}{l}\right)s^2\right]\delta(s)$$

Moment equation:

$$\left[C_{m_\delta} - \frac{1}{Sqd}(m_R l_R l + I_y)s^2\right]\delta(s)$$

Body bending equations:

$$\phi_T^{(r)}\left[C_{z_\delta} - \frac{1}{Sq}\left(m_R l_R + \frac{I_y}{l}\right)s^2\right]\delta(s)$$

(as C_{z_δ} and C_{m_δ} are negative)

The result of including these inertial terms is to add a pair of complex zeros to the overall flexible missile transfer function. These zeros will be on the $j\omega$ axis at a value

$$\omega_n = \left(\frac{T}{m_R l_R + I_y/l}\right)^{1/2} \text{rad/sec}$$

if the convention is used that $\phi_T^{(r)} = 1$. This is because the right hand side of the moment equation can be written as $(l/d)[C_{z_\delta} - (1/Sq)(m_R l_R + I_y/l)s^2]\delta(s)$, and $C_{z_\delta} = -T/Sq$.

11-8   EFFECTS OF PROPELLANT SLOSHING

Another important factor that affects the stability of large liquid-fuel missiles is the sloshing of the propellants. The so-called sloshing modes may couple with the rigid body and even the bending modes, and cause instability. The problem is further aggravated because the damping of the propellant modes is very light in large vehicles, varying inversely with tank diameter.[4]

In Appendix A of Ref. 4 it is shown that for cylindrical tanks the effects of propellant sloshing can be approximated by a series of pendulums or spring masses (one for each sloshing mode). This mechanical analog must be repeated for each tank. Normally it is sufficient to consider only the first propellant mode,[4] as the forces and moments produced by the higher-order modes are negligible. In the analysis to follow, a simple pendulum is used to derive the transfer function for a rigid missile with one tank. The analysis can be extended to include multiple tanks, but is too unwieldy to be presented here. Before proceeding with the derivation, a short discussion of the behavior of a pendulum under the influence of pivot acceleration is presented.

To illustrate this behavior, a simple pendulum, the pivot of which is being accelerated linearly with an acceleration equal to $\mathbf{a}$, is considered. This is shown in Figure 11-11, where $\mathbf{F} = m_p\mathbf{a}$ with m_p the mass of the pendulum, and two forces $\mathbf{F}_1$ and $\mathbf{F}_2$ have been added acting through the cg of the pendulum, with $\mathbf{F}_1 = \mathbf{F} = -\mathbf{F}_2$. The addition of $\mathbf{F}_1$ and $\mathbf{F}_2$ has no effect on the total summation of forces and moments acting on the pendulum. $\mathbf{F}_1$ acting on the cg of the pendulum causes the pendulum to accelerate in the direction of $\mathbf{F}_1$, but causes no rotation. However, the two forces $\mathbf{F}$ and $\mathbf{F}_2$ form a couple and impart an angular acceleration to the pendulum. The angular acceleration resulting from the couple is the phenomenon of particular interest. The moment resulting from the couple can be obtained by summing torques about any point in the body; for simplicity the torque produced by the couple is summed about the cg. Thus

$$\sum \mathbf{M}_{(cg)} = \sum \mathbf{M}_{(pivot)} = \mathbf{F} \times l = m_p\mathbf{a} \times l \qquad (11\text{-}46)$$

From this discussion it can be seen that the results of accelerating the pivot
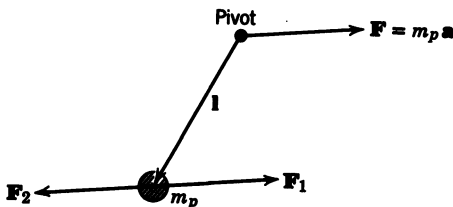
Figure 11-11   *Simple pendulum under the influence of pivot acceleration.*
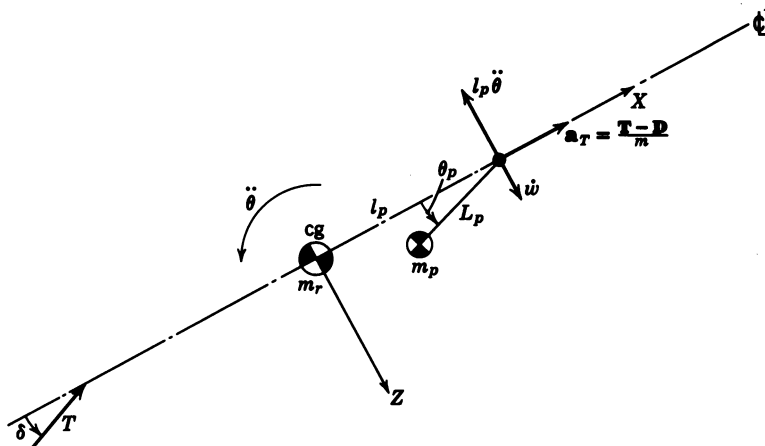
Figure 11-12 Propellant sloshing model for one tank, where m_p is the mass of the propellant in the tank; $m_r = m - m_p$ is the mass of the missile less the propellant mass; L_p is the length of the equivalent pendulum representing the first sloshing mode of one tank; and l_p is the distance between the cg of the missile, less propellant, and the pivot of the pendulum.

of a pendulum are twofold. First, it causes the whole pendulum to accelerate in the direction of the pivot acceleration, and second, it causes a moment to be produced about the pivot.

Having examined the effects of accelerating the pivot of a pendulum, the analysis of the effects of propellant sloshing are presented next. The parameters to be used are shown in Figure 11-12, and equations for relating them to the tank properties are given in Appendix A of Ref. 4. From Figure 11-12, the accelerations acting on the pivot of the pendulum are the thrust acceleration (a_T), a tangential acceleration due to pitching angular accelerations ($l_p\ddot{\theta}$), and the Z component of vehicle acceleration ($\dot{w}$). The centripetal acceleration caused by a pitch angular velocity ($l_p\dot{\theta}^2$), which is very small in comparison to a_T, is neglected. The pivot acceleration expressed in the missile axis system is then

$$\mathbf{a}_{(pivot)} = \mathbf{i}a_T + \mathbf{k}\left(\dot{w} - l_p\ddot{\theta}\right) \tag{11-47}$$

and

$$\mathbf{L}_p = -\mathbf{i}L_p + \mathbf{k}L_p\theta_p \tag{11-48}$$

using the small-angle assumption for θ_p. The moment resulting from these accelerations can be obtained by substituting Eqs. 11-47 and 11-48 into Eq. 11-46. Thus

$$\sum \mathbf{M}_{(pivot)} = m_p\mathbf{a}_{(pivot)} \times \mathbf{L}_p = \mathbf{j}\left[m_pL_p\left(l_p\ddot{\theta} - \dot{w}\right) - m_pa_TL_p\theta_p\right] \tag{11-49}$$

Now $\Sigma M_{(pivot)}$ is equal to the moment of inertia of the pendulum (I_p) times the angular acceleration of the pendulum with respect to inertial space, which can be approximated by the angular acceleration of the pendulum with respect to the earth, which is $\ddot{\theta}_p + \ddot{\theta}$. Substituting for $\Sigma M_{(pivot)}$ in Eq. 11-49 yields

$$m_p L_p \left(l_p \ddot{\theta} - \dot{w} \right) - m_p a_T L_p \theta_p = L_p^2 m_p \left(\ddot{\theta}_p + \ddot{\theta} \right) \tag{11-50}$$

where $I_p = L_p^2 m_p$. Rearranging and dividing by Sqd to nondimensionalize, Eq. 11-50 becomes

$$\frac{L_p^2 m_p}{Sqd} \ddot{\theta}_p + \frac{m_p a_T L_p \theta_p}{Sqd} + \frac{m_p L_p U \dot{\alpha}}{Sqd} - \frac{L_p m_p}{Sqd} (l_p - L_p) \ddot{\theta} = 0 \tag{11-51}$$

which is the equation describing the effects of the sloshing of the liquid propellant on the vehicle dynamics.

To obtain the transfer function for the missile, including propellant sloshing, Eq. 11-51 must be solved simultaneously with the rigid body equations. (The combination of Eq. 11-51 with the body bending equations is discussed later in this section.) This situation requires the addition of one term in each of the Z force and pitching moment equations to account for the displacement of the center of gravity of the propellant from the X axis of the missile. Due to the longitudinal acceleration of the missile there is a tension generated in the rod of the pendulum equal to $m_p a_T$ (assuming θ_p a small angle). This tension generates a force on the missile at the pivot, as shown in Figure 11-13, which results in a Z force equal to $m_p a_T \theta_p$ and a negative pitching moment equal to $m_p a_T l_p \theta_p$. The force and moment after nondimensionalizing must be added to the rigid body equations to complete the equations of motion including propellant sloshing. The final equations in Laplace transform notation, for zero initial conditions, are as follows:

$$\left(\frac{m_r U}{Sq} s - C_{z_\alpha} \right) \alpha(s) - \left(\frac{m_r U}{Sq} s - C_w \sin \Theta \right) \theta(s) - C_{z_p} \theta_p(s) = C_{z_\delta} \delta(s)$$

$$- C_{m_\alpha} \alpha(s) + \left(\frac{I_{y_r}}{Sqd} s^2 - \frac{d}{2U} C_{m_q} \right) \theta(s) + C_{m_p} \theta_p(s) = C_{m_\delta} \delta(s)$$

$$\frac{L_p m_p U}{Sqd} s \alpha(s) - \frac{L_p m_p (l_p - L_p)}{Sqd} s^2 \theta(s) + \frac{L_p^2 m_p}{Sqd} (s^2 + \omega_p^2) \theta_p(s) = 0$$

$$\tag{11-52}$$

where I_{y_r} is the moment of inertia of the missile less the propellant, $\omega_p^2 = a_T / L_p$, $C_{z_p} = m_p a_T / Sq$, and $C_{m_p} = m_p a_T l_p / Sqd$. Using the determi-
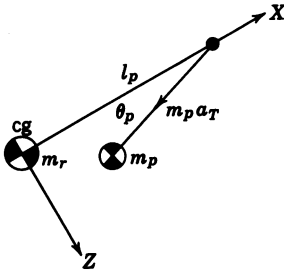
Figure 11-13 Force produced by propellant on the missile.

nants to obtain the $\theta(s)/\delta(s)$ transfer function, if $\theta(s)/\delta(s) = N/\nabla$, then

$$N = \frac{L_p^2 m_p}{Sqd} \left\{ \left[C_{m_\delta}\left(\frac{m_r U}{Sq}s - C_{z_\alpha}\right) + C_{m_\alpha}C_{z_\delta}\right](s^2 + \omega_p^2) \right.$$

$$\left. + \frac{U}{L_p}(C_{z_\delta}C_{m_p} + C_{z_p}C_{m_\delta})s\right\} \qquad (11\text{-}53)$$

and

$$\nabla = \frac{L_p^2 m_p}{Sqd} \left\{ \left[\left(\frac{m_r U}{Sq}s - C_{z_\alpha}\right)\left(\frac{I_{y_r}}{Sqd}s^2 - \frac{d}{2U}C_{m_q}s\right) - C_{m_\alpha}\left(\frac{m_r U}{Sq}s - C_w \sin\Theta\right)\right] \right.$$

$$\times (s^2 + \omega_p^2) + \left[C_{m_p}\left(\frac{m_r U}{Sq}s - C_{z_\alpha}\right) + C_{m_\alpha}C_{z_p}\right]\frac{(l_p - L_p)}{L_p}s^2$$

$$\left. + \left[-C_{m_p}\left(\frac{m_r U}{Sq}s - C_w \sin\Theta\right) + C_{z_p}\left(\frac{I_{y_r}}{Sqd}s^2 - \frac{d}{2U}C_{m_q}s\right)\right]\frac{U}{L_p}s\right\}$$

$$(11\text{-}54)$$

The first term of Eq. 11-53 contains the rigid body zero and a pair of complex zeros on the imaginary axis. The actual location of these zeros will be slightly modified by the last term. Similarly, the first term of the denominator contains the rigid body poles and the complex poles from the propellant sloshing mode, again modified by the other terms. In this case only one tank was considered in order to illustrate the technique; if two tanks had been considered, there would have been two equivalent pendulum equations and a total of four simultaneous equations, etc. The case of two propellant tanks is considered in Ref. 4 including the rigid body degrees of freedom, with a typical root locus for the control system shown in Figure 11-14. The form of the root locus is shown in Figure 11-15, which was taken from Ref. 4, p. 19.
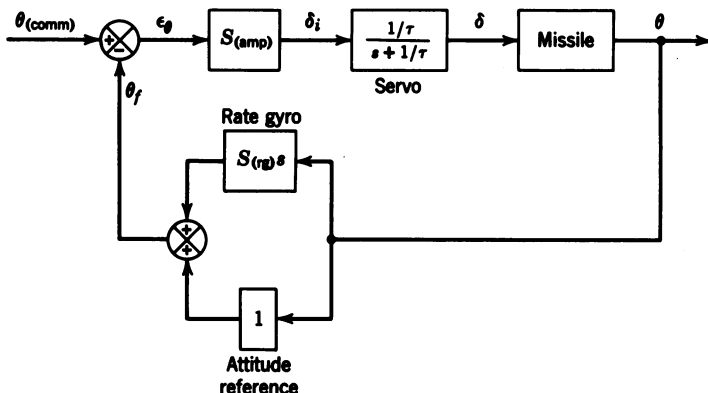
Figure 11-14 Basic control system to show effects of propellant sloshing.

From Figure 11-15 it can be seen that the root locus for the second tank is slightly unstable; however, this problem can be alleviated by the addition of mechanical baffles to provide damping.

Thus far only the rigid body modes have been considered in connection with the propellant sloshing; however, there may also be adverse coupling between the flexible modes and the propellant sloshing. In deriving Eq. 11-50 the only input was considered to be the acceleration of the pivot of the pendulum representing the sloshing mode. The flexible modes would also yield an acceleration in the direction of the Z axis. The location of the pivot of the pendulum with respect to the antinode of the flexible missile, and the frequency of the bending mode relative to the propellant sloshing frequency, determine the amount of coupling.
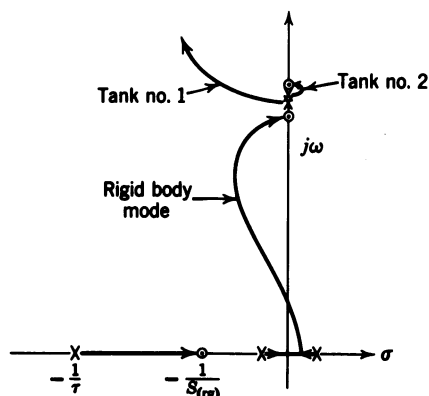
Figure 11-15 Typical root locus for ballistic missile with two propellant tanks (from Ref. 4).

11-9 COMPENSATION REQUIRED FOR BODY BENDING

Thus far the transfer function for the flexible missile has been derived to include the "tail-wags-dog" zero. The effects of propellant slosh were also discussed. Instabilities resulting from the sloshing modes normally can be controlled through the use of baffles; however, the correction of instabilities arising from the body bending modes requires some form of compensation.

As the flexible missile poles lie on or near the imaginary axis, the angle of departure of the root locus from these poles is very important. Very often the angle of departure, with no compensation for body bending, carries these poles into the right half plane (see Figure 11-19 below). To prevent this, a lag network of the form $K/[s + (1/\tau)]$ is usually added, with the pole adjusted to provide the best angle of departure for the low-frequency modes (phase stabilization) and still maintain stability of the rigid body poles. This normally takes care of the low-frequency modes, but may not completely stabilize the higher-frequency modes.

If phase stabilization (controlling the angle of departure) of the higher-frequency modes is impossible or impractical, the use of so-called "notched filters" is resorted to. The notched filter[6] is designed to attenuate frequencies associated with the higher-frequency modes so that the portion of the signal produced by the sensors at these frequencies will be sufficiently well attenuated so as to cause no stability problems. This is sometimes referred to as "gain stabilization" of the higher-frequency modes.

To illustrate the effects of compensation, the adaptive control system for advance booster systems developed by Minneapolis-Honeywell Regulator Company is used.[7] This control system employs some interesting concepts that are discussed along with the compensation for the body bending poles. Minneapolis-Honeywell used the fourth NASA Scout configuration, which is aerodynamically stable, to analyze their control system. The block diagram of the control system, with the details of the gain changer eliminated, is shown in Figure 11-16. Before simplifying the block diagram for the root locus plot, the purpose and operation of the rate gyro blender is discussed.

The main purpose of the rate gyro blender is to insure favorable first-bending-mode zero locations. It was essential that the first-mode zero have a higher natural frequency than the first-mode pole for proper first-mode phase stability for the body bending filters used in the forward loop. As shown in Eq. 11-44, the numerator of the transfer function is influenced by the amount of body bending sensed by the gyro. For this application one gyro is placed forward and the other aft of the antinode of the first body bending mode. The attenuated output of each gyro is passed through a band-pass filter centered on the first body bending frequency. The attenuation factor K is automatically adjusted so that the output of the absolute value circuits from each gyro will be equal (the output of the absolute value circuits is always positive). As the output of the forward rate gyro is attenuated by a
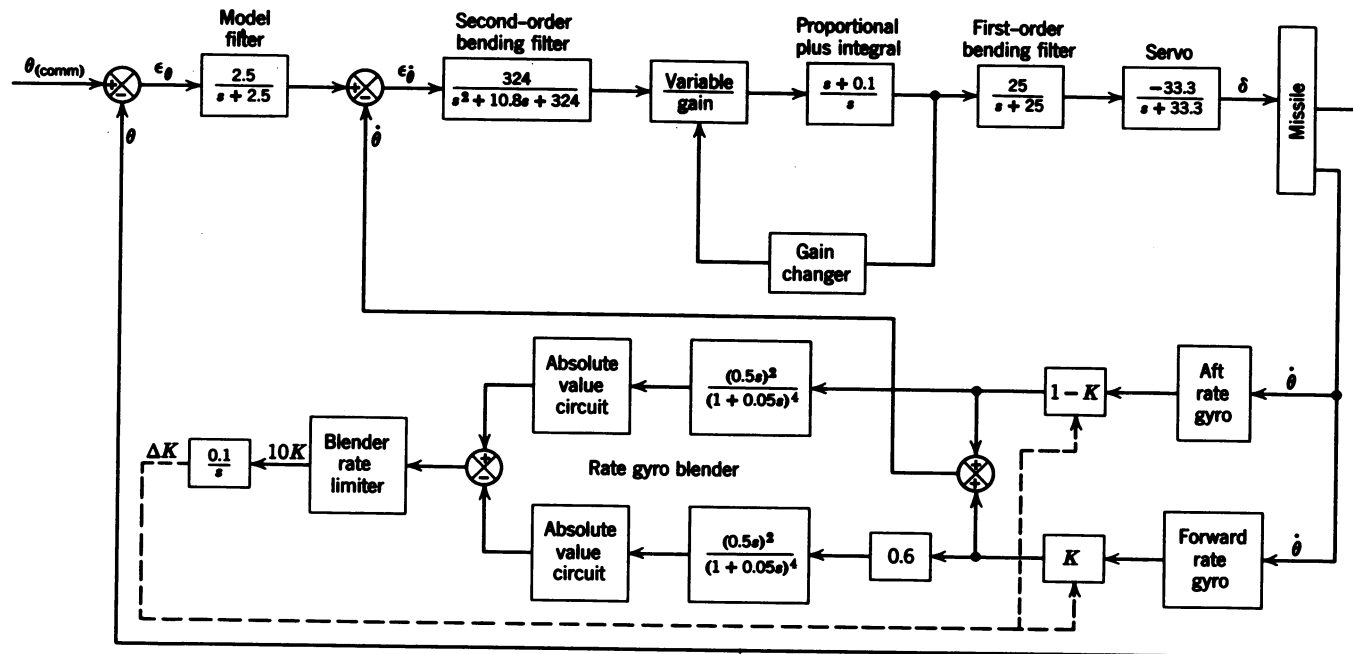
Figure 11-16 *Block diagram of control system for an advanced booster system.*
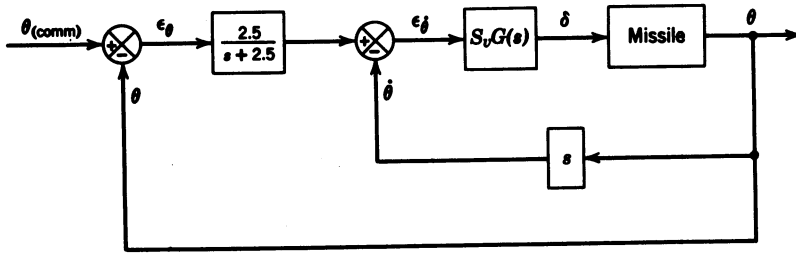
Figure 11-17 Simplified block diagram of missile control system, where S_V is the variable gain.

$$G(s) = \frac{-(33.3)(25)(324)(s+0.1)}{s(s^2+10.8s+324)(s+25)(s+33.3)}$$

fixed factor of 0.6 besides the variable factor K, the feedback signal to the control system from the forward gyro is greater than the signal from the aft gyro. This favoring of the forward gyro provides the favorable first-mode zero location. Since the output of each gyro is summed, after being attenuated by a factor of K and $1-K$, effectively there is unity feedback of $\dot\theta$. The block diagram can then be redrawn as shown in Figure 11-17.

The effect of the rate gyro blender is included in the transfer function of the missile. From Figure 11-17,

$$\epsilon_{\dot\theta} = \frac{2.5(\theta_{(comm)}-\theta)}{s+2.5} - s\theta$$

Simplifying,

$$\epsilon_{\dot\theta} = \frac{2.5\theta_{(comm)}-2.5\theta-s^2\theta-2.5s\theta}{s+2.5}$$

or

$$\epsilon_{\dot\theta} = \frac{2.5}{s+2.5}\theta_{(comm)} - \left(\frac{s^2+2.5s+2.5}{s+2.5}\right)\theta \qquad (11\text{-}55)$$

Using Eq. 11-55, an equivalent block diagram may be drawn for the control system as shown in Figure 11-18. From this figure it can be seen that the effect of passing the attitude error signal through the model filter and summing that with the $\dot\theta$ feedback is the same as that of feeding θ through a feedback filter to be summed with the signal from the model filter. The time constant of the model filter determines the zeros of the feedback filter, which, as can be seen from Figure 11-19(b), determines the approximate location of the closed loop rigid body poles, and therefore serves as the model for the rigid body poles.
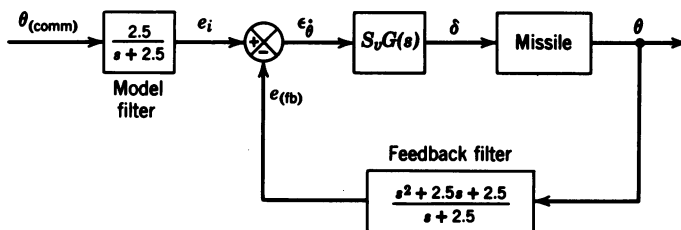
Figure 11-18 *Equivalent block diagram of the missile control system.*

Before looking at the final root locus, the purpose of the two bending filters is discussed. Figure 11-19(a) shows the angle of departure from the body bending poles for the first three body bending modes for no compensation, the first-order bending filter only, and the second-order bending filter only. From Figure 11-19(a) it can be seen that neither filter alone will phase stabilize all three bending modes. In fact, all three modes are unstable with only the first-order filter. The second-order filter used with the first-order filter provides phase stability for all the body bending modes. The second-order filter also serves another role.
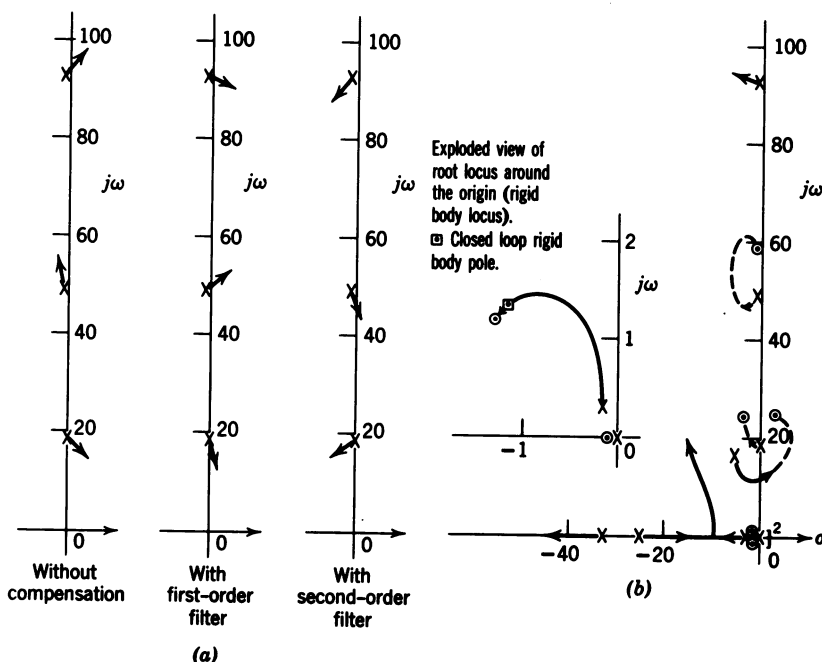
Figure 11-19 *(a) Angle of departure for the body bending poles with and without compensation. (b) Root locus of the complete system, maximum dynamic pressure.*
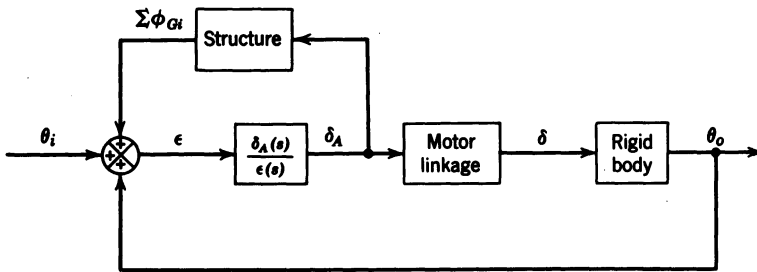
Figure 11-20 Block diagram of Vanguard control system showing flexible and rigid body loops.

As this is a self-adaptive control system using a principle similar to the MH 90 control system discussed in Chapter 6, a limit cycle must be generated by a pair of poles crossing the imaginary axis. The second-order filter provides these poles. The frequency at which the filter poles cross the imaginary axis is governed mainly by the open loop location of the filter poles and the first body bending poles and zeros. The location shown provided almost a constant frequency for this imaginary axis crossing and therefore for the limit cycle. With the second-order filter poles on the imaginary axis the closed loop rigid body poles were very near the zeros of the feedback filter [actual location shown in Figure 11-19(b)], thus providing favorable rigid body response. The final root locus is shown in Figure 11-19(b) (the dashed portion of the root locus is assumed to be the approximate locus).

For this particular missile it was possible to phase stabilize all three body bending modes; however, this is not true in every case, as can be seen by examining the compensation required for the Vanguard missile. The Martin Company considered the first three body bending modes but handled the analysis differently, as shown in Figure 11-20. For the subsequent analysis only the structure loop is considered, which is shown in more detail in Figure 11-21. The natural frequencies and the damping ratios of the first three body bending modes are

First mode: $\zeta = 0.02$, $\omega_n = 24.6$ rad/sec
Second mode: $\zeta = 0.02$, $\omega_n = 62.5$ rad/sec
Third mode: $\zeta = 8.7 \times 10^{-5}$, $\omega_n = 151.5$ rad/sec

The demodulator is part of the rigid body control system but was not included in the rigid body analysis, since the contribution of the pole at -333 to the rigid body root locus would have been negligible. The lag circuit was added to phase stabilize the first body bending mode. But as can be seen from the root locus (Figure 11-22), it also prevents system instability which would have resulted from the third body bending mode. The root locus for the flexible missile is shown in Figure 11-22; also shown are the angles of departure from the body bending poles for the system without the lag circuit.
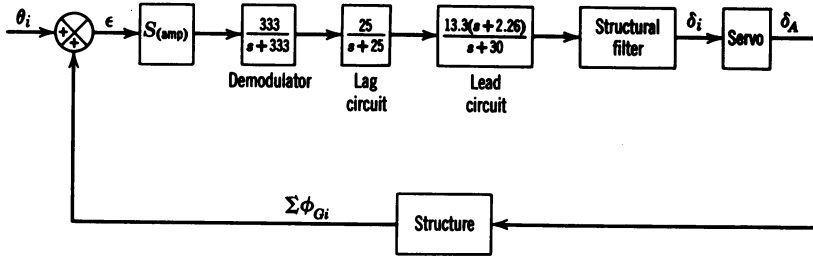
Figure 11-21 *Block diagram for flexible missile including compensators for body bending.*

$$\frac{\sum \phi_{Gi}}{\delta_A} = \frac{-0.686(s + 53)(s - 53)(s^2 - 152.2s + 14{,}500)}{(s^2 + s + 605)(s^2 + 45.5s + 2660)(s^2 + 2.51s + 3900)}$$

$$\times \frac{s^2 + 153.8s + 14{,}500}{s^2 + 3.99s + 22{,}980}$$

$$[\text{TF}]_{(\text{servo})[\delta_i;\,\delta_A]} = \frac{2750}{s^2 + 42.2s + 2750}$$

$$[\text{TF}]_{(\text{structural filter})} = \frac{(s^2 + 10s + 3597.1)(s^2 + 20s + 10{,}000.25)}{(s^2 + 10.962s + 2442.82)(s^2 + 19.04s + 14{,}724.35)}$$
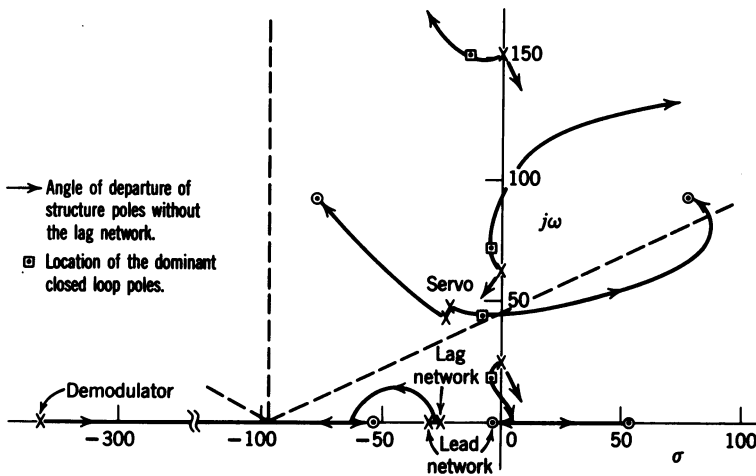
Figure 11-22 *Root locus of the flexible missile with compensation. Note: Poles and zeros not identified are from the structure.*
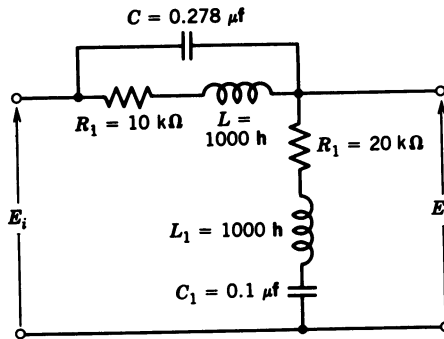
Figure 11-23 *Double-notch filter for second body bending mode.*

$$\frac{E_o(s)}{E_i(s)} = \frac{(LCs^2 + RCs + 1)\left(L_1C_1s^2 + R_1C_1s + 1\right)}{(LCs^2 + RCs + 1)\left(L_1C_1s^2 + R_1C_1s + 1\right) + LC_1s^2 + RC_1s}$$

The effect of the lag circuit is very evident from the root locus. However, as can be seen from the root locus, the damping of the second mode pole is not increased noticeably. The Martin Company found that no simple compensator would improve the damping of the second-mode pole without driving the rigid missile unstable. Their solution was to use the double-notch filter shown in Figure 11-23. The transfer function for the filter is shown with Figure 11-21. The root locus of the flexible missile with compensation and the structural filter is shown in Figure 11-24 with the location of the closed loop poles indicated for $S_{(amp)} = 7$. This gain is lower than the gain 17 used to locate the dominant closed loop poles shown in Figure 11-22. The natural frequencies and the damping ratios for the closed-loop structural poles from Figure 11-24 are

First mode: $\zeta = 0.12$, $\omega_n = 22.1$ rad/sec
Second mode: $\zeta = 0.02$, $\omega_n = 62.65$ rad/sec
Third mode: $\zeta = 0.013$, $\omega_n = 151.6$ rad/sec
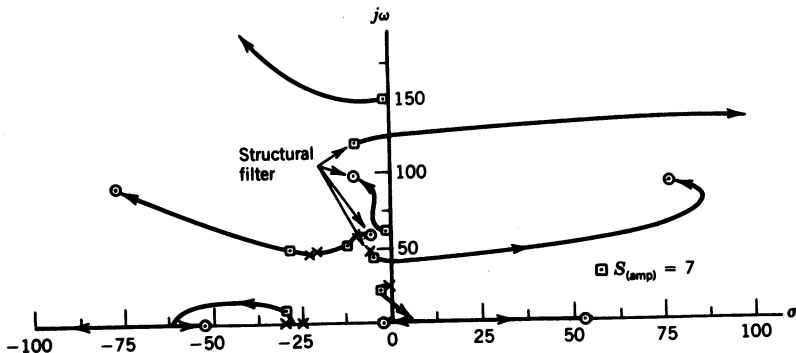
Figure 11-24 *Root locus of the flexible missile with compensation and structural filter.*
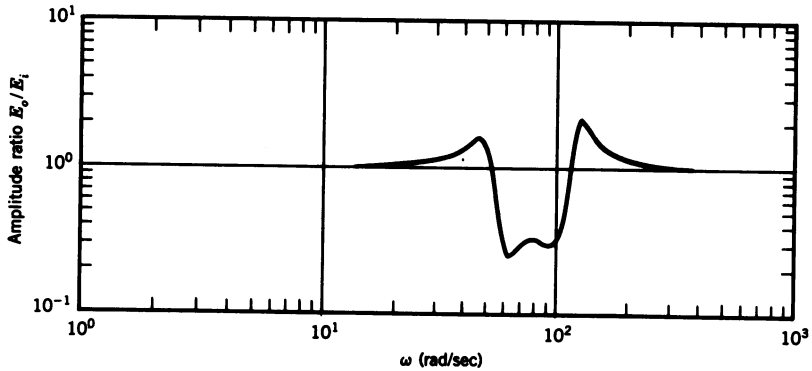
Figure 11-25 *Frequency response of the filter shown in Figure 11-23.*

A comparison of these damping ratios with the ones for the open-loop structural poles shows that the damping ratio for the second body bending mode is unchanged. The light damping of the second body bending mode is compensated for by the action of the structural filter, the frequency response of which is shown in Figure 11-25. From Figure 11-25 the attenuation of the signal at the second body bending mode frequency is 0.246, or −12.18 dB. The action of the structural filter can be seen from Figure 11-26, which shows the output of the servo δ_A for a unit step input of θ_i (see Figure 11-21).

11-10 SUMMARY

In this chapter a method for determining the transfer function of a flexible missile has been presented, as well as the rigid missile transfer function
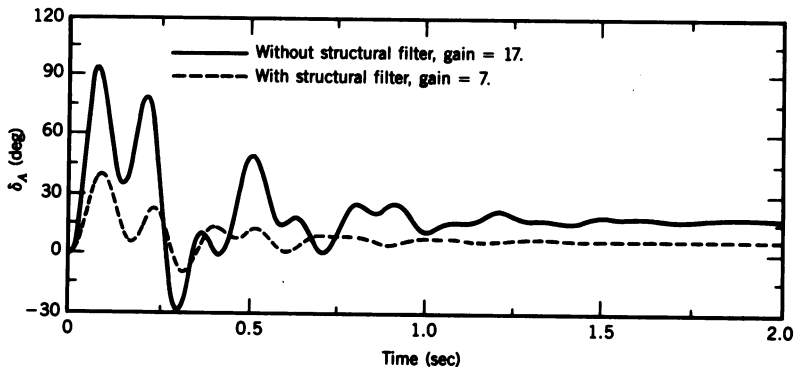
Figure 11-26 *Comparison of the unit step responses of the flexible missile (δ_A / θ_i) with and without the structural filter for gain equal to $S_{(amp)}$.*

including propellant sloshing. In deriving the flexible missile transfer function it was assumed that natural frequencies and shapes of the body bending modes were known. The usefulness of the flexible missile transfer functions depends upon the accuracy of the mode shapes and frequencies used. In some cases actual tests on a full-size missile have been made to obtain a comparison between the theoretical and actual mode shapes and frequencies.[4] Experience has shown that the frequencies are more accurately predicted than the mode shapes.

There has been no attempt in this chapter to make structures experts out of control system engineers, but only to provide them with some idea of how to use the data that they can expect to receive from the structures people.

The methods of compensation were discussed, but as in any other control system problem, the actual compensation required will vary from system to system. The determination of the required compensation may become quite involved and the compensator very complex.

REFERENCES

1. R. L. Bisplinghoff, H. Ashley, and R. L. Halfman, *Aeroelasticity*, Addison-Wesley Publishing Co., Cambridge, Massachusetts, 1955.

2. R. H. Scanlan and R. Rosenbaum, *Introduction to the Study of Aircraft Vibration and Flutter*, MacMillan Co., New York, 1951.

3. J. W. Mar, *Structural Problems in Weapons*, 16.48 Notes, Massachusetts Institute of Technology (unpublished), 1956.

4. D. R. Lukens, A. F. Schmitt, and G. T. Broucek, *Approximate Transfer Functions for Flexible-Booster-and-Autopilot Analysis*, WADD-TR-61-93, April 1961.

5. R. C. Seamans, F. A. Barnes, T. B. Garber, and V. W. Howard, "Recent Developments in Aircraft Control," *Journal of the Aeronautical Sciences*, March 1955.

6. M. W. Reed, J. A. Wolfe, and D. L. Mellen, *Advanced Flight Vehicle Self-Adaptive Flight Control System, Part IV—Notch Filter Development*, WADD-TR-60-651, Part IV, June 1962.

7. L. T. Prince, *Design, Development, and Flight Research of an Experimental Adaptive Control Technique for Advanced Booster Systems*, ASD-TDR-62-178, Part I, Nov. 1962.

<div align="right">

12

</div>

<div align="right">

Application of Statistical
Design Principles

</div>

12-1   INTRODUCTION

In many design problems the use of sinusoidal, step, or impulse functions as system inputs is inadequate. The designer may design an autopilot that gives extremely good response to a step or a pulse input, but how will this system behave under the influence of atmospheric turbulence? If the system responds rapidly, which means a high gain, then in the presence of turbulence excessive acceleration loads may be imposed on the airframe or the crew. Another application might be in the design of an automatic terrain avoidance system which would enable the aircraft to fly automatically at low levels over rough terrain. The fire control problem also has emphasized the need to evaluate a system under the influence of noise. Here the problem is generated by the desire to detect the target, compute a solution to the fire control problem, and launch the interceptor missile at the maximum range possible. This requires the system to operate accurately under the most adverse conditions, that is, extremely low signal-to-noise ratio.

   All these examples have one thing in common, that is, the response, or lack of response, of the system to a nonanalytical type of input. The atmospheric turbulence, terrain elevation, or radar noise forms a random input that cannot in general be reproduced analytically. True, the response of the terrain avoidance system can be simulated by use of an analog computer employing some typical terrain profile as an input, and the behavior of the autopilot and the fire control system under the influence of their noise inputs (turbulence and radar noise) can be simulated using a noise generator to

furnish the disturbing inputs; however, it would be useful to have an analytical means for predicting the performance of the system to these random inputs during the design phase. This then is the purpose of this chapter, to provide the control system engineer with an analytical means to predict the response of a system to random inputs. To accomplish this it is necessary to obtain the power spectral density of the random input. For this, the input must have certain statistical properties. Thus the first portion of this chapter deals with the basic statistical concepts; next a suitable error criterion is selected, followed by the definition of the correlation function, and finally the power spectral density. The rigorous mathematical derivations of the various statistical parameters are not attempted in this book. For these the reader is referred to Ref. 1 and Chapters 7 and 8 of Ref. 2.

12-2   RANDOM PROCESSES

Before discussing the characteristics of the random process some of the aspects of probability theory are discussed.

In any experiment, the output of which is dependent upon chance, the individual outcome is defined as a "sample point." Thus, in the tossing of a coin, the two outputs, a head and a tail, would be the two sample points; in the throwing of a single die there would be six sample points. All the sample points of a particular experiment make up what is called the "sample space," which consists of all the possible outcomes of the experiment. It is convenient to define a variable whose values over a sample space are determined by the various sample points of a sample space. This variable is referred to as a "random" or "stochastic" variable. In this textbook the term random variable is used. Thus for the throwing of one die, if X is considered the random variable, then X may take on values from 1 to 6 depending upon the outcome of each throw. Associated with each sample point in the sample space there is a "probability" of any event occurring; thus the probability is a measure of the likelihood that an event will occur. The probability is always a real number varying from 0 to $+1$ inclusive. The probability can be expressed mathematically as the ratio of the number of successful outcomes to the total number of outcomes if each outcome is equally likely[3]; thus

$$P(E) = \frac{S}{S + F} \tag{12-1}$$

where S is the number of successful outcomes, F is the number of failures, and $S + F$ is the total number of outcomes, or the number of sample points in the sample space. Using Eq. 12-1 the probability of throwing a 7 on one throw of two dice can be calculated. For this experiment $S = 6$ (the number of combinations making 7) and $S + F = 36$ (the total combinations). Therefore $P(E) = 6/36 = 1/6$.

Thus far in the discussion of probability, the sample space has been considered to have contained a finite number of sample points. This is not generally true in the physical world—for instance, radar noise in a fire control system or atmospheric noise in the form of turbulence. Considering the turbulence further, if a measurement were made of the velocity of the vertical gusts for a given flight path, the magnitude of the gusts would be random and the probability of measuring a gust of exactly 10 ft/sec normally would be zero. However, there would be some probability of experiencing a gust greater than some specified value, and the probability of being subjected to a gust of some velocity other than zero would be one (a certainty). If the random variable X is defined as the instantaneous value of the gusts measured, there will be a certain probability density or distribution function, $f(x)$, such that

$$P(x < X < x + dx) = f(x)\,dx \qquad (12\text{-}2)$$

Equation 12-2 states that the probability that the instantaneous velocity of the gust, as denoted by the random variable X, lies within the range of x to $x + dx$ is equal to the probability density function times the range of values, dx. If it is assumed that the velocity of the vertical gusts follows a so-called normal or Gaussian distribution,[1] then

$$f(x) = \frac{1}{\sigma\sqrt{2\pi}} e^{-(x-m)^2/2\sigma^2} \qquad (12\text{-}3)$$

where m = mean or average value of X, σ = standard deviation, and σ^2 = the variance, the average of $(x - m)^2$.

A plot of Eq. 12-3 for two values of σ is shown in Figure 12-1. The probability density function $f(x)$ must satisfy two conditions:

$$f(x) \geq 0$$

$$\int_{-\infty}^{\infty} f(x)\,dx = 1$$
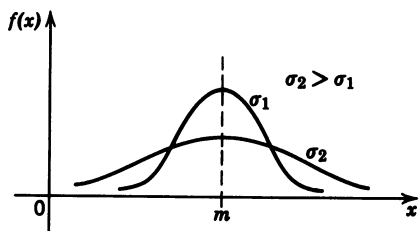
Figure 12-1 *Plot of normal probability density function for two different standard deviations.*
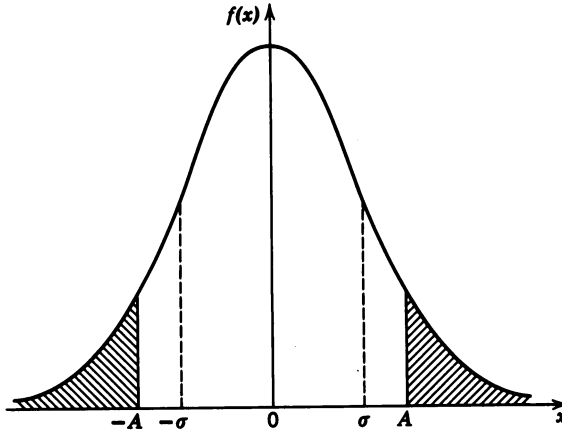
Figure 12-2 Normal probability density function for m = 0.

Returning to the discussion of the vertical wind gusts, if it is assumed that the average value of the gusts over a long flight path is zero, then $m = 0$, and the probability density function will be symmetrical about the $x = 0$ axis, as shown in Figure 12-2. If it is assumed that Figure 12-2 represents the probability density function of the gusts, then to find the probability that the magnitude of the velocity of the gusts is less than some value A (that is, $|X| < A$), it is only necessary to find the area of the unshaded portion under the curve, or mathematically,

$$P(|X| < A) = 2\int_0^A f(x)\, dx \tag{12-4}$$

$$P(|X| < A) = 2\int_0^A \frac{1}{\sigma\sqrt{2\pi}} e^{-(x^2/2\sigma^2)}\, dx \tag{12-5}$$

Let $u = x/\sigma\sqrt{2}$; then $x = u\sigma\sqrt{2}$ and $dx = \sigma\sqrt{2}\, du$. For the upper limit when $x = A$, we find $u = A/\sigma\sqrt{2}$. Substituting these values into Eq. 12-5 yields

$$P(|X| < A) = 2\int_0^{A/\sigma\sqrt{2}} \frac{1}{\sigma\sqrt{2\pi}} e^{-u^2}(\sigma\sqrt{2}\, du) \tag{12-6}$$

Simplifying,

$$P(|X| < A) = \frac{2}{\sqrt{\pi}} \int_0^{A/\sigma\sqrt{2}} e^{-u^2}\, du \tag{12-7}$$

Equation 12-7 is referred to as the "error integral." Values of this integral are tabulated in various handbooks.[4] A sketch of the error integral as a function of the upper limit is shown in Figure 12-3. As the total area under
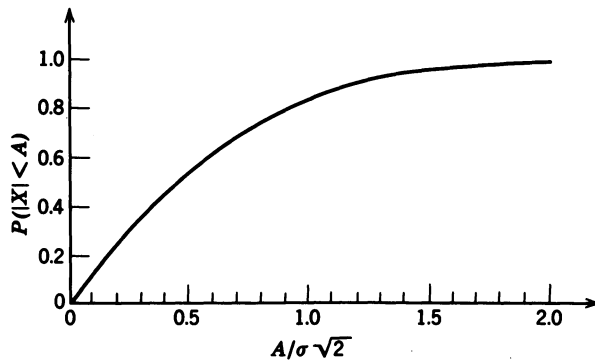
Figure 12-3 The error integral.

the curve of Figure 12-2 is 1, then $P(|X| > A) = 1 - P(|X| < A)$. The function representing the $P(|X| > A)$ is called the "complementary error function."

Having defined some of the basic probability concepts, it is now time to define "random process." A random process is a sample space, or ensemble of time functions, with the individual time functions representing the sample points. Associated with any random process is a series of probability density functions. The so-called "first probability density function" is the probability that the magnitude of any one of the random functions making up the sample space at some time t_1 lies between the two values x_1 and $x_1 + dx_1$. The "second probability density function" is the probability that the magnitude of any one of the random functions at t_1 lies between the two values x_1 and $x_1 + dx_1$, and at time t_2 that it also lies between the two values x_2 and $x_2 + dx_2$. The probability density functions can be continued to even higher orders. A complete set of these probability density functions completely defines the statistical characteristics of the random process. It should be noted that the individual functions of a random process need not be random; for example, the expression $A \cos(\omega t + \phi)$ could represent the sample space, with the randomness arising from the selection of A, ω, and ϕ.

A random process of particular interest is the "stationary random process," one for which the statistical characteristics are independent of the time origin. Thus, the first probability density function is the probability that one of the functions lies between x_1 and $x_1 + dx_1$ at any time; the second probability density function then depends only on the difference between t_1 and t_2, etc. A property of the stationary random process is the "ergodic hypothesis," which assumes that the ensemble averages equal the time averages of a single representative function of the sample space or ensemble. This means that any function making up the random process can be used to represent the ensemble if studied for a sufficient length of time. It must be remembered that the ergodic hypothesis applies only to stationary random processes; in the work to follow, it is assumed that the random process is a stationary, ergodic random process.

12-3 MEAN-SQUARE ERROR

Having defined the random process, it is now important to select a measure of the error to be minimized, as this determines which statistical characteristics of the input are important. The measure of the error chosen by Wiener is the mean-square error, which is defined as

$$\overline{e^2} = \lim_{T \to \infty} \frac{1}{2T} \int_{-T}^{T} [f_o(t) - f_d(t)]^2 \, dt \qquad (12\text{-}8)$$

where $f_o(t)$ is the actual output and $f_d(t)$ is the desired output. For most autopilots the desired output would be the command input. The decision to use the mean-square error as the error criterion is not meant to imply that this is the optimum error measure to use. In fact, as the square of the error is used, it places more emphasis on large errors than on small errors. This point is discussed in considerable detail in Ref. 2, pp. 413–415. However, as the mean-square error can be expressed easily in terms of certain statistical characteristics, such as the correlation function or the power spectral density, this error criterion is used in spite of the shortcomings mentioned.

12-4 AUTOCORRELATION FUNCTION

An important statistical characteristic of any signal is the autocorrelation function, which is a measure of the predictability of the signal at some future time based upon the present knowledge of the signal. The autocorrelation function is defined as (Ref. 2, p. 429)

$$\phi_{xx}(\tau) = \lim_{T \to \infty} \frac{1}{2T} \int_{-T}^{T} f_x(t) f_x(t + \tau) \, dt$$

$$= \lim_{T \to \infty} \frac{1}{2T} \int_{-T}^{T} f_x(t - \tau) f_x(t) \, dt \qquad (12\text{-}9)$$

which is simply the time average of the products of the values of the function, τ sec apart, as τ is allowed to vary from zero to some large value. The first expression of Eq. 12-9 indicates that the function is measured at some time t and at some later time $t + \tau$. The second expression signifies that the values of the function are taken at some time t and at an earlier time $t - \tau$; in both cases the values of the function are taken τ sec apart, whence the equivalence of the two expressions.

An examination of Eq. 12-9 indicates that if $\tau = 0$, then

$$\phi_{xx}(0) = \lim_{T \to \infty} \frac{1}{2T} \int_{-T}^{T} [f_x(t)]^2 \, dt$$

which is the mean-square value of the function as defined by Eq. 12-8. Also, if the function contains no DC or periodic component, then, in the limit(as τ approaches ∞, $\phi_{xx}(\tau)$ approaches zero; that is to say, for τ large there is no correlation between the present value of the signal and its future value.) Finally, it can be shown mathematically (Ref. 2, p. 431) that $\phi_{xx}(0) \geq \phi_{xx}(\tau)$.

To further illustrate some of the properties of the autocorrelation function, the correlation function of a sine wave and a rectangular pulse is evaluated.

Example 1. A Sine Wave. Let

$$f_\psi(t) = A \sin(\omega t + \psi) \tag{12-10}$$

where ψ is a random phase angle. Then the autocorrelation function for $f_\psi(t)$ is

$$\phi_{\psi\psi}(\tau) = \lim_{T \to \infty} \frac{1}{2T} \int_{-T}^{T} A \sin(\omega t + \psi) \cdot A \sin[\omega(t + \tau) + \psi] \, dt$$

Since the signal is periodic, it is only necessary to average over one period; thus

$$\phi_{\psi\psi}(\tau) = \frac{\omega A^2}{2\pi} \int_0^{2\pi/\omega} \sin(\omega t + \psi) \sin(\omega t + \psi + \omega\tau) \, dt \tag{12-11}$$

To simplify the integral, let $u = \omega t + \psi$; then $du = \omega \, dt$, or $dt = du/\omega$. The limits of integration are now $u = \psi$ for $t = 0$ and $u = 2\pi + \psi$ for $t = 2\pi/\omega$. With these substitutions Eq. 12-11 becomes

$$\phi_{\psi\psi}(\tau) = \frac{A^2}{2\pi} \int_\psi^{2\pi + \psi} \sin u \sin(u + \omega\tau) \, du \tag{12-12}$$

Expanding $\sin(u + \omega\tau)$ and combining yields

$$\phi_{\psi\psi}(\tau) = \frac{A^2}{2\pi} \int_\psi^{2\pi + \psi} (\sin^2 u \cos \omega\tau + \sin u \cos u \sin \omega\tau) \, du$$

The $\sin u \cos u$ can be replaced by $\frac{1}{2} \sin 2u$; making this substitution and integrating yields

$$\phi_{\psi\psi}(\tau) = \frac{A^2}{2\pi} \left[\cos \omega\tau \left(\frac{u}{2} - \frac{\sin 2u}{4} \right) \Big|_\psi^{2\pi + \psi} - \frac{1}{4} \sin \omega\tau \cos 2u \Big|_\psi^{2\pi + \psi} \right]$$
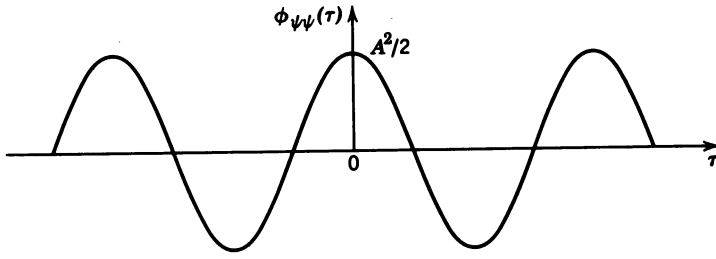
Figure 12-4 *Autocorrelation function of a sinusoidal signal.*

Substitution of the limits and simplification yields

$$\phi_{\psi\psi}(\tau) = \frac{A^2}{2}\cos\omega\tau \qquad (12\text{-}13)$$

A sketch of Eq. 12-13 is presented in Figure 12-4.

As mentioned earlier in this section, the value of the correlation function for $\tau = 0$ is the mean-square value of the sine wave.

Example 2. A Rectangular Pulse. The autocorrelation function of the rectangular pulse shown in Figure 12-5 is determined here. The autocorrelation function is given by

$$\phi_{aa}(\tau) = \lim_{T\to\infty}\frac{1}{2T}\int_{-T}^{T} f_a(t)f_a(t+\tau)\,dt \qquad (12\text{-}14)$$

As the function is zero for $|t| > b$, the averaging only need be performed over the interval of $-b$ to b. Also the integrand is zero except where the two functions $f_a(t)$ and $f_a(t+\tau)$ overlap; therefore Eq. 12-14 becomes

$$\phi_{aa}(\tau) = \frac{1}{2b}\int_{-b}^{b-|\tau|} a^2\,dt = \frac{a^2}{2b}t\Big|_{-b}^{b-|\tau|}$$
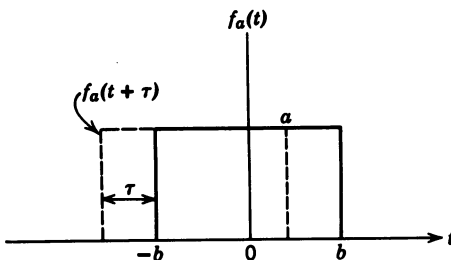
Figure 12-5 *Rectangular pulse.*

$$f_a(t) = \begin{cases} a & -b < t < b \\ 0 & |t| > b \end{cases}$$

Figure 12-6 *Autocorrelation function for the rectangular pulse shown in Figure 12-5.*
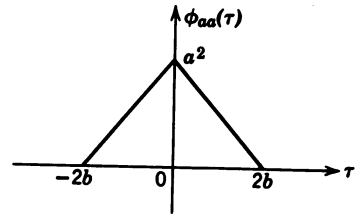
Substituting the limits yields

$$\phi_{aa}(\tau) = \frac{a^2}{2b}(b - |\tau| + b) = a^2\left(1 - \frac{|\tau|}{2b}\right) \tag{12-15}$$

The correlation function given by Eq. 12-15 is shown in Figure 12-6. The autocorrelation function shown in Figure 12-6 corresponds to several other time functions. Two of them are shown in Figure 12-7. The wave in Figure 12-7(a) has a constant period of $2b$ but a random amplitude. The value of the autocorrelation function for $\tau = 0$ is dependent only on, and equal to, the variance of the assumed amplitude distribution function (Ref. 2, pp. 433–435). The wave shown in Figure 12-7(b) has a constant amplitude of $\pm a$ but a random period of $n(2b)$, where n is a purely random variable.

(a)

(b)
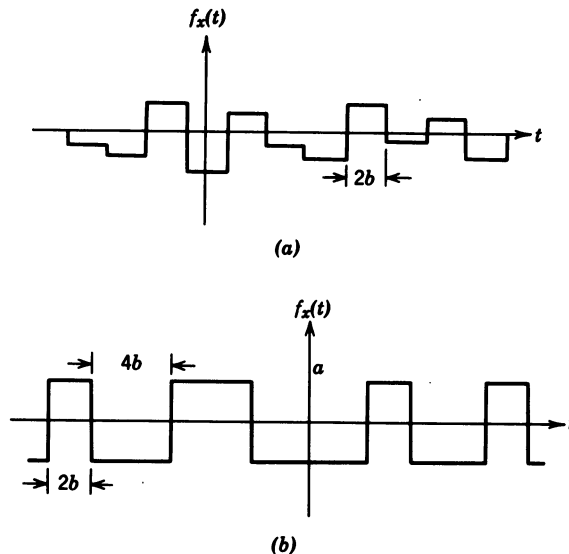
Figure 12-7 *Random square waves with the autocorrelation function shown in Figure 12-6.*

These two examples illustrate some additional properties of the autocorrelation function:

1. The autocorrelation function is an even function.
2. The autocorrelation function will contain the same periodic components as the basic signal.

One additional property not illustrated by the examples is that if the basic signal contains a DC component, the autocorrelation function approaches a constant nonzero value as τ approaches infinity.

12-5 CROSS-CORRELATION FUNCTION

Thus far the autocorrelation function of a single signal has been considered; however, in practice the input may consist of the desired signal plus noise. If the input is designated as $f_i(t) = f_s(t) + f_n(t)$, where $f_s(t)$ and $f_n(t)$ represent the signal and noise components of the input respectively, the autocorrelation function of the input can be obtained from Eq. 12-9:

$$\phi_{ii}(\tau) = \lim_{T \to \infty} \frac{1}{2T} \int_{-T}^{T} f_i(t) f_i(t + \tau) \, dt \tag{12-16}$$

Substituting for $f_i(t)$ and $f_i(t + \tau)$ yields

$$\phi_{ii}(\tau) = \lim_{T \to \infty} \frac{1}{2T} \int_{-T}^{T} [f_s(t) + f_n(t)][f_s(t + \tau) + f_n(t + \tau)] \, dt \tag{12-17}$$

Expanding the integrand yields

$$\phi_{ii}(\tau) = \lim_{T \to \infty} \frac{1}{2T} \int_{-T}^{T} f_s(t) f_s(t + \tau) \, dt + \lim_{T \to \infty} \frac{1}{2T} \int_{-T}^{T} f_s(t) f_n(t + \tau) \, dt$$
$$+ \lim_{T \to \infty} \frac{1}{2T} \int_{-T}^{T} f_n(t) f_s(t + \tau) \, dt + \lim_{T \to \infty} \frac{1}{2T} \int_{-T}^{T} f_n(t) f_n(t + \tau) \, dt \tag{12-18}$$

The first and fourth terms of Eq. 12-18 are the autocorrelation functions of the signal and the noise, respectively. The other two terms are the cross-correlation functions of the signal and the noise. The cross-correlation function is defined as

$$\phi_{sn}(\tau) = \lim_{T \to \infty} \frac{1}{2T} \int_{-T}^{T} f_s(t) f_n(t + \tau) \, dt$$

or

$$\phi_{ns}(\tau) = \lim_{T \to \infty} \frac{1}{2T} \int_{-T}^{T} f_n(t) f_s(t + \tau) \, dt \tag{12-19}$$

The cross-correlation function is a measure of the dependence of one signal upon the other. If the two signals are from independent sources, the cross-correlation functions are zero, that is $\phi_{sn}(\tau) = \phi_{ns}(\tau) = 0$, and the signals are said to be "uncorrelated." Thus the correlation function of the sum of two uncorrelated signals is simply the sum of the autocorrelation functions for each signal.

12-6 POWER SPECTRAL DENSITY

The correlation function describes the statistical properties of the signal in the time domain. It is useful, as will be seen in this section, to be able to work in the frequency domain. The Fourier transform is used to go from the time domain to the frequency domain. Taking the Fourier transform of the correlation function yields the power spectral density, denoted by

$$\Phi_{xx}(\omega) = \int_{-\infty}^{\infty} \phi_{xx}(\tau) e^{-j\omega\tau}\, d\tau \tag{12-20}$$

The autocorrelation function can then be obtained by taking the inverse Fourier transform of the power spectral density:

$$\phi_{xx}(\tau) = \frac{1}{2\pi} \int_{-\infty}^{\infty} \Phi_{xx}(\omega) e^{+j\omega\tau}\, d\omega \tag{12-21}$$

Now the autocorrelation function for $\tau = 0$ has been shown to yield the mean-square value. If the signal is a voltage, the mean-square value of the voltage is proportional to the average power. For $\tau = 0$, Eq. 12-21 reduces to

$$\phi_{xx}(0) = \frac{1}{2\pi} \int_{-\infty}^{\infty} \Phi_{xx}(\omega)\, d\omega \tag{12-22}$$

If it is assumed that the voltage is dissipated across a 1-ohm resistor, the average power in the signal is given by

$$P_{(avg)} = \frac{1}{2\pi} \int_{-\infty}^{\infty} \Phi_{xx}(\omega)\, d\omega \tag{12-23}$$

which is the integral of the area under the power spectral density curve; thus the power spectral density is a measure of the power contained in the signal as a function of frequency.

Before looking at some examples of the power spectral density, we simplify Eq. 12-20. We have

$$e^{-j\omega\tau} = \cos \omega\tau - j \sin \omega\tau \tag{12-24}$$

Substituting Eq. 12-24 into Eq. 12-20 yields

$$\Phi_{xx}(\omega) = \int_{-\infty}^{\infty} \phi_{xx}(\tau)(\cos \omega\tau - j \sin \omega\tau) \, d\tau$$

Expanding the integrand,

$$\Phi_{xx}(\omega) = \int_{-\infty}^{\infty} \phi_{xx}(\tau)\cos \omega\tau \, d\tau - j \int_{-\infty}^{\infty} \phi_{xx}(\tau)\sin \omega\tau \, d\tau \qquad (12\text{-}25)$$

As shown in Section 12-4, the autocorrelation function is an even function and the sine function is an odd function; therefore, the second integral of Eq. 12-25 is the integral of an odd function from minus infinity to plus infinity, and is zero. Equation 12-20 then reduces to

$$\Phi_{xx}(\omega) = \int_{-\infty}^{\infty} \phi_{xx}(\tau)\cos \omega\tau \, d\tau \qquad (12\text{-}26)$$

The power spectral densities of two different signals are derived in the following examples.

Example 1. A common noise used to evaluate the performance of a system under the influence of noise is "white noise." By definition white noise has a constant power spectral density, or $\Phi_{nn}(\omega) = $ constant. It is impossible to obtain a noise that has a constant frequency spectrum from minus infinity to plus infinity, because the signal would contain an infinite amount of power. However, it is possible to obtain a noise signal with a flat frequency spectrum over a range of frequencies wider than the bandwidth of the system being analyzed. This then is considered white noise for the particular application. Having defined the power spectral density of white noise, we find that the autocorrelation function for white noise is an impulse at $\tau = 0$. Then $\phi_{nn}(\tau) = u_0(t)$. The power spectral density is then

$$\Phi_{nn}(\omega) = \int_{-\infty}^{\infty} \phi_{nn}(\tau)e^{-j\omega\tau} \, d\tau \qquad (12\text{-}27)$$

but if $\phi_{nn}(\tau)$ is an impulse at $\tau = 0$ and at 0 for all other values of τ, then

$$\Phi_{nn}(\omega) = \int_{-0}^{+0} \phi_{nn}(\tau) \, d\tau$$

Since $\Phi_{nn}(\omega)$, the area under the impulse, is equal to a constant as already stated, the autocorrelation function for white noise is indeed an impulse at $\tau = 0$.

Example 2. This example is an illustration of how to obtain the power spectral density of the square wave for which the autocorrelation function was found earlier in this chapter. From Eq. 12-15

$$\phi_{aa}(\tau) = a^2 \left(1 - \frac{|\tau|}{2b}\right) \qquad \text{for} \quad -2b < \tau < 2b$$

and $\phi_{aa}(\tau)$ is zero for other values of τ. Substituting into Eq. 12-26 yields

$$\Phi_{aa}(\omega) = \int_{-2b}^{2b} a^2 \left(1 - \frac{|\tau|}{2b}\right) \cos \omega\tau \, d\tau \qquad (12\text{-}28)$$

Simplifying and dropping the absolute magnitude signs yields

$$\Phi_{aa}(\omega) = \frac{a^2}{b} \int_0^{2b} (2b - \tau) \cos \omega\tau \, d\tau \qquad (12\text{-}29)$$

Expanding,

$$\Phi_{aa}(\omega) = \frac{a^2}{b} \left[\int_0^{2b} 2b \cos \omega\tau \, d\tau - \int_0^{2b} \tau \cos \omega\tau \, d\tau \right]$$

Integrating,

$$\Phi_{aa}(\omega) = \frac{a^2}{b} \left[\frac{2b}{\omega} \sin \omega\tau \Big|_0^{2b} - \left(\frac{1}{\omega^2} \cos \omega\tau + \frac{\tau}{\omega} \sin \omega\tau \right)\Big|_0^{2b} \right]$$

Substituting the limits,

$$\Phi_{aa}(\omega) = \frac{a^2}{b} \left(\frac{2b}{\omega} \sin 2\omega b - \frac{\cos 2\omega b - 1}{\omega^2} - \frac{2b}{\omega} \sin 2\omega b \right)$$

or

$$\Phi_{aa}(\omega) = \frac{2a^2}{b} \left(\frac{1 - \cos 2\omega b}{2\omega^2} \right) \qquad (12\text{-}30)$$

But $\sin^2(\alpha/2) = (1 - \cos \alpha)/2$. Let $\alpha = 2\omega b$; then Eq. 12-30 becomes

$$\Phi_{aa}(\omega) = \frac{2a^2}{b} \left(\frac{\sin^2 \omega b}{\omega^2} \right) = 2a^2 b \left(\frac{\sin^2 \omega b}{\omega^2 b^2} \right)$$

Therefore,

$$\Phi_{aa}(\omega) = 2a^2 b \left(\frac{\sin \omega b}{\omega b} \right)^2 \tag{12-31}$$

As a check, the average power contained in the rectangular pulse is determined:

$$P_{(avg)} = \frac{1}{2\pi} \int_{-\infty}^{\infty} 2a^2 b \left(\frac{\sin \omega b}{\omega b} \right)^2 d\omega \tag{12-32}$$

Let $x = \omega b$; then $dx = b \, d\omega$. Substituting, Eq. 12-32 becomes

$$P_{(avg)} = \frac{a^2}{\pi} \int_{-\infty}^{\infty} \frac{\sin^2 x}{x^2} dx = \frac{2a^2}{\pi} \int_{0}^{\infty} \frac{\sin^2 x}{x^2} dx$$

but

$$\int_{0}^{\infty} \frac{\sin^2 x}{x^2} dx = \frac{\pi}{2}$$

Substituting,

$$P_{(avg)} = \frac{2a^2}{\pi} \left(\frac{\pi}{2} \right) = a^2$$

as before.

12-7 APPLICATION OF STATISTICAL DESIGN PRINCIPLES

The goal of this chapter is the determination of the behavior of a physical system to random inputs. This section is devoted to the determination of the mean-square error if the power spectral density of the input and the system transfer function are known.

First, let $G(s)$ denote the transfer function between the input and the output; then if s is replaced by $j\omega$ and the result denoted by $G(j\omega)$, and if the input and output are voltages, then $e_{(out)} = e_{(in)} G(j\omega)$. Squaring, $e_{(out)}^2 = e_{(in)}^2 |G(j\omega)|^2$, where $|G(j\omega)|^2$ signifies the product of the complex conjugates of $G(j\omega)$. Now e^2 is proportional to power; therefore the power spectral density of the output can be related to the power spectral density of the input in the same manner. Thus

$$\Phi_{oo}(\omega) = \Phi_{ii}(\omega) |G(j\omega)|^2 \tag{12-33}$$

where $\Phi_{oo}(\omega)$ is the power spectral density of the output and $\Phi_{ii}(\omega)$ is the
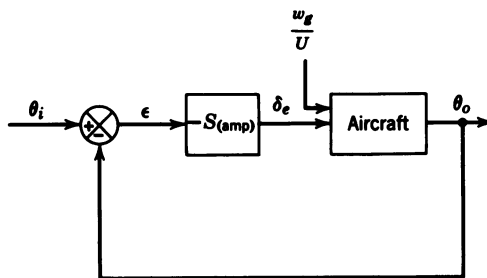
Figure 12-8   Simplified pitch control system.

power spectral density of the input. The input may be the desired input or a noise input. From Eq. 12-22 $\phi_{xx}(0) = (1/2\pi)\int_{-\infty}^{\infty}\Phi_{xx}(\omega)\,d\omega$. But $\phi_{xx}(0)$ is the mean-square value of the signal; therefore

$$\overline{e_o^2} = \frac{1}{2\pi}\int_{-\infty}^{\infty}\Phi_{oo}(\omega)\,d\omega \tag{12-34}$$

Substituting for $\Phi_{oo}(\omega)$ from Eq. 12-33 yields

$$\overline{e_o^2} = \frac{1}{2\pi}\int_{-\infty}^{\infty}\Phi_{ii}(\omega)|G(j\omega)|^2\,d\omega \tag{12-35}$$

where $\overline{e_o^2}$ is the mean-square value of the output.

The mean-square value of the pitch attitude for an aircraft with a simple control system under the influence of turbulence is now determined using Eq. 12-35. The control system is shown in Figure 12-8. The aircraft is represented by the short-period approximation. The elevator servo dynamics have been eliminated for simplicity, and a negative-gain amplifier is used for the variable gain. The turbulence input is shown as w_g/U, where w_g is the magnitude of the vertical gust. The effect of the gust is to change the angle of attack of the aircraft; and since an updraft causes a positive change in the angle of attack, $'\alpha_g = -w_g/U$, where w_g is considered negative for an updraft. The required transfer functions can be obtained from Eq. 1-128 after adding $C_{z_\alpha}'\alpha_g$ and $C_{m_\alpha}'\alpha_g$ to the right-hand sides of the force and moment equations, respectively. The equations of motion then become

$$(13.78s + 4.46)'\alpha(s) - 13.78s\theta(s) = -0.246\delta_e(s) - 4.46'\alpha_g(s)$$

$$(0.055s + 0.619)'\alpha(s) + (0.514s^2 + 0.4s)\theta(s)$$

$$= -0.71\delta_e(s) - 0.619'\alpha_g(s) \tag{12-36}$$

The transfer function then for θ output and δ_e input is

$$\frac{\theta_o(s)}{\delta_e(s)} = \frac{-1.38(s+0.309)}{s(s^2+1.21s+1.46)} \qquad (12\text{-}37)$$

and for θ output and $'\alpha_g$ input,

$$\frac{\theta_o(s)}{'\alpha_g(s)} = \frac{-1.03}{s^2+1.21s+1.46} \qquad (12\text{-}38)$$

The closed loop transfer function for $'\alpha_g$ input to θ output is of the form

$$\frac{\theta_o(s)}{'\alpha_g(s)}\bigg]_{\text{CL}} = \frac{\theta_o(s)/'\alpha_g(s)}{1+S_{(\text{amp})}[\theta_o(s)/\delta_e(s)]} \qquad (12\text{-}39)$$

Substituting the appropriate transfer functions and simplifying yields

$$\frac{\theta_o(s)}{'\alpha_g(s)}\bigg]_{\text{CL}} = \frac{-1.03s}{s^3+1.21s^2+(1.46+1.38S)s+0.426S} \qquad (12\text{-}40)$$

where S signifies $S_{(\text{amp})}$. From Eq. 12-35,

$$\overline{\theta_o^2} = \frac{1}{2\pi}\int_{-\infty}^{\infty}\Phi_{gg}(\omega)\left|\frac{\theta_o(j\omega)}{'\alpha_g(j\omega)}\right|^2 d\omega \qquad (12\text{-}41)$$

where $\Phi_{gg}(\omega)$ is the power spectral density of the gusts. The representation of the power spectral density was obtained from Ref. 5, p. 28, and is given by

$$\Phi_{gg}(\omega) = \frac{2\tau_g'\overline{\alpha_g^2}}{1+\tau_g^2\omega^2} \qquad (12\text{-}42)$$

where $'\overline{\alpha_g^2}$ is the mean-square value of the gusts and τ_g the time constant associated with the gusts. A τ_g of 2 sec is used for this analysis; then Eq. 12-42 reduces to

$$\Phi_{gg}(\omega) = \frac{'\overline{\alpha_g^2}}{\omega^2+0.25} \qquad (12\text{-}43)$$

Substituting Eqs. 12-40 and 12-43 into Eq. 12-41, after replacing s by $j\omega$,

yields

$$\frac{\overline{\theta_o^2}}{'\alpha_g^2} = \frac{1}{2\pi} \int_{-\infty}^{\infty} \frac{1.06\omega^2 \, d\omega}{(\omega^2 + 0.25)\left| -j\omega^3 - 1.21\omega^2 + (1.46 + 1.38S)j\omega + 0.426S \right|^2} \tag{12-44}$$

Breaking $\omega^2 + 0.25$ into its two complex conjugates and multiplying the $j\omega + 0.5$ term by the rest of the denominator yields

$$\frac{\overline{\theta_o^2}}{'\alpha_g^2} = \frac{1.06}{2\pi} \int_{-\infty}^{\infty} \frac{\omega^2 \, d\omega}{\left| \omega^4 - 1.71j\omega^3 - (2.07 + 1.38S)\omega^2 + (0.73 + 1.116S)j\omega + 0.213S \right|^2} \tag{12-45}$$

The method for evaluating the integral contained in Eq. 12-45 can be found in many references, and is repeated here (see Ref. 1, pp. 395–397). It should be noted in the following equations that $g_n(\omega)$ contains only even powers of ω and that the denominator is written as the product of the complex conjugates; also that $h_n(\omega)$ is the complex conjugate made up of $+ j\omega$. If

$$I_n = \frac{1}{2\pi j} \int_{-\infty}^{\infty} \frac{g_n(\omega) \, d\omega}{h_n(\omega) h_n(-\omega)} \tag{12-46}$$

$$h_n(\omega) = a_0 \omega^n + a_1 \omega^{n-1} + \cdots + a_n \tag{12-47}$$

where

$$g_n(\omega) = b_0 \omega^{2n-2} + b_1 \omega^{2n-4} + \cdots + b_{n-1} \tag{12-48}$$

and n is half the highest power of the denominator (n for h_n and g_n is the same for a particular problem). Then

$$I_n = \frac{(-1)^{n+1}}{2a_0} \frac{N_n}{D_n} \tag{12-49}$$

where

$$D_n = \begin{vmatrix} a_1 & a_0 & 0 & 0 & \cdots & 0 \\ a_3 & a_2 & a_1 & a_0 & \cdots & 0 \\ a_5 & a_4 & a_3 & a_2 & \cdots & 0 \\ \vdots & \vdots & \vdots & \vdots & & \vdots \end{vmatrix}$$

:

(this must be a square nth-order determinant), and N_n is D_n with the first column $(a_1, a_3, a_5, \dots)$ replaced by $(b_0, b_1, b_2, \dots, b_{n-1})$. But

$$\overline{e^2} = \frac{1}{2\pi} \int_{-\infty}^{\infty} \frac{g_n(\omega)\, d\omega}{h_n(\omega) h_n(-\omega)}$$

Therefore,

$$\overline{e^2} = jI_n$$

For this problem $n = 4$, and comparing the denominator of Eq. 12-45 with Eq. 12-47,

$$a_0 = 1$$
$$a_1 = -1.71j$$
$$a_2 = -(2.07 + 1.38S)$$
$$a_3 = (0.73 + 1.116S)j$$
$$a_4 = 0.213S$$

Forming D_n,

$$D_n = \begin{vmatrix} -1.71j & 1 & 0 & 0 \\ (0.73+1.116S)j & -(2.07+1.38S) & -1.71j & 1 \\ 0 & 0.213S & (0.73+1.116S)j & -(2.07+1.38S) \\ 0 & 0 & 0 & 0.213S \end{vmatrix}$$

Expanding and simplifying yields

$$D_n = -0.213S(1.39S^2 + 3.41S + 2.05) \tag{12-50}$$

Comparing the numerator of Eq. 12-45 with Eq. 12-48,

$$b_0 = 0$$
$$b_1 = 0$$
$$b_2 = 1$$
$$b_3 = 0$$

Forming N_n,

$$N_n = \begin{vmatrix} 0 & 1 & 0 & 0 \\ 0 & -(2.07+1.38S) & -1.71j & 1 \\ 1 & 0.213S & (0.73+1.116S)j & -(2.07+1.38S) \\ 0 & 0 & 0 & 0.213S \end{vmatrix}$$

Expanding and simplifying yields

$$N_n = -1.71j(0.213S) \tag{12-51}$$

Substituting Eqs. 12-50 and 12-51 into Eq. 12-49 yields

$$I_n = \frac{(-1)^5(+1.71j)}{2(1.39S^2 + 3.41S + 2.05)} \tag{12-52}$$

Therefore,

$$\frac{\overline{\theta_o^2}}{\overline{\alpha_g^2}} = \frac{0.855}{1.39S^2 + 3.41S + 2.05} \tag{12-53}$$

which gives the ratio of the mean-square error of the output to the mean-square value of the vertical gusts. From Eq. 12-53 it can be seen that increasing the amplifier gain reduces the response of the aircraft to the gusts. However, increasing the gain decreases the damping. This is one disadvantage of using the mean square as an error criterion; it tends to yield a lightly damped oscillatory system due to the dependence upon large errors.

12-8 ADDITIONAL APPLICATIONS OF STATISTICAL DESIGN PRINCIPLES

Another important application of statistical design principles is the use of cross-correlation techniques to experimentally determine the transfer function of a control system (Ref. 2, pp. 437–438). This can solve the identification problem inherent in some types of self-adaptive control systems. To accomplish this, white noise is added to the input of the system, and then the output of the system is cross-correlated with the white noise. A block diagram of the system is shown in Figure 12-9. The cross-correlation between
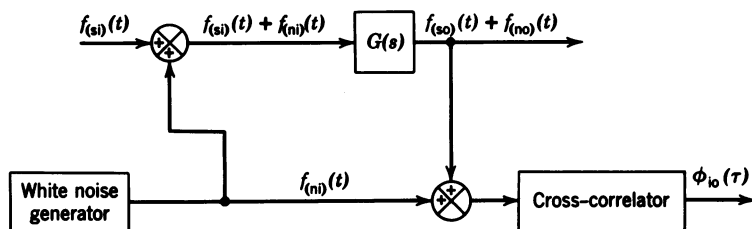
Figure 12-9   *Measurement of the system transfer function using cross-correlation.*

the white noise input and the system output is

$$\phi_{io}(\tau) = \lim_{T \to \infty} \frac{1}{2T} \int_{-T}^{T} f_{(ni)}(t - \tau) f_{(no)}(t) \, dt \qquad (12\text{-}54)$$

as the cross-correlation between the input noise and the system output from the signal is zero (the signal and the noise are uncorrelated).

Now the output of a system can be related to its input in the time domain by use of the convolution integral and the impulse response $g(t)$ of the system—$g(t)$ is the inverse Laplace transform of $G(s)$. Then

$$f_{(no)}(t) = \int_{-\infty}^{\infty} g(x) f_{(ni)}(t - x) \, dx \qquad (12\text{-}55)$$

where x is a dummy variable of integration. Substituting Eq. 12-55 into Eq. 12-54 yields

$$\phi_{io}(\tau) = \lim_{T \to \infty} \frac{1}{2T} \int_{-T}^{T} f_{(ni)}(t - \tau) \, dt \int_{-\infty}^{\infty} g(x) f_{(ni)}(t - x) \, dx \quad (12\text{-}56)$$

Interchanging the order of integration yields

$$\phi_{io}(\tau) = \int_{-\infty}^{\infty} g(x) \, dx \left[\lim_{T \to \infty} \frac{1}{2T} \int_{-T}^{T} f_{(ni)}(t - \tau) f_{(ni)}(t - x) \, dt \right] \quad (12\text{-}57)$$

The factor in the brackets of Eq. 12-57 is the autocorrelation function of $f_{(ni)}(t)$ with argument $\tau - x$,

$$\phi_{nn}(\tau - x) = \lim_{T \to \infty} \frac{1}{2T} \int_{-T}^{T} f_{(ni)}(t - \tau) f_{(ni)}(t - x) \, dt$$

Thus Eq. 12-57 can be written as

$$\phi_{io}(\tau) = \int_{-\infty}^{\infty} g(x) \phi_{nn}(\tau - x) \, dx \qquad (12\text{-}58)$$

But since the noise input is white noise, $\phi_{nn}(\tau - x)$ is an impulse (see Section 12-6), and if $\phi_{nn}(\tau - x)$ is considered the input, $\phi_{io}(\tau)$ will be the impulse response of the system (see Eq. 12-55). Then $\phi_{io}(\tau) = Ag(\tau)$ for $\phi_{nn}(\tau) = Au_0(t)$. Therefore $G(s)$ can be obtained by taking the Laplace transform of $\phi_{io}(\tau)$.

Another application of statistical design principles is the prediction of the reliability of a control system subject to random failures; however, the subject is too broad to be covered here. For information on this the reader is referred to Ref. 6.

12-9 SUMMARY

Some of the more important statistical properties have been discussed in this chapter; the main purpose has been to present a method for determining the mean-square error or output for a given condition. The material here is primarily a condensation of the material given in the references. The reader who wishes to pursue the subject further is referred to the extensive bibliography at the end of Laning and Battin's book (Ref. 1, pp. 427–429). However, the material presented here should give the reader at least a nodding acquaintance with the theory and application of statistical design.

REFERENCES

1. J. H. Laning, Jr., and R. H. Battin, *Random Processes in Automatic Control*, McGraw-Hill Book Co., New York, 1956.
2. J. G. Truxall, *Automatic Feedback Control System Synthesis*, McGraw-Hill Book Co., New York, 1955.
3. *Fundamentals of Design of Piloted Aircraft Flight Control Systems*, BuAer Report AE-61-4, 1952, Sec. 3-4, Chap. 5, Vol. I.
4. E. Jahnke and F. Emde, *Tables of Functions*, 4th ed., Dover Publications, New York, 1945, pp. 24–25.
5. R. C. Seamans, F. A. Barnes, T. B. Garber, and V. W. Howard, "Recent Developments in Aircraft Control," *Journal of the Aeronautical Sciences*, March 1955.
6. G. H. Sandler, *System Reliability Engineering*, Prentice-Hall, Englewood Cliffs, New Jersey, 1963.

13

Pilot Modeling

13-1 INTRODUCTION

The development of a mathematical model for the human pilot has been of
interest to control system engineers for many years. References dated as
early as the late 1950s can be found. Two particularly interesting references
are those by McRuer and Jex,[1] which was published in September 1967, and
by McRuer, Graham, and Krendel,[2] published in January 1967. These
references discuss in considerable depth the many factors that enter into the
human pilot's ability to perform a given task. One characteristic of the pilot
which is not modeled is his ability to adapt to changes in the environment
such as ambient illumination, temperature, vibration, and acceleration.
Another important characteristic is the ability to learn from successive
encounters with the same task. Even with proper training, such factors as
motivation, stress, workload, and fatigue affect the performance of the pilot.
Obviously all of these factors can not be included in a simple mathematical
pilot model. For this reason, when experimental tests are run to generate
data bases to be used for comparison with results obtained using a particular
pilot model, the pilots selected are highly trained and motivated subjects.
Careful analysis of the extensive experimental data that has been collected
using such subjects shows that for controlled elements represented by a pure
gain, a gain with one integration, and a gain with two integrations, the pilot
introduces sufficient lead or lag so that the slope of Bodé plot of the
G_{FL} (product of the plant and pilot model transfer functions) is -1
(-20 dB/decade) in the region of the crossover frequency.[1,3] The crossover

frequency is defined as the frequency at which the phase angle of the Bodé plot is $-180°$. The pilot model (generally referred to as the crossover model) resulting from this analysis, and its application to other plant transfer functions, will be discussed in the next section.

During this same period personnel of the Air Force Flight Dynamics Laboratory (AFFDL) at Wright-Patterson Air Force Base, Ohio, were assigned the task of preparing handling quality specifications for vertical takeoff and landing (VTOL) aircraft. It was found that conventional aircraft specifications could not be easily extended to the unconventional dynamics of VTOL aircraft, especially for the takeoff, hover, and landing phases of operation. To overcome this problem, Ronald Anderson of the AFFDL in June 1969 started work on the development of an alternate method to be used for the specification of the handling qualities for VTOL aircraft.[4] Anderson used the basic crossover model to develop a model to predict pilot ratings for a VTOL aircraft flying in the precision hover mode under gusty conditions. In the resulting model the gains and lead time constants of an X position and pitch angle pilot model were adjusted so as to minimize the pilot rating. The model and the VTOL dynamics were simulated on an analog computer, and the minimization of the pilot rating was accomplished by changing the pilot's parameters between successive runs. The pilot ratings used were based on the Cooper–Harper rating scale, discussed in the Introduction and repeated in Table 13-2 below. The ratings were calculated using an expression that is a function of the weighted rms values of the system errors and the pilot's lead time constant. The effort required for the analog approach led to the development of a digital computer program named the Paper Pilot for predicting pilot rating of a VTOL aircraft in the hover mode.[5] Anderson adapted the Paper Pilot to handle the pitch attitude tracking task for a conventional aircraft.[6] This was followed by a series of Air Force Institute of Technology theses[7-11] that reported on the application of the Paper Pilot concept to various tracking tasks such as pitch, roll, heading, and glide slope. In each case a pilot rating function was developed and the resulting ratings compared with actual pilot ratings performing the same task in a simulator. The results of these studies are discussed in Section 13-3, as well as the use of the pitch Paper Pilot to select the optimal SAS gains for a high-performance aircraft with structural bending.[12]

The applications of the Paper Pilot mentioned so far have dealt with the control of a single parameter (pitch angle, roll angle, or aircraft heading). Pollard in Ref. 13 addressed the multiaxis problem of controlling the pitch angle, roll angle, and aircraft heading simultaneously. His model employed the concepts of both the crossover model and optimal control theory in order to model the decision making capabilities of the pilot. The development of an optimum pilot model for the prediction of the pilot rating of an aircraft's handling qualities is reported in Ref. 14. These two reports will be covered in Section 13-4.

13-2 CROSSOVER MODEL

A block diagram showing the pilot in the loop for a general control system is shown in Figure 13-1. In the figure, $G_c(s)$ represents the transfer function of the vehicle being controlled, and $G_p(s)$ the pilot model, which in its simplest form is[1,2]

$$G_p(s) = \frac{S_p(\tau_L s + 1)e^{-\tau_e s}}{(\tau_I s + 1)} \tag{13-1}$$

where

S_p is the pilot gain,

τ_L is the pilot lead time constant,

τ_I is the pilot lag time constant, and

$\tau_e = \tau_i + \tau_N$ is the pilot's effective time delay, where τ_i is a pure time delay due to transport delays (time for the central nervous system to process sensed data), and τ_N is really a neuromuscular first order lag, but for low excitation frequencies can be included in τ_e.

In Refs. 1 and 2 McRuer refers to the pilot's transfer function as the pilot's describing function, and writes the expression in terms of $j\omega$ rather than the Laplace variable s. He states that without appropriate modifications the model is strictly valid only in the frequency domain. By using the Padé approximation discussed later in this section it is possible to work with the transfer function in the s domain.

The results of tracking tasks, where the human pilot controls the plant model in an attempt to minimize the observed error between a stationary random input signal and the output of the system, have shown that the combination of the pilot and most of the systems shown in Table 13-1 can be represented by[1,3]

$$G_{FL}(s) = G_p(s)G_c(s) = \frac{S_p S_c e^{-\tau_e s}}{s} \tag{13-2}$$
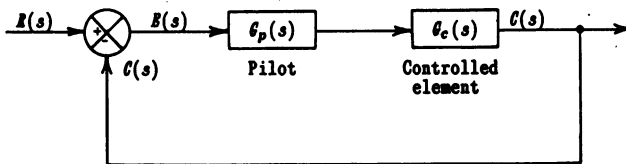
Figure 13-1 Block diagram for general tracking task with pilot in the loop.

In Ref. 1 McRuer defines the G_{FL} transfer function given in Eq. 13-2 as the "crossover model." He states that the simple crossover model is valid only near the crossover frequency, which is the frequency at which the phase angle of the Bodé plot is $-180°$. However, through the years the pilot model as given in Eq. 13-1 has been loosely referred to as the crossover model. This is the case in the reports to be discussed in the next section.

As stated earlier, the Padé approximation can be used to represent the pure time delay represented by $e^{-\tau_e s}$; this approximation is[15]

$$e^x = \lim_{(u+v)\to\infty} \frac{F_{u,v}(x)}{G_{u,v}(x)} \tag{13-3}$$

where

$$F_{u,v}(x) = 1 + \frac{vx}{(u+v)1!} + \frac{v(v-1)x^2}{(u+v)(u+v-1)2!}$$

$$+ \cdots + \frac{v(v-1)\cdots 2\times 1 x^v}{(u+v)(u+v-1)\cdots(u+1)v!} \tag{13-4}$$

$$G_{u,v}(x) = 1 - \frac{ux}{(v+u)1!} + \frac{u(u-1)x^2}{(v+u)(v+u-1)2!}$$

$$+ \cdots + (-1)^u \frac{u(u-1)\cdots 2\times 1 x^u}{(v+u)(v+u-1)\cdots(v+1)u!} \tag{13-5}$$

For the first-order approximation $u = v = 1$; then substituting $-\tau_e s$ for x yields

$$e^{-\tau_e s} = \frac{1-\tau_e s/2}{1+\tau_e s/2} = -\frac{s-2/\tau_e}{s+2/\tau_e} \tag{13-6}$$

Substituting Eq. 13-6 into the G_{FL} expression in Table 13-1 for the proportional through the roll attitude cases yields

$$G_{FL} = -\frac{\omega_c(s-2/\tau_e)}{s(s+2/\tau_e)} \tag{13-7}$$

where $\omega_c = S_p S_c$ is the gain, as will be shown from the root locus. Equation 13-7 can be normalized by multiplying the numerator and denominator by τ_e^2; this yields

$$G_{FL} = -\frac{\tau_e \omega_c(\tau_e s - 2)}{(\tau_e s)(\tau_e s + 2)} \tag{13-8}$$

TABLE 13-1   Variation of Pilot Transfer Functions for Typical Control Element Dynamics[1,3]

Type of Control	G_c	G_p	$G_{FL} = G_p G_c$	Remarks
Proportional	S_c	$\dfrac{S_p e^{-\tau_e s}}{s}$	$\dfrac{S_p S_c e^{-\tau_e s}}{s}$	
Rate or Velocity	$\dfrac{S_c}{s}$	$S_p e^{-\tau_e s}$	$\dfrac{S_p S_c e^{-\tau_e s}}{s}$	
Acceleration	$\dfrac{S_c}{s^2}$	$S_p s e^{-\tau_e s}$	$\dfrac{S_p S_c e^{-\tau_e s}}{s}$	
Roll attitude control using coord. A/C TF	$\dfrac{S_c}{s(\tau s + 1)}$	$S_p(\tau_L s + 1)e^{-\tau_e s}$	$\dfrac{S_p S_c e^{-\tau_e s}}{s}$	$\tau_L \simeq \tau$
Spiral divergence	$\dfrac{S_c}{\tau s - 1}$	$S_p e^{-\tau_e s}$	$\dfrac{S_p S_c e^{-\tau_e s}}{\tau s - 1}$	
Unstable short period	$\dfrac{S_c}{(\tau_1 s + 1)(\tau_2 s - 1)}$	$S_p(\tau_L s + 1)e^{-\tau_e s}$	$\dfrac{S_p S_c e^{-\tau_e s}}{\tau_2 s - 1}$	$\tau_L \simeq \tau_1$
Second order	$\dfrac{S_c \omega_n^2}{s^2 + 2\zeta\omega_n s + \omega_n^2}$	$S_p(\tau_L s + 1)e^{-\tau_e s}$	$\dfrac{S_p S_c \omega_n^2 e^{-\tau_e s}}{s}$	Phugoid, $\omega_n \ll 1/\tau_\theta$, $1/\tau_L \simeq \zeta\omega_n$
		$\dfrac{S_p e^{-\tau_e s}}{\tau_I s + 1}$	$\dfrac{S_c \omega_n^2}{s^2 + 2\zeta\omega_n s + \omega_n^2} \times \dfrac{S_p e^{-\tau_e s}}{\tau_I s + 1}$	Short period, $\omega_n > 1/\tau_\theta$

Then for the root locus, $\sigma = \tau_e \sigma$, $j\omega = j\tau_e \omega$, and the gain is $\tau_e \omega_c$; for the Bodé root locus, $\omega = \tau_e \omega$ and the magnitude is $1/\tau_e \omega_c$. The zero-angle root locus for G_{FL} given in Eq. 13-8 is shown in Figure 13-2, and the Bodé root locus in Figure 13-3.

From Figure 13-2 it can be seen that the normalized root locus crosses the imaginary axis at $\tau_e \omega = 2$. This results from the symmetry of the pole and zero from the Padé approximation and the pole at the origin. Also the gain (the magnitude condition) at the imaginary axis crossing is $\tau_e \omega = \tau_e \omega_c$. From Figure 13-3 the gain margin is 2 (thus $1/\tau_e \omega_c = 0.5$) and the phase margin is 36.87°. From this analysis, if $\tau_e = 0.2$ sec, then $\omega_c = 10$ and the gain for neutral stability is also 10. For $\tau_e = 0.43$ the gain margin is 4.65, which is still reasonable. Included in Ref. 1 are the comparisons of the Bodé plots of Eq. 13-2 with measured pilot–vehicle frequency responses for the proportional through the acceleration plant characteristics from Table 13-1. The results show that for all three cases the two curves compare very well for frequencies below and near the crossover frequency.

The report also states that the crossover model provides a fairly good fit even for mildly unstable plants such as the spiral divergence. For this case
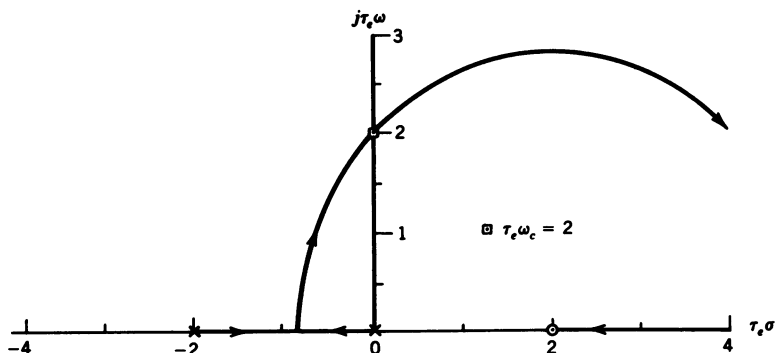
Figure 13-2   Root locus for G_{FL} given in Eq. 13-8.

the normalized forward transfer function for the root locus analysis is

$$G_{FL} = -\frac{\tau_e S_p S_c (\tau_e s - 2)}{\tau(\tau_e s - \tau_e/\tau)(\tau_e s + 2)} \tag{13-9}$$

For the spiral divergence with $1/\tau = 0.004$ (see Section 3-3) and $\tau_e = 0.43$, then $\tau_e/\tau = 0.00172$. With the unstable pole so close to the origin, the root locus will be almost identical to the one shown in Figure 13-2. For a damping ratio of 0.7, the gain is 0.54; then $\tau_e S_p S_c/\tau = 0.54$ and $S_p S_c = 333.95$. Thus it can be seen that a pilot has no problem coping with the spiral divergence mode. The root locus for G_{FL} shown in Eq. 13-9 for the unstable short period is shown in Figure 13-4, and the Bodé root locus in Figure 13-5. In Figure 13-4 the root locus is shown for $\tau_e/\tau = 0.5$ and 1. For $\tau_e/\tau = 1$, the system is always unstable. For $\tau_e = 0.2$ and $\tau_e/\tau = 0.5$ one has $1/\tau = 2.5$. In the analysis of the control system to stabilize an aircraft subject to pitch-up in
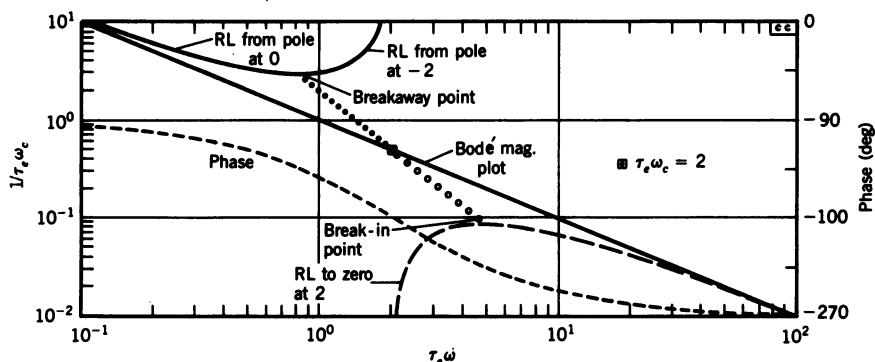
Figure 13-3   Bodé root locus for G_{FL} given in Eq. 13-8.
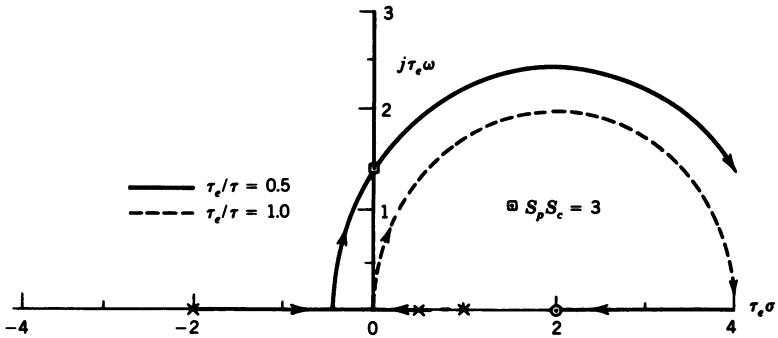
Figure 13-4 *Root locus for G_{FL} for unstable short-period plant (Eq. 13-9) for $\tau_e/\tau = 0.5$ and 1.*

Section 2-2, the unstable short-period pole was located at $s = 2.9$. The rate damping loop with $S_{(\text{rg})} = 0.527$ moved this pole to $s = 1.5$. A pilot with $\tau_e = 0.2$ would be able to stabilize this aircraft. A slower pilot with $\tau_e = 0.43$ could cope with an unstable pole at $s = 1.16$, but he would not be able to stabilize the aircraft with pitch-up unless the rate feedback gain were increased. From Figure 13-5, for $\tau_e / \tau = 0.5$ the gain margin is 3.

For the case where the controlled element has second-order dynamics such as the phugoid, short period, and Dutch roll, the pilot's compensation depends on the frequency of the second-order response. For a phugoid with a natural frequency of 0.073 rad/sec and a damping ratio of 0.032 (see Section 1-8), the value of $\zeta \omega_n$ is 0.0023. For a pilot's lead time constant τ_L of $1/0.0023$, the root locus would again be almost the same as the one shown in Figure 13-2. For higher-frequency second-order dynamics such as the short
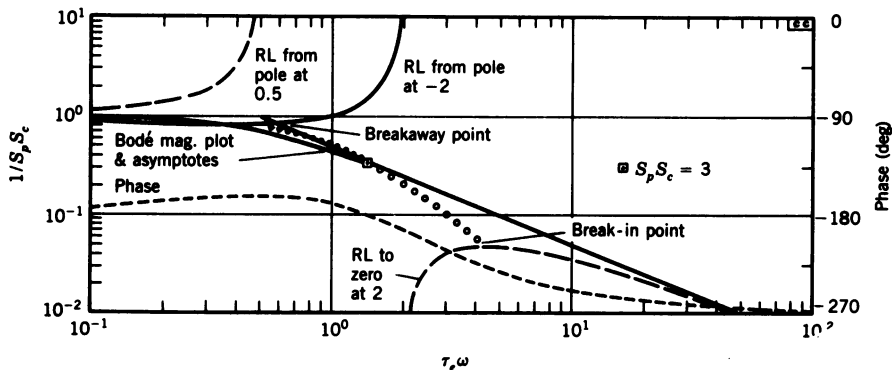
Figure 13-5 *Bodé root locus for G_{FL} for unstable short-period plant (Eq. 13-9) for $\tau_e/\tau = 0.5$.*
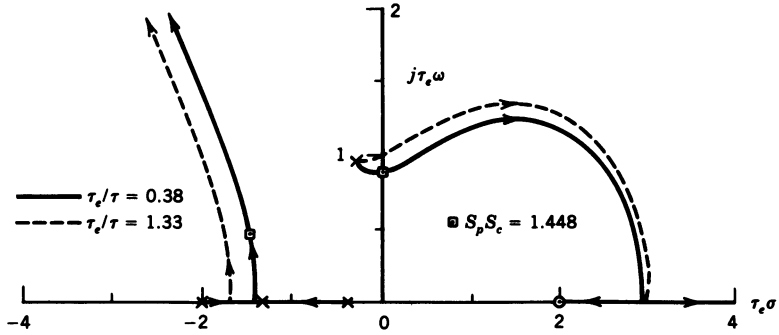
Figure 13-6 Root locus for G_{FL} for second-order plant (Eq. 13-11) for normalized pilot lag $\tau_e/\tau_I = 0.38$ and 1.33.

period and Dutch roll the G_{FL} is

$$G_{FL} = \frac{S_p S_c \omega_n^2 (s - 2/\tau_e)}{\tau_I (s + 1/\tau_I)(s + 2/\tau_e)(s^2 + 2\zeta\omega_n s + \omega_n^2)} \qquad (13\text{-}10)$$

Multiplying Eq. 13-10 by τ_e^4 to normalize the equation yields

$$G_{FL} = \frac{-S_p S_c \tau_e (\tau_e \omega_n)^2 (\tau_e s - 2)}{\tau_I (\tau_e s + \tau_e/\tau_I)(\tau_e s + 2)\left[(\tau_e s)^2 + (2\zeta\tau_e\omega_n)\tau_e s + (\tau_e\omega_n)^2\right]} \qquad (13\text{-}11)$$

For the normalized root locus values must be selected for $\tau_e\omega_n$, ζ, and τ_e/τ_I. A minimum value of 0.2 is reasonable for τ_e; then for $\omega_n = 5$ rad/sec, $\tau_e\omega_n = 1$. Selecting a value of 0.3 for ζ results in $\zeta\tau_e\omega_n = 0.3$. To decide on the value of the pilot's normalized inverse lag time constant τ_e/τ_I it is necessary to plot the other poles and zeros in the complex plane and then, using the angle condition along the imaginary axis, find a range of locations for the lag compensator pole. Using this technique, the values 0.38 and 1.33 were chosen for τ_e/τ_I. The root locus for G_{FL} given in Eq. 13-11 is plotted in Figure 13-6 for both values of τ_e/τ_I, and the Bodé root locus is plotted in Figure 13-7 for $\tau_e/\tau_I = 0.38$. For $\tau_e/\tau_I = 0.38$ the gain margin is 1.448 (3.2 dB), and for $\tau_e/\tau_I = 1.33$ the gain margin is 0.75 (-2.5 dB). For the lower value of τ_e/τ_I (for $\tau_e = 0.2$) we have $1/\tau_I = 1.9$, which is entirely reasonable. If the pilot introduces the normalized lead/lag compensator

$$G_{(\text{comp})} = \frac{\tau_L(\tau_e s + \tau_e/\tau_L)}{\tau_I(\tau_e s + \tau_e/\tau_I)} = \frac{10(\tau_e s + 1)}{\tau_e s + 10} \qquad (13\text{-}12)$$

then the angle of departure from the upper complex pole is 86.3° and the
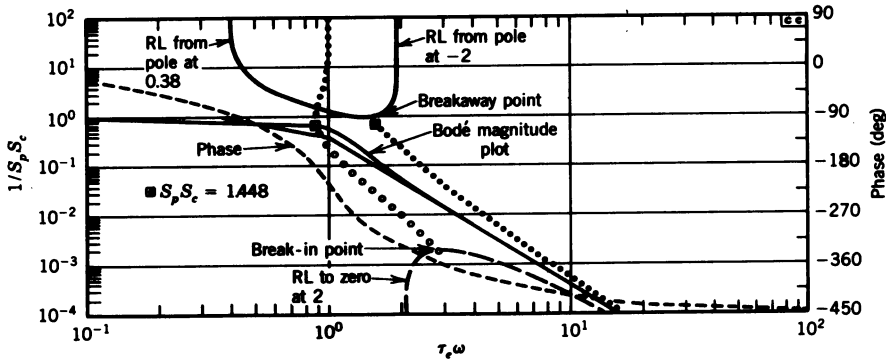
Figure 13-7 *Bodé root locus for G_{FL} for second-order plant (Eq. 13-11) for normalized pilot lag $\tau_e/\tau_i = 0.38$.*

branch crosses the imaginary axis at $\tau_e \omega = 1.647$ for $S_p S_c = 1.04$, hardly any improvement.

From this analysis it can be seen that for a wide range of control elements the dynamics of the combination of the pilot and the controlled element can be represented by three transfer functions. This completes the discussion of the crossover model for the pilot. The use of the pilot model given in Eq. 13-1 to predict the pilot rating of a new aircraft will be discussed in the next section.

13-3 THE PAPER PILOT

As mentioned in Section 13-1, R. O. Anderson in June 1969 began investigating an alternate approach for the specification of handling qualities for VTOL aircraft.[4] This work resulted in a pilot model for the prediction of pilot ratings based on a measure of the model's performance and the amount of lead generated by the pilot model. The pilot ratings were based on the Cooper–Harper scale shown in Table 13-2. Anderson used the standard crossover model in each of the two feedback loops as shown in Figure 13-8.

For each pilot model a lead time constant and gain were selected that minimized the displacement and attitude errors. The task modeled was the maintenance of a fixed hover position under gusty conditions (u_g). Anderson assumed that lead generation and closed loop performance were the *main* factors that affect pilot rating; thus, using data in Ref. 16, he developed the following pilot rating function PR:

$$PR = \text{PERF} + f(\tau_L) + 1 \qquad (13\text{-}13)$$

TABLE 13-2 Cooper–Harper Pilot Rating Scale

Controllable	Acceptable	Satisfactory without improvements	Excellent, highly desirable — pilot compensation not a factor.	1
			Good, negligible deficiencies — Pilot compensation not a factor.	2
			Fair, some mildly unpleasant deficiencies — minimal pilot compensation required.	3
		Deficiencies warrant improvement	Minor but annoying deficiencies — moderate pilot compensation required.	4
			Moderately objectional deficiencies — considerable pilot compensation required.	5
			Very objectional deficiencies — extensive pilot compensation required.	6
	Unacceptable	Deficiencies require improvements	Major deficiencies — adequate performance not attainable with maximum tolerable pilot compensation.	7
			Major deficiencies — considerable pilot compensation required for control.	8
			Major deficiencies — intense pilot compensation required for control.	9
Uncontrollable		Improvement mandatory	Major deficiencies — control will be lost during some portion of required operation.	10

where

PERF $= (\sigma - \sigma_m)/\sigma_m$ is the performance measure with a limit of 2.5, where $\sigma_m = 0.80$ is the required performance, and

$$\sigma = \sigma_{\epsilon_x} + 10\sigma_{\epsilon_q}$$

where σ_{ϵ_x} is the standard deviation of ϵ_x (ft) and σ_{ϵ_q} is the standard deviation of the pitch rate (rad/sec);

$f(\tau_L) = 2.5\tau_{L_\theta} + \tau_{L_x}$ is the work load measure with the pilot lead time constant in pitch τ_{L_θ}, limited to 1.3 sec and the pilot lead time constant in displacement, τ_{L_x}, limited to 1.2 sec.
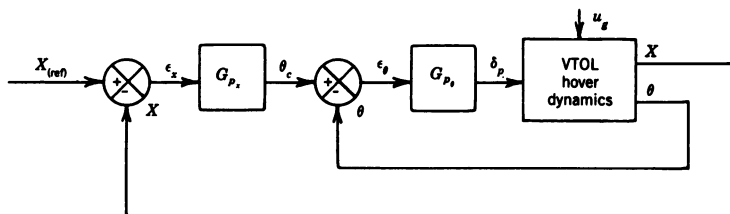
Figure 13-8 *Block diagram for VTOL hover control with pilot models.*

The 1 in Eq. 13-13 is to insure that the minimum pilot rating is 1, corresponding to excellent performance. A value of 0.44 sec was used for the pilot delay τ_e, which included 0.09 sec for τ_i and 0.35 sec for τ_N. The pilot's lag time constant τ_I was set to 0.

Anderson used an analog simulation to model the pilot and the dynamics of the VTOL aircraft in the hover mode and determined the coefficients in Eq. 13-13 by matching performance data from Ref. 16. With the PR equation developed, Anderson then used the model to predict pilot ratings for comparison with actual pilot ratings obtained from pilots flying the same task in both fixed and moving base simulators. In these tests the stability derivatives in the pitching moment and longitudinal force equations were varied to yield different vehicle dynamics. The correlation of the predicted pilot ratings with the actual pilot ratings for the same flight conditions was very good. However, as the simulation was analog, the minimization procedure was very time consuming, requiring many runs, with adjustment of the pilot model gains and time constants between each run to obtain the minimum PR. This led to the development by Dillow of the digital program, described in Ref. 5, called the Paper Pilot, for predicting the pilot rating of a VTOL aircraft in the hover mode.

Dillow used the same basic model as Anderson; however, he first minimized a cost functional, then used the values from the minimum cost functional to calculate the pilot rating. The cost functional J has the same form as Eq. 13-13 with

$$\text{PERF} = 0.218\sigma_{\epsilon_q} + 1.25\sigma_{\epsilon_x} - 1 \qquad (13\text{-}14)$$

and

$$f(\tau_L) = 2.25\tau_{L_\theta} + \tau_{L_x} \qquad (13\text{-}15)$$

with τ_{L_θ} limited to 1.3 sec and τ_{L_x} limited to 1.2 sec. With J minimized, the pilot gains S_{p_θ} and S_{p_x} are simultaneously increased by 20 per cent. If the system with the increased gains is asymptotically stable (transients decay to zero), the minimized gains are retained for the rest of the procedure. If not, the pilot gains are decreased so that the system is asymptotically stable for a 20 percent gain increase, but unstable for a 20.03 percent increase. For all gain increases both gains are increased simultaneously. The 20 percent gain margin results from the premise that an actual pilot would reduce his gain so that some positive gain margin was present. The choice of 20 percent by Dillow was strictly arbitrary. If the gains had to be reduced to provide the stability margin, then the rms values of the position and attitude error were recalculated with the adjusted gains before calculating the pilot rating. The PR is

$$\text{PR} = \text{PERF} + f(\tau_L) + 1 \qquad (13\text{-}16)$$

TABLE 13-3   Comparison of Longitudinal Paper Pilot Models: PR = PERF $+ f(\tau_L) + 1$

Task	Performance Measure PERF	Work Load Measure $f(\tau_L)$	Comments
VTOL hover (Ref. 5)	$0.218\sigma_{\epsilon_q} + 1.25\sigma_{\epsilon_x} - 1$	$2.25\tau_{L_\theta} + \tau_{L_x}$	τ_{L_θ} lim. to 1.3 τ_{L_x} lim. to 1.2
Pitch att. (Ref. 6)	$\dfrac{0.1\sigma_i^2}{0.974\sigma_i^2 - \sigma_e^2}$	$2.5\tau_L$	$\sigma_i^2 = $ var. of input $\sigma_e^2 = $ var. of error PR lim. to 10 τ_L lim. to 1.3
Pitch att. (Ref. 7)	$5.8\sigma_\theta^2 + 0.43\sigma_q^2$ for PERF ≤ 5.5 $5.5 + 0.5[(5.8\sigma_\theta^2 + 0.43\sigma_q^2) - 5.5]$ for PERF > 5.5	$0.43\tau_L$	
Pitch att. (Ref. 8)	$\sigma_\theta + 4\sigma_q$	$3.25(1 - e^{-0.154\tau_L})$	PERF lim. to 5.5

where PERF is given by Eq. 13-14 and $f(\tau_L)$ by Eq. 13-15, and where PERF is limited to 2.825. The pilot ratings PR were compared with the ratings given by actual pilots flying the same conditions in a fixed simulator. A total of 79 runs were made in which the aircraft dynamics and the gust intensities were varied. For these runs the difference between the calculated values of PR and the ratings given by the actual pilots was less than 1 for 89.9 percent of the cases, with a maximum difference of 1.69. As the ratings given by two pilots flying the same task under the same conditions can vary by as much as one pilot rating unit, the results obtained by Dillow were considered more than acceptable.

Anderson, Connors, and Dillow then applied the Paper Pilot program to the pitch attitude tracking task under gusty conditions.[6] The pilot rating equation developed by them is shown in Table 13-3 along with the equations developed by the authors of Refs. 5, 7, and 8. As can be seen from the table, the performance and work load measure equations differ for the three pitch attitude tracking tasks. Although the tasks were the same, the aircraft dynamics were not. The F-8D was used in Ref. 6, the variable stability T-33 in Ref. 7, and the F-5 and A-7 in Ref. 8. In each of these investigations the pilot rating equations were developed using one set of data and then validated against a second set of independent data. In all three cases the correlation between the pilot ratings predicted using the Paper Pilot and the ratings by actual pilots was very good to excellent.

Three other applications of the Paper Pilot are shown in Table 13-4 along with the pilot rating equations. The applications are roll angle control in Ref. 9, heading and roll angle control in Ref. 10, and glide slope control in Ref. 11, with all of the tasks performed under gusty conditions. The reasoning

TABLE 13-4 Comparison of Paper Pilots for Other Tasks: PR = PERF + $f(\tau_L)$ + 1

Task	Performance Measure PERF	Work Load Measure $f(\tau_L)$	Comments
Roll angle* (Ref. 9)	$1.31\sigma_\phi - 1$	$3.25(1 - e^{-0.76923\tau_L})$	PERF lim. to 5.75
Heading and roll control (Ref. 10)	$1.9\sigma_\psi + \sigma_r + 0.07\sigma_p$	0	PERF lim. to 6
Glide slope (Ref. 11)	$0.36175\sigma_\theta + 0.95928\sigma_q$ $+ 0.10608\sigma_d$	0	For PR > 5.5 PR = 5.5 + 0.5(PERF − 5.5)

*PR = PERF + $f(\tau_L)$ + $|1 - \omega_\phi / \omega_d|$, where ω_ϕ is the natural frequency of the numerator term of the ϕ/δ_a transfer function, and ω_d is the natural frequency of the Dutch roll mode.

behind the additional term in the roll angle control PR equation can be seen by examining the ϕ/δ_a transfer function given in Eq. 3-45. As the quadratic term in the numerator of the transfer function nearly cancels the Dutch roll quadratic, the amount of Dutch roll sensed by the pilot depends on how close the natural frequency ω_ϕ of the numerator quadratic is to the natural frequency ω_d of the Dutch roll. If both frequencies are the same, then the added term in the PR equation is zero, resulting in a lower value of PR.

The last application to be discussed is the use of the Paper Pilot model to select the optimal gains for a SAS to be used in a hypothetical aircraft.[12] The aircraft used was described in a Design Challenge at the Joint Automatic Control Conference of 1970. The flight envelope of the aircraft included Mach numbers from 0.35 to 3 with dynamic pressures ranging from 150 to 1500 lb/sq ft. The block diagram of the control system is shown in Figure 13-9. The inputs of the first two body bending modes are shown as q_b and n_{z_b}. As shown in the figure, the SAS loop contains elevator, pitch rate, and normal acceleration feedback. To compensate for the body bending modes the pitch rate and normal acceleration signals are passed through a first-order lag. An outer pitch angle loop is closed through the pilot model. It was found by the authors of Ref. 6 that for conditions of high natural frequency and low damping the Paper Pilot gave lower pilot ratings (indicating better performance) than the actual pilots. In an attempt to increase the calculated pilot rating under these conditions, the authors of Ref. 12 added a remnant δ_r, in the form of white noise input, through a first-order lag as shown in the figure. The remnant, as defined in Ref. 1, represents the difference between the response of a nonlinear system to a given input and the response of the equivalent linear system to the same input. The remnant input was scaled so that the ratio of the variance of the remnant to the variance of the stick input was 0.6. The addition of remnant was only partially successful, in that it tended to increase the values of PR for all of the cases, not just those with high natural frequency and low damping. The output of the pilot model is
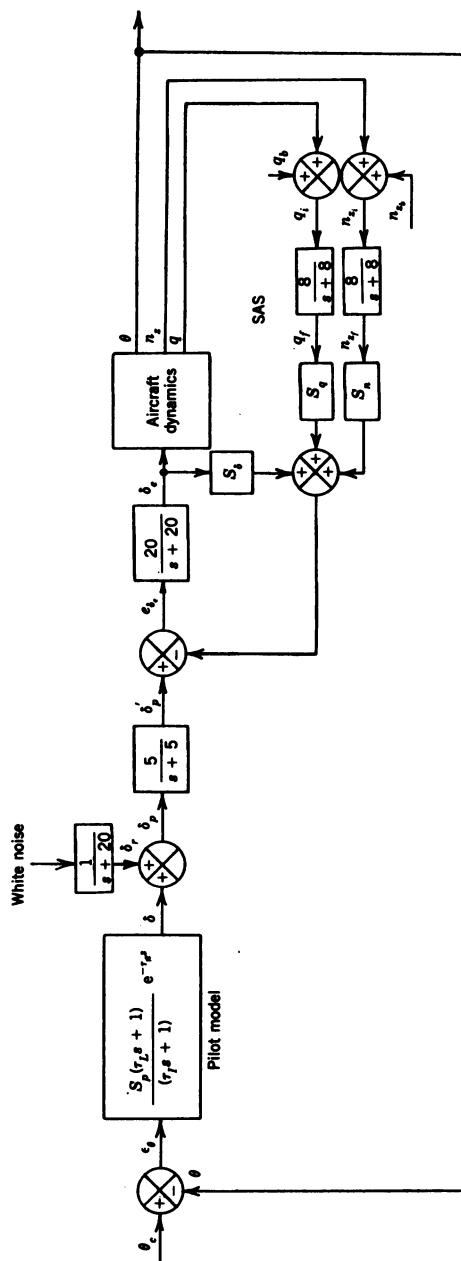
Figure 13-9 *Block diagram of SAS to be optimized, from Ref. 12.*

passed through the first-order lag to reduce an undesirable negative spike in the acceleration response. The pilot rating equation used in this study had the same form as Eq. 13-13 with

$$\text{PERF} = \frac{0.1\sigma_c}{0.974\sigma_c - \sigma_e} \tag{13-17}$$

where σ_c and σ_e are the standard deviations of the command input and pitch error respectively, $\sigma_e < 0.974\sigma_c$, and

$$f(\tau_L) = 2.5\tau_L \tag{13-18}$$

with τ_L limited to 1.3 sec. The pilot model and the pilot rating equation were tested using data from a series of Navy tests on a variable stability F-8. An examination of the optimized SAS gains by the authors showed that S_q could be scheduled as a function of $1/q$, where q is the dynamic pressure; however, no such relationship existed for S_δ. An examination of the values for S_δ indicates that it would be very difficult to come up with any form of gain schedule; thus a two-way (Mach and dynamic pressure) or three-way (Mach, altitude, and dynamic pressure) lookup table might be required. There seems to be no requirement for normal acceleration feedback, as the values of S_n varied from 0.0 to a maximum of 0.0017. The gains for Mach less than 0.86 at sea level were negative, while the rest of the values were positive. The system responses using these gains generally meet the design requirements.

As shown in this section, the Paper Pilot digital program has provided a method for the prediction of the handling qualities of aircraft for different operational tasks, and for the determination of the gains for an optimum SAS for a hypothetical aircraft. However, as shown in Tables 13-3 and 13-4, the PR equations are dependent on the aircraft dynamics as well as the task. The pilot models discussed in the next section were designed to be independent of the vehicle dynamics, and the model developed by Pollard is also task independent.

13-4   OPTIMAL PILOT MODEL

To overcome the deficiency of the Paper Pilot model discussed in the last section, Pollard in Ref. 13 developed a digital simulation of manned flight in aircraft ranging from jet fighters to large four-engine jet transports in a multiaxis, turbulent environment. The tasks included in the simulation were pitch attitude control, roll attitude control, heading control, a combination of all three, and approach and landing. The author used the linearized, uncoupled, small-perturbation 6-DOF equations of motion in the simulation (same as Eqs. 1-59 and 3-27). Thus no aerodynamic or inertial cross-coupling effects

Raw data
$\theta, \phi, \psi, \lambda, h,$
p, q, r, α

Delay
τ_e

Lead generation
$x_{new} = x_{delay}$
$+ \dot{x}_{delay}(k)(\tau_e)$

Predicted
error

Instrumentation
normalization
$\theta' = \theta/2$
$\phi' = \phi/2$
$\psi' = \psi/3$
$\lambda' = 2\lambda$
$h' = 16h$

Last
action

Yes $\dot{x}^* = x'$

No

$\dot{x}^* = 2x'$

Critical variable for
input to controller

Act on
x''_{max}

No
action
allowed

No   Yes

Distracted

Task dependence
$\theta'' = k_1\theta^*$
$\phi'' = k_2\phi^*$
$\psi'' = k_3\psi^*$
$\lambda'' = k_4\lambda^*$
$h'' = k_5h^*$
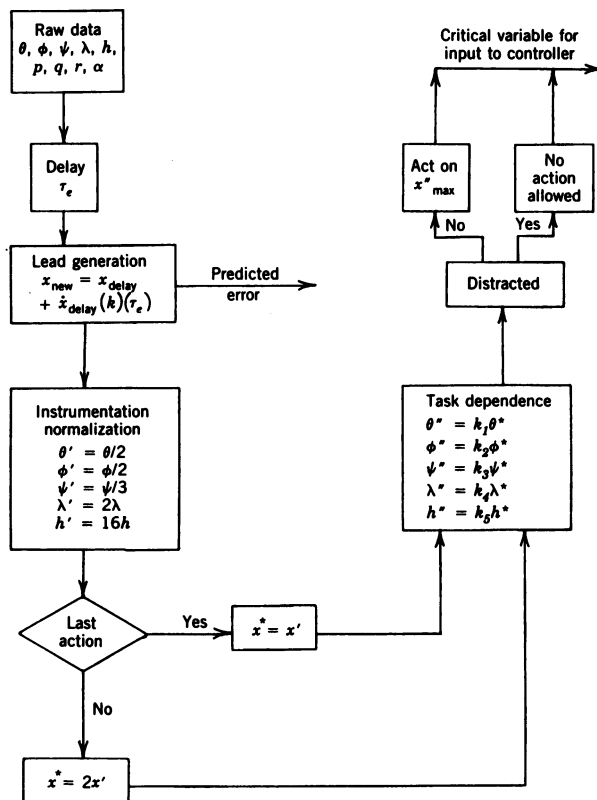
Figure 13-10 *Flow diagram for the decision process.*

were included in the simulation. For the multiaxis task, where several of the variables are being controlled at one time, it is necessary for the pilot to decide what action to perform first.

To cope with this problem Pollard developed the decision process shown in Figure 13-10. The raw data represents the deviations of the variables from the desired values from the simulation. The values of the parameters are delayed by the pilot's pure time delay τ_e, which for this study was 0.175 sec. The delayed variables are then passed through a lead term. The k in the lead generation equation was set equal to 1 for rapidly changing variables such as the attitude changes. For slowly changing variables such as glide slope and localizer deviation, the pilot is capable of predicting further ahead; thus for these variables $k = 2/\tau_e$. Since the minimum detectable deviations vary between instruments, the input variables are divided by the minimum deviations that a normal pilot will react to. All the angular quantities are in degrees. For the localizer error λ, the minimum detectable error is considered to be 0.5°; thus λ is multiplied by 2. The glide slope deviation h is multiplied by 16, as the maximum deviation is about 0.5°.
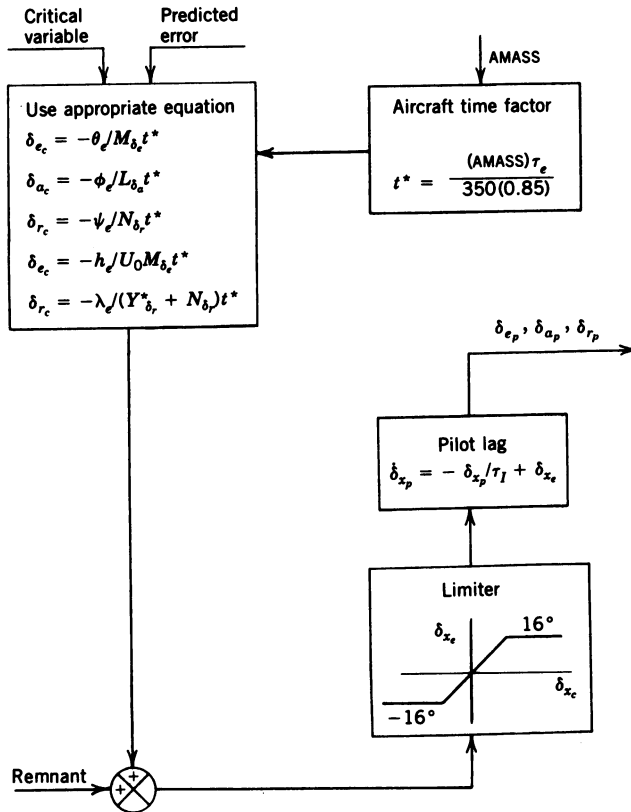
Figure 13-11 *Flow diagram for the control action implementation.*

After detecting one or more errors, the pilot must decide what corrective action to apply first; thus the pilot tends to set up a queue, where the time since the last corrective action influences the importance placed on a particular error. In this study, this was taken into account by multiplying all errors but the last one by 2. The values of the k's in the task dependence block are a function of the primary task. For instance, if the task is pitch hold, then $k_1 = 1.25$, $k_2 = k_3 = 1$, and $k_4 = k_5 = 0$. The same pattern is used for roll and heading hold, with the primary variable weighted at 1.25. For attitude hold the pitch, roll, and yaw are all weighted at 1 with $k_4 = k_5 = 0$. For landing $k_1 = 1.5$, $k_2 = k_3 = 1$, and $k_4 = k_5 = 0.2$. Finally, if the pilot is distracted no action is allowed; otherwise the maximum variable is input to the controller shown in Figure 13-11 along with the predicted error for action implementation. Pilot distraction, such as radio communication, was determined randomly with a distraction rate of 10 percent.

Based on the designated critical variable the required control system input is calculated from the corresponding predicted error. The equations for the calculation of the required control deflection can be derived by applying the

initial value theorem to the appropriate transfer function. To illustrate, consider the coordinated aircraft transfer function, which from Eq. 3-60 is

$$\frac{\dot{\phi}(s)}{\delta_{a_c}(s)} = \frac{L_{\delta_a}}{s - L_p} \tag{13-19}$$

where $L_{\delta_a} = SqbC_{l_{\delta_a}}/I_x$ and $L_p = Sqb^2C_{l_p}/2UI_x$. Applying the initial value theorem to Eq. 13-19 yields[17]

$$\lim_{s \to \infty} sF(s) = \lim_{s \to \infty} \frac{sL_{\delta_a}}{s - L_p} = L_{\delta_a} \tag{13-20}$$

Then the initial value of $\dot{\phi}/\delta_{a_c}$ is

$$\frac{\dot{\phi}_c}{\delta_{a_c}} = L_{\delta_a}$$

Then

$$\dot{\phi}_c = \delta_{a_c}L_{\delta_a} \tag{13-21}$$

Pollard assumed that the pilot will act to minimize his errors from the desired equilibrium condition. Thus for the roll angle we have

$$\phi_e + \dot{\phi}_c t^* = 0 \tag{13-22}$$

where t^* is the expected duration of $\dot{\phi}_c$ to be described later in this section. Solving Eq. 13-22 for $\dot{\phi}_c$, equating the results to Eq. 13-21, and solving for δ_{a_c} yields

$$\delta_{a_c} = \frac{-\phi_e}{L_{\delta_a}t^*} \tag{13-23}$$

By analyzing strip chart recordings of control surface inputs for different aircraft, Pollard determined that t^* could be linearly related to the mass of the aircraft:

$$t^* = \frac{(\text{AMASS})\tau_e}{350(0.85)} \tag{13-24}$$

where

AMASS is the mass of the aircraft being modeled (slugs),

350 is the reference mass (slugs), and

0.85 is a correction factor determined by Pollard from experimental data matching.

The term $Y_{\delta_r}^*$ in Figure 13-11 is equal to Y_{δ_r}/V_T, where V_T is the total velocity of the aircraft. Remnant is added to model the neuromuscular noise. The resulting control surface deflection is limited to $\pm 16°$ and then passed through a pilot lag where τ_I is assumed to be equal to τ_e. The output of the pilot lag block is the required control surface deflection for input to the aircraft equations of motion. The other control surface deflections are set at their trim values.

To calculate the pilot's rating Pollard used the total rotational rate

$$T_r = \sqrt{\sigma_p^2 + \sigma_q^2 + \sigma_r^2} \tag{13-25}$$

Then

$$PR = \begin{cases} 2+0.22T_r, & \text{for} \quad T_r < 4.5 \\ 0.615T_r + 0.35 & \text{for} \quad 4.5 \le T_r < 11 \\ 0.25T_r + 4.25 & \text{for} \quad 11 \le T_r < 23 \\ 10 & \text{for} \quad T_r \ge 23 \end{cases}$$

Using these relationships, the predicted pilot ratings were determined for the F-5, A-7, and Boeing 707 and compared with results from a hybrid man-in-the-loop simulation. For the F-5, seven out of the 12 predicted ratings were within ± 1 rating unit of the actual ratings. For the A-7, all but one of the 12 predicted ratings were within the ± 1 rating unit tolerance. For the Boeing 707, 10 simulated power approaches were made using the digital simulation. The average PR was 2.24, with a minimum value of 2.18 and a maximum value of 2.34. The actual ratings for the same task given by two different pilots were the same and equal to 2.6. Tests were also run using variable-stability NT-33 data, in which the values of θ, q, and δ_e from the digital simulation were compared with the results from an analog simulation. The standard deviations of q and δ_e for eight runs compared very well, but the values from the digital simulation for θ were consistently larger by 0.25° than the analog simulation results. The authors could find no explanation for this bias error. Despite this one discrepancy, it can be seen that the digital simulation developed by Pollard was neither task nor aircraft dependent, thus overcoming the shortcoming of the Paper Pilot model. The application of an optimal pilot model to the analysis of aircraft handling qualities will be discussed next.

Dillow and Picha in Ref. 14 applied the optimal pilot model shown in Figure 13-12 to the task of analyzing the handling qualities of several aircraft. In this study the authors considered tracking in one axis only, and assumed, based on other applications of the optimal pilot model, that the variables and their first derivatives were available. The study also included motion cues, such as angular rates, and their first derivatives.

Returning to Figure 13-12, the indications of the states of the aircraft presented by the displays are sensed by the pilot model with additive white
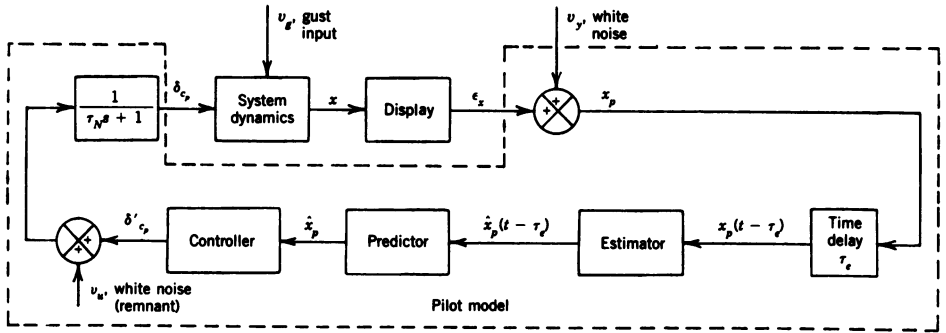
Figure 13-12 Block diagram of optimal pilot model.

noise to represent observation errors. The corrupted observations are delayed by the pilot's pure time delay. The delayed signals are then reconstructed by the optimal estimator and predictor. The controller multiplies the reconstructed signals by the optimal feedback gains determined by the quadratic cost function to be discussed later in this section. White noise or remnant is added to the output of the controller to represent control errors and neuromuscular tremor. The noisy control signal is passed through the pilot's neuromuscular lag to provide the pilot's input to the control system, thus completing the loop.

The quadratic cost function to be minimized is

$$J_p = \sum_{i=1}^{m} W_{x_i} \sigma_{x_{p_i}}^2 + R\sigma_{\delta_c}^2 \tag{13-26}$$

where

$\sigma_{x_{p_i}}^2$ is the variance of the perceived value of the ith observed variable,
$\sigma_{\delta_c}^2$ is the variance of the rate of change of the control input, and
W_{x_i} and R are weightings in the cost function.

The authors used the perceived values rather than the actual values in order to take instrument thresholds into account. The values of W_{x_i} are task dependent, but independent of the observed variables and plant dynamics.
To continue, Eq. 13-26 can be written as

$$J_p = \sum_{i=1}^{m} W_{x_i} \frac{\sigma_{x_{p_i}}^2}{\sigma_{x_i}^2} \sigma_{x_i}^2 + R\sigma_{\delta_c}^2 = \sum_{i=1}^{m} W_{x_i} K_{x_i}^2 \sigma_{x_i}^2 + R\sigma_{\delta_c}^2 \tag{13-27}$$

where $K_{x_i}^2 = \sigma_{x_{p_i}}^2 / \sigma_{x_i}^2$ and K_{x_i} is the dead zone describing function gain corresponding to x_i due to instrument threshold. For a threshold level of c_i,

$K_{x_i}^2$ is

$$K_{x_i}^2 = 1 - \text{erf}\left(\frac{\sigma_{x_i}}{\sqrt{2}\, c_i}\right) \tag{13-28}$$

where erf is the error integral described in Section 12-2. As stated in the reference, the solution of the optimal pilot model is computed iteratively, with the values of $W_{x_i} K_{x_i}^2$ computed each iteration until convergence is achieved. R in Eq. 13-27 is selected so that the neuromuscular lag $\tau_N = 0.1$ sec. In the digital program the quadratic cost function J_p is minimized using linear–quadratic Gaussian optimization theory. With J_p minimized the paper pilot rating PR is

$$\text{PR} = \begin{cases} 1 & \text{for} \quad J_p < 1 \\ \sqrt{J_p} & \text{for} \quad 1 \le \sqrt{J_p} \le 9 \\ 9 & \text{for} \quad 9 < \sqrt{J_p} < \infty \\ 10 & \text{for} \quad J_p = \infty \end{cases} \tag{13-29}$$

For $J_p = \infty$, the closed loop system would have to be unstable; thus a pilot rating of 10 is justified.

With the equations for the cost functional and the pilot rating established, the authors selected the values for the instrument thresholds and determined the weightings for the observed vector shown in Table 13-5 for four tracking tasks. The weightings were selected by the authors so that the analytic results closely matched the measured results using actual pilots. For the roll attitude task the sensing of $\dot{p}$ was assumed to be from motion cues sensed by the vestibular system.

The results of this study showed that, in general, the pilot ratings from the optimal model and the standard deviations of the observed vector agreed very well with results using actual pilots. For the longitudinal hover task, values of PR for 69.2 percent of the 26 cases were within ± 1 rating unit of the actual ratings. Of the eight cases with ratings outside the ± 1 boundary, four had values of PR that were 2 and 3 rating units greater than the actual ratings. These four cases were for conditions where the actual pilot ratings were greater than 4. For the lateral hover task, four of the 15 cases were outside the ± 1 unit boundary, with all of them greater than the actual ratings and for cases where the actual ratings were 5 or greater. For the pitch attitude case, half of the 14 cases were outside the ± 1 unit boundary. For actual ratings less than 4 the values of PR were less than the actual ratings, while for actual ratings greater than 4 the values of PR were greater than the actual ratings. All but two of the cases had values of PR that were within ± 2 units of the actual ratings. For the roll attitude task, tests were run using the F-5 and A-7 aircraft data with 16 runs made for each aircraft. All but two of the values of PR for the A-7 were less than the actual ratings, with five values

TABLE 13-5   Values of Thresholds and Weightings for Various Tracking Tasks

Task	Observed Vector x_{p_i}	Instrument Thresholds	Weightings* W_{x_i}
Longitudinal hover	θ	0.05 deg	0.0
	q	0.18 deg/sec	0.4
	x	0.07 ft	1.0
	u	0.25 ft/sec	0.0
Lateral hover	ϕ	0.44 deg	0.0
	p	1.69 deg/sec	0.4
	y	0.174 ft	1.0
	v	0.627 ft/sec	0.0
Pitch attitude	θ	0.3 deg	70.0
	q	1.08 deg/sec	7.0
Roll attitude	ϕ	0.13 deg	2.7
	p	0.47 deg/sec	1.5
	$\dot{p}$	0.5 deg/sec^2	0.02
	$\ddot{p}$	10.0 deg/sec^3	0.0

*Weightings are for angular measures in degrees and displacements in feet.

between 1 and 2 units less. The opposite trend was found for the F-15: the values of PR for four cases were more than 2 rating units greater than the actual ratings.

To summarize the results, with the exception of the roll attitude cases the values of PR tended to be greater than the actual pilot ratings for actual ratings greater than 3.5, and less than the actual ratings for actual ratings less than 3.5. This model still required that the weightings be calculated for the specific task; thus the model developed by Pollard was superior in this respect. The optimal pilot model developed by Dillow and Picha did not deal with multiaxis tasks. They stated that for multiaxis tasks, the observed variables would be sampled with the sampling ratios selected to minimize the quadratic cost function. Pollard's approach to the multiaxis task was certainly more straightforward.

This completes the discussion of pilot modeling techniques. The material presented here is primarily a condensation of the material presented in the references. The reader who wishes to pursue the subject further is referred to the extensive bibliography at the end of Ref. 3 (pp. 60–65) and the references at the end of Ref. 13 (pp. 124–127).

REFERENCES

1. D. T. McRuer and H. R. Jex, "A Review of Quasi-linear Pilot Models," *IEEE Transactions on Human Factors in Electronics*, September 1967, Vol. 8.

2. D. T. McRuer, D. Graham, and E. S. Krendel, "Manual Control of Single-Loop Systems: Part I," *Journal of the Franklin Institute*, January 1967, Vol. 283, No. 1.

3. D. T. McRuer and E. S. Krendel, *Mathematical Models of Human Pilot Behavior*, Agardograph No. 188, North Atlantic Treaty Organization, January 1974.

4. R. O. Anderson, *A New Approach to the Specification and Evaluation of Flying Qualities*, AFFDL-TR-69-120, Wright-Patterson AFB, Ohio: Air Force Flight Dynamics Laboratory, June 1970.

5. J. D. Dillow, *The "Paper Pilot" — A Digital Program to Predict Pilot Rating for the Hover Task*, AFFDL-TR-70-40, Wright-Patterson AFB, Ohio: Air Force Flight Dynamics Laboratory, March 1971.

6. R. O. Anderson, A. J. Connors, and J. D. Dillow, *Paper Pilot Ponders Pitch*, AFFDL/FGC-TM-70-1, Wright-Patterson AFB, Ohio: Air Force Flight Dynamics Laboratory, November 1970.

7. J. D. Arnold, *An Improved Method of Predicting Aircraft Longitudinal Handling Qualities Based on the Minimum Pilot Rating Concept*, M.S. thesis, GGC/MA/73-1, Air Force Institute of Technology, Wright-Patterson AFB, Ohio, June 1973.

8. R. B. Johnson, *Predicting Pitch Task Flying Qualities Using Paper Pilot*, M.S. thesis, GGC/MA/73-2, Air Force Institute of Technology, Wright-Patterson AFB, Ohio, June 1973.

9. F. R. Naylor, *Predicting Roll Task Flying Qualities with "Paper Pilot"*, M.S. thesis, GAM/MA/73-1, Air Force Institute of Technology, Wright-Patterson AFB, Ohio, September 1972.

10. C. R. Taylor, *Predicting Heading Task Qualities with Paper Pilot*, M.S. thesis, GE/MA/73-1, Air Force Institute of Technology, Wright-Patterson AFB, Ohio, June 1973.

11. D. J. Biezad, *A Method of Predicting Pilot Rating for the Pitch Handling Qualities of Aircraft Flown on the Glide Slope*, M.S. thesis, GA/MA/73A-1, Air Force Institute of Technology, Wright-Patterson AFB, Ohio, December 1973.

12. R. P. Denaro and G. L. Greenleaf, *Selection of Optimal Stability Augmentation System Parameters for a High Performance Aircraft Using Pitch Paper Pilot*, M.S. thesis, GGC/EE/73-3, Air Force Institute of Technology, Wright-Patterson AFB, Ohio, October 1972.

13. J. J. Pollard, *All Digital Simulation for Manned Flight in Turbulence*, AFFDL-TR-75-82, Wright-Patterson AFB, Ohio: Air Force Flight Dynamics Laboratory, September 1975.

14. J. D. Dillow and D. G. Picha, *Application of the Optimal Pilot Model to the Analysis of Aircraft Handling Qualities*, AFIT-TR-75-4, Air Force Institute of Technology, Wright-Patterson AFB, Ohio, August 1975.

15. C. L. Johnson, *Analog Computer Techniques*, McGraw-Hill Book Co., New York, 1956.

16. D. P. Miller and E. W. Vinje, *Fixed-Base Simulator Studies of VTOL Aircraft Handling Qualities in Hovering and Low Speed Flight*, AFFDL-TR-67-152, Wright-Patterson AFB, Ohio: Air Force Flight Dynamics Laboratory, January 1968.

17. J. J. D'Azzo and C. H. Houpis, *Linear Control System Analysis and Design: Conventional and Modern*, 3rd ed., McGraw-Hill Book Co., New York, 1988.

Appendix *A*

Review of Vector Analysis

A-1 VECTOR REPRESENTATION OF LINEAR QUANTITIES

Many physical quantities are most conveniently represented by vectors. Some of the linear quantities involved that can be represented by vectors are forces, velocity, acceleration, and position. By definition a vector has magnitude, direction, and sense (that is, plus or minus) in that direction.

Figure A-1 shows several examples of vector quantities, such as velocity, force, and position. For the velocity vector **V** and the force vector **F** the length of the arrow is proportional to the magnitude of the velocity or force, and the direction is indicated by the direction of the arrow. The position vector is a vector representing the distance and direction between two points.

A-2 VECTOR REPRESENTATION OF ROTATIONAL QUANTITIES

In addition to the linear quantities discussed in Section A-1, certain rotational quantities such as angular velocity, angular momentum, and torques can be represented by vectors. Any rotating body rotates about some instantaneous axis. The vector representing this angular velocity, ω, lies along the instantaneous axis of rotation. To determine the positive sense of the vector use the right-hand rule as illustrated in Figure A-2. As the angular momentum vector is $H = I_{(sp)}\omega$, where $I_{(sp)}$ is the moment of inertia of the body about the axis of rotation, the angular momentum vector lies along the angular velocity vector.
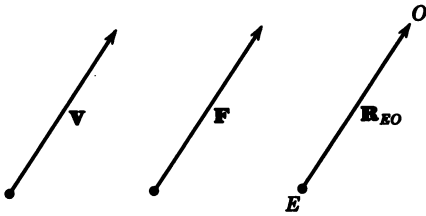
Figure A-1   Vector representation of linear quantities.
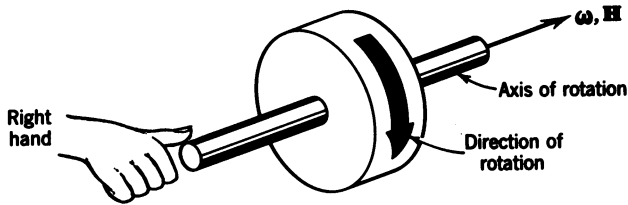
Figure A-2   Vector representation of angular velocity and angular momentum.
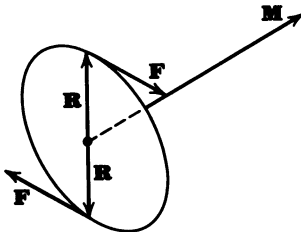
Figure A-3   Vector representation of a torque vector, where M represents the torque vector, F represents the forces of the couple generating the torque, and R represents the two lever arms.

Another important rotational quantity is the vector representation of a torque, which is shown in Figure A-3. The length of the arrow is proportional to the magnitude of the torque, which is equal to the sum of the products of the components of the forces F perpendicular to the lever arms R times the length of the lever arms. A vector expression for this is given in Section A-7.

A-3   ADDITION AND SUBTRACTION OF VECTORS

To add vectors it is necessary only to place the tail of one vector coincident with the head of the other. This procedure is continued until all the vectors have been added [see Figure A-4(a)]. To subtract the two vectors, the negative of one is added to the other [see Figure A-4(b)].
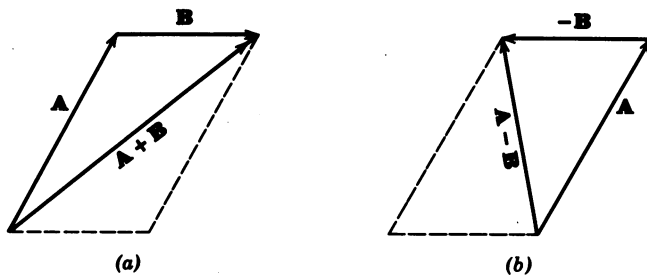
Figure A-4   *Addition and subtraction of vectors.*

A-4   MULTIPLICATION OF A VECTOR BY A SCALAR

When a vector is multiplied by a scalar quantity only the magnitude of the vector is altered; the new magnitude is equal to the old magnitude times the scalar quantity. The sign associated with the scalar quantity must be taken into account; if it is negative it reverses the sense of the vector but does not otherwise change the direction of the vector.

A-5   RECTANGULAR COMPONENTS OF VECTORS

To obtain the components of a vector, an orthogonal axis system is usually used with the axes signified by X, Y, and Z. In general this system is right-handed, which means that if the positive X axis is rotated about the Z axis toward the positive Y axis through the smallest angle, using the right hand rule, with the fingers pointed in the direction of rotation, the thumb points in the positive direction of the Z axis.

To represent vectors of unit length which lie along the X, Y, and Z axes the symbols **i**, **j**, and **k** are used in that order. Thus a vector **R** can be expressed in terms of its components along the three axes as $\mathbf{R} = \mathbf{i}R_x + \mathbf{j}R_y + \mathbf{k}R_z$, where R_x, R_y, and R_z are the magnitudes of the projections of the vector **R** (including algebraic signs), as illustrated in Figure A-5. The addition and subtraction of vectors that have been written in terms of their rectangular components can be accomplished by adding or subtracting the respective components. Thus if $\mathbf{A} = \mathbf{i}A_x + \mathbf{j}A_y + \mathbf{k}A_z$ and $\mathbf{B} = \mathbf{i}B_x + \mathbf{j}B_y + \mathbf{k}B_z$, then $\mathbf{A} + \mathbf{B} = \mathbf{i}(A_x + B_x) + \mathbf{j}(A_y + B_y) + \mathbf{k}(A_z + B_z)$.

A-6   SCALAR OR DOT PRODUCT

In equation form the dot product of two vectors is written as $\mathbf{A} \cdot \mathbf{B} = AB \cos A_{AB}$, where A_{AB} is the angle between the two vectors. Remember that the result of the dot product is a *scalar* quantity. The result of the dot
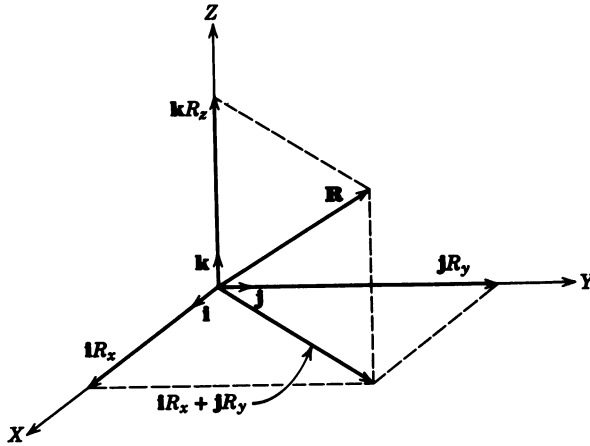
Figure A-5 *Representation of a vector in terms of its rectangular components.*

product is dependent upon the angle between the two vectors; if the vectors are perpendicular, their dot product is zero, and if they are parallel, the dot product is equal to the product of the magnitudes of the vectors. Thus $\mathbf{i} \cdot \mathbf{j} = \mathbf{j} \cdot \mathbf{k} = \mathbf{k} \cdot \mathbf{i} = 0$ and $\mathbf{i} \cdot \mathbf{i} = \mathbf{j} \cdot \mathbf{j} = \mathbf{k} \cdot \mathbf{k} = 1$; also $\mathbf{A} \cdot \mathbf{A} = A^2$, so $|\mathbf{A}| = \sqrt{\mathbf{A} \cdot \mathbf{A}}$. If the two vectors are written in terms of their rectangular coordinates, $\mathbf{A} \cdot \mathbf{B} = (\mathbf{i} A_x + \mathbf{j} A_y + \mathbf{k} A_z) \cdot (\mathbf{i} B_x + \mathbf{j} B_y + \mathbf{k} B_z) = A_x B_x + A_y B_y + A_z B_z$, as the dot products of the other unit vectors are zero.

A-7 VECTOR OR CROSS PRODUCT

The vector or cross product in equation form is $\mathbf{A} \times \mathbf{B} = \mathbf{1}_{(A \times B)} AB \sin A_{AB}$, where $\mathbf{1}_{(A \times B)}$ is a unit vector in the direction of $\mathbf{A} \times \mathbf{B}$, which by definition is normal to the plane containing the vectors $\mathbf{A}$ and $\mathbf{B}$; the positive direction is determined by use of the right-hand rule as vector $\mathbf{A}$ is rotated toward $\mathbf{B}$ through the smallest angle A_{AB}, as illustrated in Figure A-6. If the two vectors are written in terms of their rectangular components,

$$\mathbf{A} \times \mathbf{B} = (\mathbf{i} A_x + \mathbf{j} A_y + \mathbf{k} A_z) \times (\mathbf{i} B_x + \mathbf{j} B_y + \mathbf{k} B_z)$$

$$= \begin{vmatrix} \mathbf{i} & \mathbf{j} & \mathbf{k} \\ A_x & A_y & A_z \\ B_x & B_y & B_z \end{vmatrix}$$

As mentioned in Section A-2, the torque resulting from a force acting on a moment arm can be expressed by a vector equation. Referring to Figure A-3, $\mathbf{M} = 2\mathbf{R} \times \mathbf{F}$.
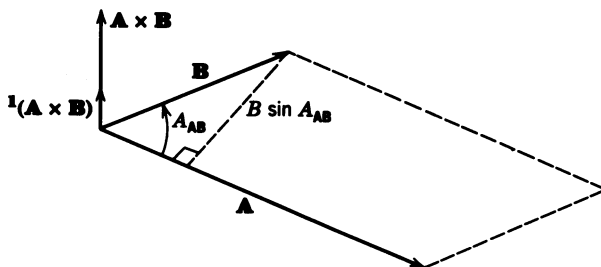
Figure A-6   *Vector or cross product of two vectors.*

A-8 MULTIPLE PRODUCTS

Besides the dot and cross products there are various combinations of these two products. Two of these combinations are of particular interest. One is the so-called "triple scalar product," which in equation form is $A \cdot (B \times C)$ and results in a scalar quantity. The factors may be rotated within the expression; thus $A \cdot (B \times C) = C \cdot (A \times B) = B \cdot (C \times A)$. The only requirement is that the cyclical order be maintained. If the three vectors are expressed in terms of their rectangular components,

$$A \cdot (B \times C) = \begin{vmatrix} A_x & A_y & A_z \\ B_x & B_y & B_z \\ C_x & C_y & C_z \end{vmatrix}$$

The other multiple product of interest is the "triple cross product," which in equation form is $A \times (B \times C)$ and results in a vector. The operation in parentheses must be performed first, for $A \times (B \times C) \neq (A \times B) \times C$. A useful expression for evaluating the triple cross product is $A \times (B \times C) = B(A \cdot C) - C(A \cdot B)$.

A-9 DIFFERENTIATION OF A VECTOR

If a vector is time dependent, it may be differentiated with respect to the scalar quantity time. The derivative of a position vector that is changing in both length and direction is illustrated in Figure A-7. The vector R can be written as $1_R R$, where 1_R is a unit vector in the direction of R. Then

$$\frac{dR}{dt} = \frac{d}{dt}(1_R R) = \frac{d1_R}{dt}R + 1_R \frac{dR}{dt} \tag{A-1}$$
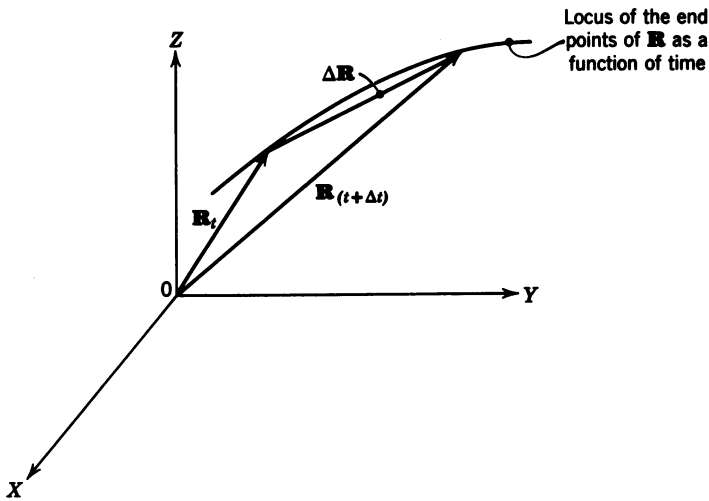
Figure A-7   *Variation of a position vector R as a function of time.*

The second term $1_R(dR/dt)$ represents the rate of change of the length of the vector as shown in Figure A-8. The first term is the rate of change of **R** due to a rotation. If ω_R denotes the angular velocity of the vectors **R** and 1_R, the tangential velocity of the tip of the vector **R** can be expressed as

$$R\frac{d1_R}{dt} = \omega_R \times R \qquad\qquad (\text{A-2})$$

and Eq. A-1 can now be written as

$$\frac{d\mathbf{R}}{dt} = 1_R\frac{dR}{dt} + \omega_R \times R \qquad\qquad (\text{A-3})$$

where $1_R\, dR/dt$ is the linear velocity caused by a change in the length of the position vector, and $\omega_R \times R$ is the tangential velocity of the tip of the position vector due to an angular velocity of the position vector. This expression is illustrated in Figure A-9.
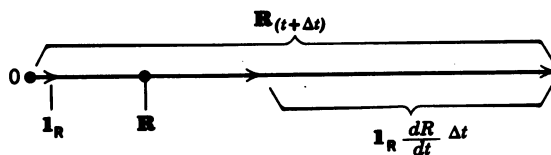
Figure A-8   *Rate of change of the length of R.*
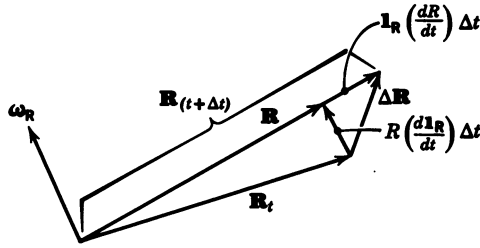
Figure A-9 *Total derivative of a position vector.*

The second derivative of a position vector is also frequently encountered; therefore, the second derivative of the vector **R** is now derived. Taking the derivative of Eq. A-3, it becomes

$$\frac{d^2\mathbf{R}}{dt^2} = \frac{d}{dt}\left(\mathbf{1_R}\frac{dR}{dt}\right) + \frac{d}{dt}(\boldsymbol{\omega_R}\times\mathbf{R}) \tag{A-4}$$

Expanding,

$$\frac{d^2\mathbf{R}}{dt^2} = \left(\frac{d\mathbf{1_R}}{dt}\right)\frac{dR}{dt} + \mathbf{1_R}\frac{d^2R}{dt^2} + \frac{d\boldsymbol{\omega_R}}{dt}\times\mathbf{R} + \boldsymbol{\omega_R}\times\frac{d\mathbf{R}}{dt} \tag{A-5}$$

we have shown that $d\mathbf{1_R}/dt = \boldsymbol{\omega_R}\times\mathbf{1_R}$. For $(d\boldsymbol{\omega_R}/dt)\times\mathbf{R}$, the $d\boldsymbol{\omega_R}/dt$ is again the derivative of a vector, but if it is assumed that the angular acceleration vector lies along the same axis as the angular velocity vector, $d\boldsymbol{\omega_R}/dt\times\mathbf{R}$ can be written as $\dot{\boldsymbol{\omega}}_\mathbf{R}\times\mathbf{R}$. Finally, if Eq. A-3 is substituted for $d\mathbf{R}/dt$ in the last term, Eq. A-5 becomes

$$\frac{d^2\mathbf{R}}{dt^2} = \mathbf{1_R}\frac{d^2R}{dt^2} + (\boldsymbol{\omega_R}\times\mathbf{1_R})\frac{dR}{dt} + \dot{\boldsymbol{\omega}}_\mathbf{R}\times\mathbf{R} + \boldsymbol{\omega_R}\times\left(\mathbf{1_R}\frac{dR}{dt} + \boldsymbol{\omega_R}\times\mathbf{R}\right) \tag{A-6}$$

Combining like terms, Eq. A-6 becomes

$$\frac{d^2\mathbf{R}}{dt^2} = \mathbf{1_R}\frac{d^2R}{dt^2} + 2(\boldsymbol{\omega_R}\times\mathbf{1_R})\frac{dR}{dt} + \dot{\boldsymbol{\omega}}_\mathbf{R}\times\mathbf{R} + \boldsymbol{\omega_R}\times(\boldsymbol{\omega_R}\times\mathbf{R}) \tag{A-7}$$

The significance of each term is as follows. The first term is the linear acceleration and results from the second rate of change of the length of the vector. The second and third terms are both tangential accelerations. The third term is probably familiar, but the second term may not be. This term is explained most easily by considering a position vector that is rotating at a constant velocity while it is changing in length. As the length of the position

ω_{rm}

$[\dot{\mathbf{R}}]_m \, dt$ = change in $\mathbf{R}$ as seen from the moving frame (observer sitting at P and rotating with the moving space).

$[\dot{\mathbf{R}}]_r \, dt$ = change in $\mathbf{R}$ as seen from the reference space or origin.

$(\omega_{rm} \times \mathbf{R}) \, dt$ = change in $\mathbf{R}$ due to rotation of moving space, that is, the location of $\mathbf{R}$ at the end of dt, if there were no motion of $\mathbf{R}$ with respect to the moving space. ω_{rm} = the angular velocity of the moving space with respect to the reference space.

$\omega_{rm} \, dt$

P

ω_{rm}

$\mathbf{R}_{(t+dt)}$ = final value of $\mathbf{R}$

$\mathbf{R}_t$ = initial $\mathbf{R}$.

Origin

Figure A-10   *Representation of the equation of Coriolis.*

vector changes, the tangential velocity of the tip must also change if the angular velocity of the vector is to remain constant. If the tangential velocity changes, there must be a tangential acceleration. The second term should not be confused with the Coriolis acceleration term discussed in Section A-10. The last term is the centripetal acceleration resulting from the rotation of this vector, and is always directed toward the center of rotation.

A-10 THE EQUATION OF CORIOLIS

The need for the equation of Coriolis arises when there are two or more axis systems rotating relative to each other; then the rate of change of a vector is different when viewed from the different axis systems. The equation of Coriolis can be stated in the following manner: The motion of an object as viewed from a reference frame is equal to the motion as seen from the moving frame, plus the motion resulting from the relative angular velocity of the moving frame with respect to the reference frame. This situation is illustrated in Figure A-10. From the vector triangle in Figure A-10, the equation of Coriolis can be written directly; thus

$$[\dot{\mathbf{R}}]_r \, dt = [\dot{\mathbf{R}}]_m \, dt + \omega_{rm} \, dt \times \mathbf{R} \qquad (A-8)$$

Dividing Eq. A-8 by the dt yields

$$[\dot{\mathbf{R}}]_r = [\dot{\mathbf{R}}]_m + \omega_{rm} \times \mathbf{R} \qquad (A\text{-}9)$$

which is the equation of Coriolis. It should be noted that $[\dot{\mathbf{R}}]_m$ is the vector velocity of the point in question as seen from the moving frame and may contain either or both of the terms given in Eq. A-3.

Another useful relation can be obtained by taking the time derivative of Eq. A-9 with respect to the reference frame. This procedure yields the second equation of Coriolis.

We have

$$[\ddot{\mathbf{R}}]_r = \left(\frac{d}{dt}\right)_r [\dot{\mathbf{R}}]_r = \left(\frac{d}{dt}\right)_r [\dot{\mathbf{R}}]_m + \left(\frac{d}{dt}\right)_r (\omega_{rm} \times \mathbf{R}) \qquad (A\text{-}10)$$

The term $(d/dt)_r[\dot{\mathbf{R}}]_m$ is the time derivative with respect to the reference frame of a vector defined in the moving frame. This requires the application of the first equation of Coriolis, which yields

$$\left(\frac{d}{dt}\right)_r [\dot{\mathbf{R}}]_m = \left(\frac{d}{dt}\right)_m [\dot{\mathbf{R}}]_m + \omega_{rm} \times [\dot{\mathbf{R}}]_m \qquad (A\text{-}11)$$

which can be written as

$$\left(\frac{d}{dt}\right)_r [\dot{\mathbf{R}}]_m = [\ddot{\mathbf{R}}]_m + \omega_{rm} \times [\dot{\mathbf{R}}]_m \qquad (A\text{-}12)$$

the last term of Eq. A-10 expanded is

$$\left(\frac{d}{dt}\right)_r (\omega_{rm} \times \mathbf{R}) = \left(\frac{d}{dt}\right)_r \omega_{rm} \times \mathbf{R} + \omega_{rm} \times \left(\frac{d}{dt}\right)_r \mathbf{R} \qquad (A\text{-}13)$$

As ω_{rm} is measured with respect to the reference frame, $(d/dt)_r \omega_{rm} = [\dot{\omega}_{rm}]_r$ and the equation of Coriolis need not be applied. However, Eq. A-9 must be substituted for $(d/dt)_r \mathbf{R}$ in Eq. A-13. Thus

$$\left(\frac{d}{dt}\right)_r (\omega_{rm} \times \mathbf{R}) = [\dot{\omega}_{rm}]_r \times \mathbf{R} + \omega_{rm} \times [\dot{\mathbf{R}}]_m + \omega_{rm} \times (\omega_{rm} \times \mathbf{R}) \quad (A\text{-}14)$$

Substituting Eqs. A-12 and A-14 into Eq. A-10 yields

$$[\ddot{\mathbf{R}}]_r = [\ddot{\mathbf{R}}]_m + [\dot{\omega}_{rm}]_r \times \mathbf{R} + 2\omega_{rm} \times [\dot{\mathbf{R}}]_m + \omega_{rm} \times (\omega_{rm} \times \mathbf{R}) \quad (A\text{-}15)$$

The significance of each term is as follows. The first term, $[\ddot{\mathbf{R}}]_m$, is the vector acceleration of the point in question as seen from the moving frame, and it may contain any or all the terms given in Eq. A-7. The second term is the tangential acceleration resulting from an angular acceleration of the moving frame with respect to the reference frame. The third term is the Coriolis acceleration; the similar-looking term in Eq. A-7 should not be confused with this term. The last term is the centripetal acceleration resulting from the rotation of the moving space with respect to the reference space. The centripetal acceleration vector always points toward and is normal to the axis of rotation.

Some Gyroscopic Theory

B-1 THE LAW OF THE GYRO[1]

The law of the gyro can be derived from Newton's law in rotational form, which states: The time rate of change with respect to inertial space of the angular momentum of a body about its center of gravity is equal to the applied torque. This can be written in equation form as

$$\mathbf{M}_{(app)} = [\dot{\mathbf{H}}]_I \tag{B-1}$$

As Eq. B-1 involves the time derivative of a vector with respect to inertial space, the equation of Coriolis must be applied. Using the earth as the moving frame,

$$[\dot{\mathbf{H}}]_I = [\dot{\mathbf{H}}]_E + \boldsymbol{\omega}_{IE} \times \mathbf{H} \tag{B-2}$$

where $\boldsymbol{\omega}_{IE}$ is the angular velocity of the earth with respect to inertial space $(0.07292115 \times 10^{-3}$ rad/sec). The gyroscope itself can be mounted on a base (aircraft, missile, etc.) that is moving with respect to the earth. Then

$$[\dot{\mathbf{H}}]_E = [\dot{\mathbf{H}}]_B + \boldsymbol{\omega}_{EB} \times \mathbf{H} \tag{B-3}$$

Also the case (Ca) of the gyroscope can be mounted on a platform so that it

can rotate relative to the base. This yields

$$[\dot{\mathbf{H}}]_B = [\dot{\mathbf{H}}]_{Ca} + \omega_{B,Ca} \times \mathbf{H} \qquad \text{(B-4)}$$

Finally the inner gimbal (Gi) can rotate relative to the case, thus

$$[\dot{\mathbf{H}}]_{Ca} = [\dot{\mathbf{H}}]_{Gi} + \omega_{Ca,Gi} \times \mathbf{H} \qquad \text{(B-5)}$$

Substituting Eqs. B-2, B-3, B-4, and B-5 into Eq. B-1, it becomes

$$\mathbf{M}_{(app)} = [\dot{\mathbf{H}}]_{Gi} + (\omega_{Ca,Gi} + \omega_{B,Ca} + \omega_{EB} + \omega_{IE}) \times \mathbf{H} \qquad \text{(B-6)}$$

But

$$\omega_{Ca,Gi} + \omega_{B,Ca} + \omega_{EB} + \omega_{IE} = \omega_{I,Gi} \qquad \text{(B-7)}$$

Then Eq. B-6 becomes

$$\mathbf{M}_{(app)} = [\dot{\mathbf{H}}]_{Gi} + \omega_{I,Gi} \times \mathbf{H} \qquad \text{(B-8)}$$

From Eq. A-3

$$[\dot{\mathbf{H}}]_{Gi} = \mathbf{1}_{\mathbf{H}} \frac{dH}{dt} + \omega_{Gi,H} \times \mathbf{H} \qquad \text{(B-9)}$$

In Eq. B-9, $\omega_{Gi,H}$ is the angular velocity of the vector $\mathbf{H}$ with respect to the inner gimbal, or the angular velocity of the spin axis with respect to the inner gimbal. This vector is made to be zero by the construction of the gyroscope, that is, there is no gimbal or bearing compliance. The term $\mathbf{1}_{\mathbf{H}} \, dH/dt$ of Eq. B-9 is constrained to be zero by maintaining the spin angular velocity of the rotor constant. This is accomplished by making the rotor part of a hysteresis-type synchronous motor and closely controlling the frequency of the excitation voltage. This procedure reduces Eq. B-9 to zero; thus, Eq. B-8 becomes

$$\mathbf{M}_{(app)} = \omega_{I,Gi} \times \mathbf{H} \qquad \text{(B-10)}$$

Equation B-10 is the "law of the gyro," which states that if a torque $\mathbf{M}_{(app)}$ is applied to a gyroscope, the inner gimbal precesses with respect to inertial space with an angular velocity $\omega_{I,Gi}$ such that Eq. B-10 is satisfied. The precession is in such a direction that the vector $\mathbf{H}$ attempts to align itself with the applied torque vector.

B-2 DYNAMIC EQUATION
OF THE SINGLE-DEGREE-OF-FREEDOM GYRO[1]

Figure B-1 shows the orientation of the gyroscopic element of a single-degree-of-freedom gyro relative to the case. In the single-degree-of-freedom gyro the outer gimbal of the two-degree-of-freedom gyro is fixed with respect to the case. The X, Y, and Z axes of the case are designated the output axis OA, the spin reference axis SRA, and the input axis IA, respectively. The output axis is synonymous with the inner gimbal axis of the two-degree-of-freedom gyro. The axes IA, OA, and SRA form a right-handed system such that $\mathbf{1}_{(IA)} \times \mathbf{1}_{(OA)} = \mathbf{1}_{(SRA)}$. The angle A_g, usually referred to as the gimbal angle, locates the spin axis of the gyroscopic element relative to the SRA, and is negative as shown in Figure B-1. As an angular velocity is normally considered the input for a single-degree-of-freedom gyro, its dynamics are determined by analyzing the gyroscopic output torque resulting from an arbitrary angular velocity of the vector **H** with respect to inertial space. The gyroscopic output torque is the reaction torque developed by the angular velocity of precession of **H** and opposes the applied torque; thus, if the gyroscopic output torque is denoted by $\mathbf{M}_g$,

$$\mathbf{M}_g = -\mathbf{M}_{(app)} = \mathbf{H} \times \boldsymbol{\omega}_{(I,\,Gi)} \qquad (B-11)$$

Now

$$\boldsymbol{\omega}_{(I,\,Gi)} = \boldsymbol{\omega}_{(Ca,\,Gi)} + \boldsymbol{\omega}_{(I,\,Ca)} \qquad (B-12)$$

and $\boldsymbol{\omega}_{(Ca,\,Gi)} = \mathbf{i}_{Ca}\dot{A}_g$, as the gyro has only one degree of freedom. The
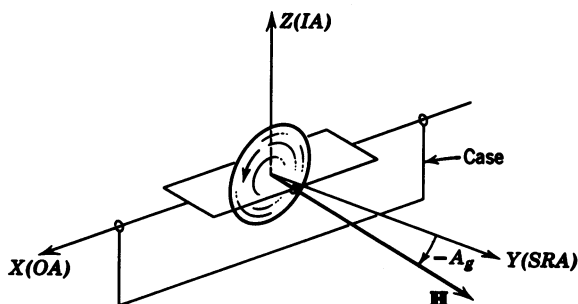
Figure B-1 Orientation of the gyroscopic element relative to the case for a single-degree-of-freedom gyro.

angular velocity of the case can be represented by its X, Y, and Z components:

$$\omega_{(I,\text{Ca})} = \mathbf{i}_{\text{Ca}}\omega_{(I,\text{Ca})X} + \mathbf{j}_{\text{Ca}}\omega_{(I,\text{Ca})Y} + \mathbf{k}_{\text{Ca}}\omega_{(I,\text{Ca})Z} \qquad \text{(B-13)}$$

Substituting into Eq. B-12

$$\omega_{(I,\text{Gi})} = \mathbf{i}_{\text{Ca}}\left(\dot{A}_g + \omega_{(I,\text{Ca})X}\right) + \mathbf{j}_{\text{Ca}}\omega_{(I,\text{Ca})Y} + \mathbf{k}_{\text{Ca}}\omega_{(I,\text{Ca})Z} \qquad \text{(B-14)}$$

The vector $\mathbf{H}$ can be resolved into the case axis system through the gimbal angle:

$$\mathbf{H} = \mathbf{j}_{\text{Ca}}H\cos A_g + \mathbf{k}_{\text{Ca}}H\sin A_g \qquad \text{(B-15)}$$

Substituting Eqs. B-14 and B-15 into Eq. B-11, and evaluating the cross product, the expression for the gyroscopic output torque becomes

$$\mathbf{M}_g = \mathbf{i}_{\text{Ca}}\left[H\omega_{(I,\text{Ca})Z}\cos A_g - H\omega_{(I,\text{Ca})Y}\sin A_g\right]$$
$$+ \mathbf{j}_{\text{Ca}}\left[H\left(\dot{A}_g + \omega_{(I,\text{Ca})X}\right)\sin A_g\right] - \mathbf{k}_{\text{Ca}}\left[H\left(\dot{A}_g + \omega_{(I,\text{Ca})X}\right)\cos A_g\right] \qquad \text{(B-16)}$$

The $\mathbf{j}_{\text{Ca}}$ and $\mathbf{k}_{\text{Ca}}$ components of Eq. B-16 represent the angular velocity of the inner gimbal about the output axis and result in a gyroscopic output torque about the Y and Z axes. The Y and Z components of the gyroscopic output torque are absorbed by the gimbal bearings and are thus of no particular interest in the analysis to follow. Taking the $\mathbf{i}_{\text{Ca}}$ component of Eq. B-16, then

$$M_{gX} = H\left(\omega_{(I,\text{Ca})Z}\cos A_g - \omega_{(I,\text{Ca})Y}\sin A_g\right) \qquad \text{(B-17)}$$

Since the input axis of the gyro lies along the Z axis of the case, $\omega_{(I,\text{Ca})Z}$ is the angular velocity of the case with respect to inertial space about the input axis of the gyro and is denoted by ω_{IA}; also $\omega_{(I,\text{Ca})Y}$ is the angular velocity of the case with respect to inertial space about the SRA and is denoted by ω_{SRA}; then Eq. B-17 can be rewritten as

$$M_{gX} = H\omega_{\text{IA}}\left[\cos A_g - \left(\frac{\omega_{\text{SRA}}}{\omega_{\text{IA}}}\right)\sin A_g\right] \qquad \text{(B-18)}$$

Equation B-18 describes the response of the gyro to the component of the angular velocity of the case with respect to inertial space that lies along the IA and SRA. The second term in the brackets of Eq. B-18 is referred to as the "coupling term." The coupling term describes the response of the gyro to angular velocities of the case with respect to inertial space about the SRA. Normally, A_g is kept small, especially in the integrating gyro (maximum

values of A_g of about 2.5° are common); thus, the coupling term can be neglected and

$$M_{gx} \simeq H\omega_{\text{IA}} \tag{B-19}$$

If $S_{(g)[\omega; M]}$ is defined as the sensitivity of the gyro for an angular velocity input to a gyroscopic output torque,

$$S_{(g)[\omega; M]} = \frac{M_{gx}}{\omega_{\text{IA}}} = H \frac{\text{g cm}^2}{\text{sec}} \tag{B-20}$$

In the remaining analysis of the single-degree-of-freedom gyro A_g is assumed to be small, and Eq. B-19 is used to describe the gyroscopic output torque resulting from an angular velocity of the case with respect to inertial space about the input axis. The single-degree-of-freedom gyro shown in Figure B-1 would be of no practical value, since there is no method provided for absorbing the gyroscopic output torque. If a spring or elastic restraint is provided that yields a torque proportional to A_g, the single-degree-of-freedom gyro becomes a rate gyro. If a viscous damper is added that yields a torque proportional to $\dot{A}_g$, an integrating gyro results. These two important single-degree-of-freedom gyros are discussed in Sections B-3 and B-4.

B-3 THE RATE GYRO

Figure B-2 shows the configuration of a typical rate gyro. Here the elastic restraint is provided by a torsion bar fixed to the inner gimbal and the case. The viscous damper is added to provide damping of the transient. Using Eq. B-19, the differential equation of the rate gyro can be written by summing
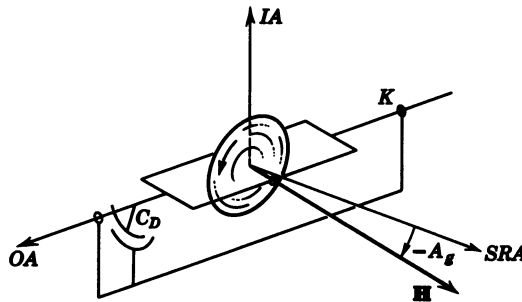
Figure B-2   *Configuration of a typical rate gyro.*

torques about the output axis:

$$M_{gx} = H\omega_{IA} = I_{OA}\ddot{A}_g + C_D\dot{A}_g + KA_g \qquad \text{(B-21)}$$

where K is the spring constant of the torsion bar (dyne cm/rad), C_D is the coefficient of damping of the viscous damper [dyne cm/(rad/sec)], and I_{OA} is the moment of inertia of the gimbal and wheel about the output axis. Dividing through by K and taking the Laplace transformation with the initial conditions zero, Eq. B-21 becomes

$$\left(\frac{I_{OA}}{K}s^2 + \frac{C_D}{K}s + 1\right)A_g(s) = \frac{H}{K}\omega_{IA}(s) \qquad \text{(B-22)}$$

Putting Eq. B-22 in the standard form of the second-order differential equation, it becomes

$$\left[\left(\frac{s}{\omega_n}\right)^2 + \frac{2\zeta}{\omega_n}s + 1\right]A_g(s) = \frac{H}{K}\omega_{IA}(s)$$

where

$$\omega_n = \left(\frac{K}{I_{OA}}\right)^{1/2} \quad \text{and} \quad \zeta = \frac{C_D}{2(KI_{OA})^{1/2}} \qquad \text{(B-23)}$$

For rapid response ω_n should be large; therefore, $K \gg I_{OA}$. In most commercial rate gyros ζ is made equal to about 0.7 and typical values of ω_n are between 150 and 400 rad/sec. The transfer function for the rate gyro for an angular velocity input to a gimbal angle output can be obtained by solving Eq. B-23 for $A_g(s)/\omega_{IA}(s)$. Thus

$$[\text{TF}]_{(rg)(\omega; A_g)} = \frac{\dfrac{H}{K}}{\left(\dfrac{s}{\omega_n}\right)^2 + \dfrac{2\zeta}{\omega_n}s + 1} \text{ sec} \qquad \text{(B-24)}$$

In the analysis of many of the applications of the rate gyro the dynamics can be neglected and the transfer function can be replaced by a sensitivity. Under these conditions, Eq. B-24 becomes

$$S_{(rg)(\omega; A_g)} = \frac{H}{K} \text{ sec} \qquad \text{(B-25)}$$

For either case the steady-state value of A_g for a step input of ω_{IA} is

$$A_g = \frac{H}{K}\omega_{IA} \tag{B-26}$$

To give the reader some conception of the magnitudes of the various parameters of a typical rate gyro, the MIT 10^4 rate gyro, developed by the Instrumentation Lab of MIT, is used as an example. For this gyro

$$H = 10^4 \text{ g cm}^2/\text{sec}$$
$$C_D = 5 \times 10^3 \text{ g cm}^2/\text{sec}$$
$$K = 3.03 \times 10^5 \text{ g cm}^2/\text{sec}^2$$
$$I_{OA} = 34 \text{ g cm}^2$$
$$\omega_n = 94.25 \text{ rad/sec}$$
$$\zeta = 0.78$$

These figures substantiate the conclusion drawn earlier that $K \gg I_{OA}$. Also, as can be seen from the figures, $K \gg C_D \gg I_{OA}$. This relation of the magnitudes of K, C_D, and I_{OA} is common in commercial rate gyros.

Since the output of the rate gyro is a signal proportional to the angular velocity of the case about its input axis with respect to inertial space, the rate gyro has found wide use in flight control systems. In these applications the sensitivity of the rate gyro is such that it cannot detect the component of earth's rate parallel to the input axis of the gyro. Thus, the gyro effectively measures the angular velocity of the case, and thus the aircraft, with respect to the earth.

B-4 RATE INTEGRATING GYRO

If the elastic restraint is removed from the rate gyro, leaving only the viscous damper, the result is referred to as a "rate integrating gyro" or just an "integrating gyro." The differential equation for the integrating gyro can be obtained from Eq. B-21 by letting $K = 0$:

$$M_{gx} = H\omega_{IA} = I_{OA}\ddot{A}_g + C_D\dot{A}_g \tag{B-27}$$

Taking the Laplace transformation of Eq. B-27 with the initial conditions zero and dividing by C_D yields

$$\left(\frac{I_{OA}}{C_D}s + 1\right)\dot{A}_g(s) = \frac{H}{C_D}\omega_{IA}(s) \tag{B-28}$$

Writing Eq. B-28 in standard form, it becomes

$$\left(\tau_{(ig)}s+1\right)\dot{A}_g(s) = \frac{H}{C_D}\omega_{IA}(s) \tag{B-29}$$

where $\tau_{(ig)} = I_{OA}/C_D$. For rapid response $\tau_{(ig)}$ must be small; therefore, $C_D \gg I_{OA}$. Typical values of $\tau_{(ig)}$ are between 0.01 and 0.002 sec. The transfer function for the integrating gyro for ω_{IA} input to a gimbal angle output can be obtained from Eq. B-29:

$$[\text{TF}]_{(ig)(\omega;A_g]} = \frac{H/C_D}{s\left(\tau_{(ig)}s+1\right)} \text{ sec} \tag{B-30}$$

As in the case of the rate gyro, the dynamics of the integrating gyro often can be neglected. Thus, Eq. B-30 reduces to

$$[\text{TF}]_{(ig)(\omega;A_g]} \simeq \frac{H/C_D}{s} \tag{B-31}$$

For either case the steady-state value of A_g for a step input of ω_{IA} is

$$A_g = \frac{H/C_D}{s}\omega_{IA} = \frac{H}{C_D}\int_0^t \omega_{IA}\,dt = \frac{H}{C_D}A_{IA} \tag{B-32}$$

where $A_{IA} = \int_0^t \omega_{IA}\,dt$. The name "integrating gyro" arises from the fact that the gimbal angle is proportional to the time integral of the input angular velocity. Because the integral of the input angular velocity is the total angle through which the gyro has rotated about its input axis with respect to inertial space A_{IA}, A_g is proportional to this angle. A sensitivity can be defined relating A_g to A_{IA}:

$$S_{(ig)(A_{IA};A_g]} = \frac{A_g}{A_{IA}} = \frac{H}{C_D} \tag{B-33}$$

The ratio H/C_D is usually about 1 but may be as large as 2.

TABLE B-1 Comparison of HIG-4 and HIG-6 Gyros

Parameter	HIG-4	HIG-6
H (g cm^2 / sec)	10^4	0.725×10^6
C_D (g cm^2 / sec)	10^4	0.427×10^6
τ (sec)	3.5×10^{-3}	2.5×10^{-3}
I_{OA} (g cm^2)	35	1070

TABLE B-2   Comparison of the Rate and Integrating Gyro

Rate Gyro	Integrating Gyro

Differential Equation

$$I_{OA}\ddot{A}_g + C_D\dot{A}_g + KA_g = H\omega_{IA} \qquad\qquad I_{OA}\ddot{A}_g + C_D\dot{A}_g = H\omega_{IA}$$

$$[TF]_{(rg)[\omega; A_g]} = \frac{\dfrac{H}{K}}{\left(\dfrac{s}{\omega_n}\right)^2 + \dfrac{2\zeta}{\omega_n}s + 1}\; \text{sec} \qquad\qquad [TF]_{(Ig)[\omega; A_g]} = \frac{H/C_D}{s\left(\tau_{(Ig)}s + 1\right)}\; \text{sec}$$

$$\omega_n = \sqrt{K/I_{OA}} \quad \zeta = \frac{C_D}{2\sqrt{KI_{OA}}} \qquad\qquad \tau_{(Ig)} = \frac{I_{OA}}{C_D} \quad C_D \ggg I_{OA}$$

$$K \gg C_D \ggg I_{OA} \qquad\qquad [TF]_{(Ig)[\omega; A_g]} \simeq \frac{H/C_D}{s}\; \text{sec}$$

$$S_{(rg)[\omega; A_g]} = \frac{H}{K}\; \text{sec} \qquad\qquad S_{(Ig)[A_{IA}; A_g]} = \frac{H}{C_D}$$

Steady-State Value of A_g for Step Input of ω_{IA}

$$A_g = \frac{H}{K}\omega_{IA} \qquad\qquad A_g = \frac{H}{C_D}\int_0^t \omega_{IA}\, dt$$

The parameters for a couple of integrating gyros are given in Table B-1 for comparison with the MIT 10^4 rate gyro. The two gyros are the HIG-4 and HIG-6 built by Minneapolis-Honeywell. The HIG stands for hermetic integrating gyro. As the gimbal angle of the integrating gyro is proportional to the integral of the input angular velocity, the integrating gyro is always used in a closed loop system. The two gyros are summarized in Table B-2.

REFERENCE

1. W. R. Weems, *An Introduction to the Study of Gyroscopic Instruments*, Instrumentation Section, Department of Aeronautical Engineering, Massachusetts Institute of Technology, 1948.

Appendix *C*

Basic Servo Theory

C-1 THE BLOCK DIAGRAM

A physical system can be represented by what is called a block diagram. A block diagram is composed of individual blocks that represent the various components of the system. The transfer function, which is the Laplace transform of the ratio of the output to the input with the initial conditions zero, is usually given for each block. The other important element in the block diagram is the summation point or points. A summation point is used for the addition or subtraction of like quantities such as voltages, forces, torques, etc. Some devices used in this text for summation or comparison are the vertical gyro, for comparison of the desired and actual vehicle attitude; the integrating gyro, which actually sums torques about its output axis; and summing amplifiers, for the summation of voltages. The symbol used to represent a summation point is shown in Figure C-1, and the sign associated with the summer indicates the operation being performed. If the quantities being summed are voltages representing the system parameters, for the case shown in Figure C-1(*a*) the voltages must be of opposite sign before being summed. Other comparison devices are synchros and potentiometers used for determining the relative positions of shafts. Still others are discussed in the literature and textbooks on servomechanisms. The derivations of the transfer functions of various electrical, mechanical, and hydraulic components are not covered here, as they can be found in such servo texts as those listed at the end of this appendix.

(a)   (b)

Figure C-1 Representation of summing points.

C-2 THE CONTROL RATIO

The control ratio is defined as the ratio of the output to the input for a closed loop system. Figure C-2 shows a block diagram of a feedback system using standard symbols. Since the sign at the summer associated with the feedback signal is negative, the system is said to have negative feedback, which is normal.

The control ratio can be derived from the relations given in Figure C-2, which yields

$$\frac{C(s)}{R(s)} = \frac{G(s)}{1 + G(s)H(s)} \tag{C-1}$$

which is the normal form of the control ratio. However, for reasons to be discussed later in the section Eq. C-1 is written here as

$$\frac{C(s)}{R(s)} = \frac{G(s)}{1 - [-G(s)H(s)]} = \frac{G(s)}{1 - [\text{TF}]_{\text{OL}}} \tag{C-2}$$

where $[\text{TF}]_{\text{OL}}$ is defined as the open-loop transfer function and consists of the product of the forward transfer function, the feedback transfer function (including the sign associated with each transfer function), and the sign at the summer corresponding to the feedback signal. Thus for Figure C-2 we have $[\text{TF}]_{\text{OL}} = -G(s)H(s)$. The control ratio is more general when written as

$R(s)$ = reference input
$E(s)$ = actuating signal
$G(s)$ = forward transfer function
$C(s)$ = controlled variable or output
$H(s)$ = feedback transfer function (= 1 in many cases)
$B(s)$ = feedback signal
$C(s)$ = $E(s)G(s)$
$B(s)$ = $C(s)H(s)$
$E(s)$ = $R(s) - B(s)$

Figure C-2 Block diagram of a typical feedback system.
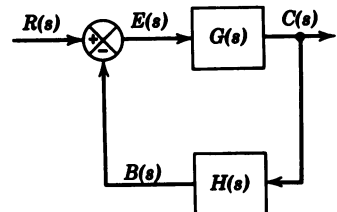
given in Eq. C-2, especially when the transfer functions may be negative, like many of the transfer functions used in this book. By using Eq. C-2, for the control ratio, the engineer determines the sign needed at the summer to yield the necessary sign for the open loop transfer function after considering the signs of the various transfer functions. As is shown later in Sections C-5 and C-7, the net sign associated with the open loop transfer function determines the type of root locus to be plotted.

There are two standard forms used in writing any transfer function. One form is obtained by making the coefficient of the highest power of s equal to unity as in

$$G(s) = \frac{K(s+1/\tau_1)}{(s+1/\tau_2)(s^2+2\zeta\omega_n s+\omega_n^2)} \tag{C-3}$$

In this form K is called the "static loop sensitivity."[1] This form of the transfer function is employed when using the root locus for analysis. The other form is obtained by making the coefficient of the lowest power of s unity. In this form Eq. C-3 becomes

$$G(s) = \frac{K'(\tau_1 s+1)}{(\tau_2 s+1)\left(\dfrac{s^2}{\omega_n^2}+\dfrac{2\zeta}{\omega_n}s+1\right)} \tag{C-4}$$

where $K' = \tau_2 K/\tau_1\omega_n^2$. The significance of K' is discussed in Section C-3.

C-3 SYSTEM TYPES

Closed loop servo systems with unity feedback are classified according to the number of pure integrations appearing in the forward transfer function, $G(s)$. Thus a Type 0 system would have no pure integrations in the forward transfer function, a Type 1, one, a Type 2, two, etc. To illustrate the significance of the various types of systems, some simple examples will now be given. The unity feedback system shown in Figure C-3 is used for all these
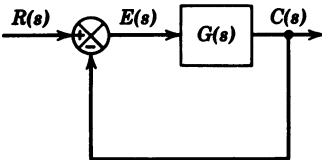
Figure C-3 *Unity feedback control system.*

examples, with

$$G(s) = \frac{K'(\tau_1 s + 1)(\tau_2 s + 1) \cdots}{s^n(\tau_a s + 1)(\tau_b s + 1) \cdots} \qquad \text{(C-5)}$$

and $n = 0, 1, 2, \ldots$. Before proceeding with the examples, the $E(s)/R(s)$ transfer function is given. From the relations given in Figure C-2,

$$\frac{E(s)}{R(s)} = \frac{1}{1 + G(s)} \qquad \text{(C-6)}$$

where $E(s)$ is now the error signal, since $H(s) = 1$.

In the following examples the steady-state value of the error is determined for different inputs for the different types of systems.

Example 1. Type 0 system, n = 0. For a unit step input, $R(s) = 1/s$; then from Eq. C-6

$$E(s) = \frac{1}{s} \left[\frac{1}{1 + G(s)} \right] \qquad \text{(C-7)}$$

To obtain the steady-state value, that is, the value of $e(t)$ as $t \to \infty$, the final value theorem must be used. The final value theorem in equation form is[1]

$$\lim_{t \to \infty} e(t) = \lim_{s \to 0} sE(s) \qquad \text{(C-8)}$$

Then from Eq. C-7

$$e(t)_{ss} = \lim_{s \to 0} \left[\frac{1}{1 + G(s)} \right] = \frac{1}{1 + K'} \qquad \text{(C-9)}$$

as

$$\lim_{s \to 0} \frac{K'(\tau_1 s + 1)(\tau_2 s + 1) \cdots}{(\tau_a s + 1)(\tau_b s + 1) \cdots} = K'$$

Therefore for a Type 0 system for a step input there is a constant error, the value of which depends on the value of K'. For this reason K' is referred to as the error coefficient (see Ref. 1, Sections 6-7, and 6-8, for a discussion of error coefficients).

For a unit ramp input, $R(s) = 1/s^2$, so

$$E(s) = \frac{1}{s^2} \left[\frac{1}{1 + G(s)} \right]$$

Then

$$e(t)_{ss} = \lim_{s \to 0} \frac{1}{s} \left[\frac{1}{1+G(s)} \right] = \infty$$

Therefore for a Type 0 system for a ramp input the error approaches ∞ as $t \to \infty$.

Example 2. Type 1 System, $n = 1$. For a unit step input,

$$E(s) = \frac{1}{s} \left[\frac{1}{1+G(s)} \right]$$

Then

$$e(t)_{ss} = \lim_{s \to 0} \left[\frac{1}{1+G(s)} \right] = 0$$

as

$$\lim_{s \to 0} \frac{K'(\tau_1 s + 1)(\tau_2 s + 1) \cdots}{s(\tau_a s + 1)(\tau_b s + 1) \cdots} = \infty$$

For a unit ramp input

$$E(s) = \frac{1}{s^2} \left[\frac{1}{1+G(s)} \right]$$

Then

$$e(t)_{ss} = \lim_{s \to 0} \frac{1}{s} \left[\frac{1}{1 + \dfrac{K'(\tau_1 s + 1)(\tau_2 s + 1) \cdots}{s(\tau_a s + 1)(\tau_b s + 1) \cdots}} \right]$$

$$= \lim_{s \to 0} \frac{1}{s + \dfrac{K'(\tau_1 s + 1)(\tau_2 s + 1) \cdots}{(\tau_a s + 1)(\tau_b s + 1) \cdots}} = \frac{1}{K'}$$

In like manner $e(t)_{ss}$ for a parabolic input, $R(s) = 1/s^3$, can be shown to be ∞. The same procedure can be followed for a Type 2 system, etc. The results are tabulated in Table C-1. It must be remembered that the classification of servos into Type 0, 1, 2, etc. is valid only for unity feedback systems; however, the steady-state value of the output or the actuating signal for any aperiodic inputs can be obtained in the manner illustrated here for nonunity feedback systems.

TABLE C-1   Steady-State Error for Various Inputs for Various Type Servo Systems

System Type	Steady-State Error for Input Indicated		
	Unit Step	Unit Ramp	Unit Parabola
0	$\dfrac{1}{1+K'}$	∞	∞
1	0	$\dfrac{1}{K'}$	∞
2	0	0	$\dfrac{1}{K'}$
3	0	0	0

C-4   ROOT LOCUS

The root locus is a convenient and useful method for determining the effects of varying the gain on the dynamics of a closed loop servo. These effects are shown analytically for a simple system and are then related to the graphical or root locus method. The system analyzed is shown in Figure C-4. For this system the closed loop transfer function is

$$\frac{C(s)}{R(s)} = \frac{\dfrac{K}{(s+1)(s+5)}}{1+\dfrac{K}{(s+1)(s+5)}} \tag{C-10}$$

Simplifying,

$$\frac{C(s)}{R(s)} = \frac{K}{(s+1)(s+5)+K} = \frac{K}{s^2+6s+K+5} \tag{C-11}$$

From Eq. C-11 it can be seen that as K is increased from zero, the roots of the quadratic in the denominator vary. Since the denominator of Eq. C-11 is the characteristic equation of the differential equation relating the output $C(s)$ to the input $R(s)$, the roots of the denominator determine the solution of the homogeneous equation and therefore the characteristics of the tran-
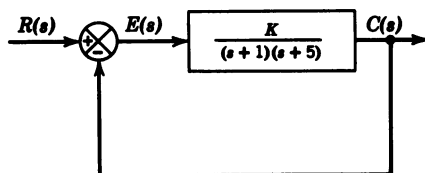
Figure C-4   *Simplified control system.*

TABLE C-2   The Roots of Eq. C-11 for Various Values of K

K	s_1	s_2
0	−1	−5
2	−1.586	−4.414
4	−3	−3
8	−3+j2	−3−j2
13	−3+j3	−3−j3
−5	0	−6

sient response of the system. The roots of the denominator of Eq. C-11 are called the poles of the closed loop transfer function. The roots of the characteristic equation can be obtained by using the quadratic formula; thus

$$s_{1,2} = -3 \pm \sqrt{9-(K+5)} \qquad\qquad (C-12)$$

From Eq. C-12 it can be seen that for $K \le 4$ the roots are real, while for $K > 4$ they are imaginary. When the roots are imaginary the general form of the characteristic equation is $s^2 + 2\zeta\omega_n s + \omega_n^2 = 0$, the roots of which are

$$s_{1,2} = -\zeta\omega_n \pm j\omega_n\sqrt{1-\zeta^2} = -\sigma \pm j\omega_d$$

The roots given by Eq. C-12 are tabulated for various values of K in Table C-2 and are plotted for all values of K in Figure C-5. Although K is generally positive, which means that negative feedback is being employed, K may be negative. As can be seen from Figure C-5, the system would be stable
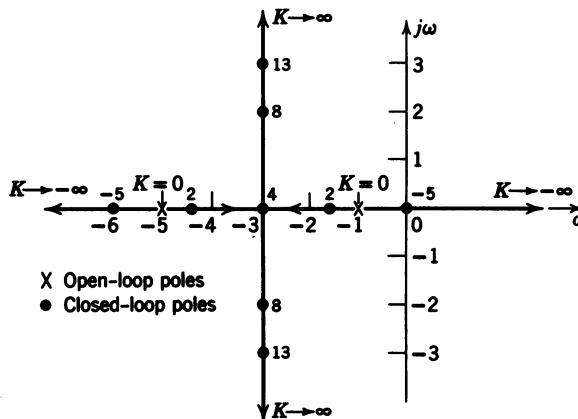
Figure C-5 A plot of all roots of Eq. C-11 for $-\infty < K < \infty$. The values of K for the roots listed in Table C-2 are indicated.

for $K > -5$. The curve shown in the figure is defined as the root locus plot of Eq. C-11. Figure C-5 was obtained by substituting various values of K into Eq. C-12 to determine the roots of the characteristic equation. For this simple example this procedure was not difficult; however, for a more complex system it would be extremely time consuming; therefore, a simpler method is needed. The rest of this appendix is devoted to the normal procedure for obtaining the root locus plot and to the interpretation thereof.

Before proceeding with the details of the construction of the root locus, the theory behind the basic rules is discussed. Figure C-5 was obtained by equating the denominator of Eq. C-11 to zero and solving for the roots for various values of K. For the root locus it is more useful to use Eq. C-10. Equating the denominator of Eq. C-10 to zero yields

$$1 + \frac{K}{(s+1)(s+5)} = 0$$

or

$$\frac{K}{(s+1)(s+5)} = -1 = 1\underline{/180°} \qquad \text{(C-13)}$$

If some value of s satisfies Eq. C-13, then for this value of s

$$\left| \frac{K}{(s+1)(s+5)} \right| = 1 \qquad \text{(C-14)}$$

and

$$\underline{/\frac{K}{(s+1)(s+5)}} = \text{an odd multiple of } 180° \qquad \text{(C-15)}$$

Equation (C-14) is referred to as the "magnitude condition" and is used to determine the value of K for a given value of s, and Eq. C-15 is referred to as the "angle condition" and is used to plot the root locus. The use of Eqs. C-14 and C-15 is first demonstrated by using the value $s = -3 + j2$ from Figure C-5. This can be done both analytically and graphically. To proceed with the analytic method, the value of s is substituted in Eq. C-13; thus

$$\frac{K}{(-3+j2+1)(-3+j2+5)} = \frac{K}{(-2+j2)(2+j2)} = -1 \qquad \text{(C-16)}$$
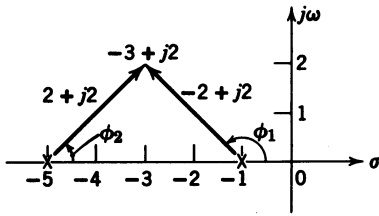
Figure C-6 Representation of the vectors from $s = -1$ and $s = -5$ to $s = -3 + j2$.

Evaluating, $K/-8 = -1$. For the magnitude condition from Eq. C-14

$$\left| \frac{K}{-8} \right| = \frac{K}{8} = 1$$

Therefore, $K = 8$ as before. For the angle condition

$$\frac{K}{-8} = \frac{K}{8 \underline{/180°}} = \frac{K}{8} \underline{/-180°}$$

Therefore the angle is $-180°$, which satisfies Eq. C-15. For the graphical method, which is normally used, examination of the two factors in the denominator of Eq. C-16 shows that they represent the vectors from $s = -1$ and $s = -5$ to the point $s = -3 + j2$. This is illustrated in Figure C-6. Each of the two vectors can be represented by its magnitude and angle. The magnitudes can be obtained by measuring the length of the vectors with a scale. From Eq. C-14, $K = |(s+1)(s+5)|$; therefore, K is equal to the product of the magnitudes of the two vectors. Measuring the two vectors yields a magnitude for each of approximately 2.82 units. Squaring this yields 7.97, or approximately 8. (Obviously any graphical method is less accurate than an analytic solution.) The angles of the two vectors are ϕ_1 and ϕ_2, which can be measured with a protractor. Here $\phi_1 = 135°$ and $\phi_2 = 45°$, and the sum is 180° as before.

Since the whole purpose of the root locus analysis is to determine the closed loop poles which determine the behavior of a system for some value of K, the final step is obtaining the closed loop transfer function from Figure C-5 for a particular value of K. Thus the closed loop transfer function for $K = 8$ is

$$\frac{C(s)}{R(s)} = \frac{8}{(s+3-j2)(s+3+j2)} = \frac{8}{s^2 + 6s + 13} \tag{C-17}$$

Section C-5 deals with the actual construction of a typical root locus and gives all the geometric short cuts.

C-5 CONSTRUCTION OF THE ROOT LOCUS

In the preceding section it was shown that it was necessary to determine the roots of the denominator of the closed loop transfer function as a function of the variable gain. This means that, in the general case, $1 + G(s)H(s)$ must be made equal to zero. In general, $G(s)H(s)$ will be of the form

$$G(s)H(s) = \frac{K(s+a_1)(s+a_2)\cdots}{(s+b_1)(s+b_2)(s+b_3)\cdots} \qquad \text{(C-18)}$$

The roots of the numerator are called the zeros of the transfer function, while the roots of the denominator are called the poles. Due to the physical nature of feedback control systems, the order of the numerator is usually less than or equal to the order of the denominator. From Eq. C-14 the "magnitude condition" can be determined, which yields

$$K = \left| \frac{(s+b_1)(s+b_2)(s+b_3)\cdots}{(s+a_1)(s+a_2)\cdots} \right| \qquad \text{(C-19)}$$

Thus K is always equal to the product of the distances from the open loop poles to a particular closed loop pole divided by the product of the distances from the open loop zeros to the same closed loop pole. For the "angle condition," from Eq. C-15

$$\angle \frac{K(s+a_1)(s+a_2)\cdots}{(s+b_1)(s+b_2)(s+b_3)\cdots} = 180(1+2m) \qquad \text{(C-20)}$$

where $m = 0, 1, 2, \ldots$, which states that the sum of the angles of the numerator terms minus the sum of the angles of the denominator terms is equal to an odd multiple of $180°$. The rest of the rules are introduced as required.

The rules given here allow the engineer to manually construct the root locus in order to obtain a first look at the potential performance of the system being analyzed and/or designed. The manual plot can also be used as a check on the correctness of a computer generated root locus using TOTAL[5] or one of the other computer-aided-design (CAD) programs listed in Section C-10. A sample root locus is drawn to illustrate the procedure.

The system to be analyzed is shown in Figure C-7, which is the same system that is discussed in Section 4-2 with the time constant of the washout circuit adjusted to yield an additional breakaway point and a break-in point.
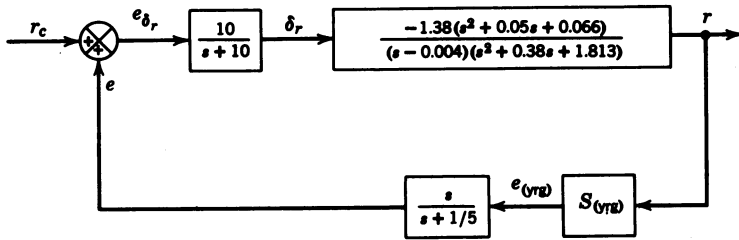
Figure C-7 *Block diagram of system to be analyzed.*

For this system,

$$[\text{TF}]_{\text{OL}} = G(s)H(s) = \frac{-13.8S_{(\text{yrg})}s(s^2+0.05s+0.066)}{(s+10)(s-0.004)(s+0.2)(s^2+0.38s+1.813)}$$

(C-21)

Then $K = 13.8S_{(\text{yrg})}$. The details of the construction are presented here.

1. *Plot the poles and zeros of $G(s)H(s)$.* See Figure C-8:

$$
\begin{aligned}
\text{Zeros:} \quad & s = 0 \\
& s = -0.025 \pm j0.256 \\
\text{Poles:} \quad & s = -10 \\
& s = -0.2 \\
& s = -0.19 \pm j1.33 \\
& s = 0.004
\end{aligned}
$$

2. *Real axis locus.* To the right of all poles and zeros the sum of all the angles from the poles and zeros is zero. After passing to the left of the pole
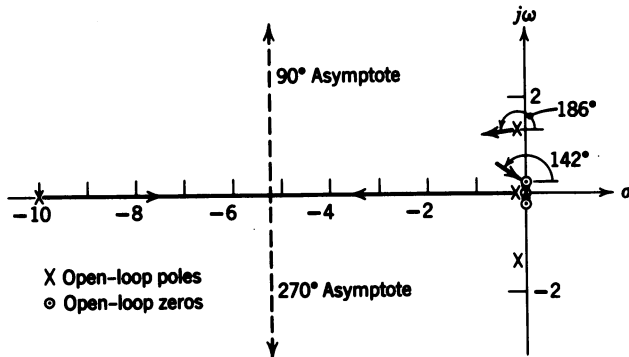
Figure C-8 *Sample problem.*

at 0.004, the sum of the angles is 180°, and to the left of the zero at the origin the sum of the angles is 360°, etc. The extent of the real axis locus is shown in Figure C-8.

3. *Real axis intercept of the asymptotes.* From Eq. C-19, if the value of the pole is equal to any of the zeros, that is, $s = -a$, then $K = \infty$; and if there are more poles than zeros in the open loop transfer function, then for $s = \infty$ in Eq. C-19, $K = \infty$. Therefore, as $K \to \infty$, part of the root locus approaches the open loop zeros; the remaining branches go to the hypothetical zeros at ∞. The branches that approach infinity approach asymptotes that are readily determined. The intercept of the asymptotes on the real axis is normally designated as σ_0, and we have

$$\sigma_0 = \frac{\sum \text{poles} - \sum \text{zeros}}{(\text{number of poles}) - (\text{number of zeros})} \qquad \text{(C-22)}$$

The summations of the poles and zeros include only the real part, since the sum of the imaginary parts of the complex conjugates of complex poles is zero. For this problem

$$\sigma_0 = \frac{(-10-0.2-0.19-0.19+0.004) - (-0.025-0.025)}{5-3}$$

or

$$\sigma_0 = \frac{(-10.576) - (-0.05)}{2} = -5.263$$

4. *Angle of the asymptotes.* The angle that the asymptotes make with the real axis is given by

$$\text{angle of the asymptotes} = \frac{(1+2m)180°}{(\text{number of poles}) - (\text{number of zeros})} \qquad \text{(C-23)}$$

where $m = 0, 1, 2, \ldots, n$ and $n = (\text{number of poles}) - (\text{number of zeros}) - 1$. For this problem,

$$\text{angle of asymptotes} = \frac{(1+2m)180°}{2}$$

For $m = 0$,

$$\text{angle of asymptotes} = \frac{180}{2} = 90°$$

For $m = 1$,

$$\text{angle of asymptotes} = \frac{3(180)}{2} = 270°$$

The asymptotes are also shown in Figure C-8. There is a real axis locus from the pole at 0.004 to the zero at the origin that cannot be shown in Figure C-8 due to the scale.

5. *Angle of departure from the complex pole.* For a point on the root locus very near a complex pole, the angle condition still must be satisfied. If the point being located is very close to the complex pole, the angles from the other poles and zeros to the point can be determined simply by measuring the angles to the complex pole itself. The angle from the complex pole to the point being located is defined as the "angle of departure," and is designated by ϕ_T. This angle cannot be measured, because the test point is too close to the complex pole; however, since the angle condition must be satisfied, ϕ_T can be determined by using Eq. C-20. This procedure is illustrated by redrawing Figure C-8 to show these angles (see Figure C-9). For simplicity the figure is not drawn to scale; the pole at 0.004 and the zero at the origin are neglected because their contribution to the angle condition is negligible. From Eq. C-20, $\underline{/\text{numerator}} - \underline{/\text{denominator}} = 180(1 + 2m)°$, or from Figure C-9

$$\psi_1 + \psi_2 - (\phi_1 + \phi_2 + \phi_3 + \phi_T) = 180(1 + 2m)° \qquad \text{(C-24)}$$

Measuring these angles from Figure C-8 and substituting into Eq. C-24 yields
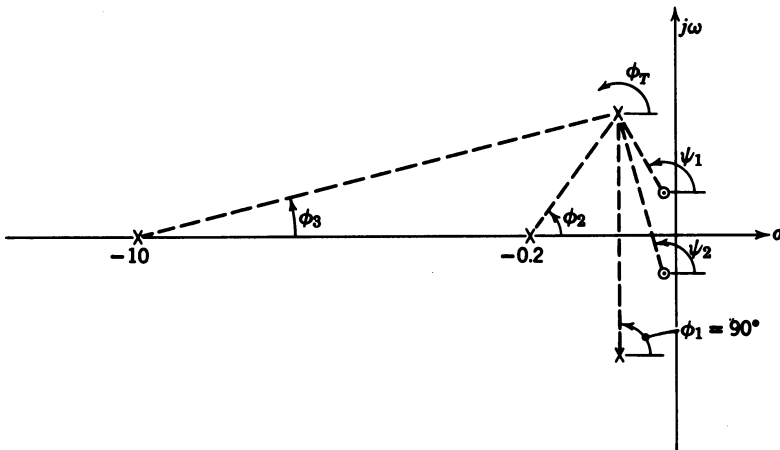
Figure C-9 *Determination of the angle of departure from the complex pole s* $= -0.19 + j1.33$. *Note: This figure is not drawn to scale.*
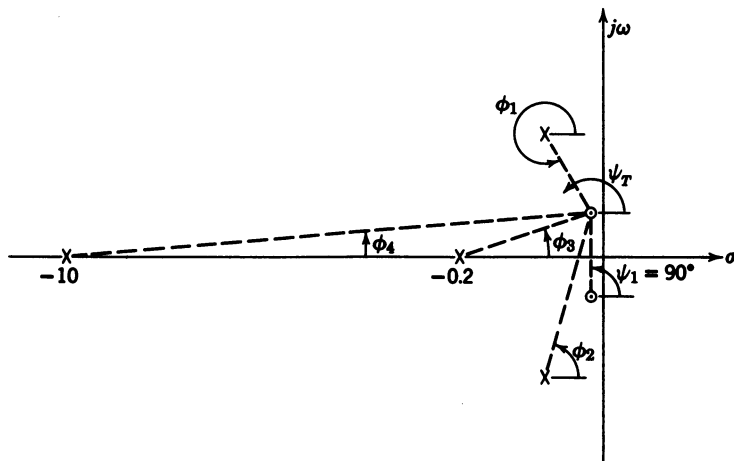
Figure C-10 Determination of the angle of arrival at the complex zero s = −0.025 + j0.256. Note: This figure is not drawn to scale.

$(97 + 95) − (90 + 88 + 8 + \phi_T) = 180(1 + 2m)°$, or $\phi_T = −174° = 186°$ (see Figure C-8).

6. *Angle of arrival at a complex zero.* The same procedure can be applied to determine the angle of arrival at a complex zero (ψ_T), which is illustrated in Figure C-10. Again from Eq. C-20,

$$\psi_1 + \psi_T − (\phi_1 + \phi_2 + \phi_3 + \phi_4) = 180(1 + 2m)° \qquad (C\text{-}25)$$

Substituting the values of the angles as measured from Figure C-8 yields $90 + \psi_T − (277 + 85 + 48 + 2) = 180(1 + 2m)°$, or $\psi_T = 180 + 322 = 502°$, which is equivalent to $502 − 360$ or $142°$ (see Figure C-8).

7. *Breakaway or break-in point on the real axis.* Referring to Figure C-8, it can be seen that there must be a transition point where the root locus leaves the real axis and proceeds toward the asymptotes. This point is referred to as a "breakaway point." There also may be a break-in point, that is, where the root locus moves onto the real axis. There are several methods for determining these breakaway or break-in points. An analytical method is discussed in Ref. 1, pp. 228–230. The method explained here is often referred to as the hills-and-dales method. Since K must increase as any pole moves from an open-loop pole to a finite zero or to a fictitious zero at infinity, then if two poles come together on the real axis and break away, the value of K at the breakaway point must be greater than its value on either side. Similarly, if the root locus breaks into the real axis, the value of K at the break-in point is lower than its value on either side. Thus to determine the existence and approximate location of the breakaway or break-in points it is only necessary
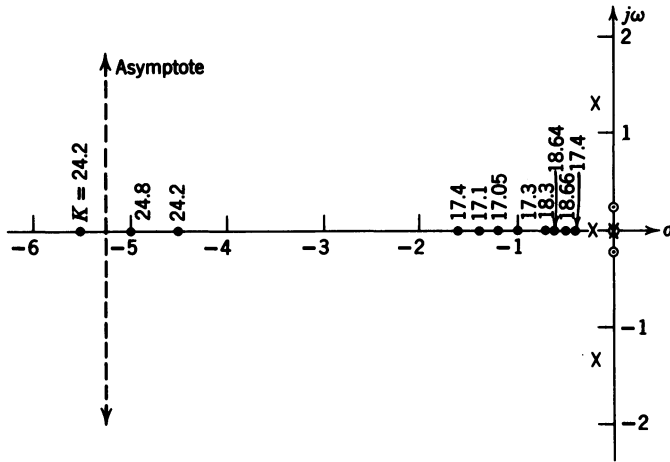
Figure C-11 *Variation of K along the real axis for the sample problem.*

to check the magnitude condition along the real axis. The results of these calculations are plotted in Figure C-11, where it can be seen that there are breakaway points near -5 and -0.5 and a break-in point near -1.2. A final check can be made by checking the angle condition about $\frac{1}{4}$ inch above the real axis in the vicinity of the maximum and minimum values of K.

8. *Imaginary axis crossing.* Routh's criterion can be used to determine the values of $j\omega$ at which the root locus crosses the imaginary axis (see Ref. 1, pp. 185–191). However, if the root locus crosses the imaginary axis, the asymptotes also must cross. It is usually easier, unless the problem is very simple, to find the imaginary axis crossing by searching for a point along the $j\omega$ axis that satisfies the angle condition (this point will be near the asymptote crossing). For this problem there is no imaginary axis crossing.

9. *Remaining plot.* After steps 1–8 have been accomplished, as applicable, it is necessary to complete the root locus by locating points that satisfy the angle condition. It is not necessary to find many points in this way. The most important part of the root locus is in the vicinity of the desired closed loop poles. The final root locus is plotted in Figure C-12 with the points actually determined by use of the angle condition indicated. Notice that by locating only four points (one of these is one of the complex closed loop poles) the rest of the root locus was determined. Actually it would have been sufficient to determine only the portion of the root locus from the complex poles to the real axis and along the real axis.

10. *Location of the closed loop poles.* After the root locus has been determined, it is necessary to determine the location of the closed loop poles. The location of the dominant pole or poles is usually dictated by the type of response desired. The dominant poles, either real or imaginary, are those
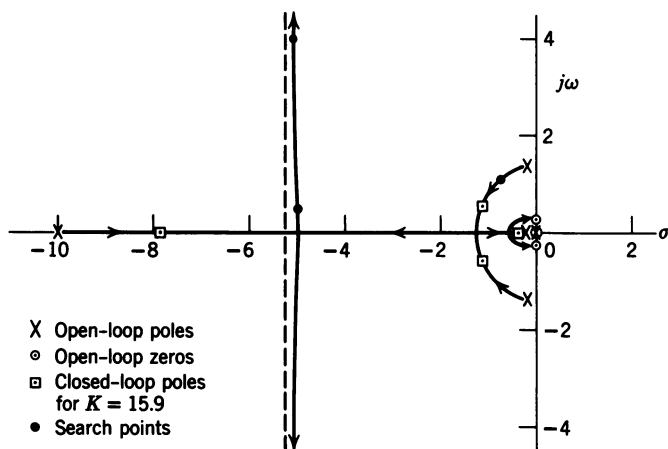
Figure C-12 Root locus for the sample problem.

closest to the imaginary axis provided they are not very close to a zero. After determining the dominant pole or poles, that is, one real pole or a pair of complex poles, the corresponding magnitude condition can be determined. The rest of the closed loop poles must satisfy the same magnitude condition. For the sample problem there is a damping ratio of 0.9 for the complex roots. Applying the magnitude condition, as given in Eq. C-19, yields

$$K = \frac{(8.86)(1.24)(2.12)(1.1)}{(1.17)(1.38)} = 15.9$$

The remaining closed loop poles must also yield the same value for K. From Figure C-11, the K for $s = -0.4$ is 17.4, and the K for $s = -0.3$ is 12.8. Therefore, there is a real axis closed loop pole between -0.3 and -0.4. The pole is closer to -0.4 than to -0.3, and is assumed to be at $s = -0.38$. The pole that started at $s = 0.004$, and is moving toward the origin, is assumed not to have moved. There is now one more closed loop pole to determine; this is the pole that started at $s = -10$ and is moving in along the real axis. From Figure C-11 it can be seen that it is to the left of $s = -5.5$. This pole can be located by checking the magnitude condition along the real axis between $s = -5.5$ and $s = -10$. However, there is a simpler way to locate at least the approximate position. Referring to Table C-2, it can be seen that the sum of the real parts of s_1 and s_2 is a constant and equal to -6; this is not a coincidence, and is always true if the number of open loop poles of $G(s)H(s)$, minus the number of zeros of $G(s)H(s)$, is equal to or greater than 2. (This characteristic of the root locus was discussed by A. J. Grant of North American Aviation, Inc., in an unpublished paper entitled "The Conservation of the Sum of the System Roots as Applied to the Root Locus

Method" dated April 10, 1953, and for this reason is often referred to as Grant's rule.[1]) The initial value of the sum of the poles is -10.576. Thus far the closed loop poles that have been determined are $s = -1.15 \pm j0.55$, $s = -0.38$, $s = 0.004$. The sum of these poles is -2.676; therefore, the remaining pole should be near -7.9. A check of the magnitude condition for $s = -7.9$ yields a K of 15.8, which is close enough. All the closed loop poles corresponding to a K of 15.9 have been determined. From Eq. C-21, $K = 13.8 S_{(yrg)}$. Then, $S_{(yrg)} = K/13.8 = 15.9/13.8 = 1.15$. For simplicity a value of 1 can be used.

The remaining step is the writing of the closed loop transfer function.

C-6   CLOSED LOOP TRANSFER FUNCTION

The closed loop transfer function is given by Eq. C-2, which is repeated here for convenience:

$$\frac{C(s)}{R(s)} = \frac{G(s)}{1 - [\text{TF}]_{\text{OL}}} \tag{C-26}$$

For this problem it is

$$\frac{r(s)}{r_c(s)} = \frac{\dfrac{-13.8(s^2 + 0.05s + 0.066)}{(s+10)(s-0.004)(s^2 + 0.38s + 1.813)}}{1 + \dfrac{Ks(s^2 + 0.05s + 0.066)}{(s+10)(s-0.004)(s+0.2)(s^2 + 0.38s + 1.813)}} \tag{C-27}$$

Simplifying,

$$\frac{r(s)}{r_c(s)} = \frac{-13.8(s+0.2)(s^2 + 0.05s + 0.066)}{(s+10)(s-0.004)(s+0.2)(s^2 + 0.38s + 1.813) + Ks(s^2 + 0.05s + 0.066)} \tag{C-28}$$

The root locus has furnished the factors of the denominator of Eq. C-28 for a K of 15.9; thus

$$\frac{r(s)}{r_c(s)} = \frac{-13.8(s+0.2)(s^2 + 0.05s + 0.066)}{(s+7.9)(s-0.004)(s+0.38)(s^2 + 2.3s + 1.64)} \tag{C-29}$$

As a check on the accuracy of the root locus and the denominator of Eq. C-29, the denominator of Eq. C-28 for $K = 15.9$ is expanded, combined, and compared with the denominator of Eq. C-29 after expanding it. From Eq.

C-28 the denominator is $s^5 + 10.576s^4 + 23.45s^3 + 20.01s^2 + 4.589s - 0.0145$, and from Eq. C-29 it is $s^5 + 10.576s^4 + 23.27s^3 + 20.1s^2 + 4.77s - 0.0194$. There is excellent agreement between the two denominators; in fact, in this case it might be considered exceptional.

Equation C-29 is the closed loop transfer function for the block diagram given in Figure C-7 for a yaw rate gyro sensitivity of 1.15. Notice that since the variable gain was in the feedback loop, the static loop sensitivity remains unchanged at 13.8. Also, the open loop pole from the washout circuit shows up as a zero in the closed loop transfer function. Thus any time the feedback loop contains a transfer function, the step shown in Eq. C-27 should be used to assure the proper form of the closed loop transfer function. This can also be accomplished by using the following equation,[1] where $G(s) = N_1(s)/D_1(s)$ and $H(s) = N_2(s)/D_2(s)$:

$$\frac{C(s)}{R(s)} = \frac{N_1 D_2}{D_1 D_2 + N_1 N_2} \qquad \text{(C-30)}$$

C-7 ZERO-ANGLE ROOT LOCUS

In Section C-5 the rules were given for the so-called 180° root locus. That is, $1 + G(s)H(s) = 0$, or $G(s)H(s) = 1\underline{/180°}$. In some instances where positive feedback is used, or—as in this book—for non-minimum-phase-angle transfer functions (that is, zeros in the right half plane), if $[\text{TF}]_{\text{OL}}$ is positive, the zero-angle root locus must be plotted. If the open loop transfer function is positive, as defined in Section C-2, then $1 - G(s)H(s) = 0$ and $G(s)H(s) = 1\underline{/0°}$. To plot the zero-angle root locus all the rules given in Section C-5 apply; the only change is the replacement of $(1 + 2m)180°$ in all the angle equations with $2m(180°)$, where $m = 0, 1, 2, \ldots$. The closed loop transfer function is obtained as described in Section C-6 for the 180° root locus.

C-8 FREQUENCY RESPONSE

Frequency response analysis yields the steady-state response of a system to sinusoidal forcing, as indicated in this book, by such figures as 1-9, 1-10, 1-11, etc. This can be accomplished by substituting $j\omega$ for s in the transfer function and then calculating the magnitude and phase angle as a function of ω. (This procedure is covered in detail in Ref. 1, Chapter 8.) At first this sounds time consuming; however, by knowing the characteristic response for a first- or second-order system, the plot for even the most complicated transfer function can be obtained by the proper combination of the appropriate first- and/or second-order responses.

1. *First-order response.* Given

$$G(s) = \frac{K}{s + 1/\tau}$$

then

$$G(j\omega) = \frac{K}{j\omega + 1/\tau}$$

Next, the transfer function must be put in the standard form for obtaining the frequency response curves. For this the form is

$$G(j\omega) = \frac{\tau K}{j\omega\tau + 1} \qquad\qquad \text{(C-31)}$$

The magnitude and phase angle of Eq. C-31 must now be plotted as a function of ω. For $\omega = 0$, $G(j\omega) = \tau K\underline{/0°}$, and as $\omega \to \infty$, $G(j\omega) \to 0\underline{/-90°}$. Also, for $\omega = 1/\tau$,

$$G(j\omega) = \frac{\tau K}{j1 + 1} = \frac{\tau K}{1.414\underline{/45°}}$$

Therefore $G(j\omega) = 0.707\tau K\underline{/-45°}$. The magnitude plot of Eq. C-31 is shown in Figure C-13, and the phase angle plot in Figure C-14. The point where $\omega = 1/\tau$ is called the "break point," and the value of ω is referred to as the "corner frequency." If the first-order term appears in the numerator, the magnitude plot breaks up at the corner frequency and the phase angle goes from 0 to $+90°$.
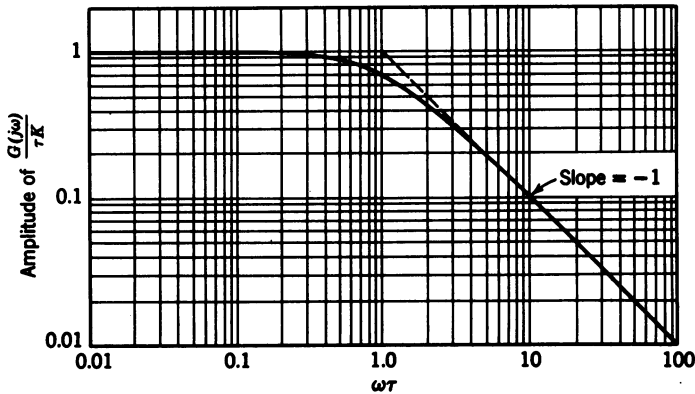
Figure C-13   *Magnitude plot for $(j\omega\tau + 1)^{-1}$.*
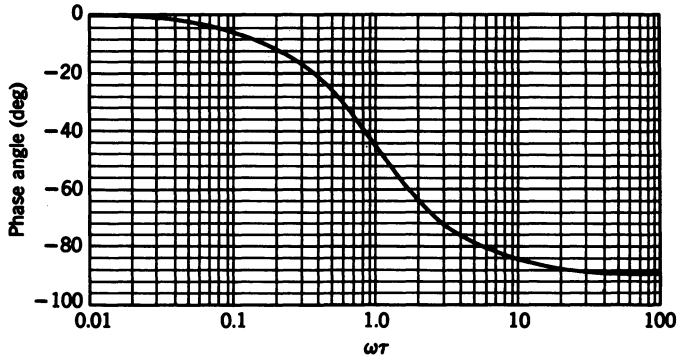
Figure C-14 Phase angle plot for $(j\omega\tau + 1)^{-1}$.

2. *Second-order response.* Given

$$G(s) = \frac{K}{s^2 + 2\zeta\omega_n s + \omega_n^2}$$

Replacing s by $j\omega$ and going to the standard form yields

$$G(j\omega) = \frac{\dfrac{K}{\omega_n^2}}{\left(\dfrac{j\omega}{\omega_n}\right)^2 + \dfrac{j2\zeta\omega}{\omega_n} + 1} \qquad (C\text{-}32)$$

Again, for $\omega = 0$, $G(j\omega) = K/\omega_n^2 \underline{/0°}$, and as $\omega \to \infty$, $G(j\omega) \to 0\underline{/-180°}$. For $\omega = \omega_n$,

$$G(j\omega) = \frac{K/\omega_n^2}{(j)^2 + j2\zeta + 1} = \frac{K/\omega_n^2}{j2\zeta}$$

Therefore $G(j\omega) = K/2\zeta\omega_n^2 \underline{/-90°}$. Thus the magnitude of $G(j\omega)$ at the corner frequency is dependent upon the damping ratio ζ. The lower ζ, the higher the gain at $\omega = \omega_n$. This phenomenon is known as "resonance." The magnitude and phase plots for various values of ζ are shown in Figures C-15 and C-16. Since the amplitude plots are plotted on a logarithmic scale, the magnitude plot for any transfer function can be obtained by adding the plots of each factor of the transfer function.
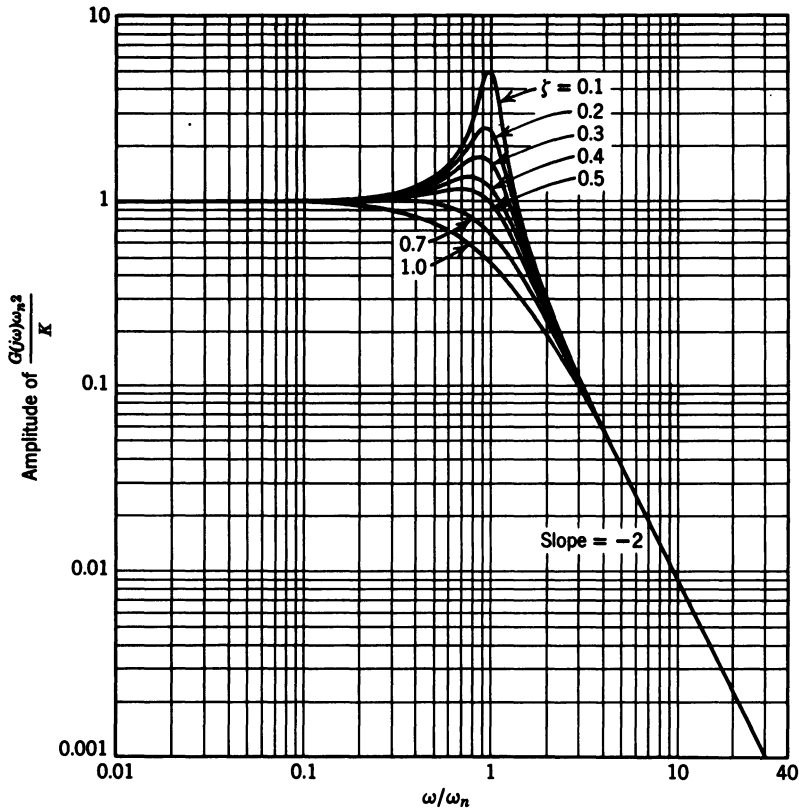
Figure C-15   *Magnitude plot for* $[(j\omega/\omega_n)^2 + j2\zeta\omega/\omega_n + 1]^{-1}$.

3. *Response of a complete transfer function.* Given

$$G(s) = \frac{14.4(s+0.25)}{s(s+10)(s^2+0.48s+1.44)}$$

Then

$$G(j\omega) = \frac{0.25(14.4)(j4\omega+1)}{14.4j\omega(j0.1\omega+1)\left[\left(\dfrac{j\omega}{1.2}\right)^2 + \dfrac{j0.4\omega}{1.2} + 1\right]}$$

$$= \frac{0.25(j4\omega+1)}{j\omega(j0.1\omega+1)\left[\left(\dfrac{j\omega}{1.2}\right)^2 + \dfrac{j0.4\omega}{1.2} + 1\right]} \qquad \text{(C-33)}$$
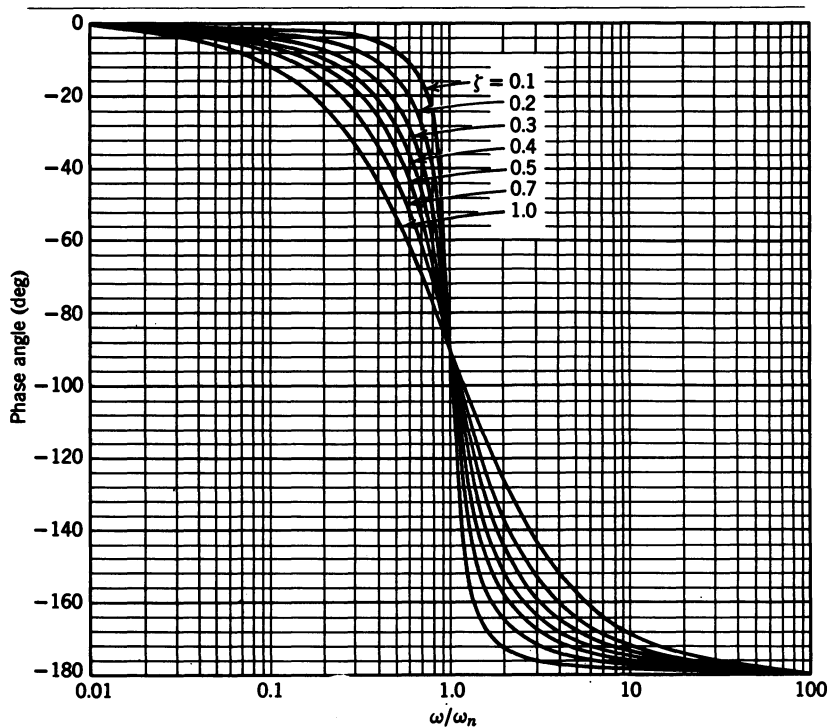
Figure C-16 Phase angle plot for $[(j\omega/\omega_n)^2 + j2\zeta\omega/\omega_n + 1]^{-1}$.
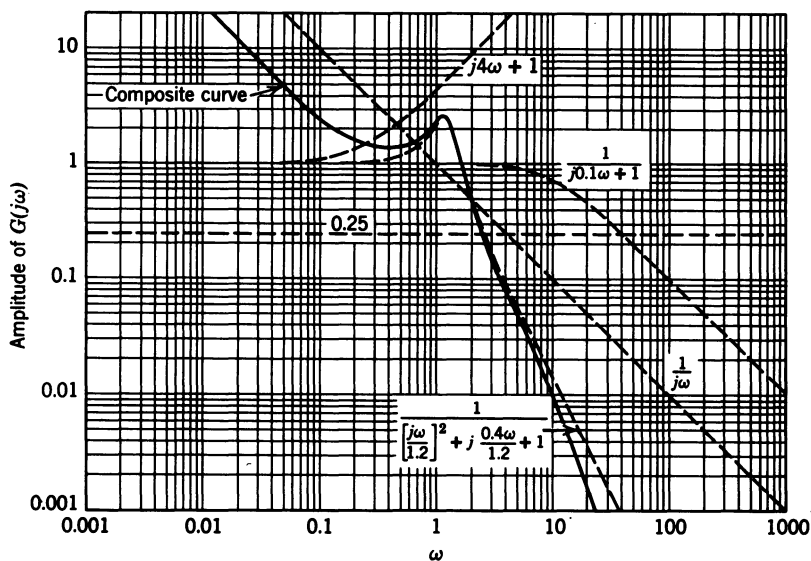
Figure C-17 Magnitude plot for Eq. C-33.
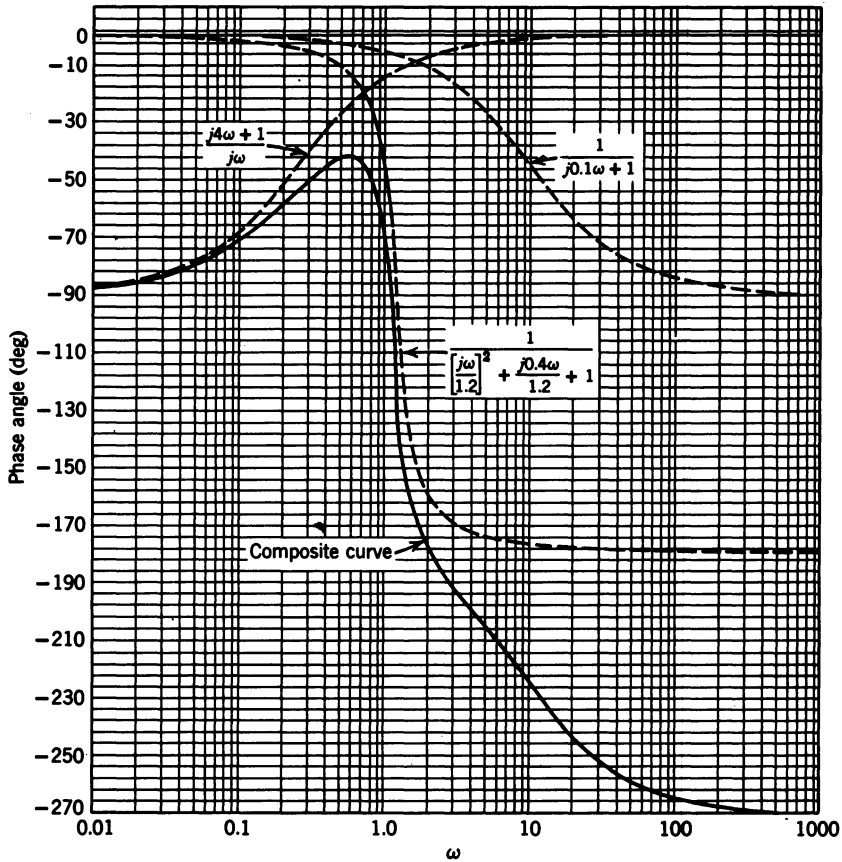
Figure C-18 *Phase angle plot for Eq. C-33.*

The magnitude and the phase plots are shown in Figures C-17 and C-18. As the factor $1/j\omega$ adds a constant phase angle of $-90°$, it is combined with the numerator factor in plotting Figure C-18. In addition to the program TOTAL,[5] two of the CAD programs cited in Section C-10 can be used to generate the frequency response plots shown in Figures C-17 and C-18.

C-9 BODÉ ROOT LOCUS DIAGRAM

Using Program CC (see next section), the Bodé root locus for the root locus shown in Figure C-12 is plotted in Figure C-19. The Bodé root locus is actually the root locus plotted on the Bodé diagram. The magnitude Bodé plot includes the asymptotes, which make it easier to identify the poles or zeros that determine the real axis portion of the root locus. For the root
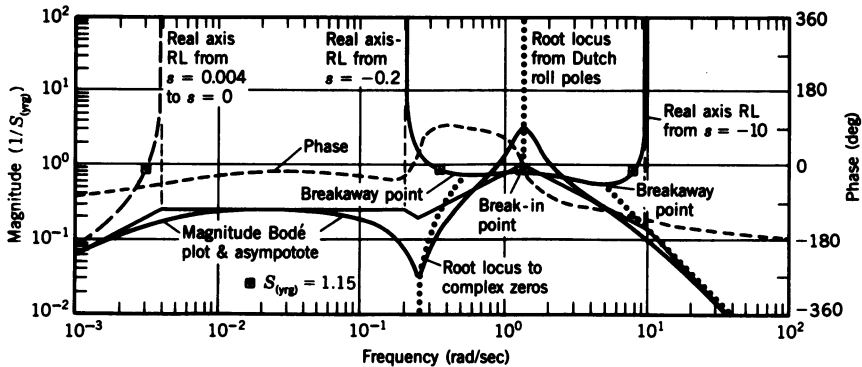
Figure C-19   *Bodé root locus for the root locus shown in Figure C-12.*

locus portion of the figure the following line types are used:

Solid, stable real axis root locus, $\sigma < 0$.

Dashed, unstable real axis root locus, $\sigma > 0$.

Solid circles, stable complex root locus (left half plane).

Open circles, unstable complex root locus (right half plane, see Figure 7-15).

For the complex portion of the root locus, the magnitude of the complex poles is plotted along the horizontal axis, with the reciprocal of the magnitude condition plotted along the vertical axis. Thus at the top of the figure $S_{(yrg)}$, as defined in Section C-5, would be 1/100, or 0.01. Then as $S_{(yrg)}$ increases from 0.01 ($1/S_{(yrg)}$ decreasing from 100), the different branches of the root locus are plotted, which are, from left to right:

1. The real axis branch from the pole at $s = 0.004$ to the zero at the origin (dashed line) becomes asymptotic to the Bodé magnitude plot as both approach zero as the frequency approaches zero.

2. The real axis branch from the pole at $s = -0.2$ heads toward the breakaway point at $s = -0.5$. After breaking away, the complex branch moves toward the complex zeros.

3. The complex branch starting at the Dutch roll poles breaks into the real axis. One pole moves to the left toward the breakaway point mentioned in item 2. The other pole moves to the right toward the breakaway point at $s = -5$. After breaking away, the complex branch is asymptotic to the high-frequency magnitude plot as the branch moves toward the zeros at infinity.

4. The real axis branch from the pole at $s = -10$ moves toward the breakaway point mentioned in item 3.

If a complex branch of the root locus crosses the imaginary axis from the left half plane (stable) to the right half plane (unstable), the solid dots become open dots (see Figure 7-15), and vice versa if the complex branch moves from the right half plane into the left half plane. By the use of two cursors on the computer monitor the gain and the frequency at the crossover point can be read accurately.

In Figure C-19 the locations of the closed loop poles for $S_{(yrg)} = 1.15$ are indicated, and the poles are

$$s = 0.0031$$

$$s = -0.36$$

$$s = -1.15 \pm j0.558 \qquad (s^2 + 2.3s + 1.88)$$

$$s = -7.92$$

A comparison of these poles with the denominator of the closed loop transfer function given in Eq. C-29 shows excellent agreement. It should be remembered that the root locus in Figure C-12 was plotted manually, the calculations having been performed using a slide rule. One distinct advantage of the Bodé root locus is the use of the logarithmic scale, which provides considerably more detail in one plot than the conventional root locus, as evidenced by the real axis branch discussed in item 1 above.

C-10   INTERACTIVE CAD PROGRAMS FOR CONTROL SYSTEM ANALYSIS AND DESIGN

There are several CAD software packages commercially available for the design and analysis of continuous- and discrete-time control systems. These packages can save the control system engineer much time in performing the many calculations required for the design and analysis of a particular control system. Some of these packages are the MATRIX$_X$ program by Integrated Systems, Inc., Santa Clara, California, and Program CC by Systems Technology, Inc., Hawthorne, California. MATRIX$_X$ performs linear systems analysis functions, matrix arithmetic, data analysis, and engineering graphics. Program CC is a complete and powerful linear and multivariable system analysis package with engineering graphics (there is also a less powerful but less expensive student version available). Also available is the MATLAB program by The Math Works, Inc., South Natick, Massachusetts, which performs matrix computations, signal processing, curve fitting, and 2D and 3D graphics.

REFERENCES

1. J. J. D'Azzo and C. H. Houpis, *Linear Control System Analysis and Design: Conventional and Modern*, 3rd ed., McGraw-Hill Book Co., New York, 1988.
2. J. G. Truxal, *Automatic Feedback Control System Synthesis*, McGraw-Hill Book Co., New York, 1955.
3. E. O. Doebelin, *Dynamic Analysis and Feedback Control*, McGraw-Hill Book Co., New York, 1962.
4. B. C. Kuo, *Automatic Control Systems*, Prentice-Hall, Englewood Cliffs, New Jersey, 1962.
5. S. J. Larimer, *An Interactive Computer-Aided Design Program for Digital and Continuous System Analysis and Synthesis* (TOTAL), M.S. thesis, GE/GGC/EE/78-2, School of Engineering, Air Force Institute of Technology, Wright-Patterson Air Force Base, Ohio, 1978; available from Defense Documentation Center (DDC), Cameron Station, Alexandria, VA 22314.

Appendix D

Fundamental Aerodynamic Principles

D-1 AERODYNAMIC FORCES

By use of dimensional analysis the equation relating the aerodynamic force on a body to the parameters of the problem can be derived.[1,2,3] The result is

$$F = C_F \frac{\rho}{2} V_T^2 S \tag{D-1}$$

where C_F is the force coefficient and is dependent on the Reynolds number $V_T l / \nu$, ρ is the air density, V_T is the velocity of the air relative to the body, and S is a characteristic area. In the equation for the Reynolds number l is a characteristic length and

$$\nu = \frac{\mu}{\rho} \frac{\text{sq ft}}{\text{sec}} = \text{kinematic viscosity}$$

where

$$\mu = \frac{\tau}{dV_T / dy} \frac{\text{lb sec}}{\text{ft}^2} = \text{coefficient of viscosity}$$

and τ is shear stress between layers of the moving fluid (due to viscosity).

527
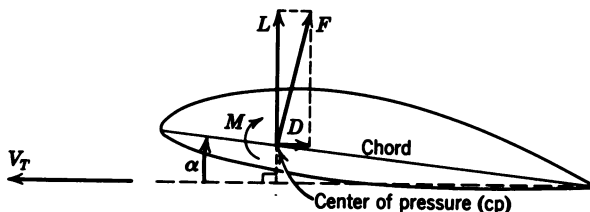
Figure D-1 *Forces acting on an airfoil.*

The characteristic area used for the study of aircraft is the wing area, which includes the entire area of wing including that portion covered by the fuselage and nacelles, but excluding wing fillets. For missile analysis the S is usually the cross-sectional area of the missile. The aerodynamic force acting on a lifting body may be resolved into two components, which are

$$\text{lift} = L = C_L \frac{\rho}{2} V_T^2 S = C_L q S \text{ lb} \tag{D-2}$$

$$\text{drag} = D = C_D \frac{\rho}{2} V_T^2 S = C_D q S \text{ lb} \tag{D-3}$$

where $q = (\rho/2)V_T^2$ is the dynamic pressure in lb/sq ft. In resolving the aerodynamic force into the lift and drag components, lift is always taken normal to V_T and drag along V_T, as shown in Figure D-1. The lift and drag are shown acting at the "center of pressure" of the airfoil. The center of pressure is defined as the point on the airfoil through which the total aerodynamic force can be considered to be acting. The center of pressure in general will not be located at the center of gravity of the airfoil; thus a moment will be produced. The positive direction of the moment is indicated in Figure D-1. To obtain a moment, the force must be multiplied by the proper moment arm; by convention the mean aerodynamic chord, c, is used; thus

$$\text{moment} = M = C_M q S c \tag{D-4}$$

The mean aerodynamic chord (MAC) is defined as the chord of an imaginary airfoil which throughout the flight range has the same force vectors as the actual three-dimensional wing. For a tapered wing

$$c = \frac{2}{3} \left(a + b - \frac{ab}{a+b} \right)$$

where a = wing root chord and b = wing tip chord.

The lift, drag, and moment coefficients are functions of the angle of attack and Mach number. Figure D-2 shows the variation of the lift and drag
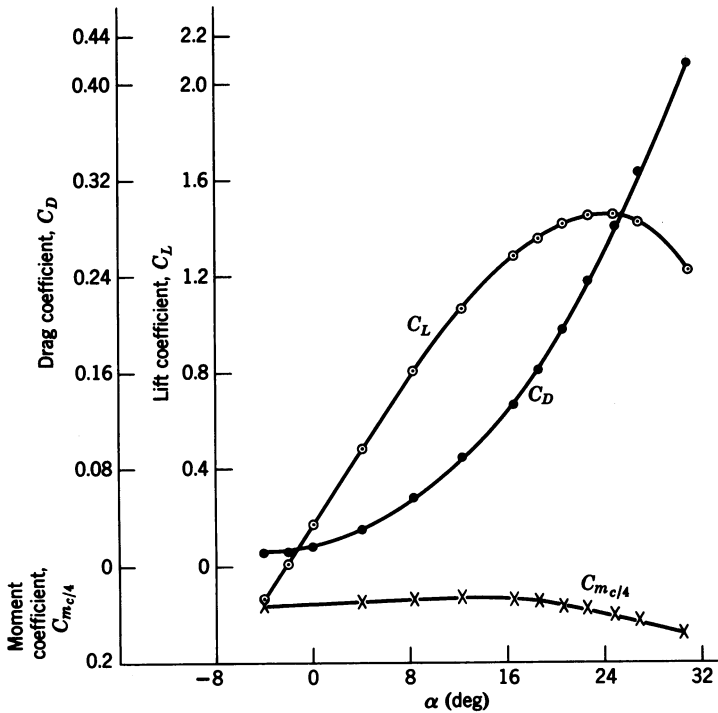
Figure D-2 Data for NACA 4521 airfoil from NACA Report 460, 1933. R = 3.15 × 10⁶; size, 5 × 30 in.; velocity, 69 ft/sec; pressure: 20.8. (Test V.D.T. 573, at L.M.A.L., April 17, 1931.) Corrected for tunnel wall effect.

coefficients and the moment coefficient about the quarter chord point with angle of attack. The lift, drag, and moment coefficients are relatively independent of Mach number for Mach numbers below 0.6 (see Figure D-3 for C_L and C_{D_p}), the widest variation occurring in the transonic region, Mach numbers between 0.6 and 1. Also, when the leading edge of the airfoil is supersonic, the lift vector is always normal to the chord.

D-2 INDUCED DRAG

An examination of Figure D-2 indicates that the drag coefficient curve is approximately parabolic while the lift coefficient curve is linear up to an angle of attack of 8°. A plot of the drag coefficient versus the square of the lift coefficient is plotted in Figure D-4, as indicated by the dashed line. The solid line is a plot of

$$C_D = C_{D_0} + \frac{C_L^2}{\pi \mathcal{R} e} \tag{D-5}$$
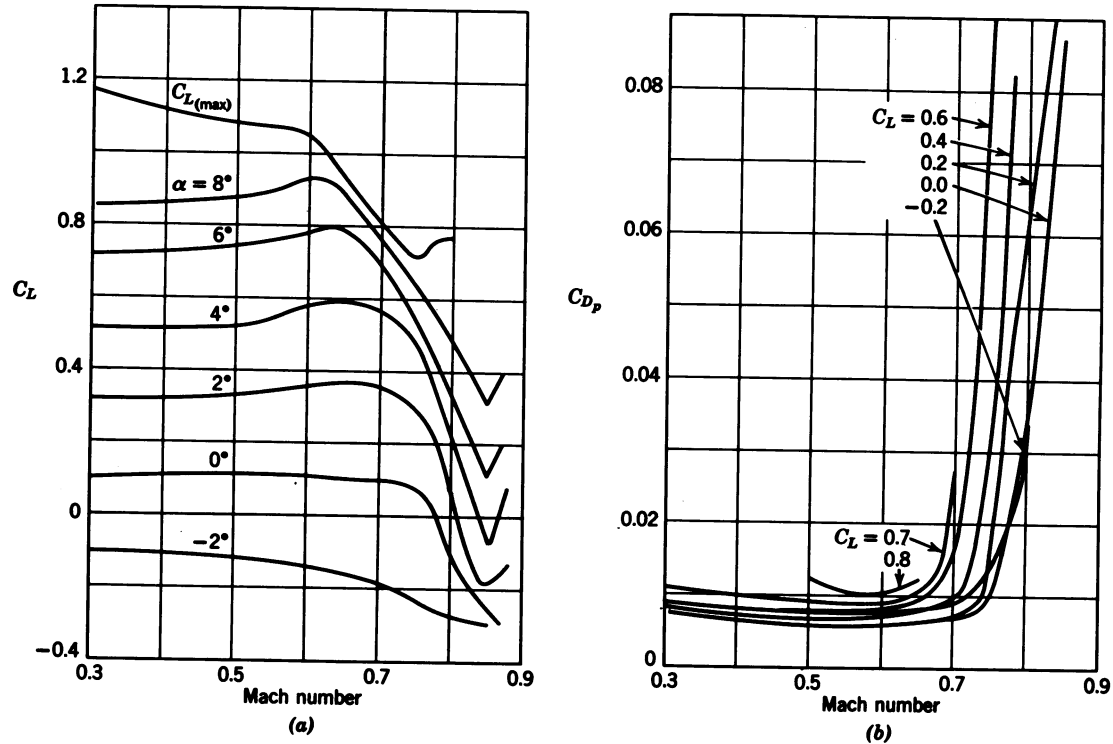
Figure D-3 Variations of lift and drag with Mach number. (a) C_L versus Mach number: BAC 53 airfoil; (b) C_{D_p} versus Mach number: BAC 53 airfoil. By permission from G. S. Schairer, "Systematic Wing Section Development," Journal of the Aeronautical Sciences, January 1947.
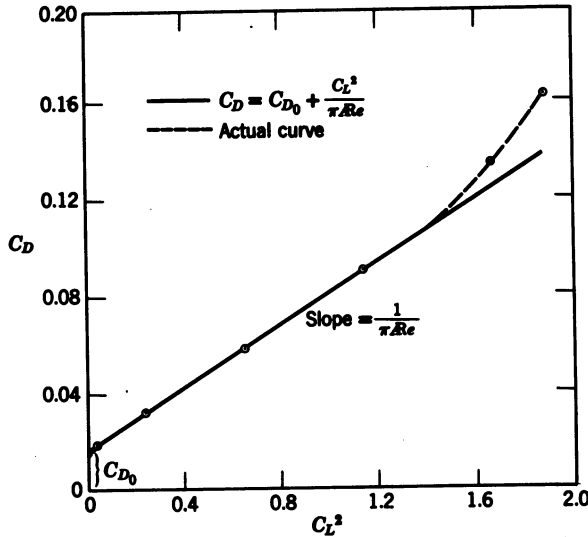
Figure D-4 Comparison of theoretical and actual plot of C_D versus C_L^2.

where C_{D_0} is the minimum parasite or profile drag and consists of friction and pressure drag, $\mathcal{R} = b^2/S$ is the aspect ratio, b is the wing span, and e is the "span efficiency factor." The span efficiency factor compensates for the nonelliptical lift distribution of the wing. The term $C_L^2/\pi\,\mathcal{R}\,e$ in Eq. D-5 is referred to as the "induced drag" and represents the change in parasite drag with angle of attack and induced drag. From Figure D-4 it can be seen that Eq. D-5 is valid over a wide range of lift coefficients, the only deviations being at extremely low values of C_L and for values of C_L greater than 1. At the high values of C_L the wing is approaching stall, and Eq. D-5 cannot be expected to be valid.

The physical cause of the induced drag is shown in Figure D-5.[1,4] The lift L' acts perpendicular to the remote relative wind V_∞, and is the lift that would
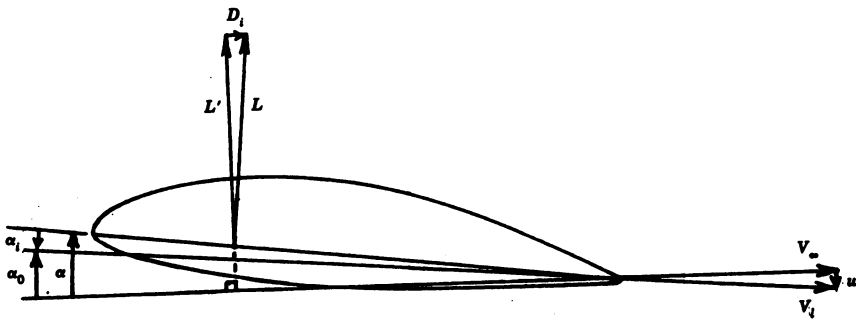
Figure D-5 Geometrical representation of induced drag.

be generated by an infinite-aspect-ratio wing. Such a wing generates no downwash; however, as described in Section 1-7, an actual wing with a finite aspect ratio generates a downwash velocity w at the wing as a result of the lifting action of the wing. The local relative wind at the wing V_l is the vector sum of V_∞ and w, as shown in Figure D-5, and the actual lift generated by the finite wing L is perpendicular to V_l. This rearward tilting of the lift vector results in the induced drag D_i. The angle through which the lift vector rotates is called the induced angle of attack α_i and is given by

$$\alpha_i = \tan^{-1} \frac{w}{V_\infty} \tag{D-6}$$

When the downwash velocity is downward as shown in Figure D-5, it is considered negative; thus for this condition α_i will be negative and the total angle of attack is

$$\alpha = \alpha_0 - \alpha_i \tag{D-7}$$

Thus it can be seen that the induced drag is a direct result of the lifting action of the wing.

D-3 CALCULATION OF STABILITY DERIVATIVES USING DATCOM

Datcom[5] is a USAF stability and control handbook that provides methods for the calculation of the subsonic, transonic, and supersonic aircraft stability derivatives. It will be used here for the calculation of the longitudinal and lateral stability derivatives for an aircraft like the F-102 for Mach 0.94 at 40,000 ft. A scaled drawing of the aircraft is shown in Figure D-6 with the basic aircraft data given in Table D-1 and the assumed airfoil characteristics in Table D-2. In Figure D-6, F.S. represents the fuselage station, which is measured in inches from the nose of the aircraft. The mean aerodynamic chord (MAC) shown for the wing is for the total wing, while the MAC indicated for the vertical tail is for the exposed tail only. The exposed wing area is the area of the wing not covered by the fuselage, or the area from the exposed root chord to the wing tip. The same convention holds for the vertical tail, where the total area includes the vertical tail extended down to the fuselage reference line (FRL) as shown in the Figure D-6. The tail length l_v indicated in Figure D-6 and listed in Table D-1 is the distance from the center of gravity of the aircraft to the $c/4$ point of the MAC of the exposed vertical tail. The aerodynamic center (a.c.) listed in Table D-2 is defined as the point on an airfoil section about which the moment coefficient is independent of the lift coefficient or angle of attack. The $c/4$ and $c/2$ sweeps are the sweep angles of the quarter chord and mid-chord lines respectively.
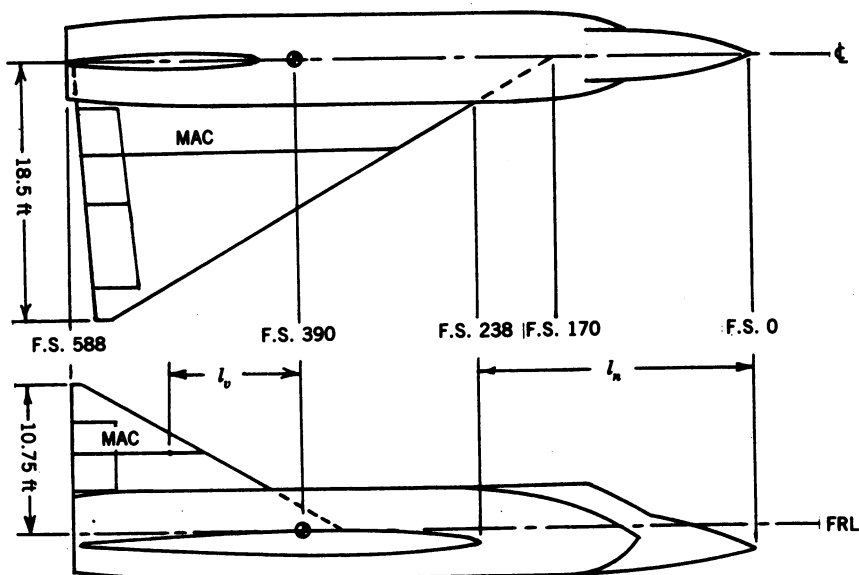
Figure D-6 *Scaled drawing of aircraft.*

Using the data from Figure D-6 and Tables D-1 and D-2, with the aid of the equations and graphs from Datcom reproduced here, the longitudinal and lateral transfer functions for the aircraft will be calculated. The longitudinal stability derivatives will be computed first. In order to calculate the longitudinal force coefficients it is first necessary to calculate the lift and drag coefficients as well as the slopes of these curves with respect to α. The zero-lift drag coefficient for the aircraft, C_{D_0}, will be calculated first by calculating the body zero-lift drag coefficient $(C_{D_0})_B$, then the wing–body zero-lift drag coefficient $(C_{D_0})_{WB}$, and finally the wing–body–tail zero-lift drag coefficient C_{D_0}.

Body Zero-Lift Drag

Skin-friction drag is assumed to be constant and equal to the value for Mach 0.6 throughout the transonic range. Then

$$C_{D_f} = C_f \frac{S_S}{S_B} \tag{D-8}$$

where

S_S is the body maximum frontal area,
S_B is the wetted or surface area of the body excluding the base area,
C_f is the skin-friction coefficient.

TABLE D-1 Aircraft Data

Aircraft Component	Parameter	Symbol	Value
Aircraft	Gross weight	W	23,000 lb
	Moments of inertia	I_x	13,566 slug ft^2
		I_y	89,357 slug ft^2
		I_z	99,695 slug ft^2
Wing	Area	S	651.2 sq ft
	Exposed area	S_e	459.6 sq ft
	Root chord	c_r	34.2 ft
	Exposed root chord	c_{re}	28.33 ft
	Tip chord	c_t	1.0 ft
	Span	b	37.0 ft
	Exposed span	b_e	31.33 ft
	Aspect ratio	$\mathcal{R}$	2.1
	Exposed aspect ratio	$\mathcal{R}_e$	2.136
	Leading edge sweep	Λ_{le}	60°
	$c/4$ sweep	$\Lambda_{c/4}$	53°
	$c/2$ sweep	$\Lambda_{c/2}$	41°
	MAC	c	22.8 ft
Vert. tail	Area	S_{vt}	118.2 sq ft
	Exposed area	S_{vt_e}	58.13 sq ft
	Exposed MAC	c_{vt_e}	9.33 ft
	Tail length	l_v	9.4 ft
Fuselage	Overall length	l_b	49.0 ft
	Maximum diameter	d	6.42 ft

TABLE D-2 Airfoil Properties[1]

Parameter	Symbol	Value
α for zero lift	α_0	0°
Section lift curve slope	$dc_l/d\alpha$	6.07/rad
Max. lift coef.	$c_{l(max)}$	0.92
Thickness to chord ratio	t/c	0.06
Section $c/4$ moment coef.	$c_{m_{c/4}}$	0.0
Aerodynamic center	a.c.	At $c/4$ point

To calculate C_f it is first necessary to obtain the cutoff Reynolds number from Figure D-7 for an input of l/k, where $l = l_b = 588$ in. and $k = 4 \times 10^{-4}$ in. from Table D-3 for standard camouflage paint, average application. Then

$$\frac{l}{k} = \frac{588}{4 \times 10^{-4}} = 1.47 \times 10^6$$
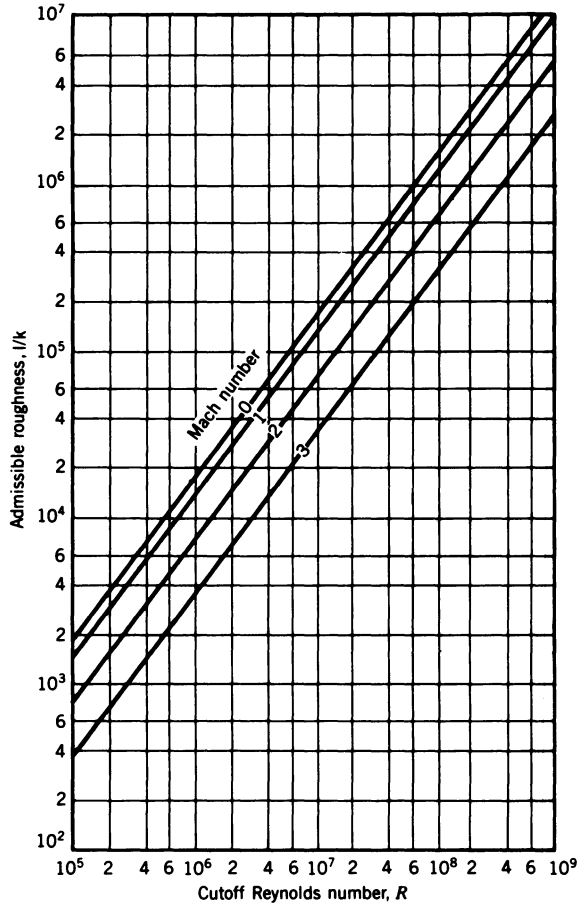
Figure D-7   *Cutoff Reynolds number.*[5]

Then from Figure D-7 the cutoff Reynolds number is approximately 1.2×10^8. The actual Reynolds number is given by

$$R = \frac{\rho V_T l}{\mu} = \frac{V_T l}{\nu} \qquad \text{(D-9)}$$

where

l is the reference length, ft

$\nu = \mu/\rho$ is the kinematic viscosity, ft^2/sec

μ is the coefficient of viscosity, slugs/ft sec

ρ is the air density, slugs/ft^3.

TABLE D-3   Representative Values of Surface-Roughness Height[5]

Type of Surface	Equivalent Sand Roughness k (10^{-3} in.)
Aerodynamically smooth	0
Polished metal or wood	0.02–0.08
Natural sheet metal	0.16
Smooth matte paint, carefully applied	0.25
Standard camouflage paint, average application	0.4
Camouflage paint, mass-production spray	1.2
Dip galvanized metal surface	6
Natural surface of cast iron	10

For 40,000 ft, $\nu = 5.056 \times 10^{-4}$. Then for $V_T = 910$ ft/sec and $l = l_b = 49$ ft, the Reynolds number for the body is

$$R = \frac{910(49)}{5.056 \times 10^{-4}} = 8.82 \times 10^7$$

As the cutoff Reynolds number is greater than the computed Reynolds number, the computed value is used. Then the value of C_f from Figure D-8 is 0.002. The value of the ratio S_S / S_B required for Eq. D-8 is obtained from
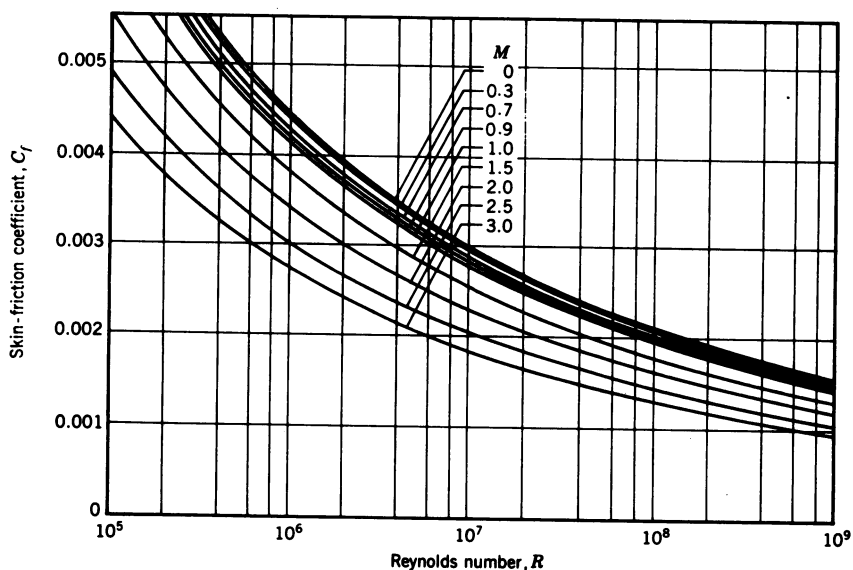
Figure D-8   Turbulent mean skin-friction coefficient on an insulated flat plate.[5]
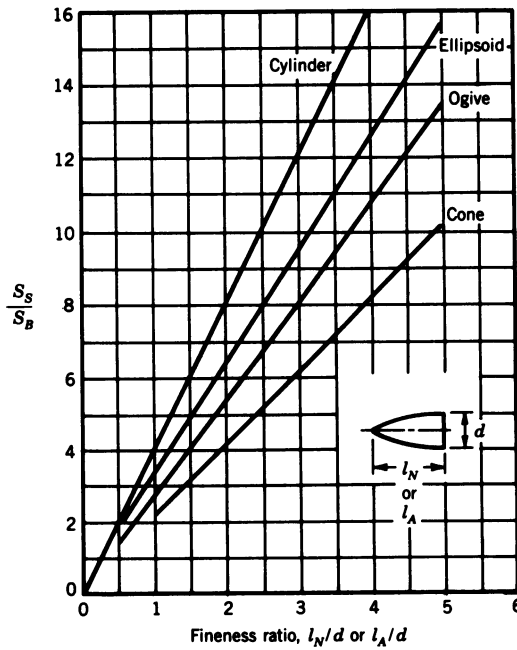
Figure D-9 *Forebody or afterbody wetted area.*[5]

Figure D-9. For the nose l_N/d is 3.1; then from Figure D-9 for a cone, S_S/S_B is 6.25. For the rest of the body l_A/d is 4.5; then from Figure D-9 for a cylinder, S_S/S_B is 17 by extrapolation. Then

$$\frac{S_S}{S_B} = 6.25 + 17 = 23.25$$

Then from Eq. D-8

$$C_{D_f} = 0.002(23.25) = 0.0465$$

The subsonic pressure drag for Mach 0.6 is

$$C_{D_p} = C_{f_{(M-0.6)}} \left[\frac{60}{(l_b/d)^3} + 0.0025 \left(\frac{l_b}{d} \right) \right] \frac{S_S}{S_B} \qquad \text{(D-10)}$$

where l_b/d is 7.63. Then substituting into Eq. D-10 yields

$$C_{D_p} = 0.002 \left[\frac{60}{(7.63)^3} + 0.0025(7.63) \right] 23.25$$

Evaluating,

$$\underline{C_{D_p} = 0.007}$$

To calculate the base-drag coefficient C_{D_b} for Mach 0.94, the subsonic base drag is calculated for Mach 0.6 and then corrected for the actual Mach number. For Mach 0.6

$$C_{D_b} = 0.029 \frac{(d_b/d)^3}{\sqrt{C_{D_{f_b}}}}$$

where $d_b/d = 0.82$ is the ratio of the base diameter to the maximum diameter and

$$C_{D_{f_b}} = C_{f_{(M-0.6)}} \frac{S_S}{S_B} + C_{D_p} = 0.002(23.25) + 0.007 = 0.054$$

Then

$$C_{D_b} = \frac{0.029(0.82)^3}{\sqrt{0.054}} = 0.07$$

The Mach number correction is accomplished by entering Figure D-10 with a calculated value of $C_{D_b}/(d_b/d)^2$ of 0.1. Then moving to the right between the top two curves to $M = 0.94$ yields a value of 0.13 for $C_{D_b}/(d_b/d)^2$, which yields

$$\underline{C_{D_b} = 0.087}$$

Neglecting wave drag, as the Mach number is below 1, then

$$\left(C_{D_0} \right)_B = C_{D_f} + C_{D_p} + C_{D_b} = 0.0465 + 0.007 + 0.087$$

Therefore

$$\underline{\left(C_{D_0} \right)_B = 0.14} \tag{D-11}$$
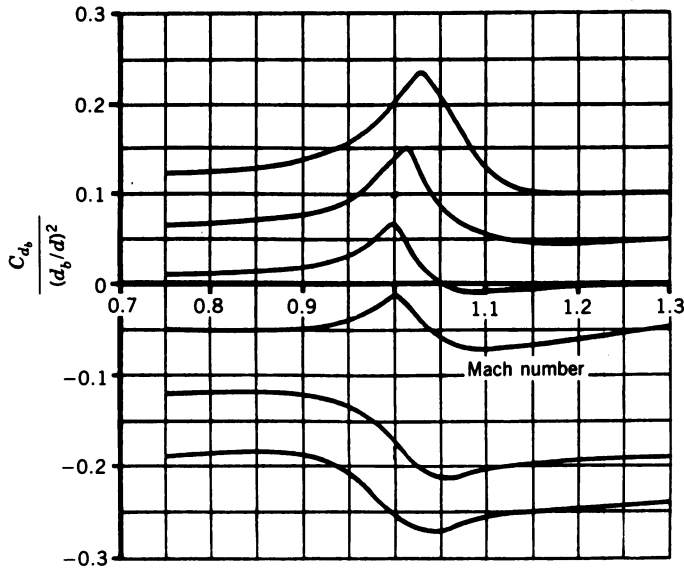
Figure D-10   *Transonic fairing for base-pressure coefficient.*[5]

Wing–Body Zero-Lift Drag

It is recommended in Datcom that the transonic zero-lift drag coefficient of a wing–body combination be approximated by adding the drag coefficients based on the total wetted area of the individual components referred to a common reference area. Then

$$(C_{D_0})_{WB} = (C_{D_0})_W + (C_{D_0})_B \frac{S_B}{S_{(ref)}}$$

where

$(C_{D_0})_W = (C_{D_f} + C_{D_w})_W$,
$(C_{D_0})_B$ is given by Eq. D-11,
$S_B/S_{(ref)} = 0.05$ is the ratio between the body base area and the wing area.

As in the case for the body, the value of C_{D_f} for the wing is calculated for Mach 0.6 and considered independent of Mach number in the transonic range. The wing wave drag in the transonic range is very difficult to estimate, and the Datcom method is only applicable to conventional, trapezoidal
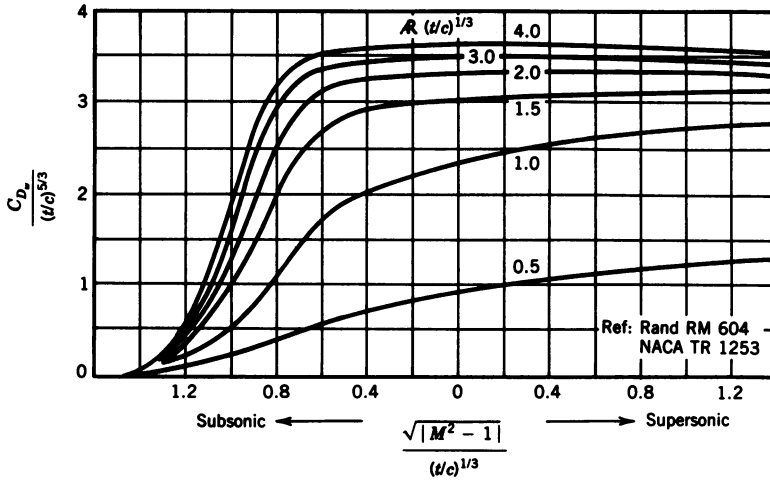
Figure D-11 *Transcnic zero-lift wing wave drag for unswept wings and round-nose airfoils.*[5]

planforms. Then

$$\left(C_{D_f}\right)_W = C_f\left[1 + L\left(\frac{t}{c}\right)\right]\frac{S_{(wet)}}{S_{(ref)}} \tag{D-12}$$

where C_f is from Figure D-8 for a Reynolds number of 4.1×10^7 based on the MAC of the wing. Then from Figure D-8, C_f is 0.00225. As the chordwise location of $(t/c)_{max}$ is at least $0.3c$, then $L = 1.2$. From Table D-2, t/c is 0.06. The value of $S_{(wet)}$ is assumed to be equal to $2S_e$, or 919.2 sq ft, and $S_{(ref)} = S = 651.2$ sq ft from Table D-1. Then substituting into Eq. D-12 yields

$$\left(C_{D_f}\right)_W = 0.00225[1 + 1.2(0.06)]919.2/651.2$$

Therefore

$$\left(C_{D_f}\right)_W = 0.0034$$

For the wing wave-drag coefficient, it is first necessary to construct a plot of C_{D_w} for an unswept wing using Figure D-11 and then correct the curve to account for the wing sweep. The values used for the construction of the plot are listed in Table D-4. For Figure D-11, $\mathcal{R}(t/c)^{1/3} = 2.1(0.06)^{1/3} = 0.82$. From Figure D-12 for the unswept wing the following values are read:

$$M_{D(\Lambda_{c/4} = 0)} = 0.925$$

$$C_{Dw\,peak(\Lambda_{c/4} = 0)} = 0.024$$

$$M_{C_{Dw\,peak(\Lambda_{c/4} = 0)}} = 1.15$$

TABLE D-4   Values for Constructing the Curve
of C_{D_w} versus M for an Unswept Wing

M	$\dfrac{\sqrt{\lvert M^2 - 1\rvert}}{(t/c)^{1/3}}$	$\dfrac{C_{D_w}}{(t/c)^{5/3}}$ (Figure D-11)	C_{D_w}
0.85	1.35	0.07	0.00064
0.9	1.11	0.3	0.0028
0.925	0.97	0.5	0.0046
0.95	0.8	0.9	0.0083
0.975	0.57	1.51	0.014
1.0	0.0	2.1	0.02
1.05	0.82	2.4	0.022
1.1	1.17	2.5	0.023
1.15	1.45	2.6 (est.)	0.024

M_D is the drag-divergence Mach number, and is defined as the Mach number for which the slope of the C_{D_w} versus M curve is equal to 0.1. For the sweep correction,

$$M_{D(\Lambda_{c/4}=n)} = \frac{M_{D(\Lambda_{c/4}=0)}}{\sqrt{\cos n}} = \frac{0.925}{\sqrt{\cos 53}} = 1.19$$

$$C_{Dw\text{ peak}(\Lambda_{c/4}=n)} = C_{Dw\text{ peak}(\Lambda_{c/4}=0)}(\cos n)^{2.5}$$

$$= 0.024(\cos 53)^{2.5} = 0.0067$$

$$M_{C_{Dw\text{ peak}(\Lambda_{c/4}=n)}} = \frac{M_{C_{Dw\text{ peak}(\Lambda_{c/4}=0)}}}{\sqrt{\cos n}} = \frac{1.15}{\sqrt{\cos 53}} = 1.48$$

Using the sweep correction values, the C_{D_w} versus M curve for the swept wing is drawn in Figure D-12. From the figure the value of the wave drag coefficient for Mach 0.94 is zero. Then

$$\underline{(C_{D_0})_W = (C_{D_f} + C_{D_w})_W = 0.0034} \tag{D-13}$$

and

$$(C_{D_0})_{WB} = (C_{D_0})_W + (C_{D_0})_B \frac{S_B}{S_{(ref)}} = 0.0034 + 0.14(0.05)$$
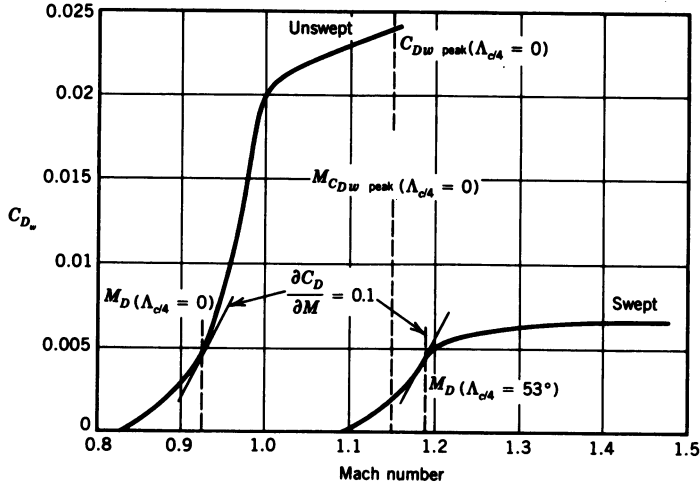
Figure D-12 Plot of zero-lift wing wave-drag coefficient for an unswept and swept wing versus Mach number.

Therefore

$$(C_{D_0})_{WB} = 0.01 \tag{D-14}$$

Wing–Body–Tail Zero-Lift Drag

The wing–body–tail zero-lift drag is

$$C_{D_0} = (C_{D_0})_{WB} + (C_{D_0})_{vt} \tag{D-15}$$

where

$$(C_{D_0})_{vt} = (C_{D_f} + C_{D_w})_{vt}$$

The Reynolds number for the vertical tail from Eq. D-9 is

$$R = \frac{910(9.33)}{5.056 \times 10^{-4}} = 1.7 \times 10^7$$

Then from Figure D-8, $C_f = 0.0026$. The equation for $(C_{D_f})_{vt}$ is

$$(C_{D_f})_{vt} = C_f \left[1 + L\left(\frac{t}{c}\right)_{vt} + 100\left(\frac{t}{c}\right)_{vt}^4 \right] (R_{L.S.})_{vt} \frac{S_{(wet)}}{S} \tag{D-16}$$
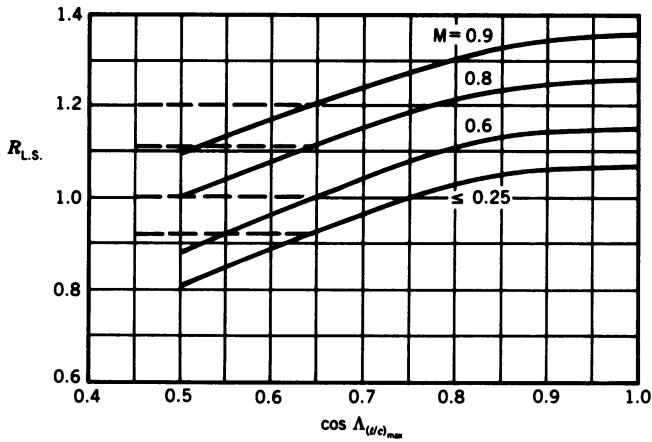
Figure D-13 *Lifting-surface correction factor for subsonic minimum drag.*[5]

where

$(t/c)_{vt} = 0.08$,

$R_{L.S.}$ is the lifting-surface correlation factor from Figure D-13,

$S_{(wet)} = 2S_{vt_e} = 2(58.13) = 116.26$,

$L = 1.2$ (see Eq. D-12).

The input to Figure D-13 requires the sweep of the maximum-t/c line of the vertical tail, which is 46.5°. Then $\cos \Lambda_{(t/c)_{max}}$ is 0.688 and $R_{L.S.}$ from Figure D-13 is 1.25. Substituting into Eq. D-16 yields

$$\left(C_{D_f}\right)_{vt} = 0.0026\left[1 + 1.2(0.08) + 100(0.08)^4\right]1.25\left(\frac{116.26}{651.2}\right)$$

Evaluating,

$$\left(C_{D_f}\right)_{vt} = 0.00064 \qquad\qquad\qquad\text{(D-17)}$$

The vertical tail wave drag is

$$\left(C_{D_w}\right)_{vt} = K\cot(\Lambda_{le})_{vt}\left(\frac{t}{c}\right)^2\frac{S_{vt_e}}{S} \qquad\qquad\text{(D-18)}$$

where K is $\frac{16}{3}$ for a biconvex airfoil section, and

$$(\Lambda_{le})_{vt} = 60°$$

Substituting into Eq. D-18 yields

$$(C_{D_w})_{vt} = \frac{16}{3} \cot 60 (0.08)^2 \frac{58.13}{651.2} = 0.0018 \tag{D-19}$$

Adding Eqs. D-17 and D-19 yields

$$(C_{D_0})_{vt} = 0.00064 + 0.0018 = 0.0024 \tag{D-20}$$

Finally, substituting Eqs. D-14 and D-20 into Eq. D-15 yields the zero-lift drag coefficient for complete aircraft:

$$C_{D_0} = 0.01 + 0.0024 = 0.0124 \tag{D-21}$$

Wing–Body Lift Curve Slope

The wing–body lift curve slope is

$$(C_{L_\alpha})_{WB} = [K_N + K_{W(B)} + K_{B(W)}](C_{L_\alpha})_e \frac{S_e}{S} \tag{D-22}$$

where

$K_N = (C_{L_\alpha})_N S_{N(ref)} / (C_{L_\alpha})_e S_e,$

$(C_{L_\alpha})_N$ is the nose lift curve slope (a value of 2/rad is a good approximation),

$S_{N(ref)}$ is the nose lift curve slope reference area [use $\pi(d/2)^2 = 32.37$ sq ft],

$(C_{L_\alpha})_e$ is the lift curve slope of the exposed wing, and

$$K_{W(B)} + K_{B(W)} = \left(\frac{d}{b} + 1\right)^2 = \left(\frac{6.42}{37} + 1\right)^2 = 1.38$$

$(C_{L_\alpha})_e$ is calculated as follows: Obtain the force-break Mach number from Figure D-14, where the thickness ratio (percent of chord) is 6. Then $(M_{fb})_{\Lambda=0} = 1$. For $\Lambda_{c/2} = 41°$ obtain $(M_{fb})_\Lambda = 1$ from Figure D-15. The theoretical value of C_{L_α} / R is obtained from Figure D-16 for $(M_{fb})_\Lambda = 1$. The value of κ is

$$\kappa = \frac{C_{l_\alpha}/\beta}{2\pi/\beta} = \frac{C_{l_\alpha}}{2\pi} = \frac{6.07}{2\pi} = 0.97$$
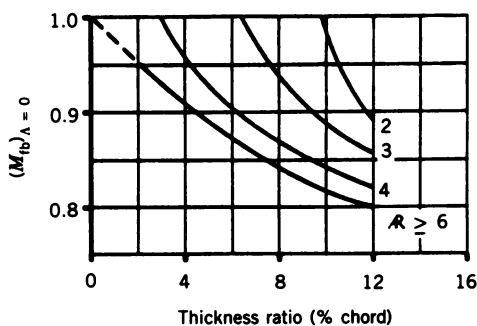
Figure D-14   *Transonic force-break Mach number for zero sweep.*[5]
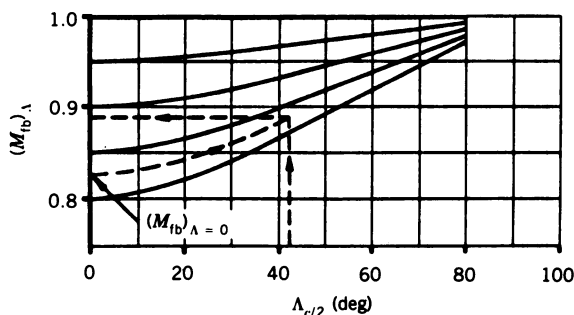
Figure D-15   *Transonic sweep correction for force-break Mach number.*[5]

$$\frac{C_{L_\alpha}}{R} = \frac{2\pi}{2 + \sqrt{\dfrac{R^2\beta^2}{\kappa^2}\left(1 + \dfrac{\tan^2 \Lambda_{c/2}}{\beta^2}\right) + 4}}$$
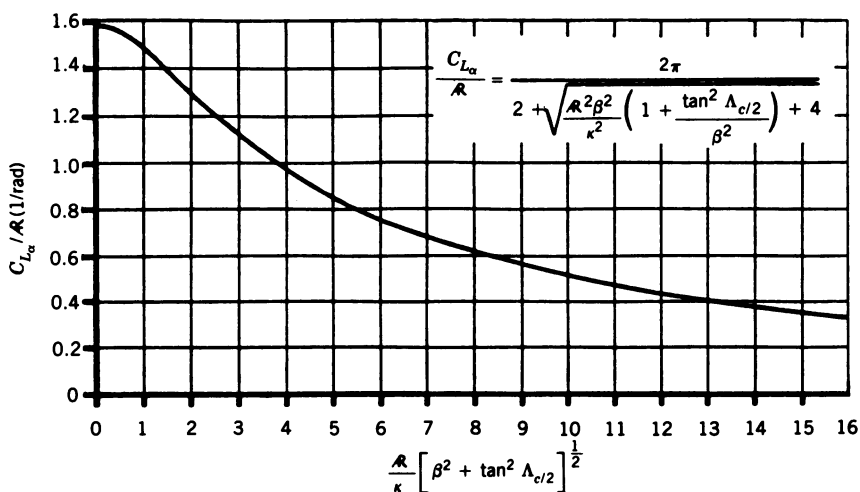
$$\frac{R}{\kappa}\left[\beta^2 + \tan^2 \Lambda_{c/2}\right]^{\frac{1}{2}}$$

Figure D-16   *Subsonic wing lift curve slope.*[5]
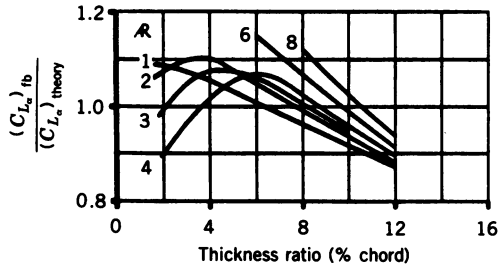
Figure D-17   *Correction to lift curve slope at force-break Mach number.*[5]

and $\beta = \sqrt{1 - M^2} = 0$ for $M = 1$. Then

$$\frac{\mathcal{R}}{\kappa} \left[\beta^2 + \tan^2 \Lambda_{c/2} \right]^{1/2} = \frac{2.136}{0.97}(0.869) = 1.9$$

From Figure D-16

$$\frac{\left(C_{L_\alpha} \right)_{\text{theory}_e}}{\mathcal{R}} = 1.3$$

Then $\left(C_{L_\alpha} \right)_{\text{theory}_e} = 1.3(2.136) = 2.78$. From Figure D-17

$$\frac{\left(C_{L_\alpha} \right)_{\text{fb}}}{\left(C_{L_\alpha} \right)_{\text{theory}}} = 1.05$$

Then

$$\left(C_{L_\alpha} \right)_{\text{fb}_e} = 1.05(2.78) = 2.92$$

From Figure D-18 $a / c = -0.05$, and from page 4.1.3.2-13 of Datcom

$$M_a = M_{\text{fb}} + 0.07 = 1.07$$

and

$$\left(C_{L_\alpha} \right)_{a_e} = \left(1 - \frac{a}{c} \right) \left(C_{L_\alpha} \right)_{\text{fb}_e} = 1.05(2.92) = 3.07$$

From Figure D-19 $b / c = 0.15$; then from page 4.1.3.2-13 of Datcom

$$M_b = M_{\text{fb}} + 0.14 = 1.14$$
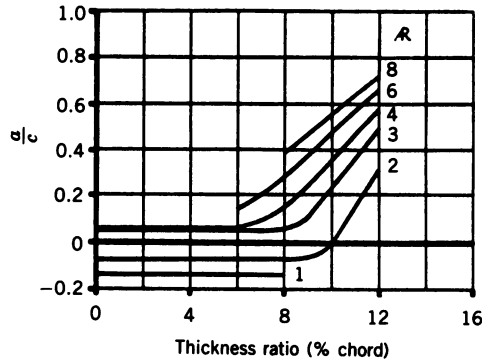
Figure D-18 *Chart for determining lift curve slope at M_a.*[5]

and

$$\left(C_{L_\alpha}\right)_{b_e} = \left(1 - \frac{b}{c}\right)\left(C_{L_\alpha}\right)_{fb_e} = 0.85(2.92) = 2.48$$

For Mach 0.6

$$\frac{\mathcal{R}}{\kappa}\left(\beta^2 + \tan^2 \Lambda_{c/2}\right)^{1/2} = \frac{2.136}{0.97}(0.64 + 0.756)^{1/2} = 2.6$$

Then from Figure D-16

$$\frac{\left(C_{L_\alpha}\right)_e}{\mathcal{R}} = 1.19$$

Then for Mach 0.6

$$\left(C_{L_\alpha}\right)_e = 2.54$$
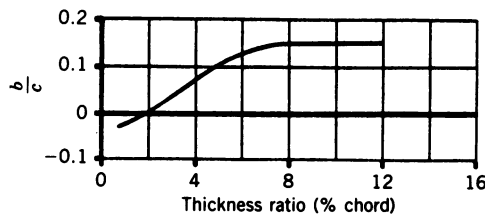
Figure D-19 *Chart for determining lift curve slope at M_b.*[5]
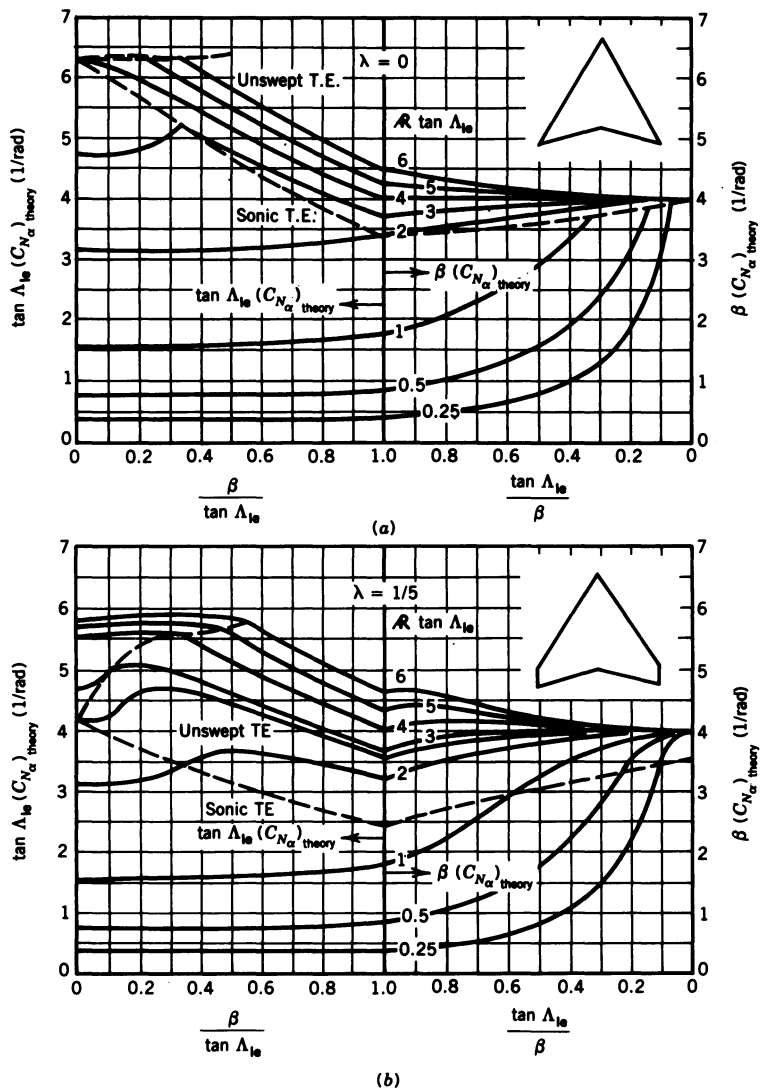
Figure D-20   *Wing supersonic normal-force curve slope.*[5]

For Mach 1.4 using Figure D-20(a) (taper ratio $\lambda = 0$)

$$\frac{\beta}{\tan \Lambda_{le}} = \frac{\sqrt{M^2 - 1}}{\tan 60°} = 0.57$$

$$Æ \tan \Lambda_{le} = 2.136 \tan 60° = 3.7$$

Then from Figure D-20(a)
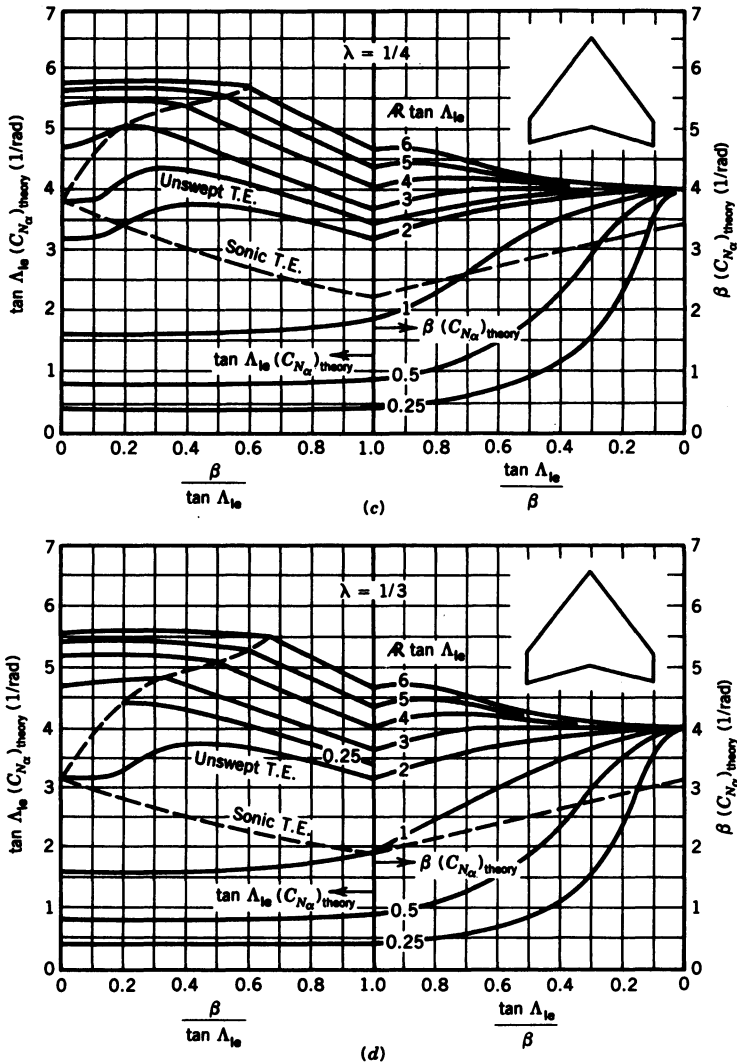
$$\tan \Lambda_{le}\left(C_{N_\alpha}\right)_{\text{theory}_e} = 4.8$$

Figure D-20 *(Continued)*

Then

$$\left(C_{N_\alpha}\right)_{\text{theory}_e} = 2.77$$

The correction for leading edge sharpness is obtained from Figure D-21, where for NACA four-digit airfoils $\Delta y = 1.6$ percent of chord. Then from page 4.1.3.2-20 of Datcom

$$\Delta y_\perp = \frac{\Delta y}{\cos \Lambda_{\text{le}}} = \frac{1.6}{\cos 60°} = 3.2$$
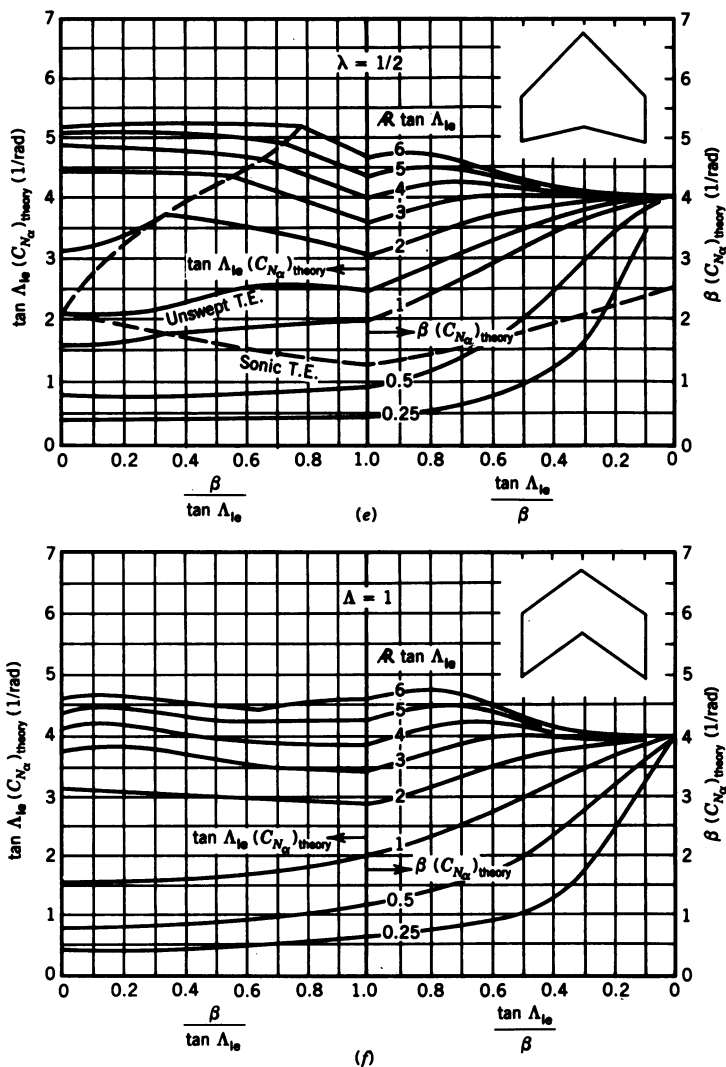
Figure D-20   *(Continued)*

Then from Figure D-22

$$\frac{C_{N_\alpha}}{\left(C_{N_\alpha}\right)_{\text{theory}}} = 0.885$$

Then for Mach 1.4

$$\left(C_{N_\alpha}\right)_e = 2.45$$
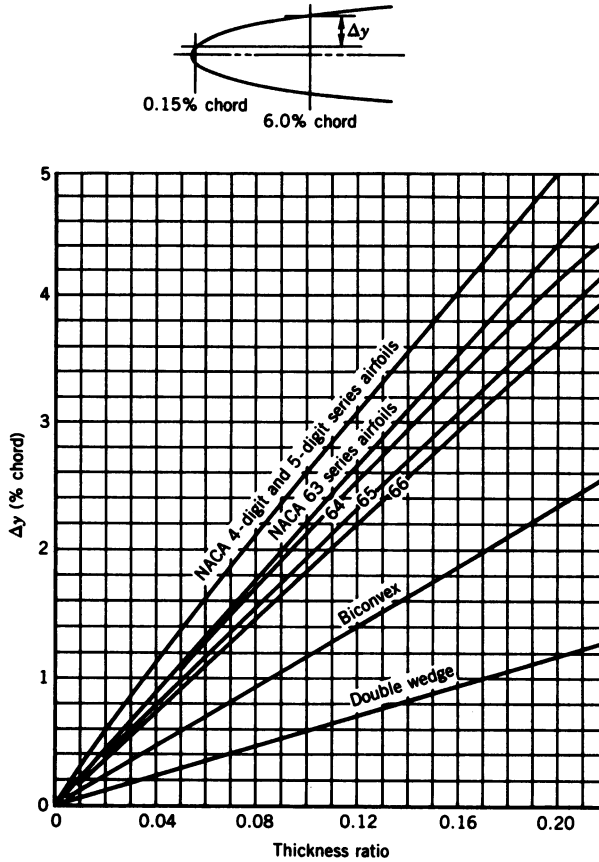
Figure D-21   *Variation of leading edge sharpness parameter with airfoil thickness ratio.*[5]

The values of the exposed wing lift curve slope just calculated are tabulated in Table D-5 and plotted in Figure D-23. Then from Figure D-23 for Mach 0.94

$$\underline{\left(C_{L_\alpha}\right)_e = 2.8/\text{rad}}$$

From Eq. D-22 K_N is

$$K_N = \frac{2(32.37)}{(2.8)(459.6)} = 0.05$$
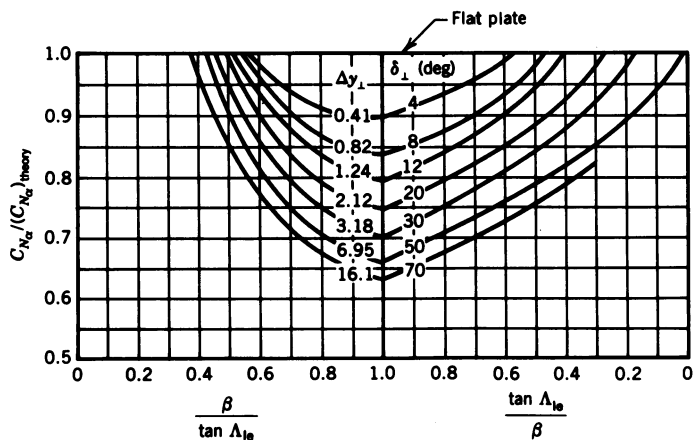
Figure D-22   *Supersonic wing lift-curve-slope correction factor for sonic-leading-edge region.*[5] $\Delta y_\perp = 5.85 \tan \delta_\perp$, *for wedge leading edge only.*

TABLE D-5   Exposed Wing C_{L_α} versus Mach Number

Mach no.	C_{L_α}
0.6	2.54
1.0	2.92
1.07	3.07
1.14	2.48
1.4	2.45
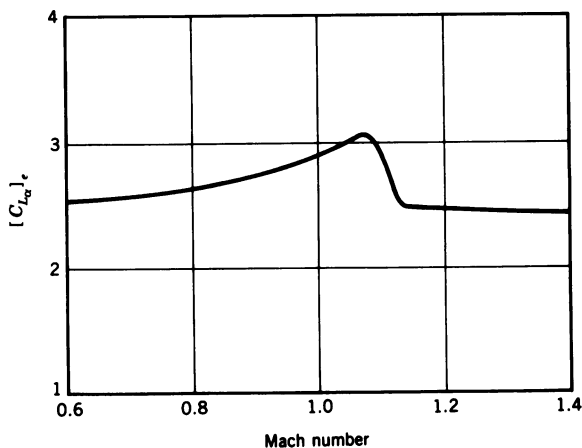
Figure D-23   *Variation of exposed wing lift curve slope with Mach number.*

Substituting into Eq. D-22 yields

$$\left(C_{L_\alpha}\right)_{WB} = (0.05 + 1.38)\left(C_{L_\alpha}\right)_e \left(\frac{459.6}{651.2}\right)$$

Evaluating,

$$\left(C_{L_\alpha}\right)_{WB} = 1.43(0.7058)\left(C_{L_\alpha}\right)_e = 1.01\left(C_{L_\alpha}\right)_e \qquad \text{(D-23)}$$

Substituting for $\left(C_{L_\alpha}\right)_e$ yields for Mach 0.94

$$\underline{\left(C_{L_\alpha}\right)_{WB} = 2.83/\text{rad}} \qquad \text{(D-24)}$$

Wing–Body Drag Due to Lift

The wing–body drag due to lift is

$$\left(C_{D_L}\right)_{WB} = \left(C_{D_L}\right)_W + \left[C_D(\alpha)\right]_B \frac{S_B}{S} \qquad \text{(D-25)}$$

where

$\left(C_{D_L}\right)_W$ is the drag due to lift of the wing
$\left[C_D(\alpha)\right]_B$ is the body drag due to angle of attack, and

$$\frac{S_B}{S} = \frac{\pi(d/2)^2}{S} = \frac{\pi(3.21)^2}{651.2} = 0.05$$

The wing drag due to lift for Mach 0.94 is calculated using Figure D-24(b), as $\mathcal{R}\tan\Lambda_{le} = 2.1\tan 60° = 3.64$. Then

$$\mathcal{R}\left(\frac{t}{c}\right)^{1/3} = 2.136(0.06)^{1/3} = 0.84$$

$$\frac{M^2 - 1}{(t/c)^{2/3}} = \frac{(0.94)^2 - 1}{(0.06)^{2/3}} = -0.76$$

Then for $\lambda = 0$, from Figure D-24(b),

$$\left(\frac{t}{c}\right)^{-1/3}\frac{C_D}{C_L^2} = 0.9$$
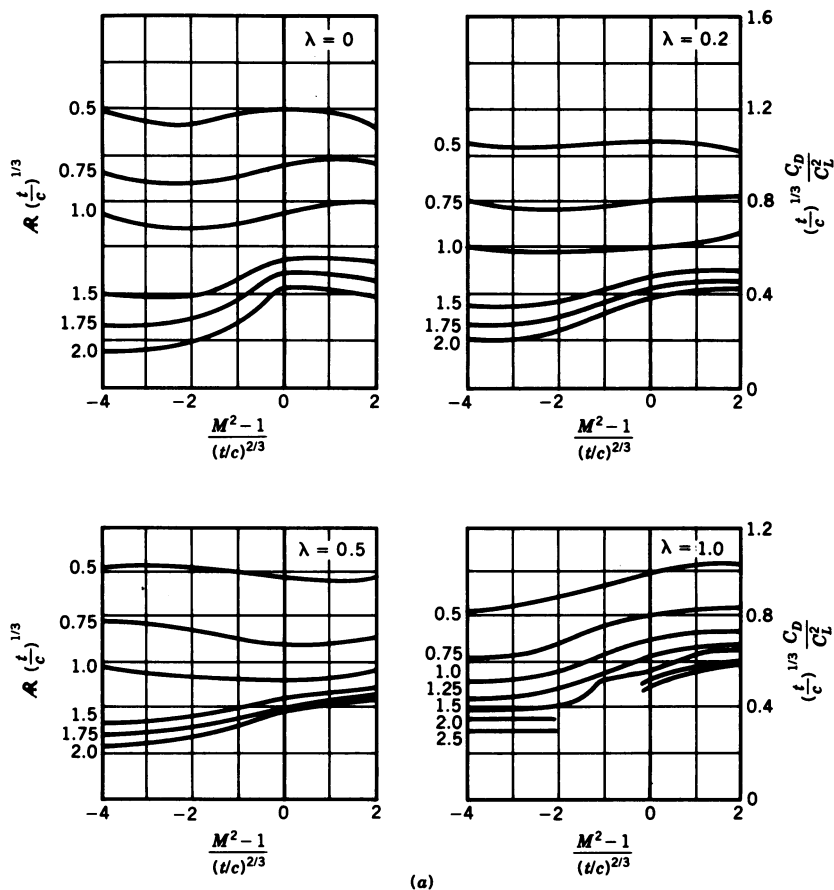
Figure D-24 (a) Transonic drag due to lift, $\mathcal{R} \tan \Lambda_{le} = 0$ (Ref. 5). (b) Transonic drag due to lift, $\mathcal{R} \tan \Lambda_{le} = 3$ (Ref. 5).

Then

$$\frac{C_D}{C_L^2} = 0.35$$

or

$$\left(C_{D_L}\right)_W = 0.35 C_L^2 = 0.35 \left[\left(C_{L_a}\right)_e \alpha\right]^2 \tag{D-26}$$

For the body

$$\left[C_D(\alpha)\right]_B = \alpha^2 \tag{D-27}$$

with α in radians.
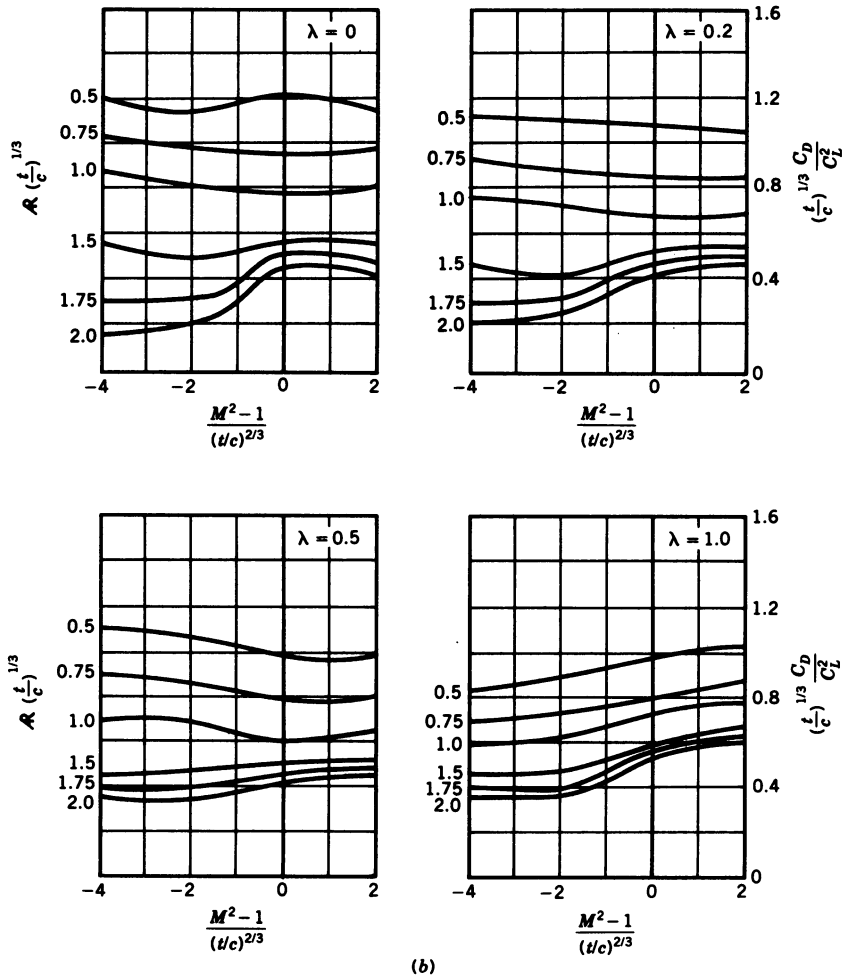
Figure D-24 *(Continued)*

Substituting Eqs. D-26 and D-27 into Eq. D-25 yields

$$\left(C_{D_L}\right)_{WB} = \left[0.35\left(C_{L_\alpha}\right)_e^2 + 0.05\right]\alpha^2 \tag{D-28}$$

Substituting for $\left(C_{L_\alpha}\right)_e$ yields

$$\left(C_{D_L}\right)_{WB} = \left[0.35(2.8)^2 + 0.05\right]\alpha^2 = 2.79\alpha^2 \tag{D-29}$$

Then

$$C_D = C_{D_0} + (C_{D_L})_{WB} \tag{D-30}$$

Substituting from Eqs. D-21 and D-29 yields

$$C_D = 0.0124 + 2.79\alpha^2 \tag{D-31}$$

Using Eqs. D-24 and D-31, C_L and C_D for the aircraft are plotted versus α in Figure D-25. The trim conditions for the aircraft can now be determined for the flight condition of Mach 0.94 at 40,000 ft. For this condition the airspeed $V_T = 910$ ft/sec and the dynamic pressure is

$$q = \frac{\rho}{2}V_T^2 = \frac{0.0005857}{2}(910)^2 = 242.5 \text{ lb/sq ft}$$

The required lift coefficient C_L then for straight and level flight is

$$C_L = \frac{W}{Sq} = \frac{23{,}000}{(242.5)(651.2)} = 0.146 \tag{D-32}$$

Then the trim angle of attack from Figure D-25 is 3°, and from Eq. D-31 or
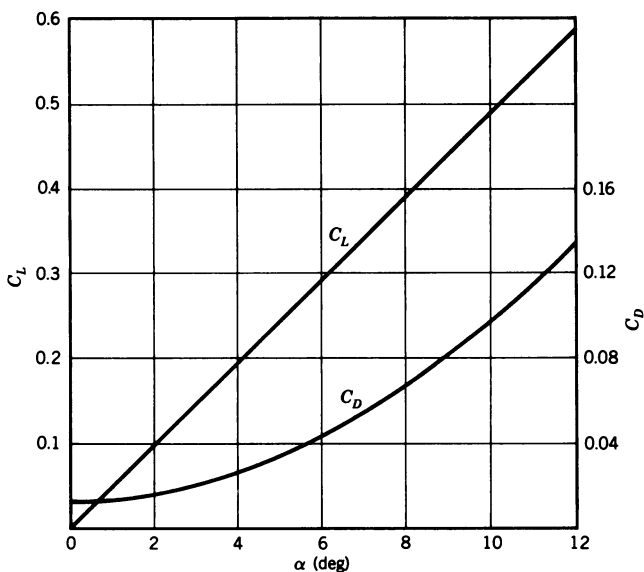
Figure D-25 *Variation of aircraft lift and drag coefficients with angle of attack.*

TABLE D-6   Results of Calculations for C_D for $\alpha = 3°$

Mach	$(C_{L_\alpha})_e$	$\dfrac{M^2 - 1}{(t/c)^{2/3}}$	$\left(\dfrac{t}{c}\right)^{-1/3}\dfrac{C_D}{C_L^2}$	$\dfrac{C_D}{C_L^2}$	$\dfrac{(C_{D_i})_{WB}}{\alpha^2}$	C_D
1.0	2.92	0.0	0.89	0.348	3.02	0.021
0.94	2.8	−0.76	0.9	0.352	2.79	0.02
0.8	2.64	−2.35	0.92	0.36	2.55	0.0194

Figure D-23

$$C_D = 0.02 \tag{D-33}$$

The value of C_{D_α} can be obtained by taking the slope of the C_D curve from Figure D-25 for $\alpha = 3°$ or by differentiating Eq. D-31. Performing the differentiation yields

$$C_{D_\alpha} = 2(2.79)\alpha \tag{D-34}$$

for α in radians. Then for $\alpha = 3°$

$$C_{D_\alpha} = 0.29/\text{rad} \tag{D-35}$$

Using Figures D-23 and D-24(b) and Eqs. D-28 and D-30, C_D can be calculated as a function of Mach number for $\alpha = 3°$. The intermediate results of these calculations as well as the final values of the drag coefficient are listed in Table D-6. A plot of C_D versus Mach number is shown in Figure D-26. From Figure D-26 for Mach 0.94,

$$\frac{\partial C_D}{\partial M} = 0.0086 \tag{D-36}$$
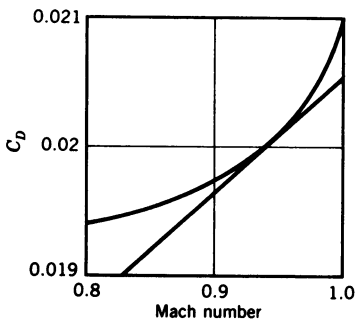
Figure D-26 Variation of aircraft drag coefficient with Mach number.

To obtain $\partial C_L / \partial M$, C_L can be calculated from

$$C_L = \left(C_{L_\alpha}\right)_{WB} \alpha$$

Substituting from Eq. D-23 yields

$$C_L = 1.01 \left(C_{L_\alpha}\right)_e \alpha$$

Evaluating for $\alpha = 3°$,

$$C_L = 0.0529 \left(C_{L_\alpha}\right)_e$$

Differentiating with respect to Mach number yields

$$\frac{\partial C_L}{\partial M} = 0.0529 \frac{\partial \left(C_{L_\alpha}\right)_e}{\partial M}$$

From Figure D-23, for Mach 0.94,

$$\frac{\partial \left(C_{L_\alpha}\right)_e}{\partial M} = 1.54$$

Then

$$\frac{\partial C_L}{\partial M} = 0.08 \tag{D-37}$$

Wing–Body Pitching-Moment-Curve Slope (Aerodynamic Center)

The aerodynamic-center location of a wing–body configuration is

$$\frac{x'_{ac}}{c_{re}} = \frac{\left(\dfrac{x'_{ac}}{c_{re}}\right)_N \left(C_{L_\alpha}\right)_N + \left(\dfrac{x'_{ac}}{c_{re}}\right)_{W(B)} \left(C_{L_\alpha}\right)_{W(B)} + \left(\dfrac{x'_{ac}}{c_{re}}\right)_{B(W)} \left(C_{L_\alpha}\right)_{B(W)}}{\left(C_{L_\alpha}\right)_N + \left(C_{L_\alpha}\right)_{W(B)} + \left(C_{L_\alpha}\right)_{B(W)}} \tag{D-38}$$

where the x'_{ac}/c_{re} coefficients are the chordwise distances measured from the apex of the exposed wing-root chord to the aerodynamic center, positive aft, divided by the exposed wing-root chord. All of the following calculations are made using exposed wing geometry. The definitions of the other coeffi-
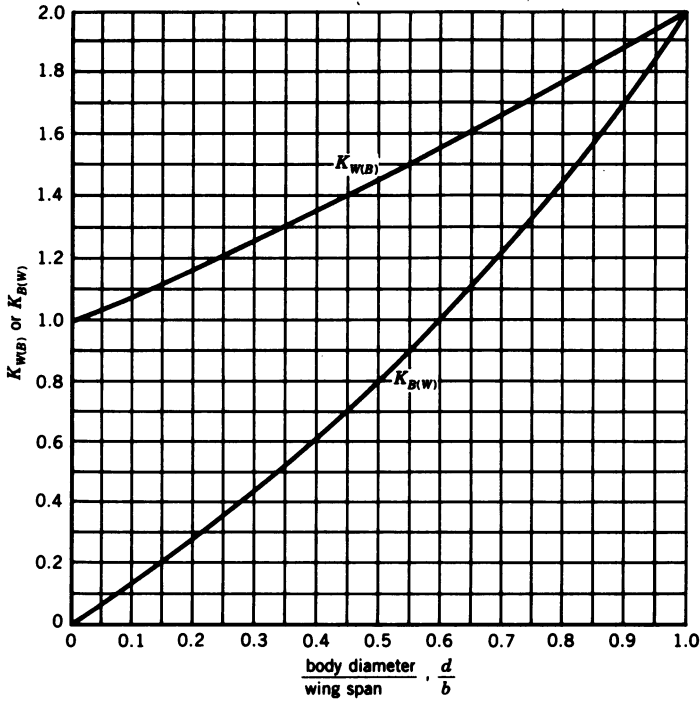
Figure D-27 Lift ratios $K_{W(B)}$ and $K_{B(W)}$ — slender-body theory, fixed incidence, all speeds.[5]

cients in Eq. D-38 are

$$(C_{L_a})_N = 2\frac{\pi d^2}{4S} = \frac{2\pi(6.42)^2}{4(651.2)} = 0.1$$

$$(C_{L_a})_{W(B)} = K_{W(B)}(C_{L_a})_e\frac{S_e}{S} = 2.8\left(\frac{459.6}{651.2}\right)K_{W(B)} = 1.976K_{W(B)}$$

$$(C_{L_a})_{B(W)} = K_{B(W)}(C_{L_a})_e\frac{S_e}{S} = 1.976K_{B(W)}$$

where $K_{W(B)}$ and $K_{B(W)}$ are interference factors from Figure D-27 for $d/b = 0.174$. Then $K_{W(B)} = 1.15$ and $K_{B(W)} = 0.26$, and

$$(C_{L_a})_{W(B)} = 1.15(1.976) = 2.27 \qquad\qquad\text{(D-39)}$$

$$(C_{L_a})_{B(W)} = 0.26(1.976) = 0.51 \qquad\qquad\text{(D-40)}$$

To calculate $(x'_{ac}/c_{re})_N$ it is necessary to determine the nose fineness ratio
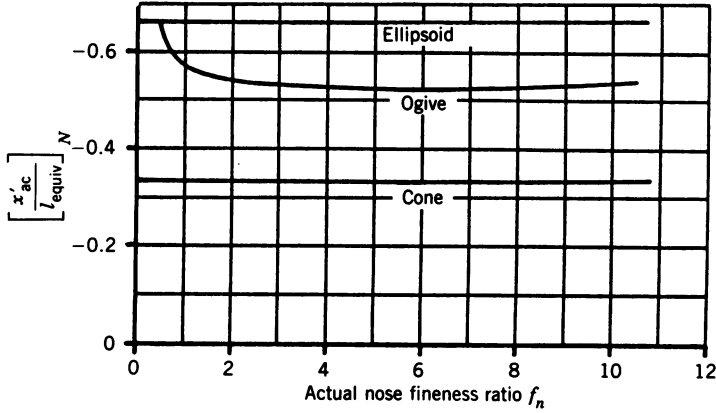
Figure D-28   *Aerodynamic-center locations of various noses (slender-body theory).*[5]

$f_n = l_n / d = 19.83 / 6.42 = 3.09$. Then from Figure D-28 for a cone,

$$\left(\frac{x'_{ac}}{l_{equiv}} \right)_N = -0.335$$

where $l_{equiv} = l_n = 19.83$, then

$$\left(\frac{x'_{ac}}{c_{re}} \right)_N = \left(\frac{x'_{ac}}{l_{equiv}} \right)_N \left(\frac{l_{equiv}}{c_{re}} \right) = -0.335 \left(\frac{19.83}{28.33} \right) = -0.23 \quad \text{(D-41)}$$

For $(x'_{ac}/c_{re})_{W(B)}$, obtain x'_{ac}/c_{re} from Figure D-29(a) for Mach 0.94. Then $\beta / \tan \Lambda_{le} = 0.34 / \tan 60° = 0.2$ and $\mathcal{R}_e \tan \Lambda_{le} = 2.136 \tan 60° = 3.7$. Then from Figure D-29($a$)

$$\left(\frac{x'_{ac}}{c_{re}} \right)_{W(B)} = \frac{x_{ac}}{c_r} = 0.57 \quad \text{(D-42)}$$

To calculate the a.c. contribution $(x'_{ac}/c_{re})_{B(W)}$ due to lift carryover of the wing on the body, as $\beta \mathcal{R}_e = 0.34(2.136) = 0.73$ is less than 4, the a.c. locations for $\beta \mathcal{R}_e = 0$ and ≥ 4 are calculated. The a.c. location for $\beta \mathcal{R}_e = 0.73$ is then determined from a curve through the value for $\beta \mathcal{R}_e = 0$ and tangent to the calculated line for $\beta \mathcal{R}_e \geq 4$, as will be shown in Figure D-32. For $\beta \mathcal{R}_e = 0$ Figure D-30 is used. Then

$$\tfrac{1}{4} \left[\mathcal{R}_e (1 + \lambda_e) \tan \Lambda_{le} \right] = \tfrac{1}{4} \left[2.163 \tan 60° \right] = 0.94$$
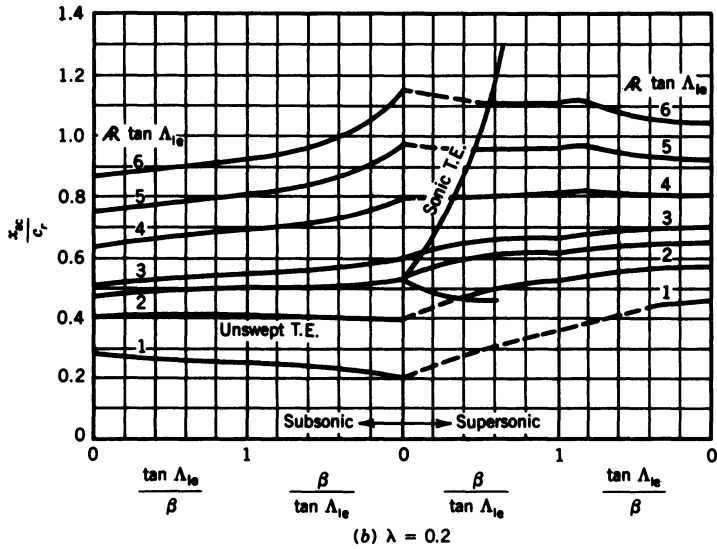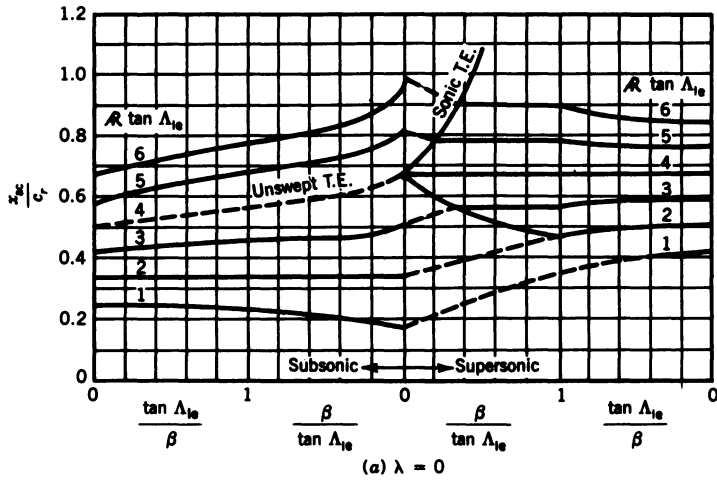
Figure D-29 Wing aerodynamic-center position.[5]

as $\lambda_e = 0$. Then for $\beta \, \mathcal{R}_e = 0$

$$\left(\frac{x'_{ac}}{c_{re}}\right)_{B(W)} = 0.47$$

For $\beta \, \mathcal{R}_e \geq 4$

$$\left(\frac{x'_{ac}}{c_{re}}\right)_{B(W)} = \frac{1}{4} + \frac{b-d}{2c_{re}} \tan \Lambda_{c/4} P$$

(c) $\lambda = 0.25$

(d) $\lambda = 0.33$
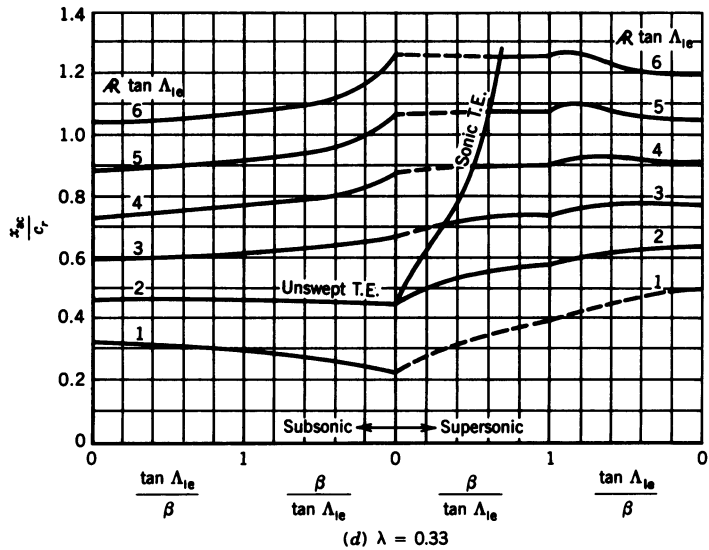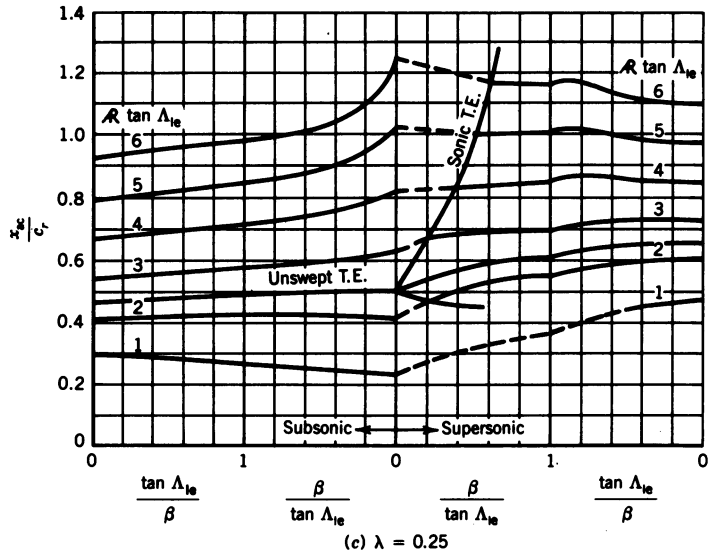
Figure D-29 (*Continued*)

where P is obtained from Figure D-31 for $k = d/b = 6.42/37 = 0.174$. Then $P = 0.218$ and

$$\left(\frac{x'_{ac}}{c_{re}}\right)_{B(W)} = \frac{1}{4} + \frac{37 - 6.42}{2(28.33)}(\tan 53°)(0.218) = 0.4$$

(e) $\lambda = 0.5$

(f) $\lambda = 0$
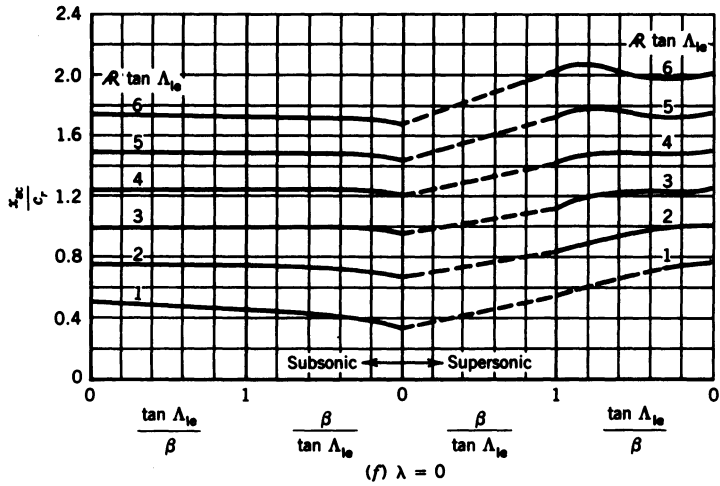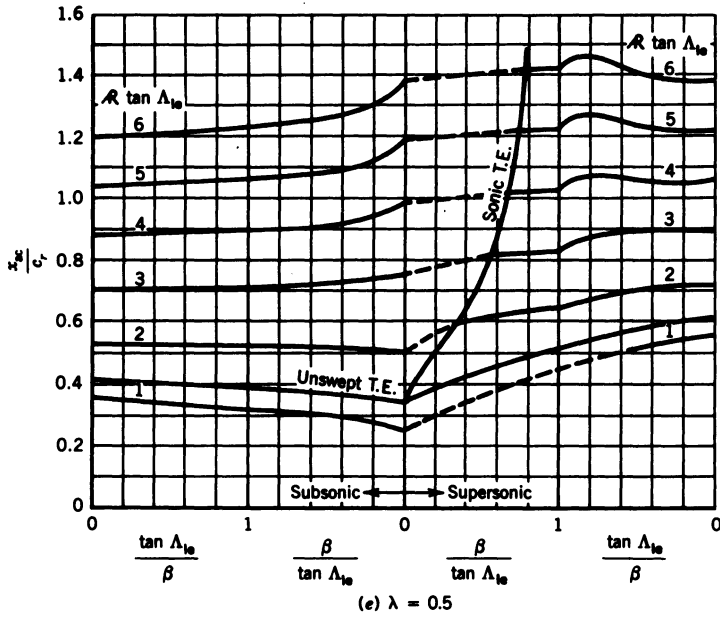
Figure D-29   (Continued)

Then from Figure D-32 for $\beta \, \mathcal{R}_e = 0.73$

$$\left(\frac{x'_{ac}}{c_{re}} \right)_{B(W)} = 0.43 \qquad \text{(D-43)}$$
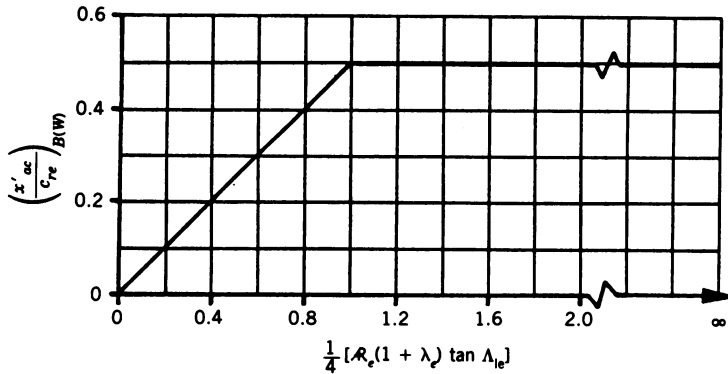
Figure D-30   Theoretical aerodynamic-center locations for $\beta \, \mathcal{R}_e = 0$ (Ref. 5).

Substituting Eqs. D-39, D-40, D-41, D-42, D-43 into Eq. D-38 yields

$$\frac{x'_{ac}}{c_{re}} = \frac{-0.23(0.1) + 0.57(2.27) + 0.43(0.51)}{0.1 + 2.27 + 0.51} = \frac{1.49}{2.88} = 0.52$$

Then

$$x'_{ac} = 0.52(28.33) = 14.7 \text{ ft} = 177 \text{ in.} \tag{D-44}$$
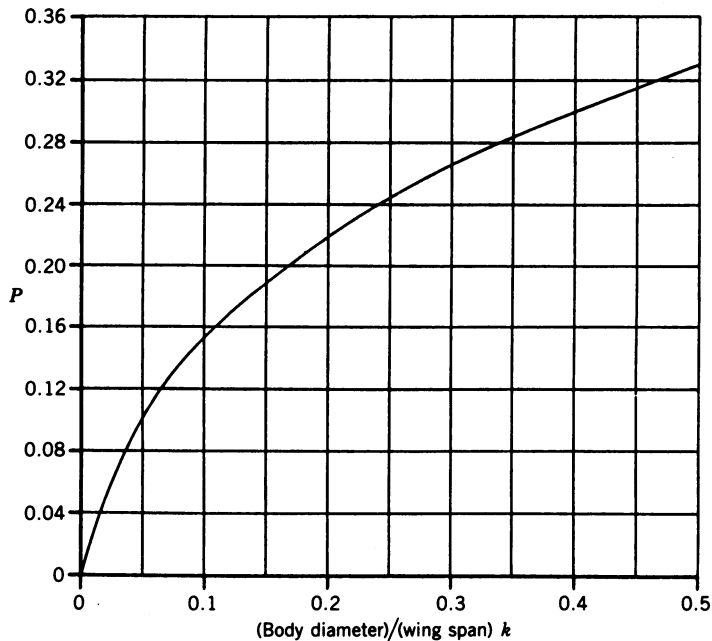
Figure D-31   Parameter used for wing-lift carryover on the body.[5]
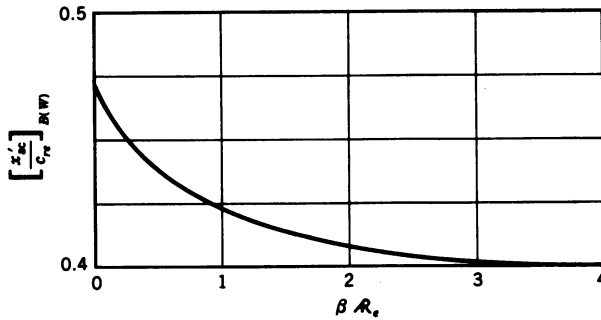
Figure D-32   Plot of $(x'_{ac}/c_{re})_{B(W)}$ versus βR_e.

Then the a.c. is at F.S. $238 + 177 = 415$ in., the static margin from Section 1-7 is

$$\text{SM} = \frac{-415 + 390}{12c_e} = \frac{-25}{12(19.17)} = -0.11 \qquad \text{(D-45)}$$

and from Eq. 1-86

$$C_{m_\alpha} = \text{SM}(C_{L_\alpha})_e = -0.11(2.8) = -0.31/\text{rad} \qquad \text{(D-46)}$$

Wing Pitching Derivatives

As a result of a pitching angular velocity of the aircraft, changes in the local angle of attack are produced that are proportional to the change in the local angle of attack. For swept-back wings an additional increment of angle-of-attack change is produced that is a function of the spanwise wing station. As a result of these local angle of attack changes, an effective angle-of-attack increment for the complete wing is produced resulting in a lift and pitching moment increment. The lift increment is represented by C_{L_q} and the pitching moment increment by C_{m_q}.[5] The equation for estimating C_{L_q} is

$$C_{L_q} = (\tfrac{1}{2} - 2\text{SM})(C_{L_\alpha})_{WB}$$

Substituting from Eqs. D-24 and D-45 yields

$$C_{L_q} = [0.5 + 2(0.11)](2.83) = 2/\text{rad} \qquad \text{(D-47)}$$

The equation for C_{m_q} is

$$C_{m_q} = \frac{(C_{L_a})_M - (C_{L_a})_{M_{cr}}}{(C_{L_a})_{M-1.2} - (C_{L_a})_{M_{cr}}} \left[(C_{m_q})_{M-1.2} - (C_{m_q})_{M_{cr}} \right] + (C_{m_q})_{M_{cr}} \quad \text{(D-48)}$$

where C_{L_a} is $(C_{L_a})_{WB}$ for the Mach number indicated and $M_{cr} = M_{fb} = 1$. Then

$$(C_{L_a})_M = 2.83$$

and using Eq. D-23 and Figure D-23,

$$(C_{L_a})_{M_{cr}} = 1.01 (C_{L_a})_{M_{cr_e}} = 1.01(2.92) = 2.95$$

Similarly

$$(C_{L_a})_{M-1.2} = 1.01(2.47) = 2.49$$

For $(C_{m_q})_{M-1.2}$

$$C_{m_q} = C'_{m_q} + \text{SM}\, C_{L_q} \quad \text{(D-49)}$$

where from Eq. D-47

$$C_{L_q} = [0.5 + 2(0.11)] (C_{L_a})_{WB} = 0.72(2.49) = 1.79$$

for $\lambda = 0$, and

$$C'_{m_q} = -\frac{3\pi\, \mathcal{R}}{16} \left[G(\beta C) F_7(N) + \frac{16 E''(\beta C)}{3} \left(\frac{F_5(N)}{F_{11}(N)} \right) \right]$$

$$- \left(\frac{d - x_{ac}}{c} \right) C'_{L_q} + 2 \left(\frac{d - x_{ac}}{c} \right)^2 C_{N_a} \quad \text{(D-50)}$$

where

   $G(\beta C)$ and $E''(\beta C)$ are obtained from Figure D-33,
   $F_5(N)$, $F_7(N)$, and $F_{11}(N)$ are obtained from Figure D-34,
   $x_{ac} = 20.52$ ft is the distance from the wing leading-edge vertex to the a.c.,
   $d = \frac{2}{3} c_{r_B}$, and c_{r_B} is the distance from the wing leading-edge vertex to the
      trailing edge of the wing-tip chord ($c_{r_B} = 33$ ft, so $d = 22$ ft),
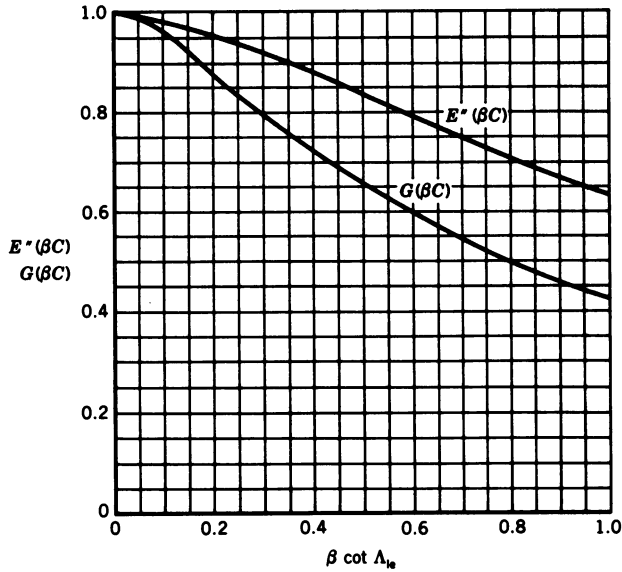
Figure D-33 *Elliptic integral factors of the stability derivative.*[5]

C_{N_α} is obtained from Figure D-20(a) for Mach 1.2, and

$$C_{L_q}' = \frac{\pi}{2} \, \mathcal{R} \, [3G(\beta C)F_3(N) - 2E''(\beta C)F_4(N)] + 2\left(\frac{d - x_{ac}}{c}\right)C_{N_\alpha}$$

$$(\text{D-51})$$

where $F_3(N)$ and $F_4(N)$ are from Figure D-35.

For the input to Figure D-33 for Mach 1.2, $\beta \cot \Lambda_{le} = 0.66 \cot 60° = 0.38$. Then $G(\beta C) = 0.74$ and $E''(\beta C) = 0.885$. For input to Figure D-34,

$$N = 1 - \frac{4 \cot \Lambda_{le}}{\mathcal{R}'} = 1 - \frac{4 \cot 60°}{2.1} = -0.1$$

Then $F_7(N) = 1.3$, $F_{11}(N) = 1.1$, $[1/(1 - N)]F_5(N) = -0.02$, and $F_5(N) = -0.022$. For C_{N_α} at Mach 1.2, $\beta/\tan \Lambda_{le} = 0.66/\tan 60° = 0.38$. As before, $\mathcal{R} \tan \Lambda_{le} = 3.7$; then from Figure D-20($a$), $\tan \Lambda_{le}(C_{N_\alpha})_{\text{theory}} = 5.3$ and $(C_{N_\alpha})_{\text{theory}} = 3.06$. As for the calculation of C_{N_α} for the wing–body lift curve slope,

$$C_{N_\alpha} = 0.885(C_{N_\alpha})_{\text{theory}} = 2.7$$
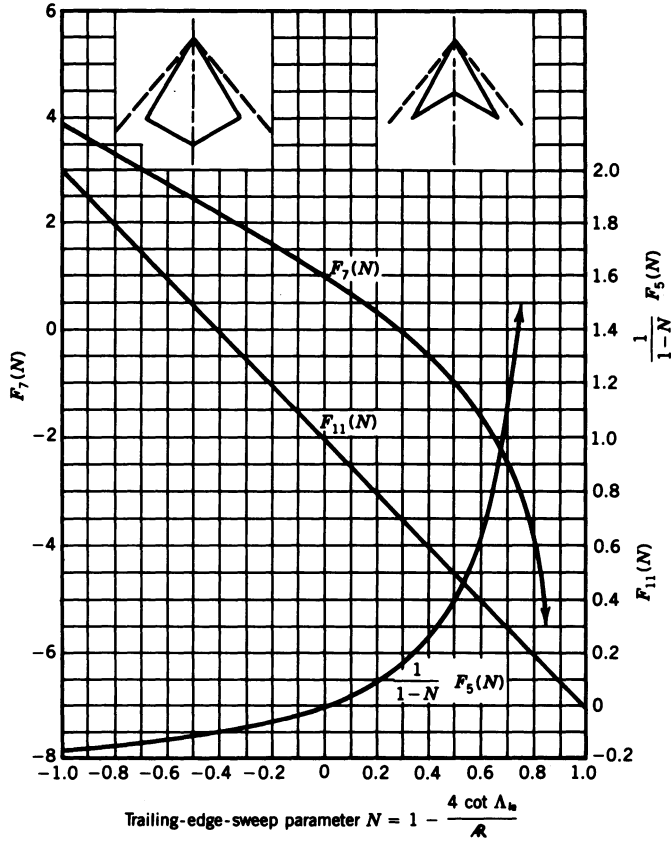
Figure D-34 *F(N) factors of the stability derivative.*[5]

From Figure D-35, $[1/(1-N)]F_3(N) = 0.95$ and $(1-N)F_4(N) = 1.07$. Then $F_3(N) = 1.045$ and $F_4(N) = 0.97$. Substituting into Eq. D-51 yields

$$C'_{L_q} = \frac{\pi}{2}(2.136)[3(0.74)(1.045) - 2(0.885)(0.97)] + 2\left(\frac{22-20.52}{22.8}\right)2.7$$

Evaluating,

$$C'_{L_q} = 2.023 + 0.35 = 2.37$$

Substituting into Eq. D-50 and noting that $(d - x_{ac})/c = 0.065$ yields

$$C'_{m_q} = \frac{-3\pi(2.136)}{16}\left[0.74(1.3) + \frac{16(0.885)}{3}\left(\frac{-0.022}{1.1}\right)\right]$$
$$- 0.065(2.37) + 2(0.065)^2(2.7)$$
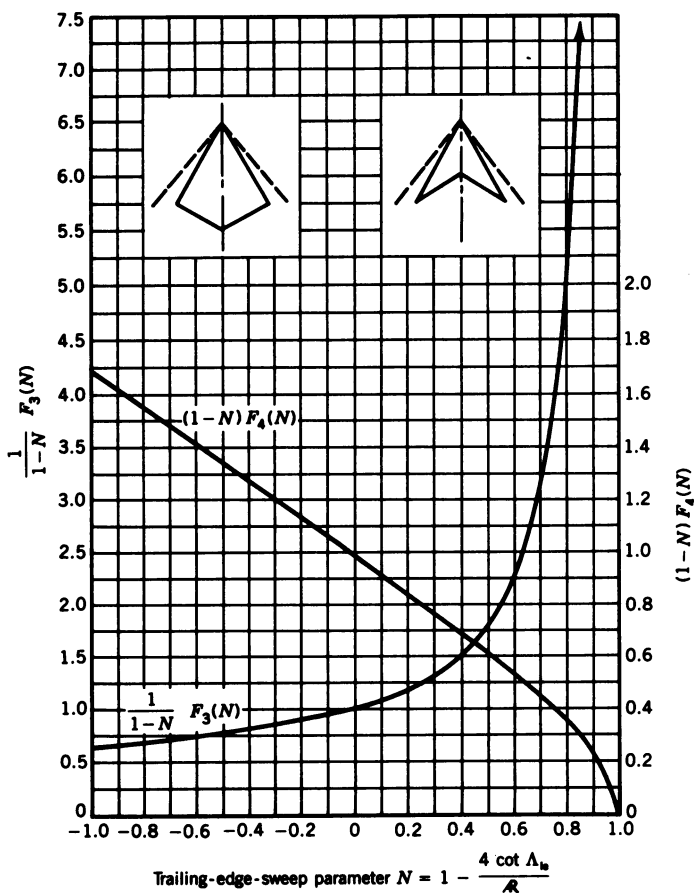
Figure D-35 *F(N) factors of the stability derivative.*[5]

Evaluating,

$$C'_{m_q} = -1.09 - 0.15 + 0.023 = -1.22$$

Substituting into Eq. D-49 yields

$$\left(C_{m_q}\right)_{M-1.2} = -1.22 - 0.11(1.79) = -1.42 \qquad \text{(D-52)}$$

For $(C_{m_q})_{M_{cr}}$ it is necessary to calculate C'_{L_q} and C'_{m_q} for Mach 1. From Table D-5, $C_{N_\alpha} = (C_{L_\alpha})_e = 2.92$; then substituting C_{N_α} into Eq. D-51 yields

$$C'_{L_q} = 2.023 + 2(0.065)(2.92) = 2.023 + 0.38 = 2.4$$

Then substituting C_{N_α} and C'_{L_q} into Eq. D-50 yields

$$C'_{m_q} = -1.09 - 0.065(2.4) + 2(0.065)^2(2.92) = -1.22$$

The value of C_{L_q} that is required for the calculation of C_{m_q} can be obtained from Eq. D-47 using $(C_{L_\alpha})_{WB}$ calculated from Eq. D-23 for Mach 1. Then $(C_{L_\alpha})_{WB} = 2.95$ and $C_{L_q} = 2.1$, and substituting C'_{m_q} and C_{L_q} into Eq. D-49 yields

$$(C_{m_q})_{M_{cr}} = -1.22 - 0.11(2.1) = -1.45 \tag{D-53}$$

Then substituting Eqs. D-52 and D-53 into Eq. D-48 yields

$$C_{m_q} = \frac{2.83 - 2.95}{2.49 - 2.95}(-1.42 + 1.45) - 1.45 = -1.44/\text{rad} \tag{D-54}$$

Wing Acceleration Derivatives

The wing acceleration derivatives $C_{L_{\dot\alpha}}$ and $C_{m_{\dot\alpha}}$ for a delta wing with no horizontal tail would result from nonquasisteady flow. As it was assumed in Section 1-7 that quasisteady flow existed, then these derivatives would be zero. Datcom does give equations for them under subsonic and supersonic conditions, but states that there is no general theory available that gives transonic values for these derivatives. As can be seen in Appendix F, $C_{m_{\dot\alpha}}$ for the F-15 from flight test data is zero; therefore, it is assumed that the wing acceleration derivatives are zero for this aircraft.

Longitudinal Equations of Motion

The longitudinal equations of motion from Eq. 1-103 for $C_{z_{\dot\alpha}}$, $C_{m_{\dot\alpha}}$, and $\Theta = 0$ are

$$\left(\frac{mU}{Sq}s - C_{x_u}\right)'u(s) - C_{x_\alpha}'\alpha(s) - C_w\theta(s) = 0$$

$$-C_{z_u}'u(s) + \left(\frac{mU}{Sq}s - C_{z_\alpha}\right)'\alpha(s) + \left(-\frac{mU}{Sq} - \frac{c}{2U}C_{z_q}\right)s\theta(s) = C_{z_{\delta_e}}\delta_e(s)$$

$$-C_{m_\alpha}'\alpha(s) + \left(\frac{I_y}{Sqc}s^2 - \frac{c}{2U}C_{m_q}s\right)\theta(s) = C_{m_{\delta_e}}\delta_e(s)$$

$$\tag{D-55}$$

From Table 1-1

$$C_{x_u} = -2C_D - U\frac{\partial C_D}{\partial u}$$

where

$$U\frac{\partial C_D}{\partial u} = U\frac{\partial C_D}{\partial aM} = \frac{U}{a}\frac{\partial C_D}{\partial M} = M\frac{\partial C_D}{\partial M}$$

and $a = 968.1$ ft/sec, the speed of sound at 40,000 ft. Then from Eq. D-36

$$U\frac{\partial C_D}{\partial u} = 0.94(0.0086) = 0.0081$$

Then from Eq. D-33

$$C_{x_u} = -2(0.02) - 0.0081 = -0.048$$

$$C_{x_a} = C_L - \frac{\partial C_D}{\partial \alpha}$$

Substituting from Eqs. D-32 and D-35 yields

$$C_{x_a} = 0.146 - 0.29 = -0.144$$

$$C_w = -\frac{W}{Sq} = -C_L = -0.146$$

$$C_{z_u} = -2C_L - U\frac{\partial C_L}{\partial u} = -2C_L - M\frac{\partial C_L}{\partial M}$$

Substituting from Eq. D-37 yields

$$C_{z_u} = -2(0.146) - 0.94(0.08) = -0.37$$

$$C_{z_a} = -C_D - \frac{\partial C_L}{\partial \alpha}$$

Substituting from Eqs. D-24 and D-33 yields

$$C_{z_a} = -0.02 - 2.83 = -2.85$$

$$C_{z_q} = -C_{L_q}$$

Substituting from Eq. D-47 yields

$$C_{z_q} = -2$$

From Eq. D-46,

$$C_{m_\alpha} = -0.31$$

From Eq. D-54,

$$C_{m_q} = -1.44$$

$$m = \frac{W}{g} = \frac{23,000}{32.2} = 714.286 \text{ slugs}$$

$$\frac{mU}{Sq} = \frac{(714.286)(910)}{(651.2)(242.5)} = 4.12 \text{ sec}$$

$$\frac{I_y}{Sqc} = \frac{89357}{(651.2)(242.5)(22.8)} = 0.025 \text{ sec}^2$$

$$\frac{c}{2U} C_{z_q} = \frac{22.8}{2(910)}(-2) = -0.025 \text{ sec}$$

$$\frac{c}{2U} C_{m_q} = \frac{22.8}{2(910)}(-1.44) = -0.018 \text{ sec}$$

For inboard trailing edge elevators 3 ft chordwise by 7 ft spanwise, the estimated values of $C_{z_{\delta_e}}$ and $C_{m_{\delta_e}}$ are -0.3 and -0.2 respectively. Substituting these values into Eq. D-55 yields

$$(4.12s + 0.048)\,'u(s) + 0.144\,'\alpha(s) + 0.146\theta(s) = 0$$

$$0.37\,'u(s) + (4.12s + 2.85)\,'\alpha(s) - 4.1s\theta(s) = -0.3\delta_e(s)$$

$$0.31\,'\alpha(s) + (0.025s^2 + 0.018s)\theta(s) = -0.2\delta_e(s) \quad \text{(D-56)}$$

Using Program CC, the longitudinal transfer functions are

$$\frac{'u(s)}{\delta_e(s)} = \frac{0.00252(s + 0.29)(s + 220.9)}{(s^2 + 1.41s + 12.75)(s^2 + 0.01s + 0.0031)}$$

$$\frac{'\alpha(s)}{\delta_e(s)} = \frac{-0.073(s + 110.06)(s^2 + 0.0116s + 0.0032)}{(s^2 + 1.41s + 12.75)(s^2 + 0.01s + 0.0031)}$$

$$\frac{\theta(s)}{\delta_e(s)} = \frac{-8(s + 0.58)(s + 0.0062)}{(s^2 + 1.41s + 12.75)(s^2 + 0.01s + 0.0031)} \quad \text{(D-57)}$$

Having completed the calculation of the longitudinal transfer functions, the lateral stability derivatives and transfer functions will be calculated. The sideslip derivatives will be calculated first.
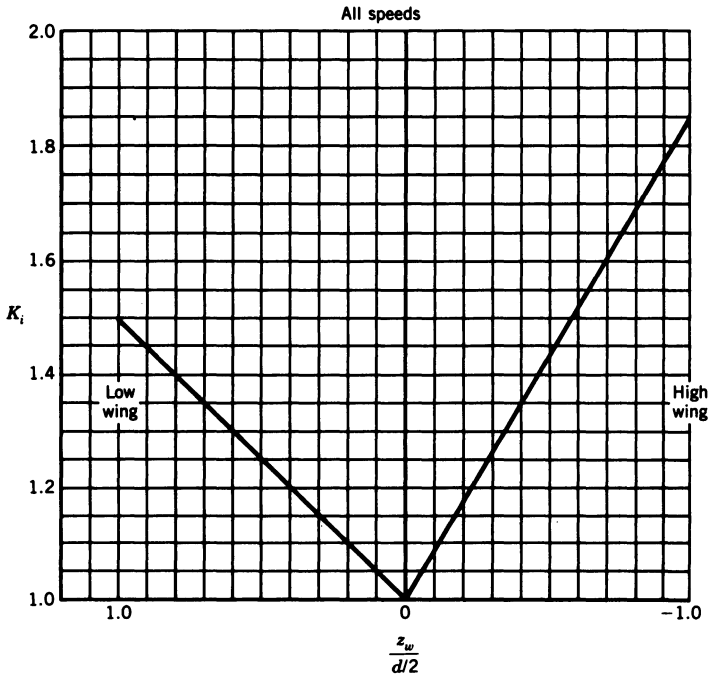
Figure D-36 *Wing–body interference factor for wing–body sideslip derivative C_{y_β}.[5] z_w = distance from body centerline to $c/4$ point of exposed wing root chord, positive for the $c/4$ point below the body centerline; d = maximum body height at wing–body intersection.*

Sideslip Derivatives

The sideslip derivatives are C_{y_β}, C_{l_β}, and C_{n_β}. The side force due to sideslip C_{y_β} results mainly from the body and is a function of the vertical location of the wing on the fuselage. The wing contribution results mainly from wing dihedral and is therefore zero for the aircraft being studied. Datcom states that there is no method available in the literature for estimating the side force due to the vertical tail in the transonic region; however, for this analysis the force will be estimated by obtaining the lift curve slope of the vertical tail panel using the subsonic equations. The contribution of the wing body to C_{y_β} is

$$\left(C_{y_\beta}\right)_{WB} = K_i \left(C_{y_\beta}\right)_B \left(\frac{\text{body ref. area}}{S}\right) \tag{D-58}$$

where

$\quad$ K_i is the wing-body interference factor from Figure D-36,

$\quad$ $\left(C_{y_\beta}\right)_B = -2/\text{rad}$ is the lift curve slope of the body as estimated earlier for the calculation of the wing–body lift curve slope,

$\quad$ body ref. area $= \pi(d/2)^2 = 32.37$ sq ft as before.
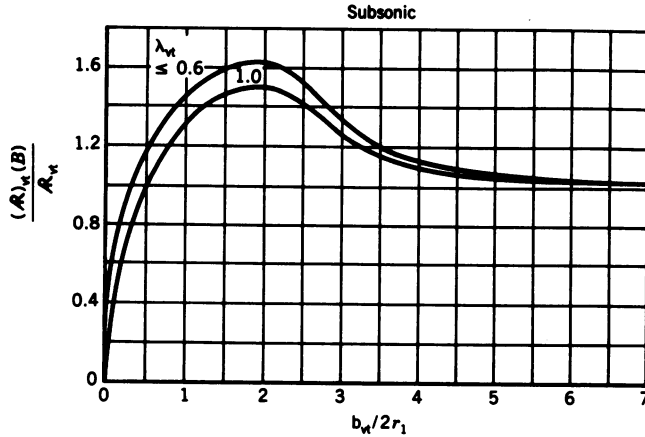
Figure D-37 Chart for estimating the sideslip derivative $(C_{y_\beta})_{v(B)}$ for single vertical tails.[5] b_{vt} = vertical-tail span measured from FRL; $2r_1$ = fuselage depth in region of vertical tail; λ_{vt} = vertical-tail taper ratio based on surface measured from FRL.

For input to Figure D-36, $z_w = 8$ in.; then $z_w/(d/2) = 0.21$, and from Figure D-36, $K_i = 1.1$. Substituting into Eq. D-58 yields

$$\left(C_{y_\beta}\right)_{WB} = 1.1(-2)\left(\frac{32.37}{651.2}\right) = -0.11/\text{rad} \qquad \text{(D-59)}$$

To obtain the lift curve slope of the exposed vertical tail it is necessary to determine the effective aspect ratio of the vertical tail using Figure D-37, where $b_{vt} = 10.75$ ft, $2r_1 = d = 6.42$ ft, and $\lambda_{vt} = 0$. The actual aspect ratio of the vertical tail is $\mathcal{R}_{vt} = b_{vt}^2/S_{vt} = (10.75)^2/118.2 = 0.98$. For input to Figure D-37, $b_{vt}/2r_1 = 10.75/6.42 = 1.67$; then $(\mathcal{R})_{vt(B)}/\mathcal{R}_{vt} = 1.61$, and $\mathcal{R}_{vt(B)} = 1.58$. For input to Figure D-16 to calculate $(C_{L_\alpha})_{vt_e}$,

$$\frac{\mathcal{R}}{\kappa}\left(\beta^2 + \tan^2\Lambda_{c/2}\right)^{1/2} = \frac{1.58}{0.97}(0.1164 + 0.704)^{1/2} = 1.48$$

Then from Figure D-16, $C_{L_\alpha}/\mathcal{R} = 1.4$ and $(C_{L_\alpha})_{vt_e} = 2.2$. Then

$$\left(C_{y_\beta}\right)_{vt} = -(C_{L_\alpha})_{vt_e}\frac{S_{vt}}{S} = -2.2\left(\frac{118.2}{651.2}\right) = -0.4$$

and

$$C_{y_\beta} = \left(C_{y_\beta}\right)_{WB} + \left(C_{y_\beta}\right)_{vt} = -0.11 - 0.4 = -0.51/\text{rad} \qquad \text{(D-60)}$$

The wing–body contribution to C_{l_β} for straight-tapered wings with zero dihedral, for sideslip angles of 5° or less at speeds up to the force-break

Mach numbers, and for low angles of attack, is

$$(C_{l_\beta})_{WB} = C_L \left[\left(\frac{C_{l_\beta}}{C_L} \right)_{\Lambda_{c/2}} K_{M_\Lambda} K_f + \left(\frac{C_{l_\beta}}{C_L} \right)_{\mathcal{R}} \right] + (\Delta C_{l_\beta})_{z_w} \frac{1}{\text{deg}} \quad \text{(D-61)}$$

where

$C_L = 0.146$ is the wing–body lift coefficient from Eq. D-32,
$(C_{l_\beta}/C_L)_{\Lambda_{c/2}}$ is the wing-sweep contribution from Figure D-38,
K_{M_Λ} is the compressibility correction to the sweep contribution from Figure D-39,
$(C_{l_\beta}/C_L)_{\mathcal{R}}$ is the aspect ratio contribution from Figure D-40,
K_f is the empirical fuselage-length-effect correction factor from Figure D-41
$(\Delta C_{l_\beta})_{z_w}$ is the increment in C_{l_β} due to the body induced effect on wing height, given by

$$(\Delta C_{l_\beta})_{z_w} = \frac{1.2\sqrt{\mathcal{R}}}{57.3} \left(\frac{z_w}{b} \right) \left(\frac{2d}{b} \right) \frac{1}{\text{deg}}$$

where $z_w/b = 0.018$ is the vertical distance from the FRL to the $c/4$ point of the root chord divided by the wing span, and $2d/b = 0.347$.

From Figure D-38 for $\Lambda_{c/2} = 41°$

$$\left(\frac{C_{l_\beta}}{C_L} \right)_{\Lambda_{c/2}} = -0.003/\text{deg}$$

From Figure D-39 for $M \cos \Lambda_{c/2} = 0.94 \cos 41° = 0.71$ and $\mathcal{R}/\cos \Lambda_{c/2} = 2.1/\cos 41° = 2.8$, we have $K_{M_\Lambda} = 1.03$. For Figure D-41, $l_f = 46.5$ ft; then $l_f/b = 46.5/37 = 1.26$, $\mathcal{R}/\cos \Lambda_{c/2} = 2.8$, and $K_f = 1$. For Figure D-40, $\mathcal{R} = 2.1$, and for $\lambda = 0$, then

$$\left(\frac{C_{l_\beta}}{C_L} \right)_{\mathcal{R}} = -0.002/\text{deg}$$

Calculating $(\Delta C_{l_\beta})_{z_w}$ yields

$$(\Delta C_{l_\beta})_{z_w} = \frac{1.2\sqrt{2.1}}{57.3} (0.018)(0.347) = 0.00019/\text{deg}$$
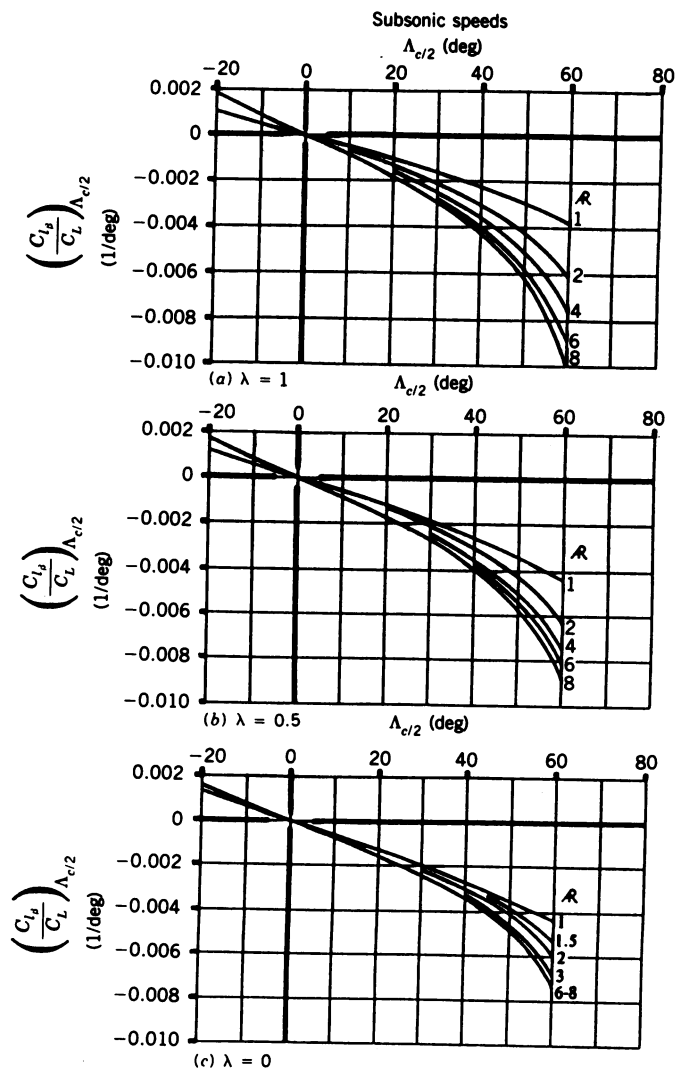
Figure D-38 *Wing sweep contribution to* C_{l_β}.[5]

Substituting into Eq. D-61 yields

$$\left(C_{l_\beta}\right)_{WB} = 0.146[(-0.003)(1.03)(1) - 0.002] + 0.00019/\text{deg}$$

Evaluating and multiplying by 57.3 yields

$$\left(C_{l_\beta}\right)_{WB} = -0.032/\text{rad}$$
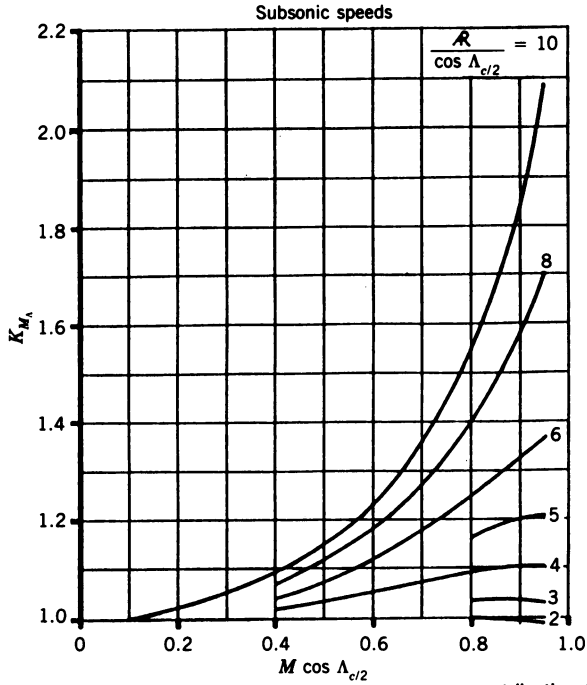
Figure D-39 *Compressibility correction factor to sweep contribution to wing* $C_{l_\beta}.^5$

The contribution of the vertical tail is assumed to be

$$\left(C_{l_\beta}\right)_{vt} = \left(C_{y_\beta}\right)_{vt} \frac{l_{vt}}{b} = -0.4\left(\frac{5.67}{37}\right) = -0.06/\text{rad}$$

where l_{vt} is the vertical distance from the FRL to the MAC of the vertical
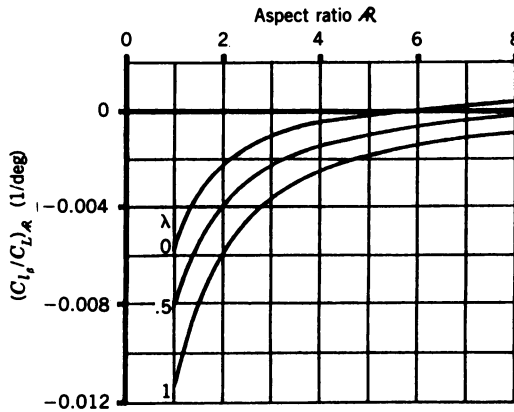
Figure D-40 *Aspect ratio contribution to wing* $C_{l_\beta}.^5$
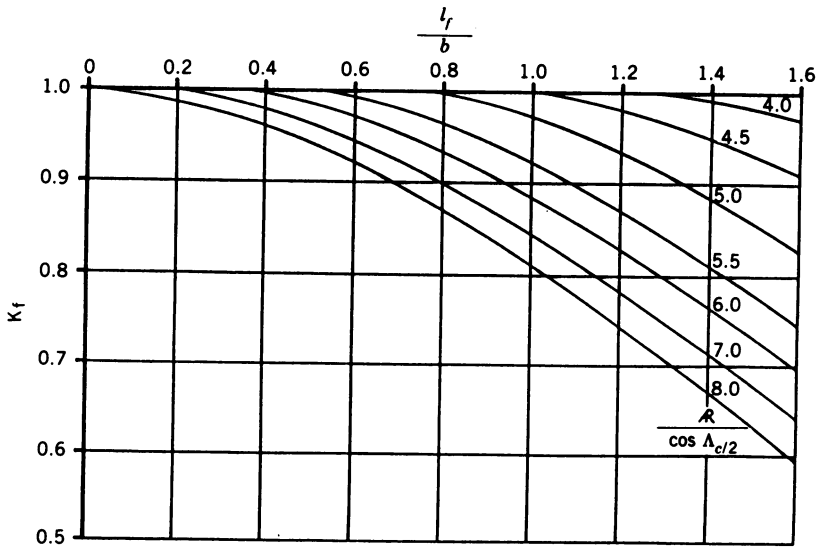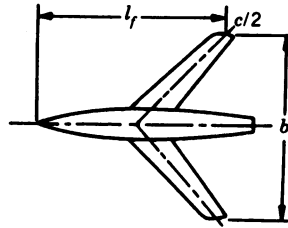
Figure D-41   *Fuselage correction factor.*[5]

tail. Then

$$C_{l_\beta} = \left(C_{l_\beta}\right)_{WB} + \left(C_{l_\beta}\right)_{vt} = -0.032 - 0.06 = -0.09/\text{rad} \qquad \text{(D-62)}$$

The wing–body yawing moment due to sideslip results from the body and the wing–body interference. The contribution of the fuselage is destabilizing, with the vertical tail providing the lateral stability. The equation for the wing–body contribution is

$$\left(C_{n_\beta}\right)_{WB} = -K_N K_R \frac{S_{B_s}}{S} \frac{l_b}{b} \frac{1}{\text{deg}} \qquad \text{(D-63)}$$

where

K_N is an empirical factor related to the sideslip derivative for the body
   plus wing–body interference from Figure D-42,
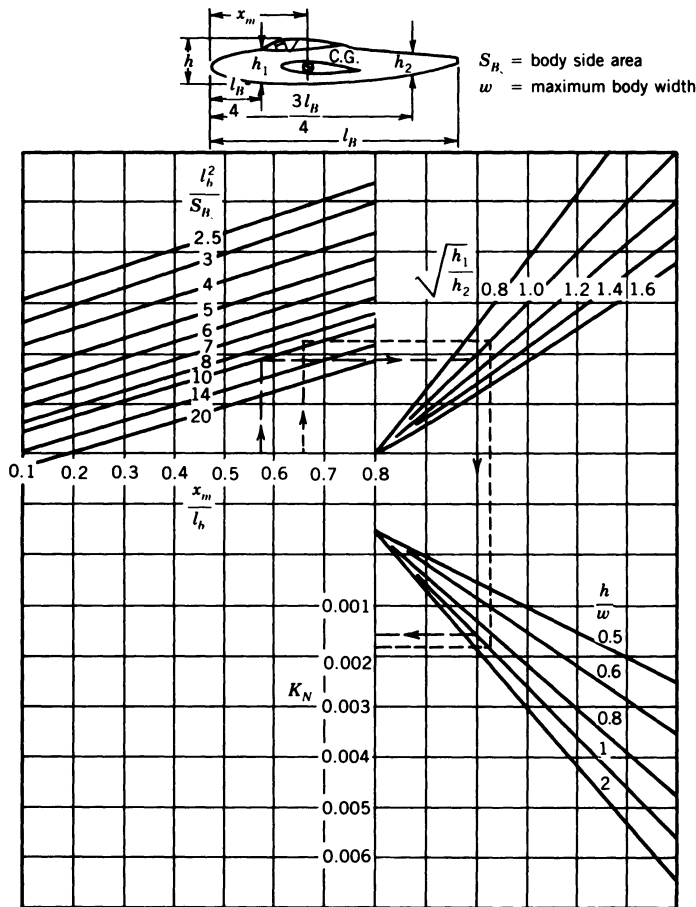
Figure D-42 *Empirical factor K_N related to sideslip derivative C_{n_β} for body + wing–body interference.*[5]

K_R is an empirical Reynolds-number factor from Figure D-43,
S_{B_s} is the projected side area of the body.

The values required for input to Figure D-42 are

$$S_{B_s} = (6.42)(36.67) + 0.5(6.42)(12.33) = 275 \text{ sq ft}$$

$$\frac{l_b^2}{S_{B_s}} = \frac{49^2}{275} = 8.73$$

$$h_1 = h_2 = d = 6.42 \text{ ft}$$
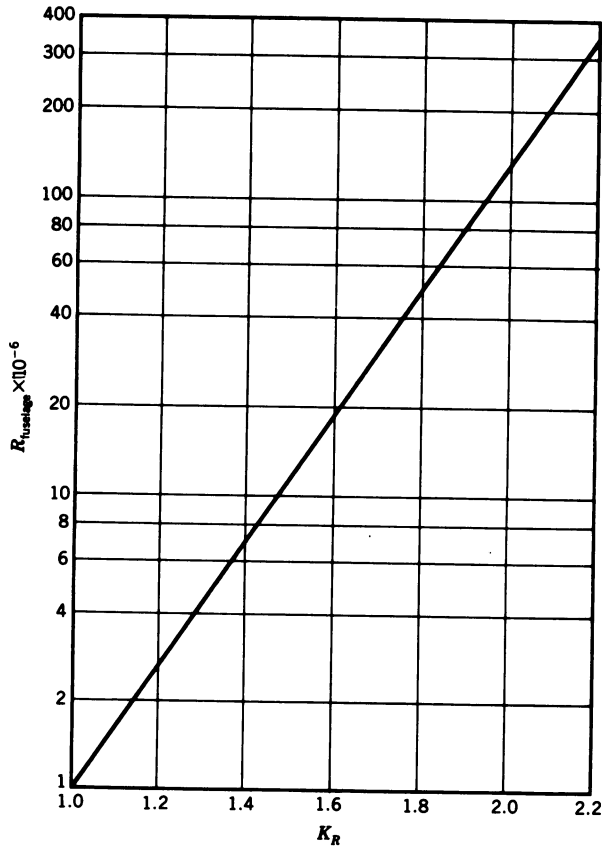
Figure D-43 *Effect of fuselage Reynolds number on wing–body C_{n_β}.*[5]

$$h_1/h_2 = 1$$

$$x_m = 32.5 \text{ ft}$$

$$\frac{x_m}{l_b} = \frac{32.5}{49} = 0.66$$

$$h/w = 1$$

Then from Figure D-42, $K_N = 0.0018$. For Figure D-43 the fuselage Reynolds number from the calculation of the skin-friction drag is 8.82×10^7; then from Figure D-43, $K_R = 1.92$. Substituting into Eq. D-63 yields

$$\left(C_{n_\beta}\right)_{WB} = -0.0018(1.92)\left(\frac{275}{651.2}\right)\left(\frac{49}{37}\right) = -0.002/\text{deg}$$

The contribution of the tail is

$$\left(C_{n_\beta}\right)_{vt} = -\left(C_{y_\beta}\right)_{vt} \frac{l_v}{b} \frac{1}{rad}$$

Substituting,

$$\left(C_{n_\beta}\right)_{vt} = 0.4\left(\frac{9.4}{37}\right) = 0.1$$

Then

$$C_{n_\beta} = 57.3\left(C_{n_\beta}\right)_{WB} + \left(C_{n_\beta}\right)_{vt} = -0.115 + 0.1 = -0.015/rad \quad \text{(D-64)}$$

As the magnitude of the tail contribution to C_{n_β} is less than that of the wing–body, the calculations just completed indicate that the aircraft is directionally unstable. This may be due to the use of the subsonic equations for these calculations. The actual aircraft is possibly only marginally stable at this flight condition. If these results were observed during the preliminary design study of an aircraft, it would indicate a potential stability problem, and reveal that a more detailed study is required.

The Dynamic Derivatives

The dynamic derivatives are the force and moment derivatives resulting from the body roll and yaw rates. The force derivatives are generally small and normally neglected. The moment derivatives are C_{l_p}, C_{l_r}, C_{n_p}, and C_{n_r}. The rolling moment due to roll rate C_{l_p} for wings with zero dihedral using the subsonic equations is

$$C_{l_p} = \left(\frac{\beta C_{l_p}}{k}\right)_{C_L = 0}\left(\frac{k}{\beta}\right) + \left(\Delta C_{l_p}\right)_{drag} \frac{1}{rad} \quad \text{(D-65)}$$

where

$\left(\beta C_{l_p}/k\right)_{C_L = 0}$ is the roll-damping parameter at zero lift from Figure D-44,
$k = c_{l_\alpha}/2\pi = 0.97$ as before,
$k/\beta = 0.97/\sqrt{1 - M^2} = 2.84,$
$\left(\Delta C_{l_p}\right)_{drag}$ is the increment in the roll-damping derivative due to drag, and is

$$\left(\Delta C_{l_p}\right)_{drag} = \frac{\left(C_{l_p}\right)_{C_{D_L}}}{C_L^2}C_L^2 - \frac{C_{D_0}}{8}\frac{1}{rad} \quad \text{(D-66)}$$
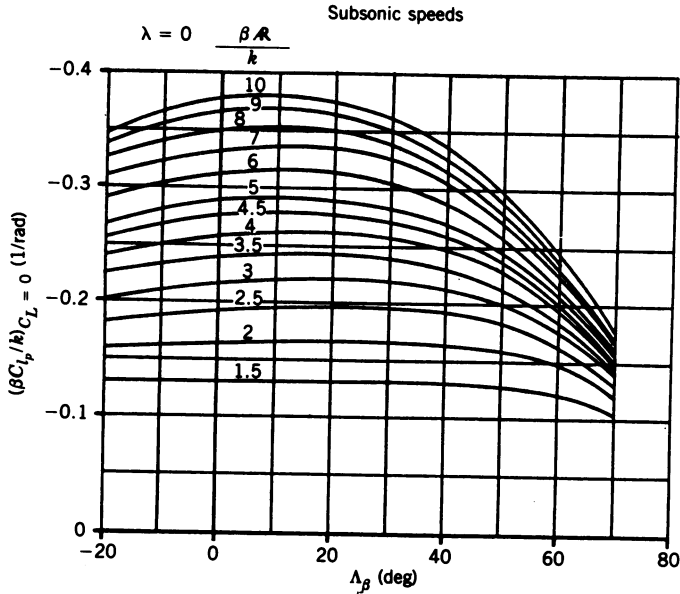
Figure D-44 *Roll-damping parameter at zero lift.*[5]

where $(C_{l_p})C_{D_L}/C_L^2$ is the drag due to the lift parameter from Figure D-45, and $C_{D_0} = 0.0124$ from Eq. D-21.

For the input to Figure D-44,

$$\Lambda_\beta = \tan^{-1}\left(\frac{\tan \Lambda_{c/4}}{\beta}\right) = \tan^{-1}\left(\frac{\tan 53°}{0.34}\right) = 75.6°$$

and $\beta \, \mathcal{R}/k = 0.34(2.1)/0.97 = 0.74$. Extrapolating from Figure D-44, $(\beta C_{l_p}/k)_{C_L=0}$ is estimated as $-0.075/\text{rad}$. From Figure D-45, $(C_{l_p})_{C_{D_L}}/C_L^2 = -0.11/\text{rad}$. Then substituting into Eq. D-66 yields

$$\left(\Delta C_{l_p}\right)_{\text{drag}} = -0.11(0.146)^2 - \frac{0.0124}{8} = -0.0039$$

Substituting into Eq. D-65 yields

$$C_{l_p} = -0.075(2.84) - 0.0039 = -0.22/\text{rad} \qquad \text{(D-67)}$$

Subsonic speeds
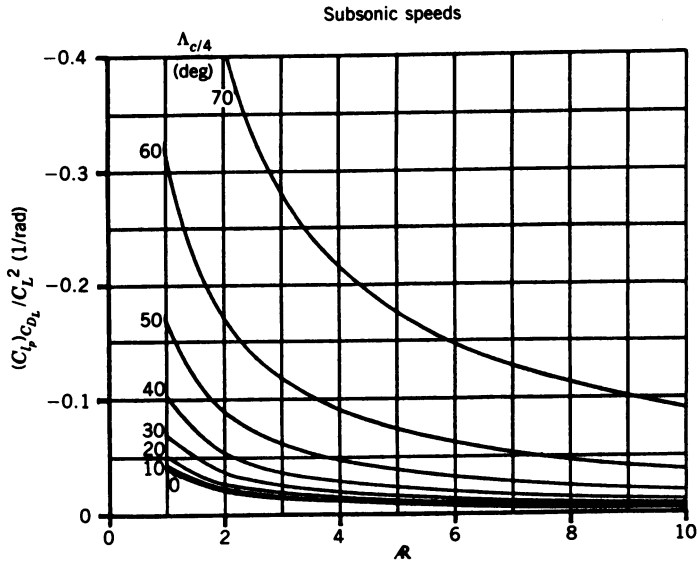
Figure D-45 *Drag-due-to-lift roll-damping parameter.*[5]

Using the subsonic equations, the rolling moment due to the yaw rate is

$$C_{l_r} = C_L \left(\frac{C_{l_r}}{C_L} \right)_{C_L = 0; M} + (\Delta C_{l_r})_{C_L} \frac{1}{\text{rad}} \qquad \text{(D-68)}$$

where

$$\left(\frac{C_{l_r}}{C_L} \right)_{C_L = 0; M} = \frac{1 + \dfrac{\mathcal{R}(1 - B^2)}{2B(\mathcal{R}B + 2\cos \Lambda_{c/4})} + \dfrac{\mathcal{R}B + 2\cos \Lambda_{c/4}}{\mathcal{R}B + 4\cos \Lambda_{c/4}} \dfrac{\tan^2 \Lambda_{c/4}}{8}}{1 + \dfrac{\mathcal{R} + 2\cos \Lambda_{c/4}}{\mathcal{R} + 4\cos \Lambda_{c/4}} \dfrac{\tan^2 \Lambda_{c/4}}{8}}$$

$$\times \left(\frac{C_{l_r}}{C_L} \right)_{C_L = 0; M = 0} \qquad \text{(D-69)}$$

where

$$B = \sqrt{1 - M^2 \cos^2 \Lambda_{c/4}} = \sqrt{1 - 0.94^2 \cos^2 53°} = 0.825,$$
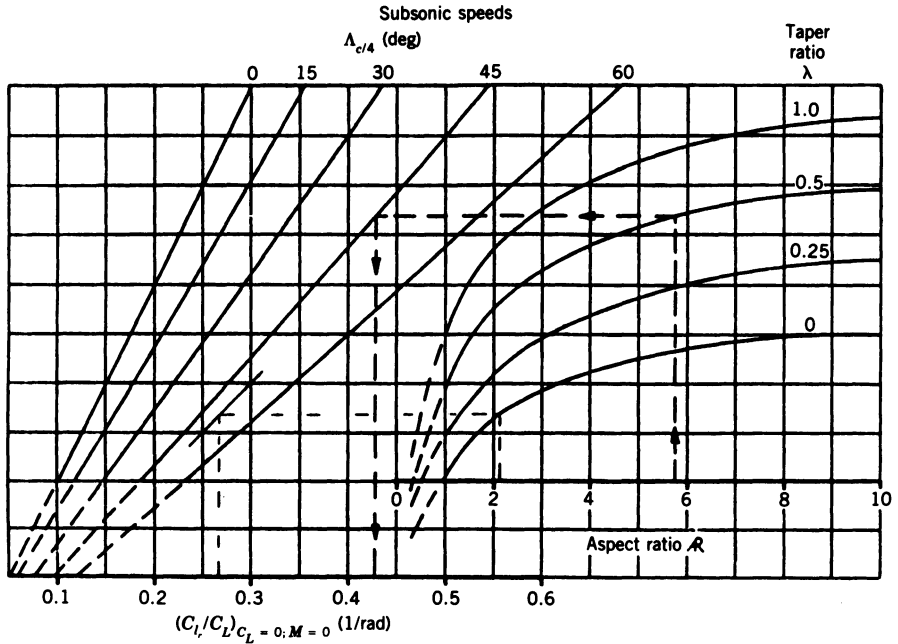
Figure D-46   *Wing yawing derivative C_{l_r}.*[5]

$(C_{l_r}/C_L)_{C_L = 0; M = 0}$ is from Figure D-46, and

$$\left(\Delta C_{l_r}\right)_{C_L} = C_L\left(\frac{C_{l_\beta}}{C_L}\right) - \left(C_{l_\beta}\right)_{\text{test}} \frac{1}{\text{rad}}$$

As the test values in Datcom were for an untapered wing with 45° sweepback, the $(\Delta C_{l_r})C_L$ term will be neglected. For Eq. D-69

$$\frac{\mathcal{R}(1 - B^2)}{2B(\mathcal{R}\, B + 2\cos \Lambda_{c/4})} = \frac{2.1(1 - 0.825^2)}{2(0.825)[2.1(0.825) + 2\cos 53°]} = 0.138$$

$$\frac{\mathcal{R}\, B + 2\cos \Lambda_{c/4}}{\mathcal{R}\, B + 4\cos \Lambda_{c/4}} = \frac{1.7325 + 2\cos 53°}{1.7325 + 4\cos 53°} = 0.709$$

$$\frac{\tan^2 \Lambda_{c/4}}{8} = \frac{\tan^2 53°}{8} = 0.22$$

$$\frac{\mathcal{R} + 2\cos \Lambda_{c/4}}{\mathcal{R} + 4\cos \Lambda_{c/4}} = \frac{2.1 + 2\cos 53°}{2.1 + 4\cos 53°} = 0.733$$

From Figure D-46

$$\left(\frac{C_{l_r}}{C_L}\right)_{C_L = 0;\, M = 0} = 0.27$$

Substituting into Eq. D-69 yields

$$\left(\frac{C_{l_r}}{C_L}\right)_{C_L = 0;\, M} = \frac{1 + 0.138 + 0.709(0.22)}{1 + 0.733(0.22)}(0.27) = \frac{1.2946}{1.16}(0.27) = 0.3$$

Substituting into Eq. D-68 yields

$$C_{l_r} = 0.146(0.3) = 0.044/\text{rad} \qquad\qquad \text{(D-70)}$$

The yawing moment due to yaw rate, C_{n_r}, is due to the wing and the vertical tail, as the contribution of the fuselage can be neglected. Then using the subsonic equations

$$C_{n_r} = (C_{n_r})_W + (C_{n_r})_{vt} \qquad\qquad \text{(D-71)}$$

where

$$(C_{n_r})_W = \left(\frac{C_{n_r}}{C_L^2}\right)C_L^2 + \left(\frac{C_{n_r}}{C_{D_0}}\right)(C_{D_0})_W$$

$$(C_{n_r})_{vt} = 2\left(\frac{l_v}{b}\right)^2 (C_{y_\beta})_{vt}$$

where

C_{n_r}/C_L^2 is the low-speed drag-due-to-lift yaw-damping parameter from Figure D-47,

C_{n_r}/C_{D_0} is the low-speed profile-drag yaw-damping parameter from Figure D-48, and

$(C_{D_0})_W = 0.0034$ from Eq. D-13.

For Figures D-47 and D-48, $x/c = -\text{SM} = 0.11$. As there are no curves for $x/c = 0.11$ in these figures, an interpolation will be made using values from the $x/c = 0$ and the $x/c = 0.2$ curves. For $x/c = 0.2$ from Figure D-47, $C_{n_r}/C_L^2 = 0.05$, and for $x/c = 0$, $C_{n_r}/C_L^2 = 0.02$. Then for $x/c = 0.11$, $C_{n_r}/C_L^2 = 0.035$. From Figure D-48 for $x/c = 0.2$, $C_{n_r}/C_{D_0} = -0.73$ and for $x/c = 0$, $C_{n_r}/C_{D_0} = -0.74$. Then for $x/c = 0.11$, $C_{n_r}/C_{D_0} = -0.735$. From
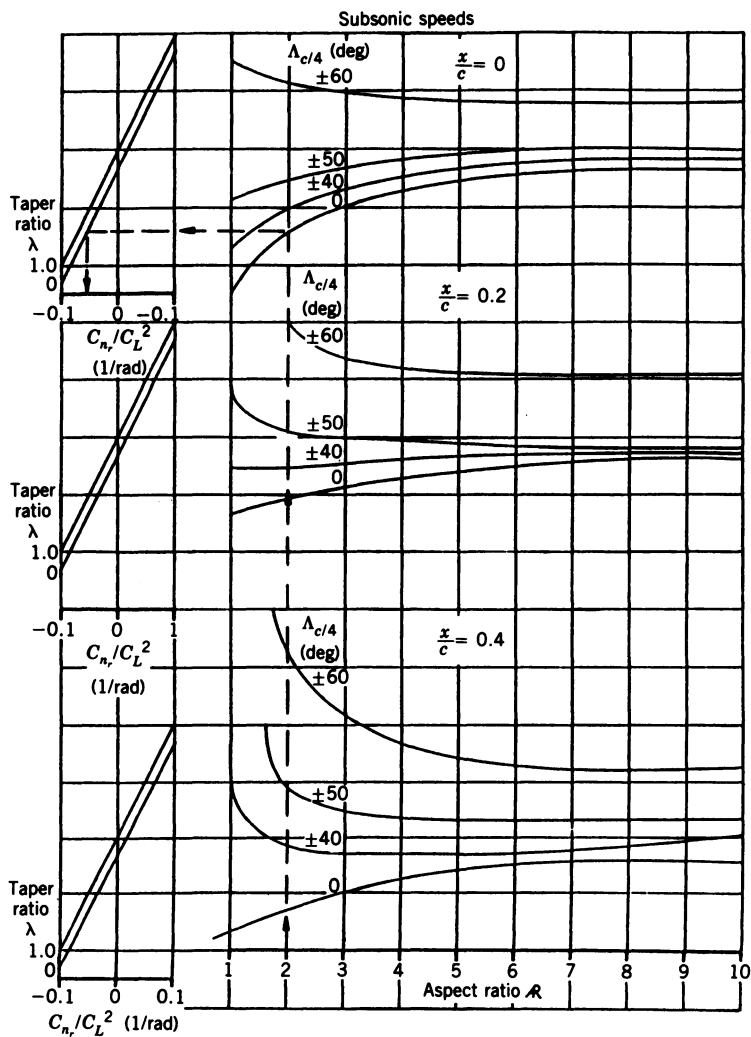
Figure D-47 *Low-speed drag-due-to-lift yaw-damping parameter.*[5] *Note: x/c = −SM.*

Eq. D-60, $(C_{y_\beta})_{vt} = -0.4$, and substituting into Eq. D-71 yields

$$C_{n_r} = 0.035(0.146)^2 - 0.735(0.0034) + 2\left(\frac{9.4}{37}\right)^2(-0.4)$$

Evaluating,

$$C_{n_r} = -0.053/\text{rad} \tag{D-72}$$
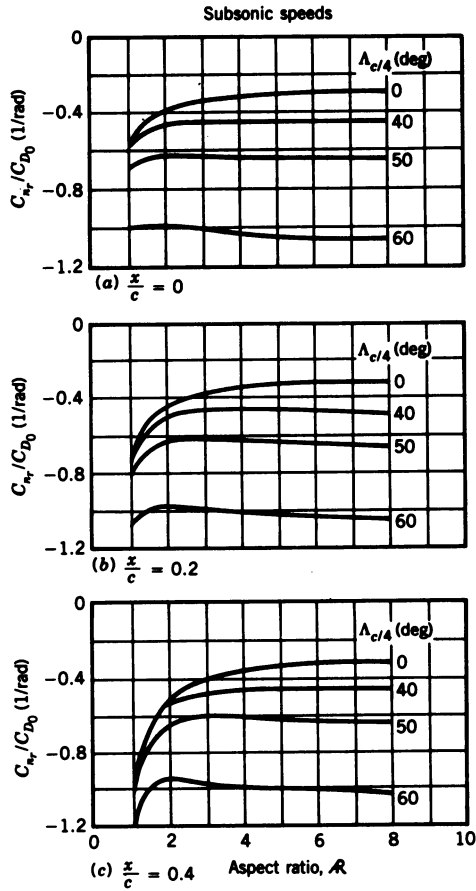
Figure D-48 Low-speed profile-drag yaw-damping parameter.[5] Note: x/c = − SM.

The yawing moment due to roll rate, C_{n_p}, is due to the differential drag of the wings and the side force on the vertical tail due to the roll rate. Then using the subsonic equations,

$$C_{n_p} = \left(C_{n_p}\right)_W + \left(C_{n_p}\right)_{vt} \tag{D-73}$$

where

$$\left(C_{n_p}\right)_W = \left(\frac{C_{n_p}}{C_L}\right)_{C_L = 0;\, M} C_L$$

$$\left(C_{n_p}\right)_{vt} = -\frac{2 l_v l_{vt}}{b^2} \left(C_{y_\beta}\right)_{vt}$$

where

$$\left(\frac{C_{n_p}}{C_L}\right)_{C_L=0;M} = \left(\frac{\mathcal{R}+4\cos\Lambda_{c/4}}{\mathcal{R}B+4\cos\Lambda_{c/4}}\right)$$

$$\times\left[\frac{\mathcal{R}B+0.5(\mathcal{R}B+\cos\Lambda_{c/4})\tan^2\Lambda_{c/4}}{\mathcal{R}+0.5(\mathcal{R}+\cos\Lambda_{c/4})\tan^2\Lambda_{c/4}}\right]\left(\frac{C_{n_p}}{C_L}\right)_{C_L=0;M=0}$$

$$C_L = 0.146$$

$$l_{vt} = 5.67 \quad \text{from } \left(C_{l_\beta}\right)_{vt} \text{ calculation}$$

$$\left(C_{y_\beta}\right)_{vt} = -0.4$$

where $B = 0.825$ from Eq. D-69, and

$$\left(\frac{C_{n_p}}{C_L}\right)_{C_L=0;M=0} = -\frac{1}{6}\left[\frac{\mathcal{R}+6(\mathcal{R}+\cos\Lambda_{c/4})}{\mathcal{R}+4\cos\Lambda_{c/4}}\right]$$

$$\times\left(\frac{\tan^2\Lambda_{c/4}}{12} - \frac{SM\tan\Lambda_{c/4}}{\mathcal{R}}\right)$$

Substituting into the equation for $(C_{n_p}/C_L)_{C_L=0; M=0}$ yields

$$\left(\frac{C_{n_p}}{C_L}\right)_{C_L=0;M=0} = -\frac{1}{6}\left[\frac{2.1+6(2.1+\cos53°)}{2.1+4\cos53°}\right]\left(\frac{\tan^2 53°}{12} - \frac{SM\tan53°}{2.1}\right)$$

$$= -0.146$$

For $(C_{n_p}/C_L)_{C_L=0;M}$,

$$\frac{\mathcal{R}+4\cos\Lambda_{c/4}}{\mathcal{R}B+4\cos\Lambda_{c/4}} = \frac{2.1+4\cos53°}{2.1(0.825)+4\cos53°} = 1.089$$

$$\frac{\mathcal{R}B+0.5(\mathcal{R}B+\cos\Lambda_{c/4})\tan^2\Lambda_{c/4}}{\mathcal{R}+0.5(\mathcal{R}+\cos\Lambda_{c/4})\tan^2\Lambda_{c/4}}$$

$$= \frac{2.1(0.825)+0.5[(2.1)(0.825)+\cos53°](\tan^2 53°)}{2.1+0.5(2.1+\cos53°)(\tan^2 53°)} = 0.8457$$

Substituting,

$$\left(\frac{C_{n_p}}{C_L}\right)_{C_L=0;M} = (1.089)(0.8457)(-0.146) = -0.134$$

and

$$(C_{n_p})_W = -0.134(0.146) = -0.02$$

$$(C_{n_p})_{vt} = -\frac{2(9.4)(5.67)}{37^2}(-0.4) = 0.03$$

Substituting into Eq. D-73 yields

$$C_{n_p} = -0.02 + 0.03 = 0.01/\text{rad} \qquad \text{(D-74)}$$

Lateral Equations of Motion

The lateral equations of motion from Eq. 3-27, assuming $J_{xz} = 0$ and for $\Theta = 0$, are

$$\left(\frac{I_x}{Sqb}s^2 - \frac{b}{2U}C_{l_p}s\right)\phi(s) - \frac{b}{2U}C_{l_r}s\psi(s) - C_{l_\beta}\beta(s) = C_{l_{\delta_a}}\delta_a(s) + C_{l_{\delta_r}}\delta_r(s)$$

$$-\frac{b}{2U}C_{n_p}s\phi(s) + \left(\frac{I_z}{Sqb}s^2 - \frac{b}{2U}C_{n_r}s\right)\psi(s) - C_{n_\beta}\beta(s) = C_{n_{\delta_a}}\delta_a(s) + C_{n_{\delta_r}}\delta_r(s)$$

$$-C_{y_\phi}\phi(s) + \left(\frac{mU}{Sq}s - C_{y_\psi}\right)\psi(s) + \left(\frac{mU}{Sq}s - C_{y_\beta}\right)\beta(s) = C_{y_{\delta_a}}\delta_a(s) + C_{y_{\delta_r}}\delta_r(s)$$

$$\text{(D-75)}$$

Summarizing the lateral stability derivatives just calculated: From Eq. D-67,

$$C_{l_p} = -0.22$$

From Eq. D-70,

$$C_{l_r} = 0.044$$

From Eq. D-74,

$$C_{n_p} = 0.01$$

From Eq. D-64,

$$C_{n_\beta} = -0.015$$

From Eq. D-72,

$$C_{n_r} = -0.053$$

From Eq. D-60,

$$C_{y_\beta} = -0.51$$

From Table 3-1,

$$C_{y_\phi} = \frac{W}{Sq} = C_L = 0.146$$

$$C_{y_\psi} = \frac{W}{Sq} \sin \Theta = 0$$

From Eq. D-62,

$$C_{l_\beta} = -0.09$$

$$\frac{mU}{Sq} = 4.12 \text{ sec}$$

$$\frac{I_x}{Sqb} = \frac{13{,}566}{(651.2)(242.5)(37)} = 0.0023 \text{ sec}^2$$

$$\frac{I_z}{Sqb} = \frac{99{,}695}{(651.2)(242.5)(37)} = 0.017 \text{ sec}^2$$

$$\frac{b}{2U} = \frac{37}{2(910)} = 0.02 \text{ sec}$$

$$\frac{b}{2U} C_{l_p} = -0.0045 \text{ sec}$$

$$\frac{b}{2U} C_{l_r} = 0.0009 \text{ sec}$$

$$\frac{b}{2U} C_{n_p} = 0.0002 \text{ sec}$$

$$\frac{b}{2U} C_{n_r} = -0.0011 \text{ sec}$$

For 3-ft chordwise × 6-ft spanwise ailerons, the lift slope per radian of deflection is assumed to be 0.26, and for a 3-ft chordwise × 5-ft spanwise rudder, $C_{y_{\delta_r}}$ is assumed to be 0.2. Then

$$C_{l_{\delta_a}} = \frac{2l_a}{b}(0.26) = \frac{2(13.17)(0.26)}{37} = 0.19$$

where l_a is the distance from the centerline of the aircraft to the spanwise

center of the aileron,

$$C_{n_{\delta_a}} = -0.0017 \quad \text{by assumption}$$

$$C_{y_{\delta_a}} = 0$$

$$C_{n_{\delta_r}} = -\frac{l_r}{b}C_{y_{\delta_r}} = -\frac{14.25(0.2)}{37} = -0.08$$

$$C_{l_{\delta_r}} = \frac{l_{vr}}{b}C_{y_{\delta_r}} = \frac{5.5(0.2)}{37} = 0.03$$

where l_r is the distance from the cg of the aircraft to the $c/4$ of the rudder, and l_{vr} is the distance from the FRL to the spanwise center of the rudder. Substituting into Eq. D-75 yields

$$(0.0023s^2 + 0.0045s)\phi(s) - 0.0009s\psi(s) + 0.09\beta(s) = 0.19\delta_a(s) + 0.03\delta_r(s)$$

$$-0.0002s\phi(s) + (0.017s^2 + 0.0011s)\psi(s) + 0.015\beta(s)$$

$$= -0.0017\delta_a(s) - 0.08\delta_r(s)$$

$$-0.146\phi(s) + 4.12s\psi(s) + (4.12s + 0.51)\beta(s) = 0.2\delta_r(s) \quad \text{(D-76)}$$

Using Program CC, the lateral transfer functions are

$$\frac{\phi(s)}{\delta_r(s)} = \frac{13.04(s + 3.83)(s - 3.92)}{(s - 0.121)(s - 0.58)(s + 0.651)(s + 2.2)}$$

$$\frac{\psi(s)}{\delta_r(s)} = \frac{-4.7(s + 2.2)(s^2 - 0.174s + 0.65)}{s(s - 0.121)(s - 0.58)(s + 0.651)(s + 2.2)}$$

$$\frac{\beta(s)}{\delta_r(s)} = \frac{0.048(s - 0.0036)(s + 2.03)(s + 97.9)}{(s - 0.121)(s - 0.58)(s + 0.651)(s + 2.2)} \quad \text{(D-77)}$$

$$\frac{\phi(s)}{\delta_a(s)} = \frac{-82.6(s - 0.87)(s + 1.06)}{(s - 0.121)(s - 0.58)(s + 0.651)(s + 2.2)}$$

$$\frac{\psi(s)}{\delta_a(s)} = \frac{0.1(s + 1.73)(s - 2.07)(s - 7.48)}{s(s - 0.121)(s - 0.58)(s + 0.651)(s + 2.2)}$$

$$\frac{\beta(s)}{\delta_a(s)} = \frac{0.1(s + 0.09)(s + 20.87)}{(s - 0.121)(s - 0.58)(s + 0.651)(s + 2.2)} \quad \text{(D-78)}$$

The directional instability resulting from the negative C_{n_β} is evident in the lateral transfer functions. The Dutch roll oscillation has been replaced by two real poles, one of which is in the right half plane ($s = 0.57$). This is the same result as was observed in Section 2-2 for a positive C_{m_α}. The negative C_{n_β}

also results in the increase in the magnitude of the spiral divergence pole ($s = 0.121$). The zeros of the rudder input transfer functions follow the same pattern as those in Section 3-4 with the exception of the ψ/δ_r transfer function, where the complex zeros are in the right half plane. For the aileron input transfer functions, the normal complex zeros of the ϕ/δ_a transfer function have been replaced by real zeros, one of which is in the right half plane. A brief analysis showed that a yaw damper similar to the one shown in Figure 4-3, along with sideslip feedback with a lead compensator in the forward path, could stabilize the aircraft.

This completes the calculation of the aircraft transfer functions using Datcom. For those interested, the four volumes of Datcom are available from Global Engineering Documents by calling (800) 854-7179.

REFERENCES

1. C. D. Perkins and R. E. Hage, *Airplane Performance, Stability, and Control*, John Wiley and Sons, New York, 1949.
2. D. O. Dommash, S. S. Sharby and T. F. Connolly, *Airplane Aerodynamics*, Pitman Publishing Corporation, New York, 1951.
3. C. B. Millikan, *Aerodynamics of the Airplane*, John Wiley and Sons, 1941.
4. A. M. Kuethe and J. D. Schetzer, *Foundations of Aerodynamics*, 2nd ed., John Wiley and Sons, 1959.
5. D. E. Hoak, R. D. Finck, et al., *USAF Stability and Control Datcom*, 1978, Flight Control Division, Air Force Flight Dynamics Laboratory, Wright-Patterson Air Force Base, Ohio.

Matrices

E-1 DEFINITION

A matrix is an array of numbers often used to systematize and simplify the writing and/or manipulation of simultaneous linear equations. The three basic matrices are as follows:

1. *Rectangular matrix:*

<div align="center">Column</div>

$$[a] = [a_{ij}] = \begin{bmatrix} a_{11} & a_{12} & \cdots & a_{1j} \\ a_{21} & a_{22} & \cdots & a_{2j} \\ a_{31} & a_{32} & \cdots & a_{3j} \\ \vdots & \vdots & & \vdots \\ a_{i1} & a_{i2} & \cdots & a_{ij} \end{bmatrix} \text{Row}$$

where the size of the matrix is expressed by calling it an $i \times j$ (read i by j) matrix. If $i = j$, then the rectangular matrix becomes a square matrix.

2. *Column matrix:*

$$\{a_i\} = \begin{bmatrix} a_1 \\ a_2 \\ a_3 \\ \vdots \\ a_i \end{bmatrix}$$

3. *Row matrix:*

$$\lfloor a_j \rfloor = \begin{bmatrix} a_1 & a_2 & a_3 & \cdots & a_j \end{bmatrix}$$

As an example of the use of matrices, the following simultaneous equations are written using matrices:

$$3x + 5y + 2z = 10$$
$$2\dot{x} - 3y + 4z = 8$$
$$-3x + 2y - 2z = -3$$

In matrix form

$$\begin{bmatrix} 3 & 5 & 2 \\ 2 & -3 & 4 \\ -3 & 2 & -2 \end{bmatrix} \begin{bmatrix} x \\ y \\ z \end{bmatrix} = \begin{bmatrix} 10 \\ 8 \\ -3 \end{bmatrix}$$

or $[A]\{B\} = \{C\}$, where

$$[A] = \begin{bmatrix} 3 & 5 & 2 \\ 2 & -3 & 4 \\ -3 & 2 & -2 \end{bmatrix}$$

$$\{B\} = \begin{bmatrix} x \\ y \\ z \end{bmatrix} \quad \text{and} \quad \{C\} = \begin{bmatrix} 10 \\ 8 \\ -3 \end{bmatrix}$$

E-2   MATRIX OPERATIONS

1. *Addition.* When adding matrices each matrix to be added must be the same size; thus $[a_{ij}] + [b_{ij}] = [c_{ij}]$ where each element $c_{ij} = a_{ij} + b_{ij}$.

Example

$$\begin{bmatrix} 1 & 2 & 1 \\ 3 & 2 & 7 \end{bmatrix} + \begin{bmatrix} 1 & -2 & 3 \\ 4 & 1 & 2 \end{bmatrix} = \begin{bmatrix} 2 & 0 & 4 \\ 7 & 3 & 9 \end{bmatrix}$$

2. *Subtraction.* Again each matrix must be the same size, and each element $c_{ij} = a_{ij} - b_{ij}$ for $[a_{ij}] - [b_{ij}] = [c_{ij}]$.

3. *Multiplication.* To multiply two matrices they must be compatible in size: the operation $[a_{ij}][b_{jk}] = [c_{ik}]$ can be performed if the number of columns of the *a* matrix is equal to the number of rows of the *b* matrix. The product matrix then has the same number of rows as the *a* matrix and the same number of columns as the *b* matrix.

Example

$$\begin{bmatrix} 1 & 2 & 4 \\ 3 & 1 & 3 \\ -1 & 2 & 7 \end{bmatrix} \begin{bmatrix} 1 & 3 \\ 2 & 2 \\ 4 & 1 \end{bmatrix} = \begin{bmatrix} 21 & 11 \\ 17 & 14 \\ 31 & 8 \end{bmatrix}$$

The element c_{11} is obtained by adding the products of the elements of the first row of the a matrix and the first column of the b matrix. Thus

$$(1)(1)+(2)(2)+(4)(4) = 21$$

In like manner

$$(3)(1)+(1)(2)+(3)(4) = 17$$

and

$$(-1)(1)+(2)(2)+(7)(4) = 31$$

To obtain the second row of the c matrix, this procedure is followed using the second column of the b matrix. *Note*: $[a][b] \neq [b][a]$

4. *Scalar multiplication.* Any matrix can be multiplied by a scalar quantity by multiplying each element of the matrix by the scalar quantity.

5. *Division.* Division can be performed only by inverting the divisor and multiplying. The inversion can be performed only for square matrices. The symbol used to indicate the inversion is a superscript -1 outside the bracket; thus the inverse of $[A]$ would be $[A]^{-1}$. If $[B]=[A]^{-1}$, then

$$[B_{ij}] = \frac{(-1)^{(i+j)}|\text{minor of } A_{ji}|}{|A_{ij}|} \qquad \text{(E-1)}$$

Example. Let

$$[A] = \begin{bmatrix} 1 & 4 & 6 \\ 3 & 2 & 7 \\ -1 & 4 & 2 \end{bmatrix}$$

Then (see Section E-4 for the method of expanding a determinant),

$$B_{11} = \frac{(-1)^2 \begin{vmatrix} 2 & 7 \\ 4 & 2 \end{vmatrix}}{\begin{vmatrix} 1 & 4 & 6 \\ 3 & 2 & 7 \\ -1 & 4 & 2 \end{vmatrix}} = \frac{4-28}{(4-28)-4(6+7)+6(12+2)}$$

or

$$B_{11} = \frac{-24}{8} = -3$$

In like manner,

$$B_{12} = \frac{(-1)^3 \begin{vmatrix} 4 & 6 \\ 4 & 2 \end{vmatrix}}{8} = \frac{-(8-24)}{8} = 2$$

and

$$B_{13} = \frac{(-1)^4 \begin{vmatrix} 4 & 6 \\ 2 & 7 \end{vmatrix}}{8} = \frac{28-12}{8} = 2$$

Finally,

$$[B] = \begin{bmatrix} -3 & 2 & 2 \\ -1.625 & 1 & 1.375 \\ 1.75 & -1 & -1.25 \end{bmatrix}$$

E-3 SPECIAL MATRICES

There are several special cases of the square matrix.

1. *Symmetric matrix.* For a symmetric matrix, $a_{ij} = a_{ji}$.

Example

$$[A] = \begin{bmatrix} 1 & 2 & -4 \\ 2 & 3 & 6 \\ -4 & 6 & 5 \end{bmatrix}$$

2. *Diagonal matrix.* For a diagonal matrix only the diagonal terms are nonzero; thus $a_{ij} = 0$ for $i \neq j$, and $a_{ij} \neq 0$ in general for $i = j$.

Example

$$\begin{bmatrix} 1 & 0 & 0 \\ 0 & 3 & 0 \\ 0 & 0 & 5 \end{bmatrix}$$

3. *Identity matrix.* A special case of the diagonal matrix in which each term in the diagonal is equal to one. The identity matrix is denoted by $[I]$.

Example

$$[I] = \begin{bmatrix} 1 & 0 & 0 \\ 0 & 1 & 0 \\ 0 & 0 & 1 \end{bmatrix}$$

Any matrix multiplied by the identity matrix yields itself. Also, $[A]^{-1}[A] = [I]$. The proof of this is left as an exercise for the student.

In Chapter 11, in the discussion of the resulting simultaneous equations using matrix techniques, the solution was obtained by multiplying both sides of the equation by the inverse of the coefficient matrix. The proof of this procedure follows.

If $[A][X] = [C]$, multiply both sides by $[A]^{-1}$.

Then

$$[A]^{-1}[A][X] = [A]^{-1}[C]$$

But

$$[A]^{-1}[A] = [I] \quad \text{and} \quad [I][X] = [X]$$

Therefore

$$[X] = [A]^{-1}[C]$$

E-4   DETERMINANTS[1]

In performing the inversion of a matrix use was made of determinants and the minors of determinants. By definition a determinant is a square array of numbers and provides a shorthand form for denoting the sum of certain products which can be formed using all the numbers of the determinant. The "order" of the determinant is the number of rows or columns. Thus

$$D = \begin{vmatrix} a_{11} & a_{12} & \cdots & a_{1n} \\ a_{21} & a_{22} & \cdots & a_{2n} \\ a_{31} & a_{32} & \cdots & a_{3n} \\ \vdots & \vdots & & \vdots \\ a_{n1} & a_{n2} & \cdots & a_{nn} \end{vmatrix} \qquad \text{(E-2)}$$

is an nth-order determinant and contains n^2 elements.

Minor of a Determinant

The minor of a determinant is the determinant formed by deleting the row and column containing a given element a_{ij}. Thus for the determinant given in

Eq. E-2, the minor of a_{22} is

$$\begin{vmatrix} a_{11} & a_{13} & \cdots & a_{1n} \\ a_{31} & a_{33} & \cdots & a_{3n} \\ \vdots & \vdots & & \vdots \\ a_{n1} & a_{n3} & \cdots & a_{nn} \end{vmatrix}$$

Expansion of a Determinant by Minors

The expansion of the determinant given in Eq. E-2 is

$$a_{11}\begin{vmatrix} \text{minor} \\ \text{of } a_{11} \end{vmatrix} - a_{12}\begin{vmatrix} \text{minor} \\ \text{of } a_{12} \end{vmatrix} + a_{13}\begin{vmatrix} \text{minor} \\ \text{of } a_{13} \end{vmatrix} - \cdots (-1)^{n-1}a_{1n}\begin{vmatrix} \text{minor} \\ \text{of } a_{1n} \end{vmatrix}$$

or

$$a_{11}\begin{vmatrix} \text{minor} \\ \text{of } a_{11} \end{vmatrix} - a_{21}\begin{vmatrix} \text{minor} \\ \text{of } a_{21} \end{vmatrix} + a_{31}\begin{vmatrix} \text{minor} \\ \text{of } a_{31} \end{vmatrix} - \cdots (-1)^{n-1}a_{n1}\begin{vmatrix} \text{minor} \\ \text{of } a_{n1} \end{vmatrix} \quad \text{(E-3)}$$

If the determinants formed by the minors in Eq. E-3 are greater than the second order, the procedure is continued until they are reduced to second-order determinants. The expansion of a second-order determinant is as follows:

$$\begin{vmatrix} a_{11} & a_{12} \\ a_{21} & a_{22} \end{vmatrix} = a_{11}a_{22} - a_{12}a_{21}$$

Example

$$D = \begin{vmatrix} 3 & -1 & 2 & 3 \\ 1 & 0 & 2 & 1 \\ 2 & 3 & 0 & 1 \\ 5 & 2 & 4 & -5 \end{vmatrix}$$

$$= 3\begin{vmatrix} 0 & 2 & 1 \\ 3 & 0 & 1 \\ 2 & 4 & -5 \end{vmatrix} + 1\begin{vmatrix} 1 & 2 & 1 \\ 2 & 0 & 1 \\ 5 & 4 & -5 \end{vmatrix} + 2\begin{vmatrix} 1 & 0 & 1 \\ 2 & 3 & 1 \\ 5 & 2 & -5 \end{vmatrix} - 3\begin{vmatrix} 1 & 0 & 2 \\ 2 & 3 & 0 \\ 5 & 2 & 4 \end{vmatrix} \quad \text{(E-4)}$$

Expanding the first term of Eq. E-4 yields

$$3\begin{vmatrix} 0 & 2 & 1 \\ 3 & 0 & 1 \\ 2 & 4 & -5 \end{vmatrix} = (3)(0)\begin{vmatrix} 0 & 1 \\ 4 & -5 \end{vmatrix} + (3)(-2)\begin{vmatrix} 3 & 1 \\ 2 & -5 \end{vmatrix} + 3(1)\begin{vmatrix} 3 & 0 \\ 2 & 4 \end{vmatrix}$$

$$= 0 - 6(-15-2) + 3(12-0)$$

$$= 0 + 102 + 36 = 138$$

The second step in the expansion just given can be skipped, as will be done in the expansion of the second term:

$$1\begin{vmatrix} 1 & 2 & 1 \\ 2 & 0 & 1 \\ 5 & 4 & -5 \end{vmatrix} = 1[1(0-4)-2(-10-5)+1(8-0)]$$

$$= 34$$

In like manner,

$$2\begin{vmatrix} 1 & 0 & 1 \\ 2 & 3 & 1 \\ 5 & 2 & -5 \end{vmatrix} = -56 \quad \text{and} \quad -3\begin{vmatrix} 1 & 0 & 2 \\ 2 & 3 & 0 \\ 5 & 2 & 4 \end{vmatrix} = 30$$

Therefore $D = 138+34-56+30 = 146$.

Use of Determinants to Solve Simultaneous Equations

Given the simultaneous algebraic equations

$$x + 2y + 3z = 6$$

$$2x - 2y - z = 3$$

$$3x + 2y + z = 2$$

Solve for x, y, and z.
   We have

$$x = \frac{\begin{vmatrix} 6 & 2 & 3 \\ 3 & -2 & -1 \\ 2 & 2 & 1 \end{vmatrix}}{\nabla} \tag{E-5}$$

where

$$\nabla = \begin{vmatrix} 1 & 2 & 3 \\ 2 & -2 & -1 \\ 3 & 2 & 1 \end{vmatrix} = 1(-2+2)-2(2+3)+3(4+6)$$

$$= 20$$

The determinant of the numerator of Eq. E-5 is obtained by replacing the column of ∇ formed by the coefficient of the unknown being solved for with

a column made up of the right hand side of the equations. Expanding,

$$x = \frac{6(-2+2)-2(3+2)+3(6+4)}{20} = 1$$

Similarly,

$$y = \frac{\begin{vmatrix} 1 & 6 & 3 \\ 2 & 3 & -1 \\ 3 & 2 & 1 \end{vmatrix}}{20} = -\frac{40}{20} = -2$$

and $z = 3$.

REFERENCE

1. W. L. Hart, *College Algebra and Trigonometry*, D. C. Heath and Co., Boston, 1959.

Appendix F

F-94A and F-15 Longitudinal and Lateral Aerodynamic Data

F-94A Data

$S = 239$ sq ft $c = 6.4$ ft
$b = 37.3$ ft $l_t = 18.5$ ft

Longitudinal Data		No Tanks					With Tip Tanks		
		Landing 1	Cruise 2	Top Speed 3	Cruise 4	Cruise 5	High Speed 6	Cruise 7	Cruise 8
h	(ft)	SL	35,000	SL	12,000	15,000	SL	12,000	15,000
V_T	(mph)	135	450	606	288	403	553	288	403
M		—	0.68	0.797	0.396	0.56	0.727	0.396	0.56
WT	(lb)	12,359	13,614	13,614	13,614	13,614	16,091	16,091	16,091
q	(psf)	46.6	161	940	148	261	781	148	261
I_x	(slug ft²)	7,169	11,029	11,029	11,029	11,029	38,732	38,732	38,732
I_y	(slug ft²)	26,545	26,543	26,543	26,543	26,543	26,723	26,723	26,723
I_z	(slug ft²)	33,009	36,801	36,801	36,801	36,801	64,575	64,575	64,575
J_{xz}	(slug ft²)	−2,557	−660	+335	−790	−200	+450	−770	−150
cg	(% MAC)	25.2	26.1	26.1	26.1	26.1	29	29	29
C_L		1.11	0.354	0.0605	0.385	0.219	0.0858	0.454	0.257
C_{L_α}	(per rad)	5.27	5.27	5.27	5.27	5.27	5.27	5.27	5.27
$C_{L_{\delta_e}}$	(per rad)	0.43	0.43	0.43	0.43	0.43	0.43	0.43	0.43
C_D		0.172	0.023	0.017	0.025	0.018	0.019	0.036	0.021
C_{D_α}	(per rad)	0.854	0.21	0	0.29	0.0644	0	0.337	0.148
$C_{D_{\delta_e}}$	(per rad)	—	—	—	—	—	—	—	—
C_{m_α}	(per rad)	−0.406	−0.44	−0.44	−0.44	−0.44	−0.44	−0.44	−0.44
$C_{m_{\delta_e}}$	(per rad)	−0.88	−0.934	−0.944	−0.934	−0.934	−0.94	−0.94	−0.94
$\frac{c}{2U}C_{m_\alpha}$	(per rad/sec)	−0.069	−0.0213	−0.0159	−0.0324	−0.0232	−0.0173	−0.0324	−0.0232
$\frac{c}{2U}C_{m_q}$	(per rad/sec)	−0.132	−0.041	−0.0305	−0.064	−0.046	−0.033	−0.064	−0.046

F-94A Data

Lateral Data	No Tanks				With Tanks		
	Landing 1	Cruise 2	Top Speed 3	Cruise 4	Cruise 5	High Speed 6	Cruise 7
C_{y_β} (per rad)	−0.86	−0.546	−0.546	−0.546	−0.546	−0.546	−0.546
$C_{y_{\delta_r}}$ (per rad)	0.149	0.149	0.149	0.149	0.149	0.149	0.149
$C_{y_{\delta_a}}$ (per rad)	—	—	—	—	—	—	—
C_{y_p} (per rad)	—	—	—	—	—	—	—
C_{y_r} (per rad)	0.45	0.287	0.287	0.287	0.287	0.291	0.291
C_{l_β} (per rad)	−0.0487	−0.0654	−0.0654	−0.0654	−0.0654	−0.0716	−0.0716
$C_{l_{\delta_a}}$ (per rad)	−0.0916	−0.114	−0.129	−0.114	−0.114	−0.0956	−0.0956
$C_{l_{\delta_r}}$ (per rad)	0.0057	0.0057	0.0057	0.0057	+0.0057	+0.0057	+0.0057
C_{l_r} (per rad)	0.278	0.107	0.043	0.115	0.065	0.0458	0.131
C_{l_p} (per rad)	−0.45	−0.39	−0.39	−0.39	−0.39	−0.39	−0.39
$C_{l_{\delta_a}}$ (per rad/sec)	—	—	—	—	—	—	—
C_{n_β} (per rad)	0.1045	0.115	0.1	0.118	0.106	0.088	0.107
$C_{n_{\delta_a}}$ (per rad)	0.0069	0.0086	0.0057	0.0090	0.0069	0.0057	0.0101
$C_{n_{\delta_r}}$ (per rad)	−0.069	−0.069	−0.069	−0.069	−0.069	−0.069	−0.069
C_{n_p} (per rad)	−0.053	−0.0145	—	−0.016	−0.0077	−0.0007	−0.0197
C_{n_r} (per rad)	−0.210	−0.134	−0.134	−0.134	−0.134	−0.134	−0.134
$C_{n_{\delta_r}}$ (per rad/sec)	−0.053	−0.0145	—	−0.016	−0.0077	−0.0007	−0.0197

F-15 Data (Combat — 50% Fuel Remaining)*

$$S = 608 \text{ sq ft} \qquad c = 15.94 \text{ ft}$$
$$b = 42.8 \text{ ft} \qquad l_t = 20.08 \text{ ft}$$

Longitudinal Data		Flight Condition 1	2	3	4
h	(ft)	20,000	5,000	20,000	40,000
V_T	(fps)	622.14	877.68	829.52	774.8
M		0.6	0.8	0.8	0.8
WT	(lb)	35,900	35,900	35,900	35,900
q	(psf)	245.2	786.9	439.9	176.1
I_x	(slug ft^2)	25,500	25,500	25,500	25,500
I_y	(slug ft^2)	166,600	166,600	166,600	166,600
I_z	(slug ft^2)	187,000	187,000	187,000	187,000
J_{xz}	(slug ft^2)	$-1,000$	$-1,000$	$-1,000$	$-1,000$
cg	(% MAC)	26.1	26.1	26.1	26.1
C_L		0.24	0.075	0.135	0.335
C_{L_α}	(per rad)	4.17	4.17	4.17	4.17
$C_{L_{i_t}}$	(per rad)	0.4	0.36	0.36	0.365
C_D		0.05	0.05	0.05	0.06
C_{D_α}	(per rad)	0.35	0.0	0.21	0.764
$C_{D_{i_t}}$	(per rad)	—	—	—	—
C_{m_α}	(per rad)	-0.29	-0.37	-0.37	-0.37
$C_{m_{i_t}}$	(per rad)	-0.5	-0.45	-0.45	-0.46
$\dfrac{c}{2U}C_{m_{\dot\alpha}}$	(per rad/sec)	0.0	0.0	0.0	0.0
$\dfrac{c}{2U}C_{m_q}$	(per rad/sec)	-0.0512	-0.036	-0.038	-0.0412

F-15 Data*

Lateral Data		Flight Condition 1	2	3	4
C_{y_β}	(per rad)	-0.92	-0.87	-0.87	-0.96
$C_{y_{\delta_r}}$	(per rad)	0.19	0.19	0.2	0.2
$C_{y_{\delta_a}}$	(per rad)	-0.01	-0.006	-0.006	0.0
C_{y_p}	(per rad)	0.14	0.06	0.135	0.11
C_{y_r}	(per rad)	0.3	0.38	0.36	0.3
C_{l_β}	(per rad)	-0.086	-0.057	-0.086	-0.14
$C_{l_{\delta_a}}$	(per rad)	0.048	0.027	0.035	0.045
$C_{l_{\delta_r}}$	(per rad)	0.007	0.004	0.004	0.003
C_{l_r}	(per rad)	0.065	0.03	0.05	0.088
C_{l_p}	(per rad)	-0.27	-0.19	-0.24	-0.27
$C_{l_{\delta_a}}$	(per rad/sec)	—	—	—	—
C_{n_β}	(per rad)	0.17	0.14	0.11	0.14
$C_{n_{\delta_a}}$	(per rad)	0.013	0.0097	0.011	0.012
$C_{n_{\delta_a}}$	(per rad)	-0.092	-0.094	-0.094	-0.093
C_{n_p}	(per rad)	-0.055	-0.02	-0.035	-0.035
C_{n_r}	(per rad)	-0.275	-0.28	-0.29	-0.3
$C_{n_{\delta_r}}$	(per rad/sec)	—	—	—	—

ρ me

Appendix G

Wind Axes

G-1 INTRODUCTION

When performing complete six-degree-of-freedom (6-DOF) simulations of aircraft and/or missiles, using either digital or hybrid computers, the use of wind axes (often called flight path axes) for the solution of the translational equations of motion rather than body axes makes lower demands on computer accuracy and bandwidth.[1]

By definition the wind axes are oriented so that the X wind axis X_W lies along the total velocity vector $\mathbf{V}_T$ of the vehicle. The wind axes are then oriented with respect to the body axes through the angle of attack α and the sideslip angle β as shown in Figure G-1. As shown in the next section, the use of wind axes causes the rate of change of the magnitude of the velocity vector to also lie along the X wind axis, and yields explicit equations for the rates of change of α and β. When body axes are used, the translational equations are solved for the rates of change of the components U, V, and W of the total velocity vector. The integration of these accelerations yields U, V, and W, which are used to calculate α and β using

$$\alpha = \tan^{-1} \frac{W}{U}$$

$$\beta = \tan^{-1} \frac{V}{U} \qquad \text{(G-1)}$$

As can be seen from Figure G-1, the correct equation for β is

$$\beta = \sin^{-1} \frac{V}{V_T}$$

$U = V_T \cos \beta \cos \alpha$
$V = V_T \sin \beta$
$W = V_T \cos \beta \sin \alpha$
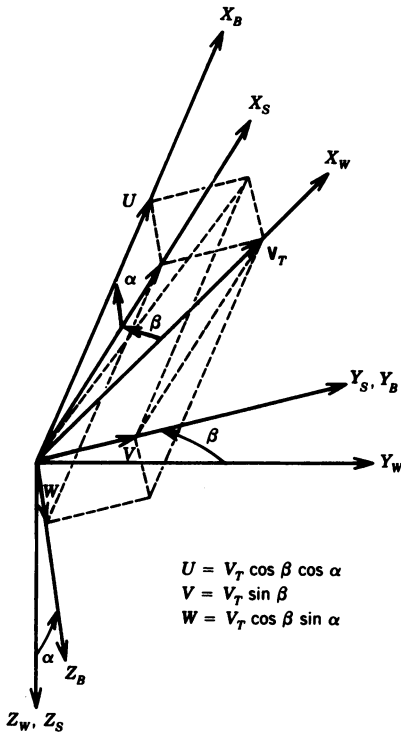
Figure G-1 *Resolution of velocity vector V_T from wind to body axes.*

The equations for $\dot{\alpha}$ and $\dot{\beta}$ are obtained by differentiating Eq. G-1 to yield

$$\dot{\alpha} = \frac{U\dot{W} - W\dot{U}}{U^2 + W^2}$$

$$\dot{\beta} = \frac{U\dot{V} - V\dot{U}}{U^2 + V^2} \tag{G-2}$$

The solution of Eq. G-2 requires both the variables and their derivatives. Thus in a digital simulation the values of the variables would be one integration time step removed from the values of the derivatives. The resulting error would be dependent upon the integration step size.

All of the complexities and inaccuracies resulting from the use of body axes are eliminated by the use of wind axes, which are derived in the next section.

G-2 DERIVATION OF THE WIND AXIS EQUATIONS OF MOTION

The wind axis equations of motion are derived from the body axis equations of motion shown in Eq. 1-33. Dividing Eq. 1-33 by the mass m yields the

body axis accelerations

$$A_{XB} = \dot{U} + WQ - VR$$
$$A_{YB} = \dot{V} + UR - WP$$
$$A_{ZB} = \dot{W} + VP - UQ \tag{G-3}$$

where A_{XB}, A_{YB}, and A_{ZB} are the accelerations resulting from the aerodynamic and gravitational forces acting on the vehicle. From Figure G-1 the body axis components of the total velocity vector are

$$U = V_T \cos \beta \cos \alpha$$
$$V = V_T \sin \beta$$
$$W = V_T \cos \beta \sin \alpha \tag{G-4}$$

Differentiating Eq. G-4 yields

$$\dot{U} = \dot{V}_T \cos \beta \cos \alpha - V_T \dot{\beta} \sin \beta \cos \alpha - V_T \dot{\alpha} \cos \beta \sin \alpha$$
$$\dot{V} = \dot{V}_T \sin \beta + V_T \dot{\beta} \cos \beta$$
$$\dot{W} = \dot{V}_T \cos \beta \sin \alpha - V_T \dot{\beta} \sin \beta \sin \alpha + V_T \dot{\alpha} \cos \beta \cos \alpha \tag{G-5}$$

Substituting Eqs. G-5 and G-4 into Eq. G-3 yields

$$A_{XB} = \dot{V}_T \cos \beta \cos \alpha - V_T \dot{\beta} \sin \beta \cos \alpha - V_T \dot{\alpha} \cos \beta \sin \alpha$$
$$\qquad + V_T Q \cos \beta \sin \alpha - V_T R \sin \beta$$
$$A_{YB} = \dot{V}_T \sin \beta + V_T \dot{\beta} \cos \beta + V_T R \cos \beta \cos \alpha - V_T P \cos \beta \sin \alpha$$
$$A_{ZB} = \dot{V}_T \cos \beta \sin \alpha - V_T \dot{\beta} \sin \beta \sin \alpha + V_T \dot{\alpha} \cos \beta \cos \alpha$$
$$\qquad + V_T P \sin \beta - V_T Q \cos \beta \cos \alpha \tag{G-6}$$

Resolving the body axis accelerations into stability axes as shown in Figure G-2(a) yields

$$A_{XS} = A_{XB} \cos \alpha + A_{ZB} \sin \alpha$$
$$A_{YS} = A_{YB}$$
$$A_{ZS} = - A_{XB} \sin \alpha + A_{ZB} \cos \alpha \tag{G-7}$$

Resolving the stability axis accelerations into wind axes as shown in Figure G-2(b) yields

$$A_{XW} = A_{XS} \cos \beta + A_{YS} \sin \beta$$
$$A_{YW} = - A_{XS} \sin \beta + A_{YS} \cos \beta$$
$$A_{ZW} = A_{ZS} \tag{G-8}$$

Substituting Eq. G-7 into Eq. G-8 yields

$$A_{XW} = (A_{XB}\cos\alpha + A_{ZB}\sin\alpha)\cos\beta + A_{YB}\sin\beta$$
$$A_{YW} = -(A_{XB}\cos\alpha + A_{ZB}\sin\alpha)\sin\beta + A_{YB}\cos\beta$$
$$A_{ZW} = -A_{XB}\sin\alpha + A_{ZB}\cos\alpha \qquad\qquad (G\text{-}9)$$

Substituting Eq. G-6 into Eq. G-9 yields

$$A_{XW} = \dot{V}_T\cos^2\beta\cos^2\alpha - V_T\dot{\beta}\sin\beta\cos\beta\cos^2\alpha$$
$$- V_T\dot{\alpha}\cos^2\beta\sin\alpha\cos\alpha + V_TQ\cos^2\beta\sin\alpha\cos\alpha$$
$$- V_TR\sin\beta\cos\beta\cos\alpha + \dot{V}_T\cos^2\beta\sin^2\alpha$$
$$- V_T\dot{\beta}\sin\beta\cos\beta\sin^2\alpha + V_T\dot{\alpha}\cos^2\beta\sin\alpha\cos\alpha$$
$$+ V_TP\sin\beta\cos\beta\sin\alpha - V_TQ\cos^2\beta\sin\alpha\cos\alpha$$
$$+ \dot{V}_T\sin^2\beta + V_T\dot{\beta}\sin\beta\cos\beta + V_TR\sin\beta\cos\beta\cos\alpha$$
$$- V_TP\sin\beta\cos\beta\sin\alpha = \dot{V}_T \qquad\qquad (G\text{-}10)$$
$$A_{YW} = -\dot{V}_T\sin\beta\cos\beta\cos^2\alpha + V_T\dot{\beta}\sin^2\beta\cos^2\alpha$$
$$+ V_T\dot{\alpha}\sin\beta\cos\beta\sin\alpha\cos\alpha - V_TQ\sin\beta\cos\beta\sin\alpha\cos\alpha$$
$$+ V_TR\sin^2\beta\cos\alpha - \dot{V}_T\sin\beta\cos\beta\sin^2\alpha + V_T\dot{\beta}\sin^2\beta\sin^2\alpha$$
$$- V_T\dot{\alpha}\sin\beta\cos\beta\sin\alpha\cos\alpha - V_TP\sin^2\beta\sin\alpha$$
$$+ V_TQ\sin\beta\cos\beta\sin\alpha\cos\alpha + \dot{V}_T\sin\beta\cos\beta + V_T\dot{\beta}\cos^2\beta$$
$$+ V_TR\cos^2\beta\cos\alpha - V_TP\cos^2\beta\sin\alpha$$
$$= V_T\dot{\beta} + V_T(R\cos\alpha - P\sin\alpha) \qquad\qquad (G\text{-}11)$$
$$A_{ZW} = -\dot{V}_T\cos\beta\sin\alpha\cos\alpha + V_T\dot{\beta}\sin\beta\sin\alpha\cos\alpha$$
$$+ V_T\dot{\alpha}\cos\beta\sin^2\alpha - V_TQ\cos\beta\sin^2\alpha + V_TR\sin\beta\sin\alpha$$
$$+ \dot{V}_T\cos\beta\sin\alpha\cos\alpha - V_T\dot{\beta}\sin\beta\sin\alpha\cos\alpha$$
$$+ V_T\dot{\alpha}\cos\beta\cos^2\alpha + V_TP\sin\beta\cos\alpha - V_TQ\cos\beta\cos^2\alpha$$
$$= V_T\dot{\alpha}\cos\beta - V_TQ\cos\beta + V_T\sin\beta(R\sin\alpha + P\cos\alpha) \qquad (G\text{-}12)$$

Solving Eqs G-10, G-11, and G-12 for $\dot{V}_T$, $\dot{\alpha}$, and $\dot{\beta}$ respectively yields

$$\dot{V}_T = A_{XW}$$
$$\dot{\beta} = \frac{A_{YW}}{V_T} - (R\cos\alpha - P\sin\alpha)$$
$$\dot{\alpha} = \frac{A_{ZW}}{V_T\cos\beta} + Q - (R\sin\alpha + P\cos\alpha)\frac{\sin\beta}{\cos\beta} \qquad\qquad (G\text{-}13)$$

$$A_{XS} = A_{XB} \cos \alpha + A_{ZB} \sin \alpha$$
$$A_{YS} = A_{YB}$$
$$A_{ZS} = -A_{XB} \sin \alpha + A_{ZB} \cos \alpha$$

(a)

$$A_{XW} = A_{XS} \cos \beta + A_{YS} \sin \beta$$
$$A_{YW} = -A_{XS} \sin \beta + A_{YS} \cos \beta$$
$$A_{ZW} = A_{ZS}$$
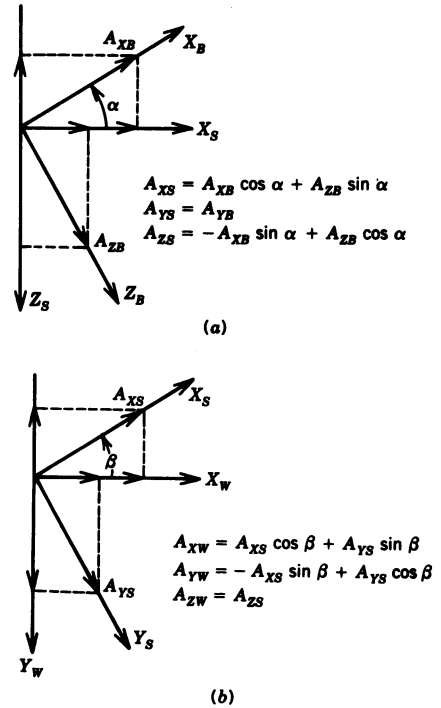
Figure G-2 *(a) Resolution of body axis accelerations to stability axes. (b) Resolution of stability axis accelerations to wind axes.*

(b)

But from Figure G-3

$$R_S = R \cos \alpha - P \sin \alpha$$

$$P_S = R \sin \alpha + P \cos \alpha \qquad\qquad (\text{G-14})$$

Substituting Eq. G-14 into Eq. G-13 yields

$$\dot{V}_T = A_{XW}$$

$$\dot{\beta} = \frac{A_{YW}}{V_T} - R_S$$

$$\dot{\alpha} = \frac{A_{ZW}}{V_T \cos \beta} + Q - P_S \frac{\sin \beta}{\cos \beta} \qquad\qquad (\text{G-15})$$

which are the wind axis equations of motion. The wind axis accelerations in

$P_S = P \cos \alpha + R \sin \alpha$
$R_S = -P \sin \alpha + R \cos \alpha$
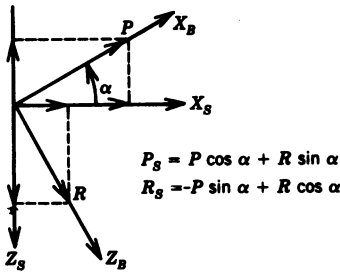
Figure G-3   Stability axis roll and yaw rates.

Eq. G-15 are given by Eq. G-8, where the stability axis accelerations are

$$A_{XS} = \left(\frac{T}{m} + g_x\right)\cos \alpha + g_z \sin \alpha - \frac{qSC_D}{m}$$

$$A_{YS} = g_y + \frac{qSC_Y}{m}$$

$$A_{ZS} = -\left(\frac{T}{m} + g_x\right)\sin \alpha + g_z \cos \alpha - \frac{qSC_L}{m} \qquad (G-16)$$

where

> T is the engine thrust in pounds, assumed to be along X_B,
>
> C_D, C_Y, and C_L are the total drag, side force, and lift coefficients respectively as shown in block 3 of Figure G-4, and
>
> g_x, g_y, and g_z are the components of gravity from Eq. 1-35.

Examination of the $\dot{\alpha}$ equation of Eq. G-15 for $\beta = 0$ shows that $\dot{\alpha} - Q = A_{ZW}/V_T = A_{ZS}/V_T$ as shown in Eq. 2-2.
   A block diagram adapted from Ref. 1 of a complete 6-DOF simulation using wind axes is shown in Figure G-4.

G-3   DEVELOPMENT OF $\dot{\beta}$ EQUATION

As mentioned in Section 4-3, $\dot{\beta}$ cannot be measured directly and the differentiation of the measured value of β would be impractical. Thus an equation to evaluate $\dot{\beta}$ from measurable quantities is required. Starting with the $\dot{\beta}$ equation from Eq. G-13 which is

$$\dot{\beta} = \frac{A_{YW}}{V_T} - (R \cos \alpha - P \sin \alpha) \qquad (G-17)$$

1. Resolution of accel. body to stability axes

2. Resolution of accel. stability to wind axes

$A_{XS} = (T/m + g_x) \cos \alpha + g_z \sin \alpha - qSC_D/m$
$A_{YS} = g_y + qSC_Y/m$
$A_{ZS} = -(T/m + g_x) \sin \alpha + g_z \cos \alpha - qSC_L/m$

T/m

A_{XS}
A_{YS}
A_{ZS}

$A_{XW} = A_{XS} \cos \beta + A_{YS} \sin \beta$
$A_{YW} = -A_{XS} \sin \beta + A_{YS} \cos \beta$
$A_{ZW} = A_{ZS}$

A_{XW}
A_{YW}
A_{ZW}

Stability axis accel.

Wind axis accel.

C_L C_Y C_D q α

β

4. Resolution of moments from stability to body axis

P_s, R_s, Q_s

α, β

h

V_T

$\delta_e, \delta_a, \delta_r$

$C_L = C_{L_0} + C_{L_\alpha}\alpha + (c/2V_T)C_{L_q}Q + C_{L_{\delta_e}}\delta_e$

$C_Y = (b/2V_T)(C_{y_p}P_s + C_{y_r}R_s) + C_{y_\beta}\beta + C_{y_{\delta_a}}\delta_a + C_{y_{\delta_r}}\delta_r$

$C_D = C_{D_0} + KC_L^2$

$c_l = (b/2V_T)(C_{l_p}P_s + C_{l_r}R_s) + C_{l_\beta}\beta + C_{l_{\delta_a}}\delta_a + C_{l_{\delta_r}}\delta_r$

$C_m = C_{m_0} + C_{m_\alpha}\alpha + (c/2V_T)C_{m_q}Q_s + C_{m_{\delta_e}}\delta_e$

$C_n = (b/2V_T)(C_{n_r}R_s + C_{n_p}P_s) + C_{n_\beta}\beta + C_{n_{\delta_a}}\delta_a + C_{n_{\delta_r}}\delta_r$

$q = (\rho/2)V_T^2, M = V_T/V_S$

C_l
C_m
C_n

q

$\mathscr{L} = Sqb(C_l\cos \alpha - C_n\sin \alpha)$

$\mathscr{M} = SqcC_m$

$\mathscr{N} = Sqb(C_l\sin \alpha + C_n \cos \alpha)$

3. Computation of aerodynamic force and moment coefficients

α

$\mathscr{L}$ $\mathscr{M}$ $\mathscr{N}$ Body axis moments

Body axis angular rates

5. Translational equations of motion

A_{XW}
A_{YW}
A_{ZW}

$\dot{V}_T = A_{XW}$

$\dot{\alpha} = Q_s - \dfrac{P_s \sin \beta}{\cos \beta} + \dfrac{A_{ZW}}{V_T\cos \beta}$

$\dot{\beta} = A_{YW}/V_T - R_s$

V_T
α
β

$\dot{P} = \dfrac{(I_y - I_z)}{I_x} QR + \dfrac{\mathscr{L}}{I_x}$

$\dot{Q} = \dfrac{(I_z - I_x)}{I_y} RP + \dfrac{\mathscr{M}}{I_y}$

$\dot{R} = \dfrac{(I_x - I_y)}{I_z} PQ + \dfrac{\mathscr{N}}{I_z}$

P
Q
R

6. Rotational equations of motion

P_s R_s Q_s Stability axis angular rates

R Q P

P
Q
R

$P_s = P \cos \alpha + R \sin \alpha$
$Q_s = Q$
$R_s = R \cos \alpha - P \sin \alpha$

α

$\dot{\Psi} = (R \cos \Phi + Q \sin \Phi)/\cos \Theta$
$\dot{\Theta} = Q \cos \Phi - R \sin \Phi$
$\dot{\Phi} = P + \dot{\Psi} \sin \Theta$

Ψ
Θ
Φ

7. Resolution of angular rates from body to stability axis

8. Computation of Euler angle rates

Euler angles

Figure G-4 *Block diagram of wind and body axis systems for 6-DOF simulation.*[1]

Substituting for A_{YW} from Eq. G-8 yields

$$\dot{\beta} = \frac{-A_{XS}\sin \beta + A_{YS}\cos \beta}{V_T} - (R \cos \alpha - P \sin \alpha) \qquad \text{(G-18)}$$

As β will be small, the $\sin \beta$ term can be neglected. Letting $\cos \beta \approx 1$ and substituting for A_{YS} from Eq. G-16 and for g_y from Eq. 1-35 yields

$$\dot{\beta} = \frac{g}{V_T}\cos \Theta \sin \Phi + \frac{qSC_Y}{mV_T} - (R \cos \alpha - P \sin \alpha) \qquad \text{(G-19)}$$

From Eq. 4-4, $a_{(lat)} = (Sq/m)C_{y_\beta}\beta$ ft/sec^2 with β in radians. But for a coordinated turn $C_Y \simeq C_{y_\beta}\beta$; then substituting into Eq. G-19 yields

$$\dot{\beta} = \frac{g}{V_T}\cos\Theta\sin\Phi + \frac{a_{(lat)}}{V_T} - (R\cos\alpha - P\sin\alpha)\ \text{rad/sec} \quad \text{(G-20)}$$

If Eq. G-20 is multiplied by 57.3°/rad and we note that 57.3°/rad times an angle or angular rate in rad or rad/sec yields the same angle or angular rate in deg or deg/sec, then Eq. G-20 becomes

$$\dot{\beta} = 57.3\frac{a_{(lat)} + g\cos\Theta\sin\Phi}{V_T} - (R\cos\alpha - P\sin\alpha)\ \text{deg/sec} \quad \text{(G-21)}$$

which is the required equation.

REFERENCE

1. G. A. Bekey and W. J. Karplus, *Hybrid Computation*, John Wiley and Sons, New York, 1968.

Appendix H

Digital Simulation of Transfer Functions

H-1 INTRODUCTION

There are numerous ways to simulate or model transfer functions in a digital simulation. Two of the more common techniques are the Tustin method, which utilizes the z transform, and the state variable method. The Tustin method uses a difference equation to represent a particular transfer function and perform the integration. The coefficients of the terms of the difference equation for the Tustin method are a function of the integration step size or update time increment Δt; thus the coefficients must be calculated in the setup portion of the simulation to allow for changing Δt during the simulation development. In addition the difference equation for a second-order transfer function requires the previous value of the derivative as well as the second previous derivative (the derivative $2 \Delta t$ old), and the previous value of the output. The state variable method, which generates first-order derivatives, presents a more straightforward approach to the digital simulation of transfer functions and will be discussed here. Two integration techniques will also be presented.

H-2 STATE VARIABLE METHOD

A transfer function of any order can be reduced to a product of first- and second-order transfer functions. The state variable method can then be applied to each of the individual transfer functions in turn. The method will initially be applied to the first-order transfer function shown in Figure H-1.
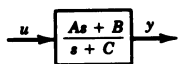
Figure H-1 General first-order transfer function.
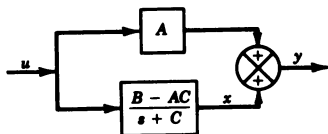
Figure H-2 Equivalent block diagram for a first-order transfer function.

Dividing the numerator by the denominator, the transfer function in Figure H-1 becomes

$$\frac{y}{u} = A + \frac{B - AC}{s + C} \tag{H-1}$$

Using Eq. H-1, the block diagram shown in Figure H-1 can be redrawn as shown in Figure H-2. From Figure H-2 the output y is

$$y = Au + x \tag{H-2}$$

with

$$x = \frac{B - AC}{s + C} u \tag{H-3}$$

Multiplying Eq. H-3 through by $s + C$, replacing sx by $\dot{x}$, and solving for $\dot{x}$ yields

$$\dot{x} = -Cx + (B - AC)u \tag{H-4}$$

From Eq. H-2

$$y = x + Au \tag{H-5}$$

By setting the appropriate coefficient (A, B, and/or C) to zero, Eqs. H-4 and H-5 can be used to model any first-order transfer function. As an example, for a pure integration, A and C would be equal to zero, Eq. H-4 would reduce to $\dot{x} = Bu$, and Eq. H-5 would become $y = x$.

The general form for a second-order transfer function is shown in Figure H-3. Dividing the numerator by the denominator, the transfer function in
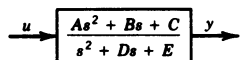
Figure H-3 General second-order transfer function.
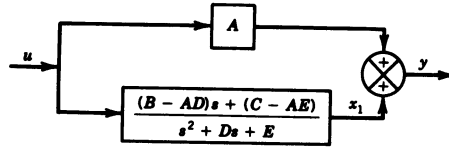
Figure H-4 *Equivalent block diagram for a second-order transfer function.*

Figure H-3 becomes

$$\frac{y}{u} = A + \frac{(B - AD)s + (C - AE)}{s^2 + Ds + E} \tag{H-6}$$

Using Eq. H-6, the block diagram shown in Figure H-3 can be redrawn as shown in Figure H-4. From Figure H-4 the output y is

$$y = Au + x_1 \tag{H-7}$$

and

$$\frac{x_1}{u} = \frac{(B - AD)s + (C - AE)}{s^2 + Ds + E} = \frac{Gs + H}{s^2 + Ds + E} \tag{H-8}$$

where

$$G = B - AD$$
$$H = C - AE$$

Multiplying Eq. H-8 through by $s^2 + Ds + E$ and solving for $\ddot{x}_1$ yields

$$\ddot{x}_1 = -Ex_1 - D\dot{x}_1 + G\dot{u} + Hu \tag{H-9}$$

In order to eliminate the $\dot{u}$ term in Eq. H-9, GDu is added and subtracted from the right hand side of the equation, which yields

$$\ddot{x}_1 = -Ex_1 - D(\dot{x}_1 - Gu) + (H - GD)u + G\dot{u} \tag{H-10}$$

Let

$$\dot{x}_1 = x_2 + Gu \tag{H-11}$$

Differentiating,

$$\ddot{x}_1 = \dot{x}_2 + G\dot{u} \tag{H-12}$$

Substituting Eq. H-12 into Eq. H-10, solving for $\dot{x}_2$, and simplifying yields

$$\dot{x}_2 = -Ex_1 - Dx_2 + (H - GD)u \tag{H-13}$$

Substituting for G and H in Eqs. H-13 and H-11 and adding Eq. H-7 yields the state variable equations for second-order transfer functions:

$$y = x_1 + Au$$

$$\dot{x}_1 = x_2 + (B - AD)u$$

$$\dot{x}_2 = -Ex_1 - Dx_2 + (C - AE - BD + AD^2)u \qquad \text{(H-14)}$$

Like the state equations for first-order transfer functions, Eq. H-14 can be used for any second-order transfer function by setting the appropriate numerator coefficients to zero. For the denominator to be second-order, the only coefficient that can be zero is D, which would result in an undamped second-order transfer function.

H-3   NUMERICAL INTEGRATION

In the digital simulation the derivatives associated with the equations of motion and those from the state variable equations representing the various system transfer functions must be integrated. The two methods presented here are trapezoidal integration and the Runge–Kutta method of order 4. Trapezoidal integration is performed using

$$x_{n+1} = x_n + \Delta t \, \frac{\dot{x}_n + \dot{x}_{n-1}}{2} \qquad \text{(H-15)}$$

where

x_n and $\dot{x}_n$ are the current values of the variable and its derivative,
$\dot{x}_{n-1}$ is the previous value of the derivative, and
x_{n+1} is the new value of the variable.

After all the integrations are performed, the old values of the derivatives must be saved before starting through the run loop again. All the integrations should be performed at the beginning or the end of the run loop, just before the run time is updated by Δt.

The recursion formula for the Runge–Kutta method of order 4 from Ref. 1 is given by

$$x_{n+1} = x_n + \frac{k_1 + 2k_2 + 2k_3 + k_4}{6} \qquad \text{(H-16)}$$

where

$$k_1 = \Delta t \dot{x}_n$$

$$k_2 = \Delta t f\left(t_n + \frac{\Delta t}{2}, y_n + \frac{k_1}{2}\right)$$

$$k_3 = \Delta t f\left(t_n + \frac{\Delta t}{2}, y_n + \frac{k_2}{2}\right)$$

$$k_4 = \Delta t f(t_n + \Delta t, y_n + k_3)$$

where $f(t, y)$ is the value of the derivative of y_n at the time and value of y_n indicated. Although the fourth-order Runge-Kutta is widely used in practice, the four calculations of each derivative may require excessive computer time. For the digital missile simulation used to obtain the results presented in Chapter 8, trapezoidal integration was used with $\Delta t = 0.0025$ sec. Both of the integration methods discussed here are subject to numerical instability if Δt is too large.

REFERENCE

1. S. D. Conte and Carl de Boor, *Elementary Numerical Analysis: An Algorithm Approach*, 2nd ed., McGraw-Hill Book Co., New York, 1972.

Appendix I

Fire Control Problem

I-1 INTRODUCTION

The basic fire control problem[1] is to direct the velocity vector of an unguided projectile, in this case a bullet, at the time of launch t_0 so the projectile and the target arrive at the same point in space at the same time t_f, thus scoring a hit. The fire control problem is similar for all projectiles in that during its time of flight (from t_0 to t_f), the projectile is in free flight under the influence of inertia and the forces generated on the projectile by its motion through the air plus the force of gravity.

The geometry of the fire control problem is shown in Figure I-1 along with the components of the prediction angle λ.

Referring to Figure I-1, the initial position of the attacking aircraft (to be referred to as the attacker) is denoted by WS_0. The velocity of the attacker relative to a coordinate system fixed to the air mass is V_A. The direction from WS_0 to the target at the time of firing t_0 is LS_0, the initial line of sight (LOS). The lead angle L is the angle between LS_0 and the final line of sight LS_f. The lead angle compensates for target motion during the time of flight of the projectile. The final position of the target is a function of the velocity and acceleration vectors of the target relative to the air mass coordinate system during the time of flight of the projectile. The angular velocity of the line of sight, ω_{LS}, is the instantaneous angular velocity of a line from the attacker to the target aircraft. The muzzle velocity of the round just before leaving the bore of the gun is V_M. Due to the angle of attack of the aircraft, the projectile will have an angle of attack with respect to the relative wind as the bullet leaves the muzzle of the gun. The resultant aerodynamic forces acting on the spinning projectile result in what is referred to as windage jump
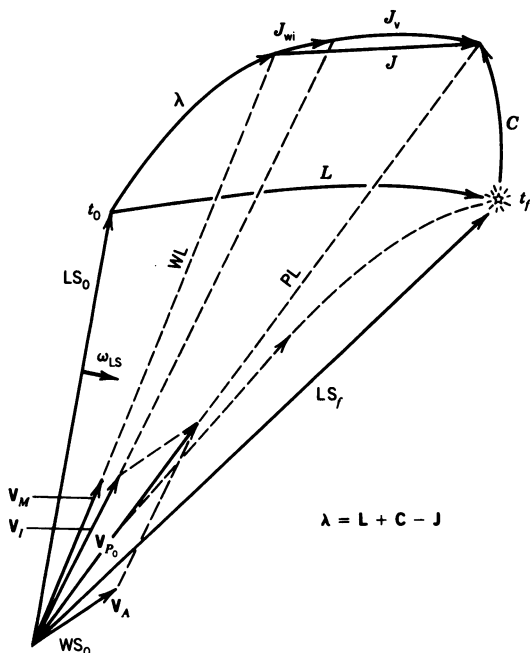
Figure I-1 *Components of the prediction angle.*[1]

J_{wi} (normally small). The effect of windage jump produces V_I, the initial velocity of the projectile with respect to the attacker. The initial velocity of the projectile with respect to air mass space is $V_{P_0} = V_I + V_A$. The angle between V_I and V_{P_0} is the velocity jump angle J_v. The total jump angle J is $J = J_{wi} + J_v$. (The treating of small angles as vectors will be discussed later in this section.) The direction of V_{P_0} is referred to as the projectile line PL. The aerodynamic and gravitational forces acting on the projectile, during the time of flight, curve the trajectory of the projectile and cause a deviation between the projectile line and the future line of sight. The correction to compensate for this curvature is the curvature correction C. Thus the prediction angle λ, which is the angle between LS_0 and the WL, is

$$\lambda = L + C - J \qquad \text{(I-1)}$$

In Eq. I-1 the components of the prediction angle have been considered vectors, where a vector angle such as L is defined as[1]

$$L \equiv 1_{(LS)_0} \times 1_{(LS)_f} \frac{L}{\sin L}$$
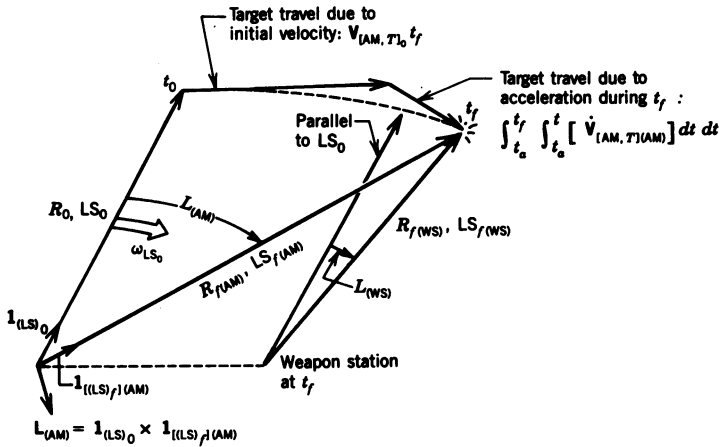
Figure I-2 Geometry of the lead angle — air mass and weapon station space.[1]

which for small angles becomes

$$L \simeq 1_{(LS)_0} \times 1_{(LS)_f} \tag{I-2}$$

Rigorously an angle cannot be treated as a vector, as the sum of finite angles is not commutative. However, for small angles up to 10°, the error is less than 1%. In the fire control problem the angles involved are normally less than 5°.

I-2   LEAD ANGLE

The lead angle, sometimes referred to as kinematic lead, compensates for target motion during the time of flight. The target motion can be broken up into two components: (1) the motion due to the target's initial velocity, and (2) the motion due to target accelerations (changes in the magnitude or direction of the velocity vector) during the time of flight. The general geometry in air mass and weapon station space is illustrated in Figure I-2. Note that although LS_0 is the same in both spaces, the direction of LS_f is dependent upon the reference space used. An important parameter in the computation of the lead angle is the angular velocity of the line of sight ω_{LS}, which is one measure of the relative motion of the two aircraft (the other is the range rate). The generation of ω_{LS} is shown in Figure I-3 in two dimensions for clarity, where $V_{[AM, T]_0}$ is the initial velocity of the target with respect to the air mass and $V_{[AM, WS]_0}$ is the initial velocity of the weapon station (attacker) with respect to the air mass. Both of these velocity vectors can be resolved into components perpendicular and parallel to R_0. The perpendicular components generate ω_{LS}, while the parallel components yield
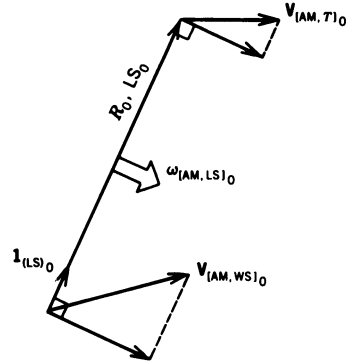
Figure I-3 *Generation of the angular velocity of the line of sight.*

the range rate. Only the perpendicular components are shown in Figure I-3. In air mass space, using the cross product, ω_{LS} is

$$\omega_{[AM,LS]_0} = \frac{\mathbf{1}_{(LS)_0} \times \mathbf{V}_{[AM,T]_0}}{R_0} - \frac{\mathbf{1}_{(LS)_0} \times \mathbf{V}_{[AM,WS]_0}}{R_0} \qquad (I\text{-}3)$$

From Figure I-3 it can be seen that the target motion is tending to rotate the LOS clockwise while the weapon station is tending to rotate it counterclockwise. As shown in Figure I-3, ω_{LS} will be counterclockwise. Equation I-3 can be written as

$$\omega_{[AM,LS]_0} = \left[\omega_{[AM,LS]_0}\right]_T - \left[\omega_{[AM,LS]_0}\right]_{WS} \qquad (I\text{-}4)$$

where

$\left[\omega_{[AM,LS]_0}\right]_T = \mathbf{1}_{(LS)_0} \times \mathbf{V}_{[AM,T]_0}/R_0$ is ω_{LS} due to target motion, and
$\left[\omega_{[AM,LS]_0}\right]_{WS} = \mathbf{1}_{(LS)_0} \times \mathbf{V}_{[AM,WS]_0}/R_0$ is ω_{LS} due to weapon station motion.

From Figure I-2 the lead angle in air mass space is

$$\mathbf{L}_{(AM)} = \mathbf{1}_{(LS)_0} \times \mathbf{1}_{[(LS)_f](AM)} \qquad (I\text{-}5)$$

The future LOS in air mass space is

$$\mathbf{1}_{[(LS)_f](AM)} = \frac{\mathbf{R}_{f(AM)}}{R_{f(AM)}} \qquad (I\text{-}6)$$

where $R_{f(AM)}$ is the future range, which from Figure I-2 is

$$\mathbf{R}_{f(AM)} = \mathbf{R}_0 + \mathbf{V}_{[AM,T]_0} t_f + \int_{t_a}^{t_f} \int_{t_a}^{t} \left[\dot{\mathbf{V}}_{[AM,T](AM)} \right] dt\, dt \qquad (I-7)$$

where

$\quad$ t_a is the time that the target acceleration starts,
$\quad$ t is the time the acceleration stops,

and $t_a \geq t_0$ and $t \leq t_f$. The magnitude of the future range is a function of the average projectile velocity $V_{[AM,P](avg)}$ and t_f:

$$R_{f(AM)} = V_{[AM,P](avg)} t_f \qquad (I-8)$$

Substituting Eqs. I-7 and I-8 into Eq. I-6 and the results into Eq. I-5 yields

$$\mathbf{L}_{(AM)} = \frac{\mathbf{1}_{(LS)_0} \times \mathbf{V}_{[AM,T]_0}}{V_{[AM,P](avg)}} + \frac{\mathbf{1}_{(LS)_0} \times \left[\int_{t_a}^{t_f} \int_{t_a}^{t} \dot{\mathbf{V}}_{[AM,T](AM)}\, dt\, dt \right]}{V_{[AM,P](avg)} t_f} \qquad (I-9)$$

$\quad$ As will be shown later, the first term of Eq. I-9 is a function of $\omega_{(LS)}$; however, there is no way to measure the target acceleration required for the second term. Captain Kendrick, in his research,[2] developed an interactive filter system that provides an improved estimate of target motion states by conditioning kinematic filter estimates of target aspect angle data, thus providing an estimate of target velocity and acceleration at the time of firing of the projectile. If the target acceleration is assumed constant during the time of flight of the projectile, then an approximation to the second term of Eq. I-9 can be made. With this research in mind, it was decided to include the target acceleration term in the future range and time-of-flight equations.

$\quad$ Returning to Eq. I-9, the first term is the angular velocity of the LOS due to target motion as shown in Eq. I-4. Then Eq. I-9 can be written as

$$\mathbf{L}_{(AM)} = \frac{R_0 [\omega_{[AM,LS]_0}]_T}{V_{[AM,P](avg)}} + \text{T.A.T.} \qquad (I-10)$$

where T.A.T. represents the second term of Eq. I-9 (target acceleration term). Solving Eq. I-4 for $[\omega_{[AM,LS]_0}]_T$ yields

$$[\omega_{[AM,LS]_0}]_T = \omega_{[AM,LS]_0} + [\omega_{[AM,LS]_0}]_{WS} \qquad (I-11)$$

Eq. I-11 could be substituted into Eq. I-10; however, as the final fire control equations will be written in weapon station space, Eq. I-10 will be first

expressed in weapon station space:

$$L_{(WS)} = \frac{R_0[\omega_{[WS,LS]_0}]_T}{V_{[WS,P](avg)}} + T.A.T. \tag{I-12}$$

Substituting weapon space for air mass space in Eq. I-11 yields

$$[\omega_{[WS,LS]_0}]_T = \omega_{[WS,LS]_0} \tag{I-13}$$

as $[\omega_{[WS,LS]_0}]_{WS} = 0$. Substituting Eq. I-13 into Eq. I-12 yields

$$L_{(WS)} = \frac{R_0[\omega_{[WS,LS]_0}]}{V_{[WS,P](avg)}} + T.A.T. \tag{I-14}$$

I-3   CURVATURE CORRECTION

The curvature correction compensates for two factors, namely:

1. The curvature of the flight path of the projectile due to the force of gravity acting on the projectile, called superelevation.
2. The curvature due to the drift of the projectile caused by the interaction between the torque produced by the rotating aerodynamic lift vector (acting at the center of pressure of the projectile), the spin angular momentum vector, and gravity (acting at the center of gravity of the projectile).

From Figure I-4 the curvature correction is the angle from the future LOS to the projectile line; thus

$$C_{(WS)} = 1_{[(LS)_f](WS)} \times 1_{(PL)(WS)} \tag{I-15}$$

where

$1_{(PL)(WS)} = V_{[WS,P]_0}/V_{[WS,P]_0}$ is a unit vector along the projectile line at the time of firing, and

$V_{[WS,P]_0}$ is the initial velocity of the projectile in weapon station space.

The future range vector is

$$R_{f(WS)} = V_{[WS,P]_0}t_f + \int_0^{t_f}\int_0^{t_f}\dot{V}_{[WS,P](WS)}\,dt\,dt \tag{I-16}$$

Figure I-4 *Geometry of curvature correction — weapon station space.*[1]

where $\dot{V}_{[WS, P](WS)}$ is the acceleration of the projectile in weapon station space, to be discussed later.

The future range can also be expressed as

$$\mathbf{R}_{f(WS)} = \mathbf{1}_{[(LS)_f](WS)} R_{f(WS)} \tag{I-17}$$

Substituting for $R_{f(WS)}$ from Eq. I-8 using weapon station space yields

$$\mathbf{R}_{f(WS)} = \mathbf{1}_{[(LS)_f](WS)} V_{[WS, P](avg)} t_f \tag{I-18}$$

Solving Eq. I-18 for $\mathbf{1}_{[(LS)_f](WS)}$ and substituting into Eq. I-15 yields

$$\mathbf{C}_{(WS)} = \frac{\mathbf{R}_{f(WS)} \times \mathbf{1}_{(PL)(WS)}}{V_{[WS, P](avg)} t_f} \tag{I-19}$$

Substituting Eq. I-16 into Eq. I-19 yields

$$\mathbf{C}_{(WS)} = \frac{\left[\int_0^{t_f} \int_0^{t_f} \dot{V}_{[WS, P](WS)} \, dt \, dt \right] \times \mathbf{1}_{(PL)(WS)}}{V_{[WS, P](avg)} t_f} \tag{I-20}$$

as $V_{[WS, P]_0} \times \mathbf{1}_{(PL)(WS)} = 0$. Now $\dot{V}_{[WS, P](WS)}$ is the acceleration of the projectile as a result of the gravitational and aerodynamic forces acting on the projectile.

Since the acceleration is with respect to weapon station space and since Newton's second law is valid only in inertial space, the theorem of Coriolis must be applied. From the developments in Refs. 1 and 3, considering the short times of flight, the projectile acceleration relative to weapon station space reduces to

$$\left[\ddot{\mathbf{R}}_{(WS,P)}\right]_{(WS)} = \dot{\mathbf{V}}_{[WS,P](WS)} = \frac{\mathbf{F}_a}{m_p} + \mathbf{g} \tag{I-21}$$

where

$\mathbf{F}_a$ represents the aerodynamic forces acting on the projectile, and m_p is the mass of the projectile.

Substituting Eq. I-21 into Eq. I-20 yields

$$\mathbf{C}_{(WS)} = \frac{\left[\int_0^{t_f}\int_0^{t_f}\left(\frac{\mathbf{F}_a}{m_p}+\mathbf{g}\right)dt\,dt\right]\times\mathbf{1}_{(PL)(WS)}}{V_{[WS,P](avg)}t_f} \tag{I-22}$$

The aerodynamic force decreases the projectile's velocity as a result of the drag, and causes the projectile to drift as a result of the lift as discussed at the beginning of this section. The magnitude of the drag force per unit mass is

$$\frac{F_D}{m_p} = \frac{C_D S}{m_p}\frac{\rho}{2}V_{[AM,P]}^2 \tag{I-23}$$

where

C_D is an empirically derived drag coefficient, and
S is the characteristic area (probably the cross-sectional area) of the projectile.

Define

$$k_D \equiv \frac{C_D S}{m_p}\frac{\rho}{2}\ 1/\text{ft} \tag{I-24}$$

But

$$\mathbf{V}_{[AM,P]} = \mathbf{V}_{[WS,P]} + \mathbf{V}_{[AM,WS]} \tag{I-25}$$

Putting Eq. I-23 into vector form and substituting Eq. I-25 yields

$$\frac{\mathbf{F}_D}{m_p} = -k_D V_{[\text{AM},P]}(\mathbf{V}_{[\text{WS},P]} + \mathbf{V}_{[\text{AM},\text{WS}]}) \qquad (\text{I-26})$$

The drift force is[1]

$$\frac{\mathbf{F}_{\text{DR}}}{m_p} = k_{\text{DR}} g \times \mathbf{1}_{(\text{PL})(\text{WS})} \qquad (\text{I-27})$$

As the aerodynamic force acting on the projectile is the sum of the drag and lift forces, then from Eqs. I-26 and I-27

$$\frac{\mathbf{F}_a}{m_p} = -k_D V_{[\text{AM},P]}[\mathbf{V}_{[\text{WS},P]} + \mathbf{V}_{[\text{AM},\text{WS}]}] + k_{\text{DR}} g \times \mathbf{1}_{(\text{PL})(\text{WS})} \qquad (\text{I-28})$$

The double integral in Eq. I-22 involves line integrals, with the direction of the vectors generally changing over the time interval of integration. If average values are used and g is assumed constant over the path of the projectile, then

$$\int_0^{t_f} \int_0^{t_f} \left(\frac{\mathbf{F}_a}{m_p} + \mathbf{g} \right) dt\, dt$$

$$= \tfrac{1}{2} \left[-k_D V_{[\text{AM},P](\text{avg})}(\mathbf{V}_{[\text{WS},P](\text{avg})} + \mathbf{V}_{[\text{AM},\text{WS}](\text{avg})}) + k_{\text{DR}} g \times \mathbf{1}_{(\text{PL})(\text{WS})} + \mathbf{g} \right] t_f^2$$
$$(\text{I-29})$$

Substituting Eq. I-29 into Eq. I-22 yields

$$\mathbf{C}_{(\text{WS})} = \frac{t_f}{2V_{[\text{WS},P](\text{avg})}}$$

$$\times \left\{ -k_D V_{[\text{AM},P](\text{avg})} \left[\mathbf{V}_{[\text{WS},P](\text{avg})} + \mathbf{V}_{[\text{AM},\text{WS}](\text{avg})} \right] \times \mathbf{1}_{(\text{PL})(\text{WS})} \right.$$

$$\left. + \left[k_{\text{DR}} g \times \mathbf{1}_{(\text{PL})(\text{WS})} \right] \times \mathbf{1}_{(\text{PL})(\text{WS})} + \mathbf{g} \times \mathbf{1}_{(\text{PL})(\text{WS})} \right\} \quad (\text{I-30})$$

Now

$$\mathbf{1}_{[(\text{LS})_f](\text{WS})} = \mathbf{R}_{f(\text{WS})} / R_{f(\text{WS})}$$

and

$$\mathbf{R}_{f(\text{WS})} = \mathbf{V}_{[\text{WS},P](\text{avg})} t_f$$

Then

$$1_{[(LS)_f](WS)} = \frac{V_{[WS,P](avg)}}{V_{[WS,P](avg)}} \tag{I-31}$$

Using Eq. I-31, the term $V_{[WS,P](avg)} \times 1_{(PL)(WS)}$ from Eq. I-30 can be written as

$$V_{[WS,P](avg)} \times 1_{(PL)(WS)} = \left[1_{[(LS)_f](WS)} \times 1_{(PL)(WS)}\right] V_{[WS,P](avg)} \tag{I-32}$$

But from Eq. I-15, $C_{(WS)} = 1_{[(LS)_f](WS)} \times 1_{(PL)(WS)}$; then from Eq. I-32

$$V_{[WS,P](avg)} \times 1_{(PL)(WS)} = C_{(WS)} V_{[WS,P](avg)}$$

Substituting this into Eq. I-30 and transposing to the left hand side yields

$$\left(1 + \frac{k_D}{2} V_{[AM,P](avg)} t_f\right) C_{(WS)}$$

$$= \frac{t_f}{2V_{[WS,P](avg)}} \Big[g \times 1_{(PL)(WS)} - k_D V_{[AM,P](avg)} V_{[AM,WS](avg)} \times 1_{(PL)(WS)}$$

$$+ \left(k_{DR} g \times 1_{(PL)(WS)}\right) \times 1_{(PL)(WS)} \Big] \tag{I-33}$$

Divide Eq. I-33 by $1 + (k_D/2)V_{[AM,P](avg)} t_f$, and define

$$k_{(sup)} \equiv \frac{1}{1 + (k_D/2)V_{[AM,P](avg)} t_f}$$

$$k_{(wi)} \equiv \frac{k_D V_{[AM,P](avg)}}{1 + (k_D/2)V_{[AM,P](avg)} t_f}$$

Then Eq. I-33 becomes

$$C_{(WS)} = \frac{t_f}{2V_{[WS,P](avg)}}$$

$$\times \Big[k_{(sup)} g \times 1_{(PL)(WS)} - k_{(wi)} V_{[AM,WS](avg)} \times 1_{(PL)(WS)}$$

$$+ k_{(sup)} k_{DR} \left[g \times 1_{(PL)(WS)}\right] \times 1_{(PL)(WS)} \Big] \tag{I-34}$$

Figure I-5 *Geometry of jump correction — air mass and weapon station space.*[1]

I-4 JUMP CORRECTION

The jump correction, as illustrated in Figure I-5, is made up of two components, namely:

    1. The windage jump correction $J_{(wi)WS}$, which compensates for the misalignment of the gun bore with the relative wind, as a result of the angles of attack and/or sideslip of the weapon station.

    2. The velocity jump correction $J_{(v)WS}$, which compensates for the difference in direction between the initial velocity of the projectile with respect to the reference space and with respect to weapon station space, as a result of the velocity of the weapon station with respect to the reference space. In this case the weapon station space is the reference space; thus the velocity jump correction is zero.

    As stated in Ref. 1, the windage jump correction is normally neglected in forward-firing air-to-air fire control; thus the derivation of the windage jump correction, although presented in Ref. 3, will not be covered here.

I-5 PREDICTION ANGLE

The final prediction angle for forward-firing air-to-air fire control can be obtained by adding Eqs. I-14 and I-34 and including the T.A.T. from Eq. I-9

after replacing air mass space with weapon station space, which yields

$$\lambda = \frac{R_0\omega_{[\text{WS, LS}]_0}}{V_{[\text{WS, }P]\text{(avg)}}} + \frac{1_{(\text{LS})_0}\times\left[\int_{t_a}^{t_f}\int_{t_a}^{t}\left[\dot{V}_{[\text{WS, }T](\text{WS})}\right]dt\,dt\right]}{V_{[\text{WS, }P]\text{(avg)}}t_f}$$

$$+\frac{t_f}{2V_{[\text{WS, }P]\text{(avg)}}}\left[k_{(\text{sup})}\mathbf{g}\times1_{(\text{PL})(\text{WS})}\right.$$

$$-k_{(\text{wi})}V_{[\text{AM, WS}](\text{avg})}\times1_{(\text{PL})(\text{WS})}$$

$$\left.+k_{(\text{sup})}k_{\text{DR}}\left[\mathbf{g}\times1_{(\text{PL})(\text{WS})}\right]\times1_{(\text{PL})(\text{WS})}\right]\quad(\text{I-35})$$

In the final mechanization of the prediction angle for the IFFC system study the T.A.T. and the drift correction (last term of Eq. I-35) were neglected.

I-6   TIME OF FLIGHT OF THE PROJECTILE[4,5]

The calculation of the time of flight of a projectile from one aircraft toward another is difficult in that the time of flight is a function of the future range, which is in turn a function of the time of flight. In addition, many variables enter into the calculations, such as air density, range rate, lead angle, target acceleration, and attacker angle of attack. The geometry relating present range, target motion, and future range is shown in Figure I-6.
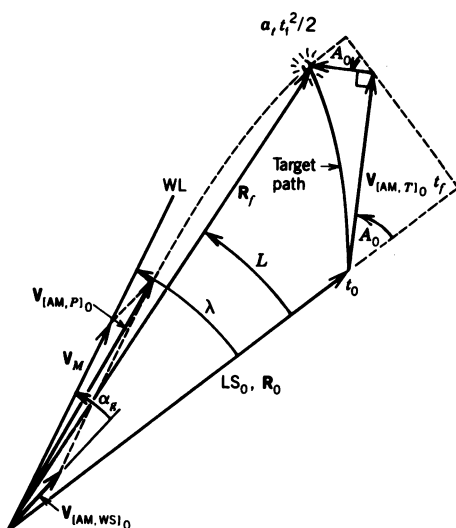
Figure I-6   Geometry for time-of-flight calculation.

In Section I-2 reference was made of a technique for estimating the target acceleration.[2] This was based on the estimation of the target angle of attack, which would yield normal accelerations resulting from target maneuvering. Thus the acceleration vector would be normal to the target velocity vector as shown in Figure I-6. Although the general fire control problem is three-dimensional, once the attacker starts tracking the target the turning planes of both aircraft are approximately coplanar. Thus the three-dimensional problem can be reduced to the two-dimensional problem shown in Figure I-6. Then from Figure I-6

$$\cos L \simeq \frac{R_0 + V_{[AM,T]_0} t_f \cos A_0 - \frac{1}{2} a_t t_f^2 \sin A_0}{R_f} \tag{I-36}$$

The velocity of the target with respect to the air mass cannot be measured by any instrumentation available to the attacker. However, the range rate $\dot{R}$, which is equal to the difference between the components of the weapon station and target velocities along the line of sight, can be measured. Then

$$\dot{R} = V_{[AM,T]_0} \cos A_0 - V_{[AM,WS]} \cos(\lambda - \alpha_g) \tag{I-37}$$

Solving for $V_{[AM,T]_0} \cos A_0$ and substituting the results into Eq. I-36 yields

$$R_f = \frac{R_0 + \{\dot{R} + V_{[AM,WS]} \cos(\lambda - \alpha_g)\} t_f - \frac{1}{2} a_t t_f^2 \sin A_0}{\cos L} \tag{I-38}$$

Equation I-38 relates the time of flight and future range through the geometry of the fire control problem. The time of flight is also a function of the ballistics of the projectile. A relation that has been used in both the F-4 and F-15 fire control systems, as given in Refs. 4 and 5, is

$$t_f = \frac{R_f}{V_{[AM,P]_0} - k_0 R_f \sigma \sqrt{V_{[AM,P]_0}}} \tag{I-39}$$

where

k_0 is an empirically derived ballistic coefficient equal to 0.00625 (ft sec)$^{-1/2}$ for a 20-mm M-56 round, and

$\sigma = \rho/\rho_0$ is the ratio of the air density at the firing altitude to the air density at sea level.

Let

$$C_B \equiv k_0 \sigma \sqrt{V_{[AM,P]_0}} \; 1/\text{sec} \tag{I-40}$$

As α_g is small, then from Figure I-6

$$V_{[AM,P]} \simeq V_{[AM,WS]_0} + V_M \qquad (I\text{-}41)$$

Substituting Eqs. I-40 and I-41 into Eq. I-39 yields

$$t_f = \frac{R_f}{V_{[AM,WS]_0} + V_M - C_B R_f} \text{ sec} \qquad (I\text{-}42)$$

Eq. I-42 could be substituted into Eq. I-38 to yield a cubic equation in t_f; however, the lead angle L and the prediction angle λ are both functions of the time of flight. To eliminate the two angles from the time-of-flight calculations, it was assumed that an estimate of the target velocity $V_{[AM,T]}$ would be available, as explained earlier. Then R_f is broken down into a component along the LOS, $R_{(fr)}$, and one perpendicular to the LOS, $R_{(ft)}$. Then from Figure I-6,

$$R_{(fr)} = R_0 + V_{[AM,T]} \cos A_0 \, t_f - \tfrac{1}{2} a_t t_f^2 \sin A_0 \qquad (I\text{-}43)$$

$$R_{(ft)} = V_{[AM,T]} \sin A_0 \, t_f + \tfrac{1}{2} a_t t_f^2 \cos A_0 \qquad (I\text{-}44)$$

The range rate is

$$\dot{R} = V_{[AM,T]} \cos A_0 - V_{(tr)} \qquad (I\text{-}45)$$

where $V_{(tr)}$ is the component of attacker velocity along the LOS, given by

$$V_{(tr)} = V_N \cos \Psi_R \cos \Theta_R + V_E \sin \Psi_R \cos \Theta_R + \dot{h} \sin \Theta_R \qquad (I\text{-}46)$$

where

   V_N and V_E are the north and east components of attacker velocity from the inertial navigation system,
   $\dot{h}$ is the altitude rate, positive up, and
   Ψ_R and Θ_R are the gimbal angles of the stabilized tracker shown in Figure 9-27.

As the range rate is known, and an estimate of $V_{[AM,T]}$ assumed, then Eq. I-45 can be solved for $\cos A_0$, which yields

$$\cos A_0 = \frac{V_{(tr)} + \dot{R}}{V_{[AM,T]}} \qquad (I\text{-}47)$$

and then

$$\sin A_0 = \sqrt{1 - \cos^2 A_0} \tag{I-48}$$

Substituting Eq. I-47 into Eq. I-43 yields

$$R_{(fr)} = R_0 + \left(V_{(tr)} + \dot{R}\right)t_f - \tfrac{1}{2}a_t t_f^2 \sin A_0 \tag{I-49}$$

The future range can be calculated from $R_{(fr)}$ and $R_{(ft)}$:

$$R_f = \sqrt{R_{(fr)}^2 + R_{(ft)}^2} \tag{I-50}$$

Using R_0 as the first estimate of R_f, Eqs. I-42, I-44, and I-47 through I-50 can be iterated to obtain the time of flight in less than 10 iterations for each update time. After the first solution, the previous value of the future range is used for the subsequent iterations.

With t_f and R_f known, the average velocity of the projectile with respect to the air mass is

$$V_{[AM, P](avg)} = R_f / t_f \tag{I-51}$$

The average velocity of the projectile relative to the attacker required for Eq. I-35 is

$$V_{[WS, P](avg)} = V_{[AM, P](avg)} - U \tag{I-52}$$

where U is the component of attacker velocity along the X axis of the aircraft, and is used because it is more nearly aligned with R_f than $V_{(tr)}$ is.

REFERENCES

1. W. Wrigley and J. Hovorka, *Fire Control Principles*, McGraw-Hill Book Co., New York, 1959.
2. J. D. Kendrick, *Estimation of Aircraft Target Motion Using Pattern Recognition Orientation Measurements*, Ph.D. dissertation, AFIT/DS/EE/78-6, Air Force Institute of Technology, 1978.
3. J. H. Blakelock, *Design of an Integrated Flight / Fire Control System Including Movable Gun and Gimbaled Line-of-Sight Tracker*, UDR-TR-79-84, University of Dayton, Dayton, Ohio, December 1979.
4. *Integrated Flight / Fire Control System, Phase I Study (F-15), Vol. I. System Definition*, Interim Technical Report, Contract No. F33615-75-C-3143, General Electric Aircraft Equipment Division, Binghamton, New York, November 1977.
5. B. Hohwiesner, *Principles of Airborne Fire Control*, lecture notes, U.S. Air Force Academy, Colorado Springs, Colorado, December 1975.

Appendix *J*

A-1 and A-4 Gunsights

J-1 INTRODUCTION[1]

The A-1 and A-4 series gun–bomb–rocket sights were developed for the U.S. Air Force by the Instrumentation Laboratory at MIT under the direction of Doctor Charles S. Draper. Their development came too late for World War II, but during the Korean War, with automatic radar ranging, these gunsights contributed to the 15:1 kill ratio of the F-16s over the MIGs. This appendix will describe the principles of operation of the A-1 sight in the air-to-air gunsight mode. The principles of operation of the A-4 sight are the same as for the A-1 sight.

J-2 PRINCIPLES OF OPERATION OF THE A-1 SIGHT[2]

A simplified schematic of the A-1 gunsight is shown in Figure J-1. The main elements of the sight are the two single-degree-of-freedom rate gyros (see Section B-3). The input axis of the elevation gyro element is parallel to the aircraft Y axis, and it therefore senses the pitch rate of the aircraft. Similarly, the input axis of the azimuth gyro element is parallel to the Z axis and senses the yaw rate of the aircraft. As a result these two gyros measure the components of the angular velocity of the aircraft perpendicular to the weapon line—that is, the angular velocity of the weapon line, which, as shown in Section I-2, is the major input for the calculation of the lead angle. It was also shown in Section I-2 that the lead angle is a function of the range from the attacking aircraft to the target aircraft. The range input is provided by the movable slide which controls the amount of elastic-restraint torque per

632
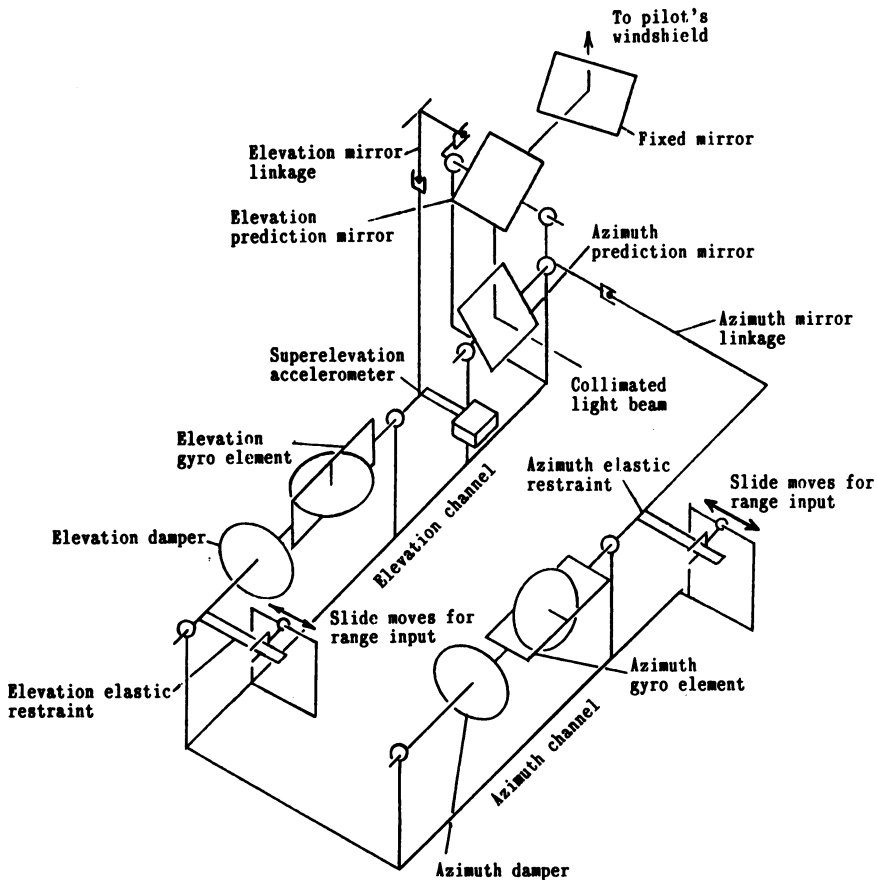
Figure J-1   *Simplified schematic of the A-1 gunsight.*

degree of rotation of the gyro element about its output axis. Under steady-state conditions the range dependent elastic-restraint torque balances the gyro output torque resulting from the angular velocity of the gyro element about its input axis. The result is a rotation of the gyro element about its output axis that is a function of the angular velocity of the gyro about its input axis and the range to the target. This operation is common to both the elevation and azimuth channels. The elevation and azimuth dampers provide the damping required for sight stability, as discussed in Section 9-1. The rotation of the gyro elements about their output axes causes the rotation of the elevation and azimuth prediction mirrors through the mirror linkages. This in turn moves the reticle on the pilot's windshield by the amount of the lead angle.

The range input can be generated by a range-only radar, as was done in the case of the F-86 in Korea, or by stadiametric ranging. The reticle

displayed on the pilot's windshield is an illuminated circle with a lighted dot, or "pipper," in the center. The pipper is used for target tracking, the reticle for stadiametric ranging. The diameter of the reticle is controlled by the pilot through the setting of the target span adjustment knob and the stadiametric range control. The mechanization of the stadiametric range control input varies from aircraft to aircraft. For the F-84D it is controlled by a rotation of the throttle grip. For manual ranging the pilot sets the target span adjustment to the wing span of the target aircraft. Then while tracking the target aircraft, the pilot adjusts the diameter of the reticle so that it spans the target, thus providing the range input.

The other important input to the prediction angle is the gravity drop correction or superelevation. This input is provided by the superelevation accelerometer, which applies a torque about the output axis of the deflection gyro element that is a function of the cosine of the pitch angle of the aircraft (if the aircraft is flying vertically—pitch angle 90°—no superelevation is required). The problem here is that this accelerometer will also sense the centripetal acceleration resulting from the pitch rate of the aircraft. The resultant error is partially compensated for by proper calibration.

As the reticle displayed on the windshield is displaced behind the target by the amount of the prediction angle, the A-1 and A-4 sights are referred to as "disturbed reticle" sights. This is in contrast to a director fire control system, where the sight is remote from the guns being controlled. In this operation the gunner tracks the target using a telescope mounted on the sight. There may be two gunners, one tracking in azimuth the other in elevation. The gyros in the sight sense the angular velocity of the sight and thus the angular velocity of the LOS. The output of the gunsight is the prediction angle: the angle by which the weapon line must lead the LOS for a hit. The guns are then driven in azimuth and elevation relative to the direction of the LOS by the amount of the prediction angle. The mounting of the tracker on the moving weapon station, as described in Section 9-2, therefore is not a true director fire control system.

This completes the discussion of the principles of operation of the A-1 sight.

REFERENCES

1. S. Lees, *Air, Space, and Instruments*, Draper Anniversary Volume, McGraw-Hill Book Co., New York, 1963.
2. C. S. Draper et al., *A-1 Sight for the Control of Gunfire from Fixed Guns, Rocketfire, and Bombing from Aircraft*, Vols. 1 and 2, Instrumentation Laboratory, Massachusetts Institute of Technology, Cambridge, Massachusetts, February 1952.

Index